Université de Lille 1 SCIENCES ET TECHNOLOGIES

Année Universitaire: 2014-2015 **N° d'ordre : 41754**

HABILITATION A DIRIGER DES RECHERCHES

Discipline: Sciences de la vie et de la santé

DIVERSITÉ DU RÉCEPTEUR AU FROID ET AU MENTHOL, TRPM8 : DU GÈNE AUX FONCTIONS

Présentée publiquement le 18 juin 2015 à Lille par,

Dr. Gabriel BIDAUX

Laboratoire de Physique des Lasers, Atomes et Molécules

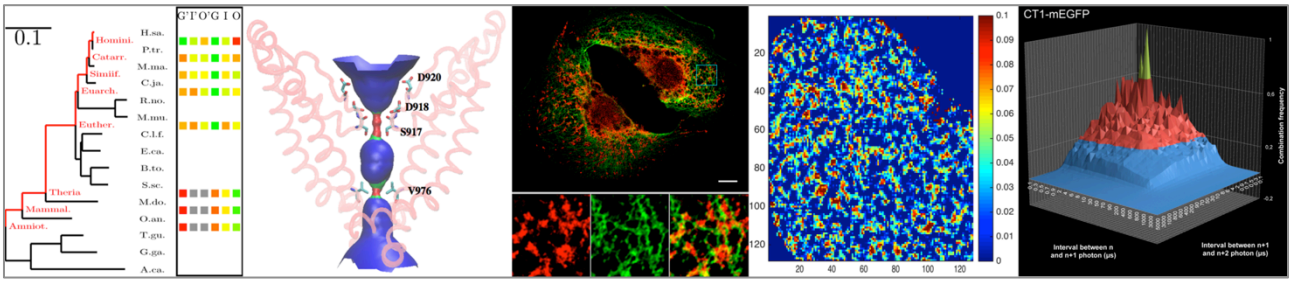

Devant la commission d'examen:

Directeur de Recherche
Dr. **Morad ROUDBARAKI,** Professeur de l'université Lille1, INSERM U1003, Lille

Rapporteurs
Dr. **Olivier BENSAUDE,** Directeur de Recherche INSERM, UMR8197, IBENS, Paris
Dr. **Fabien VAN COPPENOLLE,** Professeur de l'université Lyon 1, INSERM U1060, Lyon
Dr. **Thierry CAPIOD,** Chargé de Recherche INSERM, HDR, INSERM U1151– INEM, Paris

Examinateurs
Dr. **Natalia PREVARSKAYA,** Professeur de l'université Lille1, INSERM U1003, Lille
Dr. **Marc LEFRANC**, Professeur de l'université Lille1, PHLAM, UMR8523, Lille
Dr. **Laurent HÉLIOT**, Ingénieur de recherche CNRS, HDR, PHLAM, UMR8523, Lille

Université de Lille 1 SCIENCES ET TECHNOLOGIES

Année Universitaire: 2014-2015 **N° d'ordre : 41754**

HABILITATION A DIRIGER DES RECHERCHES

Discipline: Sciences de la vie et de la santé

DIVERSITÉ DU RÉCEPTEUR AU FROID ET AU MENTHOL, TRPM8 : DU GÈNE AUX FONCTIONS

Présentée publiquement le 18 juin 2015 à Lille par,

Dr. Gabriel BIDAUX

Laboratoire de Physique des Lasers, Atomes et Molécules

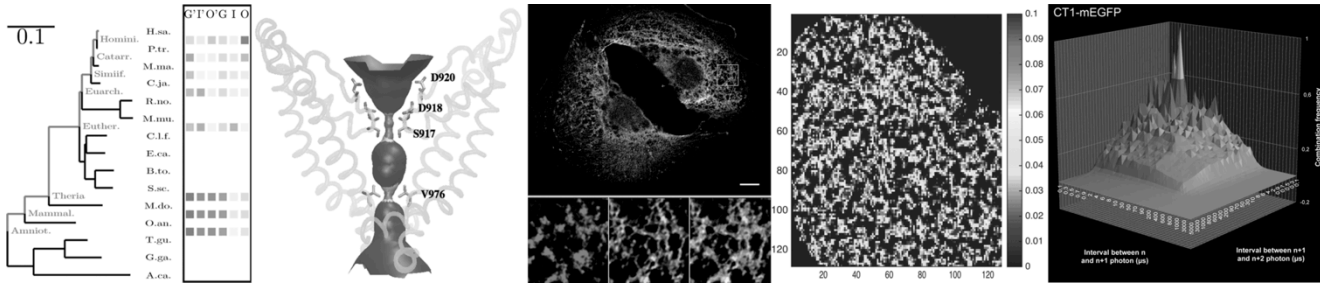

Devant la commission d'examen:

Directeur de Recherche
Dr. **Morad ROUDBARAKI,** Professeur de l'université Lille1, INSERM U1003, Lille

Rapporteurs
Dr. **Olivier BENSAUDE,** Directeur de Recherche INSERM, UMR8197, IBENS, Paris
Dr. **Fabien VAN COPPENOLLE,** Professeur de l'université Lyon 1, INSERM U1060, Lyon
Dr. **Thierry CAPIOD,** Chargé de Recherche INSERM, HDR, INSERM U1151– INEM, Paris

Examinateurs
Dr. **Natalia PREVARSKAYA,** Professeur de l'université Lille1, INSERM U1003, Lille
Dr. **Marc LEFRANC**, Professeur de l'université Lille1, PHLAM, UMR8523, Lille
Dr. **Laurent HÉLIOT**, Ingénieur de recherche CNRS, HDR, PHLAM, UMR8523, Lille

À ma femme, Anne-Sophie,

À mes enfants, Charly et Camille,

REMERCIEMENTS

Je remercie tout d'abord le Prof. Natalia Prevarskaya pour m'avoir accueilli dans son laboratoire de 2002 à 2013 et m'avoir toujours soutenu dans mes recherches en trouvant ou m'aidant à trouver des financements pour les réaliser.
Je remercie le Prof. Morad Roudbaraki pour ses conseils, sa patience et l'amitié qu'il m'a témoigné durant ces années. Merci aussi à toi d'avoir accepté d'être le directeur de recherche de cette HDR et d'y avoir consacré du temps.

Je remercie le Dr. Laurent Héliot pour m'avoir intégré à son équipe pendant 2 années et m'avoir laisser une grande liberté pour développer nos travaux dans le cadre fixé par le projet. Je le remercie aussi de m'avoir laissé continuer mon travailler sur TRPM8 et m'avoir permis de réaliser de nombreuses collaboration. Pour terminer je le remercie pour son amitié et ses précieux conseils.

Je remercie mes collègues les Drs. Olivier Bensaude, Thierry Capiod et le Prof. Fabien Van Coppenolle pour avoir accepté d'être les rapporteurs de cette HDR.
Je remercie le Prof Marc Lefranc, spécialiste de la physique non linéaire des systèmes biologiques, d'avoir accepté de participer à ce jury.

Merci à tous les collègues et les étudiants avec qui j'ai pu collaborer pendant toutes ces années, que ce soit au sein du laboratoire PHYCELL ou BCF, mais aussi à Brest, Rennes, Clermont-Ferrand, Paris, Dublin, Londres, Kiev…

Enfin, je remercie chaleureusement les Profs Fabien Van Coppenolle et Michel Ovize, pour leur confiance et leur accueil au sein de l'équipe cardioprotection du laboratoire CarMeN à Lyon.

RÉSUMÉ

Le récepteur au froid et au menthol, TRPM8, est une protéine-canal fonctionnant comme un senseur thermodynamique et est responsable de la détection du froid de part son expression dans les neurones innervant l'épiderme. Après avoir cloné 35 ARN alternatifs et ARN épissés issus du gène *trpm8*, nous avons réalisé un travail de caractérisation moléculaire, biophysique et cellulaire de ces variantes du récepteur au froid. Nous avons, en parallèle, essayé de comprendre leurs rôles dans les grandes fonctions physiologiques comme l'homéostasies de l'épiderme, la réponse au froid dans des cellules germinales ou encore le métabolisme. Le problème intrinsèque des tentatives d'association des niveaux moléculaires et cellulaires avec la physiologie est qu'il est facile de trouver des corrélations mais techniquement beaucoup plus complexe de démontrer des liens de causalité. Or, la compréhension des mécanismes moléculaires, hormis la beauté de la compréhension de l'infiniment petit, n'a de sens en biologie que lorsqu'on arrive à expliquer les effets macroscopiques. C'est dans le respect de cette démarche, que ces 2 dernières années, j'ai acquis des compétences en biophysique et en microscopie photonique avancée. En effet, le développement des outils de fluorescence permet maintenant d'envisager l'observation quantitative de mécanismes moléculaire en cellule vivante unitaire, mais aussi dans l'organisme. L'association du génie génétique, de la photonique et des modèles animaux permet donc d'envisager le développement de la physiologie moléculaire dans les prochaines années.

TABLE DES MATIÈRES

TABLE DES MATIERES

TABLE DES MATIERES

GLOSSAIRE

GLOSSAIRE

AA : acides aminés

APD : Avalanche Photo Diode

ARN POL II : ARN polymérase II

BAT : Brown Adipocyte Tissu

Ca^{2+} : ion calcique

cMOS : complementary Metal Oxide Semi-conductor

CspA : Cyclosporine A

CT1 : Cycline T1

CTD : Carboxy-terminal Domain

$E_{(FRET)}$: Efficacité de FRET

ε : brillance moléculaire apparente (nombre de photons détectés par seconde et par molécule)

Ea : Énergie d'activation

EMCCD : Electron Multiplying Charge Couplde Device

eTRPM8 : epidermal TRPM8

FCCS : Fluorescence Cross Correlation Spectroscopy

FCS : Fluorescence Correlation Spectroscopy

FRET : Förster Resonnance Energy Transfert

GPx : Glutathione Peroxidase

Gτ : fonction d'autocorrélation

Hexim : Hexamethylene-bis-acetamide-inducible

HSF1 : Heat Shock Factor 1

HSPA2 : Heat Shock Protein A2

ICS : Image Correlation Spectroscopy

IDH : Isocitrate Dehydrogenase

INV : Involucrin

IR : Ischémie-Reperfusion

IRC : Ischémie- Reperfusion Cardiaque

IRF : Instrument Response Function

K10 : Keratin 10

KO : Knock-Out

Larp7 : La RNA-binding domain of La-Related protein 7

Ma : Million d'années

MAM : Mitochondria Associated Membranes

MAM : Mitochondria-Associated Membranes

mEGFP : monomeric Enhanced Green Fluorescent Protein

mTurq2 ou mT2 : monomeric Turquoise protein, seconde version

NELF : Positive Elongation Factor

P-loop : hélice alpha formant la paroi interne du pore ionique d'un canal TRP

GLOSSAIRE

P-TEFb : Positive Transcription Elongation Facteur b

P-TEFb : Positive Transcription Elongation Factor

PALM : Photo-Activated Localization Microscopy

PB : Photon Burst (bouffé de photons)

PCH : Photon Counting Histogramm

PCR : Polymerase Chain Reaction

PMT : PhotonMultiplier Tube

P_O : probabilité d'ouverture d'un canal ionique

PSA : Prostate Specifique Antigene

PSF : Point Spread Function

PTP : Pore de perméabilité de transition

$Q_{(10)}$: mesure la variation de vitesse d'un réaction chimique suite à une variation de 10°C de la température environnante.

R0 : rayon de Förster d'un couple donneur-accepteur de fluorescence

RACE : Rapide Amplification of cDNA-ends

RE : Réticulum Endoplasmique

RER : Respiratory Exchange Ratio

ROS : Reactive Oxygen Species

Rpb1 : large sous-unité de l'ARN polymérase II

SO : SuperOxide

SOD : SuperOxide Dismutase

SPAD : Single Photon Avalanche Photo Diode

STED : STimulated Emisson Depletion

SYFP2 : Super Yellow Fluorescent Protein, version 2

TBP : TATA-Binding Protein

TCSPC : Time Correlated Single Photon Counting

TD-FLIM : Time Domain – Fluorescence Lifetime Imaging Microscopy

TFII (A/D) : Transcription Factor II sous unité A ou D

TG : TransGlutaminase

TRP : Transient Receptor Potential

UCP1,2,3 : UnCoupling Proteins 1,2 et 3

UTR : UnTranslated Region

Vf : volume focal

WAT : White Adipocyte Tissu

CURRICULUM VITAE

I. CURRICULUM VITAE

Gabriel BIDAUX, Ph.D.

Chercheur en Biologie moléculaire, cellulaire & Biophysique.

Marié, 2 enfants

Adresse personnelle :

1, rue Pierre de Coubertin

59310 Orchies

Situation professionnelle :

Chercheur associé (CDD Université Lille1) dans l'équipe Biphotonique Fonctionnelle Cellulaire

Laboratoire de Physiques des Lasers, Atomes et Molécules (PHLAM)

Equipe Biphotonique Fonctionnelle Cellulaire

UMR8523 CNRS,

Parc de la Haute Borne

50 av de Hallay

BP70478

59658 Villeneuve d'Ascq, France

gabriel.bidaux@univ-lille1.fr

gabriel.bidaux@gmail.com

DIPLOMES

2003 - 2006

Doctorat en science de la vie et de la santé, spécialité biologie moléculaire et cellulaire.

Titre de la thèse : rôle du canal TRPM8 dans la physiopathologie de la prostate humaine.

Tuteur: Pr N. Prevarskaya. (Laboratoire de physiologie cellulaire, INSERM U800, Villeneuve d'Ascq, France).

2002 - 2003

Master recherche (DEA) science de la vie et de la santé

Option biologie cellulaire et moléculaire ; Université de Lille I (USTL)

Sujet : rôle du canal TRPM8 dans la physiopathologie de la prostate humaine.

Tuteur: Pr N. Prevarskaya et Pr M. Roudbaraki. (Laboratoire de physiologie cellulaire, INSERM U800, Villeneuve d'Ascq, France).

2001 - 2002

Maîtrise de Biologie Cellulaire et moléculaire, Université de Lille I (USTL)

EXPERIENCE PROFESSIONNELLE

Juillet 2015 -

Chercheur associé.

Laboratoire INSERM U1060, CARMEN; équipe 5: cardioprotection.

Projet: Les jonctions ER-mitochondrie des cardiomyocytes et leurs modifications lors de l'ischémie-reperfusion.

http://carmen.univ-lyon1.fr

http://carmen.univ-lyon1.fr/eq5/equipe5_1.php

2013 -2015

Chercheur associé.

Université Lille 1, Equipe Biphotonique Fonctionnelle Cellulaire, Laboratoire de Physique des Lasers, Atomes et Molécules (PhLAM).

Projet: Dynamique d'assemblage du complexe P-TEFb avec le complexe d'élongation de la transcription, RNA POL II, en cellules vivantes.

http://www.phlam.univ-lille1.fr

http://nonlineaire.univ-lille1.fr/SNL/

2010 - 2013

Chercheur associé.

Université Lille 1, Laboratoire de physiologie cellulaire, INSERM U1003.

Projet 1: Rôle des isoformes du récepteur au froid TRPM8 dans l'homéostasie de l'épiderme.

Projet 2: Contrôle du métabolisme et de la thermogenèse par les isoformes du canal TRPM8 chez la souris.

http://www.phycell.univ-lille1.fr/

2007 - 2009

Chercheur Post-doctorant. Financé par un projet blanc de l'Agence Nationale de Recherche Française (ANR).

Université Lille 1, Laboratoire de physiologie cellulaire, INSERM U1003.

Projet: Rôle du canal TRPM8 dans la prostate et les testicules implication dans la fertilité?

Responsable scientifique: Pr Natalia. PREVARSKAYA.

http://www.phycell.univ-lille1.fr/

Janvier 2003 - février 2006

Chercheur Doctorant.

Université Lille 1, Laboratoire de physiologie cellulaire, INSERM U1003.

Projet: Rôle du canal TRPM8 dans la physiopathologie de la prostate.

Responsable scientifique: Pr Natalia. PREVARSKAYA.

http://www.phycell.univ-lille1.fr/

COMPÉTENCES TECHNIQUES

Techniques de biologie moléculaire:

TA Cloning, protéines de fusion (pour FRET, étude de localisation), design de siRNA, vecteur shRNA, RT-PCR, Real time PCR, Single Cell RT-PCR, RACE-PCR, mutagenèse dirigée, test d'activité promotrice, base en mRNAseq sur system SOLID 3D, formation sur les modifications du génome par TALEN, ZFN et CRISP9.

Techniques de biologie cellulaire:

Culture cellulaire : lignées cellulaires tumorales et culture primaires (épithéliales et musculaires lisse de la prostate, kératinocytes, hépatocytes et épithéliales de vessie).

Transfection (phosphate de calcium, lipofection, nucleofector).

Génération de lignée cellulaire stable ou inductible.

Techniques de Biochimie:

Western-blot, immunocytofluorescence, immunohistochimie et immunohistofluorescence (quadruple marquage) sur coupes congelées ou paraffinées, immunoprécipitation, cross-linking, test d'activité enzymatique (PLA2, Caspases, Déshydrogénases, ATP), biotinylation des protéines de surface, purification de protéines de surface , extraction de protéines recombinantes soluble ou membranaires à partir de modèle procaryote ou eucaryote, purification de microdomaines sur gradient d'iodoxanol (MAM, cavéoles).

Imagerie:

Microscopie photonique: « *Spining Disk » et « Laser Scanning Confocal », multiphotonique (*Zeiss LSM510, LSM700 et LSM780; Leica SP5).

FRET: FRAP, sensitized emission, lambda FRET, TD FLIM (TCSPC) et FD FLIM.

Imagerie de fluorescence du Calcium : Fluo-4, Rhod-2, Mag-fluo, biosenseurs Cameleon adressés dans les mitochondries, le RE, le Golgi ou le cytosol.

Imagerie de fluorescence des *DRO (dérivés actifs de l'oxygène)*: (Mitosox, BODPY C11, CellRox).

Spectroscopie corrélative de fluorescence: FCS, FCCS, bases pour l'ICS et le TICS.

Modèles Animaux

Xénogreffes sous-cutanées de cellules tumorales, puis mesures de la croissance tumorale.

Phénotypage de lignées de souris invalidées (KO).

Bioinformatique.

Maîtrise de la suite Office (Excel, Word, Powerpoint).

Maitrise de solutions statistiques et graphiques (Graphpad, Origin, PRISM).

Maîtrise de logiciels pour la biologie moléculaire (Vector NTI, SMART, Blast, Clustalw, APE, Snapgene...).

Maîtrise des logiciels analyse d'image (ImageJ), Icy.

Analyse de temps de vie : Symphotime (Picoquant), MAPI.

Programmation : bases Matlabs (écriture de scripts simples, utilisation de scripts pré-écris)

II. PUBLICATIONS

http://publicationslist.org/gabriel.bidaux

https://www.researchgate.net/profile/Gabriel_Bidaux/

24 articles, 3 revues, 1 chapitre de livre et 3 procédés de conférence publiés.

10 articles en révision/soumission/préparation

h-index: 16

*: co-premier auteur.

¶: auteur référant.

ARTICLES ET REVUES

2015

1) Anne-sophie Borowiec, Benoit Sion, Frédéric Chalmel, Antoine Rolland, Loïc Lemonnier, Tatiana De Clerck, Alexandre Bokhobza, Sandra Derouiche, Etienne Dewailly, Christian Slomianny, Claire Mauduit, Mohamed Benhamed, Morad Roudbaraki, Bernard Jégou, Natalia Prevarskaya, and **Gabriel Bidaux**. Cold/menthol channels initiate the cold shock response and protect germ cells from cold shock mediated oxydation. In preparation.
2) Laurent Héliot, Mariano Gonzalez-Pisfil, Mélanie Henry, Corentin Le Nezet, Olivier Bensaude, Bernard Vandenbunder, and **Gabriel Bidaux**. A 2-steps model for the dynamic binding of P-TEFb on the transcriptional paused complex. In preparation.
3) Samuel Blanquart, Anne-sophie Borowiec, Philippe Delcourt, Martin Figeac, Morad Roudbaraki, Natalia Prevarskaya and **Gabriel Bidaux**. Evolution of human TRPM8 isoforms. In preparation.
4) Charlotte Dubois, Artem Kondratsky, **Gabriel Bidaux**, Gilbert Lepage, Robert-Allain Toillon, Christian Slomianny, Eric Vancauwenberghe, Pascal Mariot, Morad Roudbaraki, Dominique Tierny, Jesper Vuust Moller, Natalia Prevarskaya, Guido Kroemer and Fabien Vanden Abeele. Dissecting Apoptosis Mediated by Mitochondria Calcium Overload Reveals a Tight Control of Mitochondrial Depolarization and Fission by Autophagy critical for Priming Cancer Cells to Chemotherapy. Soumis *CELL*.
5) **Gabriel Bidaux***, Miriam Sgobba*, Loic Lemonnier, Mark SP Sansom, Alexander V Zholos, Shozeb Haider. Functional and Modeling Studies of the Transmembrane Region of TRPM8 channel. Minor revision in *Biophysical Journal*.
6) **Gabriel Bidaux¶**, Anne-Sophie Borowiec, Dmitri Gordienko, George Shapovalov, Benjamin Beck, Loïc Lemonnier, Matthieu Flourakis, Matthieu Vandenberghe, Christian Slomianny, Etienne Dewailly, Philippe Delcourt, Emilie Desruelles, Abigaël Ritaine, Renata Polakowska, Jean Lesage, Mounia Chami, Roman Skryma and Natalia Prevarskaya¶. Molecular identity of the

mild cold-transducer in epidermal homeostasis. Minor revision in *PNAS*.

7) **Gabriel Bidaux¶**, Loïc Lemonnier, Anne-Sophie Borowiec, Fabien Vanden Abeele, Gilbert Lepage, Etienne Dewailly, Christian Slomianny, Bonnal Jean-Louis, Mauroy Brigitte and Natalia Prevarskaya. Targeting TRPM8 regulatory subunits in prostate cancer: towards a new drug target? In preparation for submission in *Cancer Research*.
8) **Gabriel Bidaux***,¶, Dmitri Gordienko*, Georges Shapovalov, Anne-sophie Borowiec, Matthieu Flourakis, Etienne Dewailly, Christian Slomianny and Natalia Prevarskaya¶. Novel archetype of TRPM8 channel characterized in mitochondria-associated membranes of prostate cells. Submitted in *Journal of Cell Biology*.
9) George Shapovalov, **Gabriel Bidaux**, Abigaël Ritaine, Christian Slomianny, Anne-Sophie Borowiec, Roman Skryma, Natalia Prevarskaya. Patch clamping ion channels in native subcellular membranes. Submitted in *Nature methods*.
10) Sandra Derouiche, Pascal Mariot, Marine Warnier, **Gabriel Bidaux**, Eric Vancauwenberghe, Pierre Gosset,Brigitte Mauroy, Jean-Louis Bonnal, Christian Slomianny, Philippe Delcourt, Gilbert Lepage, Natalia Prevarskaya and Morad Roudbaraki. Antibacterial agent Triclosan promotes prostate cancer progression via TRPA1 channel activation in stromal cells and VEGF secretion. In revision in *Cancer Prevention Research*.

2014

11) D. Gkika, L Lemonnier, G Shapovalov, D Gordienko, C Poux, M Bernardini, A Bokhobza, **G Bidaux**, C Degerny, K Verreman, B Guarmit, M Benahmed, Y de Launoit, R Bindels, A Fiorio Pla and N Prevarskaya. TRPM8 channel-associated factors are a novel protein family that regulates TRPM8 trafficking and activity. *Journal of Cell Biology*, accepted 12-01-2014 (ISI 5-year Impact Factor : 10.123)
12) C Dubois, F Vanden Abeel, V Lehen'kyi, D Gkika, B Guarmit, G Lepage, C Slomianny, AS Borowiec, **G Bidaux**, M Benahmed, Y Shuba, N Prevarskaya. Remodeling of Channel-Forming ORAI Proteins Determines an Oncogenic Switch in Prostate Cancer. *Cancer cell.* 2014 Jul 14;26(1):19-32. (ISI 2012, 5-year Impact Factor : 27,059)

2013

13) Anne-Sophie Borowiec, **Gabriel Bidaux**, Natascha Pigat, Vincent Goffin, Sophie Bernichtein, and Thierry Capiod. Calcium channels, external calcium concentration and cell proliferation. Review. *European Journal of Pharmacology*, accepted 11-20-2013. (ISI 2012, 5-year Impact Factor : 2,778)
14) Anne-Sophie Borowiec, **Gabriel Bidaux**, Rachida Tacine, Pauline Dubar, Philippe Delcourt, Olivier Mignen, and Thierry Capiod. Are Orai1 and Orai3 channels more important than calcium influx for cell proliferation? *BBA- Molecular Cell Research*, accepted 11-27-13. (ISI 2012, 5-year Impact Factor : 4,947)
15) Anne-sophie Borowiec, Philippe Delcourt, Etienne Dewailly, and **Gabriel Bidaux¶**. Multifactorial optimization of in vitro keratinocytes induction of differentiation. *PLos One*. 2013

Oct 7;8(10):e77507. (ISI 2012, 5-year Impact Factor : 4,244)

2012

16) **Gabriel Bidaux***,¶, Benjamin Beck, Alexander Zholos, Dmitri Gordienko, Loic Lemonnier, Matthieu Flourakis, Morad Roudbaraki, Anne-Sophie Borowiec, Jose Fernández, Philippe Delcourt, Gilbert Lepage, Yaroslav Shuba, Roman Skryma, Natalia Prevarskaya (2011) Regulation of transient receptor potential melastatin 8 (TRPM8) channel activity by its short isoforms. *J. Biol. Chem*. Accepted for publication 22th November. (ISI 5-year Impact Factor : 5,498)

17) Jose A Fernández, Roman Skryma, **Gabriel Bidaux**, Karl L Magleby, C Norman Scholfield, J Graham McGeown, Natalia Prevarskaya, Alexander V Zholos (2011). Short isoforms of the cold receptor TRPM8 inhibit channel gating by mimicking heat action rather than chemical inhibitors. *J. Biol. Chem.* Accepted for publication 22th November. (ISI 5-year Impact Factor : 5,498)

2011

18) J A Fernández, R Skryma, **G Bidaux**, K L Magleby, C N Scholfield, J G McGeown, N Prevarskaya, A V Zholos (2011). Voltage- and cold-dependent gating of single TRPM8 ion channels. *J Gen Physiol.* 137: 2. 173-95 Feb. (ISI 5-year Impact Factor : 4,712)

2010

19) A Bavencoffe, D Gkika, A Kondratskyi, B Beck, A S Borowiec, **G Bidaux**, J Busserolles, A Eschalier, Y Shuba, R Skryma, N Prevarskaya (2010) The transient receptor potential channel TRPM8 is inhibited via the alpha 2A adrenoreceptor signaling pathway. *J Biol Chem.* 285: 13. 9410-9 Mar. (ISI 5-year Impact Factor : 5,498)

20) M Monet, V Lehen'kyi, F Gackiere, V Firlej, M Vandenberghe, M Roudbaraki, D Gkika, A Pourtier, **G Bidaux**, C Slomianny, P Delcourt, F Rassendren, J P Bergerat, J Ceraline, F Cabon, S Humez, N Prevarskaya (2010). Role of Cationic Channel TRPV2 in Promoting Prostate Cancer Migration and Progression to Androgen Resistance. *Cancer Res.* 70: 3. 1225-35 Feb. (ISI 5-year Impact Factor : 8,438)

21) C Lagadec, R Romon, C Tastet, S Meignan, E Com, A Page, **G Bidaux**, H Hondermarck, X. Le Bourhis (2010) Ku86 is important for TrkA overexpression-induced breast cancer cell invasion. *Proteomics Clin Appl.* 4: 6-7. 580-90 Jul. (ISI 5-year Impact Factor : 1,912)

2009

22) Lallet-Daher, Roudbaraki, Bavencoffe, Mariot, Gackière, **Bidaux**, Urbain, Gosset, Delcourt, Fleurisse, Slomianny, Dewailly, Mauroy, Bonnal, Skryma, Prevarskaya (2009). Intermediate-conductance Ca(2+)-activated K(+) channels (IK(Ca1)) regulate human prostate cancer cell proliferation through a close control of calcium entry. *Oncogene*. 28: 15. 1792-806 Mar. (ISI 5-year Impact Factor : 7,109)

23) Michaël Monet, Dimitra Gkika, V'yacheslav Lehen'kyi, Albin Pourtier, Fabien Vanden Abeele, **Gabriel Bidaux**, Véronique Juvin, François Rassendren, Sandrine Humez, Natalia Prevarsakaya

(2009). Lysophospholipids stimulate prostate cancer cell migration via TRPV2 channel activation. *Biochim Biophys Acta.* 1793: 3. 528-539 Mar. (ISI 5-year Impact Factor : 5,016)

24) M Katsogiannou, C E Boustany, F Gackiere, P Delcourt, A Athias, P Mariot, E Dewailly, N Jouy, C Lamaze, **G Bidaux**, B Mauroy, N Prevarskaya, C Slomianny (2009). Caveolae Contribute to the Apoptosis Resistance Induced by the alpha(1A)-Adrenoceptor in Androgen-Independent Prostate Cancer Cells. *PLoS One* 4: 9. e7068. (ISI 5-year Impact Factor : 4,610)

2008

25) Charbel El Boustany*, **Gabriel Bidaux***, Antoine Enfissi, Philippe Delcourt, Natalia Prevarskaya, Thierry Capiod (2008). Capacitative calcium entry and transient receptor potential canonical 6 expression control human hepatoma cell proliferation. *Hepatology*. 47: 6. 2068-2077 Jun. (ISI 5-year Impact Factor : 11.044).

26) Florian Gackière, **Gabriel Bidaux**, Philippe Delcourt, Fabien Van Coppenolle, Maria Katsogiannou, Etienne Dewailly, Alexis Bavencoffe, Myriam Tran Van Chuoï-Mariot, Brigitte Mauroy, Natalia Prevarskaya, Pascal Mariot (2008). CaV3.2 T-type calcium channels are involved in calcium-dependent secretion of neuroendocrine prostate cancer cells. *J Biol Chem* 283: 15. 10162-10173 Apr. (ISI 5-year Impact Factor : 5,498)

2007

27) **Gabriel Bidaux***, Matthieu Flourakis*, Stéphanie Thebault, Alexander Zholos, Benjamin Beck, Dimitra Gkika, Morad Roudbaraki, Jean-Louis Bonnal, Brigitte Mauroy, Yaroslav Shuba, Roman Skryma, Natalia Prevarskaya (2007). Prostate cell differentiation status determines transient receptor potential melastatin member 8 channel subcellular localization and function. *J Clin Invest.* 117: 6. 1647-1657 Jun. (ISI 5-year Impact Factor : 16.641)

28) N Prevarskaya, R Skryma, **G Bidaux**, M Flourakis, Y Shuba (2007). Ion channels in death and differentiation of prostate cancer cells. Review, *Cell Death Differ*. 14: 7. 1295-1304 Jul. (ISI 5-year Impact Factor : 8.674)

29) Alexandre Crépin, **Gabriel Bidaux**, Fabien Vanden-Abeele, Etienne Dewailly, Vincent Goffin, Natalia Prevarskaya, Christian Slomianny (2007). Prolactin stimulates prostate cell proliferation by increasing endoplasmic reticulum content due to SERCA 2b over-expression. *Biochem J* 401: 1. 49-55 Jan. (ISI 5-year Impact Factor : 4.592)

30) Benjamin Beck, **Gabriel Bidaux**, Alexis Bavencoffe, Loic Lemonnier, Stephanie Thebault, Yaroslav Shuba, Greg Barrit, Roman Skryma, Natalia Prevarskaya (2007). Prospects for prostate cancer imaging and therapy using high-affinity TRPM8 activators. *Cell Calcium*. 41: 3. 285-294 Mar. (ISI 5-year Impact Factor : 4.165)

31) N Prevarskaya, M Flourakis, **G Bidaux**, S Thebault, R Skryma (2007). Differential role of TRP channels in prostate cancer. Review, *Biochem Soc Trans*. 35: Pt 1. 133-135 Feb. (ISI 5-year Impact Factor : 3.756)

2006

32) Florian Gackière*, **Gabriel Bidaux***, Philippe Lory, Natalia Prevarskaya, Pascal Mariot (2006) A role for voltage gated T-type calcium channels in mediating "capacitative" calcium entry? *Cell Calcium*. 39: 4. 357-366 Apr. (ISI 5-year Impact Factor : 4.165)

33) Franck Vandermoere, Ikram El Yazidi-Belkoura, Christian Slomianny, Yohann Demont, **Gabriel Bidaux**, Eric Adriaenssens, Jérôme Lemoine, Hubert Hondermarck (2006). The valosin-containing protein (VCP) is a target of Akt signaling required for cell survival. *J Biol Chem*. 281: 20. 14307-14313 May. (ISI 5-year Impact Factor : 5,498)

34) Fabien Vanden Abeele*, **Gabriel Bidaux***, Dmitri Gordienko*, Benjamin Beck, Yuri V Panchin, Ancha V Baranova, Dmitry V Ivanov, Roman Skryma, Natalia Prevarskaya (2006). Functional implications of calcium permeability of the channel formed by pannexin 1. *J Cell Biol.* 174: 4. 535-546 Aug. (ISI 5-year Impact Factor : 10.123)

35) Fabien Vanden Abeele*, Alexander Zholos*, **Gabriel Bidaux***, Yaroslav Shuba, Stephanie Thebault, Benjamin Beck, Matthieu Flourakis, Yuri Panchin, Roman Skryma, Natalia Prevarskaya (2006). Ca2+-independent phospholipase A2-dependent gating of TRPM8 by lysophospholipids. *J Biol Chem.* 281: 52. 40174-40182 Dec. (ISI 5-year Impact Factor : 5,498)

2005

36) Stéphanie Thebault*, Loïc Lemonnier*, **Gabriel Bidaux***, Matthieu Flourakis, Alexis Bavencoffe, Dimitri Gordienko, Morad Roudbaraki, Philippe Delcourt, Yuri Panchin, Yaroslav Shuba, Roman Skryma, Natalia Prevarskaya (2005). Novel role of cold/menthol-sensitive transient receptor potential melastatine family member 8 (TRPM8) in the activation of store-operated channels in LNCaP human prostate cancer epithelial cells. *J Biol Chem.* 280: 47. 39423-39435 Nov. (ISI 5-year Impact Factor : 5,498)

37) **G Bidaux**, M Roudbaraki, C Merle, A Crépin, P Delcourt, C Slomianny, S Thebault, J - L Bonnal, M Benahmed, F Cabon, B Mauroy, N Prevarskaya (2005). Evidence for specific TRPM8 expression in human prostate secretory epithelial cells: functional androgen receptor requirement. *Endocr Relat Cancer.* 12: 2. 367-382 Jun. (ISI 5-year Impact Factor : 5,443)

CHAPITRES DE LIVRES

2013

Anne-sophie Borowiec, **Gabriel Bidaux** and Thierry Capiod. Book title: Trends in Stem Cell Proliferation and Cancer Research. Chapter title: Are Calcium Channels More Important Than Calcium Influx for Cell Proliferation? *Trends in Stem Cell Proliferation and Cancer Research* 2013, pp 65-92.

III. COMMUNICATION

28 séminaires/congrès dont 17 présentations orales et 10 posters.

2015

1) FOM 2015 (Focus on Microscopy), Göttingen, Allemagne, 29 mars – 01 avril.

   Poster 1: "Photonics reveal Cycline T1-guided P-TEFb fate", par **G Bidaux**, M Gonzalez-Pisfil, M Henry, C Le Nezet, O Bensaude, X Darzacq, B VandenBunder and L Heliot.

   Poster 2: "Multimodal approach to measure molecular dynamics and interactions in living cells for studies of regulation of transcription elongation phase by P-TEFb", par M Gonzalez-Pisfil, M Henry, C Le Nezet, L Heliot, B VandenBunder and **G Bidaux**.

   Poster 3: , par "Revealing hidden FRET domains in Phasor with image segmentation", par C Le Nezet, M Henry, M Gonzalez-Pisfil ,L Heliot, B VandenBunder and **G Bidaux**.

2) **Séminaire** à l'U1060-CarMeN, Lyon (France), " Technics/methods/results : an overview from 2003 to 2015*",* invité par le Prof Michel Ovize. 8-9 janvier.

2014

3) Symposium - Equipex ImaginEx BioMed Light Electron Atomic force microscopies Days BioImaging Center Lille, 26-27 novembre 2014 (participant).
4) **Séminaire** à l'U1011-EGIDE, Lille (France), " TRPM8 isoforms regulate mouse metabolism*",* invité par le Prof Bart Staels. 22 septembre.
5) **Séminaire** à l'U1060-CarMeN, Lyon (France), " Isoforms of the cold receptor, TRPM8: the ER calcium - mitochondrial metabolism connexion, from epidermis to prostate*",* invité par le Prof Fabien Van Coppenolle. 27 juin.
6) **Séminaire** au SFR ScInBios, Brest (France), " Isoforms of the cold receptor, TRPM8: the ER calcium - mitochondrial metabolism connexion, from epidermis to prostate*",* invité par le Dr Olivier Mignen. 13 juin.
7) **Séminaire** à la réunion-bilan projet ANR_DynamIC, Villeneuve d'ascq (France)., 14 mai.
8) **Séminaire** sur l'application de la microscopie confocale pour la biologie cellulaire & moléculaire. Atelier de formation CNRS, Lille, Institut interdisciplinaire, Villeneuve d'ascq. 14 février.

2013

9) **Séminaire** à l'université de Namur (Belgique), " Governor of cold sensitivity in epidermal homeostasis*",* invité par le Prof Yves POUMAY. 6 December.
10) **Séminaire** dans le service grands brûlés du Sunnybrook Hospital de Toronto (CANADA). Invité par le Prof Marc Jeschke. "TRPM8 isoforms regulate liver metabolism*"*. du 1 au 4 Octobre.
11) **Atelier de formation** INSERM: "Genome engineering and targeting with artificial TALEs*"*, à Bordeaux (FRANCE); du 24 au 26 Avril **(participant)**.

2012

12) 12th *European Calcium Society Meeting*, Toulouse (France), du 08-12 septembre 2012; **Poster**.

13) *"*23° colloques canaux ioniques"; Giens (France); **Présentation orale**.

14) Présentation à l'IRSET à Rennes (France) sur invitation du Dr B. Jégou.

2011.

15) Matinée thématique biophotonique de l'IFR147, Villeneuve d'Ascq (France); **Présentation orale sur invitation**.

2010

16) 19° journée scientifique de l'ARTP; Paris (France); **Présentation orale**.

17) 3° journée scientifique du Cancéropôle Nord-Ouest; Deauville (France); **Présentation orale**.

18) Colloque Génomique des cancers: outils et états des lieux; Lille (France); **Poster**.

2009

19) **Séminaire** à l' IMPC, à Sophia-antipolis (France), sur invitation du Dr F. Lesage.

2008

20) **Séminaire** à l' Experimentelle und Klinische Pharmakologie und Toxikologie. Universität des Saarlandes, à Homburg (Allemagne), sur invitation du Dr V. Flockerzi.

2007

21) Symposium International "Calcium Channels & Transporters"; Manchester (Angleterre); **Poster**.

22) "4th SFB 530 Colloque: spatio–temporal interactions of cellular signaling molecules"; Homburg (Allemagne); **Poster**.

23) Séminaire, « calcium signature »; Seix (France); Présentation orale sur invitation.

2005

24) *"*16° colloques canaux ioniques"; Giens (France); **Présentation orale**.

25) *"Journées André Verbert"*; Lille (France); **Présentation orale**.

26) *"TRP channel meeting"*; Leuven (Belgium); **Poster**.

27) "3th SFB 530 Colloquium: spatio–temporal interactions of cellular signaling molecules"; Homburg (Allemagne); **Poster**.

2004

28) *"Journée Cancérologie"*; Villeneuve d'Ascq (France); **Poster**.

ACTIVITÉS DE STRUCTURATION DE LA RECHERCHE

ACTIVITÉS DE STRUCTURATION DE LA RECHERCHE

I. ENSEIGNEMENT - FORMATION - ENCADREMENT

I.1. ENSEIGNEMENT

2014-2015

Cours: "FRET and derived applications from the structure of marcomolecular complexes to biochemistry of interactions", Master 1 de Biologie.

Cours: "Electrophysiology and photonics to study biophysics of ion channels", Master 1 de Physique, option Biologie Cellulaire et Moléculaire.

2013-2014

Cours: "FRET and derived applications from the structure of marcomolecular complexes to biochemistry of interactions", Master 1 de Biologie.

Cours: " Application of FRET and FCS strategy in biology", 1ère année de master de biochimie

2003-2005.

96h de Travaux Dirigés d'électrophysiologie, 1° et 2° année de Licence.

I.2. FORMATION

2013-2014

Séminaire sur l'application de la microscopie convocable pour la biologie cellulaire & moléculaire, atelier de formation CNRS, Lille, Institut interdisciplinaire, Villeneuve d'Ascq.

2007

Intervenant dans l'atelier «imagerie calcique» du CNRS, à Seix.

I.3. ENCADREMENT

2014-2015

- Mme. Henry Mélanie ..... Ingénieur d'étude, équipe BCF, supervision dans le cadre du projet ANR « DYNAMICS »
- Mme. Ianszen Mélina ..... 2ème année de BTS à Lens

2013-2015

- Mr. Gonzalez-Pisfil Mariano Ingénieur d'étude, équipe BCF, supervision dans le cadre du projet ANR « DYNAMICS »

2013-2014

- Mme. Schulz Céline ..... Ingénieur d'étude, équipe BCF, supervision en biologie moléculaire
- Mme. Zaoui Hayat..... 2ème année de Master recherche, biophysique, à Université de Lille 1

2014

- Mr. Ruchlejmer Loic **.....** 1ère année de Master recherche à Université de Lille 1

2013

- Mme. De-Clerck Tatiana . 2ème année de BTS à Montpellier

2009-2013

- Dr. Borowiec Anne-Sophie Chercheur post-doctorant

2012

- Mme. Aimé Magalie ..... 2ème année d'école d'ingénieur, EBI, à Cergy-pontoise
- Mme. De-Clerck Tatiana.. 1ère année de BTS à Montpellier

2010

- Mme. Schulz Céline ..... 1ère année de Master recherche à Université de Lens

2006-2009

- Guénard Olivier..... 1ère année de doctorat, Université de Lille 1
- 2ème année de Master, biologie & santé, Université de Lille 1

2004-2006

- Lepage Gilbert..... Assistant-ingénieur, formation/supervision en biologie moléculaire

2003-2004

- Gauthier Julie ..... Stagiaire en biologie moléculaire

II. SUBVENTIONS

16 demandes, 7 projets financés, 2 en cours de dépôt.

2004

1) Génopôle - AAP séquençage et génotypage: « Etude de l'expression des canaux ioniques dans le cancer de la prostate : implication dans l'oncogenèse ». Rédaction à 80%. ***Accepté.***

2006

2) **ANR Blanc**: « Rôle du canal cationique TRPM8 dans la physiopathologie de la prostate et des testicules: implication dans la reproduction ». **Rédaction à 70%.** ***Accepté.***

2007

3) Projet de **Recherche collaboratif "Inter-Cancéropole" - INCA**: «Les rôles des canaux ioniques TRPM8 et TRPV6 dans le cancer de la prostate : études fonctionnelles et ciblage moléculaire pour l'élaboration de nouvelles stratégies thérapeutiques». **Rédaction à 20%.** ***Accepté.***
4) **Génopôle - AAP séquençage et génotypage:** « Etude de l'expression des quelques canaux ioniques, de leurs isoformes et de leurs protéines partenaires dans le cancer de la prostate : implication dans l'oncogenèse ». **Rédaction à 80%.** ***Accepté.***

ACTIVITÉS DE STRUCTURATION DE LA RECHERCHE

5) Consortium européen «Europump». Co-rédaction de la partie TRPM8. *Refusé.*

2009

6) **ARTP - subvention de recherche:** « Evaluation du potentiel oncogénique des isoformes du canal TRPM8 dans la cancérogenèse de la prostate ». **Rédaction à 100%. *Accepté*.**
7) **PAIR-INCA**: « Les canaux TRP oncogéniques : approche multidisciplinaire sur le potentiel oncogénique des canaux TRP pour la recherche de biomarqueurs discriminant et l'élaboration de nouvelles stratégies thérapeutiques ». **Rédaction à 50%.** *Refusé.*
8) PPF - Animalerie: « agrandissement et modernisation de l'animalerie de Lille1 ». Rédaction de la part du laboratoire U800. **Accepté.**
9) Consortium européen «IonTrac». Co-rédaction de la partie TRPM8. *Refusé.*

2011

10) **Région Nord-pas-de-Calais - Projets émergents:** « Rôle des thermorécepteurs dans le stress cellulaire induit par l'hypothermie et les substances thermo-mimétiques dans le foie: implication pour la greffe hépatique et l'amélioration de la prise en charge des patients en hypothermie ». **Rédaction à 100%.** *Refusé.*
11) **Canceropôle Nord-Ouest - Soutien de projets émergents:** « Évaluation du potentiel oncogénique des isoformes du canal TRPM8 dans la cancérogenèse de la prostate ». **Rédaction à 100%.** *Refusé pour cause de statut précaire.*
12) **Ligue contre le cancer - Financement d'un Ingénieur:** « Ultracryotomographie, analyse EDX et spectroscopie de corrélation : vers la détection des microdomaines ioniques dans les cellules de la prostate ». Rédaction à 100%. ***Accepté.***

2012

13) **ANR «projets blancs» :** « Hypothermia induced stress response in testes and infertility: role of cold receptor TRPM8 ». Rédaction à 90%, recherche de partenaires. *Refusé.*

2013

14) **ANR «projets blancs» :** « Hypothermia induced stress response in testes and infertility: role of cold receptor TRPM8 ». Resoumission de la session 2012. *Refusé.*

2015

15) **ANR « Recherche Hospitalo-Universitaire en Santé » (RHU) : « TORRID »** PI : Prof. Michel OVIZE, CARMEN INSERM U1060, équipe 5 à Lyon. G Bidaux, leader of WP2/Task2.3 « ER-mitochondria cross-talk at MAMs ». Rédaction à 90% de WP2/Task2.4. *En évaluation.*
16) **Projet FRM « Etudes Physico-chimiques innovantes pour la biologie et la médecine ».** CARMEN INSERM U1060, équipe 5 à Lyon et PHLAM, CNRS UMR8523, équipe BCF. Responsable scientifique : G. Bidaux. *Lettre d'intention.*

III. TÂCHES COLLECTIVES

III.1. SOCIÉTÉS SAVANTES

- Membre de l'European Calcium Society
- Membre de la Biophysicial Society

III.2. PEER-REVIEWER

- Plos One,
- Spinger Plus.

III.3. ÉVALUATEUR DE PROJETS SCIENTIFIQUES

- FWF (Austrian science fund) - Hertha Firnberg-Stelle - Hertha Firnberg-Position.

III.4. GESTION DE BUDGETS - COMMANDES

- Projet ANR « DYNAMICS », 2013-2015, PHLAM, équipe BCF.
- Projet ANR « TRPM8-repod », 2007-2010, INSERM U1003.
- Tests comparatifs de matériels (qPCR, broyeur de tissus…)

III.5. ORGANISATION – DÉVELOPPEMENT DE PLATEAUX DE BIOLOGIE MOLÉCULAIRE

- Laboratoire U1003 (2003-2013)
- Laboratoire PHLAM, équipe BCF (2013-2015)

ACTIVITÉS DE RECHERCHE

I. AVANT-PROPOS

Mon parcours présente l'avantage d'être simple : 11 années passées dans le laboratoire de physiologie cellulaire du Prof. Natalia Prevarskaya à Villeneuve d'Ascq, puis 2 années dans l'équipe Biphotonique Fonctionnelle Cellulaire du Dr. Laurent Héliot. Cette absence de mobilité, atypique et jugée problématique selon les critères de carrière des chercheurs, m'a par contre donné l'avantage de pouvoir travailler sur le long terme sur le canal TRPM8. J'ai par exemple initié les discussions portant sur le développement du modèle Trpm8 knock-out avec la société Genoway dès 2003. Pourtant, la lignée a vu le jour fin 2009 et le premier article portant sur ces souris a été soumis en 2013. Il va sans dire que j'ai pu ainsi observer à loisir qu'un projet de recherche ne se déroule jamais comme on a pu le préparer et la planifier.

Après ma thèse passée en décembre 2006, le Prof. Prevarskaya m'a recruté en tant que chercheur post-doctorant sur un projet ANR que j'avais écrit en partie.

En 2009, à la fin de mon contrat, le Prof. Prevarskaya m'a donné la possibilité de continuer mes travaux de recherche en tant que chercheur associé. J'étais alors responsable du développement complet de mes projets, j'encadrais « mes étudiants » et écrivais les demandes de financements compatibles avec mon statut de non-titulaire.

En 2013, je suis « parti » me former à la biologie quantitative, la biophysique et la microscopie photonique avancée dans l'équipe Dr Laurent Héliot, responsable de l'équipe BCF, à l'Institut de Recherche Interdisciplinaire à Villeneuve d'Ascq. J'y ai travaillé sur un sujet différent : la dynamique d'association du complexe P-TEFb sur l'ARN polymérase II lors de la levée de la pause de la transcription. Grâce à ces 2 années passées dans une équipe interdisciplinaire, j'ai pu gagner de nombreuses compétences en microscopie et en biophysique.

Après ce changement de thématique de 2013-2015, je me prépare à intégrer l'équipe 5 du laboratoire CARMEN, INSERM U1060, dirigée par le Prof. Michel Ovize à Lyon. Je serais en charge du développement de la partie biologie moléculaire et de la microscopie avancée.

Il est toujours délicat de synthétiser un parcours scientifique de 12 années. C'est donc dans le but de garder un esprit de synthèse et de clarté que j'ai choisi de ne présenter ici, que les travaux de fond portant sur le canal TRPM8. Néanmoins, afin de partager mon expérience récente de ces 2 dernières années au sein de l'équipe interdisciplinaire BCF, j'introduirai, dans la première partie des résultats, les développements méthodologiques auxquels j'ai participé. Cette présentation non chronologique a le mérite de mettre en lumière mon parcours de la biologie vers la biophysique, ainsi que l'apport de nouvelles méthodes de photonique dans mon travail sur le canal TRPM8 et sur mes perspectives d'avenir.

II. GÉNÉRALITÉS

Je présenterai dans le chapitre suivant des fiches de synthèse permettant à chacun de se rappeler ou d'intégrer les caractéristiques majeures de l'ion calcique, des canaux de la famille TRP. Suite à mon changement thématique en 2013, je présenterai aussi brièvement le rôle du complexe P-TEFB dans la transcription et introduirai les bases des techniques de FLIM, FRET, FCS et ICS. Ces fiches n'ont aucune volonté d'exhaustivité mais sont une aide donnée pour mieux replacer les différents contextes moléculaires, physiologiques et techniques traités dans mes travaux de recherche.

II.1. LES CANAUX TRP ET LE'ION CALCIQUE

II.1.1. LE CALCIUM

Compartimentation de l'ion calcique

L'ion divalent calcique (Ca^{2+}) est la plus petite molécule à être aussi bien compartimentalisée dans la cellule. Sa concentration est de l'ordre du mM dans la matrice extracellulaire et dans le réticulum endoplasmique, mais oscille entre 100 nM et >1 µM dans le cytosol et de 10 à 500 µM dans les mitochondries. À cause des flux incessants entre les compartiments, la concentration de Ca^{2+} cytosolique ($[Ca^{2+}]$) évolue de manière très dynamique.

Homéostasie et signal calcique

L'homéostasie calcique est par définition un équilibre entre influx et efflux. Elle est responsable du maintien de la compartimentation du calcium dans la cellule.

Le signal calcique consiste en l'intégration des mouvements de calcium sur une durée choisie. Il est donc caractérisé par des constantes de temps, d'amplitude et d'espace. Le signal calcique encode une information générée par la détection d'un stimulus et la propage jusqu'aux effecteurs qui génèrent la réponse moléculaire. Une fois ce message interprété par un réseau hiérarchisé, il entraîne l'activation ou la modulation d'une fonction cellulaire (prolifération, transcription…).

Calciosome

Nous définirons ***" LE CALCIOSOME "*** comme étant le répertoire des protéines impliquées dans l'homéostasie calcique et/ou une signature calcique. Ce calciosome est donc un ensemble de protéines caractérisables et potentiellement utilisables comme cibles dans l'optique de modifier une signature calcique spécifique dans une pathologie donnée.

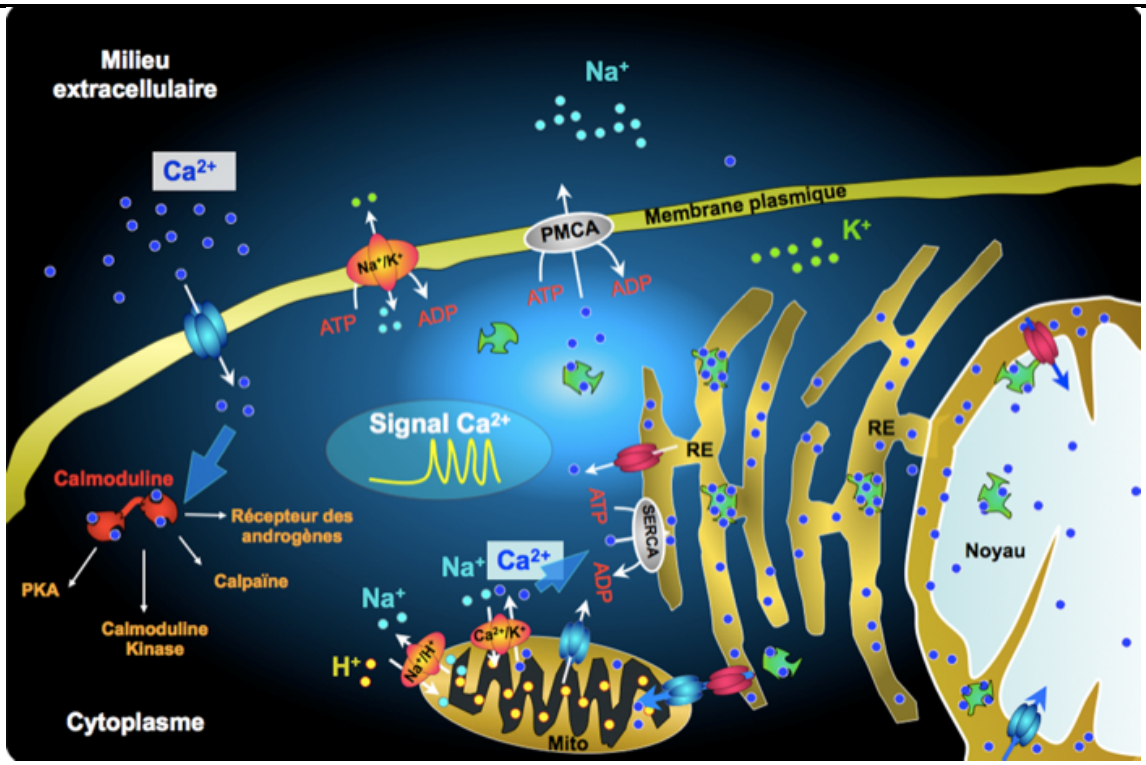

Figure 1 : schéma unifiant les notions d'homéostasie calcique, calciosome et signature calcique.

Le calciosome est constitué de trois groupes de protéines (Figure 1) : les transporteurs (de type canal ou non) assurant la diffusion facilitée ou le transport actif des ions, les protéines chélatrices permettant de contrôler le taux de calcium libre et les protéines senseurs de calcium.

Parmi ce large répertoire, la super famille des canaux TRP a émergé depuis une vingtaine d'années comme étant un groupe majeur de part la diversité de ses modes de régulation et de ses fonctions.

II.1.2. LES CANAUX TRP, thermo-senseurs et le récepteur au froid : TRPM8

Historique : de la drosophile à l'homme

Le sigle TRP, pour « Transient Receptor potential », prend son origine dans la caractérisation d'un mutant de la Drosophile présentant des problèmes de vision. En fait, le mutant présentait une réponse transitoire du processus de photo-transduction [1]. Le gène mutant incriminé codait une protéine canal dont l'ouverture était instable et donc transitoire. Depuis la fin des années 1990, de nombreuses études ont permis la caractérisation chez les mammifères des gènes orthologues et dérivés des gènes TRP et TRPL de la mouche.

Classification et structures communes

L'analyse phylogénétique de tous ces gènes a permit de les classer par groupes [2, 3]. Chez les Mammifères, les 32 gènes ont été classés en 7 sous-familles ([4], figure 10.A) :

- **TRPC (1-7)** pour « Canonique » ou « Classique » en raison de leur forte homologie avec la protéine TRP originelle de la drosophile ;

- **TRPV (1-6)** en référence au premier membre de cette famille (TRPV1 ou récepteur aux « Vanilloides ») qui fut identifié comme un canal activé par le principal composant irritant du piment rouge : la capsaicine ;
- **TRPM (1-8)** en référence également au premier membre de cette famille (TRPM1 ou « Mélastatine ») qui fut initialement cloné à partir d'une lignée cellulaire murine de mélanome ;
- **TRPML (1-3)** pour les « MucoLipines » ;
- **TRPP (1-5)** issus à l'origine de deux gènes *polycystic kidney diseases 1* et *2* (PDK1 pour TRPP1, et PDK2 pour TRPP2) regroupent actuellement cinq membres chez l'Homme ;
- **TRPN** qui ne comprend actuellement qu'un seul membre chez l'Homme et se distingue des autres TRP par la présence au niveau de son extrémité amino-terminale de nombreux domaines ankyrines répétés [5] ;
- **TRPA1** (ou « ANKTM1 »), un membre éloigné de la famille TRP [6].

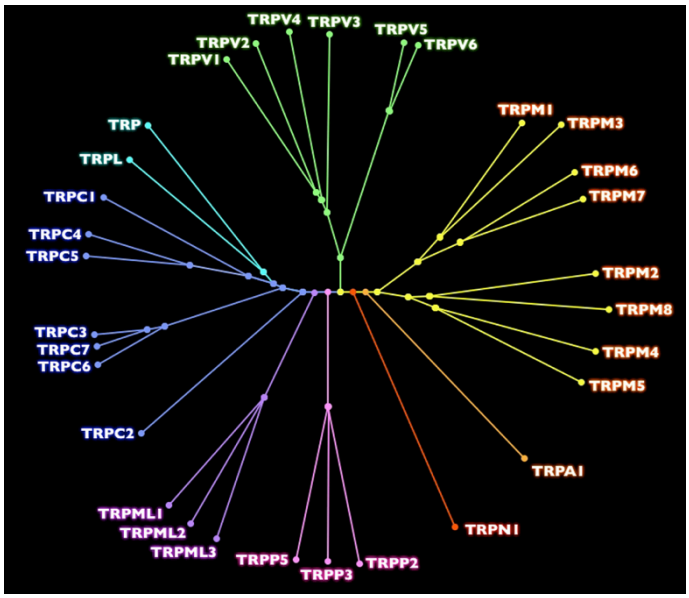

Figure 2 : arbre phylogénique des canaux de la famille TRP. Chaque couleur est associée avec une sous-famille ou groupe : TRPC, TRPV, TRPM, TRPP, TRPA, TRPN.

Les canaux d'un même groupe possèdent une structure protéique primaire et secondaire proche. La structure générale d'un canal TRP comprend 6 segments transmembranaires hydrophobes (S1 à S6), chacun séparé par de petites boucles hydrophiles (Figure 2). Les deux boucles carboxy- et amino-terminales sont cytoplasmiques et contiennent 1 à 2 zones hydrophobes relativement bien conservées ainsi que des structures en hélice alpha. La séquence comprise entre les segments transmembranaires 5 et 6 comprend une boucle P (« P-loop »), partiellement conservée par rapport à celle des canaux potassiques voltage-dépendants « Shaker », et forme le filtre de sélectivité du pore ionique. Un petit segment qualifié de domaine TRP, adjacent au 6ème segment transmembranaire, est conservé dans les canaux TRP et TRPL de la drosophile ainsi que dans les groupes C et M chez les mammifères. Ce segment serait impliqué dans la régulation de l'activité des canaux par certains lipides comme le PIP2 [7-9]. Enfin certains domaines protéiques bien connus comme les domaines ankyrines, principalement impliqués dans l'ancrage des canaux au cytosquelette, sont conservés dans la boucle amino-terminale des familles C et V.

La structure quaternaire des canaux TRP a été initialement déduite de leur homologie avec les canaux potassiques voltage-dépendants, puis la masse apparente des canaux TRPV1 et TRPM8 fut calculée par western-blot en condition non dénaturante [10, 11]. La structure 3D de TRPV1 a été plus récemment observée par cryo-microscopie électronique et reconstruite par un modèle informatique [12]. Les canaux TRP sont généralement des homotétramères (Figure 3) mais certains peuvent se combiner pour former des hétérotétramères aux propriétés électrophysiologiques différentes. Finalement, des ARNm alternatifs et des formes variables issues de l'épissage alternatif ont été clonés pour certains canaux TRP, ex : 4 pour TRPV1, 2 pour TRPV4, 9 pour TRPM3 [13-15]. Ces ARNm issus d'épissage alternatif codent soit des protéines tronquées soit des protéines présentant des insertions. Ces isoformes se comportent soit comme des canaux fonctionnels avec des propriétés électrophysiologiques modifiées soit comme des dominants négatifs bloquant la fonction de la forme « classique ». Ainsi, une petite isoforme de TRPM1, surexprimée dans le mélanome, est capable de s'associer avec la forme complète pour bloquer la translocation du canal vers la membrane plasmique.

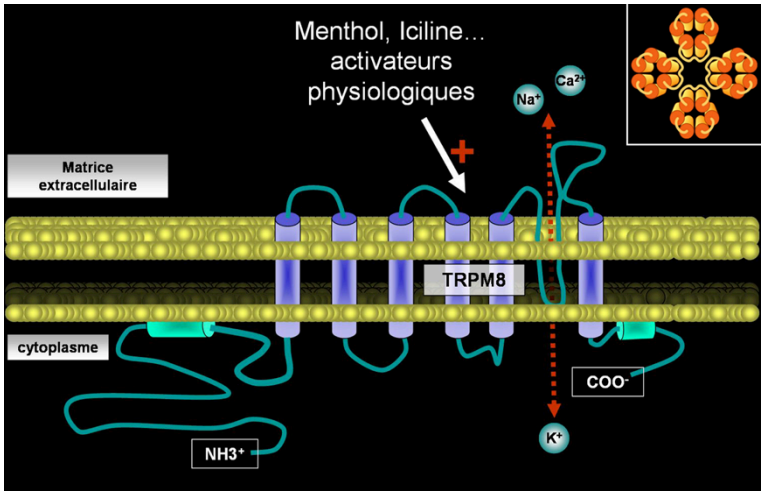

Figure 3 : représentation schématique de la structure secondaire d'un TRP monomérique (ici TRPM8) : 6 segments transmembranaires (cylindres bleus), les deux boucles terminales sont cytosoliques et la boucle-P formant le pore ionique se situe entre les deux derniers segments transmembranaires. Chaque boucle terminale cytosolique comprend une zone hautement hydrophobe (cylindre vert). Dans l'encart supérieur droit, vue du dessus d'un tétramère de TRP.

Thermorécepteurs

La thermosensation a longtemps été étudiée par l'enregistrement des dépolarisations membranaires induites par une variation de température ou par l'utilisation de substances mimant l'effet d'une variation de température, comme le menthol ou la capsaicine. Le clonage des canaux TRP a permis de caractériser certains des senseurs initiant la réponse aux variations de température. Pas moins de 7 canaux TRP présentent cette fonction. TRPA1 (ou ANKTM), TRPM8 et TRPC5 sont tous trois activés par une diminution de température [6, 16, 17]. Les canaux TRPV1, 2, 3 et 4 sont sensibles à une augmentation de température [18-22]. Les thermo-TRP couvrent une gamme de température allant de 8°C à 50°C(Figure 4) et sont inextricablement liés au phénomène de nociception pour les canaux sensibles aux températures seuil de la nociception, TRPA1 et TRPV1 [6, 23, 24]. Le détecteur de température se situe principalement dans la boucle carboxy-terminale des canaux. Ainsi l'inversion des boucles carboxy-terminales de TRPV1 et TRPM8 a permis d'inverser leurs propriétés de thermosensibilité [25].

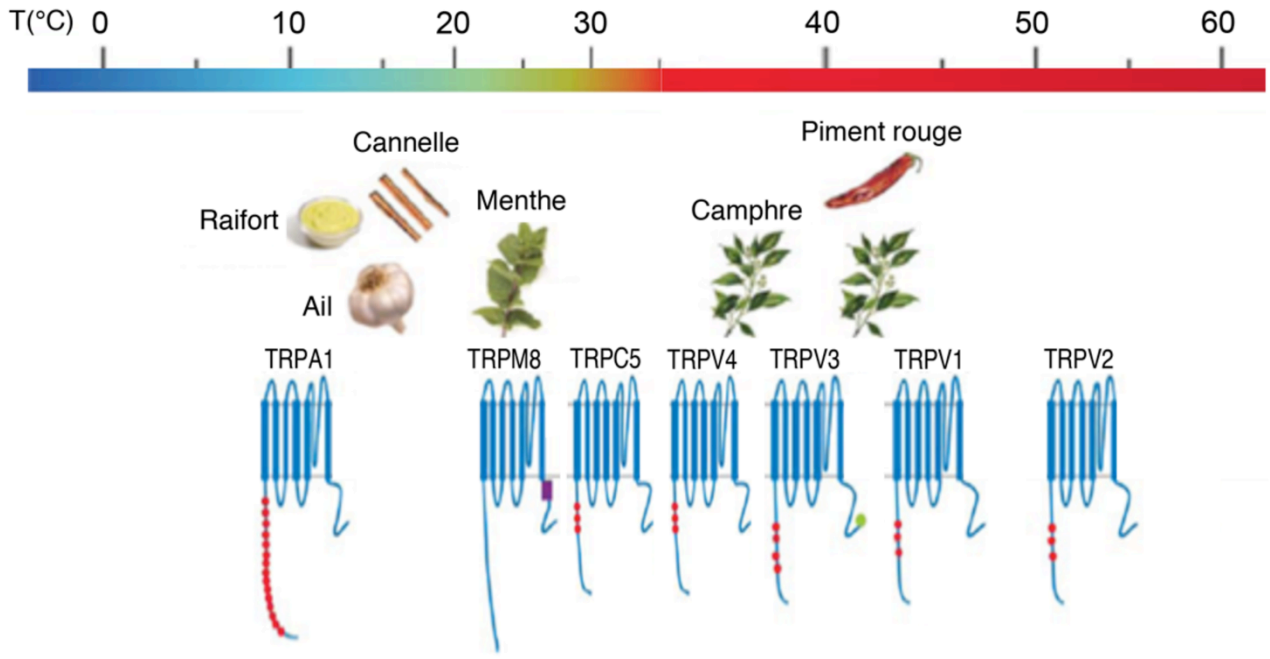

Figure 4 : schéma reportant les thermorécepteurs TRP en fonction de leurs températures d'activation. Sont ajoutées, les substances mimant les effets de la chaleur ou du froid, et parfois déclenchant la nociception. Figure adaptée de Daka A *et coll* [24].

Le principe de la thermo-activation de ces protéines repose sur la loi d'Arrhenius qui décrit la relation entre la vitesse des réactions chimiques en fonction de la température et de l'énergie [26]. Pour une réaction donnée : $A + B \leftrightharpoons AB$

Le déplacement de la réaction d'un côté ou de l'autre dépendant alors des constantes de vitesse k1 et k2. Selon loi d'Arrhenius, la constante de vitesse k est égale à :

$\boldsymbol{k = A \times e^{-\frac{Ea}{T}}}$	**k** : constante de vitesse **A** : facteur d'orientation **Ea** : énergie d'activation de la réaction **T** : température de la réaction

Appliquée à l'ouverture d'un canal ionique, cette formule est représentée ainsi :

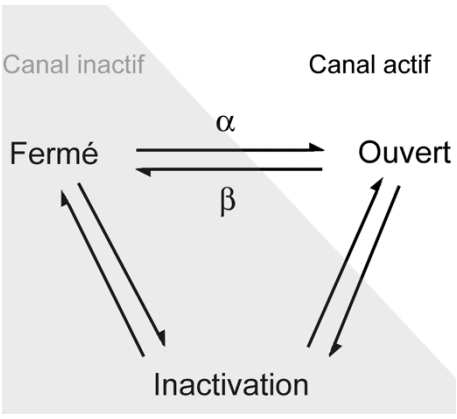

Figure 5 : Les constantes α et β représentent la vitesse de déplacement de la réaction chimique (sec^{-1}). Le rapport α/β définit le sens de déplacement de la réaction : **α/β** > 1 déplacement vers l'état d'ouverture, mais si **α/β** < 1 déplacement vers l'état fermé c'est-à-dire que le canal ne peut pas s'ouvrir. Quand **α/β = 1**, la probabilité d'ouverture du canal est de 0,5. **Le canal a alors autant de chances de s'ouvrir que de rester fermé**.

ACTIVITÉS DE RECHERCHE

Les constantes de vitesse **α** et **β** définissent le sens de la réaction (Figure 5), dans le cas d'un canal ionique cela équivaut à un changement de conformation du canal permettant les transitions ouvert-fermé. Ces constantes possèdent leur propre énergie d'activation, respectivement : **Ea,α** et **Ea,β**. En terme de thermodynamique, l'Ea représente la « barrière énergétique » que doit surpasser le système pour effectuer une transition d'un état à l'autre.

Le travail de Voets *et coll* a consisté à démontrer que les canaux thermosensibles ne possèdent pas les mêmes **Ea,α** et **Ea,β** , contrairement aux canaux non thermosensibles pour lesquels **Ea,α / Ea,β = 1** [26]. Finalement, ils ont mis en évidence que les canaux sensibles au froid sont caractérisés par **Ea,α / Ea,β < 1** (respectivement 2,98 kJ.mol^{-1} et 32,70 kJ.mol^{-1} pour TRPM8) alors que si **Ea,α / Ea,β > 1**, les canaux seront sensibles à une augmentation de température (respectivement 39,32 kJ.mol^{-1} et 4,39 kJ.mol^{-1} pour TRPV1). Ces données suggèrent que la fermeture du canal TRPM8 est presque 10 fois plus stable que son ouverture, alors que le canal TRPV1 est plus stable dans sa conformation ouverte. D'après les mesures de Brauchi *et coll* [27], l'enthalpie (ΔH) de la transition fermé-ouvert est de valeur négative et est donc une réaction exothermique. Cette émission d'énergie génère ainsi une partie de l'énergie nécessaire à la transition, diminuant d'autant le niveau de la « barrière énergétique » **Ea,α** (Figure 6).

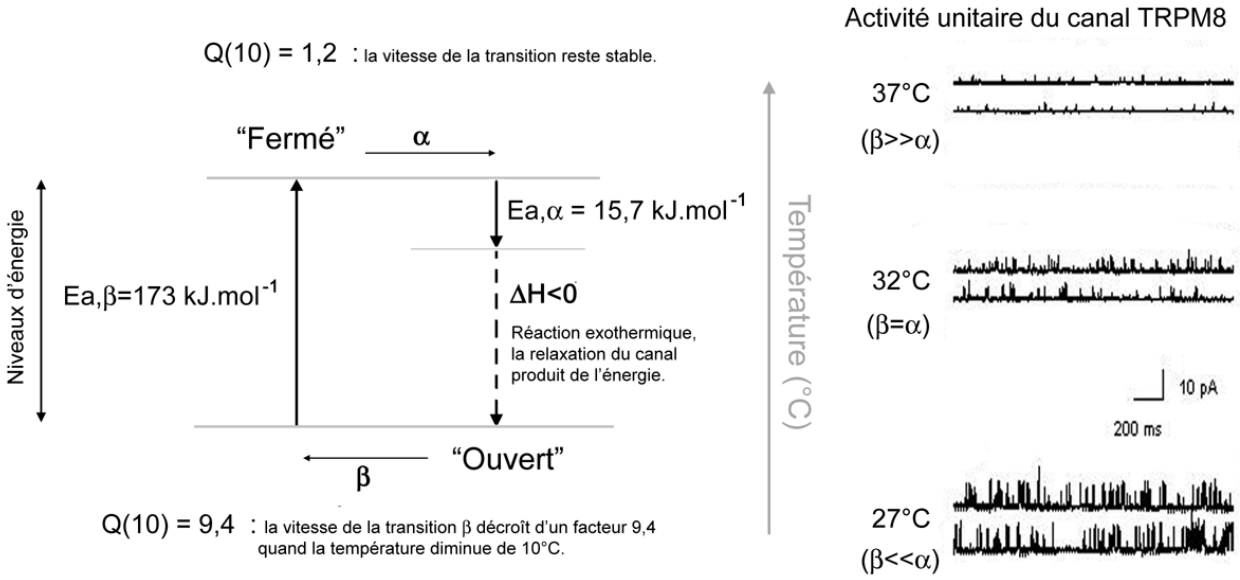

Figure 6 : représentation schématisée des transitions thermodynamiques associées à **l'ouverture** du canal TRPM8 en fonction de la température (partie gauche). La partie droite présente des enregistrements électrophysiologiques de l'activité unitaire du canal TRPM8 en fonction de la température, obtenus par la technique de Patch-clamp en configuration « cellule-attachée » (Données non publiées).

Selon les principes de la thermodynamique, plus la valeur de Ea est élevée plus sa vitesse de réaction varie avec la variation de température. Appliqués à TRPM8, ces principes relatent le fait qu'une variation de 10°C de l'environnement modifie d'un facteur 1,2 la vitesse de la réaction d'ouverture et d'un facteur 9,4 la vitesse de la réaction de fermeture [26]. Cela signifie concrètement que l'état d'ouverture du canal TRPM8

n'est que peu influencé par la variation de température, mais que la transition vers l'état « fermé » est très sensible à cette variation de température. De fait, lors de l'activation de TRPM8 par la diminution de température, la transition β diminue et quand elle devient inférieure à α, la conformation « ouvert » devient alors plus stable que la conformation « fermé ».

Le changement d'énergie vers l'état ouvert provoque une modification de la voltage-dépendance de TRPM8 avec un décalage de la courbe d'activation vers les potentiels plus négatifs (Figure 7). Ce phénomène provoque une augmentation de la probabilité d'ouverture du canal pour des potentiels de membrane identiques au potentiel de repos des cellules.

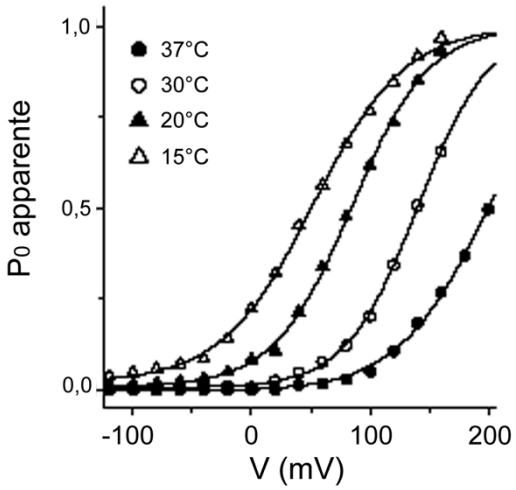

Figure 7 : évolution de la probabilité d'ouverture (P_0) apparente du canal en fonction du potentiel membranaire pour différentes températures [26]. Notez le décalage de la courbe d'activation vers des potentiels plus négatifs (rappel : le potentiel de repos des cellules varie, en général, entre -70 mV et -30 mV).

ACTIVITÉS DE RECHERCHE

II.2. P-TEFb ET LA RÉGULATION DE LA TRANSCRIPTION.

II.2.1. SÉQUENCE DE LA TRANSCRIPTION

La transcription est le mécanisme permettant la synthèse d'ARN (ARNm, ARNt, ARN non codants) à partir des gènes. Elle se divise en plusieurs étapes consécutives :

- Pré-initiation :

Recrutement la TATA-binding protein (TBP) puis du facteur de transcription II D (TFIID) sur le promoteur proximal caractérisé ou non par des éléments de type TATAA box, CAAT box, îlots CpG. L'activité hélicase de TFIID permet de séparer les brins de chromatine et d'ouvrir la fourche de réplication.

- Initiation :

Assemblage de l'ARN polymérase (ARN POL) fonctionnelle et sa stabilisation par les facteurs de transcription depuis le promoteur distal. L'équilibre entre les facteurs amplificateurs ou inhibiteurs défini une probabilité de démarrage de la transcription. Dans le cas de la synthèse d'ARNm, le facteur TFIIA phosphoryle la sérine 5 du domaine répété carboxy-terminal (CTD) de la large sous-unité de l'ARN POL II (Rpb1) ce qui initie la polymérisation (Figure 8).

- Dégagement du promoteur & Pause

Pour une certaine proportion des gènes, l'ARN POL commence la synthèse du transcrit puis s'arrête sur un site de pause situé environ 50 bases après le premier nucléotide transcrit. La pause est provoquée par le recrutement du facteur négatif d'élongation (NELF), protéine tétramérique qui s'ancre sur Rpb1 par une extrémité (NELF/A) et fixe l'ARN naissant par son autre extrémité (NELF/E) [29]. A ce stade, la transcription peut être avortée et le transcrit naissant libéré. Durant cette phase, un complexe de protection 5' est recruté sur l'extrémité de l'ARN pour prévenir toute dégradation.

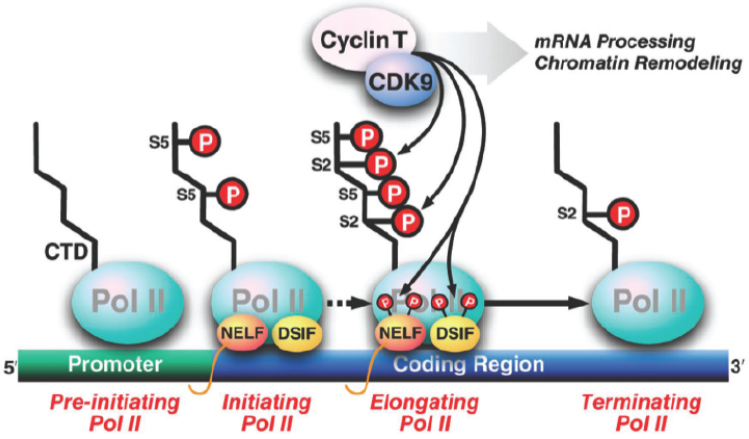

Figure 8 : modèle de contrôle de la transcription par le couple NELF / P-TEFb [28].

- Elongation

C'est le recrutement du complexe positif d'élongation (P-TEFb), dimère formé par la cycline T1 (ou T2A, T2B ou K) et la cyclin-dependent Kinase 9 (Cdk9), qui libère l'ARN POL II. L'activité kinase de P-TEFB phosphoryle NELF ce qui l'inactive et le décroche, libérant l'entrave à l'élongation. En outre, P-TEFb phosphoryle la sérine 2 (S2) des heptamères du CTD de l'ARN POL II ainsi que la protéine DSIF. La phosphorylation de DSIF augmente la processivité de l'enzyme, c'est à dire sa capacité à synthétiser de longs polymères et donc indirectement sa vitesse de transcription. La phosphorylation de la S2 du CTD de la polymérase augmenterait aussi sa processivité mais permet surtout d'assurer le recrutement du spliceosome sur la S2 des heptamères du CTD [30].

- Terminaison

L'ARN POL II reconnaît les séquences riches en A/T qui déstabilisent son interaction avec la chromatine. Ce signal marque le site de coupure 3' de l'ARN puis de sa polyadénylation terminale. L'activité kinase de P-TEFb est nécessaire à la bonne coupure 3' de l'ARN. En effet, la S2 phosphorylée du CTD de l'ARN POL II permet le recrutement du complexe de coupure 3' PCF11 [30]. Suite à la polyadénylation, un complexe de protection 3' est recruté pour prévenir l'ARN de toute dégradation.

II.2.2. P-TEFb

Biochimiquement, P-TEFb est purifié sous 2 formes : la forme libre qui est douée d'une activité kinase et la forme complexée qui est inactive. La forme complexée de P-TEFB s'agrège avec d'autres protéines autour d'un petit ARN nucléaire non codant : l'ARN 7SK (environ 200 000 molécules par cellule, contre 300 000 pour la sous-unité Rpb1 de l'ARN POL II). Ce complexe comprend principalement les protéines Hexim 1 ou 2 et Larp7. Quand il ne fixe pas P-TEFb, le complexe 7SK (Hexim, Larp7, ARN 7SK) peut interagir avec les ribonucléoprotéines nucléaire hétérogènes (hnRNP, jusqu'à 10^8 copies [31]). Les hnRNP présentent une large gamme de fonctions biologiques allant de la protection et du transport d'ARN, à la stimulation de l'action des télomérases ou de la régulation de l'épissage. Il semblerait que l'association de P-TEFb avec l'ARN 7SK soit compétitive de celle entre les hnRNP et l'ARN 7SK. Il existerait donc une relation stœchiométrique entre les complexes du type :

$$P-TEFb\ +7SK+RNP\ \Leftrightarrow P-TEFb.7SK+RNP\Leftrightarrow\ P-TEFb+7SK.RNP$$

Des résultats récents de précipitation de chromatine ont démontré que le complexe P-TEFb/7SK est recruté sur les sites actifs de transcription par son interaction avec les facteurs Brd4 et JMJD6. Ces derniers sont présents sur les éléments amplificateurs ou directement sur le site de pause dans le cas de Brd4 [32]. Un travail du groupe du Dr Olivier Bensaude a démontré qu'il existe bien un transfert : $P-TEFb.7SK+RNP\Leftrightarrow\ P-TEFb+7SK.RNP$ [33], suggérant ainsi que l'activation du complexe P-TEFb sur l'ARN POL II puisse se faire ou être facilitée par la présence de hnRNP. Ces auteurs ont suggéré que des hnRNP soient en interaction avec l'extrémités 5' de l'ARN naissant sur la polymérase puis que le complexe P-TEFB/7SK s'ancre à proximité grâce à son interaction avec des facteurs de transcription ou tout du moins des protéines liées à la chromatine [32]. L'équilibre de la réaction se déplace alors en favorisant les complexes hnRBP-ARN 7SK et libérant une fraction de P-TEFb qui s'active et permet la levée de la pause.

Ce modèle souffre d'une mauvaise connaissance des mécanismes physiques qui permettent le recrutement des complexes sur les sites de transcription. En effet, alors qu'il est connu depuis 40 ans que, chez les procaryotes, les facteurs de transcription scannent l'ADN à la recherche de leurs éléments de réponse spécifiques par le biais d'interactions électrostatiques avec l'ADN, indépendamment de la séquence [34], P-TEFB, lui, ne possède pas d'éléments de réponses spécifiques. Il est donc peu probable qu'il puisse scanner l'ADN. Néanmoins, P-TEFB interagit avec des protéines associées à l'ADN (ex : Brd4), il est donc envisageable que ces interactions affectent sa diffusion et favorisent sa recherche de sites de transcription actifs.

ACTIVITÉS DE RECHERCHE

II.2.3. DYNAMIQUE DES PROTÉINES NUCLÉAIRES

Le noyau est un compartiment délimité par l'enveloppe nucléaire, et ayant un volume moyen d'environ 250 μm^3 (250.10^{-15} L). Il est organisé en plusieurs sous-domaines définis par l'existence de différents assemblages moléculaires et par des niveaux de compactions différents de la chromatine (Figure 9). Le volume nucléaire est occupé par la chromatine, les différents corps et le nucléoplasme (phase aqueuse hors objets). La chromatine est organisée en territoire chromosomique au sein desquels les polymères d'ADN évoluent par une diffusion contrainte les empêchant d'homogénéiser les différents territoires.

Au sein du nucléoplasme, on compte plusieurs structures dont les nucléoles (structures fibrillaires, lieu de synthèse de nombreux ARN ribosomiques), les corps de Cajal (taille≈µm), les corps PML (taille≈µm), les domaines SC35 (taille>µm), les paraspeckles (taille ≈ µm). Ces différents corps et domaines sont principalement le lieu de maturation des petits ARN nucléaires non codants (snRNA ; impliqués dans l'épissage alternatifs) ainsi qu'un lieu de stockage de protéines nécessaires à l'entretien des fonctions nucléaires. Dans de ce milieu très chargé en peptides, acides nucléiques et comprenant des structures massives comme la chromatine et les différents corpuscules, la diffusion des protéines n'est pas souvent linéaire et l'accessibilité à un site actif peut relever du parcours du combattant. En effet, pour rechercher sa cible au sein du noyau, une protéine de concentration limitée (entre 10 000 et 1 000 000 de molécules pour les facteurs de transcription) et régie par un mouvement brownien subissant les phénomènes d'obstruction, ou est régie par un mouvement anomale sous-diffusif quand elle subit les contraintes induites par son interactome. Ainsi, l'interaction avec un complexe peu diffusif aura tendance à restreindre le mouvement d'une protéine et donc à limiter son accession à son site d'activité lointain. A l'inverse, une interaction peut permettre de libérer une protéine et ainsi augmenter sa diffusion que ce soit pour l'éloigner d'un site actif ou pour augmenter sa capacité à le rejoindre. La dynamique des protéines nucléaires participe donc pleinement à la régulation de leur fonction et la caractérisation biophysique de cette dynamique est une composante essentielle dans l'étude de la régulation des activités des protéines nucléaires.

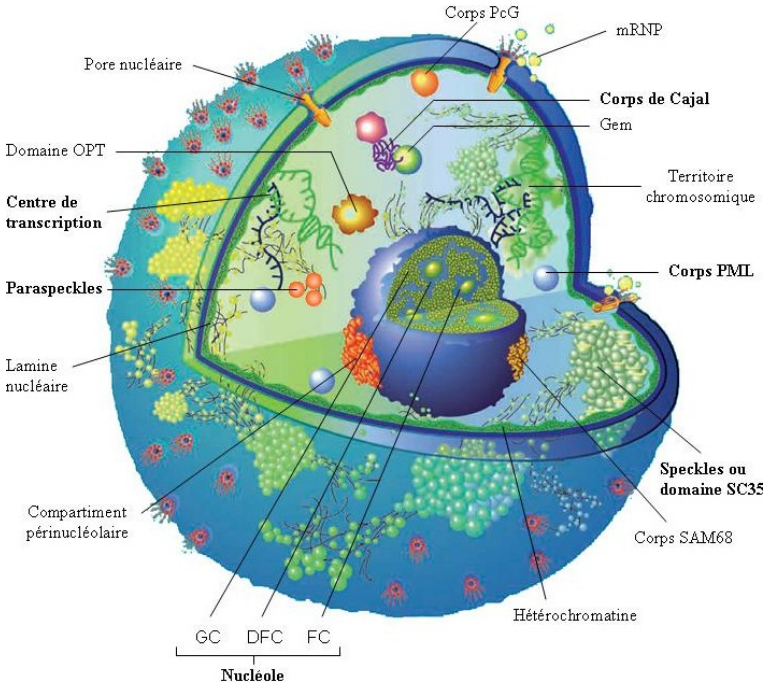

Figure 9 : représentation schématique de la structure du noyau des cellules eucaryotes (adapté de [35]).

II.3. INTRODUCTION AUX TECHNIQUES DE PHOTONIQUES AVANCÉES

II.3.1. TIME DOMAIN – FLUORESCENCE LIFETIME IMAGING MICROSCOPY (TD-FLIM)

La microscopie d'image en temps de vie de fluorescence est une technique pouvant s'appliquer à tous les fluorochromes. Elle permet de mesurer un changement de l'état ou de l'environnement de ce fluorochrome indépendamment de sa concentration. Ceci rend le FLIM très utile pour obtenir des données quantitatives et permet de transformer les sondes dites non-ratiométriques en sondes ratiométriques. Cette technique repose sur la mesure du temps de demi-décroissance de la fluorescence émise par un fluorochrome suite à son excitation.

Le temps de vie de fluorescence d'une molécule dans une cellule vivante peut être mesuré par 2 méthodes : la méthode des **domaines fréquentiels** et la méthode des **domaines temporels**. La méthode temporelle fait appel à un laser pulsé (fréquence 10-80 MHz en fonction du temps de vie des fluorochromes) dont le déclenchement ("trigger") est synchronisé à un système de détection de type comptage de photon unique (détermination du temps d'arrivée exact de chaque photon) ou un système de « portes » électroniques permettant de retarder les photons afin de les discriminer en fonction de leur temps d'arrivée. Les photons sont comptabilisés et distribués en fonction de leur délai d'arrivée sur un histogramme de comptage de photon (Figure 10).

Il existe 2 méthodes pour mesurer le temps de vie depuis cet histogramme : **une méthode d'ajustement** et **une méthode calculée**.

La méthode d'ajustement consiste à trouver la fonction représentant la décroissance exponentielle de l'histogramme de comptage de photon. Cette fonction est caractérisée par une constante correspondante au temps de vie moyen.

L'alternative graphique consiste à déterminer la valeur de délai d'arrivée de photon correspondant à 37% de l'amplitude (1/e) de la courbe.

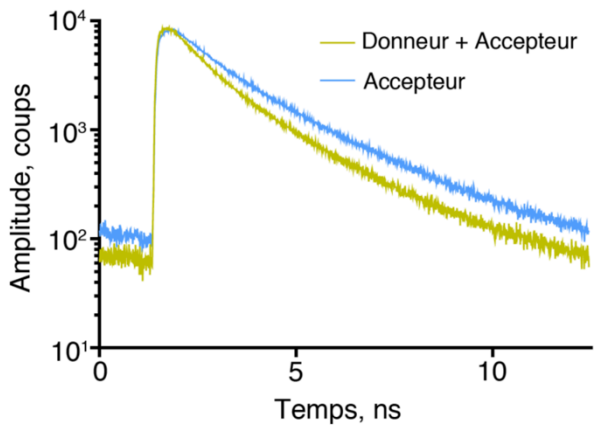

Figure 10 : histogramme de comptage de photons.

Méthode calculée : pour chaque pixel, la transformation de Fourier de cet histogramme de comptage de photon calcule un nombre réel et un nombre complexe que l'on reporte sur le phaseur ou vecteur de phase (Figure 11) [36].

La valeur du temps de vie de phase est alors donnée par la formule :

Eq. (1) $$\tau_{\varphi} = \frac{1}{\omega}\tan(\varphi)$$

On obtient, de fait, une valeur de temps de vie pour chaque pixel de l'image. On peut ensuite analyser la distribution de ces temps de vie afin de déterminer s'il y a une ou plusieurs populations puis les séparer. On peut aussi réaliser une segmentation de l'image pour sectionner des domaines (x ,y) en associant le temps de vie de chaque pixel à l'une des populations.

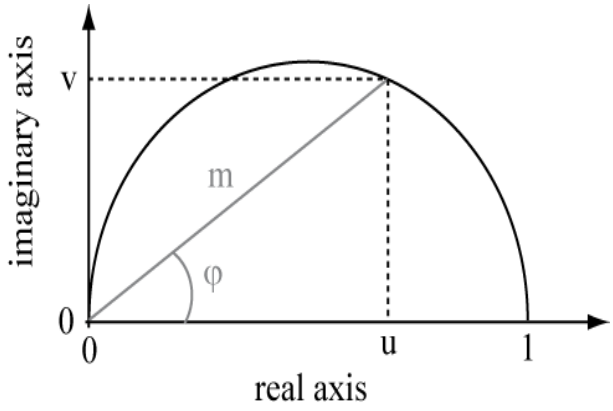

Figure 11 : Phaseur. u et v sont les coordonnées dans l'espace de Fourier, de la décroissance du temps d'arrivée des photons. M et phi sont le module et la phase, respectivement, et sont calculés à partir de la projection du point (u,v) depuis l'origine.

II.3.1. FÖRSTER RESONNANCE ENERGY TRANSFERT (FRET)

La technique de FRET repose sur le transfert d'énergie par résonnance entre 2 molécules dans un rayon maximal dépendant du rayon de Förster (R0) de ce couple de fluorochromes. Les protéines fluorescentes dérivées de la GFP ou de la RFP présentent des R0 compris entre 4,5 et 6,5 nm ce qui permet d'obtenir des signaux FRET entre 2 fluorochromes distants jusqu'à 8-9 nm. Physiquement, le principe du transfert d'énergie consiste en l'absorption d'une fraction de l'énergie (par résonnance) du donneur par l'accepteur. Ceci accélère la relaxation du donneur (transition des états supérieurs à S1 vers S1) et lui permet d'émettre plus rapidement après excitation ses propres photons (transition S1 vers S0). La conséquence est que le temps de vie du donneur décroît (figure 10, p32). En pratique, on excite la protéine fluorescente donneur de fluorescence puis : 1) soit on enregistre les photons émis par la protéine acceptrice de fluorescence, 2) soit on mesure le temps de vie de fluorescence de la protéine donneuse de fluorescence, 3) soit on mesure le changement d'anisotropie du donneur.

Cette diminution du temps de vie permet de connaître l'efficacité de FRET (E_{FRET} ; équation 1) ainsi que le pourcentage de donneur engagé dans un couple de FRET selon les formules 1 et 2, respectivement.

Eq 2) $$E_{(FRET)} = 1 - \left(\frac{\tau DA}{\tau D}\right)$$

Le résultat de FRET peut être analysé sur un phaseur [37] de sorte à établir une carte d'E_{FRET} dans laquelle chaque pixel possède sa propre valeur. La distribution de ces valeurs d'E_{FRET} peut alors servir à calculer la valeur moyenne et son écart-type.

La technique de FRET peut être utilisée pour différentes mesures :

- interaction protéine-protéine ou plus strictement oligomérisation au sein d'un complexe protéique,
- changement de conformation (FRET intramoléculaire), réalisé en greffant le donneur et l'accepteur de FRET sur la même protéine,
- suivi dynamique d'un clivage peptidique,
- mesure de concentration d'un ligand libre ou mesure d'une activité kinase en utilisant un bio-senseur,
- information sur la topologie des zones de FRET au sein de la cellule.

II.3.2. FLUCTUATIONS (FLUORESCENCE) CORRELATION SPECTROSCOPY (FCS)

La FCS consiste en une analyse de corrélation de fluctuations temporelles du signal de fluorescence. Le principe consiste à illuminer le volume focal (Vf) et d'enregistrer les variations de fluorescence à l'aide d'un détecteur à faible niveau de bruit (ex. une photodiode à avalanche afin d'obtenir un comptage des photons ; Figure 12). Le régime d'acquisition dépend principalement du temps mort du détecteur (autour de 80-100 ns). Une fois le tracé obtenu pour une durée typique de 20-30 secs, on effectue une autocorrélation du signal pour détecter des motifs répétés dans les fluctuations de fluorescence, ce qui trahit la présence répétée d'évènements de diffusion possédant des propriétés physiques similaires. L'autocorrélation consiste d'abord en un décalage de la courbe d'intensité, réalisé en augmentant le déphasage d'un temps τ compris entre l'unité temporelle minimale (100 ns), jusqu'à l'échelle de la seconde ou dizaine de secondes. Chaque tracé déphasé d'une valeur (τ) est ensuite multiplié par le tracé d'origine (t), puis l'intégrale du signal sous la moyenne est soustraite à l'intégrale du signal au dessus de la moyenne pour chaque valeur de déphasage (τ0,τ +1...τ+n). On peut alors ajuster cette fonction d'autocorrélation avec différents modèles qui prennent en compte la nature de la

Eq. (3) $$G(\tau) = \frac{\langle \delta I(t) \delta I(t+\tau) \rangle}{\langle I(t) \rangle^2}$$

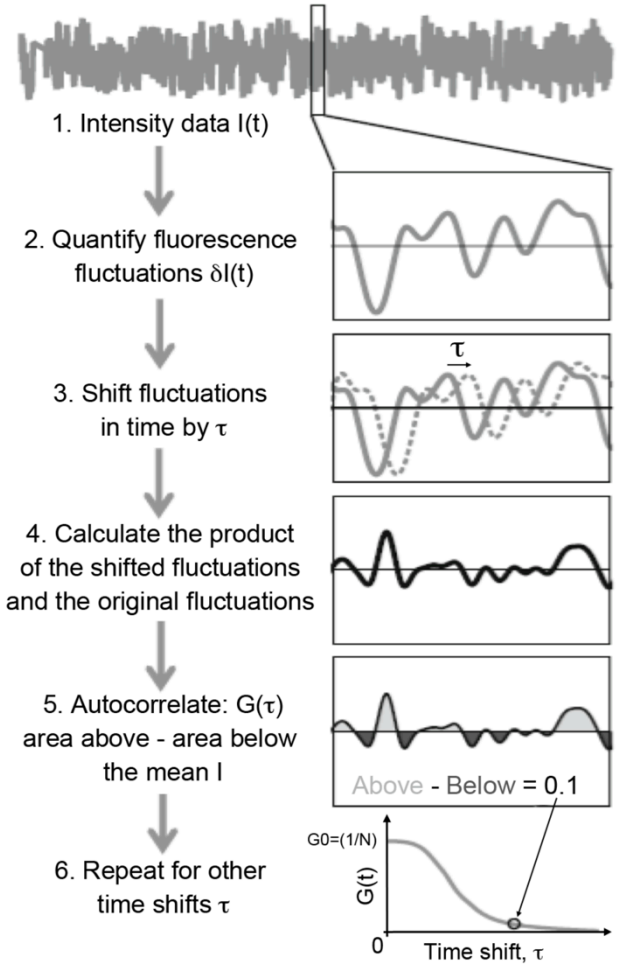

Figure 12 : chaine d'opération composant l'acquisition et l'analyse FCS.

diffusion (brownien, anomale) et de la fixation. La valeur G0 à l'origine est égale à 1/N (N étant le nombre moyen de molécules dans Vf), et le temps médian de résidence, τ_D, égal à la valeur déphasage obtenue pour G0/2. Comme on connaît la taille du volume focale et qu'on a calculé N, on peut déterminer **la concentration moyenne** de nos chimères fluorescentes (typiquement entre 20 et 500 nM) utilisées. Comme, on connaît le **temps de résidence moyen** dans Vf et comme on connaît la taille du Vf, on peut déterminer **le coefficient de diffusion**, D ($\mu m^2/s$). La fonction s'ajustant le mieux à la fonction d'autocorrélation est acceptée comme correspondant au meilleur modèle du modèle. On peut en extraire des caractéristiques intrinsèques à la nature de la diffusion : marcheur libre (mouvement brownien), fraction libre / fraction liée, sous-diffusion ou super-diffusion et/ou de la fixation (fraction libre / fraction liée).

II.3.1. IMAGE CORRELATION SPECTROSCOPY (ICS)

Le principe de l'ICS consiste à réaliser une corrélation spatiale (Eq. 4) entre les pixels en déphasant l'image selon l'axe x (ξ) puis selon l'axe y (η) [38, 39].

Eq. (4) $$r_{11}(\xi,\eta)_j = \frac{\langle \delta i(x+\xi,y+\eta)\delta i(x,y)\rangle}{\langle i\rangle^2}$$

La fonction d'autocorrélation 2D, $r_{1,1}(\xi,\eta)_j$ est ensuite ajustée avec une fonction gaussienne (Figure 13) afin de déterminer :

- le nombre de particule par pixel : $\frac{1}{r1,1(0,0)}$
- la résolution (taille du pixel si l'autocorrélation est de bonne qualité)
- la densité des particules.

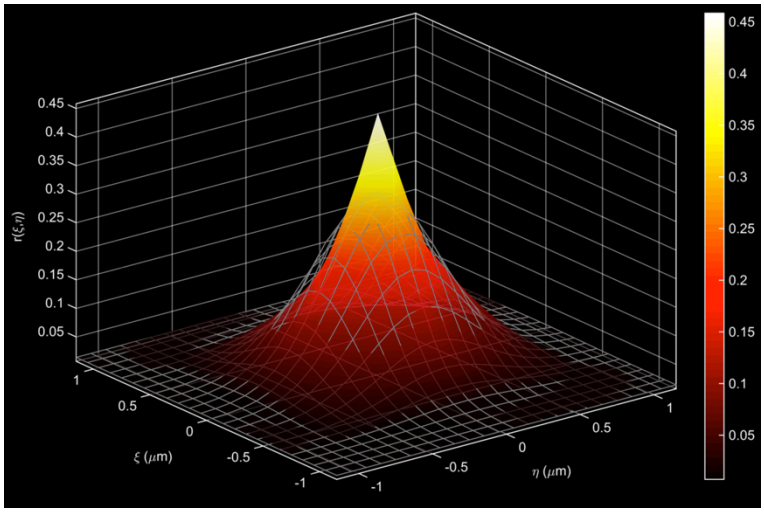

Figure 13 : fonction d'autocorrélation 2D d'une image avec ajustement gaussien (maillage).

III. RÉSULTATS

III.1. BIOLOGIE. Le récepteur au froid, TRPM8 : du gène à l'organisme.

III.1.1. TRPM8: ÉVOLUTION & DIVERSITÉ

Contexte

Dans mon travail de thèse sur TRPM8, nous avions démontré, bien qu'indirectement, la nécessaire existence d'isoformes du canal TRPM8 [40, 41]. En 2007, j'ai donc entrepris de les cloner. Cette simple tâche a nécessité 2 années de mise au point et d'amélioration de la RACE-PCR puis du clonage des 42 ARN trouvés…La diversité de structure des ARN et des protéines associées m'a ébahi et je me suis demandé dans quelle mesure cette diversité du récepteur au froid était issue d'une sélection étalée dans le temps.

L'analyse phylogénétique des canaux TRP a révélée que les TRP du groupe Canonical (TRPC) présentent le plus d'homologie avec les 2 canaux TRP des insectes (Drosophila melanogaster). A contrario, le groupe Melastatin (TRPM) est un des plus récent et parmi ceux-ci le canal TRPM8 est le dernier apparu, probablement après duplication de TRPM2 [42]. Cette étude suggère d'ailleurs que l'ancêtre du gène *trpm8* a été perdu chez les poissons. Néanmoins, aucune espèce extérieure à la superclasse des tétrapodes ne possédant ne le gène *trpm8*, il est donc aussi probable que ce dernier soit apparu par duplication de TRPM8 chez les tétrapodes. Les thermorécepteurs à la chaleurs TRPV2 et TRPV3 sembleraient aussi présenter un cas de figure identique. C'est particulièrement intéressant car cela pourrait être la démonstration que la spéciation a créé un système de thermo-détection chez les organismes poïkilothermes puis l'a affiné chez les homéothermes.

C'est sur la base de ce postulat, que nous avons avec mon collègue le Dr Samuel Blanquart (INRIA, Lille) décidé d'analyser l'évolution des formes humaines des ARNm et isoformes protéiques de TRPM8.

Objectifs

Réaliser l'analyse phylogénétique des ARNm humains de TRPM8 et prédire l'existence d'orthologues chez les mammifères.

Résultats

Le premier challenge technique de ce projet aura été la réalisation d'une RACE-PCR de qualité, j'entends par là : permettant l'amplification de séquence >2500 pb, et sensible, c'est à dire permettant la détection et le clonage d'ARN faiblement exprimés (sortant au delà de 35 cycles en qPCR à partir de 50ng d'équivalent cDNA). Après optimisation de notre protocole avec le Prof Morad Roudbaraki, nous sommes parvenus à cloner la forme longue de TRPM8, de la zone du pore jusqu'à l'extrémité 5', soit environ 2900 pb. En outre, nous avons cloné 10 bases supplémentaires à l'extrémité 5' de l'ARN par rapport à la référence publiée sur Genebank. Ceci a réduit la distance entre le premier nucléotide de transcription et la TATAA box de 35 à 25 pb, c'est à dire la distance consensuelle d'une TATAA box (-25). Les critères de qualité et de sensibilité de notre expérience étaient donc bien remplis. Nous avons alors réalisé les RACE-3' et 5' du gène *trpm8* sur des cDNA extraits de 4 organes/tissus humains : prostate, foie, testicule et épiderme. Sur 300 colonies bactériennes positives, 110 présentaient de nouvelles séquences. Après analyses, nous avons sorti 19

nouveaux exons que je qualifie d'alternatifs (contre 26 exons « classiques » pour la forme longue). Parmi les exons alternatifs, 12 étaient des exons 5' initiateurs de transcription, 4 étaient des exons 3' terminateurs de transcription et les 3 restants étaient des exons cassettes. Nous parlerons d'ARN alternatifs dans le cas de séquence ARN provenant de l'utilisation soit d'un promoteur alternatif soit d'un site alternatif de terminaison de transcription du gène *trpm8*. Les nouveaux exons cassettes sont eux des exons issus de

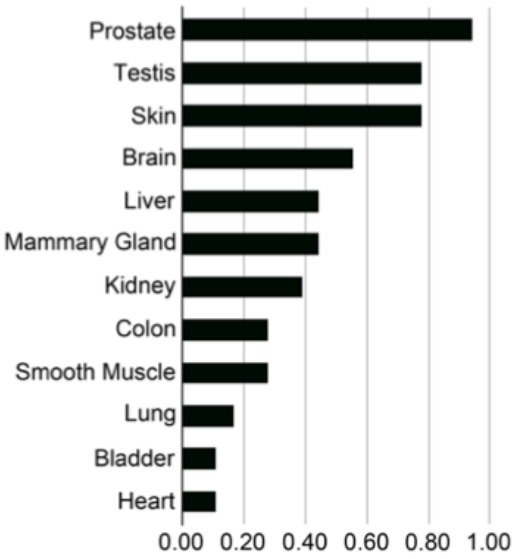

Figure 14 : expression normalisée des 19 nouveaux exons alternatifs dans des organes/tissus humains.

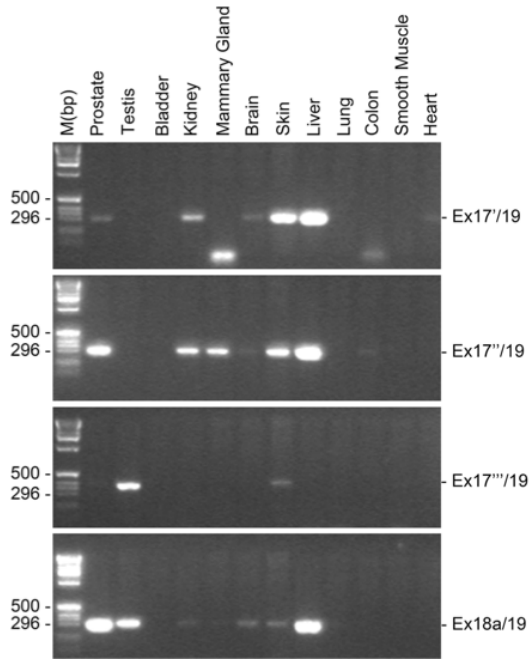

Figure 15 : exemple de détection de paires [exons alternatifs – exon core] dans différents organes/tissus humains par PCR.

l'épissage alternatif (variant d'épissage ou splice variant). Je tiens à la différence qui n'est pas bien décrite dans les livres et articles scientifiques, mais il existe bel et bien des différences spatiales, temporelles et mécanistiques entre la transcription alternative et l'épissage alternatif.

Du point de vue de l'expression tissulaire, nous avons observé une expression hétérogène de ces 19 exons (Figures 14 et 15). Nous n'avons pas détecté d'exons alternatifs de TRPM8 qui soient « tissu-spécifique », mais on peut parler de « motif/empreinte tissu-spécifique » au sens ou il existe des groupes d'exons exprimés spécifiquement au sein d'un organe.

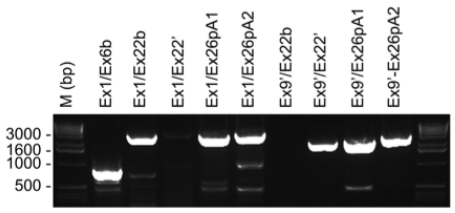

Figure 16 : PCR montrant l'amplification de segments d'ADNc deTRPM8 dans la prostate humaine. Les couples d'amorces ciblent les exons dénotés [initiateur/terminateur].

Nous avons ensuite réalisé des PCR longue-distance et clonages systématiques pour chaque paire [exon initiateur / exon terminateur], qu'ils soient classiques ou alternatifs. Ce travail a été réalisé sur les 4 organes utilisés initialement pour effectuer les RACE-PCR. Nous avons cloné environ 40 séquences, dont 34 étaient intègres et entièrement séquencées. Il est intéressant de noter que chaque couple [initiateur – terminateur] n'était pas exprimé dans les 4 organes testés (figure 16).

L'analyse du positionnement des prometteurs alternatifs et sites alternatifs de terminaison de la transcription sur le gène *trpm8* offre des indices sur la nature (canaux ou non) et la structure (nombre de segments transmembranaires) des protéines TRPM8. La figure 17 montre l'alignement des exons formant ces 34 ARN

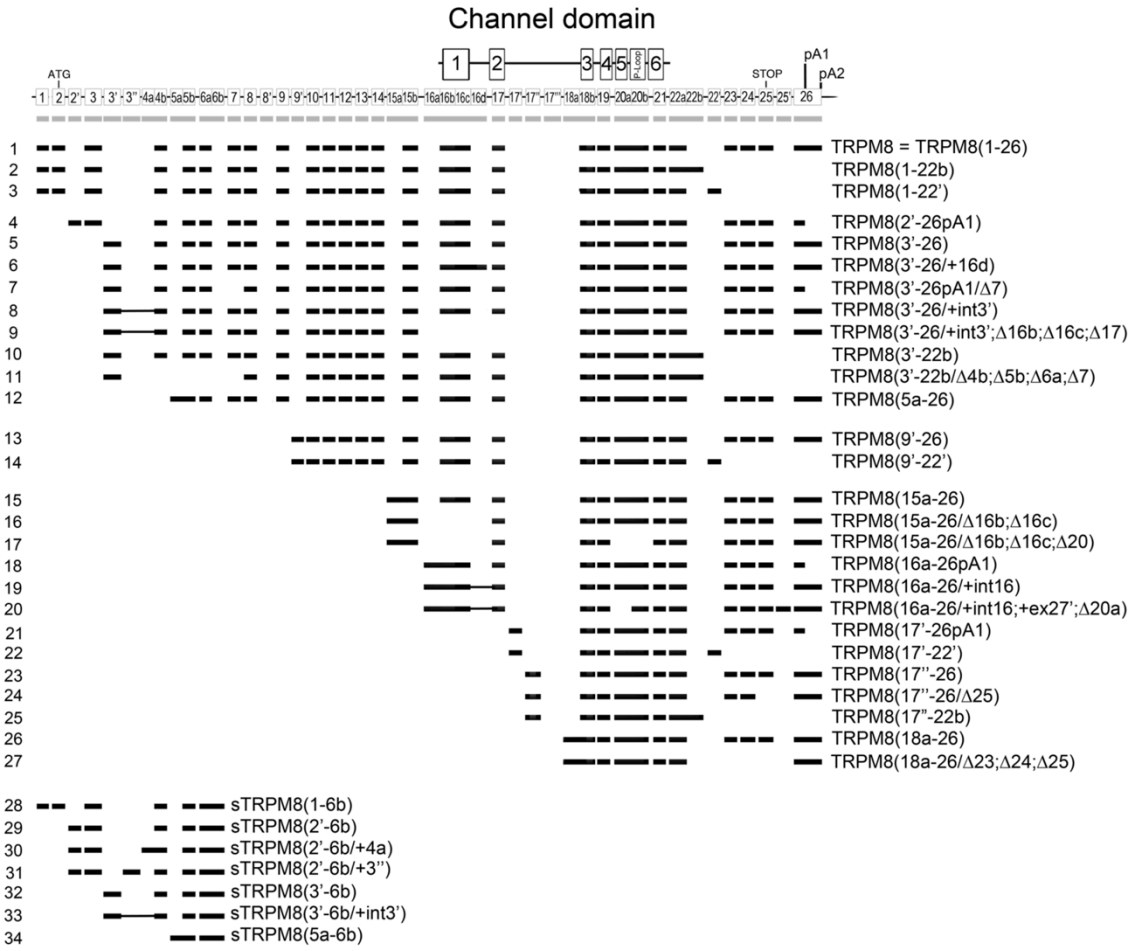

Figure 17 : schéma représentant les structures exoniques des ARNm TRPM8 alignées en phase avec les domaines protéiques : segments transmembranaires (1 à 6), pore (p-loop). Les codons ATG et STOP de la forme longue sont représentés ainsi que son site de polyadénylation (pA2). Notez qu'il existe, dans les ARN alternatifs, un site de polyadénylation plus amont que pA2 sur l'exon 26 (pA1). Les traits fins entre les exons représentent des introns complets retenus dans les ARN. Les ARN ont été dénommé selon le code suivant : (exon initiateur – exon terminateur / exons ajouté (+) ou supprimé (Δ) par épissage alternatif).

de TRPM8, dont la séquence classique (1) ainsi que le positionnement des segments transmembranaires (S1 à S6) et la boucle (p-loop) formant le filtre de sélectivité du canal.

Au niveau protéique, il est important de noter que :

- tous les ARNm ne codent pas de protéines (figure 18),
- il existe une redondance dans l'encodage de protéines par différent ARNm (figure 34).

Cette redondance peut permettre un contrôle différentiel de la transcription (promoteurs différents donc facteurs de transcription différents) servant à exprimer la même protéine à partir de réseaux de facteurs de transcription différents.

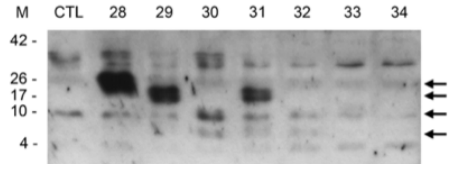

Figure 18 : western-blot montrant la détection d'isoformes TRPM8 étiquetées avec un épitope HA. Les numéros indiquent l'isoformes selon la nomenclature de la figure 33.

Comme nous le verrons plus loin dans ce manuscrit, certaines de ces isoformes sont des sous-unités régulatrices quand d'autres sont des canaux fonctionnels arborant une structure différente de celle du récepteur au froid et au menthol. Étant donné que certaines de ces isoformes sont des récepteurs au froid et possèdent une expression exclusive vis à vis de la forme longue (ex. l'épiderme exprime un forme courte mais pas la forme longue), je me suis demandé si ces isoformes étaient des produits de l'évolution de la forme longue. Il semble en effet tout à fait raisonnable de se dire que l'évolution a enrichi la famille des thermorécepteurs de nouveaux membres et de nouvelles fonctions au court du temps.

L'analyse phylogénétique est robuste quand elle est réalisée sur des séquences suffisamment longues et quand elle est fait sur la séquence protéique, ce qui permet de s'affranchir des variations de type neutre ou silencieuse. Le problème de notre étude était que tous les exons initiateurs et terminateurs de transcription sont des exons non codant dont la taille moyenne est de 120 pb. Autrement dit, la simple analyse par homologie de séquence est statistiquement bien trop faible pour pouvoir reconstruire avec assurance des ancêtres communs.

Nous avons donc opté pour une approche plus laborieuse et plus intégrée qui a consisté à analyser les facteurs suivants :

- la proportion de sites homologues (n sites conservés / N sites totaux),
- la conservation des sites accepteur et donneur d'épissage,
- la conservation des codons putatifs « start » et « stop » en phase avec le cadre de lecture de la séquence de TRPM8,
- la proportion de sites homologues sur le promoteur proximal,
- la vitesse d'évolution des séquences des exons ou promoteurs par rapport aux exons classique (exons de la forme longue de TRPM8). Par exemple, la vitesse d'évolution (longueur de la branche sur l'arbre phylogénétique) d'un exon du TRPM8 Homo sapiens depuis l'ancêtre commun Catarrhini (regroupe l'homme, le chimpanzé et le macaque dans notre analyse) est normalisé sur la vitesse d'évolution moyenne de l'ensemble des exons classiques (groupe interne). On peut aussi connaître le taux d'évolution du groupe externe, servant de référence. Dans l'exemple précédant, il s'agira de calculer le taux d'évolution de l'exon chez le macaque (Macaca mulata). Ceci nous permet de savoir si l'exon humain a subit une forte pression de sélection depuis un ancêtre déterminé et de le comparer à une espèce issue du même ancêtre mais ayant divergé de la branche des Homo. Un taux d'évolution très important dans le groupe externe et dans le groupe interne laisse penser que la séquence n'était pas conservée alors qu'un taux d'évolution important dans le groupe externe mais faible dans le groupe interne suggèrerait que la séquence humaine a été conservée depuis l'ancêtre commun mais que l'espèce externe l'a perdue.

L'analyse des exons classiques formant la forme longue du récepteur au froid et au menthol révèle par exemple que l'exon 1 et donc le promoteur de la forme humaine n'ont pas pu émerger avant l'apparition des Eutheria (Figure 19). L'exon 2, comprenant le codon start (ATG) de la protéine TRPM8 humaine, est conservé depuis les Eutheria, bien qu'il pouvait être utilisé chez les Theria mais sans l'exon 1 et sans le codon « start » de la séquence humaine. Les exons de 3 à 24 ont dans l'ensemble tous émergés chez les amniotes, voire plus probablement chez les Tétrapodes [42]. L'exon 25 codant le codon STOP semble,

comme l'exon 2, s'être stabilisé chez les Eutheria. Pour terminer, l'exon 26 est une séquence dérivée partagée de l'ancêtre Eutheria. En conclusion, on peut donc déjà observer que la forme longue de TRPM8, qui semble être apparue chez les Tétrapodes (-380 Ma), a en fait continué à évoluer à ses extrémités 5' et 3' en intégrant puis conservant de nouveaux sites initiateurs et terminateurs de traduction ainsi que des séquences terminales non traduites (UTR) 5' et 3'. La séquence humaine de TRPM8 est dérivée de l'évolution orthologue de l'ancêtre des Eutheria (-125 Ma).

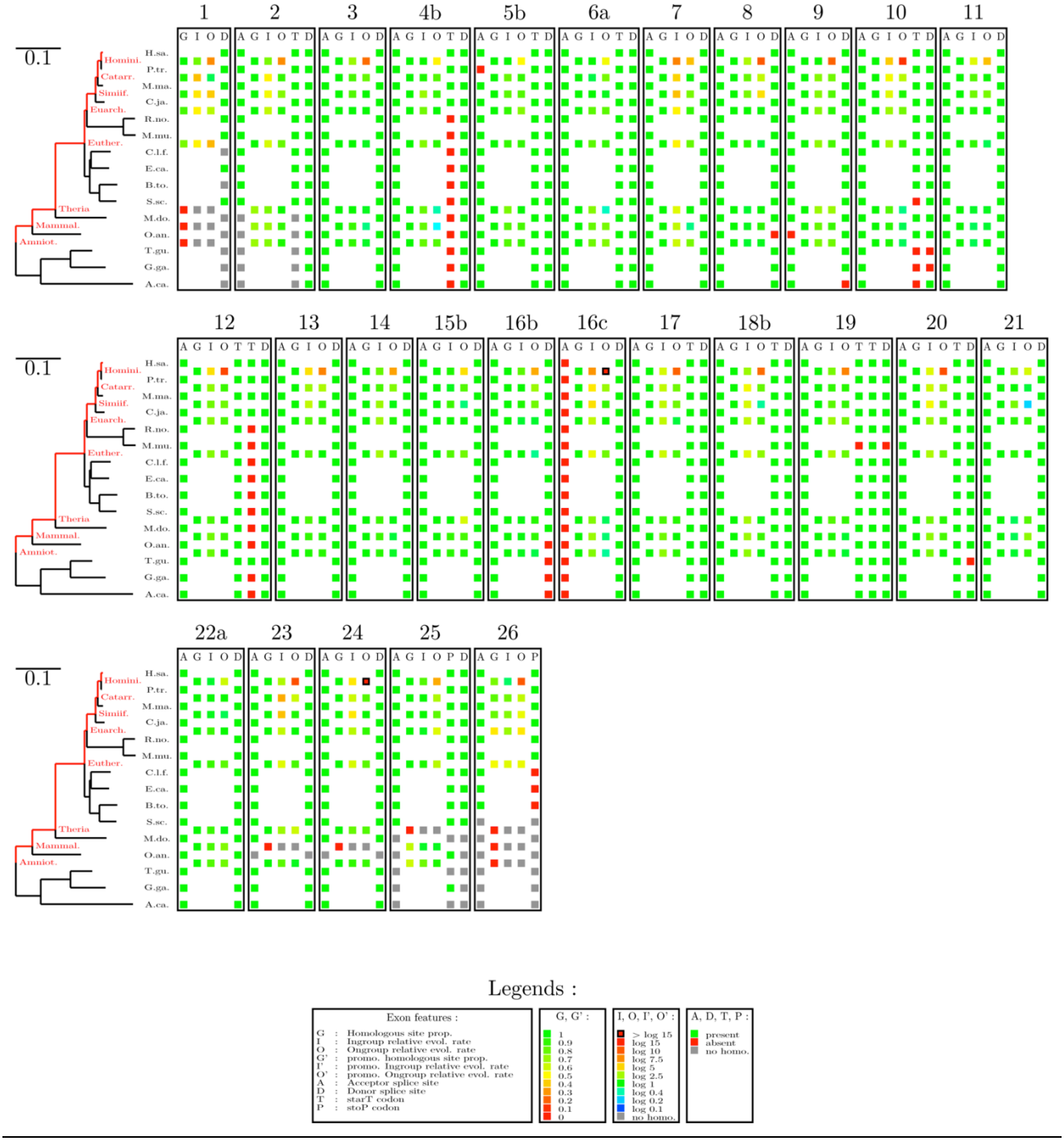

Figure 19 : analyse phylogénétique des exons TRPM8 classiques d'Homo sapiens. G & G' : proportion de conservation de la séquence exonique & promotrice. Pour chaque ancêtre commun, un taux d'évolution de l'exon humain est calculé en normalisant la vitesse d'évolution de l'exon par la vitesse d'évolution moyenne de l'ensemble des exons classiques (I ; ingroup ; tracé rouge depuis l'ancêtre) ou avec les espèces issues de cet ancêtre mais ayant divergé de la branche humain (O ; outgroup ; tracé noir depuis l'ancêtre). A & D : accepteur & donneur d'épissage. T & P : codon start & stop.

ACTIVITÉS DE RECHERCHE

Sans entrer ici dans une analyse exhaustive de notre travail, la divergence entre les exons alternatifs et les exons classiques (hors exon 1 et 26) est frappante comme nous pouvons l'observer sur la figure 20. Les exons 16a et 18a sont des dérivés partagés de l'ancêtre Eutheria alors que l'exons 17'' est dérivé partagé de l'ancêtre des primates Simiformes. L'exon 17' est lui conservé depuis les Eutheria, mais il a été perdu antérieurement par les rongeurs. Les exons terminateurs de transcription 6b et 22' sont des dérivés partagés des ancêtres primates Simiformes et Catarrhini, respectivement. On peut noter aussi que depuis l'ancêtre commun des hominidés, les exons 6b et 22' d'Homo sapiens ont peu évolué contrairement à ceux de Pan troglodytes (chimpanzé). Ces exemples démontrent bien que la conservation des exons alternatifs s'est effectué au long de la sélection des espèces et que bien qu'une séquence puisse avoir été sélectionnée et conservée, elle continue à évoluer et peu même disparaître chez certaines espèces.

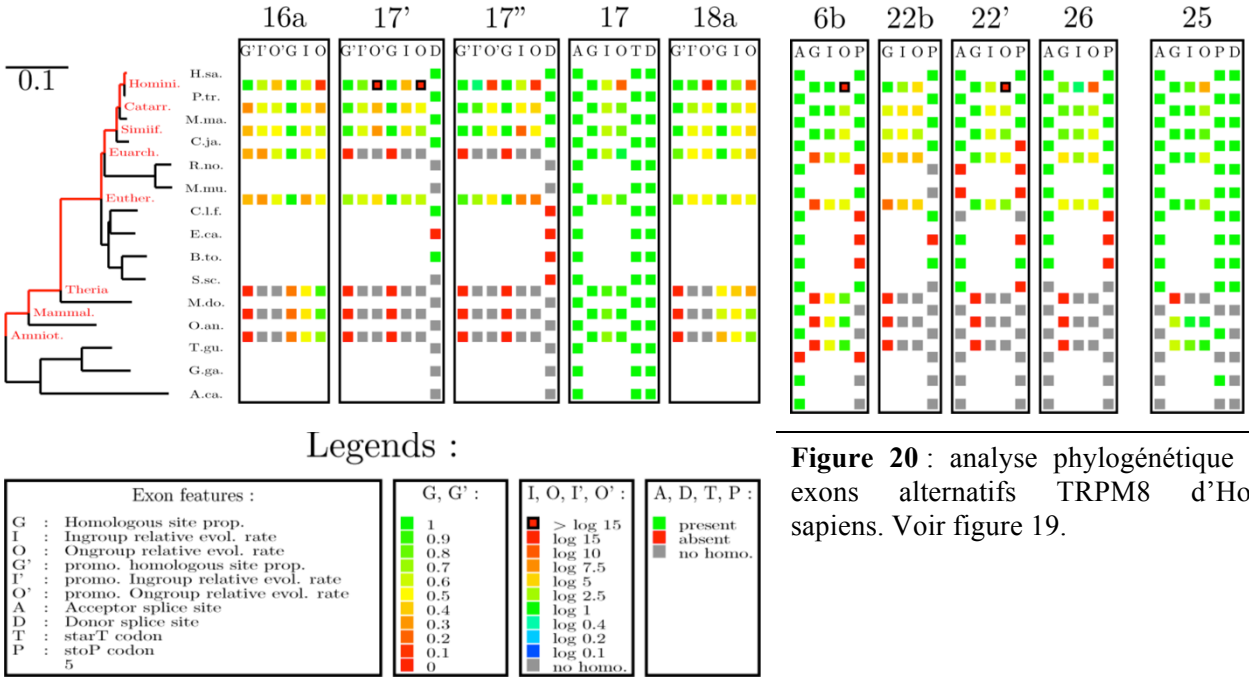

Figure 20 : analyse phylogénétique des exons alternatifs TRPM8 d'Homo sapiens. Voir figure 19.

La compilation de l'ensemble de ces analyses nous permet d'évaluer de quel ancêtre chaque isoforme humaine de TRPM8 est dérivée et donc d'estimer la période de conservation de la séquence. Dans cette optique, nous avons donner un ordre d'importance à chaque paramètre étudié : [donneur et accepteur d'épissage ; codon start/stop] > [homologie de séquence, taux d'évolution. Une fois la période de conservation d'un exon connu, nous avons recherché parmi chaque exon constituant un ARN alternatif, la période la plus récente de conservation. La distribution des séquences ARN du TRPM8 humain par date probable de conservation indique que sur les 33 ARN alternatif validés, 9 sont conservés depuis la divergence des Euthériens en Placentaires et Marsupiaux il y a environ -125 millions d'années (Figure 21).

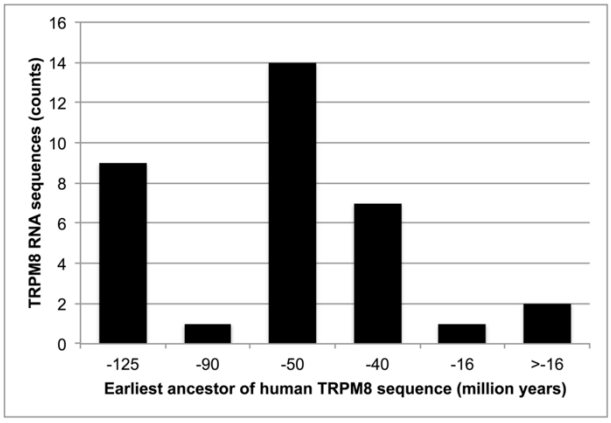

Figure 21 : distribution des 34 ARN de TRPM8 chez l'homme en fonction de leur période probable de conservation.

1 autre isoforme est dérivée partagée d'un ancêtre Euarchontoglires (-90 Ma) ayant divergé en Glires (rongeurs, lapins) et en Euarchontes (incluant les primates). 14 ARNm semblent conservés depuis la spéciation des primates Simiformes (-50 Ma), groupe excluant les primates Strepsirrhini (lémuriens). 7 ARN alternatifs du gène *trpm8* chez l'homme sont conservés depuis la divergence entre les primates de l'infra-ordre des Simiformes (-40 Ma) divisant les Platyrrhini et les Catarrhini (incluant les hominidés et les cercopithèques). Pour terminer, 1 ARN est dérivé partagé chez les grands singes (Hommes, chimpanzés, bonobos, gorille et orang-outang) et 2 ARN semblent ne pas avoir d'ancêtres communs avec les Hominidés ce qui suggère que les séquences sont probablement toujours en train d'évoluer.

Conclusion & Perspectives

Dans ce travail, nous avons, d'une part, mis évidence la diversité et la complexité des séquences produites par le gène humain *trpm8*. Nous avons montré qu'il existe une redondance dans l'encodage des protéines et que si la sélection naturelle a conservé ce système c'est raisonnablement parce qu'il offre un/des avantage(s). On peut, par exemple, suggérer que la mise sous contrôle de plusieurs ARN redondants par plusieurs promoteurs soit requis pour exprimer la protéine dans des tissus ne possédant pas les mêmes réseaux de facteur de transcription. On peut aussi envisager que ce système permette un contrôle quantitatif de cette protéine par le biais de n promoteurs générant des ARN caractérisés par des temps de demi-vie différents. Ainsi, la synthèse d'ARN redondants depuis différents promoteurs pourrait augmenter de un niveau de complexité la régulation de la quantité de la protéine finale.

D'autre part, nous avons démontré que l'évolution du gène humain du récepteur au froid est un processus assez récent mais continu. Bien qu'on assume que la forme longue du récepteur existe depuis au minimum l'apparition des tétrapodes (-380 Ma), la séquence humaine du gène *trpm8* codant l'ARN de la forme longue n'a commencé son évolution orthologue que depuis -125 Ma. Plusieurs processus d'exonisation (création d'un exon par mutation aléatoire de la séquence d'ADN) sont apparus et ont été sélectionnés au cours de l'évolution créant ainsi de nouvelles formes d'ARN. Il semblerait que cette évolution soit toujours un processus actif chez les hominidés puisque les séquences les plus jeunes ne sont peut être pas encore conservées.

La limite de ce type d'approche rétrograde dans laquelle on évalue le début d'une évolution orthologue de la séquence ancestrale est qu'elle ne permet pas d'infirmer l'existence d'isoformes protéiques. Il est en effet possible que, suite à une évolution paralogue, des ARN de structures légèrement divergentes puissent exister et coder des protéines similaires jouant un rôle biologique identique.

Production associée

Article 2 : Samuel Blanquart, Anne-sophie Borowiec, Philippe Delcourt, Martin Figeac, Morad Roudbaraki, Natalia Prevarskaya and Gabriel Bidaux. Article en cours de rédaction.

Nos travaux ont servi de base à la création du **consortium CG-ALCODE** :

Principal investigator (Inria): Samuel Blanquart, EPI BONSAI, Inria Lille Nord Europe / CRIStAL UMR 9189.

Principal investigator (partner): Anne Bergeron, professor, UQÀM Université du Québec à Montréal, Canada.

Other participants: LIRMM, UMR 5506 CNRS / Université de Montpellier 2.

Teams' web site: http://thales.math.uqam.ca/~cgalcode/

Encadrement, Collaborations et tâches associés

- Dr. Anne-sophie Borowiec, chercheuse post-doctorante,

Gestion complète du projet.

Collaboration Nationale et interdisciplinaire avec le Dr. Samuel Blanquart de l'INRIA.

III.1.2. TRPM8 : RELATION STRUCTURE-FONCTION DU PORE IONIQUE

Contexte

De nombreuses études combinant biologie moléculaire et patch-clamp ont permis de déterminer les propriétés électrophysiologiques du canal TRPM8 ainsi que certains de ses domaines fonctionnels. Mais peu de données sur la relation entre la conformation du canal et les résidus essentiels étaient connus.

Objectifs

Modéliser la structure tridimensionnelle du domaine ionique de TRPM8 et valider le modèle par une stratégie de mutagenèse couplée à l'électrophysiologie.

Résultats

Initialement basée sur la structure du canal potassique shaker, Kv1.2 [43], notre étude a été modifiée par la publication de la structure du canal TRPV1 réalisée par cryomicroscopie électronique à la fin de l'année 2013 [12], et ce pendant la première évaluation de notre article.

Pore ionique & filtre de sélectivité.

Le modèle calculé par nos collègues les Dr. Haider et Sgobba a mis en évidence l'existence d'un double anneau de résidus aspartate (DDDD918 et DDDD920) dans le pore du canal (Figure 22). Nos résultats ont démontré que seul l'anneau en position 920 jouait un rôle dans la sélectivité cationique du canal. L'anneau 918 jouant lui un rôle dans la stabilisation et la fermeture du pore. En outre, les différentes substitutions réalisées démontrèrent que la charge de l'anneau D920 était plus importante que la nature du squelette protéique formant la paroi du pore. Cette propriété de l'anneau d'aspartates de TRPM8 diverge de celle des canaux TRPV6 et TRPV5 chez lesquels la structure de la chaine latéral des résidus formant l'anneau est plus importante que la charge [44, 45]. Ceci peut être expliqué par le fait que TRPM8 est un canal cationique non-sélectif alors que TRPV5 et V6 sont des canaux très sélectifs à l'ion calcique. Ces derniers possèdent des résidus supplémentaires chargés négativement qui participent à leur sélectivité pour les cations divalents. A l'inverse, le canal TRPM4 est un canal perméable aux cations monovalents et possède les 2 anneaux d'acides aspartiques

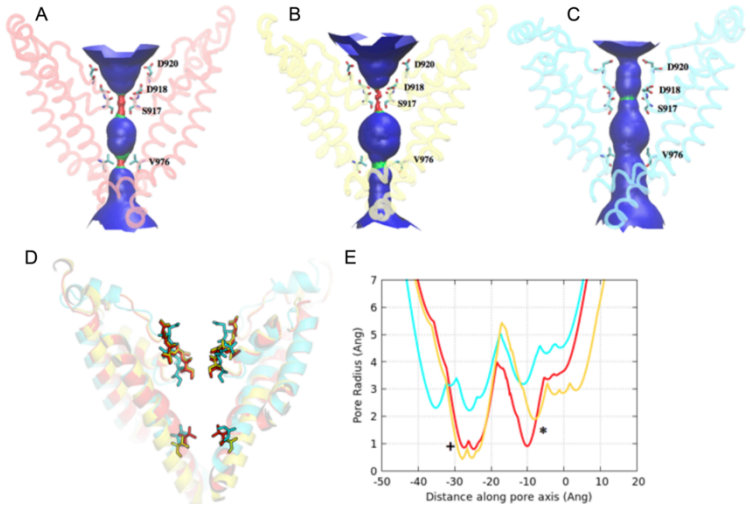

Figure 22 : filtre de sélectivité de TRPM8. (A) Les chaines des résidus D^{918} et D^{920} forme 2 anneaux chargés négativement dans la bouche du pore. Au fur et à mesure de l'ouverture du pore (B et C), les anneaux s'ouvrent pour former un conduit suffisant pour le passage des ions calciques hydratés (D). Résidus clefs formant le filtre de sélectivité, coupe transversale du pore. (E) Le pore du canal forme le filtre de sélectivité. Les couleurs indiquent la taille du pore compare à la taille d'une molécule d'eau: rouge (<), vert (~) et bleu (>). (C) Profil d'énergie Poisson-Boltzmann tous les 1 Å le long de l'axe du pore

comme TRPM8. Néanmoins, contrairement à TRPM8, les 2 anneaux semblent impliqués dans la sélectivité de TRPM4 [46].

P-loop et activation par le menthol et le froid.

Une autre caractéristique intrigante qu'a révélée notre étude concerne le rôle essentiel de la tyrosine 908 dans l'activation du canal par le froid et le menthol. De nombreuses études réalisées par mutagenèse dirigée ont mis en évidence le rôle de résidus allant du segment S2 à la boucle Carboxy-terminal de TRPM8 dans la sensibilité au menthol et à l'iciline (pour une synthèse, lire [47]). Une autre étude a démontré que la sensibilité au froid était principalement portée par un domaine de la boucle Carboxy-terminale [48]. Aucune donnée sur l'implication de résidus du pore n'était connue pour TRPM8, mais une étude avait démontré le rôle de la p-hélice du pore dans l'activation du thermorécepteur à la chaleur, TRPV1, par le camphre [49]. En effet, l'interaction du camphre avec TRPV1 induirait une rotation de la p-hélice, déclenchant une ouverture du pore ionique de manière indépendante de l'activation par la chaleur. Notre étude montre que la suppression de la chaine latérale du résidu 908 supprime l'activation par le froid et le menthol. Sa substitution par la phénylalanine n'induit pas de changement notable, suggérant que c'est la nature aromatique de la tyrosine plutôt que le groupement hydroxyle qui est impliquée dans la fonction. La substitution de la tyrosine 908 par le tryptophane supprime presque totalement l'activation par le froid et le menthol, confirmant que le type de noyau aromatique soit essentiel. La tyrosine 908 forme en fait des empilements pi (pi stacking) avec les noyaux aromatiques de la tyrosine 905 et la phénylalanine 912. La suppression de la Y905 abolissant complétement le fonctionnement du canal.

Dans le but d'évaluer statistiquement, la nature dominante ou mineure de la mutation, j'ai proposé une analyse basée sur la combinatoire en assumant que la tétramérisation du canal se fait comme un processus aléatoire, incorporant les monomères de manière stochastique. En co-transfectant un plasmide sauvage et un plasmide mutant à un ratio [1 :3], la distribution attendue des tétramères est donnée dans la figure 23.

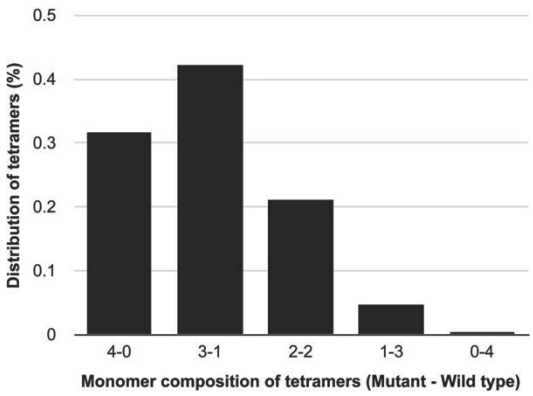

Figure 23 : fréquence d'assemblage des différents tétramères wt/mutant TRPM8 dans une cellule transfectée par un ratio 1/3 de plasmide wt/mutants.

Cette analyse nous a permis de mettre en évidence que les mutations de l'anneau D920 sont de type « fortes » ou dominantes, c'est à dire que la mutation d'un des quatre résidus de l'anneau suffit à obtenir la perte de densité maximale du courant. A l'inverse, la mutation du résidu Y908 est du type « faible » puisque l'effet maximal n'est atteint que quand on favorise les homotétramères mutants.

Pour terminer, nous nous sommes intéressés aux liaisons inter-monomères afin d'évaluer leur importance dans la stabilité du canal. En effet, des études antérieures s'étaient opposées sur le rôle exclusif des boucles amino- et carboxy-terminales dans la tétramérisation. Comprendre le rôle respectif des boucles cytosoliques et des liaisons inter-monomériques du domaine ionique est un point capital pour prédire la stabilité des isoformes tronquées comme nous le verrons plus loin dans ce manuscrit. Nos travaux montrent

que quelques résidus sélectionnés sur la base du modèle structural se révèlent essentiels à la bonne conformation et donc à l'activité du canal. Néanmoins, nos expériences de biotinylation de surface et les co-transfection avec le plasmide sauvage montrent respectivement que ces mutants sont adressés normalement à la membrane plasmique et qu'ils sont au moins partiellement actifs. Ceci suggère donc que la mutation d'un seul résidu ne compromet pas la tétramérisation en elle-même mais interfère avec la bonne conformation de la protéine, diminuant son temps d'ouverture.

Conclusion & Perspectives

En conclusion, ce travail a démontré que le filtre de sélectivité de type cationique non-sélectif de TRPM8 est principalement dû à l'anneau de résidus D920. Nous avons aussi montré que la compromission de l'assemblage des tétramères ne peut se faire sans altérations majeures du domaine ionique, ce qui laisse à penser que les isoformes tronquées du canal TRPM8 pourraient être des canaux fonctionnels. Pour terminer, nous avons isolé un résidu clef de l'activation par le froid et le menthol, Y908, présent dans l'hélice alpha de la boucle p. Ce travail permet d'expliquer structurellement pourquoi les modèles électrophysiologiques de « gating » du canal TRPM8 considéraient que les mécanismes d'activation par le menthol et par l'iciline sont 2 mécanismes distincts [50]. D'autre part, les modes d'activation par le froid, le menthol, la voltage-dépendance sont partiellement différents mais cumulatifs [51] et ont comme principale caractéristique de diminuer la durée des états de fermeture à constante longues [52]. Comme il a été montré que l'activation par le menthol implique de nombreux résidus répartis du S4 à la boucle carboxy-terminale et comme l'activation par le froid requière aussi un domaine du C-terminus, on peut envisager que l'activation du canal TRPM8 par le froid et le menthol requièrent un certains nombre de changements conformationnels impliquant les segments transmembranaires, la boucle carboxy-terminale et le filtre de sélectivité.

Production associée

Article 3 (annexes) : **Gabriel Bidaux**, Miriam Sgobba, Loic Lemonnier, Anne-Sophie Borowiec, Lucile Noyer, Alexander V Zholos, Shozeb Haider ; Functional and Modelling Studies of the Transmembrane Region of the TRPM8 channel ; en révision dans *Biophysical Journal*.

Article 4 : José A. Fernández, Roman Skryma, **Gabriel Bidaux**, Karl L. Magleby, C. Norman Scholfield, J. Graham McGeown, Natalia Prevarskaya, and Alexander V. Zholos; Voltage- and cold-dependent gating of single TRPM8 ion channels; *J Gen Physiol*.

Encadrement, Collaborations et tâches associés

Collaboration internationale avec le Dr Shozeb HAIDER (UCL School of Pharmacy, London, UK) et le Prof. Alexander Zholos (Educational and Scientific Centre "Institute of Biology" Taras Shevchenko Kiev National University, Ukraine).

ACTIVITÉS DE RECHERCHE

III.1.3. DIVERSITÉ DES ISOFORMES DE TRPM8 DANS LA PROSTATE

Contexte

La prostate est un petit organe situé en dessous de la vessie et devant la vésicule séminale. Cette glande exocrine, appartenant à l'appareil génital masculin, englobe le canal éjaculateur et la partie supérieure de l'urètre. La prostate est composée de deux couches histologiques principales : le stroma fibromusculaire et le tissu glandulaire consistant en un épithélium pseudo-stratifié incluant cellules épithéliales et cellules neuroendocrines (figure 24). Ces deux tissus sont séparés l'un de l'autre par une lame basale (figure 2A). La partie glandulaire de la prostate est le siège d'une sécrétion exocrine intense représentant environ 30% du sperme. Les composés du liquide prostatique sont nombreux; parmi ceux-ci, au moins le zinc, l'antigène spécifique de la prostate (PSA) et la neutral α-glucosidase interviennent directement dans l'activation des spermatozoïdes [53, 54].

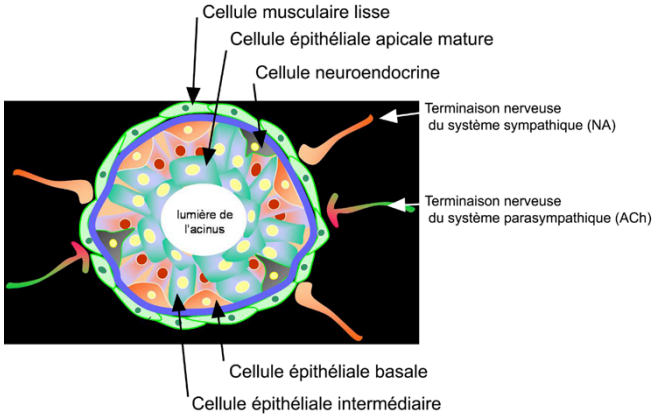

Figure 24 : représentation schématique de la structure cellulaire d'un acinus prostatique. À noter : le stroma (zone noire) est formé d'un mélange de fibroblastes, de cellules musculaires lisses et de fibres protéiques de type collagène.

Pathologie.

L'adénocarcinome de la prostate est la principale pathologie mortelle affectant cet organe. Avec plus de 40 309 cas déclarés et environ 10 004 décès par an en France [55]. L'adénocarcinome de la prostate est la seconde cause de mortalité par cancer chez l'homme après le cancer du poumon. Initialement androgéno-dépendant, l'adénocarcinome peut devenir androgéno-indépendant suite à un traitement antihormonal. Le gène *trpm8* est surexprimé dans l'adénocarcinome de la prostate [56-59]. Plusieurs brevets ont été déposés au fil des ans dans le but de protéger l'utilisation de TRPM8 comme cible thérapeutique. Il existe donc un intérêt particulier des compagnies pharmaceutiques, mais rien de probant n'a pour l'instant était publié. En outre, le rôle de ce thermorécepteur dans la prostate reste inconnu.

Objectifs

Caractériser la régulation de l'expression et de l'activité de TRPM8 dans la physiologie et la physiopathologie de la prostate.

Résultats & Conclusion

RÉSUMÉ DES TRAVAUX DE THÈSE ET DE POST-DOCTORAT (2003-2009)

Le canal TRPM8 fut cloné en 2001 à partir d'un échantillon d'ADNc de prostate humaine et démonstration fut faite de sa surexpression dans le PCa. Nous avons démontré que la transcription du gène *trpm8* est sous le contrôle du récepteur des androgènes (Bidaux *et al*, ERC, 2005). Nous avons donc stipulé que la perte ou la forte diminution d'expression dans des biopsies pouvait être révélateur de l'apparition de l'hormono-indépendance. Nous avons ensuite démontré que la forme classique de TRPM8 fonctionne sur le plasmalemme mais aussi dans les membranes du réticulum endoplasmique (RE) [41]. Nous avons poursuivi en démontrant l'existence, sans parvenir à la cloner, d'au moins une isoforme de TRPM8. Nous avions démontré que cette forme est tronquée et que sa localisation est restreinte aux endomembranes. En outre, nous avons mis en évidence son expression dans les cellules épithéliales intermédiaires n'exprimant pas le récepteur aux androgènes [40].

Ce travail a été complété par plusieurs collaborations internes dans lesquelles nous avons :

- réalisé une étude pharmacologique démontrant l'activation de TRPM8 par une classe de molécules dérivées de l'iciline, les WS [51],
- caractérisé une voie d'activation du canal TRPM8 par la phospholipase A2 indépendante du calcium [60],
- démontré l'inhibition du canal TRPM8 par la voie du récepteur alpha 2 adrénergique [61].

Production associée

Article 5 : **G Bidaux**, M Roudbaraki, C Merle, A Crépin, P Delcourt, C Slomianny, S Thebault, J - L Bonnal, M Benahmed, F Cabon, B Mauroy, N Prevarskaya (2005). Evidence for specific TRPM8 expression in human prostate secretory epithelial cells: functional androgen receptor requirement. *Endocr Relat Cancer*.

Article 6 : Stéphanie Thebault*, Loïc Lemonnier*, **Gabriel Bidaux***, Matthieu Flourakis, Alexis Bavencoffe, Dimitri Gordienko, Morad Roudbaraki, Philippe Delcourt, Yuri Panchin, Yaroslav Shuba, Roman Skryma, Natalia Prevarskaya (2005). Novel role of cold/menthol-sensitive transient receptor potential melastatine family member 8 (TRPM8) in the activation of store-operated channels in LNCaP human prostate cancer epithelial cells. *J Biol Chem*.

Article 7 : **Gabriel Bidaux***, Matthieu Flourakis*, Stéphanie Thebault, Alexander Zholos, Benjamin Beck, Dimitra Gkika, Morad Roudbaraki, Jean-Louis Bonnal, Brigitte Mauroy, Yaroslav Shuba, Roman Skryma, Natalia Prevarskaya (2007). Prostate cell differentiation status determines transient receptor potential melastatin member 8 channel subcellular localization and function. *J Clin Invest*.

Article 8 : Benjamin Beck, **Gabriel Bidaux**, Alexis Bavencoffe, Loic Lemonnier, Stephanie Thebault, Yaroslav Shuba, Greg Barrit, Roman Skryma, Natalia Prevarskaya (2007). Prospects for prostate cancer imaging and therapy using high-affinity TRPM8 activators. *Cell Calcium*.

Article 9 : A Bavencoffe, D Gkika, A Kondratskyi, B Beck, A S Borowiec, **G Bidaux**, J Busserolles, A Eschalier, Y Shuba, R Skryma, N Prevarskaya (2010) The transient receptor potential channel TRPM8 is inhibited via the alpha 2A adrenoreceptor signaling pathway. *J Biol Chem*.

ACTIVITÉS DE RECHERCHE

PETITES ISOFORMES DE TRPM8

Contexte

Dès mon stage de DEA (2002-2003), je me suis passionné pour l'existence d'ARN alternatifs de TRPM8 et je clonais 2 petits ARN s'arrêtant à l'exon 7. Il fallut un certains nombre d'années pour que nos compétences techniques soient suffisantes pour réussir à étudier ces petites isoformes non-canal (sM8) car contrairement à leurs homologues du canal TRPC2 se comportant comme des dominant négatif [15], les sM8 ont une activité beaucoup plus ciblée et parcimonieuse.

Objectifs

Nous avons donc entrepris d'étudier les sM8 par des approches multimodales avec pour objectif de caractériser leurs effets sur l'activité de la forme longue du canal TRPM8

Résultats

Nos études ont abouti en 2011. Nous avons démontré que l'ARN sM8α codent deux protéines de 6 (sM8-6) et 18 kDa (sM8-18), alors que l'ARN sM8β code, de manière redondante à sM8α, la forme de 6 kDa. Ces 2 protéines se comportent comme des sous-unités régulatrices du canal TRPM8 en diminuant sa sensibilité au froid et au menthol par une modification de sa voltage-dépendance. En effet, bien que n'ayant jamais réussi à caractériser une interaction entre sM8 et TRPM8 par une approche biochimique de co-immunoprécipitation, nous avons démontré l'existence d'un signal FRET spécifique en cellules vivantes. Ceci suggère que les conditions de l'IP étaient probablement trop astringentes. La contrainte majeure étant probablement la nécessité de réaliser l'IP sur glace ou à 4°C. En effet, nous avons démontré que l'interaction entre sM8 et TRPM8 s'affaiblit quand on diminue la température d'incubation des cellules vivantes de 37°C à 21°C [62]. Cette dépendance à la température et cette faible affinité d'interaction expliquent pourquoi ces sM8 ne se comportent pas comme des dominants négatifs.

Les expériences d'électrophysiologie en configuration cellule entière ont mis en évidence un changement de la voltage-dépendance du canal TRPM8 en présence de l'isoforme sM8-6. Ce décalage de la voltage-dépendance induit une moindre sensibilité au froid et au menthol. Ainsi, on peut observer sur la figure 25 que l'équilibre entre les constantes d'ouverture (α) et de fermeture (β) du canal est atteint à 30,95°C pour le canal seul, contre 27,30°C en présence de l'isoforme sM8-6. La conséquence directe en est que pour atteindre un même niveau d'ouverture du canal en présence de sM8-6, il faut abaisser la température plus fortement.

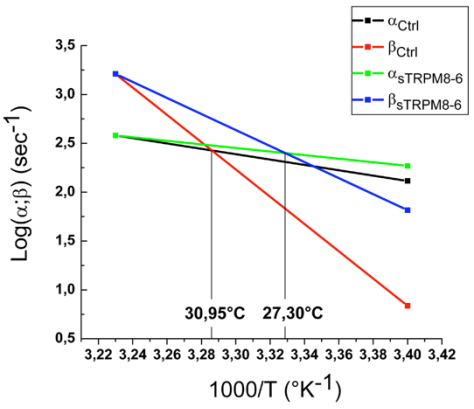

Figure 25 : graphique reportant la valeur des vitesse de transition ouvert-fermé (α) et fermé-ouvert (β) en fonction de le température .

L'explication mécanistique tient au fait que d'un point de vue thermodynamique, on peut considérer que le canal TRPM8 voit son entropie augmenter quand on abaisse la température ce qui provoque des transitions conformationnelles impliquant plusieurs domaines de la protéine qui aboutissent à l'ouverture

transitoire du canal. Les enregistrement de l'activité du canal unitaire montre des ouvertures très brèves que des durées longues comme le font certains canaux (ex : BK). Le canal TRPM8 est un système non-isolé qui mesure la diminution d'entropie du système pour voir la sienne augmenter (Q_{10}=9.4 soit environ 173 kJ.mol^{-1}, contre Q_{10}=1 environ de pour la dénaturation thermo-induite des protéines). Quand son entropie augmente car il émet de la chaleur pour faire baisser son entropie, il oscille donc constamment entre état ouvert et état fermé. Quand la température remonte au dessus de 35°C, l'entropie du milieu augmente et celle du canal décroit de manière stable permettant une stabilisation de l'état fermé.

D'un point de vue biophysique, on traduit cela par le fait que l'ouverture du canal induit une transition des états fermés à longues constantes de temps vers des états fermés à courtes constante de temps [52]. Notre collaboration avec l'équipe du Prof Alexander Zholos, à Belfast à cette époque, démontra que l'isoforme sM8-6 stabilise le canal TRPM8 en position fermé (figure 26) en renforçant les états fermés caractérisés par des constantes de temps longues [63]. Autrement dit, le canal voit sa capacité de senseur entropique réduite.

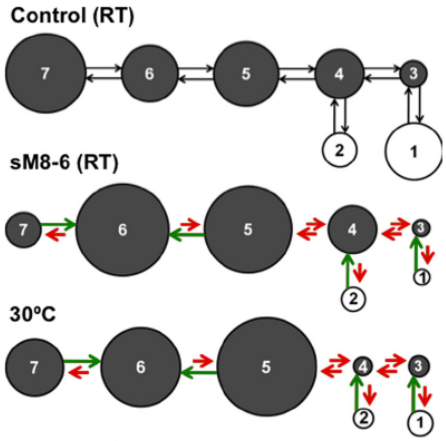

Figure 26 : représentation schématique des variations des constantes de temps de fermeture (cercles pleins) et d'ouverture (cercles vides) du canal TRPM8 à 21°C (RT), 30°C et à 21°C en présence de l'isoforme sM8-6.

Du point vue structural, nous avons alors démontré que cette stabilisation de l'état fermé du canal TRPM8 était corrélée à la stabilisation d'une conformation « serrée » du tétramère formé par les boucles carboxy-terminales du canal. À l'opposé, l'ouverture du canal par le froid et le menthol requière une relaxation de ce C-terminus tétramérique.

De 2009 à 2011, comme décrit précédemment, nous avons cloné un grand nombre d'isoformes de TRPM8 dont de nouvelles sM8. Comme certaines d'entres elles étaient exprimées dans la prostate cancéreuse, de manière concomitante à des formes « canal », nous avons évalué l'impact de la dérégulation de l'expression des sM8 sur les cellules cancéreuses.

Comme reporté dans l'**article 11** en annexe, nous avons développé une méthode de destruction soustractive des isoformes par groupe, basée sur l'utilisation de petits ARN interférents (Voir figure 27).:

[1] TRPM8 seul

[2] sM8 + TRPM8

[3] TRPM8-I + TRPM8

ACTIVITÉS DE RECHERCHE

Ce travail a révélé que la destruction de la forme longue de TRPM8 ou la destruction concomitante de cette dernière et des isoformes canal n'avait que peu d'effet sur la croissance des cellules androgéno-réfractaires LNCaP C4-2b. Au contraire, la destruction des sM8 (concomitant à la destruction de la forme longue à cause de leur forte homologie de séquence) entraine une mort par apoptose de 20 à 25% des cellules après 3 jours et une induction de $p21^{waf1}$, un inhibiteur du cycle cellulaire, dans environ 20% des cellules survivantes. Au niveau de la population, l'impact est un effet cytostatique important de la croissance cellulaire. Nos résultats mettent aussi en évidence une corrélation positive entre le niveau d'expression de l'ARN sM8(2'-6b) (équivalent à sM8α dans l'article précédant) et le taux d'apoptose. Ainsi lorsqu'on augmente le niveau d'expression de cet ARN d'un facteur 10 ou 800, on observe une augmentation de l'apoptose de 3 et 8 fois respectivement suite à la destruction des sM8 par le siRNA siM8-6a. Par homologie, lorsqu'on augmente de 6 fois l'expression de l'ARN (3'-6b), codant pour sM8-6, le taux d'induction de p21 augmente de 9 à 10 fois dans les cellules préalablement transfectées avec le siM8-6a. Autrement dit, il existe une spécificité dans l'induction de l'apoptose et de p21, les 2 mécanismes étant dépendants de la destruction d'une isoforme sM8 différente.

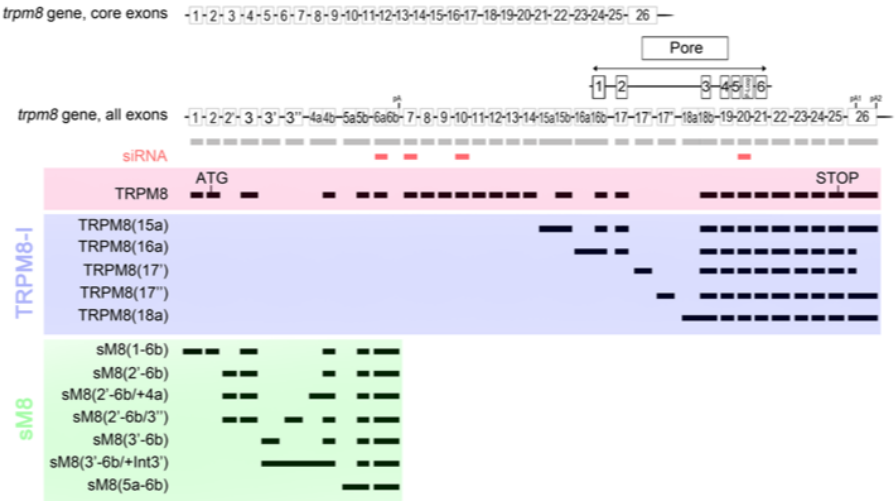

Figure 27 : rappel sur la structure des isoformes de type sM8 (surlignées en vert) en comparaison de la forme longue de TRPM8 (surlignée en rouge) et des isoformes-canal de 36 kDa (TRPM8-I, surlignées en bleu). Les barres oranges en face de « siRNA »reportent les exons ciblés par les différents ARN interférents utilisés.

Les mécanismes induisant ces réponses suite à la suppression des sM8 sont diverses. Nous avons par exemple démontré que la suppression ou l'inhibition concomitante des isoformes canal de TRPM8 et des sM8 abolit aussi bien l'apoptose que l'induction de p21. De plus, l'expression de l'ARN sM8α est corrélée négativement à l'expression des isoformes canal de TRPM8 et aux stocks de Ca^{2+} réticulaire. Bien que les différents effets observés semblent s'agencer de manière non-linéaire, il parait évident d'après nos données que l'apoptose induite par la suppression des sM8 implique une dérégulation de l'activité des isoformes canal TRPM8 et de l'homéostasies calcique réticulaire.

Conclusion & Perspectives

En conclusion, nous avons cloné et caractérisé de petites isoformes et ARN alternatifs de TRPM8 qui jouent le rôle de sous-unité régulatrices de la forme longue de TRPM8, et probablement des isoformes canal. Nos travaux partant de la biophysique et la biochimie du canal et de ses isoformes nous a entrainé vers une étude plus translationnelle.

En effet, plusieurs articles avaient évoqué de manières peu convaincantes l'utilisation de TRPM8 comme cible thérapeutiques dans le cadre du traitement du cancer de la prostate [64, 65]. Dans notre dernier travail, nous montrons que le ciblage des sous-unités régulatrices du canal, induisant une modification de l'activité des formes canal et de l'homéostasie calcique réticulaire, provoque un effet beaucoup plus important sur l'apoptose et la prolifération des cellules cancéreuses de la prostate que la destruction des formes canal (Figure 28).

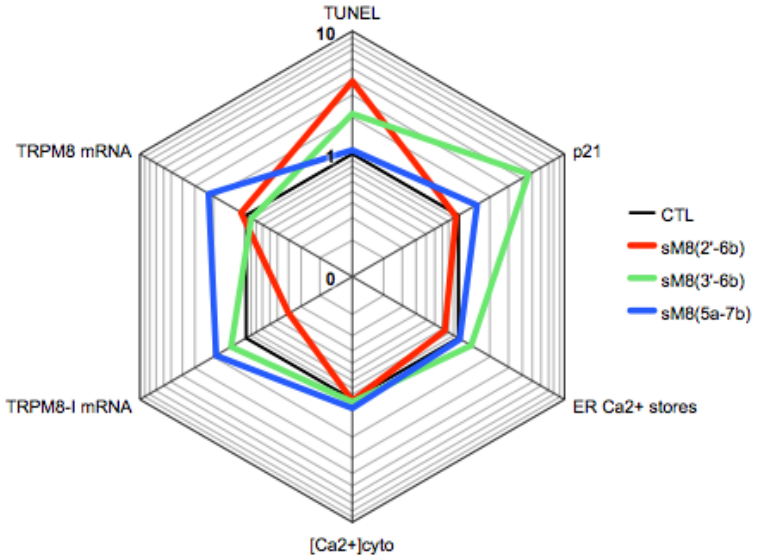

Figure 28 : schéma représentant la complexité des connexions entre l'expression des isoformes de TRPM8, l'apoptose, l'induction de p21 et l'homéostasie calcique dans les cellules cancéreuses de la prostate.

Ce travail pourrait aider à changer de paradigme en focalisant l'attention des recherches sur des moyens de déstabiliser l'activité des canaux ioniques plutôt que de les inhiber ou les activer directement. Néanmoins, une recherche plus aboutie permettrait de mieux comprendre les cascades de dérégulation conduisant de manière non-linéaire aux phénotypes observés.

Production associée

Article 10 : **Gabriel Bidaux***, Benjamin Beck*, Alexander Zholos, Dmitri Gordienko, Loic Lemonnier, Matthieu Flourakis, Morad Roudbaraki, Anne-Sophie Borowiec, Jose Fernández, Philippe Delcourt, Gilbert Lepage, Yaroslav Shuba, Roman Skryma, Natalia Prevarskaya (2011) Regulation of transient receptor potential melastatin 8 (TRPM8) channel activity by its short isoforms. *J. Biol. Chem*.

Article 11 : Jose A Fernández, Roman Skryma, **Gabriel Bidaux**, Karl L Magleby, C Norman Scholfield, J Graham McGeown, Natalia Prevarskaya, Alexander V Zholos (2011). Short isoforms of the cold receptor TRPM8 inhibit channel gating by mimicking heat action rather than chemical inhibitors. *J. Biol. Chem*.

Article 12 (annexes) : **Gabriel Bidaux**, Anne-Sophie Borowiec, Loïc Lemonnier, Charlotte Dubois, Céline Schulz, Fabien Vanden Abeele, Gilbert Lepage, Emilie Desruelles, Philippe Delcourt, Christian Slomianny, Morad Roudbaraki, Jean-Louis Bonnal, Brigitte Mauroy, Pascal Mariot, and Natalia Prevarskaya. Soumission *Cancer Research*.

Encadrement, Collaborations et tâches associés

- Dr. Anne-sophie Borowiec, chercheuse post-doctorante,
- Mr Olivier Guénard, Master 2 recherche et 1ère année de thèse,
- Mm Céline Schulz, Master 1.

Gestion du projet.

Financement Association pour la Recherche sur les tumeurs de la Prostate obtenu pour la réalisation de l'étude portant sur la destruction des sM8.

TRPM8-36 & MAM

Contexte

En 2007, nous avons publié un article décrivant l'expression de TRPM8 au cours de la différenciation des cellules épithéliales de prostate et au cours de leur cancérisation. Dans ce travail, nous détections, sans les avoir clonées, des isoformes canal de TRPM8 actives sur les membranes du RE et démontrions que la forme longue de TRPM8 était fonctionnelle aussi bien sur la membrane plasmique que sur le RE.

Objectifs

Suite aux travaux précédemment décrits, nous avons entrepris des travaux afin de cloner les isoformes de TRPM8 exprimées au niveau des membranes du RE.

Résultats

Après avoir mis au point la technique de RACE-PCR et au clonage massif des ARN alternatifs de TRPM8, l'analyse et le regroupement des isoformes par classes a vu l'émergence d'un groupe fortement représenté dans les cellules de la prostate : les isoformes de 36kDa. Contrairement à la forme longue de TRPM8, ces isoformes ne possèdent au maximum que 4 segments transmembranaires puisqu'elles ne possèdent pas les séquences codant le S1 et le S2. Comme publié précédemment [40], ces isoformes sont exprimées plus fortement que la forme longue dans les cellules primaires de prostate humaine cancéreuses alors que dans les cellules normales, la forme longue est prépondérante.

En utilisant des approches de biochimie et de microscopie photonique et électroniques, nous avons démontré que les TRPM8-36 sont exprimées dans des nanodomaines du réticulum appelés Mitochondria Associated Membrane, MAMs (Figure 29).

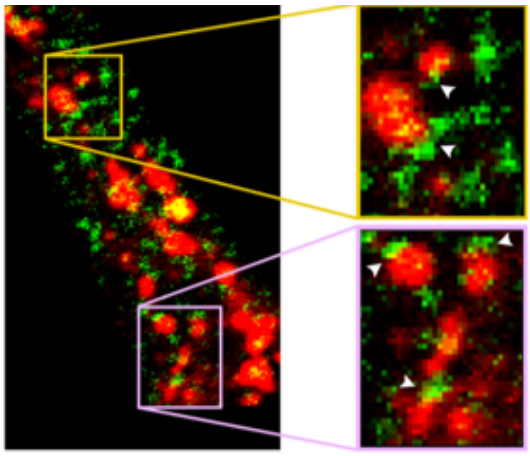

Figure 29 : immuno-marquage de TRPM8 (vert) et ATP synthétase (rouge) dans des cellules LNCaP. Tête de flèches : MAM.

Une collaboration fructueuse avec mes collègues électrophysiologistes Dr Dmitri Gordienko et George Shapovalov a permis de démontrer que ces isoformes sont des canaux fonctionnels dans le RE. A cette fin, nous avons aussi développé une stratégie de préparation des protéines endogènes des MAMs et leur intégration dans des GUV (Giant Unilamellar Vesicules) permettant de réaliser des expériences de Patch-clamp sur des protéines-canal intracellulaires, natives et conformées. Ce travail fait l'objet d'un dépôt de brevet.

Pour terminer cette étude, j'ai utilisé la technique de FRET-FLIM dans l'équipe du Dr. Laurent Héliot, pour mesurer la concentration basale de calcium dans le RE et les mitochondries grâce au biosenseur Cameleon adressé spécifiquement dans l'un des 2 organites.

Cette approche ratiométrique permet une mesure directe du taux de calcium dans les organites sans dépendance à la concentration de la sonde. J'ai ainsi démontré que la suppression des canaux TRPM8-36 entraine une augmentation de la concentration de Ca^{2+} libre réticulaire corrélée à une diminution de la concentration de calcium libre mitochondrial dans les cellules cancéreuses de la prostate (Figure 30). Ces résultats démontrent bien le rôle fonctionnel des TRPM8-36 dans le transfert de Ca^{2+} du RE vers les mitochondries et alors que la forme longue est principalement adressée à la membrane plasmique où elle fait entrée du Ca^{2+} depuis la matrice extracellulaire.

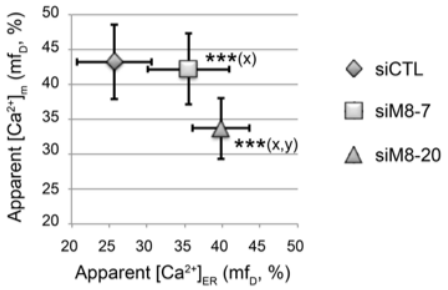

Figure 30 : concentration moyenne apparente de Ca^{2+} dans le RE et les mitochondries des cellules LNCaP C4-2b contrôles (siCTL), sans forme longue de TRPM8 (siM8-7), sans TRPM8-36 et TRPM8 (siM8-20).

Conclusion & Perspectives

La structure des différentes classes de TRPM8 régit donc probablement leur localisation subcellulaire et leur associe donc un signal calcique spécifique. Ce dernier relai une information jusqu'à un groupe d'effecteurs, ce qui génère une réponse biologique spécifique. Dans le cas des isoformes TRPM8-36, le signal calcique se propage jusqu'aux mitochondries. D'une part, les MAM étant des nanodomaines hautement actifs dans le métabolisme des lipides et des stéroïdes [66-68], et le Ca^{2+} étant un cofacteur de nombreuses enzymes, il est probable que les isoformes de TRPM8 participent à la modulation de ces voies anaboliques par le contrôle fin de la quantité de Ca^{2+} libre dans le cytosol à l'interface mitochondrie-RE. D'autre part, dans les mitochondries, il est bien documenté que le Ca^{2+} en provenance du RE sert à réguler l'activité de la pyruvate déshydrogénase, de l'isocitrate déshydrogénase et de l'oxoglutarate déshydrogénase [69-71]. Il est donc possible que l'activité des isoformes TRPM8-36 participent à la modulation de la bioénergétique mitochondriale. En toute vraisemblance, on peut même spéculer sur le fait que ces mécanismes soient aussi possibles dans d'autres types cellulaires et tissus dans lesquels les isoformes TRPM8-36 sont exprimées.

Production associée

Article 13 (annexes) : **Gabriel Bidaux***, Dmitri Gordienko*, Georges Shapovalov*, Anne-sophie Borowiec, Loic Lemonnier, Etienne Dewailly, Christian Slomianny and Natalia Prevarskaya ; Novel isoform of TRPM8 channel characterized in mitochondria-associated membranes of prostate cells. Soumission *Journal of Cell biology*.

Demande d'inventivité auprès de la SATT Nord De France Valo. Brevet IntraChan.

Encadrement, Collaborations et tâches associés

- Dr Anne-sophie Borowiec, chercheuse post-doctorante,

Gestion du projet.

ACTIVITÉS DE RECHERCHE

III.1.4. LE RÉCEPTEUR AU FROID MODULE L'HOMEOSTASIE DE L'ÉPIDERME

Contexte

L'ÉPIDERME

Anatomiquement, l'épiderme est la couche superficielle de la peau dont la surface est formée de cellules mortes kératinisées. Il est formé d'un tissu épithélial stratifié, kératinisé, pavimenteux et non vascularisé qui recouvre le derme. Les kératinocytes sont le principal type cellulaire représenté dans ce tissu. L'homéostasie extrêmement dynamique de l'épiderme (21 à 28 jours pour la transformation d'un kératinocyte basal en cornéocyte, 10% de l'épiderme humain renouvelé chez jour) est due au fort taux de prolifération et de différenciation, permanentes, aux termes desquelles les kératinocytes se transforment en cellules mortes (cornéocytes), s'éliminant régulièrement par desquamation.

L'épiderme des mammifères se décompose classiquement en 4 strates (figure 31) :

- le *stratum basalum* ou *germinativum* inclus les cellules souches dont la division permet le renouvellement de l'épiderme tout en maintenant un stock de progéniteurs.

- le *stratum spinosum* contient des kératinocytes initiant leur différenciation en synthétisant les kératines nécessaires à la transformation finale en cornéocytes. Dans cette couche épineuse, on trouve aussi des mélanocytes, des cellules immunitaires de Langerhans et des terminaisons nerveuses.

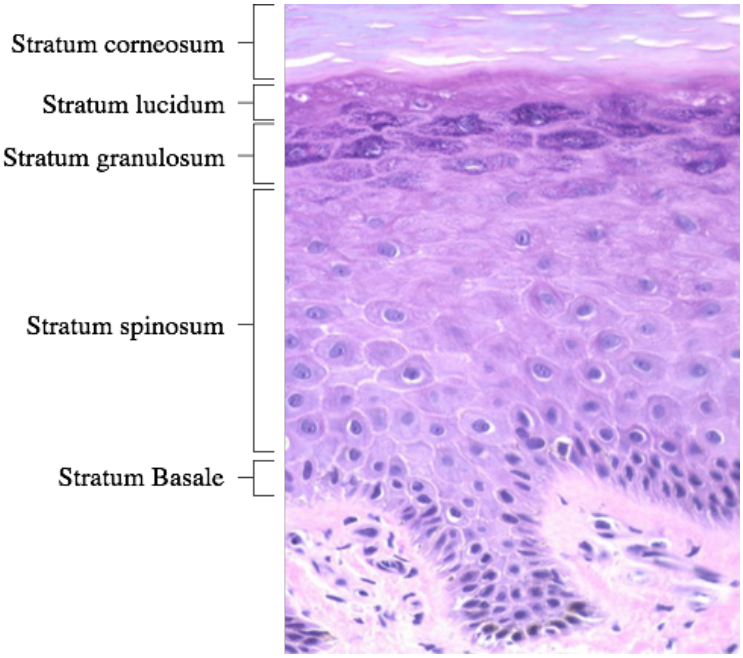

Figure 31 : coloration d'une section transversale de peau humaine montrant l'organisation multi-stratifiée de l'épiderme.

- le *stratum granulosum* est la dernière couche de cellules vivantes. Les kératinocytes y synthétisent la profillagrine qui sera clivée dans la partie haute de cette strate ou dans le stratum lucidum dans l'épiderme humain (couche intermédiaire entre la couche granulaire et la couche cornée). Les transglutaminases activent le pontage des kératines entre elles formant ainsi une coque rigide qui donnera sa résistance et son hydrophobicité à la couche cornée.

- le *stratum corneum*, les kératinocytes y meurt par un processus d'apoptose incomplet, conduisant à la suppression du noyau, mais la conservation de l'armature formée par les filaments de kératines et l'inclusion de vésicules lipidiques.

Fonctions biologiques.

- *Rôle de barrière protectrice*. L'épiderme est une barrière hydrophobe permettant de limiter l'évaporation de l'eau des organismes. Elle permet aussi de protéger l'organisme des agressions physico-chimiques de l'environnement.

- *Rôle de senseur*. L'épiderme inclus les cellules de Merkel capables de détecter les variations de pression puis de transmettre l'information aux terminaisons des fibres sensorielles présentent dans le stratum spinosum. Ces dernières expriment aussi des thermorécepteurs de la famille des TRP, comme TRPM8 [72, 73]. Néanmoins des travaux suggèrent que la capacité à détecter une variation de température nécessite un détecteur et un référentiel. Ce dernier consisterait en un détecteur interne aux kératinocytes. Ainsi, il a été reporté que le canal TRPV3 dans les kératinocytes, lors de son activation par une augmentation de température, induit une libération d'ATP extracellulaire qui va activer les récepteurs purinergiques sur les terminaisons nerveuses des neurones de la racine postérieure de la moelle épinière (DRG pour « Dorsal Root Ganglia »). Ce mécanisme a pour conséquence de moduler la réponse des neurones DRG à la détection directe de température par leurs propres canaux TRPV3 [74, 75].

Etant en contact direct avec l'extérieur de l'organisme, la température moyenne de l'épiderme est plus basse (environ 32°C ; [76]) que la température corporelle (37°C). Cette caractéristique a des conséquences directes sur la sensation de température, mais pourrait aussi avoir des effets notables sur la physiologie de l'épiderme en modulant par exemple les activités enzymatiques et donc indirectement l'homéostasie de l'épiderme. Pourtant, il existe peu d'informations relatives à ce sujet. Dans la même veine, il n'existe que 1 article reportant la détection d'un canal « TRPM8-like » dans les kératinocytes [77].

Objectifs

Caractériser l'impact de la baisse légère de température sur la physiologie des kératinocytes en culture.

Cloner puis déterminer le rôle de cette protéine TRPM8-like dans l'épiderme.

Résultats

Dans un premier temps, incapable de reproduire les résultats d'une partie de la littérature défendant l'induction de la différenciation par la méthode dite du « Ca^{2+} switch » (augmentation de la concentration de Ca^{2+} dans un milieu sans sérum d'environ 70 µM à plus de 1 mM), nous avons réalisé une lecture attentive et la plus exhaustive possible de ce sujet. Ce travail nous a mené à modifier le protocole défendu par certains de nos collègues car nous avons montré que cette absence de sérum est, certes favorable au maintien du phénotype kératinocytaire et à la prolifération, mais défavorable à la différenciation des kératinocytes [78]. Il est stupéfiant de notre que cela était déjà référencé dans le papier originel présentant l'intérêt de la supplémentation par de l'extrait pituitaire bovin dans un milieu sans sérum, papier datant de 1983… Contrairement à ce que nombre d'articles simplifient depuis une dizaine d'année, nous avons aussi démontré que le niveau d'induction de la kératine 10 (K10) dans les kératinocytes en culture primaire, utilisé comme marqueur de différenciation, est loin d'atteindre son niveau d'expression dans l'épiderme (il y a un facteur d'au moins 10x). Moins de 5% de kératinocytes se différenciant au dessus de la monocouche de cellules expriment la K10 à un niveau jugé comparable à son expression dans l'épiderme…

ACTIVITÉS DE RECHERCHE

Suite à cette calibration préparatoire des conditions de culture et du protocole de différenciation, nous avons évalué l'effet d'une incubation des kératinocytes à 31°C et 25°C pendant 3 jours. Cette baisse de la température d'incubation est corrélée à une chute de la prolifération. Cet effet était attendu puisque la diminution de température induit une diminution de l'activité de nombreuses réactions chimiques et que la prolifération est très consommatrice d'énergie et de produits issus de ces réactions chimiques. Nous avons, par la suite, évalué le taux de différenciation par une approche large allant de l'expression des ARN et protéines, au dénombrement des kératinocytes exprimant des marqueurs de différenciation. Le nombre de marqueurs a été élargi car il est souvent limité à 1 à 3 dans les études, ce qui est très limitant pour développer de bonnes interprétations. En effet, il est impossible d'assumer que la variation d'expression d'un si petit nombre de marqueurs représente bien une évolution du phénotype et non pas une simple variation d'expression limitée à 3 gènes. Nos résultats démontrent que l'incubation à 31°C est favorable à l'augmentation du niveau d'expression de marqueurs de différenciation mais aussi à l'augmentation de la proportion de cellules qui se différencient (Figure 32).

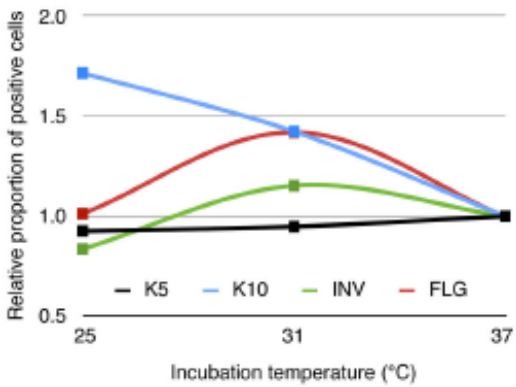

Figure 32 : proportion relative de kératinocytes exprimant un marqueur basal (K5) et des marqueurs de différenciation (K10, INV, TG) et triée par cytométrie de flux.

Nous avons en outre démontré pour la première dans une culture de kératinocytes primaires, que la culture à 31°C en présence de sérum permet d'observer la polymérisation de la K10 suite à l'activation des transglutaminases (Figure 33). Ce processus de différenciation tardive n'est observé que dans moins de 1% des cellules de nos cultures.

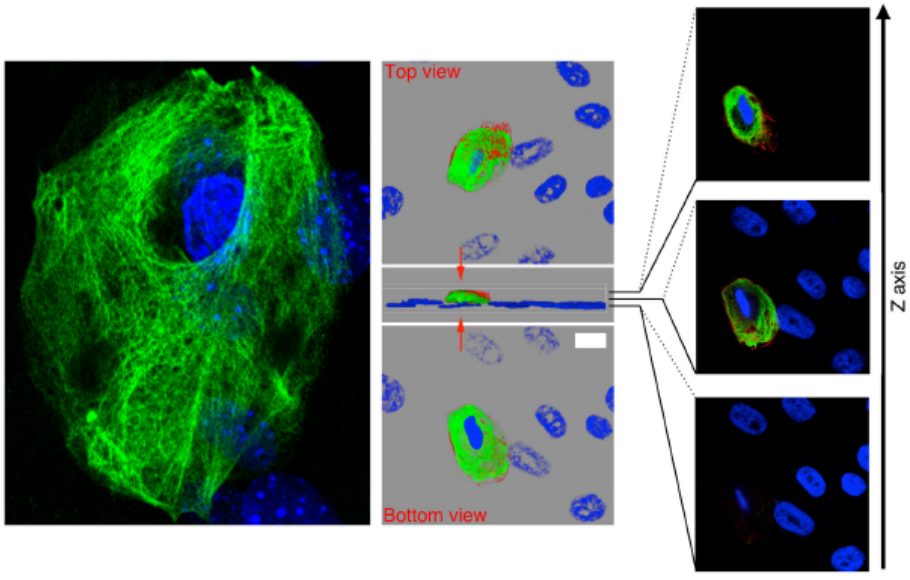

Figure 33 : image confocale et reconstruction 3D de la coquille formée par la K10 (vert) polymérisée dans un kératinocyte différencié et reposant sur la monocouche de kératinocytes basaux. Les noyaux sont colorés par la technique de Hoecht.

Dans un second temps, pour comprendre pourquoi et comment la baisse de température vers 32°C pouvait favoriser la différenciation des kératinocytes, nous avons cloné puis caractérisé une isoforme canal de TRPM8 dans les kératinocytes comme présenté dans l'article 14 (annexes). Cette isoforme, eTRPM8, de structure proche des isoformes TRPM8-36 présentées dans le chapitre précédant, est un canal de 40 kDa composé de 4 segments transmembranaires et du domaine ionique. eTRPM8 est un canal fonctionnel exprimé dans les membranes du RE des kératinocytes de mammifères, faiblement dans la couche basal et plus fortement dans les couches différenciées de l'épiderme. Nous avons mis en évidence que notre lignée de souris présentant une inactivation fonctionnelle de TRPM8 (délétion des S3, S4, S5 et la P-loop) avaient un épiderme modifié présentant une moindre épaisseur de la couche granulaire et de la couche cornée. Cette diminution de la différenciation des kératinocytes *in situ* a été reproduite en culture et nous avons démontré qu'elle est associée à une diminution de la concentration de Ca^{2+} dans les mitochondries ainsi qu'une diminution de la quantité ATP et une augmentation parallèle du superoxide (SO). On observe une corrélation entre la thermo-dépendance de la proportion de kératinocytes différenciés (figure 32) et la thermo-dépendance de la concentration d'ATP (figure 34). Nous en avons conclu que l'activation modérée de TRPM8 à 32°C suffit à booster la concentration de Ca^{2+} dans la matrice des mitochondries, ce qui engendre une augmentation de la synthèse d'ATP par emballement du cycle de Krebs et de la chaine OXPHOS (oxydation – phosphorylation). Une conséquence connue de l'augmentation d'activité de la chaine de respiration cellulaire est la synthèse du SO. Or les kératinocytes présente la particularité d'avoir une expression faible des superoxide dismutases (SOD ; enzymes transformant le SO en H_2O_2), au regard de l'expression des catalases et gluthation-peroxidases servant à détoxifier H_2O_2. Ce qui a pour conséquence de favoriser l'accumulation de SO. Or nous avons démontré que la surexpression de la SOD1 entraine une diminution de l'induction de la transglutaminase à 31°C, un marqueur de différenciation tardive, concomitante à une augmentation du nombre de cellules exprimant les marqueurs de différenciation plus précoces que sont K10 et INV.

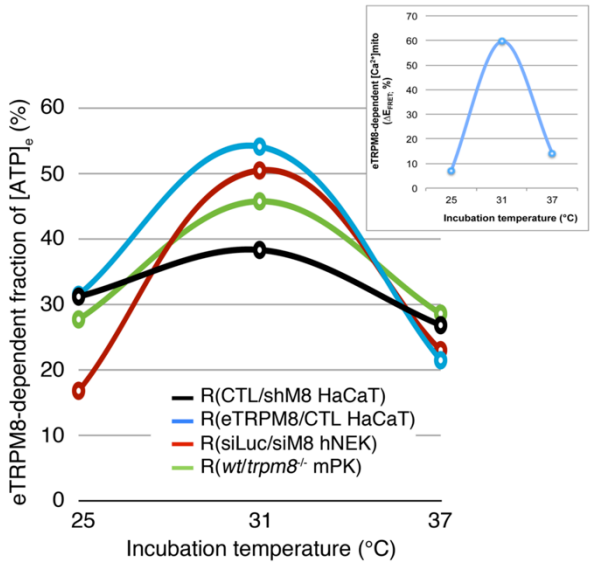

Figure 34 : eTRPM8 favorise la synthèse d'ATP. La figure représente la part de la concentration d'ATP stimulée à différentes températures par l'expression de eTRPM8. Encart : concentration de Ca^{2+} dans les mitochondries.

Conclusion & Perspectives

En conclusion, nous avons démontré qu'une nouvelle isoforme de TRPM8, à 4 segments transmembranaires, se comporte comme un canal fonctionnel dans les nanodomaines du RE des kératinocytes. Cette isoforme est activable par le froid, le menthol et l'iciline comme la forme longue de TRPM8. Comme résumé sur la figure 35, l'activation de eTRPM8 transduit le stimulus « froid » en libérant

du calcium du RE en face des mitochondries qui le recaptent immédiatement. Cette augmentation de la concentration de Ca^{2+} mitochondrial module la synthèse d'ATP et de SO. Ces derniers stimulent la différenciation terminale des kératinocytes, ce qui à l'échelle de l'épiderme augmente l'épaisseur des couches cornées et granulaires.

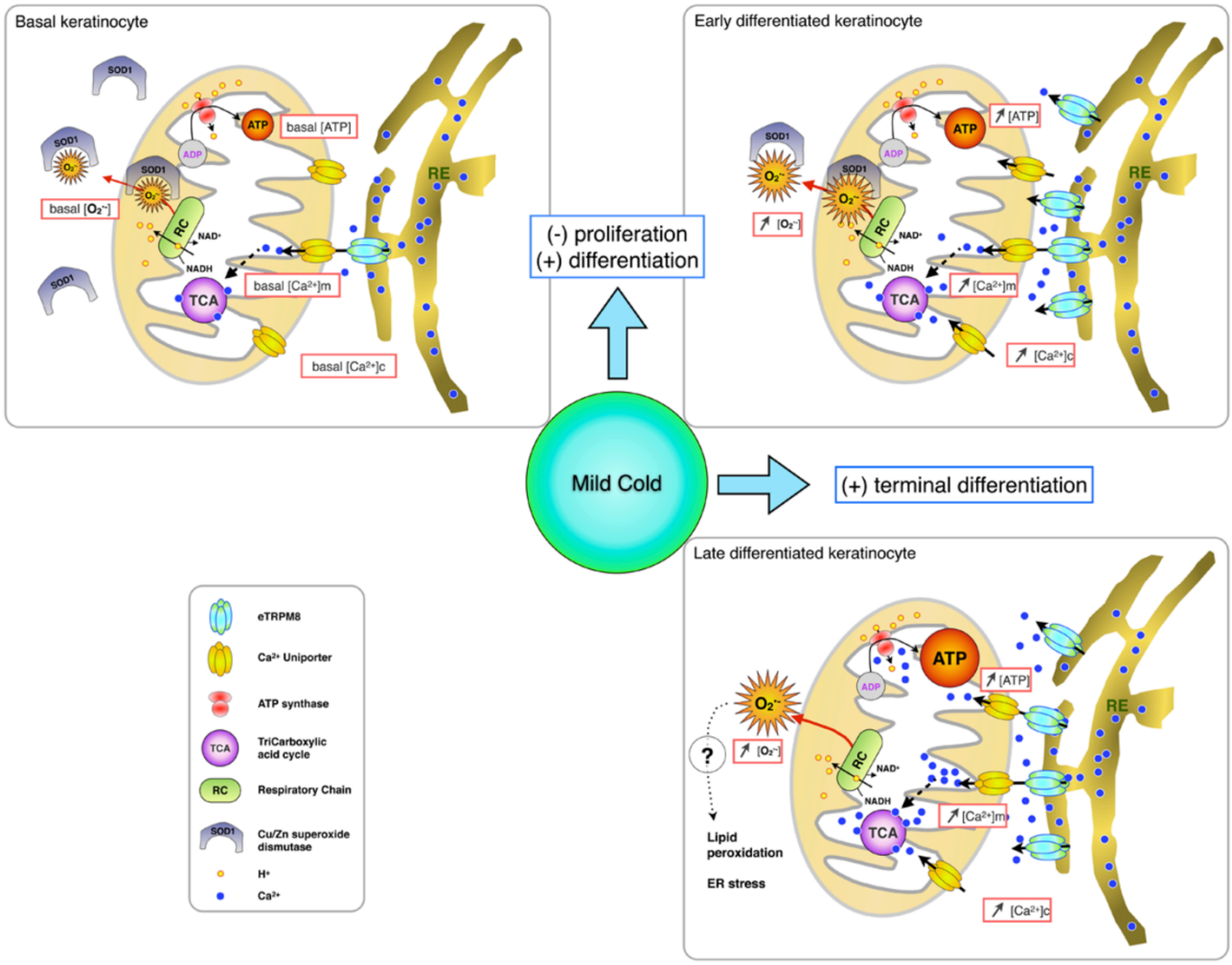

Figure 35 : schéma résumant la régulation par le froid de la balance prolifération / différenciation des kératinocytes via l'activation de l'isoforme eTRPM8.

Production associée

Article 14 : Anne-sophie Borowiec, Philippe Delcourt, Etienne Dewailly, and **Gabriel Bidaux**. Multifactorial optimization of in vitro keratinocytes induction of differentiation. *PLos One*. 2013 Oct 7;8(10):e77507.

Article 15 (annexes) : **Gabriel Bidaux**, Anne-Sophie Borowiec, Dmitri Gordienko, George Shapovalov, Benjamin Beck, Loïc Lemonnier, Matthieu Flourakis, Matthieu Vandenberghe, Christian Slomianny, Etienne Dewailly, Philippe Delcourt, Emilie Desruelles, Abigaël Ritaine, Renata Polakowska, Jean Lesage, Mounia Chami, Roman Skryma and Natalia Prevarskaya. Molecular identity of the mild cold-transducer in epidermal homeostasis. Minor revision in *PNAS*.

Encadrement, Collaborations et tâches associés

- Dr Anne-sophie Borowiec, chercheuse post-doctorante,

III.1.5. TRPM8 PRÉVIENT L'OXYDATION DES CELLULES GERMINALES INDUITE PAR LE FROID

Contexte

LA SPERMATOGENESE

Le testicule, gonade mâle, est un organe externe au pelvis contenu dans le scrotum afin d'être à une température moyenne se situant entre 2-4°C sous la température corporelle.

Le testicule a 2 fonctions principales :

- la spermatogenèse (production de spermatozoïdes)
- la stéroïdogenèse (production de la testostérone, hormone stéroïdienne)

La spermatogenèse est le processus de différenciation des cellules germinales en spermatozoïdes. Elle prend place dans les tubules séminifères contenus dans le testicule. Les spermatogonies réalisent de nombreuses mitoses pour entretenir le stock de cellules progénitrices. Une partie de ces spermatogonies se différencie en spermatocytes I qui deviennent des spermatocytes II après la première division de méiose (figure 36). La seconde division de méiose transforme les spermatocytes en spermatides qui migrent vers la lumière du tubule et se différencie en spermatozoïdes.

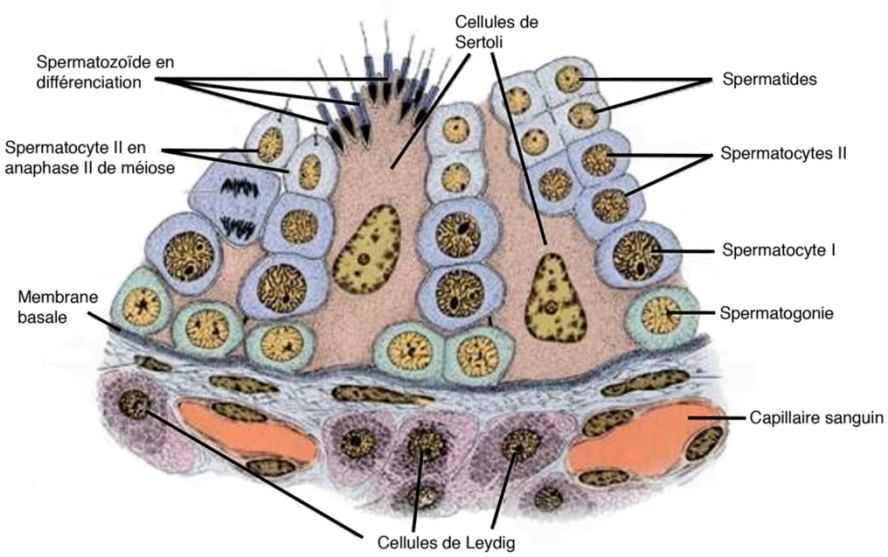

Figure 36: représentation partielle d'une coupe transversale de tubule séminifère (lumière en haut).

Les cellules germinales sont très sensibles aux variations de l'environnement. Une hausse de la température scrotale par chauffage ou par la rétention pathologique des testicules à l'intérieur du corps (Cryptorchidie) conduit à l'apoptose des cellules germinales et induit la stérilité de l'individu. L'hypothermie des testicules augmente le taux de cellules apoptotiques [79-82]. Ainsi, la régulation fine des mécanismes de réponses aux variations de température du scrotum est essentielle au bon déroulement de la spermatogenèse [79]. Bien que TRPM8 ait été détecté dans les spermatozoïdes [83-85], rien n'est connu sur son expression dans les cellules germinales au long de la spermatogenèse. Rien non plus n'est connu sur le rôle éventuel d'un récepteur au froid dans les cellules germinales soumises à un refroidissement.

ACTIVITÉS DE RECHERCHE

Objectifs

Caractériser l'expression et le rôle des canaux TRPM8 dans la réponse à l'hypothermie des cellules germinales de souris.

Résultats

Nos résultats de criblage des isoformes de TRPM8 sur les testicules de souris et humains ont montré l'expression d'au moins 5 isoformes-canal de TRPM8. Nous avons réalisé ce travail par une approche non discriminante des isoformes, en considérant que ce que nous voulions étudier était la réponse physiologique consécutive à l'activation de toutes les isoformes de TRPM8 dans les cellules germinales.

Après une phase de mise au point de l'hypothermie sur le scrotum des souris CTL et KO-TRPM8 par mon collègue le Dr Benoit Sion à Clermont-Ferrand. Nous avons réalisé des mesures d'expression de gènes et d'apoptose sur les testicules des animaux et des cellules germinales isolées soumis à l'hypothermie. Ces travaux ont mis en évidence une corrélation notable entre la thermo-dépendance de l'induction de l'apoptose et la thermo-dépendance du taux de substances activés en oxygène (ROS), suggérant que le choc hypothermique induisait une augmentation de la concentration de ROS dans les cellules germinales responsable de l'apoptose d'une fraction des cellules germinales. Grâce à un large criblage de gènes impliqués dans le cycle cellulaire, la signalisation, le stress réticulaire, la réponse au stress thermique, le découplage mitochondrial et la détoxification des ROS, nous avons démontré que l'expression des canaux TRPM8 en condition basale ou d'hypothermie légère (20°C) réprime l'expression des gènes de réponse au choc thermique : HSF1 et HSPA2 mais augmente l'expression de la gluthation-peroxidases 4, GPx4 (Figure 37). Dans la condition d'hypothermie sévère (4°C), l'expression de TRPM8 induit l'expression de la glutathion-peroxydase 5 (GPx5) et de la protéine de découplage UCP3.

		TRPM8-mediated fold-induction of gene expression		
Markers of:	**Gene:**	**8°C**	**20°C**	**32°C**
Germ cell markers	*mMagea4*	1.23	1.47	1.52
	mTnp1	1.21	1.31	1.53
	mPrm2	1.08	0.82	1.12
Cold/Heat shock Proteins	*mHSF1*	1.05	0.79	0.64
	mHSF2	0.94	0.97	1.00
	mCIRBP	0.96	1.20	0.89
	mHSPA1	1.14	1.23	1.28
	mHSPA2	0.89	0.72	0.66
Mitochondrial Uncoupling	*mUCP3*	2.40	1.78	0.88
Oxydation	*mSOD1*	1.04	1.19	1.22
	mGPX2	1.72	2.23	0.83
	mGPX4	1.08	1.53	1.60
	mGPX5	6.90	5.35	0.73

Figure 37 : ratio d'expression des gènes dans les cellules germinales isolées de souris CTL divisé par leur expression dans les cellules germinales isolées de souris KO-TRPM8 soumises à une incubation à différentes températures pendant 1h.

Comme UCP1 dans les adipocytes bruns, UCP2 et UCP3 par leur action découplante [86], c'est à dire découplant l'activité de la chaine de respiration cellulaire de la synthèse d'ATP, peuvent participer à la génération de chaleur. En outre, il semblerait que l'expression et l'activité de protéines découplantes soient induites par le SO [87] et que l'expression d'UCP3 participe à la détoxification des ROS (dont SO) dans les cardiomyocytes [88]. Il est intriguant de constater que la protéine UCP2 est induite dans les cellules germinales assujetties à l'hyperthermie et qu'elle participe aussi à la détoxification des ROS [89].

Conclusion & Perspectives

Ce travail est un pont entre le rôle de eTRPM8 dans l'homéostasie de l'épiderme (chapitre précédant) et le rôle global des isoformes de TRPM8 dans le métabolisme de la souris (chapitre suivant). En effet, nous démontrons la connexion entre les isoformes de TRPM8 localisées dans les MAMs et la synthèse de ATP/ROS par les mitochondries. Nous mettons aussi en exergue la connexion entre cette accumulation de molécules oxydantes et l'induction des protéines découplantes de la famille UCP. Dans l'épiderme, nous avons démontré que la production de ROS croît linéairement avec la baisse de la température, mais qu'en condition d'hypothermie légère (32°C), la production d'ATP est prépondérante. A l'inverse, vers 20-25°C, l'accumulation de ROS devient prépondérante et la synthèse d'ATP s'effondre. En corrélant nos travaux et les données de la littérature, nous suggérons que l'effondrement de la synthèse d'ATP est la conséquence de plusieurs effets :

- une inhibition directe des enzymes par l'oxydation (pour revue, voir [90])
- l'induction du découplage qui entraine une chute de capacité de synthèse d'ATP par l'ATP synthétase
- la diminution globale d'activité enzymatique à ces températures.

Le rôle résiduel de TRPM8 à température physiologique peut paraître, à première vue, contradictoire. En effet, comment un canal fermé pourrait avoir un rôle de régulateur de la prolifération des kératinocytes et de protection contre les ROS dans les cellules germinales. Néanmoins, nous et d'autres équipes avons démontré que le canal TRPM8 est activé par des lipides endogènes comme le phosphatidylinositol [8] ou les lysophospholipides [60]. Dans les kératinocytes et les cellules germinales, cette activité basale de TRPM8 pourrait donc être due pour partie à la température (30°C-32°C) et pour partie aux lipides. Cette activation résiduel en stimulant une synthèse de ROS à un niveau modéré pourrait stimuler l'expression des enzymes détoxifiantes à un niveau basal plus élevé et donc permettre de réguler le niveau basal de ROS. L'induction de protéines découplantes pourrait participer à limiter l'oxydation lors de stimuli transitoires, mais pourrait aussi être un mécanisme générateur de chaleur permettant de tamponner légèrement l'échange de calories avec l'extérieur. Ceci sera d'autant plus vrai que l'inertie calorifique et la résistivité thermique de l'organisme est faible.

Production associée

Article 16 (annexes) : Anne-sophie Borowiec, Benoit Sion, Frédéric Chalmel, Antoine Rolland, Loïc Lemonnier, Tatiana De Clerck, Alexandre Bokhobza, Sandra Derouiche, Etienne Dewailly, Christian Slomianny, Claire Mauduit, Mohamed Benhamed, Morad Roudbaraki, Bernard Jégou, Natalia Prevarskaya, and **Gabriel Bidaux**. Cold/menthol channels initiate the cold shock response and protect germ cells from cold shock mediated oxydation. En préparation.

Encadrement, Collaborations et tâches associés

- Dr Anne-sophie Borowiec, chercheuse post-doctorante,
- Mme De Clerck Tatiana, étudiante en BTS,

Gestion complète du projet et des collaborations Nationales avec les laboratoires INSERM U1107 à Clermont-Ferrand et INSERM U 1085 à Rennes.

ACTIVITÉS DE RECHERCHE

III.1.6. ISOFORMES DE TRPM8 & DÉPENSE ÉNERGÉTIQUE

Contexte

MÉTABOLISME & THERMOGENÈSE

Le **métabolisme de base** est constitué de l'ensemble des réactions chimiques (enzymatiques et acido-basiques) qui se déroulent au sein d'un être vivant pour lui permettre notamment de se maintenir en vie, de se reproduire, de se développer et de répondre aux stimuli de son environnement. On distingue d'une part l'**anabolisme**, qui représente l'ensemble des voies de biosynthèse des constituants cellulaires, et d'autre part le **catabolisme**, qui représente l'ensemble des voies de dégradation de ces constituants cellulaires en petites molécules pour en libérer l'énergie par oxydation ou pour rebâtir d'autres constituants cellulaires (polymères peptidiques ou nucléiques par exemple). L'intensité du métabolisme de base détermine la quantité de nutriments à ingérer pour apporter des calories à l'organisme. Les nutriments (acides gras, protéines, carbohydrates) fournissent un apport énergétique indispensable aux réactions enzymatiques et un apport structurel nécessaire à la reconstruction continue des molécules composant les cellules.

La transformation et la distribution de ces composés organiques au sein de l'organisme implique de nombreux organes : système digestif, foie, pancréas. Des tissus dédiés participent au stockage des ressources énergétiques : tissu gras sous-cutané (adipocytes blancs). Les organes de locomotion, de thermogenèse, le système cardiovasculaire, le système immunitaire, sphère uro-génitale, et le cerveau sont des systèmes effecteurs qui consomment de l'énergie et des nutriments.

Le **métabolisme énergétique** vise à produire des molécules d'adénosine triphosphate (ATP) principalement à partir du catabolisme des carbohydrates ou celui des lipides. Ces réactions sont majoritairement de type aérobies car elles sont oxydantes (phosphorylation oxydative), bien que la dégradation du glucose puisse se faire en condition d'anaérobie lactique.

Chez les **organismes homéothermes** (par opposition aux poïkilothermes), la maintenance de la température corporelle est une source de consommation d'énergie importante. En effet, en dehors de la zone de thermoneutralité (température extérieure pour laquelle un organisme nu ne consomme pas d'énergie pour maintenir sa température : 28-30°C chez l'homme), les organismes homéothermes consomment de l'énergie pour soit se refroidir, soit se réchauffer. La thermolyse fait principalement appel à la sudation qui élimine des calories dans l'eau libérée par les glandes sudoripares. Le système de thermogenèse varie selon les organismes et implique plusieurs mécanismes :

- alimentation,
- l'exercice physique,
- **micro-contractions ou frissons** (5 à 10 par secondes), consistent en une augmentation du tonus musculaire, n'entravent en rien les mouvements,
- **thermogenèse de non-frisson** (chez les mammifères hibernants ; jusqu'à 7-8 ans pour l'homme). Fait appel au découplage mitochondrial entre la consommation d'O_2 et la production d'ATP.

Le **découplage mitochondrial** fait appel à la protéine UCP1 qui découple la consommation d'O_2 de la production d'ATP en créant une fuite de proton depuis l'espace inter-membranaire vers la matrice mitochondriale. Ceci ayant pour effet de diminuer le gradient de proton et entraine une diminution de l'activité de l'ATP synthétase bien que l'oxydation du NADH, H^+ et du FADH2 continue au niveau de la chaine de respiration cellulaire. Du point de vue général de l'organisme, un haut couplage entre la respiration cellulaire (consommation d'O_2) et la synthèse d'ATP est favorable au stockage des calories. Au contraire, un fort découplage des réactions OXPHOS entraine une consommation efficace des calories qui peut être associée à une absorption importante de nutriments pour compenser les pertes d'énergie par production de chaleur. En effet, les réactions d'oxydation du NADH, H^+ et FADH2 sont **exergoniques** ($\Delta rG° = -219$ kJ/mol pour l'oxydation du NADH,H^+) alors que la synthèse d'ATP est une réaction endergonique ($\Delta rG° = 30,5$ kJ/mol). Dans un milieu possédant une certaine inertie thermique et une résistance thermique, l'augmentation des réactions exergoniques couplée à la diminution des réactions endergoniques provoque un **effet exothermique**, c'est à dire une production de chaleur. Ainsi dans l'organisme des enfants ou celui des mammifères hibernants, la diminution de la température du corps est détectée par le système nerveux central qui induit *via* les voies beta-adrénergiques l'expression d'UCP1 dans les adipocytes bruns. Ces derniers possèdent un très grand nombre de mitochondries auxquelles ils doivent leur couleur brune ainsi que de substantielles réserves lipidiques. La stimulation adrénergique provoque une hausse de l'activité métabolique mitochondriale concomitante à une augmentation du découplage mitochondrial, induisant une production massive de chaleur.

Un travail récent a montré que le canal TRPM8 serait exprimé dans les adipocytes bruns et que l'ingestion de menthol induirait une augmentation de l'expression d'UCP1 dans les adipocytes bruns, conduisant à une augmentation de la dépense énergétique sous forme de chaleur [91]. D'autres études ont mis en évidence l'expression de TRPM8 dans le pancréas [92] et le foie [93] alors qu'une autre étude montrait implication dans le contrôle de l'insulinémie [94]. Cependant, la démonstration claire de l'expression de la forme longue de TRPM8 ou d'une isoforme n'est pas toujours faite clairement. D'autres part, les études réalisées sur une lignée KO TRPM8 utilisent en général la lignée du Prof. A. Patapoutian (La Jolla, USA) ou celle du Prof. D. Julius (San Franscico, USA) dans lesquelles seule la forme longue de TRPM8 est supprimée [72, 73].

Objectifs

L'objectif de cette étude est de caractériser l'expression des isoformes de TRPM8 dans les organes impliqués dans l'anabolisme et la thermogenèse et s'appuie sur la lignée KO fonctionnel de TRPM8 que nous avons développée.

Résultats

Le phénotypage de notre lignée KO TRPM8 (KOM8) a été confié en partie à l'Institut Clinique de la souris à Illkirch et en partie au Dr Emilie Caron du laboratoire INSERM U 837, Centre de recherche Jean-Pierre Aubert à Lille.

ACTIVITÉS DE RECHERCHE

Ce phénotypage a révélé que notre lignée présente une augmentation significative de la masse musculaire et une diminution de la masse grasse de réserve (sous-cutanée) avec diminution de taille des adipocytes, ce qui entraine une diminution de l'adiposité. Ce phénotype correspond aux critères d'un phénotype dit « maigre ». Nos analyses ne démontrent aucun changement dans l'absorption des nutriments au niveau intestinal et une capacité d'adaptation normale à des régimes sucrés ou gras. Par contre, nos données révèlent une extraction de calories plus importante des aliments ainsi qu'une ingestion d'eau et d'aliments accrue en régime riche en carbohydrates (60% sucres) mais moindre en régime gras (45% lipides). L'activité motrice est augmentée et sur un test d'effort, les animaux KOM8 courent plus loin et plus longtemps. La consommation d'O_2 est accrue tout comme la dépense énergétique (calorie transformée en chaleur, évaluée par la respiration).

L'analyse de l'expression des ARN alternatifs de TRPM8 a révélé l'expression d'isoformes-canal tronquées, de type TRPM8-36, dans le foie et le tissu adipocytaire brun (BAT). Cependant, la forme longue de TRM8 n'a pas été détectée dans ces organes. Nous n'avons pas détecté d'expression notable d'isoformes de TRPM8 ni dans le muscle squelettique ni dans le tissu adipocytaire blanc (WAT).

Le criblage de nombreux gènes jouant un rôle dans les vois métaboliques fut réalisé par qPCR sur le foie, le BAT, le WAT et le Soleus. Ce criblage a révélé que la suppression de TRPM8 est associée à:

- une diminution de 50% de l'expression d'UCP2 dans le foie mais une augmentation de 100% d'UCP1 dans le BAT,
- une diminution de GPx2 et GPx3 dans le foie mais une augmentation de GPx2 dans le WAT et de SOD3 dans le Soleus,
- l'augmentation de plusieurs Cyclo-oxygénases de la chaine d'oxydation cellulaire dans le BAT,
- l'augmentation de la citrate synthase et des isocitrate déshydrogénases 3A et 3B (IDH3A et IDH3B) dans le BAT, mais une diminution d'IDH3A dans le foie,
- une augmentation de la cétonisation dans le foie et le WAT,
- une augmentation de la gluconéogenèse, une diminution de la β-oxydation et une diminution de la synthèse d'acides gras monosaturés dans le foie.

Le bilan de ce criblage est qu'on observe une diminution du métabolisme hépatique indiquant que les isoformes de TRPM8 sont promotrices de cette activité. Par contre, on observe une forte augmentation de l'activité catabolique dans les BAT. Cette dernière pourrait être responsable de la majorité de l'augmentation de la dépense énergétique observée chez les animaux KOM8. Par induction, cela indique que les isoformes de TRPM8 dans les BAT possèdent une activité de répression de la thermogenèse des BAT dans des conditions de température externes de 21°C.

Nous avons voulu vérifier si la thermogenèse stimulée et la dépense énergétique globale par le froid divergeaient entre les animaux CTL et les KOM8. Les expériences ont été réalisées dans des cages métaboliques avec une période d'adaptation de 24h à 10, 20 ou 30°C sur des groupes d'animaux nourris *ad libitum* puis mis à jeûner. À noter que les animaux à jeun n'ont pas pu poursuivre l'expérience à 10°C suite l'apparition de mortalité.

On observe tout d'abord que l'activité locomotrice des souris est en bonne partie indépendante de la présence de nourriture (figure 38A). Les animaux à jeun ne présentent pas d'augmentation de mouvements pour

rechercher de la nourriture. On voit par contre que les animaux KOM8 ont une activité motrice légèrement augmentée par rapport aux CTL durant la journée, et que cette augmentation est nettement amplifiée la nuit dans les conditions à 20°C et à 30°C. Il semblerait que la nuit, à une température ambiante de 10°C, les animaux limitent leurs mouvements pour limiter les pertes d'énergie. A contrario, on observe une augmentation de l'activité motrice des animaux nourris à 10°C en phase diurne. Il semblerait donc que les animaux cherchent un régime d'activité musculaire optimal pour générer un peu de chaleur en limitant les grosses déperditions d'énergie liées à la suractivité motrice nocturne.

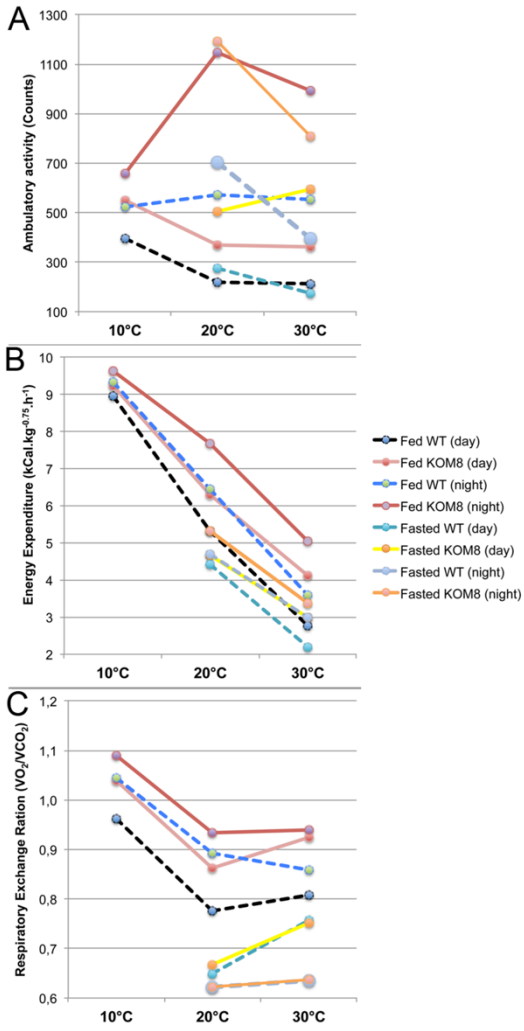

Figure 38 : thermo-dépendance de l'activité ambulatoire (A), de la dépense énergétique (B) et du quotient respiratoire (C) chez les animaux CTL et KOM8 placés dans des environnements à différentes températures.

La dépense énergétique des animaux KOM8 est plus élevée que celle des CTL à 30°C et à 20°C (figure 38B), mais elle semble atteindre un plateau à 10°C puisque la dépense énergétique des animaux CTL atteint la même valeur que celle des animaux KOM8. D'autre part, on observe une augmentation similaire de la dépense énergétique des souris CTL et KOM8 durant la phase nocturne. L'activité locomotrice accrue des souris KOM8 ne semble donc pas être responsable de l'augmentation de la dépense énergétique. Il faut noter que la différence maximale de dépense énergétique entre les animaux CTL et KOM8 est atteinte à la thermoneutralité. C'est donc le métabolisme de base qui est augmenté chez les souris KOM8. L'ingestion de nourriture ne semble pas vraiment affecter la dépense énergétique puisque les animaux KOM8 à jeun continuent d'avoir une dépense énergétique plus élevée que celles des animaux CTL.

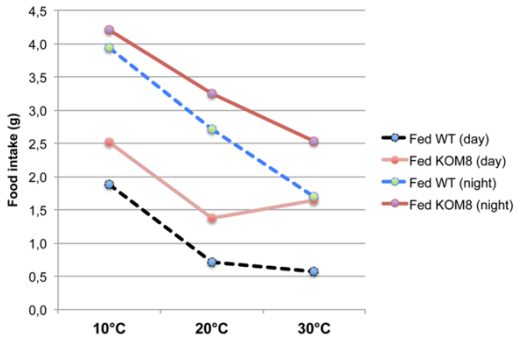

Figure 39 : masse cumulée de nourriture ingérée par les souris CTL et KOM8 placées dans des environnements à différentes températures.

Le calcul du quotient respiratoire (V_{O2}/V_{CO2} ; Figure 54C) démontre une forte utilisation de la glycolyse comme carburant énergétique, ce qui était attendu pour cette série réalisée avec un régime riche en carbohydrates (65%). On constate que la mise à jeun des animaux CTL comme KOM8, induit une nette diminution du RER (<0,7) ce qui traduit l'utilisation des lipides comme carburant principal. C'est à dire que les animaux utilisent leurs réserves caloriques. Cette utilisation des réserves est plus

marquée à 20°C qu'à la thermoneutralité, ce qui couplé à l'augmentation de dépense énergétique, démontre la consommation d'énergie affectée à la thermogenèse. On observe aussi que plus les animaux mangent (Figure 39) plus leur production d'énergie dépend de la qualité des nutriments. Ainsi dans le cas du régime riche en carbohydrates, les souris dans les cages régulées à 10°C voient leur RER augmenter autour de 1 ce qui signifie qu'elles utilisent la glycolyse comme carburant majeur de leur production d'énergie. Notez que dans le cas du régime riche en lipide, les souris CTL comme les souris KOM8 utilisent principalement les lipides comme carburant (RER de 0,6).

Il est intéressant de noter que la lignée KOM8 du Dr Patapoutian, inactivée pour la forme longue de TRPM8, ne présente pas de différence basal de dépense énergétique, ni de phénotype maigre.

Conclusion & Perspectives

En conclusion, la suppression fonctionnelle et ubiquitaire des isoformes de TRPM8 induit un profond bouleversement dans le régime basal de la thermogenèse. Ainsi, il semblerait que les isoformes participent au contrôle du métabolisme basal au niveau hépatique et dans le BAT par le biais du contrôle de l'activité de découplage. Ceci entraine une moindre efficacité de production d'énergie et par conséquent un brûlage plus rapide des calories générant le phénotype « maigre ».

Production associée

Article 17 : Anne-sophie Borowiec, Gabriel Bidaux, Emilie Caron, Brian Finan, Matthias Tschöp and Natalia Prevarskaya and Gabriel Bidaux. Article en cours de rédaction.

Encadrement, Collaborations et tâches associés

Gestion du projet.

Collaboration internationale : Dr Brian Finan et Prof. Matthias Tschöp (Institute for Diabetes and Obesity (IDO), Helmholtz Zentrum Munich, Germany)

III.2. INGENIERIE : Développement de méthodes d'analyse d'image pour la biologie quantitative.

Une partie de mon activité de recherche a, depuis le début, consisté en le développement d'outils de biologie moléculaire ou de méthodes d'analyses. Cette facette de mon travail de recherche s'est nettement accrue quand j'ai rejoint l'équipe BCF dont une grosse partie de l'activité consiste à développer des techniques de microscopie linéaire ou non-linéaire et des méthodes d'analyse permettant de quantifier les évènements biologiques. Dans le but de mettre en exergue la démarche d'ingénierie de mon parcours, je décrirai dans cette section les développements majeurs que j'ai initiés, réalisés ou dans lesquels j'ai participé ces deux dernières années.

Ce travail fut réalisé dans le cadre du projet ANR DynamIC (Dynamique et interactions de complexes intranucléaires par microscopie), coordonné par le Dr Laurent Héliot et en collaboration avec les Dr Oliver Bensaude et Xavier Darsacq à l'ENS, Paris. Le postulat de travail de notre groupe était d'utiliser la complémentarité des méthodes existantes : FRET, FCS, SPT (Figure 40) et de développer de nouvelles méthodes permettant de relier les premières entre elles et ainsi de s'affranchir de leurs limites, dans le but d'étudier la dynamique des interactions entre protéines en cellules vivantes.

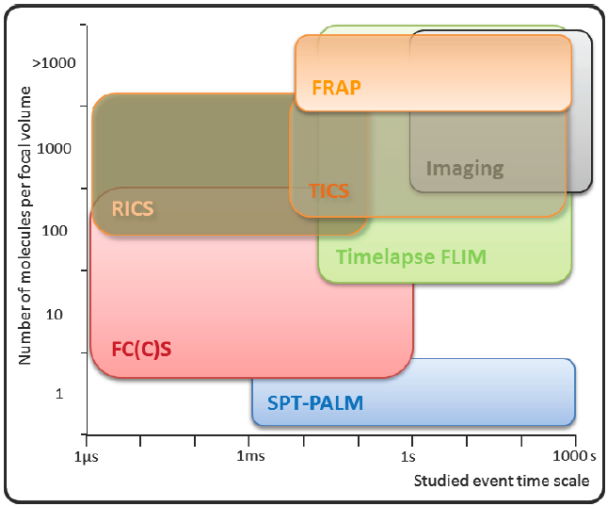

Figure 40 : complémentarités et limites spatiales et temporelles des techniques de microscopie et nanoscopie.

III.2.1. CORRÉLATION TEMPORELLE DE DÉTÉCTION DE PHOTONS : CARACTÉRISATION DE L'OLIGOMERISATION DE PROTÉINES FLUORESCENCES PAR FCS

Contexte

L'analyse de la diffusion des molécules par la technique de FCS offre une très bonne résolution temporelle (de la µs à la minute) sans informations sur la distribution spatiale. Une des contraintes de la FCS est d'acquérir sur la durée dans un volume restreint sans induire le photoblanchiment des molécules les plus lentes. Ainsi, si deux populations sont en présence, une diffusive rapide représentant 90% de la population totale et une diffusive lente comptant pour 10% de la population totale, les autocorrélations auront tendance à masquer la seconde. Dans le cas de notre modèle nous cherchons à mesurer la dynamique d'interaction entre la Cycline T1 (CT1) et la sous-unité majeure de l'ARN polymérase II (Rpb1). Cependant, les analyses FCS ne nous permettent de détecter qu'une population rapide de CT1 dont le temps de résidence moyen dans le volume focal (Vf) est de 1 ms. Or nous savons, par nos analyses de FRET, qu'une partie des molécules de CT1 se lie à l'ARN POL II sur l'ADN de manière suffisamment stable pour visualiser des nanodomaines d'interaction. Bien que la FCS favorise les populations de molécules caractérisées par une dynamique rapide,

il paraît envisageable de discriminer la fraction diffusive de la fraction liée à l'ADN, considéré comme immobile.

Objectifs

Nous cherchons donc à développer une méthode d'analyse de nos enregistrements de FCS qui nous permettrait d'isoler cette sous-population dans le but de pouvoir la caractériser bio-physiquement.

Résultats

Lors du stage de master de Mme Hayat ZAOUI, que je co-encadrais avec Corentin Le Nezet, nous avons posé les bases de cette nouvelle méthode.

Nous avons commencé par effectuer des acquisitions FCS de 600 sec en limitant le photoblanchiment au maximum. Ces acquisitions furent réalisées avec une photodiode à avalanche (SPAD). Dans un premier temps, nous avons recherché des évènements diffusant lentement (de la seconde à la minute) et peu nombreux donc masqués dans nos courbes d'autocorrélation de FCS à cause de leur faible fréquence temporelle par rapport aux fluctuations microsecondes de la fraction diffusive. Dans cette optique, nous avons effectué un lissage du tracé à la fréquence de 1 Hz (Figure 41). En parallèle, nous avons calculé, à chaque seconde) le nombre de molécules et la brillance moléculaire (nombre de photons détectés par seconde et par molécule) grâce à la méthode d'histogramme de comptage de photon, PCH [95]. Cette analyse montre que des déflections importantes ont lieu sur des échelles de temps allant de 10 à 60 s. Ces variations de fluorescence sont associées à une variation du nombre de molécules moyennes dans le volume focal (Vf) plutôt qu'à une variation de la brillance.

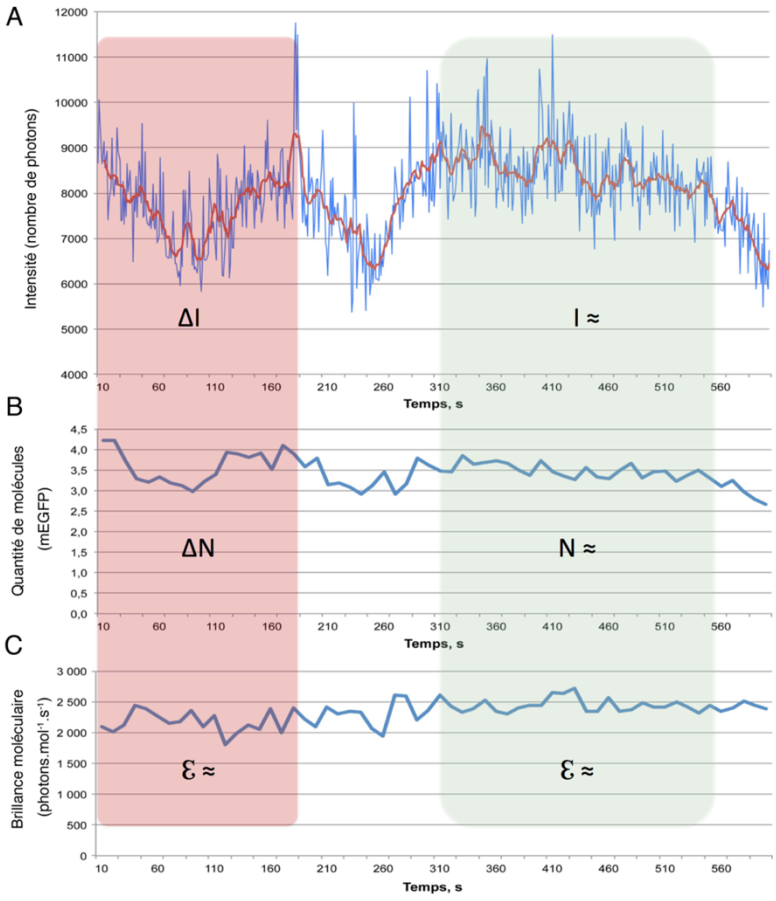

Figure 41 : tracé de FCS lissé à 1Hz et analyses PCH associées. **A.** Détection des photons provenant des molécules CT1-mEGFP dans le Vf pendant 600 sec. **B.** Courbe d'évolution du nombre de molécules au court du temps. **C.** Courbe d'évolution de la brillance moléculaire (ε) moyenne au cours du temps. Zone rouge : corrélation entre la baisse du nombre de photons et la baisse du nombre de molécules, sans relation directe avec l'évolution de la brillance moléculaire. Zone verte : segment stable pour les 3 paramètres.

Cette échelle de temps correspond à la dynamique attendue de gros éléments comme les boucles de

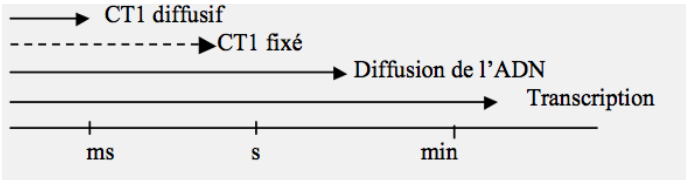

Figure 42 : représentation comparative de la durée de la transcription d'un gène avec la cinétique de diffusion des différentes composantes de notre système d'étude.

chromatine [96, 97], les nucléoles ou encore les larges zones de surconcentration de la cycline T1 dans le noyau (Figure 41).

Nous aurions pu attendre que le calcul du nombre de molécules nous informe sur la présence de molécules liées à un site de transcription en plus des molécules diffusant librement (soit une augmentation du nombre de molécules attendues). Cependant, nous n'avons détecté que des diminutions temporaires du N. Ceci peut s'expliquer par le photoblanchiment des molécules liées à la chromatine. Ainsi, à puissance laser similaire, on observe un photoblanchiment rapide de la fluorescence de l'histone H2A avec une demi-décroissance allant de 300ms à 3s en fonction de la concentration initiale de molécules mEGFP. Ceci implique que si des molécules de CT1 se fixent sur la chromatine dans le Vf et pour un temps supérieur à leur constante de photoblanchiment, ces molécules seront photo-blanchies avant de sortir du Vf que ce soit sous forme libre ou sous forme complexée à la chromatine. Nous devrions alors être capable d'observer des photons surnuméraires liés au transit de molécules CT1 fixées sur la chromatine et observer leur photoblanchiment ou leur sortie du Vf suite au mouvement de la chromatine (Figure 43).

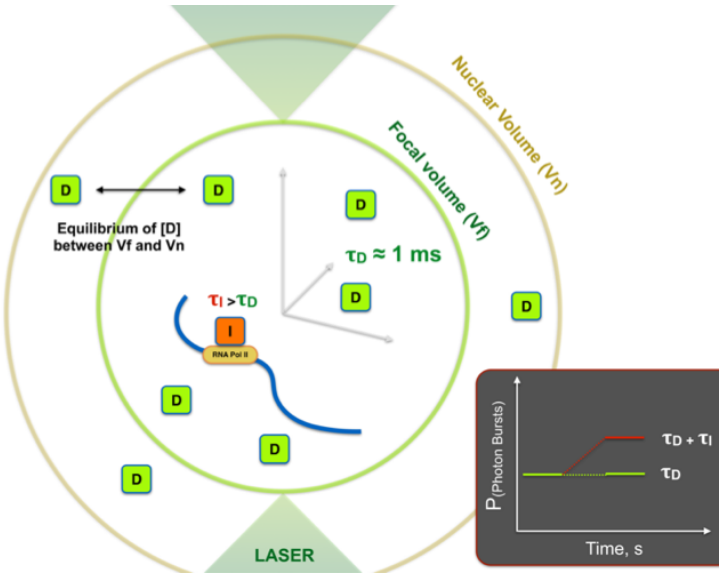

Figure 43 : schéma expliquant la théorie des bouffées de photons (PBs). Grâce à la diffusion rapide de CT1, on postule que l'équilibre des concentrations est vrai en tout point du noyau et que donc la quantité de molécules diffusant librement à travers Vf est stable (cf. Figure 12). Ce n'est pas vrai pour la fraction de CT1 liée à la chromatine. On peut donc s'attendre à avoir, *en absence d'évènement de photoblanchiment*, 2 niveaux de fluorescence : le niveau basal = fraction diffusante et le niveau 1 associant fraction mobile et liée à la chromatine.

La bouffée de photon.

Notre idée a donc été de considérer que le transit de molécules surnuméraires mEGFP fixées sur la chromatine devrait introduire une petite hétérogénéité dans le nombre de photon (Figure 44). Le photoblanchiment ne pouvant pas totalement supprimer mais plutôt diminuer la durée de ces « bouffées de photon » ou photon

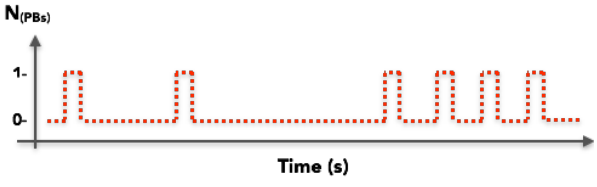

Figure 44 : schéma représentant l'hétérogénéité des bouffées de photons au cours du temps.

bursts (PBs).

Nous avons commencé par déterminer le seuil minimal d'arrivée de plusieurs photons appartenant à un PB. Ce seuil fut fixé à l'arrivée consécutive de 3 photons séparés par un intervalle de 200ns (3 fois le temps mort du détecteur).

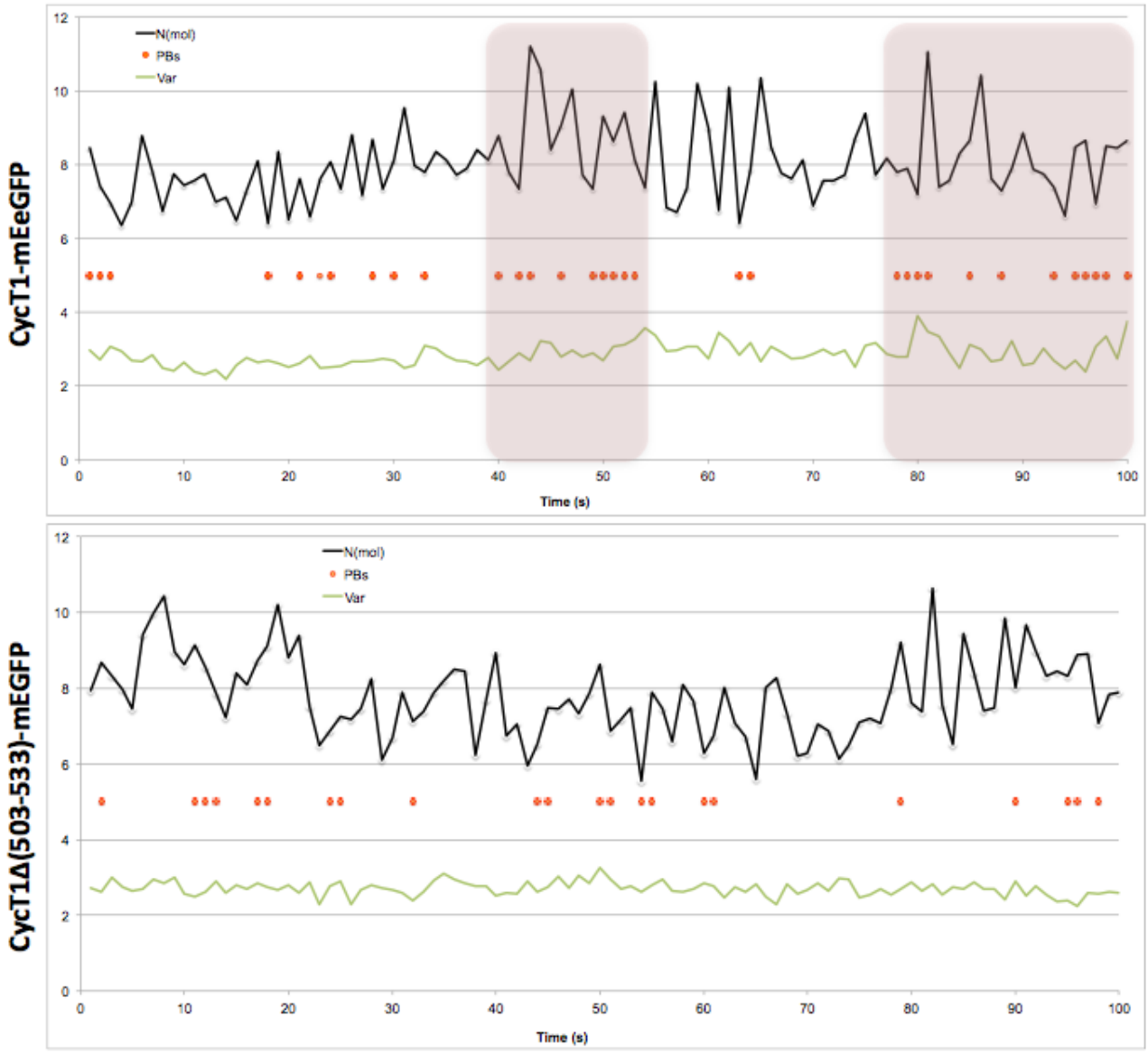

Figure 45 : tracés 1Hz montrant l'évolution du nombre de molécules mEGFP, N (courbes noires), de la variance de N (courbes vertes) et de la détection de PBs (points orange) dans des cellules U2OS transfectées soit avec la forme sauvage de CT1 soit avec un mutant de CT1 ayant une interaction diminuée avec l'ARN POL II (CT1Δ(503-533)). N et variance de N ont été calculé par PCH, avec un bin de 100 µs, sur des intervalles de 1s.

On observe dans la figure 45, une plus forte détection de PBs dans la condition CT1 sauvage qu'avec son mutant incapable de s'associer à Rpb1, ce qui était prédit par les données de biochimie démontrant une moindre interaction (voir une suppression) de l'interaction du mutant avec la sous-unité Rpb1 de l'ARN POL II. Cette densité plus élevée traduit donc probablement la fixation temporaire de molécules CT1 sur Rpb1. Néanmoins, nous avons caractérisé quelques limites inhérentes à la méthode et au système.

Problème 1 : dépendance du nombre de bouffées de photons au nombre de photons totaux (nombre de molécules)

Il existe une relation entre le nombre de photon détectée et le nombre de PBs détectés (Figure 46). Ceci vient du fait que la probabilité d'obtenir des PBs dépend de la probabilité de détecter 3 photons dans un intervalle maximal de 2*200ns. Cette probabilité dépendant du nombre de photon émis convolué par l'IRF du système. Le nombre de photons émis dépend, à puissance laser constante, du nombre de protéines dans le Vf et de la brillance moléculaire (stable pour des particules monomériques, variables pour des agrégats). En conclusion, plus les photons sont émis, plus on a de chance de détecter 3 photons dans un intervalle de 2*200ns. Cette limite rend caduque le simple comptage du nombre de PBs par unité de temps. En effet, il est quasiment impossible de comparer le nombre de PBs sur des tracés de durée égale car le nombre de molécules dans nos conditions d'acquisition varie entre 3 et 15 molécules moyennes par Vf (entre 40 et 200 nM). Néanmoins, cette limite ne remet pas en cause l'analyse de l'hétérogénéité de la distribution des arrivées des PBs comme on pouvait l'observer sur la figure 45. Pour quantifier cette hétérogénéité, nous avons calculé la distribution de ces intervalles entre 2 PBs (Figure 47).

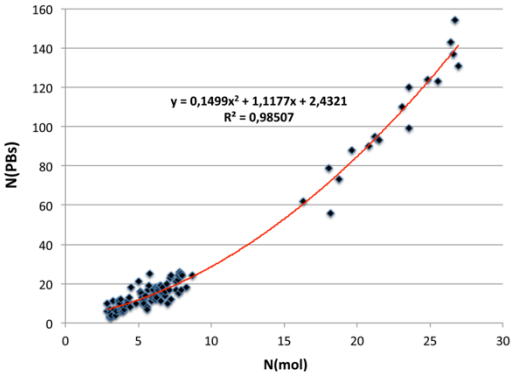

Figure 46 : relation entre nombre de PBs, N(PBs), et nombre de molécules, N(mol). Données acquises sur une protéine CT1-mEGFP en cellule vivant par FCS.

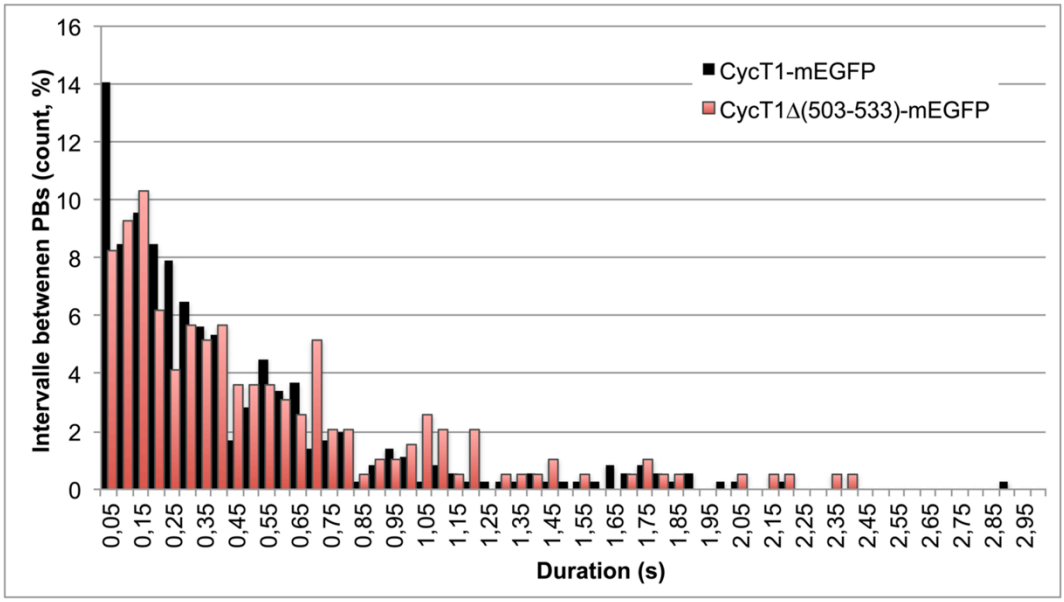

Figure 47 : distribution des intervalles séparant 2 PBs dans des cellules U2OS exprimant soit CT1 soit le mutant CT1Δ(503-533).

Sur des tracés de 100s comptant entre 8.10^5 et 10^6 photons, on observe une nette augmentation (x 1,8) du nombre de PBs séparés par un intervalle inférieur à 50ms dans la condition CT1-mEGFP par rapport au mutant de CT1 déficient pour interagir avec l'ARN POL II. Ces résultats révèlent la présence de plus fortes densités locales de PBs caractérisant l'interaction de CT1 avec l'ARN polymérase II.

ACTIVITÉS DE RECHERCHE

Problème 2 : Afterpulse

Les détecteurs de type APD et SPAD utilisent une matrice de silicium semi-conductrice (jonction p-n) soumise à un fort champ électrique. Les photons entrants sont absorbés par la zone d'absorption ($i_{(p-)}$) et créant des paires électron-trou qui se propagent en sens inverse par diffusion dans la couche p^+ pour les trous et la couche p pour les électrons (Figure 48). Au niveau de la jonction p-n les électrons ionisent en cascade la matrice générant de nouvelles paires électron-trou, créant l'amplification du signal par avalanche. L'accumulation de trous à la cathode et d'électrons à l'anode génère le photo-courant.

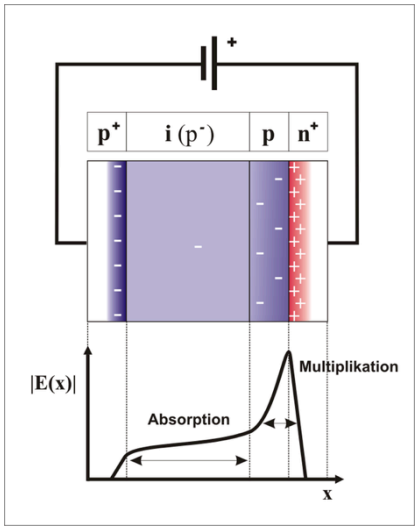

Figure 48 : schéma de fonctionnement d'une photodiode à avalanche.

Les SPAD fonctionnent sur le même principe mais en mode Geiger, c'est à dire avec un courant appliqué supérieur au courant de claquage du semi-conducteur (seuil au dessus duquel le semi-conducteur se comporte comme un conducteur linéaire). Ceci permet à un seul électron d'engendrer une avalanche exponentielle permettant ainsi de booster le gain jusqu'à un facteur 10^6 et donc de générer un photo-courant supérieur au bruit suite à l'impact d'un unique photon. Les 2 principales propriétés de ces détecteurs sont le rendement quantique (42% pour notre SPAD) et le dark count (250 cps), c'est à dire le nombre de déclenchements d'avalanche en absence de stimulus externe (dû à une stimulation thermique ou un effet quantique de la matrice). La limite technique inhérente aux systèmes à avalanche est l'afterpulse. Suite à une première excitation de l'APD, le piégeage d'un ou plusieurs électrons dans la couche p peut libérer une seconde avalanche sans excitation par un photon. L'afterpulse du détecteur peut être vu comme une probabilité (3% sur notre détecteur sur une durée allant de 70 à 500 ns après une première avalanche) de générer un signal faux positif consécutif à un vrai signal. La probabilité d'obtenir un afterpulse secondaire (consécutif à un afterpulse primaire) semble heureusement quantité négligeable. Dans notre hypothèse de travail sur les PBs, la génération d'un afterpulse peut intervenir sur le 2° ou 3° photon d'un PBs. Ceci à pour conséquence de générer un fort bruit et donc limiter notre capacité à détecter des évènements rares.

Une solution pour supprimer l'afterpulse consiste à inactiver l'APD pour un temps supérieur au temps moyen de l'afterpulse, en général < 500 ns (le temps mort de notre SPAD est de 80 ns). Néanmoins, augmenter le temps mort signifie aussi diminuer la probabilité de détection de photons rapprochés, ce qui n'est pas indiqué dans notre méthode. Une solution alternative consiste à utiliser un détecteur dit hybride qui est dépourvu d'afterpulse (Figure 49).

C'est pourquoi, pour évaluer, l'importance de l'afterpulse dans la génération de nos PBs, nous avons testé un détecteur GaAsP Hybride (Hamamatsu). Ce type de détecteur récent utilise le principe d'un PMT en détectant les photons grâce à une photocathode puis en accélérant les électrons de sorte qu'ils génèrent un forte stimulation sur la matrice de silicium de la photodiode en aval [98]

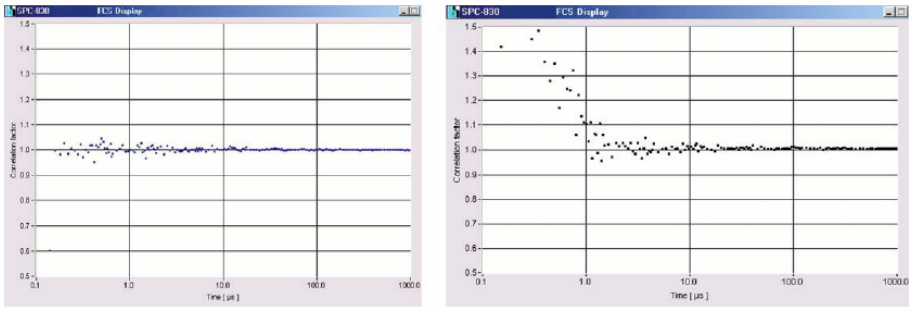

Figure 49 : comparaison des autocorrélations issues d'un PMT hybride (gauche) et d'un PMT standard (droite) sous illumination constante à un taux de comptage de photon de 10 kHz [98].

Nos premiers résultats, sur notre nouveau détecteur GaAsP hybride, montrent que le nombre de PBs de 3 photons espacés de 2*200 ns a diminué de 50% par rapport aux données acquises avec un SPAD. Ceci suggère donc que 90% des PBs détectés avec le SPAD étaient formés d'au minimum 2 photons détectés et un afterpulse. Le nombre de PBs de 3 photons espacés de 200 ns étant faible dans les tracés issus du détecteur hybride, Corentin Le Nezet a développé une autre méthode d'analyse, basée sur la fréquence de combinaison des durées des intervalles séparant les 2 premiers photons et les 2ème et 3ème photons détectés.

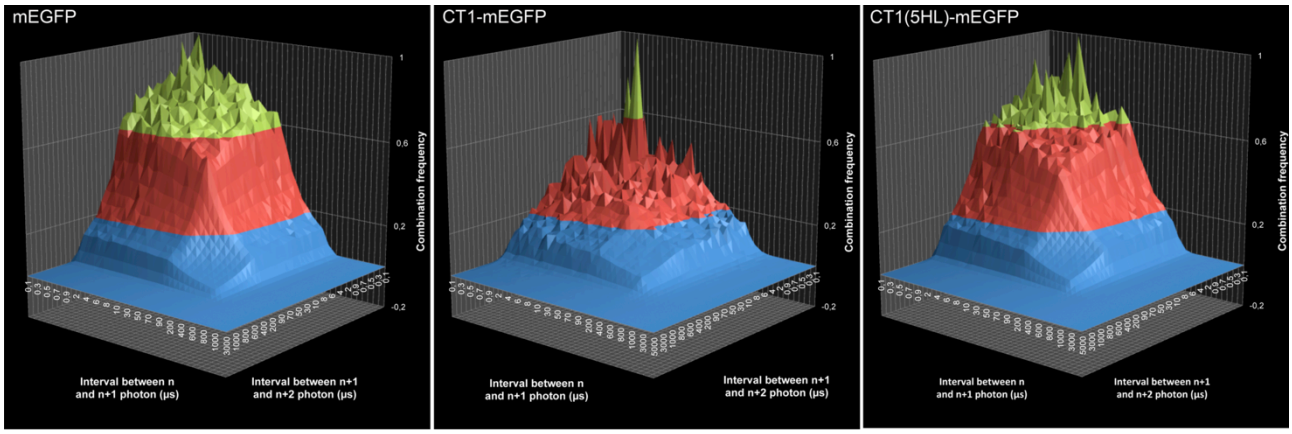

Figure 50 : fréquence observée de combinaison des durées des intervalles séparant les photons n/n+1 et n+1/n+2 pour la mEGFP libre, la cycline T1 (CT1-mEGFP) et un mutant de la cycline T1 déficient pour l'interaction avec la sous-unité Rpb1 de l'ARN POL II. Le code couleur représente 20% (bleu) et 40% (rouge et vert) de la fréquence.

Comme présenté sur la figure 50, on observe dans le cas de la mEGFP libre que 60% des groupes de 3 photons ont des intervalles équiprobables entre les 2 premiers photons et le 2° au 3° photon d'une durée maximale de 8 µs (valeur maximale observée des intervalles entre 2 photons). On observe aussi que seulement 20% des groupes de 3 photons combinent un premier intervalle de 400 ns avec des intervalles maximaux de 400 ns, contre 80% avec des intervalles compris entre 400 ns et 8 µs. A l'inverse, dans le cas de CT1-mEGFP, on observe que seul 35% des groupes de 3 photons ont des intervalles équiprobables entre les 2 premiers photons et le 2° au 3° photon d'une durée maximale de 8 µs. On voit aussi que 60% des groupes de 3 photons combinent un premier intervalle de 400-600 ns sont suivis d'un intervalle maximum

400-600 ns. On observe donc une récurrence des intervalles courts (environ 1 évènement par minute) dans le cas de CT1-mEGFP qu'on n'observe ni dans le cas de la mEGFP libre, ni avec le mutant CT1 déficient pour l'interaction avec l'ARN polymérase II.

Nos travaux démontrent donc que la récurrence des intervalles courts des groupes de 3 photons dans la condition CT1 est spécifiquement due à la fraction de CT1 liée à l'ARN POL II et donc très probablement à la chromatine. Nos données mettent aussi en évidence une détection rare de l'ordre de 1'événement par minute, ce qui correspond à peut prêt au temps de résidence de la chromatine dans le volume focale. On s'est donc demandé dans quelles limites la différence de diffusion des 2 populations pouvaient être responsable de la récurrence des durées des intervalles. Néanmoins, la comparaison entre l'atto-488, diffusant à environ 536 $\mu m^2/s$, et la mEGFP, diffusant à environ 70 $\mu m^2/s$, ne démontre aucune différence de fréquence de combinaison des intervalles n à n+2 similaire. Ce résultat suggère donc que la contribution de la cinétique de diffusion ne peut générer de PB. Comme d'après nos collègues mathématiciens, la génération de PB ne peut être mathématiquement dépendante que de la brillance totale dans le Vf, la seule explication cohérente serait que plusieurs molécules de CT1 s'oligomérisent en s'associant avec Rpb1. Dans ce cas, les oligomères de CT1-mEGFP se comporteraient comme un émetteur unique dont la brillance moléculaire serait égale au produit du nombre de molécules oligomérisées et de la brillance moléculaire. Notre données suggèrent donc, en l'absence actuelle d'un modèle mathématique solide pour les valider, que notre méthode permet d'extraire, des tracés FCS, la contribution minoritaire des CT1 oligomériques fixées sur l'ARN polymérase…ce qui était l'objectif initial de ce travail.

Conclusion & Perspectives

Ce travail est toujours en cours et nous évaluons la possibilité de calibrer un système *in vitro* dans le but de démontrer que la récurrence des intervalles (entre 400 et 600 ns) nait bien de l'oligomérisation de molécules fluorescentes. Nous évaluons aussi la possibilité d'estimer le nombre de molécules oligomérisées en fonction de la durée moyenne des intervalles récurrents.

Une collaboration avec le Dr Hugues BERRY (INRIA Rhone-Alpes Université de Lyon LIRIS UMR5205), portant sur la modélisation du comportement de molécules oligomérisées sur l'ADN et diffusant lentement à travers le Vf de FCS, devrait nous aider à expliquer et clarifier nos données.

Production associée

- Un article méthodologique sera réalisé.
- Un logiciel sera développé sous Matlabs pour automatiser l'analyse de grandes séries de données.

Encadrement, Collaborations et tâches associés

- Mme ZAOUI Hayat, Master 2 biophysique.
- Mr LE NEZET Corentin, IR, analyse des intervalles entre les trains de photons.

III.2.2. OPTIMISATION DU COUPLE DONNEUR-ACCEPTEUR POUR LE FRET

Contexte

La qualité et la sensibilité de mesure d'un événement de FRET dépendent principalement du **rapport signal/bruit** du système (électronique et biologique).

Le **bruit** est la composante du bruit électronique du système (IRF du laser, bruit blanc du détecteur), de l'autofluorescence et des phénomènes de cross-excitation / cross-émission des protéines fluorescentes. Le bruit électronique dépendant du système utilisé, il est difficile de le réduire. Les phénomènes de cross-émission et cross-excitation peuvent être limités par le choix des fluorochromes et des filtres du chemin optique.

Le **signal** est dépendant de la sensibilité de la détection (rendement du détecteur), de la concentration des protéines fluorescentes en interaction et de l'efficacité de FRET, $E_{(FRET)}$ (Eq. 5). Comme le but est de travailler dans des conditions proches de la physiologie, il est déconseillé de jouer sur la concentration des protéines pour augmenter le signal. Le rendement du détecteur étant fixe, nous ne pouvons optimiser que l'$E_{(FRET)}$. Comme rappelé dans le chapitre précédant, l'$E_{(FRET)}$ d'un système est directement dépendante de 1) la distance entre le donneur et l'accepteur de fluorescence et 2) du rayon de Förster (Eq. 6).

Eq. (5) $$E_{(FRET)} = \frac{1}{1+\left(\frac{R}{R0}\right)^6}$$

Eq. (6) $$R0 = 0{,}2108.[\kappa^2.\Phi_D.J(\lambda).\eta^{-4}]^{1/6}$$

κ : facteur d'orientation du dipôle (2/3 par défaut), (

η : indice de réfraction du milieu (1,3342 dans l'eau à 25°C)

Φ_D : rendement quantique du donneur (%)

$J(\lambda)$: intégrale de recouvrement des spectres ($L.mol^{-1}.cm^{-1}.nm^4$)

Il existe donc, conceptuellement, 2 solutions permettant d'augmenter le R0 :

- choisir/améliorer les propriétés des fluorochromes : κ, ΦD et $J(\lambda)$.
- favoriser le positionnement des fluorochromes pour qu'ils se situent dans un rayon, R de moins de 10 nm. Il faut aussi prendre en compte l'encombrement stérique au sein des complexes supramoléculaires et l'obstruction au couplage des fluorochromes que la densité locale de protéine peut représenter dans ces complexes.

Objectifs

Développer un système de FRET possédant un meilleur rapport signal/bruit et une moindre dépendance à l'encombrement stérique des complexes supramoléculaires P-TEFb/ARN POL II permettant l'étude d'association de protéines dans des gammes de concentration physiologique.

Méthodes

En octobre 2013, après avoir effectué un référencement des diverses protéines fluorescentes disponibles et calculé l'$E_{(FRET)}$ en fonction de R (Figure 51), j'ai sélectionné le couple mTurquoise2 (mTurq2) [99] et SYFP2.

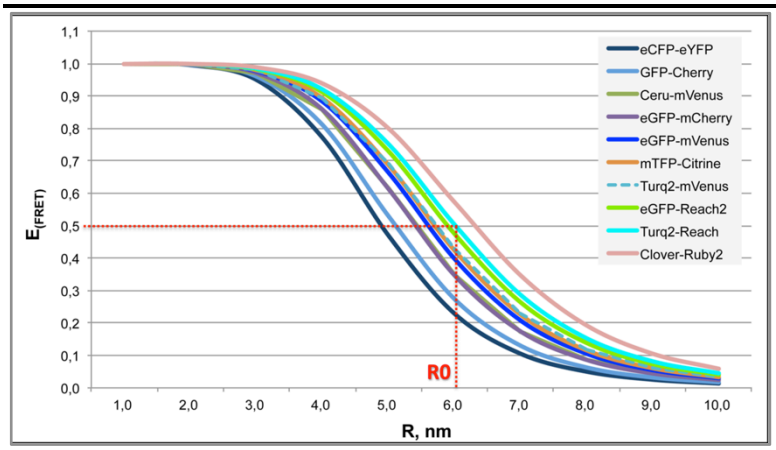

Figure 51 : graphique représentant l'évolution de l'efficacité de FRET $E_{(FRET)}$ en fonction de la distance entre le donneur et l'accepteur de FRET (R) pour 10 couples de fluorophores. Le rayon de Förster, R0, du couple mTurquoise2/Reach est reporté graphiquement pour une $E_{(FRET)}$ de 50%.

Le R0 du couple Clover/ruby2 était meilleur que celui de mTurq2/SYFP2 mais le rendement quantique de la mTurq2 (93%) et sa stabilité (50% de la stabilité de la EGFP) étaient meilleurs que ceux de Clover (76%, 25% de la stabilité de la EGFP) [100]. Au delà de l'importance de l'E_{FRET}, l'optimisation d'une expérience de TD-FLIM requiert un rapport signal/bruit optimisé. C'est pourquoi le rendement quantique et la stabilité du donneur de fluorescence sont essentiels.

La description d'une variante sombre de la protéine fluorescente Venus, Reach [101], m'a aussi interpellé. Les caractéristiques de cette protéine en faisaient un excellent accepteur d'énergie pour le FRET. Les auteurs de l'article décrivant Reach l'avaient utilisée en couple de FRET avec la GFP en démontrant que la perte de 90% de l'émission de fluorescence de Venus suite à sa mutation permettait de s'affranchir des problèmes de cross-excitation. Néanmoins, bien que l'efficacité de couple EGFP/Reach (R0 = 5,90 nm), soit meilleure que nombre d'autres couples, dont mTurq2/SYFP2 (R0 = 5,72 nm), la très grande proximité des spectres d'excitations de la EGFP et de Reach provoque un phénomène de cross-excitation. Malgré sa faible fluorescence, Reach qui possède un temps de vie très bas (0,3 ns) va émettre des photons très rapides lors d'une expérience de FRET-FLIM et contaminera la fluorescence émise par la GFP. La conséquence néfaste sera de faire décroitre le temps de vie apparent de l'EGFP, et ce, indépendamment de l'existence d'un phénomène de FRET.
J'ai cependant profité du plus grand décalage entre les spectres d'excitation de la mTurq2 et de la Reach, puis testé l'absence de cross-excitation, afin de vérifier leur compatibilité. Le R0 de ce couple est un des meilleurs actuellement (6,0 nm) et le rendement quantique de la mTurq2 nous permet de la détecter même a faible concentration (100-500 nM).

Dans l'optique de limiter les problèmes liés à l'encombrement stérique des protéines et à la limitation de l'espace disponible au sein des complexes supramoléculaires comme celui de l'ARN POL II, j'ai créé un vecteur permettant de normaliser et évaluer l'impact de la taille du peptide de liaison (séquence d'acides aminés séparant les protéines d'intérêt et l'étiquette fluorescente). La particularité de ce vecteur est de posséder 2 paires de sites de restriction permettant de réduire la taille du peptide de liaison en une restriction/ligation (Figure 52). Ce vecteur, pVLL, basé sur le squelette du vecteur pEGFP, possède ainsi un peptide de liaison de 42 AA pouvant être réduit à 22 et 12 AA.

Nous avons développé une gamme de vecteurs pVLL(42) incluant les protéines mTurq2, mEGFP, SYFP2, Reach, mNeptune et mDendra2, greffées en N ou en C-terminale de la chimère finale. Ces vecteurs sont prédigérés par les 2 sites de restrictions utilisés pour introduire le gène d'intérêt (NheI/AgeI ou SacII/NotI) et congelés.

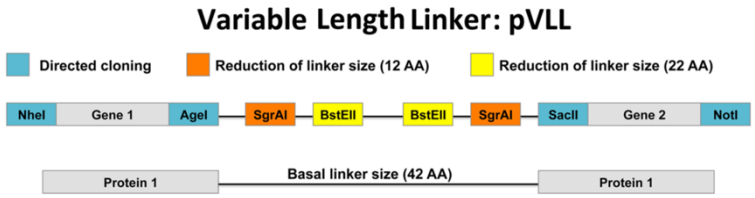

Figure 52 : schéma récapitulant les sites de restrictions imposés dans le site de clonage du vecteur pVLL. Les paires de sites BstEII et SgrAI sont utilisées pour réduire la taille du peptide de liaison de 42 AA à 22 et 12 AA respectivement.

Résultats

Les tests réalisés en FLIM-FRET sur des tandems fluorescents de mTurq2/SYFP2 ou mTurq2/Reach, construits dans les vecteurs pVLL(42/22/12) ont démontré que le couple mTurq2/Reach possède une $E_{(FRET)}$ moyenne de valeur double de celle du couple mTurq2/SYFP2 (Figure 53). Comme les tailles et structures des chimères sont comparables, on peut calculer que la distance moyenne obervée séparant les fluorochromes ne diverge pas énormément (7,68 nm). Une explication plausible est que les peptides de liaison sont flexibles et qu'ils offrent suffisamment de mobilité aux fluorochromes des tandems pour générer un FRET maximal, indépendamment de la taille des peptides de liaison. A la distance de 7,68 nm, le couple mTurq2/Reach, devrait générer une $E_{(FRET)}$ moyenne de 0,19... Le calcul expérimental du R0 du couple mTurq2/Reach selon nos données indique un R0 compris entre 6,6 et 6,8 nm, contre 6,0 nm calculés selon les données de la littérature. Une détermination plus précise du R0 de ce couple permettrait de valider ces calculs. Néanmoins, j'ai montré que la version Reach2 (double mutation) de la SYFP2 améliore grandement la sensibilité de notre système de FRET.

J'ai ensuite déterminé l'importance de la taille du linker en mesurant $E_{(FRET)}$ moyenne entre

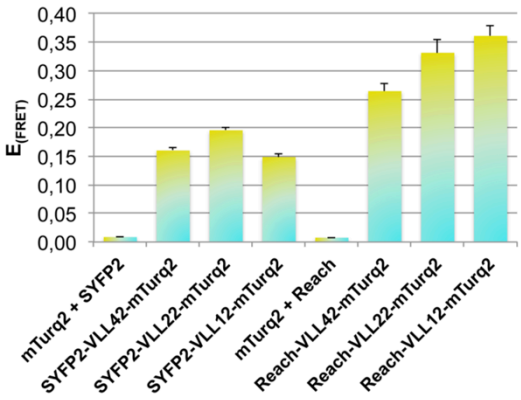

Figure 53 : efficacités de FRET ($E_{(FRET)}$) de couples de fluorochormes (+) ou de tandems dans lesquels les 2 fluorochromes sont séparés par des peptides de liaison de 3 tailles différentes : 42, 22 et 12 AA (VLL42/22/12). Acquisitions réalisées en TD-FLIM dans des cellules U2OS vivantes.

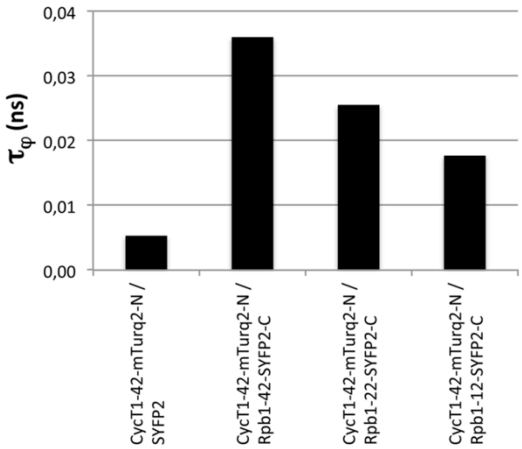

Figure 54 : efficacités de FRET ($E_{(FRET)}$) de tandems de protéines CT1-mTurquoise2 et SYFP2 ou Rpb1-SYFP2. Acquisitions réalisées en TD-FLIM dans des cellules U2OS vivantes.

les protéines CT1 et Rpb1 (Figure 54). Ce travail de criblage a été effectué par la méthode de FLIM dans le domaine des fréquences (non développé dans l'introduction). Cette dernière présente l'avantage de sacrifier la résolution spatiale pour une meilleure résolution temporelle et elle est plus rapide à analyser. Il est à noter qu'avec notre système de FRET mTurq2/Reach avec un peptide de liaison de 42 AA, nous avons détecté un signal de FRET faible entre CT1 et Rpb1 alors qu'avec un couple ECFP/EYFP fusionné sans peptide de liaison sur CT1 et Rpb1 respectivement, nous ne sommes pas parvenus à détecter de FRET. Dans chaque configuration, nous avons aussi évalué l'effet du positionnement en N- ou C-terminal de la protéine d'intérêt dans la chimère fluorescente. Il est apparu qu'en fonction de la protéine d'intérêt, les 3 cas de figures pouvaient être rencontrés : pas de différence, préférence pour le N ou le C-terminus.

Conclusion & Perspectives

Dans ce travail, j'ai donc démontré que la préparation et l'amélioration des outils de FRET est une composante essentielle de la réussite d'une expérience de FLIM-FRET et ce d'autant plus que la concentration du donneur et la force du FRET sont faibles. En outre, l'évolution très rapide des protéines fluorescentes ces dernières années, oblige à une veille technologique régulière pour profiter de toutes les optimisations possibles.

Production associée

- **ARTICLE 1:** Laurent Héliot, Mariano Gonzalez-Pisfil, Mélanie Henry, Corentin Le Nezet, Olivier Bensaude, Bernard Vanden Bunder and Gabriel Bidaux. A 2-steps model for the dynamic binding of P-TEFb on the transcriptional paused complex. En préparation.
- **POSTER à FOM (Focus On Microscopy), mars 2015 :** "Photonics reveal Cycline T1-guided P-TEFb fate", par **G Bidaux**, M Gonzalez-Pisfil, M Henry, C Le Nezet, O Bensaude, X Darzacq, B VandenBunder and L Heliot.

Encadrement, Collaborations et tâches associés

- Mr GONZALEZ-PISFIL Mariano, expériences de FLIM,
- Mme HENRY Mélanie, réalisation d'une partie des protéines de fusion dans pVLL.

III.2.3. SEGMENTATION D'IMAGE ET CORRÉLATION D'IMAGE POUR LA CARACTÉRISATION DE NANODOMAINES DE FRET

Contexte

La méthode la plus courante pour analyser des données de FRET consiste à calculer soit le temps de vie moyen (FLIM) ou l'$E_{(FRET)}$ (FLIM ou méthode ratiométrique) de toute l'image ou de la région d'intérêt choisie. Cette méthode est rapide et fonctionnelle dans de nombreux cas. Mais elle ne fournit aucune information sur la carte des interactions dans la cellule, et dans notre cas dans le noyau.

De plus, il existe des cas de figures pour lesquels les variations de temps de vie ou d'$E_{(FRET)}$ sont minimes et se situent dans une zone d'incertitude (moins de 1,5% d'$E_{(FRET)}$) ou zone grise (Figure 55). Cette zone grise est la zone dans laquelle on peut détecter un signal de FRET significatif même en absence d'interaction réelle. Ainsi la simple diffusion des fluorochromes dans une cellule vivante crée des rencontres aléatoires susceptibles de générer du FRET. Ainsi, bien qu'on observe une légère diminution de l'$E_{(FRET)}$ entre les mutants de CT1 (incapables d'interagir avec Rpb1 d'après les données de biochimie) et Rpb1, la différence n'est pas significative (t-test). De même, la protéine libre Reach exprimée en même temps que CT1-mTurq2 suffit à générer une $E_{(FRET)}$ moyenne du même ordre de grandeur que celle générée par CT1-mTurq2 et Rpb1-Reach. On peut donc se demander si CT1 génère un FRET en interagissant avec Rpb1 ou en la rencontrant aléatoirement. La même question se pose pour les mutants de CT1 avec Rpb1.

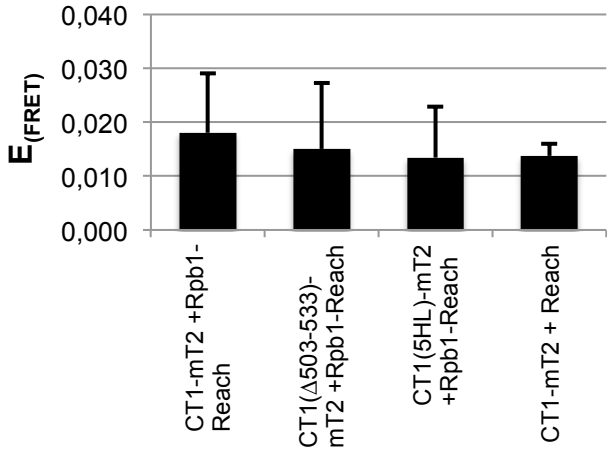

Figure 55 : histogramme reportant l'$E_{(FRET)}$ entre CT1-mTurquoise2 ou ses mutants et Rpb1-Reach, ou CT1-mTurquoise2 et la protéine Reach libre.

Objectifs

Développer une méthode et des outils d'analyses automatisés permettant de discriminer entre les évènements de FRET dépendant d'interactions les évènements de FRET induits par la rencontre aléatoire de molécules n'interagissant pas, pour des $E_{(FRET)}$ moyennes inférieures à 2%.

Résultats

Nous avons posé l'hypothèse que la nature de la dynamique des molécules peut être responsable du masquage d'évènements de FRET discrets. En effet, l'$E_{(FRET)}$ moyenne d'une image est régie par l'équation suivante :

Eq. (7) $$Emean = Epix \times \left(\frac{Npix,FRET}{Npix,tot}\right)$$

E_{mean} : $E_{(FRET)}$ moyenne.
E_{pix} : $E_{(FRET)}$ par pixel.
$N_{pix,FRET}$: le nombre de pixels dans lesquels le FRET a lieu.
$N_{pix,Tot}$: le nombre de pixel total.

ACTIVITÉS DE RECHERCHE

[1] Dans le cas d'un donneur et d'un accepteur de fluorescence libres de diffuser indépendamment et n'interagissant pas ensemble, des événements de FRET discrets vont se produire dans quasiment tous les pixels de sorte que $E_{mean} = E_{pix}$. D'après nos données, E_{mean} due aux rencontres aléatoires entre les protéines des couples : mTurq2/Reach, CT1-mTurq2/Reach et mTurq2/H2A-Reach se situe entre 1 et 1,5% (Figure 56.1). On peut donc supposer que $E_{pix} < 1,5\%$.

[2] Dans le cas de 2 molécules diffusives interagissant même faiblement, $E_{pix} > 1,5\%$ et donc $E_{mean} > 1,5\%$ (Figure 56.2). Ce cas de figure donnera donc toujours une $E_{(FRET)}$ supérieure à la zone grise et pourra donc être analysé facilement par le calcul de la valeur moyenne de l'$E_{(FRET)}$ sur l'image.

[3] Dans le cas de 2 molécules diffusant à des régimes très différents, voir en considérant que l'une des 2 molécules est immobile au regard de la vitesse d'acquisition, on peut prédire que le FRET n'aura lieu que dans les pixels où le partenaire immobile se trouve. Donc $N_{pix,FRET} < N_{pix,Tot}$ (Figure 56.3). La conséquence est que, pour $E_{mean} < 1,5\%$ plus le partenaire immobile aura une distribution spatiale limitée, plus le ratio $N_{pix,FRET} / N_{pix,Tot}$ diminuera et plus E_{pix} sera forte. Ceci induit que si le FRET existe dans des nanodomaines limités en nombre, l'analyse globale moyenne apparaitra sous forme d'une $E_{(FRET)}$ faible.

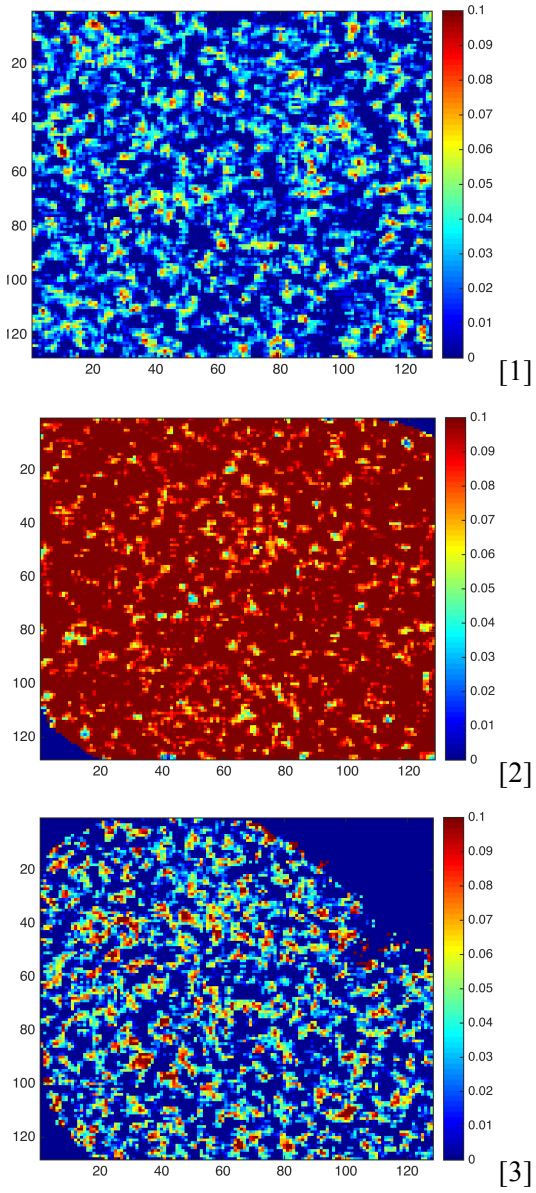

Figure 56 : cartographie d'$E_{(FRET)}$. Images 128x128 pixels affichant une $E_{(FRET)}$ seuillée et montrant des noyaux de cellules U2OS exprimant les paires de protéines fluorescentes suivantes : mTurq2/H2A-Reach (gauche, cas [1]), CT1-mTurq2/Cdk9-Reach (centre, cas [2]) et CT1-mTurq2/Rpb1-Reach (droite, cas [3]).

Ayant déterminé que la contrainte portant sur l'étude d'événements de FRET discrets est une limitation spatiale de la détection, nous avons choisi de réaliser des cartes d'$E_{(FRET)}$ puis de les analyser par segmentation d'image. Dans ce but, suite à l'analyse de nos images en temps de vie par la méthode du phaseur, nous avons développé des scripts sous Matlabs afin de générer des images de temps de vie. Dans le but d'exclure au maximum les faux-positifs, nous soustrayons ensuite à l'image l'$E_{(FRET)}$ moyenne des images du donneur seul (mTurq2) soit 1%. Les premiers résultats présentés dans la figure 27 semblent confirmer les 3 situations décrites. Dans le cas [1], on observe une variation d'$E_{(FRET)}$ allant de 0 à 4% contre plus de 6% pour l'ensemble des pixels de la condition [2]. Enfin dans le cas [3], on observe que CT1 et Rpb1

forment des nanodomaines de FRET (taille moyenne 500nm) possédant des efficacités supérieurs à 8% mais dont le nombre de pixel (5 pixels en moyenne par domaines) ne représente pas plus de 5% des pixels de la carte.

La simple observation des nanodomaines de FRET n'étant pas un aboutissement, nous avons cherché des stratégies de quantification qui permettraient de mieux déterminer les variations de l'interaction des formes sauvages et mutantes de CT1 avec Rpb1 ou l'histone H2A (marqueur de la chromatine). La stratégie consiste à isoler les clusters de pixels possédant des valeurs d'$E_{(FRET)}$ supérieures à la valeur d'$E_{(FRET)}$ correspondant à 90% de la distribution des pixels de la condition donneur seul soit environ 4% (Figure 57). La carte est ensuite binarisée afin d'attribuer la valeur 1 aux pixels ayant une valeur >0 et une valeur 0 aux pixels ayant une valeur ≤ 0.

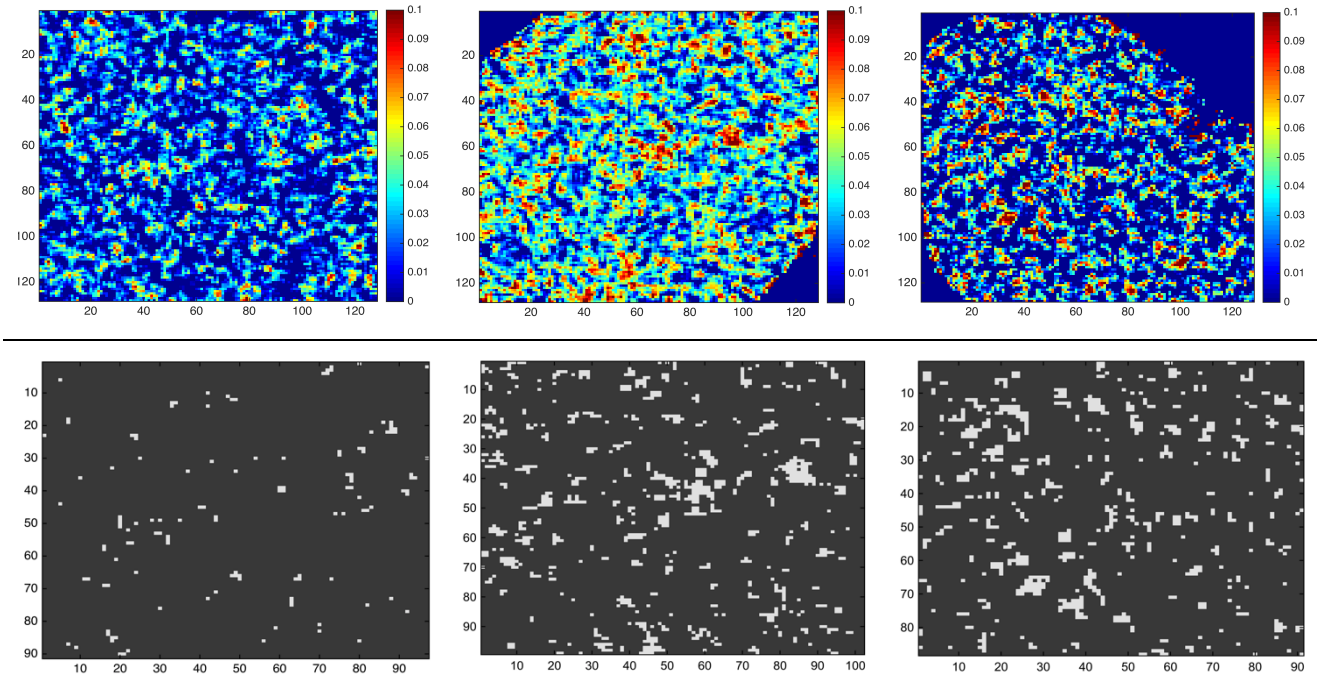

Figure 57 : cartographie en $E_{(FRET)}$ (haut) et segmentation d'image appliquée sur une zone restreinte de l'image en $E_{(FRET)}$ (bas). Expériences réalisées sur des cellules exprimant les paires de protéines fluorescentes suivantes : mTurq2/H2A-Reach (gauche), CT1-mTurq2/H2A-Reach (centre) et CT1-mTurq2/Rpb1-Reach (droite).

La quantification des clusters peut s'effectuer par simple numération grâce au logiciel gratuit Icy (http://icy.bioimageanalysis.org). Cependant, nous testons actuellement une méthode d'analyse d'image correlation spectroscopy (ICS) basée sur les scripts Matlabs de l'équipe du Prof. Paul Wiseman [39]. L'intérêt de l'ICS appliquée à des clusters est que d'une part le rayon moyen des particules et la densité des particules calculés se réfèrent non plus aux pixels mais directement aux clusters et d'autre part que l'ICS ne nécessite pas de fixer un seuil minimum, arbitraire, de nombre de pixels à partir duquel on considère avoir affaire à un cluster (Figure 58).

ACTIVITÉS DE RECHERCHE

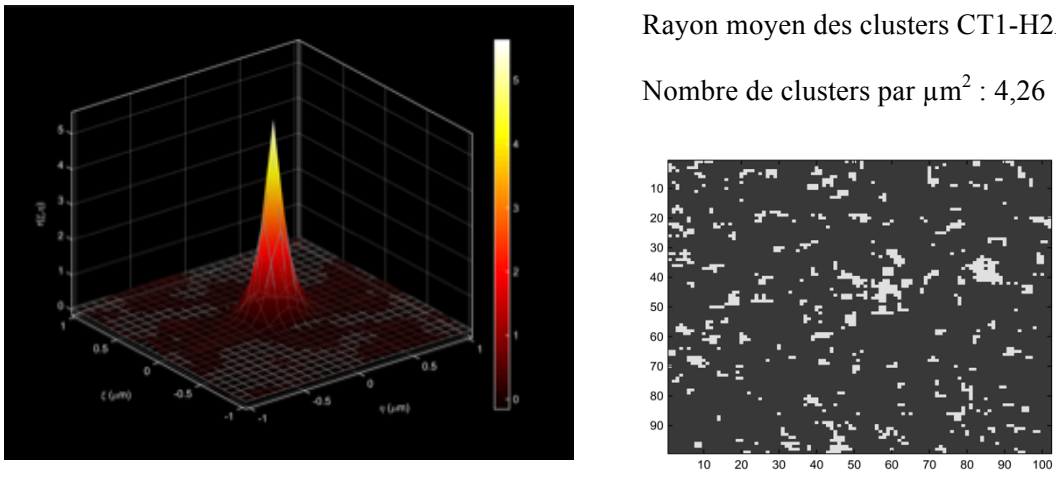

Rayon moyen des clusters CT1-H2A : 250nm

Nombre de clusters par μm^2 : 4,26

Figure 58 : ajustement Gaussien sur une autocorrélation r(ξ,η) de l'image segmentée (bas à droite).

Conclusion & Perspectives

Ce travail, dont le principe méthodologique est bien avancé, est toujours en cours. Nous développons l'automatisation des analyses dans le but de sortir des données de toutes nos images et ainsi obtenir des quantifications et statistiques associées pour valider la stratégie.

Nos premiers résultats suggèrent que nous sommes capables de visualiser et de quantifier le nombre et la taille des nanodomaines sur lesquels les protéines CT1, ARN POL II et Brd4 (résultats non montrés) interagissent. Il semblerait aussi que le segment de CT1, dont la suppression induit une perte d'interaction avec l'ARN POL II dans des expériences de pull-down ou de co-immunoprécipitation, conserve une légère capacité d'interaction sur ces nanodomaines. Il sera intéressant de comprendre si l'interaction résiduelle dépend toujours de l'ARN POL II ou d'autres protéines comme Brd4. Nous comparerons ensuite les résultats d'interaction (FRET) et de diffusion (FCS, PBs) et de suivi de particules uniques (SPT) obtenus sur la gamme de mutants de CT1. Notre objectif est de démontrer que les mécanismes moléculaires régulant la diffusion de P-TEFb ne se réduisent pas à ses partenaires sur le site actif de transcription, et que la sous-diffusion de P-TEFb participe au contrôle de sa présence sur l'ARN POL II.

Production associée

- **ARTICLE 1:** Laurent Héliot, Mariano Gonzalez-Pisfil, Mélanie Henry, Corentin Le Nezet, Olivier Bensaude, Bernard Vanden Bunder and Gabriel Bidaux. *A 2-steps model for the dynamic binding of P-TEFb on the transcriptional paused complex*. En préparation.

Alternativement, un article méthodologique est envisagée.

- **POSTER à FOM (Focus On Microscopy), mars 2015 :** "Photonics reveal Cycline T1-guided P-TEFb fate", par **G Bidaux**, M Gonzalez-Pisfil, M Henry, C Le Nezet, O Bensaude, X Darzacq, B VandenBunder and L Heliot.

Encadrement, Collaborations et tâches associés

- Mr GONZALEZ-PISFIL Mariano, acquisition d'une partie des expériences de FLIM,
- Mr LENEZET Corentin, IR, développement des scripts Matlabs.

CONCLUSION & PERSPECTIVES

I. CONCLUSION

Au cours de ces 12 dernières années, j'ai eu la chance et le privilège de pouvoir faire évoluer une thématique de fond : l'étude du récepteur au froid, TRPM8. Au grés des idées et des collaborations, mes collègues et moi-même sommes parvenus à mener une large étude du gène *trpm8* et de ses protéines associées en partant de la régulation de la transcription, à la démonstration de la fonctionnalité d'isoformes-canal à 4 segments transmembranaires en passant par la génération d'ARN alternatifs. Nous avons étudié aussi bien l'histoire de l'évolution de TRPM8 que son rôle dans l'homéostasie tissulaire, dans le métabolisme énergétique et dans la thermogenèse des mammifères. Ce travail s'est appuyé sur une grande variété de techniques et de spécialités dont l'intérêt final fut d'essayer de relier les évènements moléculaires et cellulaires à la physiologie de l'organisme, ce qu'on pourrait résumer en le terme : physiologie moléculaire. Bien que la dénomination semble séduisante car intégrant les évènements moléculaires dans le contexte de l'organisme, il existe en vérité un gouffre entre les caractérisation biophysiques et moléculaires des canaux, leurs effets au niveau cellulaire et les effets biologiques finaux dans l'organisme. La plupart de nos interprétations découlent en effet de corrélation entre les effets micro- et macroscopiques. Il n'est pas toujours techniquement possible de pouvoir contrôler (activer/stopper) les mécanismes moléculaires dans le contexte de l'organisme. Pourtant les outils issus de l'optogénétique commencent à permettre ce genre d'expérimentations et devraient à l'avenir nettement améliorer notre capacité à vérifier la causalité, et non plus la simple corrélation, entre les effets micro- et macroscopiques.

Suite au changement thématique en 2013, j'ai beaucoup appris et apprécié la recherche interdisciplinaire à l'œuvre dans l'équipe BCF. La recherche interdisciplinaire, cette notion vague pour nombre d'entre nous, mais limpide pour Bernard et Laurent. Il ne s'agit pas simplement d'utiliser les techniques issues de la chimie, des maths et de la physique pour faire avancer nos projets car ceci se résume à la consommation de savoir-faire ou de la prestation de service. Il s'agit de sortir des certitudes de notre formation et du confort des outils que nous maîtrisons. Il s'agit en fait pour le biologiste de se frotter à une vision différente des systèmes qu'il étudie, aux formules et modèles mathématiques, aux lois des statistiques, à la physique quantique et l'électronique ou encore à la thermodynamique. Enfin, il s'agit d'un cercle vertueux entre disciplines consistant à aider nos collègues à avancer dans leur discipline afin à notre tour de pouvoir bénéficier de leur progrès et ainsi de suite… Mes 2 années dans l'équipe BCF furent donc riches en apprentissage, en collaborations et m'ouvrent de nouvelles perspectives.

Du point de vue humain, j'ai eu la chance de travailler durant ces 12 années avec des gens passionnés et efficaces qu'il s'agisse de mes étudiants ou de mes collaborateurs.

Riche de ce parcours et de mon bagage scientifique et technique, je suis persuadé que je pourrai mettre en œuvre dans un cadre nouveau cette interdisciplinarité qui m'a tant apporté.

II. PERSPECTIVES : ICHÉMIE-REPERFUSION CARDIAQUE

A compter du 01 juillet 2015, je rejoins l'équipe cardioprotection, dirigée par le PU-PH Michel Ovize, au sein du laboratoire CARMEN, INSERM U1060 à Lyon.

L'équipe cardioprotection travaille sur les mécanismes moléculaires contrôlant la mort des cardiomyocytes dans le cadre de l'ischémie-reperfusion (IR). Leurs compétences techniques et forces de travail vont de la biochimie des mitochondries isolées à la physiologie des cardiomyocytes et des modèles animaux d'ischémie-reperfusion. Je rejoins cette équipe avec à charge de développer la partie biologie moléculaire et photonique et m'appuyant sur l'expertise et le réseau acquis ces dernières années.

Je participe déjà avec le laboratoire CARMEN à l'appel d'offre Réseau Hospitalo-Universitaire ainsi qu'à l'appel d'offre « pionniers de la recherche » de la fondation pour la recherche médicale.

II.1. RÔLE DES NANODOMAINS RE-MITOCHONDRIE DANS L'IRC

Contexte

Les nanodomaines MAMs forment un pontage physique entre les mitochondries et le RE. La protéine NLRP3 est localisée sur l'ensemble des membranes du RE mais se relocalise dans les MAM pour former la structure nommée inflammasome avec les protéines ASC et caspase-1 [102]. Cet inflammasome active alors la caspase 1 qui induit à son tour l'apoptose. L'interaction entre l'inflammasome et la jonction ER-mitochondrie serait transitoire car il a été montré que l'inflammasome est libéré dans le cytosol où il mature la pro-IL-1β. L'IR est caractérisé par du stress du RE, une surcharge mitochondriale en Ca^{2+} et une augmentation de la production de ROS qui sont tous des activateurs potentiels de l'inflammasome [103]. L'équipe du Prof. Ovize a récemment montré que l'hypoxie-réoxygénation, associée à la mort cellulaire, induit un rapprochement des jonctions ER- mitochondrie dans la région périnucléaire des cardiomyocytes, ce qui facilite le transfert de Ca^{2+} du RE vers les mitochondries [104]. Cette équipe a aussi mis en évidence que la cyclosporine A (CspA), un inhibiteur du pore de perméabilité de transition (PTP), déstabilise les tethers IP3R/GRP75/VDAC réduisant ainsi le transfère de Ca^{2+} entre MAM et mitochondries [104].

Objectifs

Par une approche multimodale utilisant la protéomique, la lipidomique, la biologie moléculaire, la biochimie et la nanoscopie, nous caractériserons les protéines des MAMs dans les cardiomyocytes avant et après IR. Nous vérifierons si l'inflammasome à protéines NLRP3 est bien recruté dans les MAMs pour y être activé dans les cardiomyocytes et les macrophages. Nous examinerons ensuite l'effet du pré- ou post-conditionnement avec les analogues de la CspA sur l'activation de l'inflammasome.

Une autre partie de la stratégie que je mettrai en place sera l'utilisation et le design de biosenseurs permettant les acquisitions multiplexes en temps réel sur cellule vivante. En effet, la mesure conjointe, en temps réelle, du taux de calcium, du taux d'ATP et de ROS, mais aussi des métabolites limitant des voies de synthèse ou

de lyse des lipides et des carbohydrates offrira une meilleure compréhension des liens de causalités entre tous ces processus et la mort cellulaire.

Grâce au développement de nouveaux bio-indicateurs, encodés génétiquement, et par l'utilisation de la technique de FLIM-FRET, j'aiderai les collègues travaillant sur l'activation du PTP à caractériser la dynamique d'assemblage de ces constituants et je créerai un système rapporteur fluorescent permettant de quantifier leur assemblage. Ce système pourra être utilisé pour les tests pharmacocinétiques.

II.2. NANOSCOPY, MICROSCOPIE 3D ET ENDOSCOPIE

Contexte

Ces dernières années ont été riches d'avancées majeures dans la microscopie photonique. La plus célèbre est sans doute le contournement de la limite de diffusion d'Ernst Abbe qui a permit d'entrer dans l'ère de la super-résolution et de la nanoscopie. Néanmoins, selon moi, les systèmes de super-résolution ne sont pas encore à maturité pour la recherche en biologie au delà des belles images ils sont très peu voir pas résolus temporellement ce qui limite leur utilisation pour étudier l'évolution de systèmes moléculaires au cours du temps. Cependant, l'observation directe des nanodomaines requière ces techniques. A ce titre, la photo-conversion de la méthode PALM offre probablement un intérêt supérieur au STED car on peut envisager de coupler la photo-conversion au FRET pour observer directement le couplage entre 2 protéines au sein des nanodomaines.

En comparaison, la technique, moins médiatique, de la feuille de lumière permet d'étudier le développement de petits organismes en 3D et en temps réel (ex : Zebra fish, Caenorabditis elegans, des organoïdes en culture…). Ce système permet en outre, quand on le couple à la technique de clarification d'organes [105, 106] de réaliser la reconstruction 3D d'un organe entier (Figure 59).

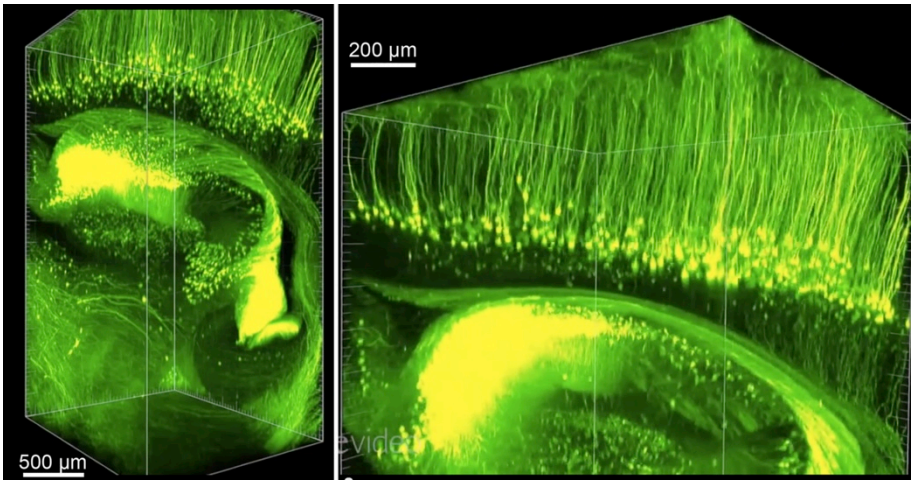

Figure 59 : cerveau clarifié de souris adulte exprimant le eYFP dans les neurones. Reconstruction 3D obtenue après imagerie à 0° et 180 ° permettant d'acquérir jusqu'à 12 mm de profondeur.

L'endoscopie consiste en l'utilisation d'un endoscope, fibre optique se terminant par un micro-objectif [107], pour réaliser l'imagerie sur un organe vivant *in situ* et en limitant la chirurgie associée. Les avancées techniques portant sur les fibres et les objectifs permettent maintenant de réaliser de l'imagerie multiphotonique et d'analyser les temps de vie des molécules autofluorescentes [108] ou de sondes fluorescentes [109, 110]. Très récemment, une solution technique a été proposée pour réaliser un endoscope

2-photon super-résolu intégrant la technique de déplétion (STED). Ce système améliore la résolution sagittale d'un facteur 3, soit environ 75 nm (x,y) [111].

L'optogénétique est une méthode visant à photo-convertir une protéine modifiée par génie génétique de sorte à induire l'activation d'une réponse biologique.

Dans le domaine de la recherche en cardiologie, l'optogénétique a ouvert la voie à des systèmes de contrôle de l'activité pacemaker ne souffrant pas de la stimulation nociceptive associée à la méthode classique des chocs électriques [112-114]. La démonstration a aussi été faite que cette approche pouvait corriger les arythmies cardiaques [115].

L'alliance de la microscopie par feuille de lumière et l'optogénétique a ainsi récemment permis de suivre en temps réel les battements cardiaques de l'embryon de Zebra fish et de les stopper par photo-activation [116].

Les avancées de l'optogénétique et de la microscopie sur organe/tissu ont permis de réaliser de très grosses avancées ces dernières années. Couplée à l'évolution rapide des protéines fluorescence et des méthodes d'analyses spectrales, on peut envisager sans problème d'être capable de mesurer *in vivo* les variations de plusieurs métabolites/protéines d'intérêt dans les 5-10 ans à venir.

Objectifs

À court terme, je mettrai en place la clarification du cœur de souris pour pouvoir reconstruire en 3D le volume de l'infarctus, mais aussi marquer les cellules immunitaires et les vaisseaux pour évaluer l'importance de l'inflammation autour et dans la zone de l'infarctus. Une fois la création d'un modèle moyen obtenu pour un protocole d'IR spécifique, nous pourrons évaluer les améliorations induites par le pré- et post-conditionnement des analogues CspA ou autres molécules.

À moyen terme, sachant que le transfert de Ca^{2+} depuis le RE vers les mitochondries semble être un des éléments déclencheurs de la mort cellulaire suite à l'ischémie-reperfusion, nous pourrions concevoir un système de contrôle de la vidange du Ca^{2+} réticulaire par photo-activation. Des souris génétiquement modifiées et exprimant ce système pourraient permettre d'étudier l'effet de la modulation de la concentration de Ca^{2+} dans les mitochondries en phase de pré- (avant l'IR) et post-conditionnement (après l'ischémie mais avant la reperfusion) sur la survie des cardiomyocytes. Ce système pourrait être couplé à des systèmes rapporteurs permettant de suivre l'activation de l'inflamasomme, la formation du PTP et l'activation des caspases afin de quantifier l'intensité et la dynamique de l'apoptose.

L'utilisation de l'endoscopie multiphotonique pourrait aussi nous permettre de confronter les résultats acquis sur les cardiomyocytes isolés avec ceux acquis sur le cœur *in vivo*.

Il va sans dire qu'en cas de réussite de ces challenges techniques, nous pourrons mettre en évidence les liens de causalités entre les mécanismes moléculaires et les symptômes des pathologies.

RÉFÉRENCES BIBLIOGRAPHIQUES

RÉFÉRENCES BIBLIOGRAPHIQUES

1. Minke, B., *Drosophila mutant with a transducer defect.* Biophys Struct Mech, 1977. **3**(1): p. 59-64.
2. Montell, C., *Physiology, phylogeny, and functions of the TRP superfamily of cation channels.* Sci STKE, 2001. **2001**(90): p. RE1.
3. Clapham, D.E., L.W. Runnels, and C. Strubing, *The TRP ion channel family.* Nat Rev Neurosci, 2001. **2**(6): p. 387-96.
4. Birnbaumer, L., et al., *A comparison of the genes coding for canonical TRP channels and their M, V and P relatives.* Cell Calcium, 2003. **33**(5-6): p. 419-32.
5. Montell, C., *Thermosensation: hot findings make TRPNs very cool.* Curr Biol, 2003. **13**(12): p. R476-8.
6. Story, G.M., et al., *ANKTM1, a TRP-like channel expressed in nociceptive neurons, is activated by cold temperatures.* Cell, 2003. **112**(6): p. 819-29.
7. Liu, B. and F. Qin, *Functional control of cold- and menthol-sensitive TRPM8 ion channels by phosphatidylinositol 4,5-bisphosphate.* J Neurosci, 2005. **25**(7): p. 1674-81.
8. Rohacs, T., et al., *PI(4,5)P2 regulates the activation and desensitization of TRPM8 channels through the TRP domain.* Nat Neurosci, 2005. **8**(5): p. 626-34.
9. Liu, D. and E.R. Liman, *Intracellular Ca2+ and the phospholipid PIP2 regulate the taste transduction ion channel TRPM5.* Proc Natl Acad Sci U S A, 2003. **100**(25): p. 15160-5.
10. Kedei, N., et al., *Analysis of the native quaternary structure of vanilloid receptor 1.* J Biol Chem, 2001. **276**(30): p. 28613-9.
11. Dragoni, I., E. Guida, and P. McIntyre, *The cold and menthol receptor TRPM8 contains a functionally important double cysteine motif.* J Biol Chem, 2006.
12. Liao, M., et al., *Structure of the TRPV1 ion channel determined by electron cryo-microscopy.* Nature, 2013. **504**(7478): p. 107-12.
13. Arniges, M., et al., *Human TRPV4 channel splice variants revealed a key role of ankyrin domains in multimerization and trafficking.* J Biol Chem, 2006. **281**(3): p. 1580-6.
14. Oberwinkler, J., et al., *Alternative splicing switches the divalent cation selectivity of TRPM3 channels.* J Biol Chem, 2005. **280**(23): p. 22540-8.
15. Chu, X., et al., *Identification of an N-terminal TRPC2 splice variant which inhibits calcium influx.* Cell Calcium, 2005. **37**(2): p. 173-82.
16. McKemy, D.D., W.M. Neuhausser, and D. Julius, *Identification of a cold receptor reveals a general role for TRP channels in thermosensation.* Nature, 2002. **416**(6876): p. 52-8.
17. Peier, A.M., et al., *A TRP channel that senses cold stimuli and menthol.* Cell, 2002. **108**(5): p. 705-15.
18. Cortright, D.N., et al., *The tissue distribution and functional characterization of human VR1.* Biochem Biophys Res Commun, 2001. **281**(5): p. 1183-9.
19. Caterina, M.J., et al., *A capsaicin-receptor homologue with a high threshold for noxious heat.* Nature, 1999. **398**(6726): p. 436-41.
20. Peier, A.M., et al., *A heat-sensitive TRP channel expressed in keratinocytes.* Science, 2002. **296**(5575): p. 2046-9.
21. Delany, N.S., et al., *Identification and characterization of a novel human vanilloid receptor-like protein, VRL-2.* Physiol Genomics, 2001. **4**(3): p. 165-74.
22. Benham, C.D., M.J. Gunthorpe, and J.B. Davis, *TRPV channels as temperature sensors.* Cell Calcium, 2003. **33**(5-6): p. 479-87.
23. Gori, T., et al., *The effect of ischemia and reperfusion on microvascular function: a human in vivo comparative study with conduit arteries.* Clin Hemorheol Microcirc, 2006. **35**(1-2): p. 169-73.
24. Dhaka, A., V. Viswanath, and A. Patapoutian, *Trp ion channels and temperature sensation.* Annu Rev Neurosci, 2006. **29**: p. 135-61.

25. Brauchi, S., et al., *A hot-sensing cold receptor: C-terminal domain determines thermosensation in transient receptor potential channels.* J Neurosci, 2006. **26**(18): p. 4835-40.
26. Voets, T., et al., *The principle of temperature-dependent gating in cold- and heat-sensitive TRP channels.* Nature, 2004. **430**(7001): p. 748-54.
27. Brauchi, S., P. Orio, and R. Latorre, *Clues to understanding cold sensation: thermodynamics and electrophysiological analysis of the cold receptor TRPM8.* Proc Natl Acad Sci U S A, 2004. **101**(43): p. 15494-9.
28. Cho, S., S. Schroeder, and M. Ott, *CYCLINg through transcription: posttranslational modifications of P-TEFb regulate transcription elongation.* Cell Cycle, 2010. **9**(9): p. 1697-705.
29. Narita, T., et al., *Human transcription elongation factor NELF: identification of novel subunits and reconstitution of the functionally active complex.* Mol Cell Biol, 2003. **23**(6): p. 1863-73.
30. Gu, B., D. Eick, and O. Bensaude, *CTD serine-2 plays a critical role in splicing and termination factor recruitment to RNA polymerase II in vivo.* Nucleic Acids Res, 2013. **41**(3): p. 1591-603.
31. Dreyfuss, G., V.N. Kim, and N. Kataoka, *Messenger-RNA-binding proteins and the messages they carry.* Nat Rev Mol Cell Biol, 2002. **3**(3): p. 195-205.
32. Liu, W., et al., *Brd4 and JMJD6-associated anti-pause enhancers in regulation of transcriptional pause release.* Cell, 2013. **155**(7): p. 1581-95.
33. Barrandon, C., et al., *The transcription-dependent dissociation of P-TEFb-HEXIM1-7SK RNA relies upon formation of hnRNP-7SK RNA complexes.* Mol Cell Biol, 2007. **27**(20): p. 6996-7006.
34. Lin, S. and A.D. Riggs, *The general affinity of lac repressor for E. coli DNA: implications for gene regulation in procaryotes and eucaryotes.* Cell, 1975. **4**(2): p. 107-11.
35. Spector, D.L., *Nuclear domains.* J Cell Sci, 2001. **114**(Pt 16): p. 2891-3.
36. Redford, G.I. and R.M. Clegg, *Polar plot representation for frequency-domain analysis of fluorescence lifetimes.* J Fluoresc, 2005. **15**(5): p. 805-15.
37. Leray, A., et al., *827Spatio-temporal quantification of FRET in living cells by fast time-domain FLIM: a comparative study of non-fitting methods.* PLoS One, 2013. **8**(7): p. e69335.
38. Petersen, N.O., et al., *Quantitation of membrane receptor distributions by image correlation spectroscopy: concept and application.* Biophys J, 1993. **65**(3): p. 1135-46.
39. Wiseman, P.W. and N.O. Petersen, *Image correlation spectroscopy. II. Optimization for ultrasensitive detection of preexisting platelet-derived growth factor-beta receptor oligomers on intact cells.* Biophys J, 1999. **76**(2): p. 963-77.
40. Bidaux, G., et al., *Prostate cell differentiation status determines transient receptor potential melastatin member 8 channel subcellular localization and function.* J Clin Invest, 2007. **117**(6): p. 1647-57.
41. Thebault, S., et al., *Novel role of cold/menthol-sensitive transient receptor potential melastatine family member 8 (TRPM8) in the activation of store-operated channels in LNCaP human prostate cancer epithelial cells.* J Biol Chem, 2005. **280**(47): p. 39423-35.
42. Saito, S. and R. Shingai, *Evolution of thermoTRP ion channel homologs in vertebrates.* Physiol Genomics, 2006. **27**(3): p. 219-30.
43. Chen, X., et al., *Structure of the full-length Shaker potassium channel Kv1.2 by normal-mode-based X-ray crystallographic refinement.* Proc Natl Acad Sci U S A, 2010. **107**(25): p. 11352-7.
44. Voets, T., et al., *Outer pore architecture of a Ca2+-selective TRP channel.* J Biol Chem, 2004. **279**(15): p. 15223-30.

RÉFÉRENCES BIBLIOGRAPHIQUES

45. Nilius, B., et al., *The single pore residue Asp542 determines Ca2+ permeation and Mg2+ block of the epithelial Ca2+ channel.* J Biol Chem, 2001. **276**(2): p. 1020-5.
46. Nilius, B., et al., *The selectivity filter of the cation channel TRPM4.* J Biol Chem, 2005. **280**(24): p. 22899-906.
47. Latorre, R., et al., *ThermoTRP channels as modular proteins with allosteric gating.* Cell Calcium, 2007. **42**(4-5): p. 427-38.
48. Brauchi, S., et al., *Dissection of the components for PIP2 activation and thermosensation in TRP channels.* Proc Natl Acad Sci U S A, 2007. **104**(24): p. 10246-51.
49. Marsakova, L., et al., *Pore helix domain is critical to camphor sensitivity of transient receptor potential vanilloid 1 channel.* Anesthesiology, 2012. **116**(4): p. 903-17.
50. Chuang, H.H., W.M. Neuhausser, and D. Julius, *The super-cooling agent icilin reveals a mechanism of coincidence detection by a temperature-sensitive TRP channel.* Neuron, 2004. **43**(6): p. 859-69.
51. Beck, B., et al., *Prospects for prostate cancer imaging and therapy using high-affinity TRPM8 activators.* Cell Calcium, 2007. **41**(3): p. 285-94.
52. Fernandez, J.A., et al., *Voltage- and cold-dependent gating of single TRPM8 ion channels.* J Gen Physiol, 2011. **137**(2): p. 173-95.
53. Elzanaty, S., et al., *The impact of epididymal and accessory sex gland function on sperm motility.* Hum Reprod, 2002. **17**(11): p. 2904-11.
54. Carpentier, M., et al., *Reduced fertility in male mice deficient in the zinc metallopeptidase NL1.* Mol Cell Biol, 2004. **24**(10): p. 4428-37.
55. Remontet, L., et al., *Cancer incidence and mortality in France over the period 1978-2000.* Rev Epidemiol Sante Publique, 2003. **51**(1 Pt 1): p. 3-30.
56. Bidaux, G., et al., *Evidence for specific TRPM8 expression in human prostate secretory epithelial cells: functional androgen receptor requirement.* Endocr Relat Cancer, 2005. **12**(2): p. 367-82.
57. Fuessel, S., et al., *Multiple tumor marker analyses (PSA, hK2, PSCA, trp-p8) in primary prostate cancers using quantitative RT-PCR.* Int J Oncol, 2003. **23**(1): p. 221-8.
58. Kiessling, A., et al., *Identification of an HLA-A*0201-restricted T-cell epitope derived from the prostate cancer-associated protein trp-p8.* Prostate, 2003. **56**(4): p. 270-9.
59. Tsavaler, L., et al., *Trp-p8, a novel prostate-specific gene, is up-regulated in prostate cancer and other malignancies and shares high homology with transient receptor potential calcium channel proteins.* Cancer Res, 2001. **61**(9): p. 3760-9.
60. Vanden Abeele, F., et al., *Ca2+-independent phospholipase A2-dependent gating of TRPM8 by lysophospholipids.* J Biol Chem, 2006. **281**(52): p. 40174-82.
61. Bavencoffe, A., et al., *The transient receptor potential channel TRPM8 is inhibited via the alpha 2A adrenoreceptor signaling pathway.* J Biol Chem, 2010. **285**(13): p. 9410-9.
62. Bidaux, G., et al., *Regulation of transient receptor potential melastatin 8 (TRPM8) channel activity by its short isoforms.* J Biol Chem, 2011.
63. Fernandez, J.A., et al., *Short Isoforms of the Cold Receptor TRPM8 Inhibit Channel Gating by Mimicking Heat Action rather than Chemical Inhibitors.* J Biol Chem **(to be published in the same volume)**.
64. Zhang, L. and G.J. Barritt, *Evidence that TRPM8 is an androgen-dependent Ca2+ channel required for the survival of prostate cancer cells.* Cancer Res, 2004. **64**(22): p. 8365-73.
65. Valero, M.L., et al., *TRPM8 ion channels differentially modulate proliferation and cell cycle distribution of normal and cancer prostate cells.* PLoS One, 2012. **7**(12): p. e51825.
66. Bionda, C., et al., *Subcellular compartmentalization of ceramide metabolism: MAM (mitochondria-associated membrane) and/or mitochondria?* Biochem J, 2004. **382**(Pt 2): p. 527-33.

67. Raturi, A. and T. Simmen, *Where the endoplasmic reticulum and the mitochondrion tie the knot: the mitochondria-associated membrane (MAM).* Biochim Biophys Acta, 2013. **1833**(1): p. 213-24.
68. Rusinol, A.E., et al., *A unique mitochondria-associated membrane fraction from rat liver has a high capacity for lipid synthesis and contains pre-Golgi secretory proteins including nascent lipoproteins.* J Biol Chem, 1994. **269**(44): p. 27494-502.
69. Denton, R.M., J.G. McCormack, and N.J. Edgell, *Role of calcium ions in the regulation of intramitochondrial metabolism. Effects of Na+, Mg2+ and ruthenium red on the Ca2+-stimulated oxidation of oxoglutarate and on pyruvate dehydrogenase activity in intact rat heart mitochondria.* Biochem J, 1980. **190**(1): p. 107-17.
70. McCormack, J.G. and R.M. Denton, *Role of calcium ions in the regulation of intramitochondrial metabolism. Properties of the Ca2+-sensitive dehydrogenases within intact uncoupled mitochondria from the white and brown adipose tissue of the rat.* Biochem J, 1980. **190**(1): p. 95-105.
71. Hansford, R.G. and D. Zorov, *Role of mitochondrial calcium transport in the control of substrate oxidation.* Mol Cell Biochem, 1998. **184**(1-2): p. 359-69.
72. Bautista, D.M., et al., *The menthol receptor TRPM8 is the principal detector of environmental cold.* Nature, 2007. **448**(7150): p. 204-8.
73. Dhaka, A., et al., *TRPM8 is required for cold sensation in mice.* Neuron, 2007. **54**(3): p. 371-8.
74. Mandadi, S., et al., *TRPV3 in keratinocytes transmits temperature information to sensory neurons via ATP.* Pflugers Arch, 2009. **458**(6): p. 1093-102.
75. Moqrich, A., et al., *Impaired thermosensation in mice lacking TRPV3, a heat and camphor sensor in the skin.* Science, 2005. **307**(5714): p. 1468-72.
76. Smith, A.D., et al., *The validity of wireless iButtons and thermistors for human skin temperature measurement.* Physiol Meas, 2010. **31**(1): p. 95-114.
77. Denda, M., M. Tsutsumi, and S. Denda, *Topical application of TRPM8 agonists accelerates skin permeability barrier recovery and reduces epidermal proliferation induced by barrier insult: role of cold-sensitive TRP receptors in epidermal permeability barrier homoeostasis.* Exp Dermatol, 2010. **19**(9): p. 791-5.
78. Boyce, S.T. and R.G. Ham, *Calcium-regulated differentiation of normal human epidermal keratinocytes in chemically defined clonal culture and serum-free serial culture.* J Invest Dermatol, 1983. **81**(1 Suppl): p. 33s-40s.
79. Blanco-Rodriguez, J. and C. Martinez-Garcia, *Mild hypothermia induces apoptosis in rat testis at specific stages of the seminiferous epithelium.* J Androl, 1997. **18**(5): p. 535-9.
80. Macdonald, J. and R.G. Harrison, *Effect of low temperatures on rat spermatogenesis.* Fertil Steril, 1954. **5**(3): p. 205-16.
81. Yazawa, T., et al., *Abnormal spermatogenesis at low temperatures in the Japanese red-bellied newt, Cynops pyrrhogaster: possible biological significance of the cessation of spermatocytogenesis.* Mol Reprod Dev, 2003. **66**(1): p. 60-6.
82. Zhang, Z., et al., *Functional analysis of the cooled rat testis.* J Androl, 2004. **25**(1): p. 57-68.
83. De Blas, G.A., et al., *TRPM8, a versatile channel in human sperm.* PLoS One, 2009. **4**(6): p. e6095.
84. Gibbs, G.M., et al., *Cysteine-rich secretory protein 4 is an inhibitor of transient receptor potential M8 with a role in establishing sperm function.* Proc Natl Acad Sci U S A, 2011. **108**(17): p. 7034-9.
85. Martinez-Lopez, P., et al., *TRPM8 in mouse sperm detects temperature changes and may influence the acrosome reaction.* J Cell Physiol, 2011. **226**(6): p. 1620-31.
86. Vidal-Puig, A.J., et al., *Energy metabolism in uncoupling protein 3 gene knockout mice.* J Biol Chem, 2000. **275**(21): p. 16258-66.

RÉFÉRENCES BIBLIOGRAPHIQUES

87. Echtay, K.S., et al., *Superoxide activates mitochondrial uncoupling proteins.* Nature, 2002. **415**(6867): p. 96-9.
88. Liu, D., et al., *Human stanniocalcin-1 suppresses angiotensin II-induced superoxide generation in cardiomyocytes through UCP3-mediated anti-oxidant pathway.* PLoS One, 2012. **7**(5): p. e36994.
89. Zhang, K., et al., *Uncoupling protein 2 protects testicular germ cells from hyperthermia-induced apoptosis.* Biochem Biophys Res Commun, 2007. **360**(2): p. 327-32.
90. Mailloux, R.J., X. Jin, and W.G. Willmore, *Redox regulation of mitochondrial function with emphasis on cysteine oxidation reactions.* Redox Biol, 2014. **2**: p. 123-39.
91. Ma, S., et al., *Activation of the cold-sensing TRPM8 channel triggers UCP1-dependent thermogenesis and prevents obesity.* J Mol Cell Biol, 2012. **4**(2): p. 88-96.
92. Cucu, D., et al., *Characterization of functional transient receptor potential melastatin 8 channels in human pancreatic ductal adenocarcinoma cells.* Pancreas, 2014. **43**(5): p. 795-800.
93. Fonfria, E., et al., *Tissue distribution profiles of the human TRPM cation channel family.* J Recept Signal Transduct Res, 2006. **26**(3): p. 159-78.
94. McCoy, D.D., et al., *Enhanced insulin clearance in mice lacking TRPM8 channels.* Am J Physiol Endocrinol Metab, 2013. **305**(1): p. E78-88.
95. Chen, Y., et al., *The photon counting histogram in fluorescence fluctuation spectroscopy.* Biophys J, 1999. **77**(1): p. 553-67.
96. Chuang, C.H., et al., *Long-range directional movement of an interphase chromosome site.* Curr Biol, 2006. **16**(8): p. 825-31.
97. Marshall, W.F., et al., *Interphase chromosomes undergo constrained diffusional motion in living cells.* Curr Biol, 1997. **7**(12): p. 930-9.
98. Becker, W., et al., *FLIM and FCS detection in laser-scanning microscopes: increased efficiency by GaAsP hybrid detectors.* Microsc Res Tech, 2011. **74**(9): p. 804-11.
99. Goedhart, J., et al., *Structure-guided evolution of cyan fluorescent proteins towards a quantum yield of 93%.* Nat Commun, 2012. **3**: p. 751.
100. Lam, A.J., et al., *Improving FRET dynamic range with bright green and red fluorescent proteins.* Nat Methods, 2012. **9**(10): p. 1005-12.
101. Ganesan, S., et al., *A dark yellow fluorescent protein (YFP)-based Resonance Energy-Accepting Chromoprotein (REACh) for Forster resonance energy transfer with GFP.* Proc Natl Acad Sci U S A, 2006. **103**(11): p. 4089-94.
102. Zhou, R., et al., *A role for mitochondria in NLRP3 inflammasome activation.* Nature, 2011. **469**(7329): p. 221-5.
103. Menu, P., et al., *ER stress activates the NLRP3 inflammasome via an UPR-independent pathway.* Cell Death Dis, 2012. **3**: p. e261.
104. Paillard, M., et al., *Depressing mitochondria-reticulum interactions protects cardiomyocytes from lethal hypoxia-reoxygenation injury.* Circulation, 2013. **128**(14): p. 1555-65.
105. Chung, K., et al., *Structural and molecular interrogation of intact biological systems.* Nature, 2013. **497**(7449): p. 332-7.
106. Tomer, R., et al., *Advanced CLARITY for rapid and high-resolution imaging of intact tissues.* Nat Protoc, 2014. **9**(7): p. 1682-97.
107. Rivera, D.R., et al., *Compact and flexible raster scanning multiphoton endoscope capable of imaging unstained tissue.* Proc Natl Acad Sci U S A, 2011. **108**(43): p. 17598-603.
108. Lagarto, J., et al., *Application of time-resolved autofluorescence to label-free in vivo optical mapping of changes in tissue matrix and metabolism associated with myocardial infarction and heart failure.* Biomed Opt Express, 2015. **6**(2): p. 324-46.
109. Jung, J.C., et al., *In vivo mammalian brain imaging using one- and two-photon fluorescence microendoscopy.* J Neurophysiol, 2004. **92**(5): p. 3121-33.

110. Hirano, M., Y. Yamashita, and A. Miyakawa, *In vivo visualization of hippocampal cells and dynamics of Ca2+ concentration during anoxia: feasibility of a fiber-optic plate microscope system for in vivo experiments.* Brain Res, 1996. **732**(1-2): p. 61-8.
111. Gu, M., H. Kang, and X. Li, *Breaking the diffraction-limited resolution barrier in fiber-optical two-photon fluorescence endoscopy by an azimuthally-polarized beam.* Sci Rep, 2014. **4**: p. 3627.
112. Wengrowski, A.M., et al., *Optogenetic release of norepinephrine from cardiac sympathetic neurons alters mechanical and electrical function.* Cardiovasc Res, 2015. **105**(2): p. 143-50.
113. Williams, J.C. and E. Entcheva, *Optogenetic versus Electrical Stimulation of Human Cardiomyocytes: Modeling Insights.* Biophys J, 2015. **108**(8): p. 1934-45.
114. Vogt, C.C., et al., *Systemic gene transfer enables optogenetic pacing of mouse hearts.* Cardiovasc Res, 2015. **106**(2): p. 338-43.
115. Bingen, B.O., et al., *Light-induced termination of spiral wave arrhythmias by optogenetic engineering of atrial cardiomyocytes.* Cardiovasc Res, 2014. **104**(1): p. 194-205.
116. Mickoleit, M., et al., *High-resolution reconstruction of the beating zebrafish heart.* Nat Methods, 2014. **11**(9): p. 919-22.

Annexes

I. ARTICLE 3

ARTICLE 3

Functional and Modelling Studies of the Transmembrane Region of the TRPM8 channel

Gabriel Bidaux[1,2,3*], Miriam Sgobba[4*], Loic Lemonnier[1,2], Anne-Sophie Borowiec[1,2], Lucile Noyer[1,2], Srdan Jovonovic[6], Alexander V Zholos[5#], Shozeb Haider[6#]

[1] Inserm, U1003, Laboratoire de Physiologie Cellulaire, Equipe labellisée par la Ligue contre le Cancer, Villeneuve d'Ascq, F-59650, France
[2] Laboratory of Excellence, Ion Channels Science and Therapeutics, Université de Lille 1, Villeneuve d'Ascq, F-59650, France
[3] Laboratoire Biophotonique Cellulaire Fonctionnelle. Institut de Recherche Interdisciplinaire, Villeneuve d'Ascq, USR3078 CNRS, France
[4] Centre for Cancer Research and Cell Biology, Queen's University of Belfast, BT9 7BL, Belfast, UK
[5] Department of Biophysics, Educational and Scientific Centre "Institute of Biology" Taras Shevchenko Kiev National University, Kiev 03187, Ukraine
[6] UCL School of Pharmacy, 29-39 Brunswick Square, London WC1N 1AX, UK

* These authors made Equal Contributions
# Corresponding authors - a.zholos@qub.ac.uk and shozeb.haider@ucl.ac.uk

Running Title: Structure-function relationship of TRPM8 TM region

Keywords
TRPM8/ cold receptor/ selectivity filter/ oligomerization/ molecular model

Abstract
Members of the Transient Receptor Potential (TRP) ion channel family act as polymodal cellular sensors, which aid in regulating Ca^{2+} homeostasis. Within the TRP family, TRPM8 is the cold receptor that forms a non-selective homotetrameric cation channel. In the absence of TRPM8 crystal structure, little is known about the relationship between structure and function. Inferences of TRPM8 structure have come from mutagenesis experiments coupled to electrophysiology, mainly regarding the fourth TM helix (S4), which constitutes a moderate voltage-sensing domain, and about cold sensor and PIP_2 binding sites, which are both located in the C-terminus of TRPM8.
In this study we use a combination of molecular modelling and experimental techniques to examine the structure of the TRPM8 TM and pore helix region including the conducting conformation of the selectivity filter. The model is consistent with a large amount of functional data and was further tested by mutagenesis. We present structural insight into the role of residues involved in intra- and inter-subunit interactions and their link with the channel activity, sensitivity to icilin, menthol and cold, and impact on channel oligomerization.

Introduction

The Transient Receptor Potential (TRP) ion channel family is ubiquitously present throughout mammals [1]. There are 28 members of the mammalian TRP channel superfamily, which form six subfamilies based on sequence similarity and homology [2]. Many TRP channels act as polymodal cellular sensors that respond to chemical and physical changes in both local and global environment. They respond to a variety of different gating stimuli including intra- and extracellular messengers, chemical, mechanical and osmotic stress, temperature, growth factors and depletion of intracellular Ca^{2+} stores [3]. Activation of these non-selective cation channels triggers not only Na^+ influx and membrane depolarisation, but also Ca^{2+} influx from extracellular matrix to cytosol as well as from the ER stores to cytosol for channels located in the ER membranes [4]. TRP-mediated Ca^{2+} signalling leads to specific biological effects such as induction of proliferation, modulation of the electrical activity of excitable cells in the brain and heart, sensory perception and vascular contractility. Given the importance of Ca^{2+} signalling in all cell types and the role of TRP channels in regulating Ca^{2+} homeostasis, it is not surprising that an abnormality in TRP channel function often results in pathogenesis of several diseases including channelopathies like mucolipidosis, polycystic kidney diseases, hypertension and hypomagnesaemia with hypocalcaemia [2].

Among the TRP family, TRPM8 is the primary cold receptor expressed in DRG neurons [5, 6], and is also sensitive to substances, which mimic cold sensation, such as menthol and icilin. Interestingly, TRPM8 has been originally cloned from human prostate, as it is overexpressed in prostate and other tumors [7]. It was found to be located at both plasma and endoplasmic reticulum membranes of prostate cells [8, 9]. Although endogenous TRPM8 activation is still poorly understood in human prostate, phosphatidylinositol 4,5-bisphosphate, PIP_2, [10] and lysophospholipids [11] regulate its activity. Furthermore, it has been reported that lysophospholipids sensitize TRPM8 to cold [12], modifying its threshold of activation that has been reported to be around 32°C in recombinant TRPM8 channels expressed in lipid bilayers [13]. Taken together, the studies that have characterized TRPM8 gating by menthol, icilin and cold, concluded that conformational shifts leading to TRPM8 opening was different and dependent of the activator.

In the absence of a crystal structure, information about TRPM8 structure has been obtained mainly by site-directed mutagenesis followed by electrophysiological characterisation, with the aim to define selectivity-related sites, PIP_2 binding sites and both menthol and icilin binding sites [14, 15]. Although several critical amino acids have been characterized no binding sites have yet

ARTICLE 3

been clearly defined [16]. TRPM8 monomers associate as homotetramers to form a non-selective cation channel whose permeability to Ca^{2+} is about 0.97-3.2 compared to that for Na^{+} [5, 6], though selectivity filter has not been studied. Similar to all other TRPs, a functional channel is formed by four subunits where each subunit consists of six transmembrane (TM) spanning regions (S1-S6), a short pore helix between S5 and S6 and intracellular N- and C-terminal domains. Little is known about TRPM8 structure-function relationship apart from that the fourth TM helix (S4) constitutes a moderate voltage-sensing domain and that both cold sensor and PIP_2 binding sites are located in the C-terminus of TRPM8 [17]. Stabilization of the tetramers has been poorly characterised and three studies report paradoxical data. Phelps *et al* (2007) suggested that TM were sufficient for tetramerization [18], while other teams reported that the C-terminal Coiled-coil domain was sufficient by itself [19] or in addition to other domains [20]. Rationalisation to structure has previously been based on the low homology with voltage gated K^{+} (K_V) and cyclic-nucleotide gated channels [21].

In this study we have used a combination of computational molecular modelling and experimental methodologies to examine the structure of the TRPM8 TM and pore helix regions based on their homology with the recently published structure of TRPV1 [22, 23]. We present structural insight into the role of residues involved in intra- and inter-subunit interactions and their link with the channel activity, sensitivity to icilin, menthol, and cold, and impact on channel oligomerization.

Materials and Methods

Site-directed Mutagenesis.

TRPM8 mutants have been performed on TRPM8 pcDNA4.TO.A vector [4] using the Phusion® Site-Directed Mutagenesis Kit (Finnzymes) as recommended. Briefly, wild-type (WT) TRPM8pcDNA4 vector was amplified with PCR using 5'-phosphorylated, degenerated forward primer and 5'-phosphorylated reverse primer on the adjacent sequence. Parental vectors were digested with Dpn I restrictase for 2-4 hours at 37°C. After sybergreen agarose gel purification with Wizard® SV Gel and PCR Clean-Up System (Promega), linearized TRPM8mut/pcDNA4.TO.A were ligated with T4 ligase (Promega) at 14°C overnight. After transformation in JM109 bacteria, colonies were screened by PCR and plasmids extracted prior to sequencing.

Cell culture and transient transfection.

Human Embryonic Kidney (HEK) 293 cells were grown in DMEM (Invitrogen) supplemented with 10% fetal calf serum (Seromed, Poly-Labo).

Cells were transfected with 2 µg of each construct and 0.2 µg of pmaxGFP using either NucleofectorTM (Amaxa, Gaithersburg, Maryland, USA) or FuGENE HD reagent (Roche Diagnostics, France). For control experiments, WT TRPM8 plasmid was used. Cells were used for patch-clamp experiments 24 hours after transfection.

Electrophysiology

Macroscopic membrane ion currents were recorded at 37°C using the patch-clamp technique in its whole cell configuration. The currents were acquired using a HEKA PC-9 amplifier (HEKA Elektronik Dr. Schulze GmbH, Germany) and analyzed offline using Origin 6.1 software (OriginLab Corporation, USA). Regular extracellular solution (osmolarity 310 mosmol/l) contained (in mM): 150 NaCl, 5 KCl, 10 HEPES, 10 Glucose, 1 $MgCl_2$, 2 $CaCl_2$, pH, 7.3 (adjusted with NaOH). Selectivity experiments were carried out at room temperature using a different extracellular solution of the following composition (in mM): 100 TEA-Cl, 10 HEPES, 10 Glucose, pH 7.3 (adjusted with TEA-OH) in which were added 50 mM of either NaCl, KCl, CsCl or $CaCl_2$. The intracellular pipette solution (osmolarity 290 mosmol/l) contained (in mM): 140 CsCl, 10 HEPES, 8 EGTA, 1 $MgCl_2$, and 4 $CaCl_2$ (100 nM free Ca^{2+}), pH 7.3 (adjusted with CsOH). Patch pipettes were fabricated from borosilicate glass capillaries (WPI, England). The resistance of the pipettes varied between 3 and 5 MΩ. Necessary supplements were added directly to the respective solutions, in concentrations that would not significantly change the osmolarity. Changes in the external solutions were carried out using a multibarrel puffing micropipette with common outflow that was positioned in close proximity to the cell under investigation. During the experiment, the cell was continuously superfused with the solution via a puffing pipette to reduce possible artefacts related to the switch from static to moving solution and vice versa.

Results are expressed as mean ± SEM. Icilin was purchased from Tocris Cookson Inc. (England), all other chemicals were from Sigma-Aldrich (France).

Cell surface biotinylation.

HEK293 cells were transfected with 6 µg of WT or mutant TRPM8 plasmids for 3 million cells in 10 cm dishes. After a 40h-transfection, the biotinylation assay was performed prior to cell homogenization in 1 ml lysis buffer. Briefly, cells were washed 2 times with Phosphate Buffer Saline (PBS) complemented with 1 mM $MgCl_2$ and 0.5 mM $CaCl_2$ at pH 8.2 (PBSB). Cells were incubated in PBSB containing 0.5 mg/ml EZ-Link Sulfo-NHS-LC-LC-Biotin (Thermo Scientific Pierce Protein Biology Products, USA), on ice for 30 min. After 2 washouts with PBSB containing 1 mM Glycine, followed with 1 wash with PBS, cells were lysed in 1X RIPA buffer as described elsewhere [4]. Protein concentrations were determined with BCA assay (Thermo Scientific Pierce Protein Biology Products, USA). 50 µg of total protein extract were frozen in order to be used as an internal control, since 500 µg of proteins were pulled-down with 100 µl of NeutrAvidin Agarose (Thermo Scientific Pierce Protein Biology Products, USA) on a rotating wheel at 4°C overnight. Beads were centrifuged for 2 min at 250 g and supernatant was removed. Beads were then suspended in 1 mL of 0,5X RIPA buffer prior to a further centrifugation. This step was repeated 2 times. Finally, pelleted beads were suspended in 2X Laemmli sample buffer, and incubated at 30°C for 45 min. Samples were thereby analyzed by immunoblotting.

Immunoblotting.

Total protein and acrylamide electrophoresis were performed as described previously [24]. Immunoblotting was processed as follows: after the PVDF membrane were blocked in 5% TNT-milk (15mM Tris buffer pH 8,

140mM NaCl, 0.05% Tween 20 and 5% non-fat dry milk) with 5% donkey serum (Chemicon International Inc., USA) at room temperature for 30 min, they were soaked in a in 1% TNT milk with either 1/1,000 anti-TRPM8 antibody (Abcam, ab109308, lot GR47573-2, 2013) or with 1/1,500 Mouse Anti- c-Myc Monoclonal Antibody (Life Technologies™) at +4°C overnight. After three washes, the membranes were incubated in anti rabbit IgG or anti mouse IgG secondary antibodies coupled to horseradish peroxidase-linked (Chemicon International Inc., USA), diluted in 3% TNT-milk (1/20,000) for 1 h prior to be rinsed three times. Afterward, the membranes were processed for chemiluminescent detection using Luminata™ Forte, Western HRP Substrate (Merck Millipore, USA) according to the manufacturer's instructions. The blots were then exposed to X-Omat AR films (Eastman Kodak Company, Rochester, NY).

Calculations of the expected total current in a mixed population of mutant and WT TRPM8 channels.

Proportions of mutant monomers to WT monomers (4-0, 1-3, 2-2, 3-1 and 4-0) represent the different tetrameric structures in a single cell transfected with both WT and mutant TRPM8 vectors. Giving that tetramer assembling is a stochastic process, their distribution in a cell has been calculated by multiplication of the probability to obtain each tetramer (0.316, 0.105, 0.035, 0.012 and 0.003, respectively), with the number of permutations giving each tetramer (respectively 1, 4, 6, 4 and 1), and were respectively 0.316, 0.420, 0.211, 0.088 and 0.003 as presented in the **Figure S4**. This distribution assumes that mutant homotetramers are stable proteins. If not, their probability of appearance would be inferior to 0.316 and would be 0 if mutant homotetramers could not be oligomerized.

Total relative TRPM8 currents expected for mix population of mutant and WT TRPM8 channels in a single cell, assuming their proportion was 3:1, were estimated as the sum of relative currents of each type of tetramers in the population weighted with a probabilistic distribution (**Table S1**). Relative currents are the normalization of the averaged maximal amplitude of current density of mutant TRPM8 homotetramers in single cells by the averaged maximal amplitude of current density of wild type TRPM8 homotetramer in single cells. This value was then, 1 for WT homotetramers and for mutant/WT heterotetramer for weak mutations (carrying a mutant effect only when the four monomers of a channel were mutated), 0 for current-killer mutant homotetramers and dominant, current-killer mutant/WT heterotetramers and was experimentally determined for other conditions (labeled R). It should be noted that we could not determine the relative current of mutant/WT heterotetramers carrying a stoichiometry-dependent mutation in whole cell experiment. Therefore, we assumed, by default, that a mutation was stoichiometry-dependent when the recorded total current was comprised in the range given by values for a dominant and weak mutation.

Computational Modeling

Homology model of transmembrane region of TRPM8 and refinement of the selectivity filter

The sequence of human TRPM8 was taken from Uniprot (Q7Z2W7). To investigate the relationship between the selectivity filter, P-helix and SF-S6 extracellular loop, three homology models of the TRPM8 transmembrane region were generated using TRPV1 structure as a template and represented the three conformations of TRPV1 in open (PDB code 3J5Q), intermediate (PDB code 3J5R) and closed state (PDB code 3J5P). All models were generated with Modeller v9.14 [25]. Sequence alignment was performed using ClustalW [26], then manually modified to be consistent with the PSIPRED secondary structure prediction [27] and previous work by Kalia and Swartz [28]. To enforce the homotetrameric folding of the channel, symmetry restraints were applied to the four subunits. The models were subjected so conjugate gradient energy minimisations using GROMACS software. The quality and the stereochemical properties of the final models were assessed after each step using PROCHECK version 3.4.4 [29]. Pore dimension were evaluated by the HOLE program [30].

Results

Structural Architecture of TRPM8

TRPM8 is a homotetramer and secondary structure prediction performed with Psipred [27, 31] predict intracellular N- and C-terminal domains and a transmembrane (TM) region. Each TRPM8 TM segment consists of six helices (S1-S6), a short pore helix (P-helix), and an ascending loop (between P-helix and S6), which includes the selectivity filter (SF) and an extracellular linker. Four SF loops, one from each subunit, along with S5-P-S6 helices, arrange around the central axis, with four-fold symmetry, to form the pore that allows the permeation of cations across the membrane (Fig 1). Helices S1-S4 surround the central ion channel and associate with the S5-P-S6 region of the adjacent subunit, through domain swap organisation [22, 23]. Just proceeding S6 helix is a 20 amino-acid α-helical TRP domain containing the conserved WxxQ signature sequence. It has been proposed to engage in subunit assembly or allosteric modulation of channel gating [1, 21, 32]. This helix, which sits at the interface of the inner membrane, also interacts with S1 and S4-S5 linker. Another short helix-turn-helix region has been predicted between S2 and S3 helices, which similar to the TRP domain, runs parallel along the inner leaflet of the membrane (Fig S3). Three homology models of TRPM8 TM region were built using the recently solved structures of TRPV1, in open (PDB code 3JPQ), intermediate (PDB code 3J5R) and closed (PDB code 3J5P) states, as templates. The different states are categorised based on the conformation of the residues in the SF and lower gate in the S6 helix [23]. In the closed state, the ion-conducting pathway is constricted at the SF and the lower gate. In the intermediate state, the SF is constricted, while the lower gate is open. Finally, in the open state, both the SF and the lower gate are expanded and the pore is dilated without any constrictions (Fig 2). The narrowest points in the pore are observed between diagonally opposite carbonyl oxygen at S^{917} in the SF and between the side chains of V^{976} in the lower gate (Fig 2e). The Cα RMSD between the closed (Fig 2a), intermediate (Fig 2b) and the

ARTICLE 3

open (Fig 2c) conformations of the models ranged between 0.8 Å – 1.5 Å.

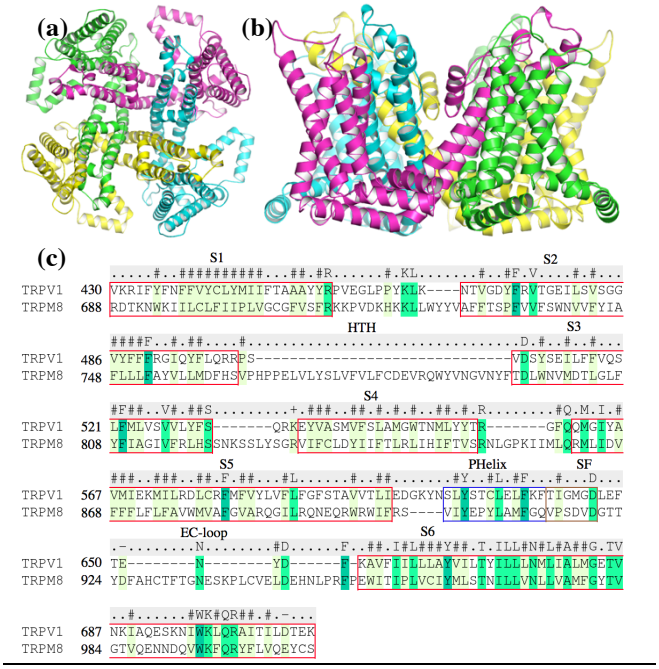

Figure 1. (a) Homology model of the human TRPM8 TM region, as viewed from the extracellular side. Each monomer has been highlighted with different colours. (b) Side view of the human TRPM8 TM region. The intra- and extracellular sides have been labelled (c) Sequence alignment between the TM regions of human TRPV1 and TRPM8. S1-S6 TM helices are enclosed in red, P-helix in blue and SF in brown boxes. The regions are labelled above the sequence including the predicted Helix-turn-helix segment (between S2-S3 helices) and the EC-loop between SF and S6 helix. The colours are based on sequence conservation, where dark green represents total conservation. The conserved residues are also annotated above the alignment.

The relatively low difference in RMSD between different conformations is a result of the static nature of S1-S4 domains during channel activation within the TRP family [23]. The predominant differences are observed only in S5-P-S6 helices. Similar to the TRPV1 structure, the pore profiles support a dual gating mechanism involving substantial conformational changes in both, SF and the lower gate [22, 23].

The percentage identity in the TM helices ranges between 20-30%. The Cα RMSD between the model and the template is 0.9Å (closed/intermediate) and 1.2 Å (open) and lies within the expected range for proteins sharing 20-30% sequence identity [33]. However, in cases where sequence identity is low, it is essential to validate the predictive power of the model by making novel mutations [34]. The SF sequence is ^{917}SDVD^{920}, where both backbone carbonyl and side chain carboxylic oxygen atoms point into the central ion conduction pathway. The structural difference between the Na^+/K^+ and Ca^{2+} channel SFs is functionally relevant for the ion permeation and selectivity. In particular, while in Na^+ and K^+ channels, sodium and potassium ions are coordinated by the peptide backbone, in Ca^{2+} channels the side chains of conserved D/E residues located in the SF are responsible for the chelation of ions [35]. Atomistic structures of the SF in Ca^{2+} channels have been previously modelled and different Ca^{2+}-coordination patterns were described, all having a ring formed by the side chains of the D/E residues located in the SF [36]. TRPM8 Asp^{920} is a highly conserved amino acid within the TRP family (Fig 1C and S1), where as Asp^{918} is substituted by a glutamate residue in several TRPM channels (Fig S1). Neutralization of the Asp^{920} orthologous residue of TRPM4 channel by an alanine substitution results in a non-functional channel [37], suggesting that it forms the main component of TRPM4 SF. Furthermore, mutation of the equivalent residue in TRPV1 (Asp^{646}) has also shown to result in a non-functional channel [38, 39].

In TRPM8, the D^{918} and D^{920} side chains from each subunit form two rings (referred to as DDDD rings), one at the top (towards the extracellular side of the channel) and one at the bottom of the SF. The negative charges of Asp^{918} or Asp^{920} have been implicated in coordinating Ca^{2+} ions in the SF. The side chain conformations adopted by Asp^{918} and Asp^{920} are distinct in open and closed states (Fig 3). In the closed conformation, the negatively charged side chains of Asp^{918} are positioned perpendicular to the pore axis and makes hydrogen bonds with the backbone nitrogen atoms of Val^{919} (Fig 3a,b). This interaction reduces the flexibility of the selectivity filter and locks it in a conformation that constricts the dimensions of the pore (Fig 2d,e). In the open state, the aspartate side chains of Asp^{918} point away from the central pore and position in a small cavity created by the rearrangement of the pore helices and the SF (Fig 3c). As a result of the tilt of the pore helix away from the central axis of the channel and conformational changes in the SF, the side chains of Asp^{920} reorient and point towards the inner cavity of the central pore of the channel ready to coordinate Ca^{2+} ion (Fig 3f). Organization and function of DDDD rings in TRPM8 selectivity filter.

We next investigated which and how the DDDD rings could be involved in ion conduction. Based on site-directed mutagenesis strategies developed for the study of catalytic sites of enzymes [40], we have created several TRPM8 mutants prior to comparing their electrophysiological properties with the wild type (WT) TRPM8 channel by the mean of Patch-clamp technique using the whole cell configuration. As shown in Fig 3g, substitution of D^{918} by alanine (neutral, small side chain), glutamic acid (negatively charged, polar, longer side chain) or asparagine (neutral, polar, medium side chain) had no significant effect on TRPM8 activity. Conversely, alanine and asparagine substitution of D^{920} (Fig 3h) respectively reduced and almost abolished TRPM8 current in response to sequential treatment with cold (22°C), icilin (10 µM) and menthol (500 µM), while substitution with glutamic acid did not alter TRPM8 current (For peak current data, see Supplementary section).

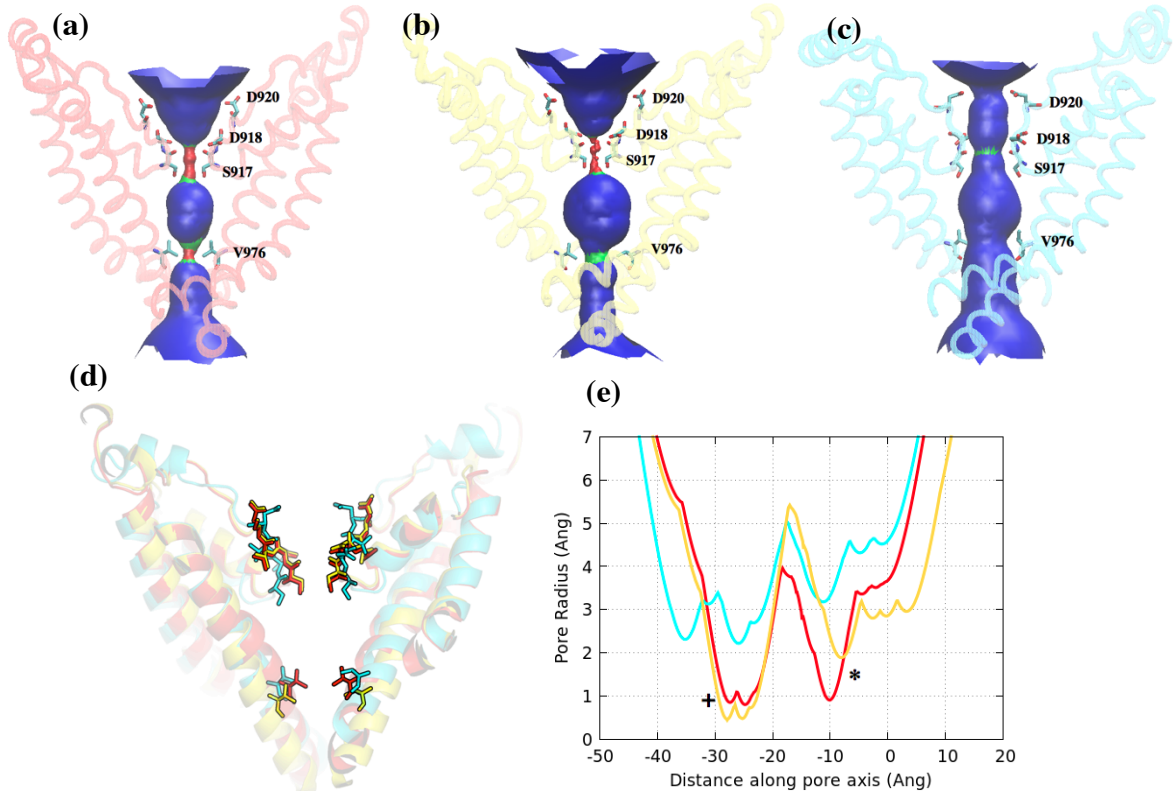

Figure 2. Pore profile of the human TRPM8 model in (a) closed/red (b) intermediate/yellow and (c) open/cyan conformations. Only two, diagonally opposite subunits have been shown for clarity. The solvent accessible pathway as generated using HOLE software is illustrated as red (radius < size of a water molecule), green (radius ~ size of a water molecule), and blue (radius > size of a water molecule) surface. The residues that align the SF and the lower gate have been rendered as sticks. (d) Superimposition of the three models highlights the conformational changes in the SF and the lower gate. (e) The pore radius profile of the three models. '+' corresponds to the SF and '*' denotes the lower gate region.

Since mutants of the TRPM8 channel were detected at cell surface with biotinylation assay, suppression of TRPM8 current could not have been the result of misfolding or from issues in channel translocation (Fig S4). Moreover, as shown in Fig S5, these mutations did not affect channels core electrophysiological properties such as I/V relationship, or general shape of the traces. Ion selectivity of wild-type TRPM8, $D^{918}A$ and $D^{920}A$ mutants was quantified on the basis of the shifts in reversal potentials caused by the replacement in the extracellular solution of 50 mM Na^+ with equimolar concentrations of either K^+, Cs^+ or Ca^{2+}. Mutations did not affect permeation sequence, which remained $Ca^{2+}>K^+\approx Cs^+\approx Na^+$ as previously described [5]. Recorded permeability values for wild-type TRPM8 (n=14), $D^{918}A$ (n=7) and $D^{920}A$ (n=7) mutants were respectively: P_K/P_{Na}=1.08±0.02, 1.06±0.01, and 1.08±0.02; P_{Cs}/P_{Na}=1.04±0.01, 1.03±0.01, and 1.07±0.03; P_{Ca}/P_{Na}=6.25±1.28, 8.67±2.96, and 5.05±0.49, showing no significant difference between wild-type TRPM8 and mutants selectivity. To further understand whether the peptide backbone *per se* might be involved in TRPM8 SF, we substituted V^{919} with an isoleucine. As shown in Fig 3i, $V^{919}I$ mutant did exhibit similar responses to cold, icilin and menthol than wild-type TRPM8. Our results therefore suggest that both the negative charge and the length of the side chain of D^{920} constitute the TRPM8 SF for cations, while D^{918} is not involved in this SF primary function. In order to assess a putative complementary role of $DDDD^{918}$ ring in the pore backbone, we performed double point mutations on D^{918} and D^{920} (Fig 3j). While $D^{918}N/D^{920}N$ double mutant was inactive, a strong decrease of current was detected with the $D^{918}A/D^{920}A$ mutant (87.4%, 80.8% and 87.5% decrease for cold, icilin and menthol-activated currents, respectively), and no significant effect was observed with $D^{918}E/D^{920}E$ mutant. Current reduction of the $D^{918}A/D^{920}A$ mutant without any apparent changes in channel electrophysiological properties (Fig S5) is likely triggered by the destabilization of the ion conduction pathway in the pore, which indicated a structural role for the $DDDD^{918}$ ring. Finally, to determine if coordination by four D^{920} is required for a functional channel, we expressed heteromeric TRPM8 ($D^{920}E$)/wild type (WT) channels and determined the role of $D^{920}A$ mutation. To address this, WT TRPM8 vector was concomitantly transfected with either empty vector or with mutant TRPM8 ($D^{920}A$). A calculation model was built to predict qualitative variations in the behaviour of three types of mutations (dominant, weak and stoichiometry-dependent) and two kinds of phenotypes (current-killer and current-reducer).

ARTICLE 3

A dominant mutation should affect both mutant/WT hetero- and homotetramers, a weak mutation should only affect mutant homotetramers, and stoichiometry-dependent mutation should partially and gradually affect mutant/WT heterotetramers incorporating an increasing proportion of mutant monomers. Characterizing the type of a mutation might help to estimate the importance and role of its associated endogenous amino acid. Therefore, we calculated the frequency of tetramer structures formation assuming that the ratio of wild type and mutant TRPM8 proteins would be, on average, equal to the ratio of transfected plasmids (Fig S6). Then, in cells co-expressing a 3:1 ratio of mutant TRPM8 and WT TRPM8, we determined the theoretical normalized TRPM8 current (Table S1) for each of the six possible cases: dominant/current-killer, dominant/current-reducer, weak/current-killer, weak/current-reducer, stoichiometry-dependent/current-killer, and stoichiometry-dependent/current-reducer. Experimental values (mean ± SEM) were finally compared to this model in order to determine the nature of each mutation. It has to be noted that stoichiometry-dependent mutants could not be determined because of the inherent unknown decrease rate of current for each kind of heterotetramer formed in a channel population (Table S1). Stoichiometry-dependent mutations were therefore selected by elimination of both dominant and weak types. Co-expression of WT TRPM8 and $D^{920}A$ mutant (Fig S7) triggers a decrease in current amplitude slightly bigger, but not significantly, than the one observed in Fig 3h, with the $D^{920}A$ homotetramers (59.9% of control for cold, 46.5% of control for icilin and 45.1% of control for menthol). With regards to our model, we concluded that $D^{920}A$ is likely a dominant mutation - suggesting that the $DDDD^{920}$ ring would lose its function even with one of the four Asp^{920} mutated to Alanine.

In accordance with previous findings that orthologous residues of D^{920} (TRPM8), in TRPM4, TRPV1 and TRPV6, were critical for ion conduction, we have experimentally confirmed that D^{920} residue in TRPM8 channel is the main component of TRPM8 SF [37-39, 41]. Our data demonstrates that in the open state conformation of the SF, side chains of D^{920} residue align the pore, making it accessible for hydrated ions and that negative charges are required for cation coordination and flux through TRPM8 pore.

P-helix is critical for cold and menthol but not icilin activation of TRPM8

The structure of the TRPV1 channel has revealed that a short α helix (P-helix) is localized in close spatial conformation with S5 and S6 of the same monomer as well as with S6 of the adjacent monomer. T^{633} in the P-helix of TRPV1 is critical for its activation by camphor [42]. In addition, the F^{640} residue, also present in the P-helix, is involved in opening/closure of TRPV1, TRPV2 and TRPV3 [43]. F^{640} substitution with leucine sensitized TRPV1 activity to lower capsaicin concentration and to lower temperatures than for WT TRPV1 [39]. Finally, the P-helix is a dynamic component of the pore whose conformational shift participates in the gating of TRPV1 channel [22, 23] and may also be central to gating in other TRP family members [44]. Since our TRPM8 structural model suggests that the P-helix conformation is similar to that of TRPV1, we investigated whether TRPM8 P-helix can be stabilized by interactions with adjacent TM domains and if it was involved in ligand gating.

Y^{905} is a critical residue of the P-helix and is positioned in hydrophobic pocket that is surrounded by V^{903}, I^{904}, Y^{908}, L^{909} (same subunit) and W^{954} and I^{957} (adjacent subunit) (Fig 4a). It is located at the beginning of the P-helix in our

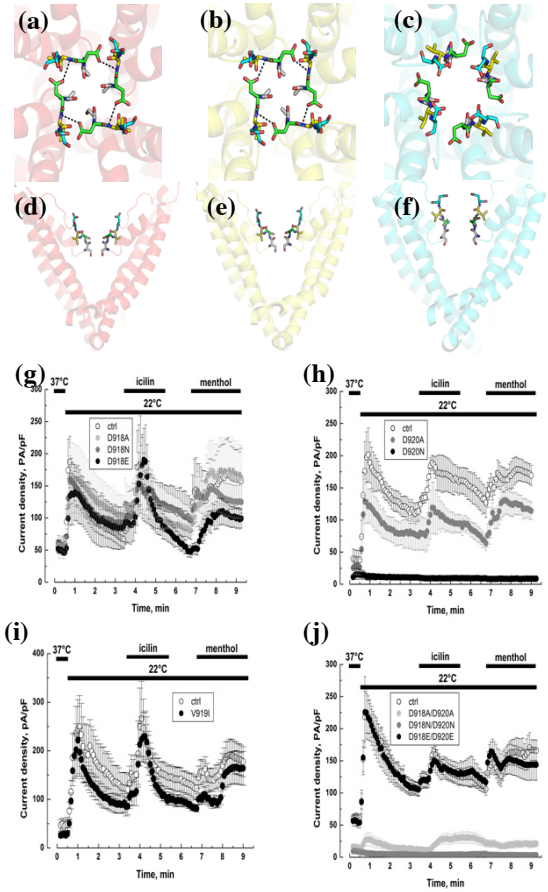

Figure 3. Selectivity filter in human TRPM8 model. In the (a) closed/red and (b) intermediate/yellow conformation, D^{918} makes hydrogen bonds with the backbone nitrogen of V^{919}. This interaction is lost in the (c) open/cyan state, where the side chains of D^{918} are pointing into a cavity between the SF and P-helix. The side chains of D^{920} point towards the pore. Side view of the different conformations of the SF are illustrated in (d,e,f). Side chains of S^{917} (white), D^{918} (green), V^{919} (yellow) and D^{920} (cyan) are rendered as sticks. Whole-cell recordings at +100mV showing TRPM8 currents induced with either cold (22°C), or Icilin (10 μM), or Menthol (500 μM) for HEK cells transfected with (g) D^{918}* TRPM8 mutants (h) D^{920}* TRPM8 mutants (i) $V^{919}I$ mutant and (j) D^{918}*/D^{920}* double TRPM8 mutants - * represents the substituted amino acids. Cells transfected with wild type TRPM8 were used as control (ctrl).

models and makes π-stacking interactions with Y^{908} from

the same subunit. A tilt of P-helix, away from the pore during channel activation, positions Y^{905} in close proximity to the adjacent subunit (Fig 4b). However, no hydrogen bonding is observed within this hydrophobic cluster. This is similar to the P-helix interactions in several other TRP channels, including TRPV1, where the flexible architecture permits the channel permeable to large cations [45, 46]. Y^{905} substitution with an alanine, a tryptophan or a phenylalanine led to very different consequences on TRPM8 activity. While complete removal of the aromatic group in Y^{905}A mutant totally prevented channel activation, removal of hydroxyl group in Y^{905}F did not affect TRPM8 current (Fig 4c). The substitution of the benzyl side chain by an indole group strongly decreased TRPM8 current regardless of the stimulus. This suggests that Y^{905} stabilize the conformation of the P-helix likely via π-stacking. As previously reported for all other current-generating TRPM8 mutants in this study, there were no apparent changes in Y^{905}W and Y^{905}F electrophysiological properties at the whole cell level (Fig S5). Co-expression of Y^{905}A mutation with WT TRPM8 (Fig S7) generates a dramatic decrease in channel activity (49.3%, 28% and 46.4% respectively for cold, icilin and menthol). Calculations suggested that Y^{905}A substitution induced a stoichiometry-dependent mutation triggering a killer-current phenotype, suggesting that Y^{905} mutation does not abolish tetramerization, but rather modify P-loop spatial positioning which in turn hinders ion conduction through the pore.

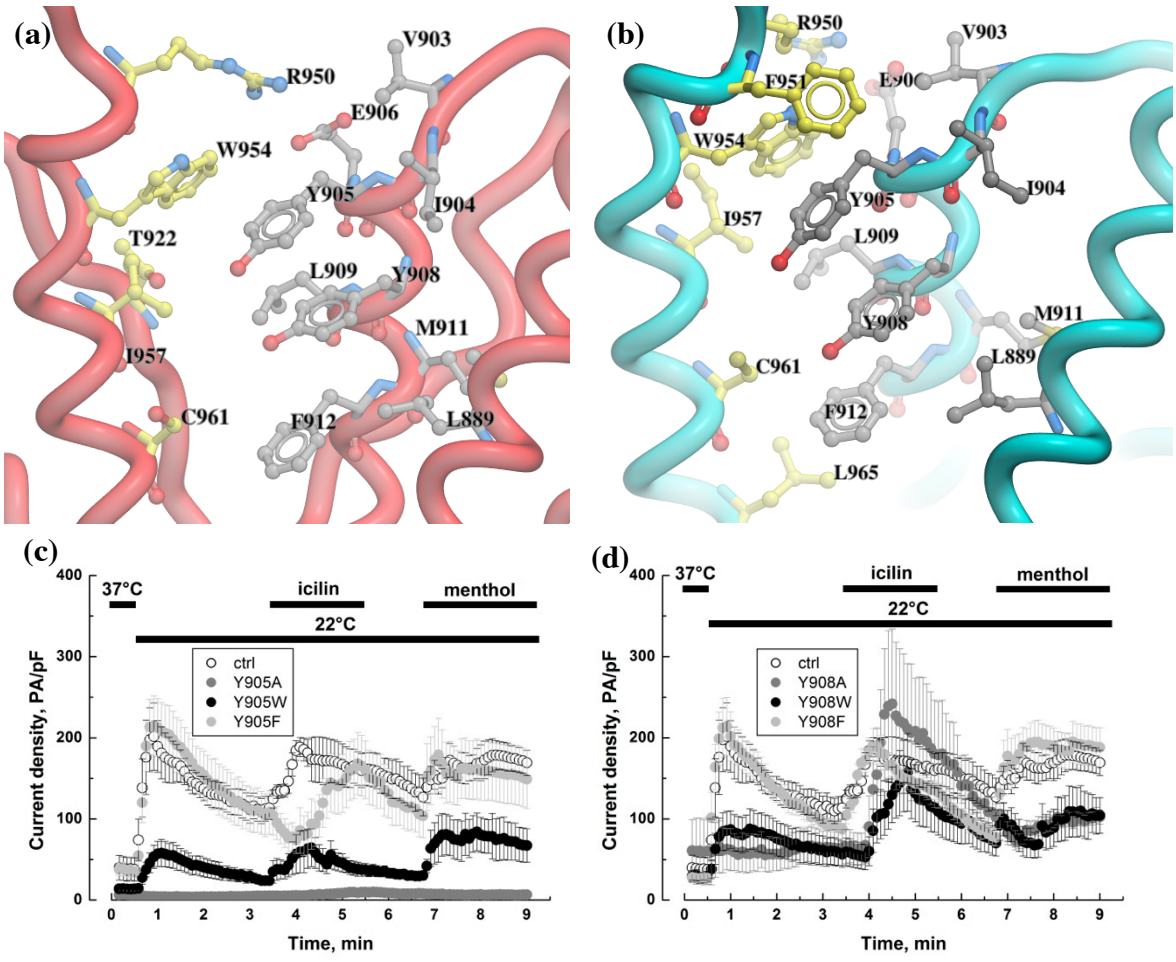

Figure 4. Inter-subunit hydrophobic cluster between P- and S6 helices in (a) closed and (b) open conformations. The side chains from one subunit are coloured grey and those from adjacent subunit are rendered as yellow sticks. Whole-cell recordings at +100mV of TRPM8 currents induced with either cold (22°C), or Icilin (10 µM), or Menthol (500 µM) for HEK cells transfected with (c) Y^{905}A, Y^{905}F or Y^{905}W TRPM8 mutants and (e) Y^{908}A, Y^{908}F or Y^{908}W TRPM8 mutants. Cells transfected with wild type TRPM8 were used as control (ctrl).

Y^{908} is a conserved residue among TRPM channels and its side chain is buried towards the S5-S6 helices (Fig 4a,b). It makes π-stacking interactions with Y^{905}. Y^{908} mutations provided us with some new data on how TRPM8 senses cold and menthol stimuli. Suppression of the phenol side chain (Y^{908}A) or its substitution by an indole side chain (Y^{908}W) triggered an almost complete loss of sensitivity to both cold and menthol application while responses to icilin where similar to WT TRPM8 (Fig 4d). Conversely, the removal of the hydroxyl group in Y^{908}F did not

ARTICLE 3

modify TRPM8 currents in response to cold, icilin and menthol. The mutants were properly targeted to the plasmalemma (Fig S4), and once again retained all the apparent electrophysiological properties of wild type TRPM8 (Fig S5).

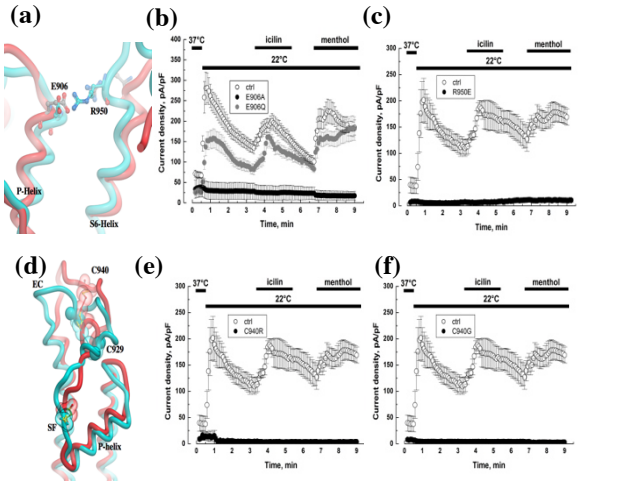

Figure 5. Residues involved in conformation of P-helix and of SF-to-S6 extracellular loop. The closed conformation is coloured red and the open state is coloured cyan. The interactions between (a) E^{906} and R^{950} are rendered as sticks and (d) disulphide bond formed by C^{929}-C^{940} are illustrated as transparent balls Whole-cell recordings at +100mV of TRPM8 currents induced with either cold (22°C), or Icilin (10 µM), or Menthol (500 µM) for HEK cells transfected with (b) E^{906}A or E^{906}Q TRPM8 mutant (c) R^{950}E TRPM8 mutant, (e) C^{940}G TRPM8 mutant, and (f) C^{940}R TRPM8 mutant. Cells transfected with wild type TRPM8 were used as control (ctrl).

Co-expression of Y^{908}A mutant with wild-type TRPM8 (3:1 ratio) induced a significant decrease of cold-activated currents (34.7%), but not of menthol-activated ones (15%, Fig S7). This suggests that Y^{908}A is a weak, current killer mutation for cold activation, and probably for menthol activation as well, since the four P-helices must be mutated to make the channel insensitive to cold and menthol. We can thus conclude that the P-helix is involved in cold and menthol gating of TRPM8 channel, while icilin activation does not involve the P-helix in the same manner. In addition, our results suggest that Y^{908} could be implicated in a functional π-stacking interaction involved in cold and menthol activation of TRPM8. In our previous studies, we observed a similar effect on TRPM8 ligand gating when co-expressing TRPM8 with its short isoforms [47, 48]. Indeed, short TRPM8 isoforms interacted with the C-terminus of TRPM8, leading to an increased stability of the closed conformation of the channel. In the light of our new data, it is therefore likely that, while interacting with TRPM8 channel, the short isoforms induce a shift of the P-helix conformation or position similar to the one operated in Y^{908}A mutant. Finally, this study confirms that conformational shifts occurring during cold and menthol activation of TRPM8 are different from the one occurring after icilin stimulation [47]. Strikingly, the two key tyrosines of the P-helix, Y^{905} and Y^{908}, exhibited π-stacking interactions. E^{906} is another important amino acid involved in P-helix function. It forms an ion pair interaction with R^{950}, present in the SF-S6 EC loop of the adjacent subunit (Fig 5a). The structural role of E^{906} in maintaining the interactions to spatially position the P-helix is assessed by its crucial role in the channel. Substitution of E^{906} with alanine completely inactivates TRPM8 channel (Fig 5b), while its substitution with a polar neutral side chain of glutamine partially restores its activity (Fig 5b). As presented in Fig S7, co-expression experiments of E^{906}A with WT TRPM8 (3:1 ratio) had almost no impact on TRPM8 activity, except for a mild effect on cold-mediated current. According to our model, these values were within the range of expected values for a weak, current-killer mutation. Similarly, R^{950} substitution to glutamate exhibited no detectable current when expressed in HEK cells, though channel expression at cell surface was found to remain unchanged (Fig S4). R^{950} showed a weak current-killer behaviour when co-expressed (3:1 ratio) with WT TRPM8 (Fig S7).

The side chain of E^{893} (S5 helix) is positioned adjacent to Y^{908} in the P-helix (Fig 6). The side chains do not form bonded interactions with any neighbouring residues in both, open and closed states. The expression of E^{893}A mutants resulted in a mild decrease in detectable currents. This is consistent with the model suggesting the tolerance to the short hydrophobic side chain of alanine and the non-critical position of E^{893}side chain.

Stabilization of the SF-to-S6 Extracellular Loop.

N^{934} residue is localized in the extracellular loop formed between SF and S6. It has been reported to be N-glycosylated and to modulate cold and menthol-sensitivity of the channel [49]. It is thought that C^{929} and C^{940} residues could form a disulfide bond [50], stabilizing the extracellular loop (Fig 5d). We therefore studied the stabilization of this extracellular loop by mean of its interaction with other domains of the TRPM8 pore.

Firstly, we confirmed that substitution of C^{940} with either glycine or arginine completely abolished TRPM8 activity (Fig 5e,f). The mutant channel was found at cell surface, though to a lesser amount than in control (Fig S4). Co-expression experiments of wild-type TRPM8 with both C^{940} mutants in a 1:3 ratio led to normal channel activity (Fig S7). Cold-induced current was in the range expected for weak, current-killer mutations demonstrating an important but not critical role of the extracellular loop in TRPM8 activity.

Discussion

Selectivity filter in TRPM8 channels

Two models of selectivity filter are classically recognized for ion channels: the oxygen-coordinated backbone of Na^+ and K^+ channels [51] and a ring of D/E residues in the outer-mouth of Ca^{2+}-selective channels [35]. Comparatively, the great family of TRP channels can be divided in three groups characterized with their ion selectivity: 1) calcium-selective TRPV5 and TRPV6 channels [52], 2) monovalent-selective TRPM4 and TRPM5 [53], 3) non-selective cationic channels, such as TRPM8 (P_{Ca}/P_{Na} = 3; [5]). Several studies and our current work have demonstrated the importance of the DDDD

ring in the outer mouth of the pore in TRPV5 (D^{542}), TRPV6 (D^{541}), TRPM4 (D^{984}) [37, 54, 55] and TRPM8 (D^{920}) channels. Substitution of this aspartic acid with short and neutral alanine significantly decreases current density in TRPV5 and TRPV6 channels and modifies slightly the Ca^{2+}-selectivity. Nilius and co-workers explained that the side chains of DDDD ring were essential to stabilize the diameter of the TRPV6 outer pore at about 5.2 Å [54]. One should note that hydrated Ca^{2+} diameter is about 4.1 Å while Na+ and K+ diameters are 3.6 and 3.3 Å, respectively [56]. Substitution of this negatively charged and polar DDDD ring with an uncharged but polar NNNN ring whose side chains length are similar, decrease calcium permeability and slightly decrease the monovalent current density without affecting the monovalent selectivity [57]. This demonstrated that the electronegative oxygen of this side chain (at physiological pH) cannot fully substitute for the negative charge of aspartate to confer Ca^{2+} permeability and facilitates transportation of monovalent ions with the same efficiency. Furthermore, Nilus *et al* demonstrated that swapping the TRPV6 SF to TRPM4 channels makes this latter permeable to Ca^{2+}, even though it does not confers TRPV6 conductance [37]. Moreover, TRPM4 SF is characterized by a second inner ring of DDDD side chains, which have been demonstrated to be involved in stabilization of the SF [37]. In this study, we have demonstrated that the open state conformation of the TRPM8 SF shows a mix pattern of TRPV5/V6 SF and TRPM4/5 SF.

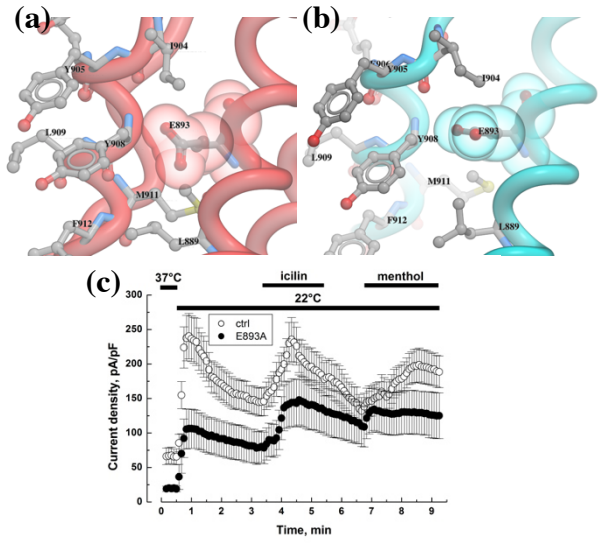

Figure 6. Molecular interactions of E^{893} in (a) closed/red and (b) open/cyan conformation. (c) Whole-cell recordings at +100mV of TRPM8 currents induced with either cold (22°C), or Icilin (10 µM), or Menthol (500 µM) for HEK cells transfected with E^{893}A TRPM8 mutant.

We have identified that the DDDD ring conserved in TRP family was essential for the pore of TRPM8. Similar to TRPV5, we identified that both the length of the side chain and negative charges are essential in TRPM8. However, the negative charge of TRPM8 D^{920} plays a greater role than its homologous residue in TRPV5/V6 SFs because it controls not only Ca^{2+} permeability but also monovalent cation permeability, unlike in TRPV5/V6 [41, 57]. The second DDDD ring, conserved in TRPM4, is not involved in the SF function of TRPM8 channel since its single mutation does not significantly alter TRPM8 current, contrary to what happens in TRPM4 [37]. However, when the two DDDD rings were mutated to alanine, no current was recorded. This suggests that the two DDDD rings may structurally participate to the stabilization of the pore, likely by forming coordinated repulsive forces, even though only the most outward ring is necessary for coordination of cations. It is also important to note the lack of apparent effect that these mutations had on channel electrophysiological properties such as I/V relationship and reversal potential. This leads us to conclude that all the mutants tested in the current study do not significantly impact TRPM8 channel selectivity for cations, as demonstrated for D^{918}A and D^{920}A. While this observation does not preclude that single channel properties such as open probability or conductance are altered in these mutants, our results show that channels behaviour followed tightly the expected distribution associated with current-killer and current-reducer mutations (**Supplementary Table S1**), thus validating our predictive model.

P-helix involvement in the activation of TRPM8 channel.

Although the structural determinants of SF activity have been studied in TRP channels, the function and role of P-helix is less described. Only two studies reported on the role of the P-helix structure in i) Camphor sensitivity of TRPV1 [42] and ii) in pH sensitivity of TRPV5 [44]. In the present study, we emphasize the close interdependence between P-Helix and external loop linking SF and TM domain S6 (SF-S6 extracellular loop). Similar to previous work by McIntyre and co-workers [50], removal of the disulfide bond (C^{929}-C^{940}) of TRPM8 did not impair its translocation to plasmalemma in cell surface biotinylation assay. We therefore believe that the absence of TRPM8 (C^{940}R) current is more related to an intrinsic issue of the channel than to a matter of translocation efficacy. Also, SF-S6 extracellular loop interacts with the P-helix via the E^{906}-R^{950} ion pair interaction. Disruption of the disulphide bond in the SF-S6 extracellular loop is likely to trigger a conformational change that alters interaction with the P-helix [50]. We also demonstrated that Y^{908} in the P-helix is crucial for menthol and cold-mediated TRPM8 activity, even though it is not involved in icilin sensitivity. By analogy with TRPV1 [42] and TRPV5 [44], we propose that either menthol binds to the P-helix or that menthol-binding site on TRPM8 (S1-S2 pocket) induces a conformational shift of the pore domain and requires rotation of the P-helix. In previous work, we demonstrated that short non-channel TRPM8 isoforms (sM8-6) [58, 59] stabilizes the TRPM8 channel in its closed conformation leading to a decrease in menthol and cold sensitivity, but without modifying icilin sensitivity. We further demonstrated that this isoform could interact with the cytosolic C-terminus of

ARTICLE 3

TRPM8 that consequently maintains the pore in closed conformation. However, because sM8-6 isoform does not interfere with the icilin-activated current density [58], it is very unlikely that sM8-6 isoform interacts directly with the P-helix. Altogether, our results suggest, for the first time, a complex physical link between the C-terminus, P-helix and the SF-S6 extracellular loop required for the menthol and cold-mediated opening of the TRPM8 channel. Other studies have highlighted the requirement of S1 and S2 [16] helices, S4 voltage-sensor [60] and C-terminus [61] in menthol-mediated TRPM8 opening. In the light of present knowledge, we propose that i) menthol induces large shift of TRPM8 conformation involving several distinct domains, ii) cold induces conformation shift of a module composed of C-terminus, P-helix and SF-S6 extracellular loop, while iii) icilin activation appeared to be restricted to the intracellular loop between S2 and S3 [62], S2 [16] and S3 TM domains [62]

Conclusion

In conclusion, we have systematically constructed a model of the TM region of the TRPM8 channel. The model is consistent with a large amount of published data and enables previous experimental findings to be explained. This provides significant validation of the model, as none of this was used in its construction. The model was further tested based on novel mutagenesis and functional analysis. Our results lead us to suggest that the ring formed by D^{920} in the selectivity filter is essential for cation conduction and the involvement of P-helix and the SF-S6 extracellular loop in menthol and cold sensitivity. The model predicts several interactions in the P-helix and SF-S6 extracellular loop that are important in stabilisation of a functional conformation of the channel. In the absence of any crystal structure, this model provides specific suggestions towards understanding TRPM8 structure-function relationship.

Acknowledgements

SH would like to thank UCL for the Excellence Fellowship.

Abbreviations

TRPM transient receptor potential melastatin; ER endoplasmic reticulum; TM transmembrane; TRPV transient receptor potential vallinoid; SF selectivity filter; DRG dorsal root ganglion; HEK Human embryonic kidney; WT wild type

Author Contribution

GB, LL, ASB, LN conducted the experiments; MS, SJ, SH constructed the molecular model, GB, LL, MS, SH wrote the manuscript, GB, AZ, SH designed the study

Conflict of Interest

The authors declare no conflict of interest

References

1. Venkatachalam, K. and C. Montell, *TRP channels.* Annu Rev Biochem, 2007. **76**: p. 387-417.
2. Nilius, B., et al., *Transient receptor potential cation channels in disease.* Physiol Rev, 2007. **87**(1): p. 165-217.
3. Clapham, D.E., *TRP channels as cellular sensors.* Nature, 2003. **426**(6966): p. 517-24.
4. Bidaux, G., et al., *Prostate cell differentiation status determines transient receptor potential melastatin member 8 channel subcellular localization and function.* J Clin Invest, 2007. **117**(6): p. 1647-57.
5. McKemy, D.D., W.M. Neuhausser, and D. Julius, *Identification of a cold receptor reveals a general role for TRP channels in thermosensation.* Nature, 2002. **416**(6876): p. 52-8.
6. Peier, A.M., et al., *A TRP channel that senses cold stimuli and menthol.* Cell, 2002. **108**(5): p. 705-15.
7. Tsavaler, L., et al., *Trp-p8, a novel prostate-specific gene, is up-regulated in prostate cancer and other malignancies and shares high homology with transient receptor potential calcium channel proteins.* Cancer Res, 2001. **61**(9): p. 3760-9.
8. Thebault, S., et al., *Novel role of cold/menthol-sensitive transient receptor potential melastatine family member 8 (TRPM8) in the activation of store-operated channels in LNCaP human prostate cancer epithelial cells.* J Biol Chem, 2005. **280**(47): p. 39423-35.
9. Zhang, L. and G.J. Barritt, *Evidence that TRPM8 is an androgen-dependent Ca2+ channel required for the survival of prostate cancer cells.* Cancer Res, 2004. **64**(22): p. 8365-73.
10. Rohacs, T., et al., *PI(4,5)P2 regulates the activation and desensitization of TRPM8 channels through the TRP domain.* Nat Neurosci, 2005. **8**(5): p. 626-34.
11. Vanden Abeele, F., et al., *Ca2+-independent phospholipase A2-dependent gating of TRPM8 by lysophospholipids.* J Biol Chem, 2006. **281**(52): p. 40174-82.
12. Andersson, D.A., M. Nash, and S. Bevan, *Modulation of the cold-activated channel TRPM8 by lysophospholipids and polyunsaturated fatty acids.* J Neurosci, 2007. **27**(12): p. 3347-55.
13. Zakharian, E., C. Cao, and T. Rohacs, *Gating of transient receptor potential melastatin 8 (TRPM8) channels activated by cold and chemical agonists in planar lipid bilayers.* J Neurosci, 2010. **30**(37): p. 12526-34.
14. Latorre, R., et al., *ThermoTRP channels as modular proteins with allosteric gating.* Cell Calcium, 2007. **42**(4-5): p. 427-38.
15. Latorre, R., et al., *A cool channel in cold transduction.* Physiology (Bethesda), 2011. **26**(4): p. 273-85.
16. Bandell, M., et al., *High-throughput random mutagenesis screen reveals TRPM8 residues specifically required for activation by menthol.* Nat Neurosci, 2006. **9**(4): p. 493-500.
17. Brauchi, S., et al., *Dissection of the components for PIP2 activation and thermosensation in TRP channels.* Proc Natl Acad Sci U S A, 2007. **104**(24): p. 10246-51.
18. Phelps, C.B. and R. Gaudet, *The role of the N terminus and transmembrane domain of TRPM8 in channel localization and tetramerization.* J Biol Chem, 2007. **282**(50): p. 36474-80.
19. Tsuruda, P.R., D. Julius, and D.L. Minor, Jr., *Coiled coils direct assembly of a cold-activated TRP channel.* Neuron, 2006. **51**(2): p. 201-12.
20. Erler, I., et al., *Trafficking and assembly of the cold-sensitive TRPM8 channel.* J Biol Chem, 2006. **281**(50): p. 38396-404.
21. Latorre, R., C. Zaelzer, and S. Brauchi, *Structure-functional intimacies of transient receptor potential channels.* Q Rev Biophys, 2009. **42**(3): p. 201-46.

22. Liao, M., et al., *Structure of the TRPV1 ion channel determined by electron cryo-microscopy.* Nature, 2013. **504**(7478): p. 107-12.
23. Cao, E., et al., *TRPV1 structures in distinct conformations reveal activation mechanisms.* Nature, 2013. **504**(7478): p. 113-8.
24. Beck, B., et al., *Prospects for prostate cancer imaging and therapy using high-affinity TRPM8 activators.* Cell Calcium, 2007. **41**(3): p. 285-94.
25. Sali, A. and T.L. Blundell, *Comparative protein modelling by satisfaction of spatial restraints.* J Mol Biol, 1993. **234**(3): p. 779-815.
26. Larkin, M.A., et al., *Clustal W and Clustal X version 2.0.* Bioinformatics, 2007. **23**(21): p. 2947-8.
27. Buchan, D.W., et al., *Scalable web services for the PSIPRED Protein Analysis Workbench.* Nucleic Acids Res, 2013. **41**(Web Server issue): p. W349-57.
28. Kalia, J. and K.J. Swartz, *Exploring structure-function relationships between TRP and Kv channels.* Sci Rep, 2013. **3**: p. 1523.
29. Laskowski, R.A., et al., *PROCHECK: a program to check the stereochemical quality of protein structures.* J. Appl. Cryst., 1993. **26**: p. 283-291.
30. Smart, O.S., et al., *HOLE: a program for the analysis of the pore dimensions of ion channel structural models.* J Mol Graph, 1996. **14**(6): p. 354-60, 376.
31. Nugent, T. and D.T. Jones, *Transmembrane protein topology prediction using support vector machines.* BMC Bioinformatics, 2009. **10**: p. 159.
32. Ramsey, I.S., M. Delling, and D.E. Clapham, *An introduction to TRP channels.* Annu Rev Physiol, 2006. **68**: p. 619-47.
33. Russell, R.B., et al., *Recognition of analogous and homologous protein folds: analysis of sequence and structure conservation.* J Mol Biol, 1997. **269**(3): p. 423-39.
34. Antcliff, J.F., et al., *Functional analysis of a structural model of the ATP-binding site of the KATP channel Kir6.2 subunit.* EMBO J, 2005. **24**(2): p. 229-39.
35. Sather, W.A. and E.W. McCleskey, *Permeation and selectivity in calcium channels.* Annu Rev Physiol, 2003. **65**: p. 133-59.
36. Cheng, R.C., D.B. Tikhonov, and B.S. Zhorov, *Structural modeling of calcium binding in the selectivity filter of the L-type calcium channel.* Eur Biophys J, 2010. **39**(5): p. 839-53.
37. Nilius, B., et al., *The selectivity filter of the cation channel TRPM4.* J Biol Chem, 2005. **280**(24): p. 22899-906.
38. Garcia-Martinez, C., et al., *Identification of an aspartic residue in the P-loop of the vanilloid receptor that modulates pore properties.* J Biol Chem, 2000. **275**(42): p. 32552-8.
39. Winter, Z., et al., *Functionally important amino acid residues in the transient receptor potential vanilloid 1 (TRPV1) ion channel--an overview of the current mutational data.* Mol Pain, 2013. **9**: p. 30.
40. Peracchi, A., *Enzyme catalysis: removing chemically 'essential' residues by site-directed mutagenesis.* Trends Biochem Sci, 2001. **26**(8): p. 497-503.
41. Voets, T., et al., *Outer pore architecture of a Ca2+-selective TRP channel.* J Biol Chem, 2004. **279**(15): p. 15223-30.
42. Marsakova, L., et al., *Pore helix domain is critical to camphor sensitivity of transient receptor potential vanilloid 1 channel.* Anesthesiology, 2012. **116**(4): p. 903-17.
43. Myers, B.R., C.J. Bohlen, and D. Julius, *A yeast genetic screen reveals a critical role for the pore helix domain in TRP channel gating.* Neuron, 2008. **58**(3): p. 362-73.
44. Yeh, B.I., et al., *Conformational changes of pore helix coupled to gating of TRPV5 by protons.* EMBO J, 2005. **24**(18): p. 3224-34.
45. Chung, M.K., A.D. Guler, and M.J. Caterina, *TRPV1 shows dynamic ionic selectivity during agonist stimulation.* Nat Neurosci, 2008. **11**(5): p. 555-64.
46. Salazar, H., et al., *Structural determinants of gating in the TRPV1 channel.* Nat Struct Mol Biol, 2009. **16**(7): p. 704-10.
47. Bidaux, G., et al., *Regulation of transient receptor potential melastatin 8 (TRPM8) channel activity by its short isoforms.* J Biol Chem, 2011.
48. Fernandez, J.A., et al., *Short isoforms of the cold receptor TRPM8 inhibit channel gating by mimicking heat action rather than chemical inhibitors.* J Biol Chem, 2011.
49. Pertusa, M., et al., *N-glycosylation of TRPM8 ion channels modulates temperature sensitivity of cold thermoreceptor neurons.* J Biol Chem, 2012. **287**(22): p. 18218-29.
50. Dragoni, I., E. Guida, and P. McIntyre, *The cold and menthol receptor TRPM8 contains a functionally important double cysteine motif.* J Biol Chem, 2006. **281**(49): p. 37353-60.
51. Khalili-Araghi, F., E. Tajkhorshid, and K. Schulten, *Dynamics of K+ ion conduction through Kv1.2.* Biophys J, 2006. **91**(6): p. L72-4.
52. den Dekker, E., et al., *The epithelial calcium channels, TRPV5 & TRPV6: from identification towards regulation.* Cell Calcium, 2003. **33**(5-6): p. 497-507.
53. Ullrich, N.D., et al., *Comparison of functional properties of the Ca2+-activated cation channels TRPM4 and TRPM5 from mice.* Cell Calcium, 2005. **37**(3): p. 267-78.
54. Voets, T., et al., *Mg2+-dependent gating and strong inward rectification of the cation channel TRPV6.* J Gen Physiol, 2003. **121**(3): p. 245-60.
55. Dodier, Y., et al., *Topology of the selectivity filter of a TRPV channel: rapid accessibility of contiguous residues from the external medium.* Am J Physiol Cell Physiol, 2007. **293**(6): p. C1962-70.
56. Conway, B.E., *Ionic hydration in chemistry and biophysics.* Journal of Solution Chemistry, 1982. **11**(3): p. 221-222.
57. Nilius, B., et al., *The single pore residue Asp542 determines Ca2+ permeation and Mg2+ block of the epithelial Ca2+ channel.* J Biol Chem, 2001. **276**(2): p. 1020-5.
58. Bidaux, G., et al., *Regulation of activity of transient receptor potential melastatin 8 (TRPM8) channel by its short isoforms.* J Biol Chem, 2012. **287**(5): p. 2948-62.
59. Fernandez, J.A., et al., *Short isoforms of the cold receptor TRPM8 inhibit channel gating by mimicking heat action rather than chemical inhibitors.* J Biol Chem, 2012. **287**(5): p. 2963-70.
60. Voets, T., et al., *TRPM8 voltage sensor mutants reveal a mechanism for integrating thermal and chemical stimuli.* Nat Chem Biol, 2007. **3**(3): p. 174-82.
61. Brauchi, S., et al., *A hot-sensing cold receptor: C-terminal domain determines thermosensation in transient receptor potential channels.* J Neurosci, 2006. **26**(18): p. 4835-40.
62. Chuang, H.H., W.M. Neuhausser, and D. Julius, *The super-cooling agent icilin reveals a mechanism of coincidence detection by a temperature-sensitive TRP channel.* Neuron, 2004. **43**(6): p. 859-69.

ARTICLE 3

Supplementary Information

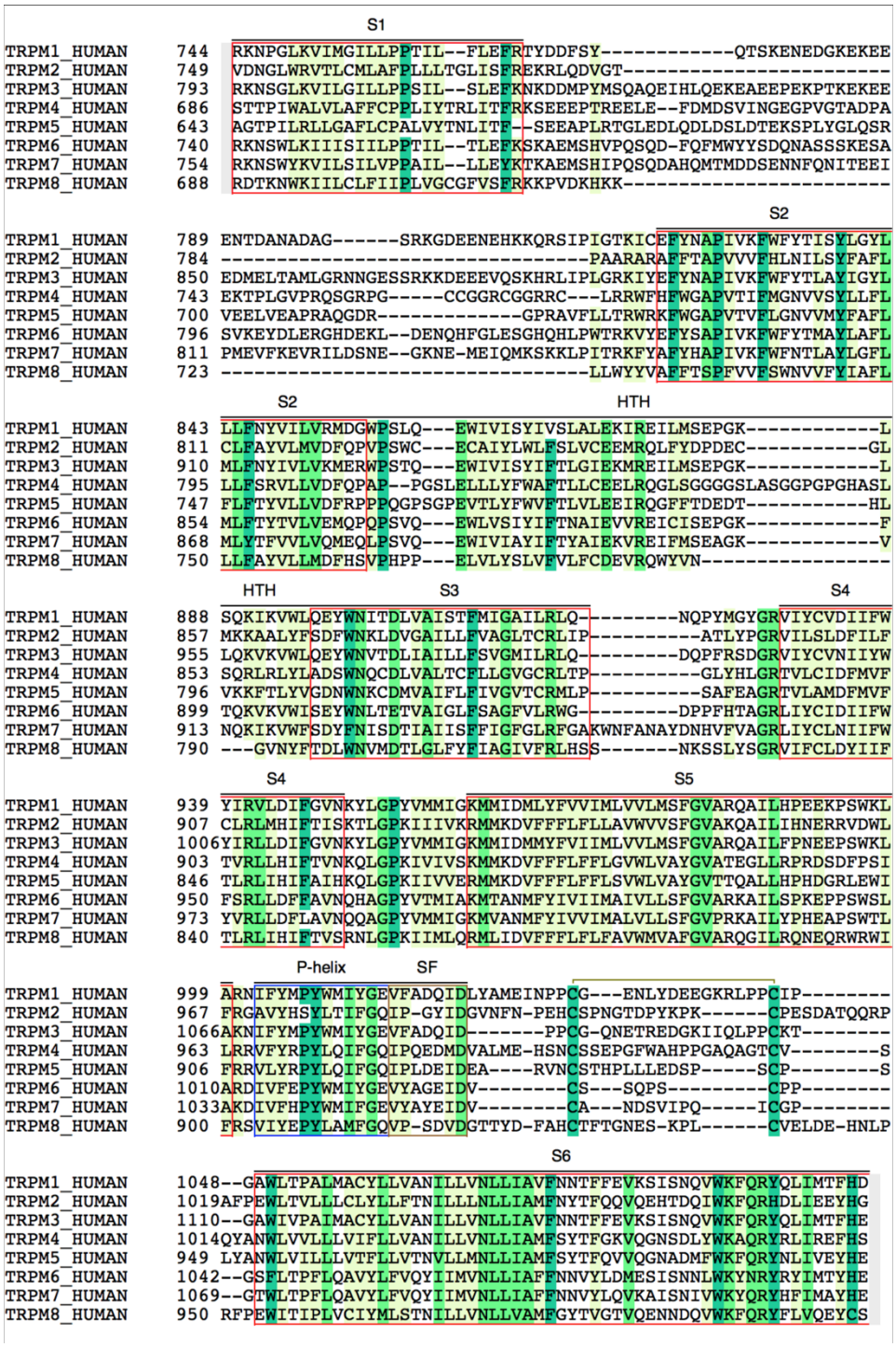

Supplementary Figure S1. Multiple sequence alignment of the transmembrane regions within the TRPM ion channel family.

Supplementary Figure S2. Secondary structure prediction of the transmembrane region of TRPM8.

ARTICLE 3

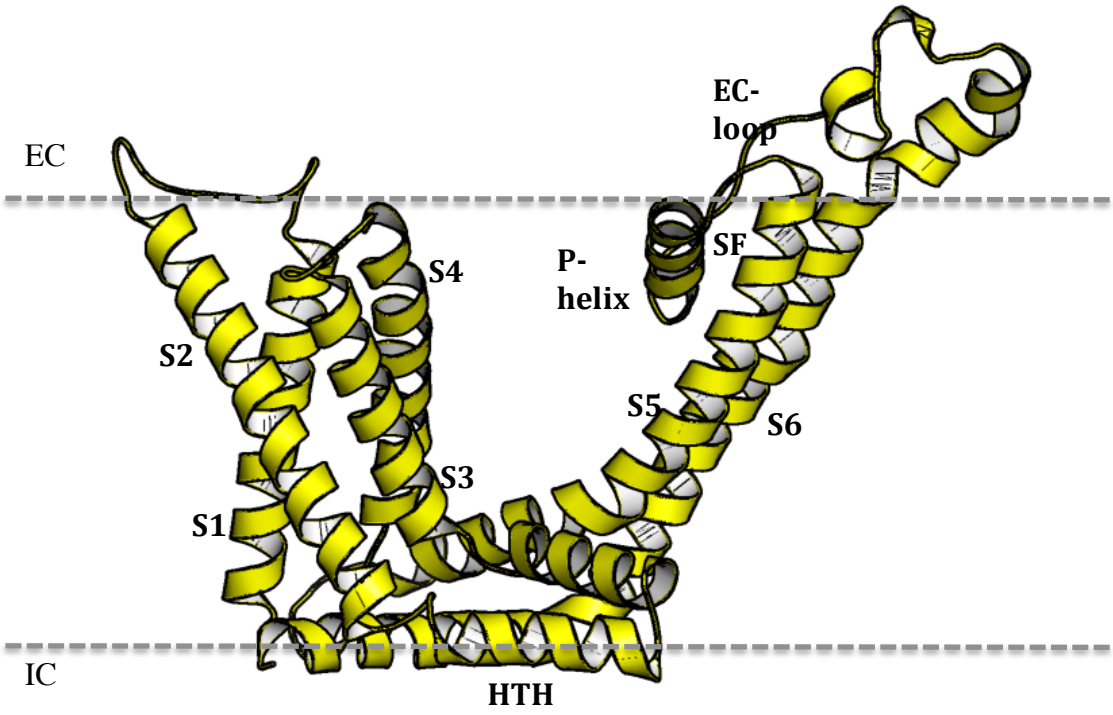

Supplementary Figure S3. A monomeric chain of TRPM8 TM region (green) as positioned in the lipid bilayer. The top and the lower boundary of the lipid bilayer have been illustrated as a grey line. Four identical chains come together to form a functional channel

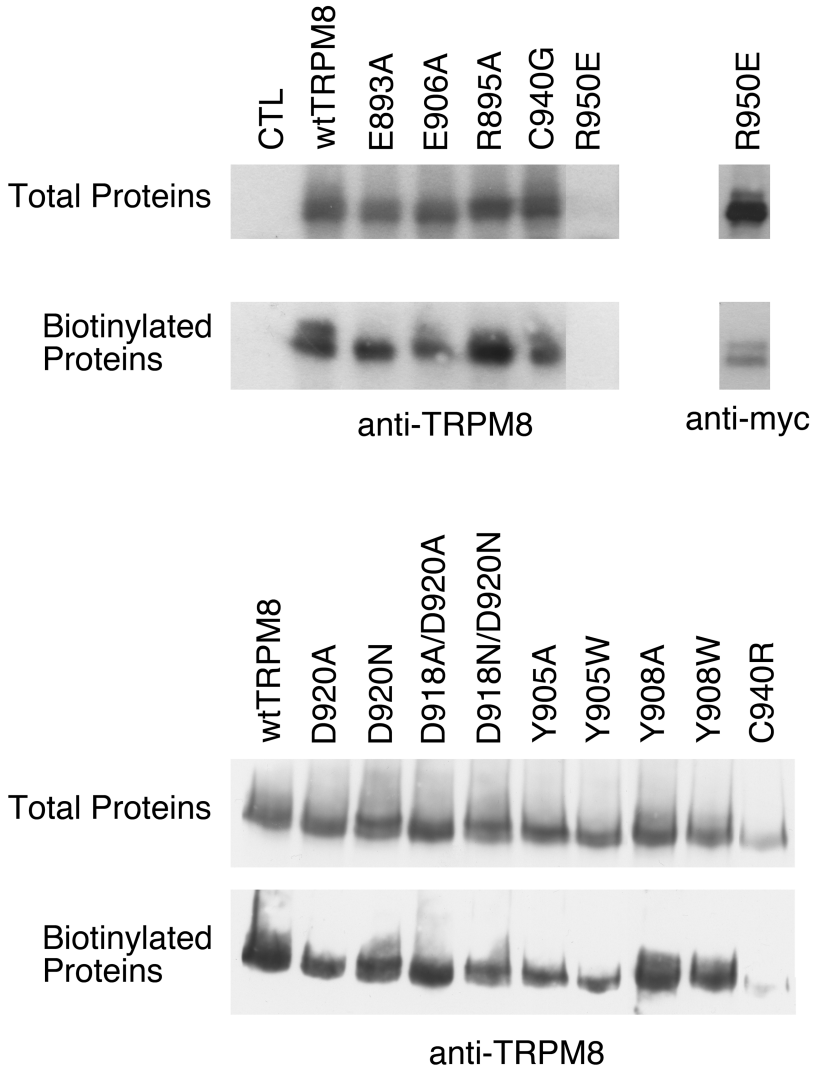

Supplementary Figure S4. Cell surface biotinylation of *wild-type* and mutant TRPM8 proteins in HEK cells. Immunoblottings showing the detection of TRPM8 proteins in total protein extracts (Total Proteins) after pull-down of biotinylated proteins with neutravidin beads (Biotinylated Protein). Proteins were detected with antiTRPM8 antibody except TRPM8 ($R^{950}A$), which was revealed with anti-myc antibody.

ARTICLE 3

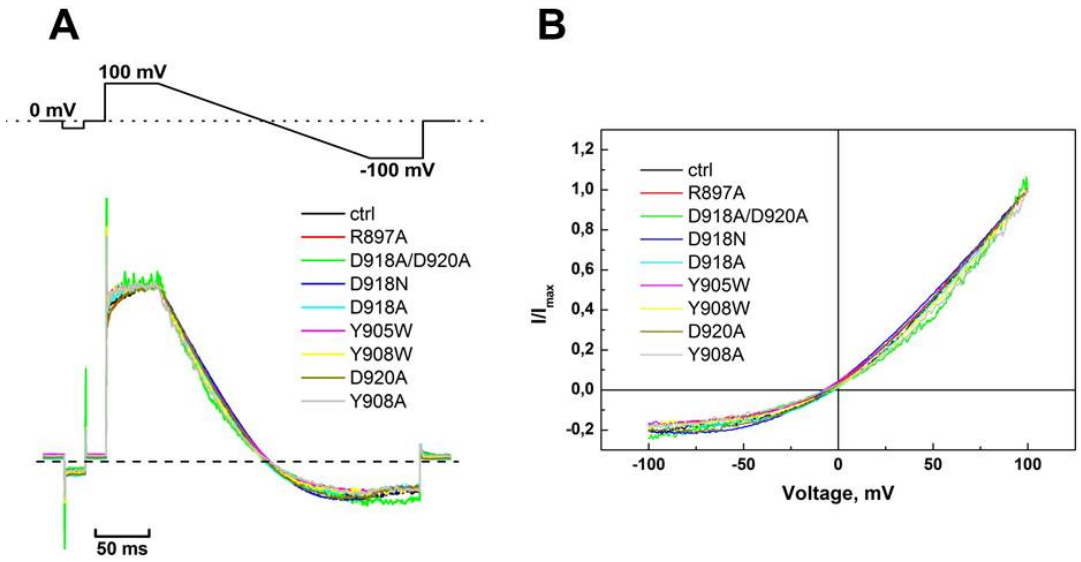

Supplementary Figure S5. TRPM8 mutant proteins exhibit unaltered electrophysiological properties. **A**: Normalized whole-cell traces of representative cells transfected with wild type (ctrl) or mutant TRPM8 proteins and stimulated with the voltage ramp protocol presented above. Corresponding current/voltage relationships are shown in **B**.

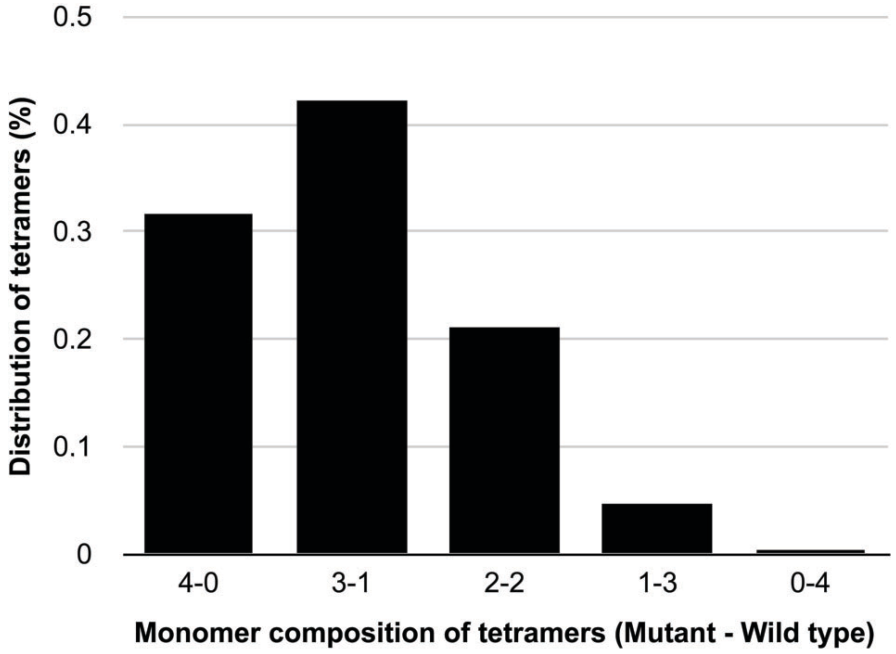

Supplementary Figure S6. Stochastic assembling of mutant and wild type TRPM8 monomers in a single cell. Probabilistic distribution of the different type of tetramers in cells co-transfected with a 3:1 ratio of mutant TRPM8 and WT TRPM8 channels.

ARTICLE 3

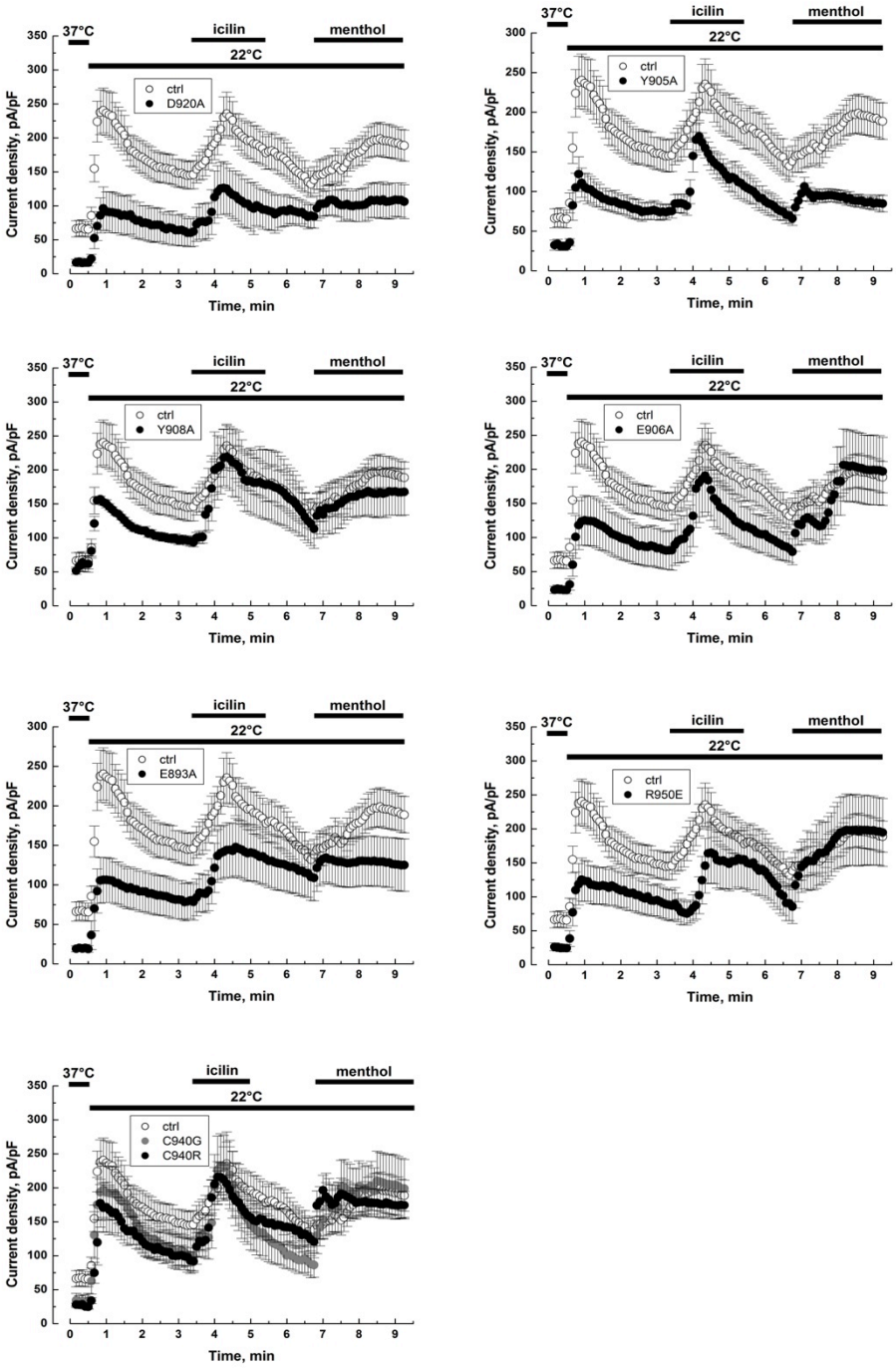

Supplementary Figure S7. Whole-cell recordings at +100mV of TRPM8 currents induced with either cold (22°C), or Icilin (10 µM), or Menthol (500 µM) for HEK cells concomitantly transfected with wild type TRPM8 and one specific TRPM8 mutant at a ratio 1:3. Cells transfected with wild type TRPM8, alone, were used as control (ctrl).

		Monomer proportion in each tetramer (Mutant - Wild type)					
	Homotetramers	**4-0**				**0-4**	
	Frequence of assembling	**1**				**1**	Total relative current
Relative current	WT					**1**	**=1.000**
	Current-killer mutation	**0**					**=0.000**
	Current-reducer mutation	**R**					**=R**
	Heterotetramers (Mutant - WT)	**4-0**	**3-1**	**2-2**	**1-3**	**0-4**	
	Frequence of assembling	***0.316***	***0.422***	***0.211***	***0.047***	***0.004***	
Relative current	Dominant/current-killer mutation	**0**	**0**	**0**	**0**	**1**	**=0.004**
	Dominant/current-reducer mutation	**R**	**R**	**R**	**R**	**1**	**=0.996xR+0.004**
	Weak/current-killer mutation	**0**	**1**	**1**	**1**	**1**	**=0.684**
	Weak/current-reducer mutation	**R**	**1**	**1**	**1**	**1**	**=0.316xR+0.684**
	Stoichiometry-dependent/current-killer mutation	**0**	**0<A<1**	**0<B<1**	**0<C<1**	**1**	=0.422xA+0.211xB+0.047xC+0.004 (1)
	Stoichiometry-dependent/current-reducer mutation	**R**	**R<a<1**	**R<b<1**	**R<c<1**	**1**	=0,316xR+0.422xA+0.211xB+0.047xC+0.004 (2)

(1): A<B<C
(2): a<b<c

Supplementary Table S1. Model for calculation of the expected whole cell current in a mixed population of wild type and mutant TRPM8 channels. The relative current represents the normalization of the averaged maximal amplitude of current density of mutant TRPM8 homotetramers in single cells by the averaged maximal amplitude of current density of wild type TRPM8 homotetramer in single cells. The total relative current is the sum of relative currents of each type of tetramers in the population weighted with the probabilistic distribution.

Plasmid	**Peak current (pA/pF), Cold (22°C)**	**Peak current (pA/pF), Icilin (10 µM)**	**Peak current (pA/pF), Menthol (500 µM)**
CTL	187.1±40	183.2±75.8	168.5±56.2
D918A	162.4±54	165.4±52	173.9±51.7
D918N	159.1±37.6	154±33.6	145±32.8
D918E	139.7±43.2	190.3±49	110.6±19.9
D920A	128.8±34.5	119.1±40.2	130.7±23.5
D920N	13.7±6.3	9.4±2.1	8.8±1.4
D918A/D920A	28.2±10.4	31.6±9.3	21.4±4.7
D918E/D920E	223.8±30.5	164.8±13.9	170.7±23.1
D918N/D920N	6.3±1.1	31.6±9.3	21.4±4.7
V919I	222.1±69.2	228.6±53	166.5±33.9
Y905A	4.4±0.4	7.1±1.5	6.7±2.1
Y905W	57.9±16.7	64.4±23.2	84.1±23.2
E893A	7.5±2.3	23.4±9.8	26.4±11.1
E906A	38.2±23.6	24.6±17.4	17.4±11.2
R950E	5.9±0.6	6.2±0.8	11.5±3.5
Y908A	62.8±25.3	241.8±92.3	102.5±8.9
Y908W	87.7±25	157.2±48	109.2±31.6
C940G	4.3±0.6	3.9±1.5	3±0.1
C940R	13.4±9.2	3.5±0.3	3.3±0.5

Supplementary Table S2. Summary of our patch-clamp results on single TRPM8 mutants when expressed in HEK293. Control (CTL) represents wild-type TRPM8 expressed in the same model. All data are presented as mean±SEM and show current density values obtained at +100mV following application of cold, icilin or menthol (n=3-8).

II. ARTICLE 12

ARTICLE 12

Targeting TRPM8 regulatory subunits in prostate cancer: towards a new drug target?

Gabriel Bidaux[1,2,§], Anne-Sophie Borowiec[1,§], Loïc Lemonnier[1], Charlotte Dubois[1], Céline Schulz[1], Fabien Vanden Abeele, Gilbert Lepage[1], Emilie Desruelles[1], Philippe Delcourt[1], Christian Slomianny[1], Morad Roudbaraki[1], Jean-Louis Bonnal[1], Brigitte Mauroy[1], Pascal Mariot[1], and Natalia Prevarskaya[1]

[1] Inserm, U-1003, Equipe labellisée par la Ligue Nationale contre le cancer, Villeneuve d'Ascq, F-59655 France; Université des Sciences et Technologies de Lille (USTL), Villeneuve d'Ascq, F-59655 France.

Running title: Pro oncogenic effect of short TRPM8 isoforms in prostate cancer.
To whom correspondences should be addressed: Gabriel Bidaux; gabriel.bidaux@gmail.fr

[§]Contributed equally.

[2]Laboratoire de Physique des Lasers, Atomes & Molécules, Equipe Biophotonique Cellulaire Fonctionnelle, Parc scientifique de la Haute Borne, Villeneuve d'Ascq, France.

Abstract

Since its cloning a decade ago, the transient receptor potential melastatin channel member 8 (TRPM8) has emerged as a promising prognostic marker and a putative therapeutic target in prostate cancer (PCa). Though TRPM8 expression in PCa has been extensively studied, its biological function in the epithelial prostate cells is still debated. We recently characterized several TRPM8 channel isoforms in prostate cells and demonstrated their increased expression in advanced prostate tumors, while the expression of the full length cold and menthol TRPM8 channel is decreased, otherwise repressed. Moreover, we recently cloned truncated non-channel TRPM8 isoforms (sM8s) in PCa cells and proposed that they could function as regulatory subunits of the full length TRPM8 channel. In the present study, we investigated the biological outcomes of the sM8s suppression in PCa cells. We report that sM8s suppression triggers endoplasmic reticulum stress, induction of $p21^{waf1}$ and induction of apoptosis in PCa cells. Besides, we show that the concomitant knockdown of sM8s and the knockdown/inhibition of TRPM8 channel isoforms decrease the stress response reducing the induction of $p21^{waf1}$ and inhibiting apoptosis. Altogether, our results suggest that targeting sM8s, rather than the full length TRPM8, could be an efficient therapeutic strategy to inhibit prostate cancer growth.

Introduction

Prostate cancer (PCa) is the most common tumor and the second cause of cancer-related death in men living in Western Europe and North America. Recent advances in cancer research have provided strong evidences that PCa originates from the basal proliferating compartment, likely from stem cell progenitors [1]. However, these cancer basal cells still partially differentiate into cells expressing both luminal [1, 2] and stem cell markers and are able to propagate advanced tumors. This luminal-like phenotype of PCa cells, balancing between proliferating and differentiated phenotypes, is particularly consistent with the low proliferating rate of PCa and their increased resistance to apoptosis [3], which is partly stimulated by androgen receptor [4]. Different anti-cancer strategies are studied worldwide such as inducing PCa cell death with vectorized drugs or gene editing/silencing technologies (see selected reviews [5, 6]), promoting differentiation into luminal epithelial cells which are further subjected to apoptosis, or stimulating the patient's immune response to induce a T-cell based immunotherapy [7].

For 20 years, an increasing number of reports have demonstrated that alterations of calcium (Ca^{2+}) homeostasis and/or Ca^{2+} signals interfere with the signaling pathways controlling apoptosis, proliferation, differentiation, secretion and migration [8, 9]. Indeed, a deregulation of ER Ca^{2+} homeostasis processes have been reported in PCa, such as the overexpression of the anti-apoptotic protein Bcl-2 or the Ca^{2+} leak through translocon during Unfolding Response Protein, UPR, both correlated to a decrease in ER Ca^{2+} content [10, 11]. Along this line, a new anti-cancer strategy, based on the remodeling of the network of Ca^{2+}-transporting proteins [12], has emerged by the mean of knockdown strategies or treatment with drugs modifying the pathological Ca^{2+} homeostasis in PCa cells [13]. Among Ca^{2+} channels, TRPM8 (TRP, Melastatine member 8) has emerged as a putative therapeutic target in PCa [14-17]. Indeed, we and others have reported i) an increased expression and activity of TRPM8 channel in intracapsular prostate tumors [18], ii) a strong decrease in TRPM8 expression in androgen-dependent extracapsular PCa and in androgen-dependent metastasis [19], iii) an almost complete suppression of TRPM8 expression in prostates of patients treated preoperatively with anti-androgen therapy [20] due to its absolute requirement on functional androgen receptors (AR) [17, 21]. Furthermore, we reported that a TRPM8 channel isoform was present in the intermediate/transient amplifying normal epithelial prostate cells as well as in PCa and metastasis. Finally, we demonstrated that several TRPM8 channel isoforms are expressed and active in the endoplasmic reticulum (ER) membranes of prostate cells (Unpublished data, Bidaux et al).

TRPM8 is composed of six transmembrane domains with a pore P-loop between the fifth and sixth domains and intracellular N- and C-terminal regions [16, 22, 23]. The TRPM8 isoforms show different structures which can be classified in two groups: channel-like isoforms possessing a minimum of 2 transmembrane domains and a P-loop (Unpublished data, Bidaux et al), and regulatory non-channel isoforms. The latter, labeled short isoforms or sM8, could act as regulatory sub-units modulating the

activity of TRPM8 channel-like isoforms [24, 25]. We also reported that prostate tumors might (over)express splice variants of these sM8 isoforms, although the biological consequences of this altered expression remain elusive.

While TRPM8 has been previously suggested as a valuable putative therapeutic target, only one proof of concept has been reported so far, demonstrating that T-cell-based immunotherapy could be achieved by targeting the plasmalemmal TRPM8 channel expressed in an heterologous cell model [15]. In the present study, we wondered whether a modification in sM8 expression level may trigger significant biological consequences in prostate cancer cells. To do so, we first detailed our previous classification of sM8 family by cloning 3 new alternate mRNA. Using a siRNA-based strategy to decipher their role of non-channel isoforms, we then demonstrated that suppression of sM8 isoforms induced ER stress, $p21^{waf1}$ induction and apoptosis. Finally, we showed that the inhibition of TRPM8 channel isoforms reduced the sM8 knockdown-mediated induction of $p21^{waf1}$ and apoptosis. Altogether, our results infer that sM8 isoforms participate in resistance against pro-apoptotic signals in prostate cancer cells and consequently that targeting sM8 isoforms rather than the TRPM8 channel itself could be an appropriate and beneficial strategy to fight prostate cancer.

Materials and Methods

Cell lines culture. The LNCaP, DU145 and PC-3 cell lines were purchased from the American Type Culture Collection (ATCC). LNCaP C4-2b cell line and CWR22Rv1 was a generous gift from Dr. F. Cabon, Paris. Cells were amplified in RPMI medium 1640 (Gibco®) supplemented with 10% fetal calf serum (FCS) and kanamycin (100 µg/ml). For experiment, cells were cultured in RPMI medium 1640 (Gibco®) supplemented with 2% FCS, 1mM Sodium pyruvate, 1.5mM $CaCl_2$, and kanamycin (100 µg/ml). TRPM8-36nducible HEK cell line was established as described elsewhere (ref Cell calcium Ben) and was grown in Dulbecco's minimal essential media (DMEM) (Gibco) including 4.5 g/l Glucose and 1.8 mM Ca^{2+}, and was supplemented with 10% FCS and Kanamycin (100 µg/ml).

Primary culture of human prostate cancer epithelial cells (PrPCa). Human prostate tissue specimens were obtained from resection surgeries performed on clinical indications in the Urology Department at l'Hôpital St. Philibert (Lille, France). All specimens came from patients who had not received anti-androgen therapy. In addition, all specimens were diagnosed by an anatomopathological examination. After patient surgery, the connective tissues were eliminated and the epithelial nodules were cut into small fragments of about 1-2mm^3 in a 100mm diameter dish filled with 3ml of RPMI 1640 medium. Fragments of tissue were washed in clean RPMI medium prior to their transfer in culture dishes. About 7 explants were put in BD *Primaria* ™ 100 mm Cell Culture *Dishes with 1 to 1.5 ml of basal PrPCa medium for 2-3 days – to let the explants adhere on the dish surface. Thereafter, extra medium was added, and renewed twice a week for 4 to 5 weeks or until cells outspreading from explants reached confluence. Before carrying out experiments, cells were detached with a 30 min incubation in 9 ml of a PBS solution containing 0.5mM EDTA. One ml of trypsin was then added for a further 5 min-incubation. Cells were collected and centrifuged prior to their resuspension in basal PrPCa medium. After a 1-day recovery period, cells were transfected and induced in the induction PrPCa medium. Basal PrPCa medium was: Keratinocyte-SFM medium* (Gibco®) supplemented with EGF, BPE and kanamycin (100 µg/ml). *Induction PrPCa medium was: Keratinocyte-SFM medium* (Gibco®) supplemented with EGF, BPE, kanamycin (100 µg/ml), 2% FCS and 1.7 mM $CaCl_2$.

All experiments on human tissues were performed according to the "CP 01/33" regulations issued by the "Comité Consultatif de Protection des Personnes dans la Recherche Biomedicale de Lille" (CCPPRB).

Transfection. Cells were transfected with plasmids using nucleofector technology (Lonza). Briefly, 1 million cells were transfected with 2 µg of total vectors and then seeded on precoated dishes with polylysine. SiRNA (25nM) transfection was performed with HiPerfect (Qiagen) as described by the manufacturer. Cell lines were transfected once and experiments were performed 3 days after transfection. PrPCa were transfected twice with 3 days recovery between transfections and experiments were performed 3 days after the second transfection. siRNAs are listed in Table 1.

Group suppression of TRPM8 isoforms. We postulated that group suppression of TRPM8 isoforms could result in different cellular and molecular phenotypes. We also assumed that a subtractive comparison should reveal informations about the biological function of a specific group of TRPM8 isoforms. For instance, while siM8-6a silenced both sM8 and TRPM8, siM8-7 silenced only TRPM8. We thus expected to attribute the biological variations between both siRNAs, specifically, to sM8 knockdown (KD). To address this strategy, we developed series of siRNAs targeting different TRPM8 exons spanned over the TRPM8 gDNA. siRNAs were labeled in reference to the TRPM8 exons they were targeting (i.e siM8- exon number). Efficiency of siRNA on TRPM8 silencing was measured in TRPM8-36 inducible HEK cells transfected with 50 nM of siRNA for 48h (**Fig S1A**). qPCR (**Fig S1A**) and western-blot (**Fig S1B and S1C**) experiments validated two siRNAs targeting TRPM8 (siM8-7 and siM8-10), three siRNA targeting the sM8s in addition to TRPM8 (siM8-4b, siM8-6a and siM8-6a.2) and two siRNAs targeting TRPM8-36 in addition to TRPM8 (siM8-19 and siM8-20) (**Fig 1A**). The specificity of siRNA is usually guaranteed by the use of low siRNA concentrations (below 100 nM), and by comparing their biological effects with the ones induced by a control siRNA. This latter is usually assumed to be a RNA sequence which does not match with genome sequences of the host organism. However, this does not completely guaranty the absence of off-target effects. A further control could be achieved by the mean of degenerated sequences, which only diverge from the original siRNA by one or two base substitutions. We therefore designed two siM8-6a mutants and quantified their respective

efficiency by qPCR (**Fig S1D**). Both siM8-6a(M1) and siM8-6a(M3) showed a partial silencing effect on sM8 mRNA.

Subcutaneous xenograft. Six-week old male swiss nude mice (Charles River Laboratories, France) were injected with LNCaP C4-2b cells. Six million cells were injected into both flanks of each mouse. Cells were prepared in a mixture composed of 50 % PBS and 50 % BD-Matrigel® (BD Bioscience, France). Tumors were measured twice a week using a caliper and animals were sacrificed 12 weeks after injection unless the mice had to be sacrificed earlier if the total tumor size reached 10% of the animal weight.

Tumor volume was calculated using the following formula: Volume (in mm3) = length (in mm)*depth (in mm) *width (in mm)*π/6.

On the day of sacrifice, tumors were weighed and divided for further immuno-histochemical, western blot and RT-PCR experiments. At least 10 animals per condition were used. *In vivo* experiments were conducted on mice according to the agreement provided by the local ethical comity (protocol CEEA 202012).

5'-RACE PCR. 5' alternate extremities of short TRPM8 isoforms (sM8) were cloned with SMART RACE-PCR, following the manufacturer procedures (Clonetech). Briefly, total mRNA of LNCaP cells were treated with DNAse 1 for 15 minutes prior to phenol/chloroform purification. After ethanol precipitation of mRNA, first strand cDNA were synthesized with Prime script Reverse Transcriptase (Takara) from 2 µg of mRNA using SMART oligonucleotides. To clone sM8 mRNA, 5'-RACE-PCR was performed with phusion polymerase (Finzymes) for 35 cycles with TRPM8 specific backward oligonucleotide: CACAATATTCTCCTCTGAACTCCT. After cleaning up PCR mix on columns (Nucleospin extract II, Macherey Nagel), nested-PCR was performed on 1 µl of RACE purified DNAs with phusion polymerase. Amplicons were visualized on agarose gel with syber green on a Dark reader, blue light table (Ozyme). After excision of bands, DNA was recovered with Nucleospin extract II (Macherey Nagel). Terminal adenylation of DNAs was then performed with Taq gold polymerase prior to cloning PCR products in pGem-T easy vector (Promega). Colonies were controlled by EcoRI digestion and positive clones were submitted to sequencing.

Cloning of sM8 mRNA. Specific primers, based on RACE sequences, were designed and used to amplify cDNA with Taq Gold polymerase from LNCaP mRNA, prepared as described above. Amplicons were ligated in pGemTeasy vector (Promega). Cloning primers were: **TRPM8/exon1**: GAGAGACCAGCAGGATCCTTGG, **TRPM8/exon2'**: TGACCTGTGGGAAGTGGCACTG, **TRPM8/exon3'**: ATGGAGAGAGAAGAGGAACATCAG, **TRPM8/exon5a**: GAAGTTGGGAGGGAATGCTAAAC, TRPM8exon7a/R: GAGATTGCTGAGAACACATTTTAATGAAC. After PCR screening, clones were subjected to sequencing. Both TRPM8 splice variants were then inserted in pcDNA4.TO.A (Invitrogen).

HA-tagged fusion proteins. The forward PCR oligonucleotide includes the Not I restriction site and conserves the endogenous Kozak sequence. The backward PCR oligonucleotide incorporates a substitution of the STOP codon prior to the HA sequence followed with a Xho I restriction site. After PCR amplification, PCR products were digested overnight at 37°C, and finally subjected to agarose gel purification and DNA recovery (Wizard SV gel, Promega). pcDNA4.TO.A vector has been opened with both Not I / Xho I before dephosphorylation with Antarctic Phosphatase (New England Biolabs). Restricted PCR products and dephoshorylated vector were ligated overnight at 4°C with T4 ligase (New England Biolabs) prior to transformation in JM109 chemo-competent bacteria. Final plasmids were extracted and checked before sequencing.

Real-time PCR. After total mRNA extraction and purification with TRI REAGENT® (Sigma-Aldrich), mRNA were subjected to DNAse treatment (Ambion) with 0.25µl DNAse per µg of RNA for 25 min at 25°C. Afterwards, 10 µg DNAse-treated mRNAs were purified in a phenol/chloroform/AIA solution (Fluka) complemented with 5% Sodium Acetate 3M. 10% Sodium Acetate 3M and 2.5Volumes of 100% Ethanol were added to the aqueous phase and kept at -20°C overnight in order to precipitate mRNAs . After a brief wash in 70% Ethanol, pellets were left to dry and then re-suspended in 30 µl water. After an agarose gel check of mRNA quality, 2µg of mRNA were subjected to reverse transcription as reported elsewhere [26]. Real-time quantitative PCR was performed on a Cfx C1000 system (Biorad). For each reaction, 12.5 ng of cDNA were placed in a final reaction mixture of 15µl containing 7.5µl of 2x SsoFast™ EvaGreen® Supermix (Biorad) and 200nM primer pairs (see Table 1). The housekeeping gene Glyceraldehyde-3-phosphate dehydrogenase (GAPDH) was used as an endogenous control to normalize variations in RNA extractions, the degree of RNA degradation and variability in RT efficiency. To quantify the results, we used the comparative Ct method. The PCR protocol was: an initial 30 sec denaturation step at 95° C, and 40 cycles of [4 sec at 95° C, 30 sec at 60° C] and a final dissociation curve to control the specificity of the amplification.

The respective quantification of full length TRPM8 mRNA and TRPM8-36 encoding mRNAs was performed as described: TRPM8 mRNA was detected with primers targeting exons 7 and 8, whereas TRPM8-36 mRNAs (in addition of TRPM8 mRNA) were measured with primers targeting exons 19 and 20. Note that, as the efficiency of the two primers' pairs was considered equal, the level of TRPM8-36 mRNAs was estimated as the subtraction of ΔΔCt(7-8) value to ΔΔCt(19-20) value.

Immunoblotting. An ice-cold buffer (pH 7.2) containing 10 mM PO4Na2/K buffer, 150 mM NaCl, 1 g/100 ml sodium deoxycholate, 1% Triton X-100, 1% NP40, a mixture of protease inhibitors (Sigma-Aldrich), and a phosphatase inhibitor (sodium orthovanadate; Sigma-Aldrich) was applied to previously PBS-washed cells in dishes. After 30 min incubation on ice, the protein extract was transferred into 1.5 ml tubes and sonicated. After 10 minutes of centrifugation at 15,000 g, the pellet was

transferred into a clean tube prior to a determination of the protein concentration using a BCA Protein Assay (Pierce). An SDS-page was performed using 25 µg of total protein loaded into a 10% polyacrylamide gel . After electrophoresis, proteins were transferred to a nitrocellulose membrane using a semi-dry electroblotter (Bio-Rad). The membrane was blocked in a TNT +5% (W/V) milk (15 mM Tris buffer, pH 8, 140 mM NaCl, 0.05% Tween 20, and 5% non-fat dried milk) for 30 min at room temperature, then soaked in the primary antibody diluted in TNT +1% milk for either 2 h at room temperature or overnight at +4°C. After three washes in TNT, the membrane was soaked in the secondary antibody diluted in TNT+1% milk for 1h at room temperature. The membrane was processed for chemiluminescence detection using Luminata Forte Western HRP Substrate (Millipore) according to the manufacturer's instructions. After a 10 min bath in Re-blot PLus Mild SOlution (Millipore), membrane was blotted again. The primary antibodies were: rabbit anti-TRPM8 (Ab109308, Abcam), rabbit anti-HA tag (Sc-805, Santa Cruz) and goat anti-GA3PDH (Sc-20357, Santa Cruz).

ImmunocytoFluorescence. Experiments were performed on LNCaP C4-2b cells plated on 35 mm glass bottom dishes (MatTek Inc) or on 6 µm - thick slices of the LNCaP C4-2b tumors or from *wt*, 5 *trpm8*$^{-/-}$ mice or 5 *trpm8*$^{-/-}$ *(DJ)* mice, obtained with Microm HM355S (Thermo Scientific Inc). After paraffin removal, antigen retrieval was achieved in a citrate buffer boiled 4 times for 5 minutes in a microwave oven and rinsed three times in PBS. Before immunocytofluorescence, LNCaP C-42b cells were fixed with 4% formalin in PBS for 10 min on ice prior to 3 PBS washes. Cells/tumors slices were subjected to blocking and permeabilization with PBS + 1.2% gelatine + 0.2% Tween + 0.2M glycine for 30 min at 37°C. The slides/dishes were then incubated with primary antibodies 2 h at 37°C. After thorough rinsing in PBS/gelatine, the slides/dishes were treated with the corresponding secondary antibody: either Dye light 488-labeled anti-rabbit IgG (Jackson ImmunoResearch; dilution, 1/2000) or Alexa fluor 546-labeled anti-mouse IgG (Molecular Probes; dilution, 1/4000) diluted in PBS/gelatine for 1 h at ambient temperature. After rinsing twice in PBS/gelatine and once in PBS with 1/200 Dapi for 10 min at ambient temperature, the slides were mounted with Mowiol® and examined under a confocal microscope. The primary antibodies used were: rabbit anti-TRPM8 (Ab109308, Abcam), mouse anti-p21waf1 (Clone SX118, Dako), rabbit anti- cytokeratin 14 (PRB-155P-100, Covance), rabbit anti- cytokeratin 5 (PRB-160P-100, Covance), mouse anti-cytokeratin 18 (Sc-51582, Santa Cruz) and mouse anti-Vimentin (Clone V9, Dako).

Flow cytometry. Flow cytometry was performed with a CyAn™ ADP Analyser. Cells were harvested, split into 1 million cell samples in 15 ml tubes before fixation with 1ml of 70% Ethanol at -20°C overnight. Cells were washed twice with PBS / 4% BSA / 0,1% Triton X100 and finally incubated at RT for 30 min. Cell were then pelleted by centrifugation at 250 xg for 8 min at 20°C.

For analysis of immunolabeled cell population, mouse anti- p21waf1 (Clone SX118, Dako) primary antibody was diluted in 100 µl PBS-BT at 1/200 and incubated with cells at ambient temperature for 1h. After a first quick wash in PBS, a second wash was done at RT for 30 min. Cells were incubated with rabbit anti-Ki67 antibody coupled to FITC (Ab27619, Abcam) and/or secondary antibodies specific to the host animal of the primary antibodies, antirabbit IgG coupled to Dye Light-488 (Jackson ImmunoResearch; dilution 1/2000) or anti-mouse IgG coupled to Alexa Fluor 647 (Jackson ImmunoResearch; dilution 1/4000) at RT for 30 min. After two PBS washouts for a total incubation time of 30 min at ambient temperature, cells were suspended in 500 µl of PBS and then analyzed.

For TUNEL (terminal deoxynucleotide transferasemediated dUTP—biotin nickend labelling) experiments, cells were pelleted and then suspended in 100 µl of labeling solution (TUNEL-TMR red, Roche) at room temperature for 30 min. Cells were washed once in PBS at ambient temperature for 10 min.

For cell cycle analysis, cells were suspended in 250 µl PBS / 4% BSA / 0,1% Triton X100 with Ribonuclease A (200 µg/ml) and incubated at room temperature for 15 min. After addition of 250 µl of PBS containing 30 µg/ml of propidium iodide, cells were further incubated at room temperature for 30 min to 1 hour. Data were analyzed with FlowJo software (version 8.7).

The flow cytometer was calibrated with rainbow beads before each experiment. 405, 488 and 642 wavelength lasers were used according to fluorescent reporters. Data were analyzed with Summit software (v 4.3.1).

Apoptosis quantification. Alternatively to TUNEL experiments, cells were stained with 5 µg/ml Hoescht 33258 for 10 min at room temperature and mounted in glycergel (DAKO). Nuclear morphology (condensed and fragmented) was analyzed on an upright Axio Imager.A1 microscope (Zeiss, Germany). The percentage of apoptotic cells was determined by counting at least 500 cells in random fields.

Viability Assay. Cells were transfected with siRNA in 100 mm dishes overnight. The day after, cells were dispatched in 96-well plates at a density of 5,000 cells per well in 100 µl RPMI medium. After 6 hours of incubation, experiments started as day 0, and treatments were applied by adding 100 µl of treatment-containing medium. From day 1, half of the medium was changed daily. CellTiter 96® AQ_{ueous} Non-Radioactive Cell Proliferation Assay (Promega) was used to determine the number of viable cells each day.

Wide-field Ca^{2+} imaging. Calcium imaging experiments have been performed as described previously [19]. Briefly, $[Ca^{2+}]_c$ was measured using ratiometric dye fura-2 (2 µM) and quantified according to the Grynkiewicz equation [27]. The bath solution (HBSS (Hank's Balanced Salt Solution)) contained 142 mM NaCl, 5.6 mM KCl, 1 mM $MgCl_2$, 2 mM $CaCl_2$, 0.34 mM Na_2HPO_4, 0.44 mM KH_2PO_4, 10 mM HEPES and 5.6 mM glucose. The osmolarity and pH of external solutions were adjusted to 310 $mOsm.l^{-1}$ and 7.4, respectively. The cells were continuously perfused with the HBSS solution and chemicals were added *via* a perfusion system.

Confocal imaging. Confocal imaging was performed using a confocal microscope (LSM 780, Carl Zeiss MicroImaging, Inc) with a plan-Apochromat 40×/1.3 NA oil immersion objective and equipped with a thermo-controlled chamber. 405, 488, 561, 633 nm laser lines were used for excitation. Emission wavelengths were designed to produce no overlap between the four fluorophores. 1024*1024 pictures were acquired frame by frame with an averaging of 8 to reduce noise.

Data analysis. Each experiment was repeated at least three times and the results were expressed as mean ± S.E.M. The data were analyzed and graphs plotted using Origin 5.0 software (Microcal, Northampton, MA). InStat3 (GraphPad Software Inc, SanDiego, USA) was used for statistical analysis and mean values were compared using either unpaired t test with Welch's corrected test (2 groups) or One-way ANOVA with Dunnett multiple comparison post-test (≥3 groups). Statistical significance was denoted by (*) for $P<0.05$, (**) for $P<0.01$ or (***) for $P<0.001$.

Results

Expression of multiple TRPM8 isoforms in prostate cancer cell lines. TRPM8 was originally cloned in human prostate 12 years ago [16]. To date, several studies have reported an androgen-dependent regulation of *TRPM8* [17, 20, 21] and its overexpression during prostate carcinogenesis [14, 15, 28]. Based on functional evidence, we suggested that a TRPM8 isoform is localized in endoplasmic reticulum (ER) membranes [18, 19]. We then recently cloned multiple TRPM8 alternate mRNAs and splice variants in human prostate epithelial cells and characterized the properties of these TRPM8 isoforms [24, 25]). We propose a rational classification of these TRPM8 isoforms based on their structure (**Fig 1A**). Accordingly, the TRPM8 isoforms family is composed of i) the TRPM8 channel: the cold and menthol full length receptor, 130 kDa, referred to as TRPM8 in the text and encoded by the TRPM8(1-26) mRNA; ii) the 36 to 40kDa isoform family which are N-terminal truncated cold and menthol activated channels (Bidaux et al, PNAS; Unpublished data, Bidaux et al): referred to as TRPM8-36 in this work, encoded by TRPM8(15a-26), TRPM8(17'-26), TRPM8(17''-26) and TRPM8(18a-26) mRNA. Note that TRPM8(16a-26) is a non-coding mRNA. In addition to these channel proteins, we previously cloned and characterized an alternate mRNA, sM8α, and its splice variant, sM8β [24], which are now respectively renamed sM8(2'-6b) and sM8(2'-6b/+4a) (**Fig 1A**).

In the present study, using RACE-PCR, we have cloned additional sM8 encoding mRNAs, which exhibit alternate 5' exons (**Fig 1A**). The five novel sM8 mRNA and accompanying splice variants were: sM8(1-6b), sM8(2'-6b/+3'') which incorporates the new cassette exon 3'', sM8(3'-6b) whose transcription starts with the new alternate exon 3', sM8(3'-6b/+intron3') characterized by insertion of the intron 3' and sM8(5a-6b) whose transcription starts with the new alternate exon 5a (**Fig 1A**). PCR fingerprinting revealed the expression of all the TRPM8 and sM8 mRNAs described above, in human normal prostate as well as in androgen-dependent LNCaP, androgen-refractory LNCaP C4-2b and androgen-independent PC-3 cell lines (**Fig 1B**). Except for TRPM8(18a-26) mRNA, all TRPM8 mRNAs encoding TRPM8-36 isoforms were detected at a significant level in prostate cancer cell lines. Note that sM8(3'-6b) was found only in cancer cells while sM8(1-6b) and sM8(5a-6b) appeared down-regulated in cancer cell lines compared to normal prostate.

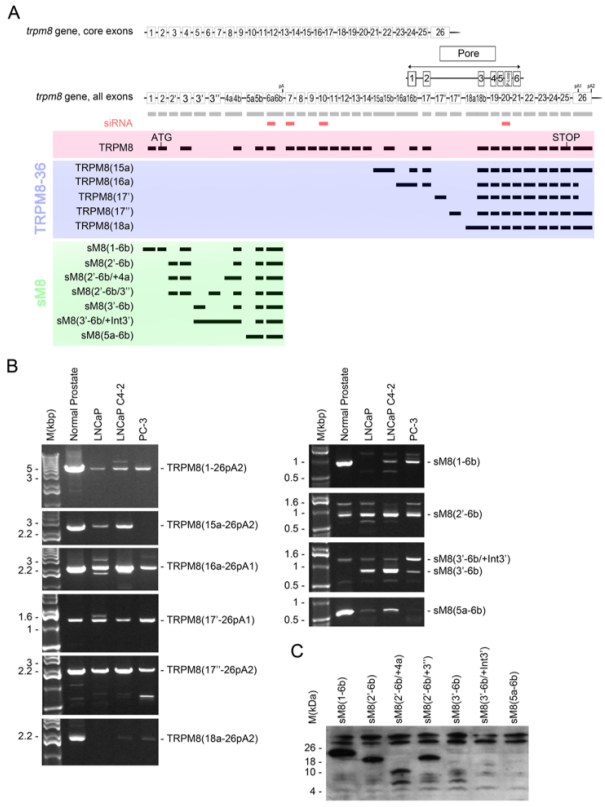

FIGURE 1. *Trpm8 gene encodes 5 alternate TRPM8 mRNA and 2 splice variants in human prostate.* **A.** Genomic DNA map (not to the scale) represents the core exons of full length TRPM8. Alternate exons are labeled with prime or second sign when are forming a cassette exon, and with "a" or "b" when they are forming the 5' or 3' supplemental part of a core exon respectively. Transmembrane domains and p-loop of the TRPM8 channel are aligned with their encoding exons. Full-length TRM8 is showed in the red area (TRPM8) while channel-like TRPM8 isoforms are highlighted in blue (TRPM8-36) and short TRPM8 isoforms are highlighted in green (sM8). siRNA targeting TRPM8 are represented as small red squares aligned with the homologous TRPM8 exons. **B.** Full length amplification of TRPM8 cDNAs by PCR reveals the expression of TRPM8 mRNAs in normal prostate tissue, androgen-dependent prostate cancer cell line, LNCaP, androgen-refractory prostate cancer cell line, LNCaP C4-2b, and androgen-independent prostate cancer cell line, PC-3. Each PCR reaction was performed with 100 ng of cDNA. **C.** Western-blot showing the detection of HA-tagged sM8 isoforms in total protein extract of HEK cells. Cells have been transfected with vector encoding sM8 mRNA for 24h. 75 µg of total protein extract were loaded on each well. Experiments have been reproduced 3 times independently.

ARTICLE 12

A divergence in the sM8 fingerprinting was noticeable between LNCaP and PC-3 cell lines, suggesting that the selection of the first exon could depend on the androgen receptor expression and activity. Since sM8 may act as negative regulatory sub-unit of the cold and menthol receptor [24], and because TRPM8 channel has been considered as a target of interest in cancer therapy [28], we wondered whether sM8 knockdown (KD) could affect prostate cancer cell growth.

sM8 knockdown decreases cell growth of prostate cancer cell lines and impaired tumor implantation in mice. Two studies reported that the inhibition or suppression of TRPM8 inhibit both cell survival [21] and proliferation of LNCaP cells [29]. On the contrary, in all prostate cell lines that we have tested in the present study, the suppression of either TRPM8 alone (siM8-7, siM8-10) or TRPM8 and TRPM8-36 (siM8-20) did not result in any significant changes in cell growth (**Fig 2A**). Nevertheless, the concomitant suppression of both sM8 group and TRPM8 resulted in a significant reduction of cell growth (**Fig 2A)** in LNCaP, LNCaP C4-2b and PC-3 cell lines. Because the suppression of TRPM8 alone did not modify cell growth, one might conclude that the decrease in prostate cell growth originates from the suppression of the sM8 group. Cell growth kinetic studies showed a cytostatic effect of sM8 knockdown (KD) in LNCaP C4-2b cells (**Fig 3B**), LNCaP (**Fig S2A**), but only a more moderate effect in PC-3 cells (**Fig S2B**). Mutant siM8-6a(M1) did not modify the growth of LNCaP C4-2b cells (**Fig 2B**) or LNCaP cells (**Supp Fig S2A**), suggesting that the siM8-6a cytostatic effect was highly specific and related to sM8 KD. Conversely, in PC-3 cells, siM8-6a and siM8-6a(M1) induced a slight and similar decrease in cell proliferation, therefore probably unrelated to sM8 KD. We next injected LNCaP C4-2b cells subcutaneously in male nude mice and report here both efficiency of tumor implantation and growth rate. As shown in **table 1**, the efficiency of tumor implantation was strongly impaired by the injection of siM8-6a at a frequency of 1 injection every 3 days over a 2 weeks period. In animals where tumor implantation was not impaired, no significant change in tumor growth rate was observed with either siCTL or siM8-6a (Table 1). However, strong divergence occurs in siM8-6a in which 2 populations can be observed: 1) as CTL, 2) low growth (37,34 ± 11,68 mm^3/day). Microscopic observation of LNCaP C4-2b cells revealed that siM8-6a treatments produced cell unhealthiness (**Fig S2C**) characterized by retraction of cell extensions, loss of contrast, and detachment from the underlying matrix, while siM8-7 (TRPM8 KD cells) did not alter cell morphology. Mutant siM8-6a(M1) also led to cell alterations, though less pronounced than those induced by siM8-6a..

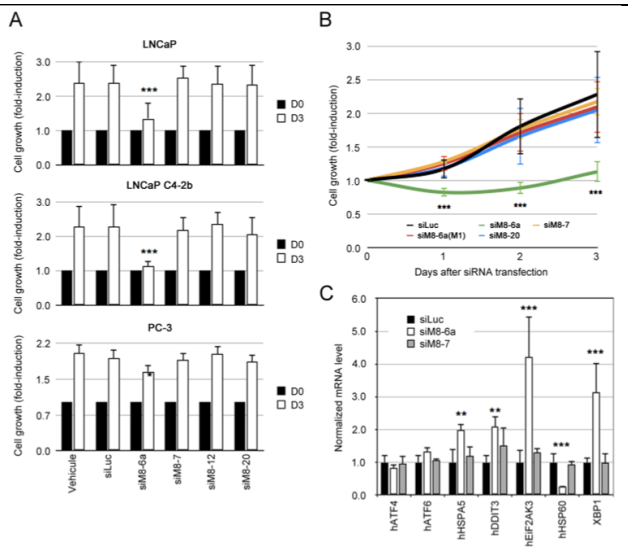

FIGURE 2. *Silencing of sM8 isoforms reduces cell growth of prostate cancer cell lines and triggers stress in endoplasmic reticulum.* **A.** Cell growth of LNCaP, LNCaP C4-2b and PC-3 cells was measured with CellTiter 96® AQ_{ueous} Non-Radioactive Cell Proliferation Assay (Promega), as described in *Materiels and Methods*, after 2 or 3 days of culture. Average values at day 2 or 3 were then normalized to values at D0. Experiments were performed three times independently. **B.** Kinetic of the LNCaP C4-2b cell growth following an identical procedure than the one described in **A.** Cells were transfected with either control siRNA (siLuc) or anti-TRPM8 siRNA (siM8-6a, siM8-7, siM8-20), labels refers to the target TRPM8 exon. A mutant siRNA targeting exon 6a and showing a limited efficiency, siM8-6a(M1), has been transfected to assess the sequence-specificity of the effect of siM8-6a transfection on cell growth. Experiments were performed four times independently. **C.** Gene expression was estimated with real time PCR after a 3-day siRNA transfection of LNCaP C4-2b cells. Top panel displays human genes involved in stress of endoplasmic reticulum: *ATF4, ATF6, HSPA5, DDIT3 (Chop), EIF2AK3 (PERK), HSP60 and XBP1*. Experiments were performed three times independently. Values are expressed as Mean ± SD.

We detected by qPCR a significant induction of ER stress markers *HSPA5*, *DDIT3* (CHOP), *EIF2AK3* (PERK), and spliced *XBP1* (**Fig 2C**), but no induction of mitochondrial stress markers (**Fig S3B**). This ER stress was confirmed with an increased expression of grp78 proteins (**Fig S3A**). The observed cytostatic effect induced by sM8 KD could thus result from the induction of ER stress simultaneous. Since ER stress and energy stress are known inducer of cell cycle arrest and apoptosis [30-33], we next measured the level of apoptosis and cell proliferation.

.

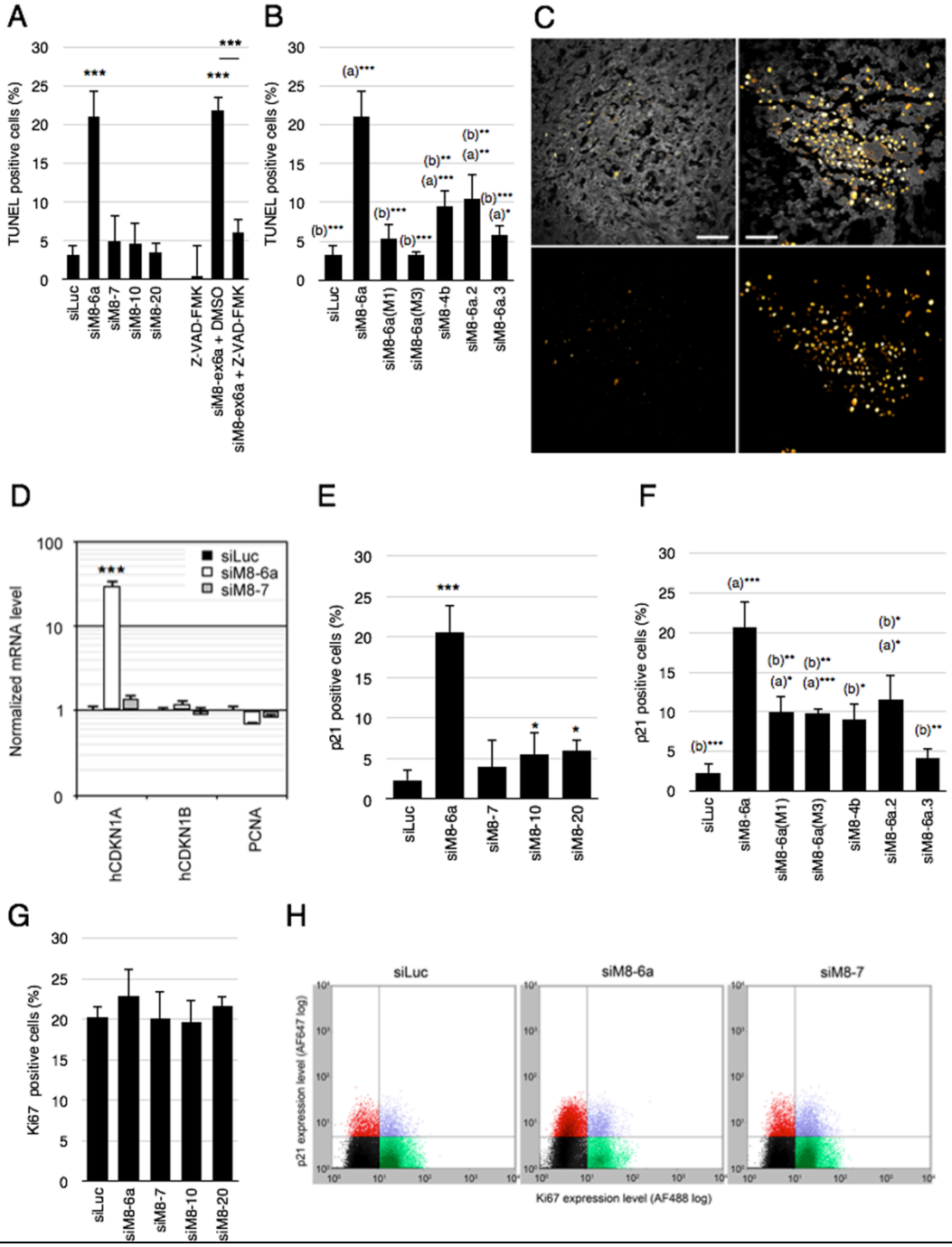

FIGURE 3. *Silencing of sM8 isoforms induces apoptosis and increases p21waf1 positive cell population of prostate cancer cells.* **A.** Terminal deoxynucleotidyl transferase dUTP nick end labeling (*TUNEL*) reaction was performed on LNCaP C4-2b cells with nucleotide coupled to tetramethyl rhodamine (TMR) before cell counting was achieved by flow cytometry. Values in the graph represent the proportion of apoptotic cells. This reveals induction of apoptosis after a 3-day transfection with siRNA targeting TRPM8 exon 6a. No significant variation of the apoptosis is detected with other anti-TRPM8 siRNA (siM8-7, siM8-10, siM8-20) compared to the control siRNA (siLuc). This induction of apoptosis is strongly reduced in cells treated with the general inhibitor of caspases: Z-VAD-FMK. **B.** Percentage of apoptotic cells is also increases by transfection of other siRNA targeting exons expresses in both sM8 isoforms and in the full length TRPM8 channel, while mutants of the siM8-6a siRNA fail to trigger apoptosis. **C.** TUNEL reports the detection of apoptosis in tumors developed subcutaneously in mice after injection of LNCaP C4-2b cells. Left panels show CTL tumor and right panels show low growth rate tumors developed in siM8-6a-injected mice. Top panels are merge images of autofluorescence (excited at 633nm) and TUNEL, while bottom panels only show TUNEL (Orange Hot LUT). Scale bars: 30 µm. **D.** Gene expression was estimated with real time PCR after a 3-day siRNA transfection of LNCaP C4-2b cells. Panel shows genes coding for cell cycle inhibitor $p21^{waf1}$ and $p27^{kip}$ (respectively *CDKN1A* and *CDKN1B*), and the *PCNA* gene coding for the proliferating cell nuclear antigen, which is expressed during cell cycle. **E.** and **F.**, show increase of the $p21^{waf1}$ and Ki67 positive cells, respectively, after transfection of cells with siRNA

targeting different groups of TRPM8 isoforms. **G.** Specificity of $p21^{waf1}$ induction in sM8 KD cells is estimated as a proportion of p21waf1 immunolabeled cells and sorted by flow cytometry. **H** shows the distribution of $p21^{waf1}$ and Ki67 immunolabeled cells reported by flow cytometry (representative experiment shown). Red area represents the p21+/Ki67- cell population, while the violet area represents the p21+/Ki67+ cell population and the green area p21-/Ki67+ cell population. Experiments were performed three times independently. Values are expressed as Mean ± SD.

sM8 knockdown induces apoptosis and p21waf1 expression in quiescent LNCaP C4-2b cells. Apoptotic cells labeled by terminal deoxynucleotidyl transferase dUTP nick end labeling (*TUNEL*) have been sorted out by flow cytometry analysis. As reported in **figure 3A**, siM8-6a transfection induced a strong increase in apoptosis (21.12 ± 3.39%), which was efficiently diminished (6.12 ± 1.79%) by a zVAD.fmk treatment, a general inhibitor of caspases. siM8-6a mutants (M1 and M3) failed to induce apoptosis in LNCaP C4-2b cells (**Fig 3B**). Supplemental siRNAs targeting both sM8 isoforms and full-length TRPM8 channel (siM8-4b, siM8-6a.2 and siM8-6a.3) significantly triggered apoptosis, although less efficiently than siM8-6a (**Fig 3B**). Histopathology analysis of *in situ* tumors revealed a strong induction of apoptosis in tumors characterized by the lowest growth rate in siM8-6a injected mice (**Fig 3C**). This suggests that apoptosis is a major component of decrease growth rate of *in vitro* and *in situ* LNCaP C4-2b cells. Though such apoptosis could explain the cytostatic effect reported in **figure 2B**, we next checked whether siM8 KD induced a parallel decrease in cell proliferation. We focused on $p21^{waf1}$, a protein restricting cell cycle at both G1/S and G2/M transition [34, 35] and which is implicated in triggering concomitantly cell cycle arrest and apoptosis [36-38]. We measured a strong and concomitant induction of the *CDKN1A* gene coding for the cell cycle inhibitor $p21^{waf1}$ (**Fig 3D, bottom panel).** Using flow cytometry (FACS), we estimated the proportions of cell population expressing $p21^{waf1}$ proteins. Analyses presented in **figure 3E** reveals that sM8 KD increased by 20.63 ± 3.53% the number of $p21^{waf1}$ positive cells, while TRPM8 KD or TRPM8-36 KD resulted in 5.46 ± 1.51% and 6.02 ± 1.29% decreases, respectively. This $p21^{waf1}$ induction was significantly reduced with siM8-6a mutants (10.0 ± 4.15% (M1) and 9.87 ± 0.84% (M3)), (**Fig 3F**). SiM8-4b and siM8-6a.2 also significantly induced $p21^{waf1}$ expression, even though they were less efficient than siM8-6a. These results demonstrated that maximal $p21^{waf1}$ induction was specifically mediated by sM8 KD. We thus studied by FACS a cell cycle marker, Ki67, expressed from G1/S checkpoint until the exit of mitosis [39]. As shown in **Fig 3G**, Ki67 positive cell population was unexpectedly unaffected by sM8 KD. Besides, the dual distribution of $p21^{waf1}$ and Ki67 labeled cells revealed that sM8 KD mediated a strong increase of $p21^{waf1}$ in Ki67 negative cells (**Fig 3H**). Cell cycle analysis was carried out on LNCaP C4-2B cells labeled with propidium iodide and transfected with siLuc (**Fig S4A**), siM8-6a (**Fig S4B**) or siM8-7 (**Fig S4C**) for three days. Only a 7 % decrease in the proportion of cells in G2/M phase was found in cells knocked down with either siM8-6a or siM8-7 (**Fig S4D**), suggesting that this slight drop in G2/M cell proportions was dependent on TRPM8 but not on sM8 KD. A strong increase in the subG1 cell sub-population (**Fig S4B** and **S4D**) also confirmed a specific induction of apoptosis in sM8 KD cells. Altogether, our results demonstrate that sM8 KD triggers a concomitant induction of apoptosis and $p21^{waf1}$ expression independently of cell cycle phase. Since we cloned five alternate sM8 mRNA and two splice variants, we wondered which ones were involved in the sM8 KD response. According to their mRNA and protein fingerprints in PCa, we developed C4-2b cell clones stably overexpressing sM8(2'-6b), sM8(3'-6b) or sM8(5'-6b). A sM8(2'-6b) clone resistant to siM8-6a treatment was also developed to check for specificity. As reported in the **figure 4A**, mRNA expression levels were measured by qPCR. Transfection of these sM8s expressing C4-2b cell clones with siM8-6a modified the distribution of the cell population in flow cytometry (**Fig 4B**), and clearly showed two distinct populations: 1) apoptotic or 2) $p21^{waf1}$ induced cells (also see, **Fig S6)**. The percentage of apoptotic cells was strongly increased in clones overexpressing sM8(2'-6b) in an mRNA concentration-dependent manner. On the contrary, the overexpression of the sM8(2'-6b) mRNA resistant to siM8(6a) protected cells from apoptosis (**Fig 4B and 4C)**. Surprisingly, sM8(2'-6b) overexpression did not sensitize siM8(6a) transfected cells to $p21^{waf1}$ induction (**Fig 4D**). The overexpression of sM8(3'-6b) sensitized C4-2b cells to apoptosis, though to a lesser extent than did sM8(2'-6b). Conversely, the overexpression of sM8(3'-6b) was found to drastically increase $p21^{waf1}$ expression. Finally, the non-coding sM8(5b-6a) mRNA did not antagonize apoptosis or $p21^{waf1}$ induction after sM8 KD in prostate cancer cells. These results, altogether, suggest that knockdown of sM8(2'-6b) mRNA potently activates apoptosis while knockdown of sM8(3'-6b) strongly induces $p21^{waf1}$. We thus wondered whether apoptosis and $p21^{waf1}$ induction mediated by sM8 knockdown implicated functional TRPM8 channels. *Apoptosis of LNCaP C4-2b cells knocked down for the short TRPM8 isoforms is dependent on TRPM8 channel isoforms.* We previously reported that sM8s are negative regulatory subunits of the full length TRPM8 channel [24, 25]. Along this line, we postulated that sM8 could also modulate the activity of TRPM8-36. Thus, sM8 KD-induced apoptosis could be due to a deregulation of TRPM8-36. To assess such a possibility, we carried out a concomitant transfection of siM8-6a (targeting sM8 and TRPM8) with either sM8-10 (targeting only TRPM8) or sM8-20 (targeting TRPM8-36 and TRPM8).

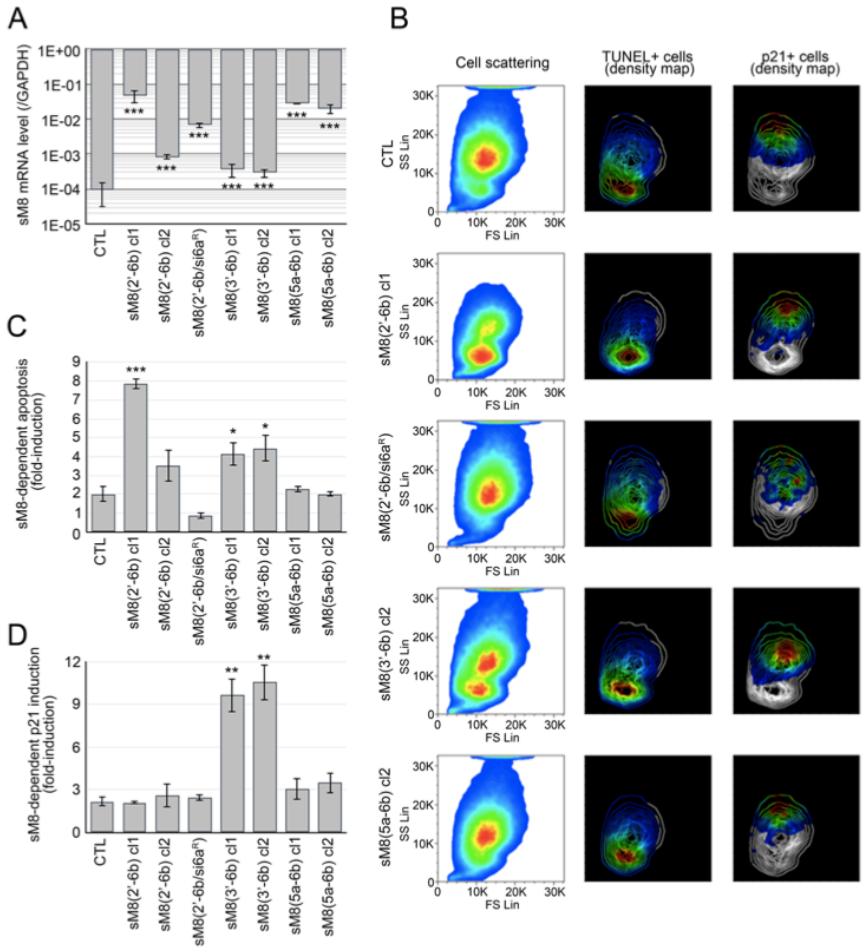

FIGURE 4. *LNCaP C4-2b clones overexpressing a selective sM8 isoform become sensitized to either apoptosis or p21waf1 induction following sM8 knockdown.* **A.** LNCaP C4-2b clones overexpressing a single sM8 isoform shows variable levels of sM8 mRNA expression as reported by qPCR. sM8(2'-6b/si6a^{R}) mRNA has been mutated in order to resist to siM8(6a)-mediated silencing. **B.** Overexpression of sM8 isoforms modifies the distribution of cells as represented in the pseudo-color cell scattering plots where cells are sorted by size (Forward scattering light; FS Lin) and by granularity (Side scattering light: SS Lin). Visualization of the apoptotic and p21^{waf1} expressing cell sub-populations is shown as the merge of a contour plot (scattering of cells by size and granularity) and density pseudo-color plot representing the distribution of either TUNEL or p21^{waf1} positive cells. Pseudo-color code represents density from the lowest (blue) to highest (red). Each plot represents about 1 million cells. **C.** Bar diagram plot shows the fold-induction of apoptosis rate, induced by transfection of siM8(6a), in cell C4-2b clones normalized by the apoptosis rate in wild type LNCaP C4-2. Control (CTL) was figured out as the average of apoptotic rates of two cell clones expressing the empty vector pcDNA4. **D.** As C. but shows the fold-induction of cells expressing p21^{waf1}. Experiments were performed three times independently. Values are expressed as Mean ± SD.

We then quantified the populations of cells engaged in apoptosis or showing induction of p21^{waf1}. As shown on **figure 5A**, the transfection of LNCaP C4-2b cells with siM8-6a and either siM8-10 or siM8-20 drastically diminished the TRPM8 fluorescence level. However, only siM8-20, inducing an additional TRPM8-36 KD, counteracted the p21^{waf1} induction and apoptosis triggered by siM8-6a KD (**Fig 5A,5B and 5C**). This infers TRPM8-36 isoforms are required for p21^{waf1} and apoptosis induction in sM8 KD LNCaP C4-2b cells while full length TRPM8 is not involved. To confirm the requirement of functional TRPM8-36 channels in the induction of p21^{waf1} and apoptosis, LNCaP C4-2b cell line was transfected with 25 nM of either siM8-6a or control siM8-7 for 3 days, and TRPM8-36 were either activated with a 500 µM menthol daily treatment or inhibited with a 10 µM BCTC treatment (Unpublished data, Bidaux et al). Menthol treatment did not significantly modify p21^{waf1} induction, but unexpectedly diminished sM8 KD-mediated apoptosis (**Fig 5D and 5E**, respectively). BCTC treatment decreased both p21^{waf1} induction and apoptosis (**Fig 5D and 5E**, respectively). Note that cells transfected with siM8-7, or with siM8-20 (**data not shown**) showed apoptosis after BCTC treatment to a similar level to the one of siM8-6a transfected cells. This suggests that, in addition to its inhibitory effect on TRPM8, BCTC exerts a further, TRPM8-36-independent, induction of apoptosis in LNCaP C4-2b cells. Nevertheless, our data confirm that sM8 KD-mediated p21^{waf1} induction and apoptosis require functional TRPM8-36 channel isoforms.

sM8 knockdown also induces apoptosis and p21^{waf1} in primary culture of prostate cancer epithelial cells. Since

ARTICLE 12

next-generation sequencing appeared, genomes and genetics aberrations of prostate cell lines have been extensively characterized.

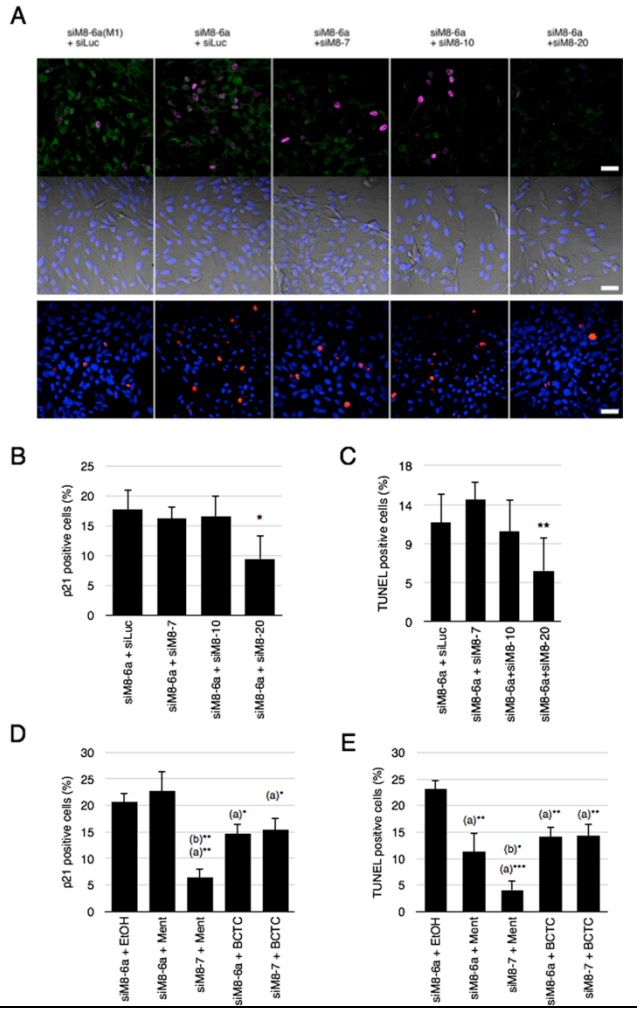

FIGURE 5. *Apoptosis and p21waf1 induction of sM8 knockdown C4-2b cells requires TRPM8 channel isoforms (TRPM8-36).* **A.** Immunocytofluorescence detects TRPM8 channel proteins (green), $p21^{waf1}$ (magenta) and TUNEL (red) in LNCaP C4-2 cultures after a 3-day transfection with siRNA. Nuclei were counterstained with Dapi (blue). Scale bar represents 10 µM. **B.** Flow cytometry counting shows a decrease of $p21^{waf1}$ expressing or TUNEL positive (**C.**) cells following the concomitant transfection of siM8-6a and siRNAs targeting the pore region (siM8-20). No variation of $p21^{waf1}$ or apoptosis induction is visible in cells in which a concomitant knockdown was achieved for the full length TRPM8 channel (siM8-7 and siM8-10) and sM8 isoforms. Addition of TRPM8 agonist, menthol (500 µM), in the medium of cells transfected with siM8-6a does not modify $p21^{waf1}$ induction (**D**), but significantly decreases apoptosis (**E**). Addition of 10 µM BCTC in the medium of LNCaP C4-2b cells transfected with siM8-6a, a known antagonist of the TRPM8 channel, reduces both $p21^{waf1}$ induction and apoptosis to the same level than in cells knockdown for TRPM8 (siM8-7).. Values are expressed as Mean ± SD.

We therefore checked the relevance of our hypothesis in primary cultures of prostate cancer epithelial cells, as we previously did [18]. We measured the percentage of $p21^{waf1}$ and TUNEL positive cells in primary cultures of prostate cancer epithelial cells (PrPCa) derived from two independent resection specimens of human prostate (**Fig 5A**). First of all, cell types were characterized with flow cytometry in our primary cultures (**Fig S6**) and were found to encompass almost 90% epithelial cells among which 75% were basal cells expressing keratin 5 and 14, and the other 25% were apical cells expressing keratin 5 and 18. Transfection of anti-TRPM8 siRNAs did not affect the proportions of the different phenotypes. Primary cultures proliferated slowly (doubling time was about 8 days) compared to prostate cancer cell lines (doubling time of LNCaP cell lines was about 32 hours). This is further supported by the fact that more than 40% of cells expressed $p21^{waf1}$ (**Fig 6B**), while less than 2% were positive for Ki67 (**Fig 6C**). After two siRNA transfections within 3 days of interval, silencing efficiency reached 50% - as compared to 90% in LNCaP cell lines. sM8 KD induced a significant increase in $p21^{waf1}$ and TUNEL positive cells, though with less potency than in LNCaP C4-2b cell line. Statistics revealed a 23%-increase in the $p21^{waf1}$ positive cells population (**Fig 6B**) which was further enhanced with menthol treatment (+39%) and reversed by BCTC treatment. Suppression or inhibition of TRPM8-36 did not modify the rate of proliferative cells (**Fig 6C**). Apoptotic cells were found to be 2.7-fold more abundant in the sM8 KD PrPCa cell population (**Fig 6D**). Menthol addition increased by 3.5-fold the number of apoptotic cells, while BCTC fully inhibited both sM8 KD and menthol effects. Altogether, these results show that sM8 KD promotes $p21^{waf1}$ expression and apoptosis in PrPCa as it does in LNCaP C4-2b cell line, and confirm the requirement of TRPM8-36 activity in this effect.

sM8 mRNAs/isoforms differentially regulate the expression of TRPM8 and TRPM8-36 mRNA and alters Ca^{2+} homeostasis. Finally, we aimed at understanding whether knockdown of sM8 isoforms could interfere with Ca2+ homeostasis and TRPM8 channel expression. Negative feedback loop exerted by RNA/protein on their mother-gene transcriptional activity have been reported for different genes (for review, see [40]). By performing qPCR with primers pairs matching different sequences of the TRPM8 gene, we measured which TRPM8 isoforms were altered by sM8 KD. TRPM8-36 mRNA levels decreased within cells transfected with siM8-10 and siM8-20 (Fig 7A, right panel). As expected, TRPM8-36 mRNA levels were unchanged after transfection with siM8-7, which indeed does not match with TRPM8-36 sequences. Strikingly, a strong and unexpected increase of TRPM8-36 mRNA level was detected in sM8s KD cells (siM8-6a), while a smaller effect was observed in cells transfected with the mutant siM8-6a(M1). This induction of TRPM8-36 in sM8 KD cells implies that the endogenous sM8 isoforms could exert a negative control on the transcription of TRPM8-36. To confirm this, we measured TRPM8 mRNAs expression in C4-2b clones in relation with the expression of various sM8 isoforms.

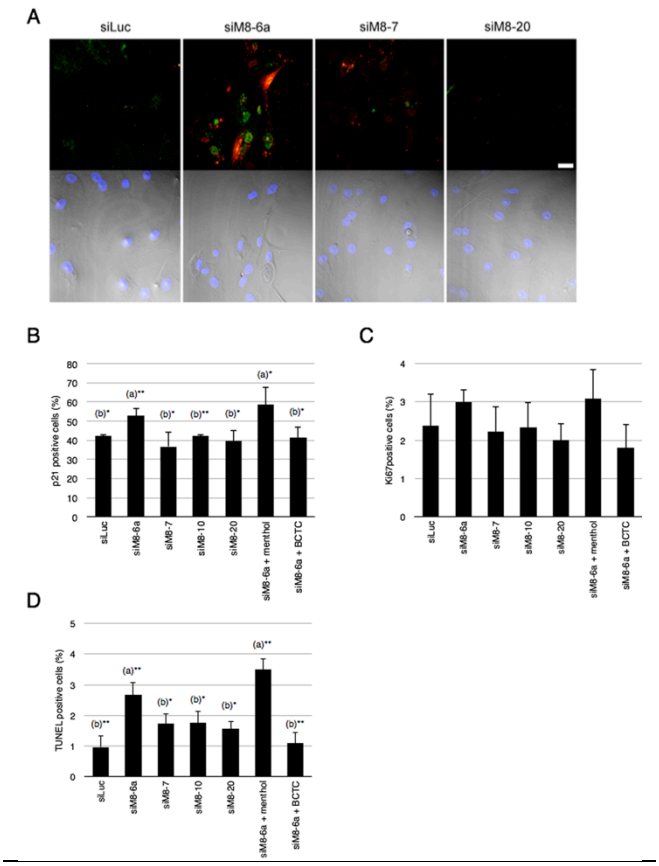

FIGURE 6.

sM8 knockdown results in p21waf1 induction and increase of apoptosis in primary cultures of prostate epithelial cancer cells. **A.** Immunocytofluorescence, on the top, shows the concomitant TUNEL labeling of apoptotic nuclei (red) and immunodetection of p21waf1 (green) in a primary culture of prostate epithelial cancer cells. Below are presented merged images of bright field and dapi fluorescence (405 nm). Panels **B**, **C and D** represent the percentage of $p21^{waf1}$ positive cells, the percentage of Ki67 positive cells and the percentage of TUNEL positive cells, respectively, after transfection with siRNA (for details see Materials and Methods). Menthol (500µM) or BCTC (10µM) have been added daily in the medium of cells transfected with siM8-6a for the 3 last days of the experiment. Experiments were performed three times independently. Values are expressed as Mean ± SD.

As reported in the figure 7B, both full length TRPM8 and TRPM8-36 expression increased only in cells overexpressing the non-coding sM8(5a-6b) mRNA. However, a decrease in TRPM8-36 expression was found in cells overexpressing sM8(2'-6b) at high level (right panel). This suggests that TRPM8-36 induction in sM8 KD cells is, indeed, mediated by the specific silencing of sM8(2'-6b) mRNA. Since we previously reported that the full-length TRPM8 channel and its channel isoforms were functional in ER membranes [18], we hypothesized that either variations in their expression or knockdown of the sM8 regulatory subunits could modify ER Ca2+ homeostasis. We thus quantified ER Ca2+ content and steady-state cytosolic Ca2+ concentration ([Ca2+]cyto) in LNCaP C4-2b cells transfected with siRNAs targeting TRPM8 and in LNCaP C4-2b clones overexpressing various sM8 isoform. Although the suppression of a functional calcium channel in ER membranes could be expected to modify ER Ca2+ homeostasis, silencing of a non-channel isoform would unlikely be able to directly alter ER Ca2+ homeostasis unless this suppression would modify the expression and/or activity of a Ca2+ transporters. The concomitant suppression of sM8s and TRPM8 (siM8-6a) induced a significant increase in ER Ca2+ content and an increase in [Ca2+]cyto (Fig 7C and 7D, respectively). The suppression of full-length TRPM8 itself did not alter ER Ca2+ content and only slightly increased [Ca2+]cyto but to a lesser extent than in siM8-6a transfected cells. The overexpression of sM8(2'-6b) in LNCaP C4-2b cells decreased ER Ca2+ content without altering [Ca2+]cyto. Lastly, the overexpression of the non-coding sM8(5a-6b) mRNA induced a significant increase in [Ca2+]cyto (Fig 7E and 7F, respectively). Altogether, this suggests that the level of expression of non-channel isoforms encoded by sM8(2'-6b) mRNA is associated with changes in ER Ca2+ content.

Discussion

In the present study, we have cloned novel short TRPM8 non-channel isoforms sM8s in prostate cancer cells and characterized their roles in cell cycle, survival and ER Ca^{2+} homeostasis. We have shown that sM8 knockdown induced $p21^{waf1}$ expression and apoptosis in prostate cancer cells. We have also demonstrated that the sensitivity to sM8 knockdown was related to the level of expression of two different short isoforms, sM8(2'-6b) and sm8(3'-6b) mRNAs. These results thus suggest that sM8 isoforms participate in resistance against pro-apoptotic signals in prostate cancer cells.

In 2011, we characterized a new short TRPM8 mRNA (sM8α) and its splice variant (sM8β) and we demonstrated that both of these mRNA encoded two sM8 protein isoforms: sM8-6 and sM8-18. The latters behaved as negative regulatory subunits of the full-length TRPM8 channel in plasmalemma [24, 25]. In the current study, by the mean of a systematic cloning of cDNA sequences generated by 5'-RACE-PCR starting from the terminal exon, 6b, we isolated 3 additional alternate mRNAs and 2 splice variants. We showed that, among these 7 mRNAs, 5 encoded 4 different proteins while 2 were likely none-coding mRNA. Long none-coding mRNAs were originally thought to be products of either mRNA degradation or mistranscription but growing evidences have more recently revealed their involvement in the regulation of the expression of their mother-gene (for review, see [40]). Along this line, we found that the expression level of the non-coding sM8(5a-6b) mRNA was correlated to the level of full length TRPM8 mRNA – suggesting that sM8(5a-6b) could be involved in a positive loop of transcriptional regulation of the *trpm8* gene. This would explain why both sM8(5a-6b) and full-length TRPM8 mRNAs are concomitantly down-regulated in prostate cancer cell lines compared with normal prostate samples (Fig. 1B). Conversely, we showed that the expression level of coding sM8(2'-6b) mRNA, previously labelled sM8α, was inversely

ARTICLE 12

correlated to the expression level of TRPM8-36 and independent of full length TRPM8 expression.

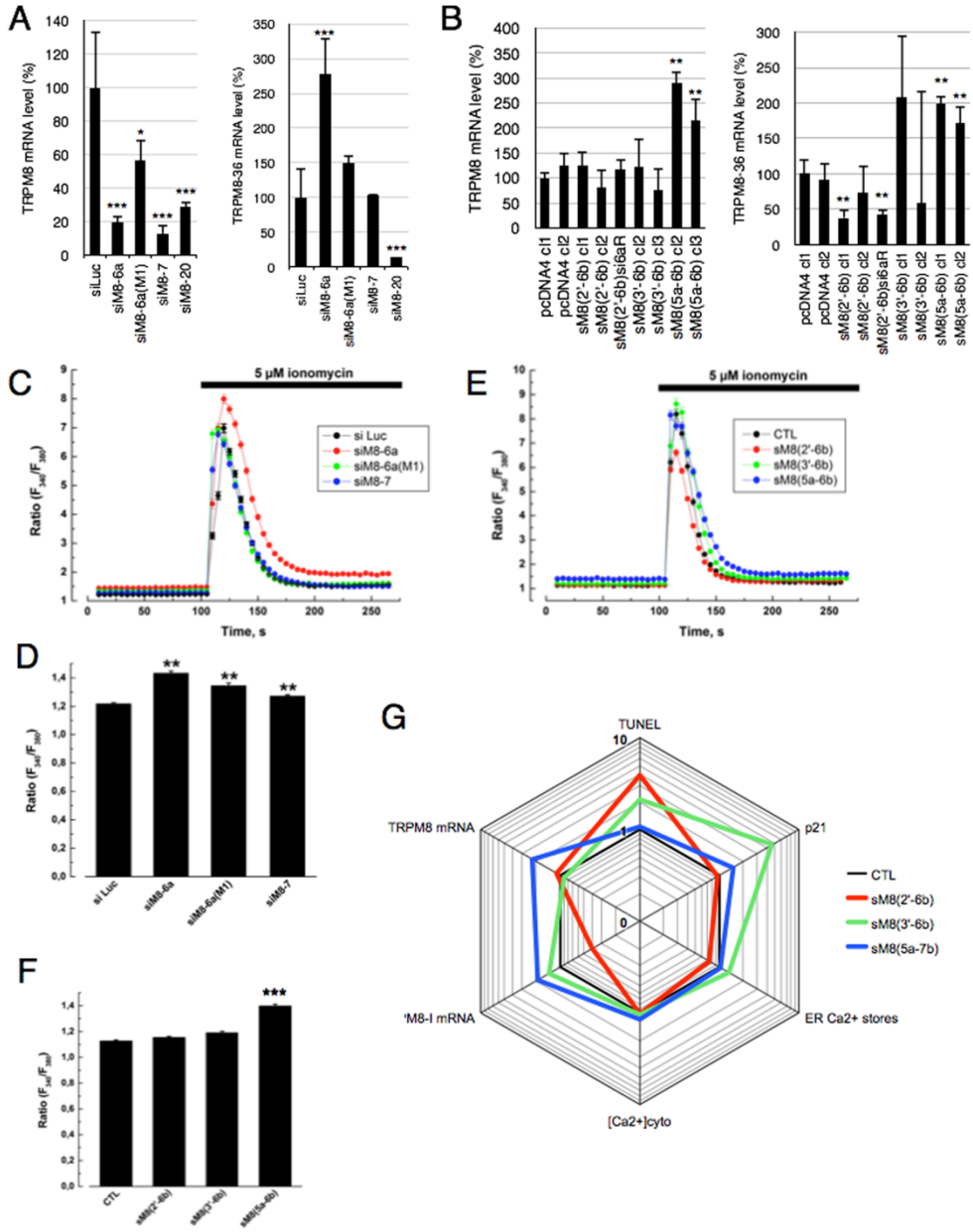

FIGURE 7. *Level of expression of sM8 isoforms is correlated to level of expression of TRPM8 channel isoforms and to ER Ca^{2+} stores.* **A.** Bar diagram plots show expression level of TRPM8 mRNA (left panel) and of TRPM8-36 (right panels) as measured by the mean of qPCR. Knockdown of sM8 isoforms and full length TRPM8 with siM8-6a (left panel, calculations described in M&M section) induces expression of TRPM8-36 (right panel), although neither mutant siM8-6a(M1) nor specific KD of TRPM8 channel, siM8-7, modify TRPM8-36 expression. **B.** mRNA levels of TRPM8 (left panel) and TRPM8-36 (right panel, calculations described in M&M section), measured by qPCR, in C4-2b clones overexpressing sM8 isoforms are presented in bar diagram plots. **C.** Time course of Ca^{2+} imaging experiments realized on LNCaP C4-2b cells 3 days after transfection with 50 nM of siRNAs targeting luciferase (si Luc, n=387) or TRPM8 (siM8-6a, n=348; siM8-6a(M1), n=184 and siM8-7, n=345). Experiments were carried out in the absence of extracellular calcium, 5 µM ionomycin were added as indicated on the graph. Corresponding averaged values are summarized in the bar diagram plot presented in (**D.**). **E.** Time course of Ca^{2+} imaging experiments carried out in different LNCaP C4-2b clones: control clone (CTL), n=344; sM8(2'-6b), n=307; sM8(3'-6b), n=302; sM8(5a-6b), n=280. Experimental protocol is the same as presented in (**C**). Corresponding averaged values are summarized in the bar diagram plot shown in (**F.**). **G.** Logarithmic radar plot summarizes the complexity of variations happening in C4-2b clones overexpressing sM8 isoforms after transfection of the siM8-6a. The rates of apoptosis (TUNEL) and of $p21^{waf1}$ expression (p21), ER Ca^{2+} content of ER stores (ER Ca^{2+} stores), Ca^{2+} concentration in cytosol ([Ca^{2+}]cyto) and TRPM8 and TRPM8-36 mRNA levels were normalized on the related values calculated in the control clones (CTL).

This suggests that the sM8-dependent regulation of TRPM8 and TRPM-36 transcription is a finely tuned and specific mechanism that occurs in addition of consensual regulation mechanisms of transcription and translation. However, the antagonist effects we observed suggest that a single cell may, likely, not express the whole variety of sM8s at the same level of expression. Strikingly, in the sM8-KD cell population, we observed 3 cell sub-populations: one insensitive to sM8-KD, one ongoing apoptosis and one subjected to p21 induction and growth arrest. Since we showed that overexpression of sM8(2'-6b) sensitized to sM8-KD mediated apoptosis, and sM8(3'-6b) overexpression sensitized to p21 induction, this suggests that these 3 cell sub-populations are actually characterized by different fingerprints of sM8s expression. In term of therapeutic design, this implies that sM8-KD should be reserved to low proliferative prostate tumors expressing sM8(2'-6b)/TRPM8-36 mRNAs or to tumors expressing sM8(3'-6b)/ /TRPM8-36 mRNAs and characterized by a higher rate of proliferation. Please note that sM8(3'-6b) mRNA has been characterized in prostate cancer cell line but was found to incorporate intron 3' in normal prostate cells. It is thus likely that the splicing on intron 3' occurs in proliferative cancer cells like metastasis derived from a prostate tumor.

Apoptotic and cytostatic effects of sM8-KD on prostate cancer cells require activity of TRPM8 channel isoforms. Indeed, either the suppression or the inhibition of TRPM8-36 blocked apoptosis and p21 induction in sM8-KD cells, while the suppression of full length TRPM8 channel - always concomitant to silencing of sM8s - did not impeach cell death and p21 induction. This suggests that silencing of sM8s alters not only TRPM8 expression but also TRPM8-36 activity. Since TRPM8-36 are localized in ER membranes and since measuring the activity of channels in intracellular membranes is technically impossible in living cells, we measured ER Ca^{2+} content to demonstrate that suppression or overexpression of sM8s modified Ca^{2+} homeostasis. sM8(2'-6b) isoform demonstrates the highest effect that suggests a link, or at least a correlation, between modification of ER Ca^{2+} homeostasis and apoptosis. Other and we demonstrated that cell death of cells is a finely-tuned mechanism link to ER Ca^{2+} stores (for review see [9]). However, we previously reported that in prostate cancer cells overexpressing the anti-apoptosis protein Bcl-2, ER Ca^{2+} content was lowered [11]. This contradictory results may suggest that cell death is not a direct consequence of changes in ER Ca^{2+} content, but either involved parallel independent mechanisms, or that variation in ER Ca^{2+} content, whatever its orientation, is critical for triggering apoptosis.

In conclusion, our results demonstrate that targeting sM8 expression/activity is a far better strategy to inhibit cell growth and induce apoptosis of PCa cells than targeting the full length TRPM8 channel. *In vivo* gene silencing has emerged in the past decade as a potential strategy to trigger cell death inside tumors. However, improvement of siRNA vectorization must still be achieved to efficiently and specifically target cancer cells and to deliver siRNAs at the required concentration. In this study, we showed that transfecting primary cultures of human PCa cells is less efficient that transfecting LNCaP C4-2b cell line and lead to a partial and attenuated effect of sM8 KD. We believe that, in a near future, therapeutic strategies should target a combination of genes to prevent secondary effects without decreasing efficiency or inducing relapse. Silencing of sM8 could participate to that king of strategy which would rely on the stimulation of ER stress.

Authors' Contribution

Conception and design: G.B., AS.B., L.L.
Acquisition of data, methodology: G.B., AS.B., L.L., C.D., C.Sc., F.VA., G.L., E.D., C.Sl., M.R., JL.B., B.M.
Analysis and interpretation of data: G.B., AS.B., L.L., C.D., F.VA.
Writing / review: G.B., AS.B., L.L., P.M., N.P.
Study supervision: G.B. and N.P.

Aknowledgements

Mr Laurent Allart for his technical support
Prof Robert-Alain Toillon for his kind advises on cell cycle analysis.

Grant support

This work was supported by grants from INSERM, Ministère de l'Education Nationale, Ligue Nationale Contre le Cancer, the Region Nord-Pas-de-Calais, Agence Nationale de Recherche, Association de Recherche sur les Tumeurs de la Prostate.
Dr Anne-sophie Borowiec was supported by a grant of "foundation pour la recherché médicale".

References

1. Stoyanova, T., et al., *Prostate cancer originating in basal cells progresses to adenocarcinoma propagated by luminal-like cells.* Proc Natl Acad Sci U S A, 2013.
2. Kwon, O.J., et al., *Prostatic inflammation enhances basal-to-luminal differentiation and accelerates initiation of prostate cancer with a basal cell origin.* Proc Natl Acad Sci U S A, 2014. **111**(5): p. E592-600.
3. McKenzie, S. and N. Kyprianou, *Apoptosis evasion: the role of survival pathways in prostate cancer progression and therapeutic resistance.* J Cell Biochem, 2006. **97**(1): p. 18-32.
4. Shiota, M., A. Yokomizo, and S. Naito, *Pro-survival and anti-apoptotic properties of androgen receptor signaling by oxidative stress promote treatment resistance in prostate cancer.* Endocr Relat Cancer, 2012. **19**(6): p. R243-53.
5. Oh, Y.K. and T.G. Park, *siRNA delivery systems for cancer treatment.* Adv Drug Deliv Rev, 2009. **61**(10): p. 850-62.
6. Reischl, D. and A. Zimmer, *Drug delivery of siRNA therapeutics: potentials and limits of nanosystems.* Nanomedicine, 2009. **5**(1): p. 8-20.
7. Joniau, S., et al., *Current vaccination strategies for prostate cancer.* Eur Urol, 2012. **61**(2): p. 290-306.
8. Prevarskaya, N., R. Skryma, and Y. Shuba, *Calcium in tumour metastasis: new roles for known actors.* Nat Rev Cancer, 2011. **11**(8): p. 609-18.
9. Shapovalov, G., et al., *TRP channels in cell survival and cell death in normal and transformed cells.* Cell Calcium, 2011. **50**(3): p. 295-302.

ARTICLE 12

10. Hammadi, M., et al., *Modulation of ER stress and apoptosis by endoplasmic reticulum calcium leak via translocon during unfolded protein response: involvement of GRP78.* FASEB J, 2013. **27**(4): p. 1600-9.
11. Vanden Abeele, F., et al., *Bcl-2-dependent modulation of Ca(2+) homeostasis and store-operated channels in prostate cancer cells.* Cancer Cell, 2002. **1**(2): p. 169-79.
12. Dubois, C., F. Vanden Abeele, and N. Prevarskaya, *Targeting apoptosis by the remodelling of calcium-transporting proteins in cancerogenesis.* FEBS J, 2013. **280**(21): p. 5500-10.
13. Dubois, C., et al., *Differential effects of thapsigargin analogues on apoptosis of prostate cancer cells: complex regulation by intracellular calcium.* FEBS J, 2013. **280**(21): p. 5430-40.
14. Fuessel, S., et al., *Multiple tumor marker analyses (PSA, hK2, PSCA, trp-p8) in primary prostate cancers using quantitative RT-PCR.* Int J Oncol, 2003. **23**(1): p. 221-8.
15. Kiessling, A., et al., *Identification of an HLA-A*0201-restricted T-cell epitope derived from the prostate cancer-associated protein trp-p8.* Prostate, 2003. **56**(4): p. 270-9.
16. Tsavaler, L., et al., *Trp-p8, a novel prostate-specific gene, is up-regulated in prostate cancer and other malignancies and shares high homology with transient receptor potential calcium channel proteins.* Cancer Res, 2001. **61**(9): p. 3760-9.
17. Bidaux, G., et al., *Evidence for specific TRPM8 expression in human prostate secretory epithelial cells: functional androgen receptor requirement.* Endocr Relat Cancer, 2005. **12**(2): p. 367-82.
18. Bidaux, G., et al., *Prostate cell differentiation status determines transient receptor potential melastatin member 8 channel subcellular localization and function.* J Clin Invest, 2007. **117**(6): p. 1647-57.
19. Thebault, S., et al., *Novel role of cold/menthol-sensitive transient receptor potential melastatine family member 8 (TRPM8) in the activation of store-operated channels in LNCaP human prostate cancer epithelial cells.* J Biol Chem, 2005. **280**(47): p. 39423-35.
20. Henshall, S.M., et al., *Survival analysis of genome-wide gene expression profiles of prostate cancers identifies new prognostic targets of disease relapse.* Cancer Res, 2003. **63**(14): p. 4196-203.
21. Zhang, L. and G.J. Barritt, *Evidence that TRPM8 is an androgen-dependent Ca2+ channel required for the survival of prostate cancer cells.* Cancer Res, 2004. **64**(22): p. 8365-73.
22. McKemy, D.D., W.M. Neuhausser, and D. Julius, *Identification of a cold receptor reveals a general role for TRP channels in thermosensation.* Nature, 2002. **416**(6876): p. 52-8.
23. Peier, A.M., et al., *A TRP channel that senses cold stimuli and menthol.* Cell, 2002. **108**(5): p. 705-15.
24. Bidaux, G., et al., *Regulation of transient receptor potential melastatin 8 (TRPM8) channel activity by its short isoforms.* J Biol Chem, 2011.
25. Fernandez, J.A., et al., *Short isoforms of the cold receptor TRPM8 inhibit channel gating by mimicking heat action rather than chemical inhibitors.* J Biol Chem, 2011.
26. Gackiere, F., et al., *A role for voltage gated T-type calcium channels in mediating "capacitative" calcium entry?* Cell Calcium, 2006. **39**(4): p. 357-66.
27. Grynkiewicz, G., M. Poenie, and R.Y. Tsien, *A new generation of Ca2+ indicators with greatly improved fluorescence properties.* J Biol Chem, 1985. **260**(6): p. 3440-50.
28. Erdmann, K., et al., *Elevated expression of prostate cancer-associated genes is linked to down-regulation of microRNAs.* BMC Cancer, 2014. **14**: p. 82.
29. Valero, M.L., et al., *TRPM8 ion channels differentially modulate proliferation and cell cycle distribution of normal and cancer prostate cells.* PLoS One, 2012. **7**(12): p. e51825.
30. Urra, H., et al., *When ER stress reaches a dead end.* Biochim Biophys Acta, 2013. **1833**(12): p. 3507-17.
31. Sano, R. and J.C. Reed, *ER stress-induced cell death mechanisms.* Biochim Biophys Acta, 2013. **1833**(12): p. 3460-70.
32. Jones, R.G., et al., *AMP-activated protein kinase induces a p53-dependent metabolic checkpoint.* Mol Cell, 2005. **18**(3): p. 283-93.
33. Okoshi, R., et al., *Activation of AMP-activated protein kinase induces p53-dependent apoptotic cell death in response to energetic stress.* J Biol Chem, 2008. **283**(7): p. 3979-87.
34. Deng, C., et al., *Mice lacking p21CIP1/WAF1 undergo normal development, but are defective in G1 checkpoint control.* Cell, 1995. **82**(4): p. 675-84.
35. Niculescu, A.B., 3rd, et al., *Effects of p21(Cip1/Waf1) at both the G1/S and the G2/M cell cycle transitions: pRb is a critical determinant in blocking DNA replication and in preventing endoreduplication.* Mol Cell Biol, 1998. **18**(1): p. 629-43.
36. Kim, S.Y., et al., *Lactococcus lactis ssp. lactis inhibits the proliferation of SNU-1 human stomach cancer cells through induction of G0/G1 cell cycle arrest and apoptosis via p53 and p21 expression.* Ann N Y Acad Sci, 2009. **1171**: p. 270-5.
37. Zhang, Y., et al., *Recombinant human decorin suppresses liver HepG2 carcinoma cells by p21 upregulation.* Onco Targets Ther, 2012. **5**: p. 143-52.
38. Seo, H.S., et al., *Induction of apoptotic cell death by phytoestrogens by up-regulating the levels of phospho-p53 and p21 in normal and malignant estrogen receptor alpha-negative breast cells.* Nutr Res, 2011. **31**(2): p. 139-46.
39. Endl, E., et al., *Analysis of cell cycle-related Ki-67 and p120 expression by flow cytometric BrdUrd-Hoechst/7AAD and immunolabeling technique.* Cytometry, 1997. **29**(3): p. 233-41.
40. Guil, S. and M. Esteller, *RNA-RNA interactions in gene regulation: the coding and noncoding players.* Trends Biochem Sci, 2015. **40**(5): p. 248-256.

TABLE 1

	Tumor implantation, % of mice injected (size of cohorts)
siLuc	70 (10)
siM8-6a	40 (10)
	Tumor growth, mm^3/day
siLuc	73,71 ± 3,65
siM8-6a	61,42 ± 25,60

TABLE 1: percentage of tumor implantation as the percentage of mice exhibiting visible tumors.

TABLE 2

siRNA label	5'-3' RNA sense sequence
siLuc	CUUACGCUGAGUACUUCGA
siM8-4b	CAAGAAACACACCAAGGAA
siM8-6a	GGAGUUCAGAGGAGAAUAU
siM8-6a(M1)	GGAGUUCAGAAGAGAAUAU
siM8-6a(M3)	GGAGUUCAGAGAAGAAUAU
siM8-6a.2	GGGGAGGUGGUGAGAGAUA
siM8-7	UCUCUGAGCGCACUAUUCA
siM8-10	GGGAUGAAAUUGUGAGCAA
siM8-12	GGAAACUGGUUGCGAACUU
siM8-19	GUAUUCUGGACGAGUCAUU
siM8-20	UAUUCCGUUCGGUCAUCUA

TABLE 2: list of oligonucleotides used in this study.

ARTICLE 12

SUPPLEMENTAL DATA

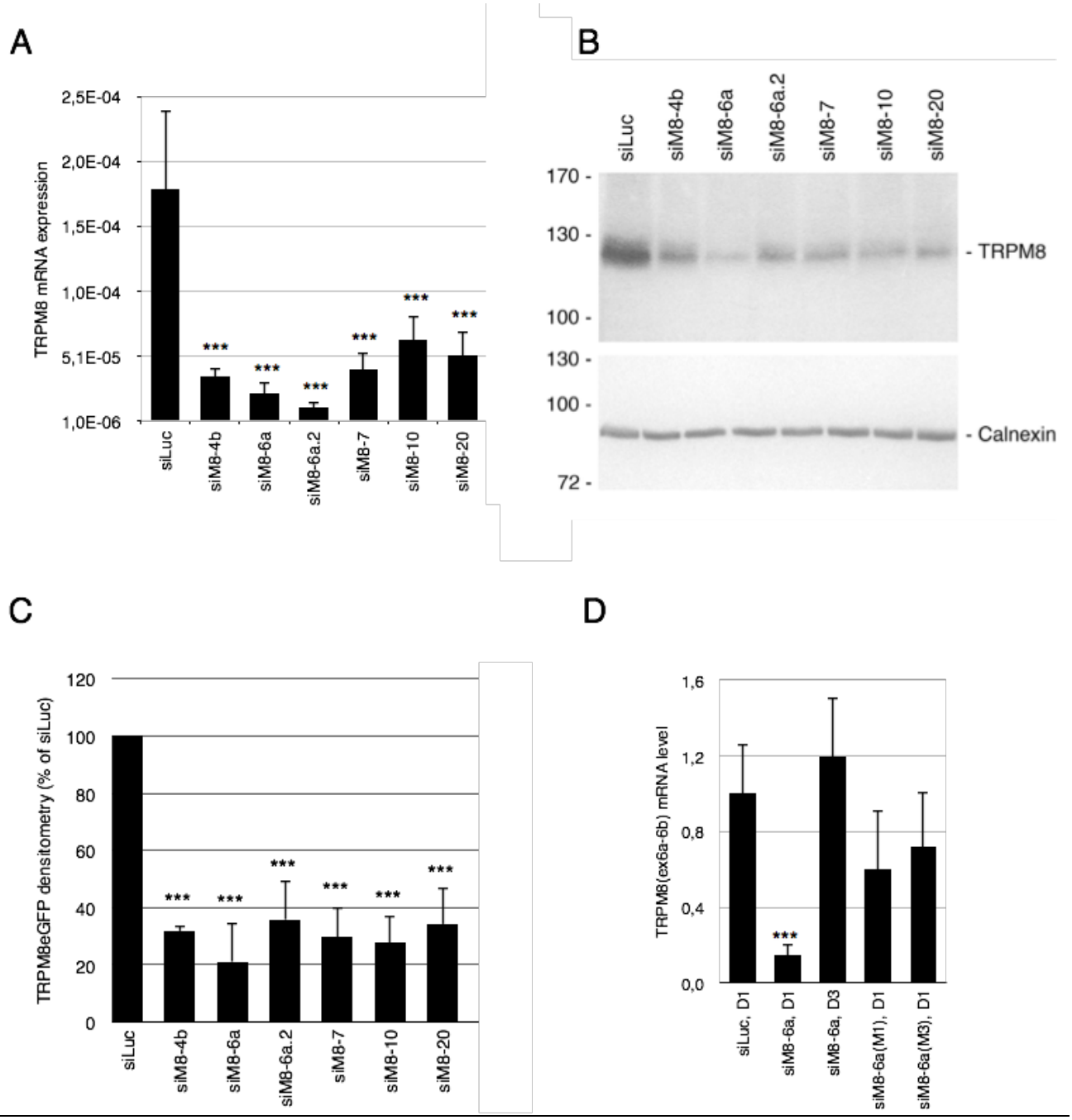

FIGURE S1 *Silencing efficiency of anti-TRPM8 siRNAs.* **A.** Bar diagram plot shows quantification of TRPM98 mRNA level in TRPM8-36nducible HEK cells after transfection of anti-TRPM8 siRNAs. **B.** Western-blot shows expression of TRPM8 channel in TRPM8-36nducible HEK cells after transfection of anti-TRPM8 siRNAs. 50 µg of total protein extract were loaded on each well. **C.** Bar diagram plot represents the quantification of TRPM8 proteins detected by immunoblotting by densitometry. Values are normalized on siLuc value. **D.** Silencing of native sM8 mRNAs in LNCaP C4-2b cells following a 48h siRNA transfection. TRPM8 mRNA level has been measured from exon 6a to exon 6b to specifically detect sM8 transcripts, and were quantified by the mean of qPCR. Values are normalized on siLuc value. All experiments were performed three times independently. Values are expressed as Mean ± SD.

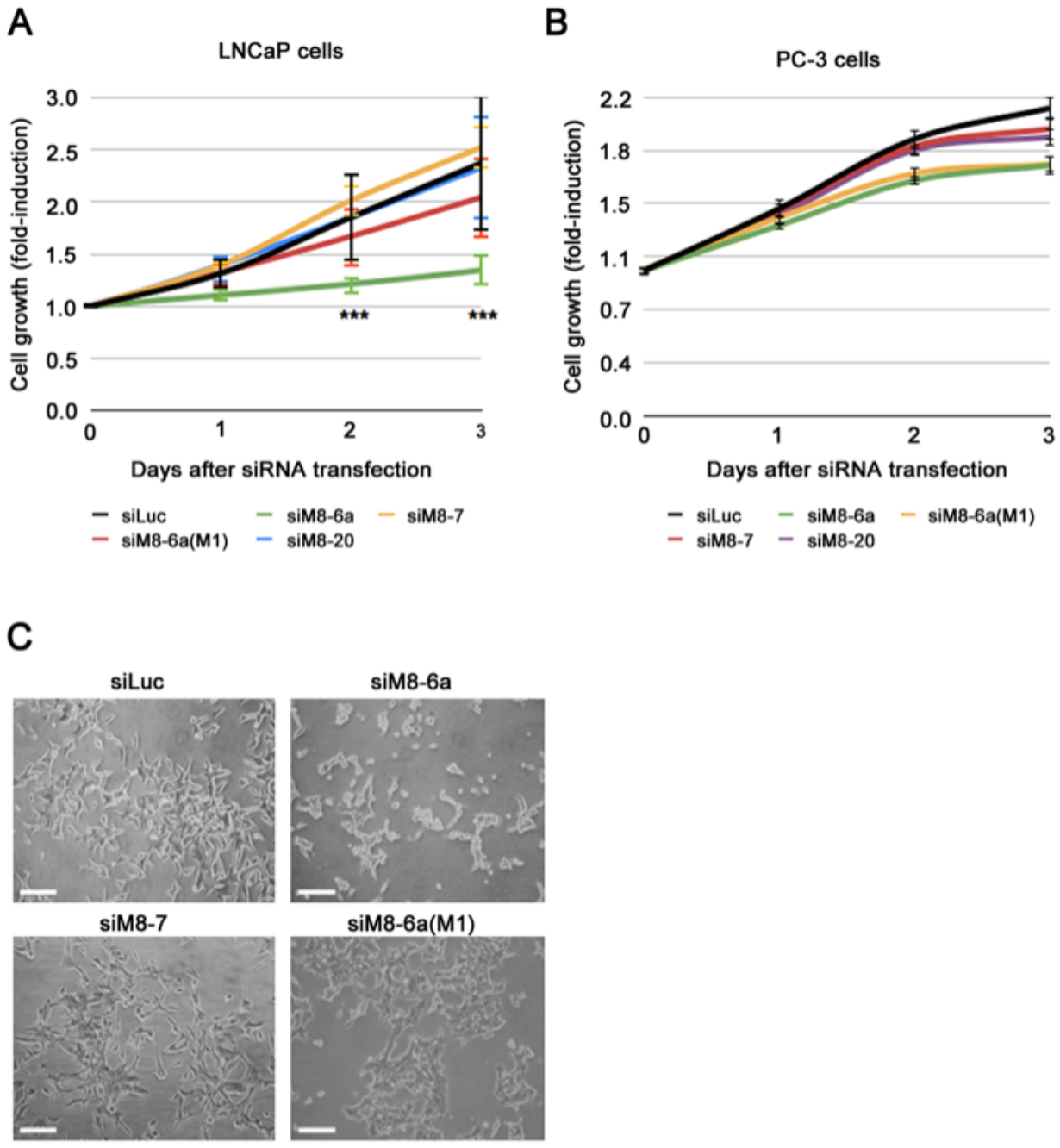

FIGURE S2 *Suppression of sM8 isoforms inhibits cell growth of androgen-dependent LNCaP and androgen-refractory LNCaP C4-2b cells.* **A.** and **B.** Growth kinetic of LNCaP and PC-3 cell lines, respectively. siRNA targeting selective groups of TRPM8 isoforms were transfect at day 0**.** Estimation of cell number was achieved usin the CellTiter 96® AQ_{ueous} Non-Radioactive Cell Proliferation Assay (Promega), as described in *Materiels and Methods*. Experiments were performed three times independently. Values are expressed as Mean ± SD. **C.** Phase-contrast images of LNCaP C4-2b cells after a 3-day siRNA transfection. Scale bar represents 50 µM.

ARTICLE 12

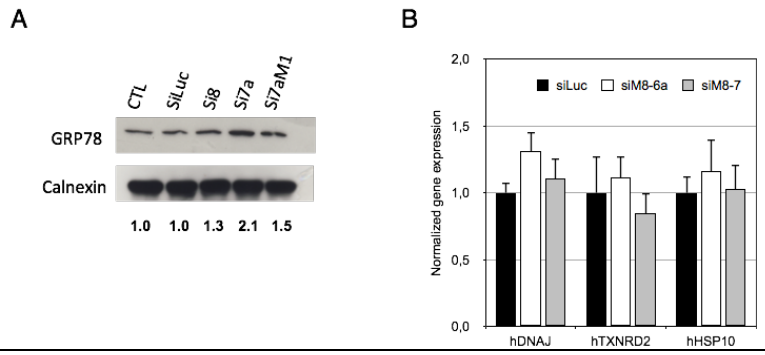

FIGURE S3 *sM8 knockdown does not modify expression of genes implicated in mitochondrial stress.* Expression of genes involved in mitochondrial stress: *DNAJ, TXRND2, HSP10* was estimated with qPCR after a 3-day siRNA transfection of LNCaP C4-2b cells. Experiments were performed three times independently. Values are expressed as Mean ± SD

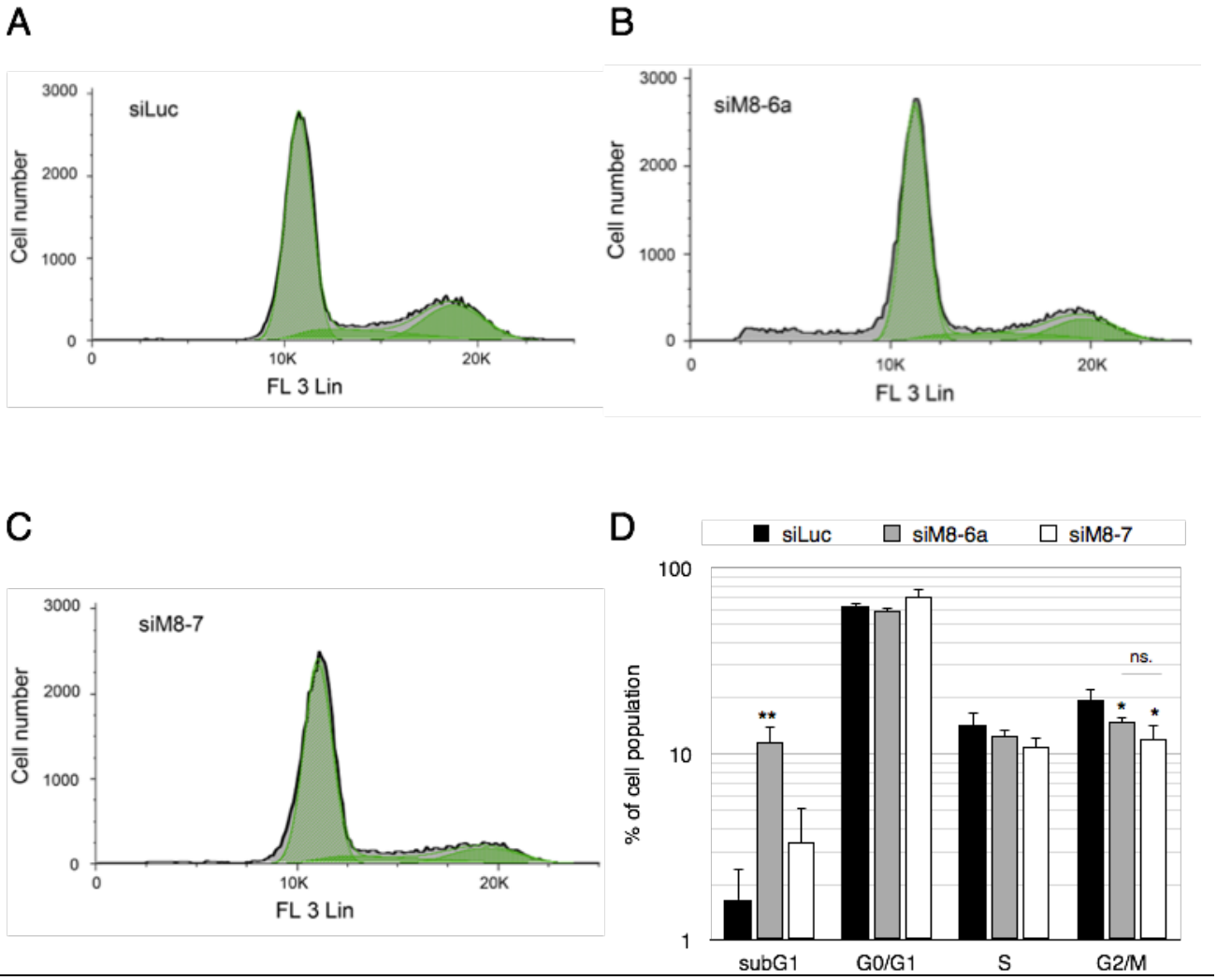

FIGURE S4 *sM8 knockdown does not significantly modify cell cycle distribution of LNCaP C4-2b cells.* Cell cycle analysis by flow cytometry was performed in LNCaP C4-2b cells transfected with siLuc (**A**), siM8-6a (**B**) or siM8-7 (**C**) for 3 days. Distributions of cells by their DNA content (FL 3 lin, x axe) are fitted with the Dean-Jett-Fox model to estimate the cell sub-populations in subG1, G0/G1, S and G2/M phases. Experiments were performed three times and average values of the cell sub-populations were figured out. **D.** Bar diagram plot represents the mean ± SD of the cell sub-population at the different phase of the cell cycle.

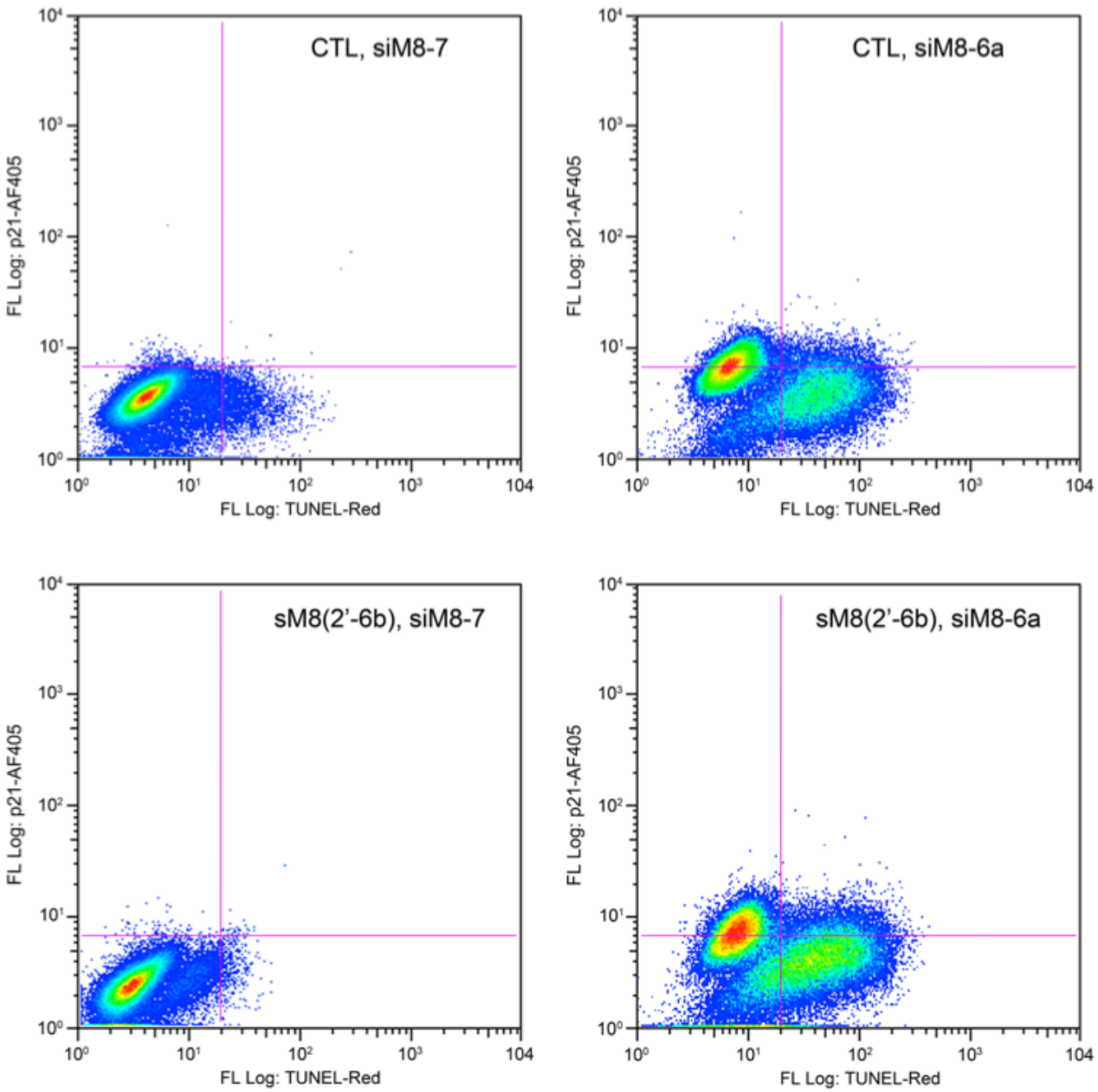

FIGURE S5. *Distribution of p21^{waf1}-immunolabeled and TUNEL-positive cells* reported by flow cytometry (representative experiment shown) in a population of LNCaP C4-2b cells (CTL) or sM8(2'-6b)-overexpressing C4-2b cells transfected with either siM8-7 or siM8-7a, knocking down TRPM8 or TRPM8+sM8, respectively. Pseudo-color code represents density from the lowest (blue) to highest (red). Experiments were performed three times independently.

ARTICLE 12

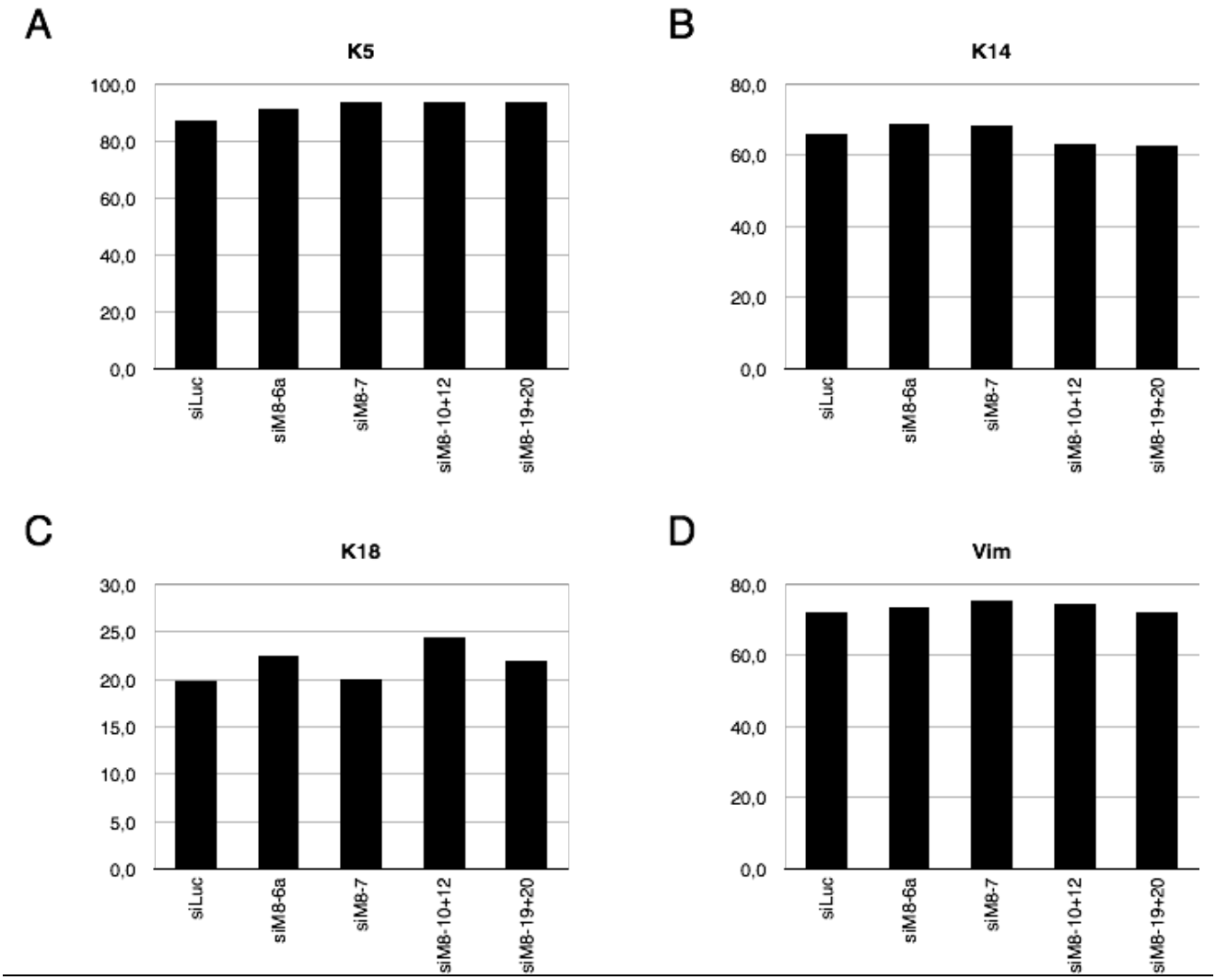

FIGURE S6 *Distribution of the different cell types in the primary culture of prostate cancer cells (PrPCa) is not affected by transfection of siRNA targeting the TRPM8 mRNAs.* The proportion of PrPCa cells expressing keratin 5 (K5), keratin 14 (K14), keratin 18 (K18) or vimentin (VIM) has been estimated with flow cytometry. Cells were previously transfected with either siRNA. Histograms represents a representative experiments. Experiments were performed three times independently.

III. ARTICLE 13

ARTICLE 13

Novel isoform of TRPM8 channel characterized in mitochondria-associated membranes of prostate cells

Gabriel Bidaux[1,2,*], Dmitri Gordienko[1,3,*], Georges Shapovalov[1,*], Anne-sophie Borowiec[1], Loic Lemonnier[1], Etienne Dewailly[1], Christian Slomianny[1] and Natalia Prevarskaya[1]

[1]Inserm, U-1003, Equipe labellisée par la Ligue Nationale contre le cancer, Villeneuve d'Ascq, F-59655 France; Université des Sciences et Technologies de Lille (USTL), Villeneuve d'Ascq, F-59655 France.
[2]Laboratoire de Physique des Lasers, Atomes et Molécules, Equipe Biophotonique Cellulaire Fonctionnelle, UMR 8523, Parc scientifique de la Haute Borne, Villeneuve d'Ascq, France.
[3]Laboratory of Molecular Pharmacology and Biophysics of Cell Signalling, State Key Laboratory of Molecular and Cell Biology, Bogomoletz Institute of Physiology, Kiev, Ukraine

*: Authors contributed equally to the work

Running title: TRPM8 isoforms in MAM of prostate cancer cells

To whom correspondences should be addressed:
Dr Gabriel Bidaux: Laboratoire Biophotonique Cellulaire Fonctionnelle, Institut de Recherche Interdisciplinaire, USR3078 CNRS, Parc scientifique de la Haute Borne, Villeneuve d'Ascq, F-59655 France. Tel: +33 (0) 362-531-733. Fax: +33 (0) 362-531-701. gabriel.bidaux@gmail.fr.
Prof. Natalia Prevarskaya: Laboratoire de physiologie cellulaire, Inserm, U-1003, Bat SN3, 2 étage, Université des Sciences et Technologies de Lille (USTL), Villeneuve d'Ascq, F-59655 France. Tel: +33 (0) 320-336-018. Fax: +33 (0) 320-434-066. Natalia.Prevarskaya@univ-lille1.fr.

Keywords: TRP channel, MAMs, alternate transcription, ER Calcium fluxes, mitochondria, prostate

ABSTRACT

The transient receptor potential melastatin channel 8 (TRPM8) is a promising prognostic marker and putative therapeutic target in prostate cancer (PCa). However, the nature of the TRPM8 isoforms and their role in PCa are still debated. Here, we report the cloning of five TRPM8 alternate mRNAs which may encode two N-terminally truncated TRPM8 isoforms: TRPM8-38 and TRPM8-35. These TRPM8 isoforms exhibit an unconventional structure with 4 transmembrane domains (TMs) instead of 6 TMs characteristic for the TRP channel archetype. We also demonstrate that in PCa cells TRPM8-35 is expressed at significantly higher level than other TRPM8 isoforms and forms functional channel, which, in contrast to classical TRPM8, is located in the endoplasmic reticulum (ER) microdomains known as mitochondria associated membranes (MAMs). These results demonstrate that several channel proteins encoded by the same gene may have different structure and cellular localization. The TRPM8-35 isoform in the MAMs of PCa epithelial cells participates in calcium homeostasis of the ER and mitochondria.

INTRODUCTION

During last decade the transient receptor potential melastatin 8 channel, TRPM8, has emerged as a putative therapeutic target for PCa (Bidaux et al, 2005; Fuessel et al, 2003; Kiessling et al, 2003; Tsavaler et al, 2001). In a previous study, we detected the expression of a N-terminal truncated channel-like TRPM8 isoform and showed its specific activity in ER membranes of prostate cells (Bidaux et al, 2007). In this line, Phelps *et al* demonstrated that sequence between the 40th and the 80th amino acid was essential for translocation of the protein to the plasmalemma (Phelps & Gaudet, 2007). Besides, these authors demonstrated that TMs are the main component of tetramerization and that the coiled-coil domain at the C-terminus is required for cold/menthol-sensitivity of TRPM8 (Phelps & Gaudet, 2007). In 2008, another study confirmed that a N-terminal truncated TRPM8 protein encoded by the gDNA segment from exon 18 to 3' UTR was a menthol-sensitive protein (Sabnis et al, 2008). We previously showed that a TRPM8 isoform was confined to the membranes of endoplasmic reticulum (ER) of epithelial prostate cells during intermediate/transit amplifying stage, and in PCa and metastasis (Bidaux et al, 2007). These studies, altogether, suggested that alternate (promoter and/or termination site) transcription is an important determinant of diversity of the TRPM8 protein structure that, in turn, is essential for cellular localization and function.

Expression of calcium channels in ER membrane is actually thought to participate to the capacitive calcium entry (CCE) by homology with inositol triphosphate receptors (IP3R) and ryanodine receptors (RYR) activity in ER. However, ER is a segmented organelle with specific microdomains dedicated to specific functions such as ER-plasmalemmal junction, ER-Golgi or ER-mitochondria junction (for review, see(Levine & Rabouille, 2005)). While the first is related to CCE, the latter refers to the physical coupling of mitochondria-associated ER membranes (MAMs) with mitochondria (Wang et al, 2000). MAMs are functional domains gathering enzymes involved in lipid metabolism (Lewin et al, 2002; Stone & Vance, 2000) and the Ca^{2+} channel, IP3R, which connects the ER Ca^{2+} stores to the mitochondrial matrix (Robb-Gaspers et al, 1998a; Robb-Gaspers et al, 1998c). This tight coupling between the ER and mitochondria facilitates mitochondrial Ca^{2+} uptake either by robust increase of Ca^{2+} concentration in the ER-mitochondria "nanodomains" (Poburko et al, 2008) or via

direct "Ca^{2+} tunneling" from the ER to mitochondria (Giacomello et al, 2010; Ishii et al, 2006; Shkryl & Shirokova, 2006). $[Ca^{2+}]_m$ plays an important role in cell bioenergetics and ATP synthesis in particular. Ca^{2+}-dependent regulation of ATP synthesis involves several mechanisms, including tricarboxylic acid cycle's Ca^{2+}-dependent dehydrogenase regulation (for review see (Harris & Das, 1991)) and Ca^{2+} binding by ATP synthase beta subunit (complex F1) itself (Hubbard & McHugh, 1996).

Here we report the cloning of five alternate TRPM8 mRNA generated from five internal promoters localized in introns 14, 15, 16 (2 different transcription start sites) and 17, and terminated at two different sites in exon 26. Four of these alternate TRPM8 mRNA, namely TRPM8(15a), TRPM8(17'), TRPM8(17'') and TRPM8(18a), redundantly encodes three highly similar proteins: TRPM8-40, TRPM8-38 and TRPM-35. The predicted structures of these TRPM8 isoformes likely include 4 TM and the P-loop. Since in prostate cells, TRPM8-35 is expressed at significantly higher level than other TRPM8 isoforms, we analyzed its functional properties. We found that TRPM8-35 is localized in mitochondria-associated ER membranes (MAMs) where it functionally coupled ER Ca^{2+} stores with the $[Ca^{2+}]$ of mitochondrial matrix. The ability of TRPM8-35 to act as a Ca^{2+}-permeable channel was confirmed by patch-clamp recording of the single channel activity from giant unilamelar vesicles (GUV), incorporating recombinant and native proteins (Shapovalov et al, submitted).

RESULTS

New sub-types of TRPM8 channel identified in human prostate epithelial cells.

Using differential PCR screenings to characterize TRPM8 mRNA in human prostate epithelial cells, we previously detected a 5'-truncated TRPM8 mRNA but did not cloned it then (Bidaux et al, 2007). Here using 5'-RACE PCR from the pore encoding sequence (exon 20) we cloned 5 alternate 5'-extremities and 1 alternate 3'-extremity of TRPM8 mRNAs. Internal quality control for the RACE PCR was performed with the cloning of the 5' extremity of the full length TRPM8 mRNA in human prostate. We succeeded in amplifying of 2,900 bp (GenBank accession number: KC692993) and improved the definition of the first transcribed nucleotide (+1) of the TRPM8 mRNA by detecting of 10 additional bases upstream to the published +1 (NM_024080.4). This shifts the new +1 nucleotide 25 bases downstream of the TATAA box. Although previously published +1 nucleotide was identified 35 bases downstream (Bidaux et al, 2005), this location does not match consensus distance between TATAA box and +1 (from 15 to 25 bp). Novel alternate starting or ending exons were labeled with regards to their position relative to the core exons. Cassette exons, included into a core intron, were labeled with "comas", while 5' or 3' supplemental part of a core exon were labeled a and b, respectively (**Fig. 1A**). Full length PCR was performed to amplify the cloned alternate TRPM8 mRNAs in total mRNA extract from human prostate tissue by pairing each starting exon with each ending exon in order to clone all TRPM8 mRNAs. As shown in the Figure 1A, five alternate TRPM8 mRNA were cloned, namely, TRPM8(15a) (GenBank accession number: xxxxxx), TRPM8(16a) (GenBank accession number: xxxxxx), TRPM8(17') (GenBank accession number: xxxxxx), TRPM8(17'') (GenBank accession number: xxxxxx) and TRPM8(18a) (GenBank accession number: xxxxxx); for sequences please see S**upplemental material**. Note that the 3' cleavage site of TRPM8(16a) and TRPM8(17') is upstream of the classical 3' cleavage site in the full length TRPM8 mRNA (**Fig. 1A**). Full length PCR fingerprinting of TRPM8 mRNA expression (**Fig. 1B**) was performed on (1) cancer cell lines: LNCaP (androgen-dependent), LNCaP C4-2b (androgen-refractory), PC-3 (androgen-independent), and on (2) long term (>20 days) primary culture of epithelial cells from normal human prostate (PrPE) and human prostate cancer (PrPCa-1 and PrPCa-2) resection specimens. Except TRPM8(18a), all alternate mRNAs were detected in prostate cancer cell lines, while TRPM8(15) was found in androgen-dependent and androgen-refractory but not in androgen-independent PC-3 cell line. Note that the low expression level observed in the primary culture may result from changes caused by a long-term cell culturing and may not reflect the level of TRPM8 expression in the tissue of tumor (Bidaux et al, 2007). Nevertheless, TRPM8(17') mRNA was detected in the two independent primary cultures of the epithelial prostate cancer cells. qPCR quantification of both N-terminus- and pore region-encoding mRNA sequences confirmed the strong discrepancy between normal prostate tissue, prostate cancer cell lines and primary culture of prostate epithelial cells (**Fig. 1C**). This is in agreement with previous findings that full-length TRPM8 (here detected through exon 7-8 expression) is down-regulated in advanced prostate cancer cells (Kiessling et al, 2003) and in the long-term primary culture of human resection specimens (Bidaux et al, 2007). As shown on the annotated sequences of TRPM8 mRNAs in **supplemental material**, several putative open reading frames (ORF) were found for each mRNA. Since prediction of ORF is always a random challenge, we expressed recombinant TRPM8 isoforms in HEK cells and performed immunoblotting with an anti-TRPM8 antibody on 25 µg of total protein extract. TRPM8(15a) mRNA generates two majors doublet of protein at about 35 and 40 kDa (**Fig 1D**) which, regarding the ORF size prediction, correspond to the expected sizes. TRPM8(16a) mRNA was untranslated, while TRPM8(17') and TRPM8(17'') were translated giving rise to several proteins with masses expected for the proteins encoded by the different ORFs: 38, 35, 28, 26 and 22 kDa . Finally, translation of TRPM8(18a) mRNA gave rise to 26 and 22 kDa proteins. It is likely that the weak consensus Kozak sequences of the first upstream AUG codons causes escaping from the first-AUG rule (Kozak, 1986). Alternative possibility is that AUG codon in the 5' UTR (Rogozin et al, 2001) impairs the scanning model of AUG selection so that the translation is initiated at several alternate AUG codons (for review see (Kozak, 2002)). However, since truncated 5' and 3' UTR and heterologous expression are likely to generate artifacts, such as wrong usage of AUG codon, we checked the expression of native TRPM8 isoforms in LNCaP C4-2b

ARTICLE 13

cells, which were transfected with either control small interfering RNA (siCTL) or siRNA targeting the pore region of TRPM8 (siM8-20).

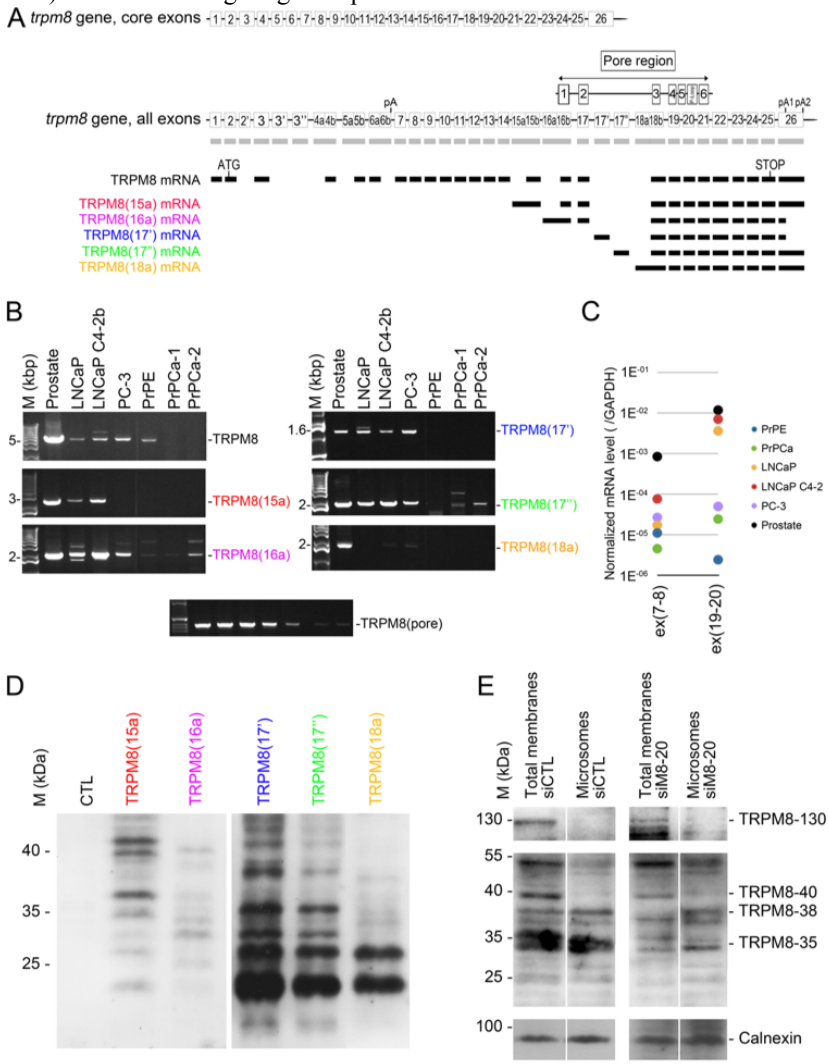

FIGURE 1. *Alternate TRPM8 mRNAs, generated by means of internal promotor, encode new kind of TRPM8 channel structure in the epithelial cells of human prostate.* **A,** Schematic representation (*trpm8* gene, core exons) of the *trpm8* gene with its core exons (top). In schematic representation (*trpm8* gene, all exons) of both core and new alternate exons (middle) the labeling reflects: "comas" – a cassette exon, a small letter - 5' or 3' supplemental part of a core exon. Transmembrane domains (TM) and p-loop of the channel pore (pore region) are aligned with their encoding exons. Exon structure (bottom) of alternate TRPM8 mRNAs: TRPM8(15a), TRPM8(16a), TRPM8(17'), TRPM8(17'') and TRPM8(18a). Note that the 3' cleavage site of TRPM8(16a) and TRPM8(17'), polyadenylation site (pA1), is upstream of the classical 3' cleavage site in the full-length TRPM8 mRNA (pA2). **B,** Full length amplification of TRPM8 cDNAs by PCR reveals a differential expression of the TRPM8 mRNAs in normal prostate tissue (Prostate), androgen-dependent prostate cancer cell line (LNCaP), androgen-refractory prostate cancer cell line (LNCaP C4-2b), androgen-independent prostate cancer cell line (PC-3), primary culture of normal prostate epithelial cells (PrPE) and the two samples of primary culture of prostate cancer epithelial cells (PrPCa-1 and PrPCa-2). Each amplification was performed with 100 ng of high-quality cDNA. TRPM8 pore region (TRPM8-pore) was amplified as an internal control of TRPM8 amount in the cDNA mixture. **C,** qPCR quantification of TRPM8 exon pair (8-9) and (21-22) demonstrate the variations in proportion of 5'-truncated alternate mRNA relative to the full length TRPM8 mRNA in prostate cancer cell lines, normal prostate tissue and primary culture of prostate epithelial cells. Data points represent mean values for 3 different samples. **D.** Immunoblotting of total protein lysates (25 µg) extracted from 1 million HEK cells transfected with 3 µg of plasmid encoding different TRPM8 isoforms. TRPM8 proteins were revealed with anti-TRPM8 antibodies (Abcam). Cells transfected with an empty pcDNA4.TO.A vector were used as a negative control (CTL). Experiment has been performed three times independently. **E.** Immunoblotting performed on either total membrane proteins or microsomes (50 µg) extracted from 1 million LNCaP C4-2b cells, transfected with either control siRNA (siCTL) or anti-TRPM8 siRNA (siM8). TRPM8 proteins were revealed with anti-TRPM8 antibodies (Abcam) and were labeled according to their apparent molecular weight on gel and to their expected ORF sizes: 130 kDa, 40 kDa, 38 kDa and 35 kDa. Experiment has been performed three times independently.

In the latter case, all TRPM8 channel isoforms are knocked-down. The western blot analysis was performed on protein extracts from either total membrane fractions or microsomes (**Fig. 1E**). The absence of the smaller bands (around 25 kDa) in the western blot (**Fig. 1E**) confirms further our hypothesis that these small proteins, detected in the overexpression experiments (**Fig. 1D**), are likely to be the artifacts of truncated 5' and 3' UTR and heterologous expression. Nonetheless, a doublet of 35 kDa TRPM8 protein (TRPM8-35) was present in both, total membrane and microsomal membrane fractions obtained from the cells transfected with control siRNA, but was absent in the TRPM8 knocked-down cells (**Fig. 1E**). Finally, a single 38 kDa protein was detected in total membrane fractions, but not in microsomal membrane fractions obtained from the cells transfected with control siRNA, and was almost silenced (please see **Fig. 1E**) in the TRPM8 knocked-down cells. Note that full-length classical TRPM8 was detected in total membrane fractions but not in the microsomal membrane fractions and was suppressed by the siM8-20 treatment. Altogether, the results presented in the Figure 1 suggest that TRPM8(15a) mRNA encodes a doublet of TRPM8-40 and TRPM8-35 isoforms while both TRPM8(17') and TRPM8(17'') mRNAs encode a doublet of TRPM8-38 and TRPM8-35 isoforms. Detection of TRPM8-38 and TRPM8-35 in microsomal membrane fraction demonstrates their expression in the ER, while the less abundant TRPM8-40 isoform, which was not observed in the microsomal membrane fractions, is likely to be localized in other cellular membranes of prostate cells.

TRPM8 isoforms are localized in MAMs of the ER.
Confocal detection of immunolabeled TRPM8 and the ER marker Calnexin in LNCaP C4-2 cells transfected with TRPM8(17')-encoding vector revealed their colocalization, thus confirming that TRPM8-38 and TRPM8-35 isoform are expressed in the ER membranes (**Fig S1A-C**). Confocal detection of immunolabeled TRPM8 and ATP synthase F0 as a marker of mitochondria (**Fig. 2A**) in LNCaP C4-2b cell line revealed that some of the TRPM8 "clusters" are associated with mitochondria, while the others do not. We have previously demonstrated that in short term cultures (< 6 days after cell isolation) the endogenous level of the expression of TRPM8 proteins in prostate epithelial cells is higher than during long-term culturing and than inLNCaP cell line. Immunodetection of endogenous TRPM8 in these cells revealed a "network"-like pattern consistent with the ER structure (Bidaux et al, 2007). The fluorescence image processing revealed inhomogeneity in this "network" and colocalization of the TRPM8-enriched ER elements and mitochondria (**Fig. 2B**), suggesting the expression of native TRPM8 in mitochondria associated membranes (MAMs) of the ER. More direct demonstration of MAMs was achieved with transmission electronic microscopy (TEM). In electron micrographs of LNCaP C4-2b cells mitochondria are seen to be closely associated with the ER tubular network (**Fig. 3A**), so that on enlarged image fragments (Fig. 3B-C) the membranes of mitochondria are virtually fused with the membranes of some ER tubules. Using high-pressure freezing substitution (HPF/FS) and immuno-electron microscopy we conducted the detection of Calnexin (**Fig. 3D**).

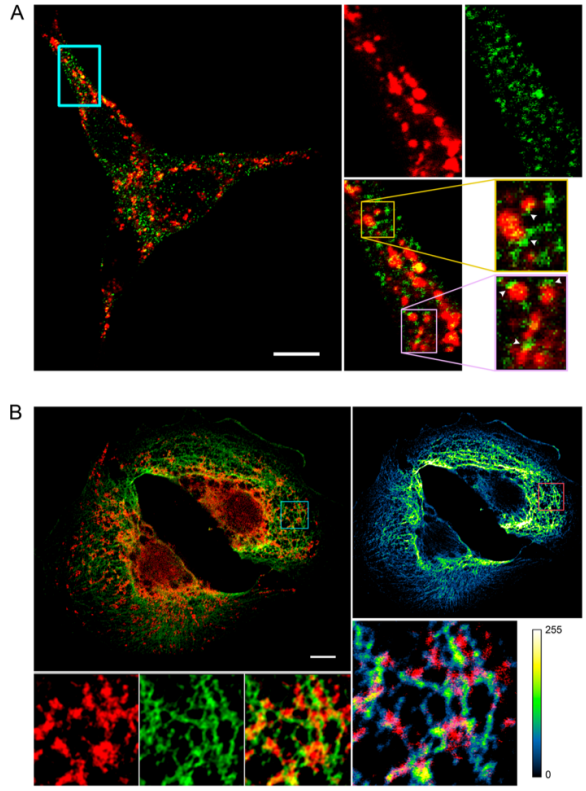

FIGURE 2. *Immunodetection of TRPM8 in LNCaP C4-2b cells reveals "hotspots" in the ER membranes in close association with mitochondria.* **A,** Immunofluorescence confocal image of three LNCaP C4-2b cells (left) demonstrates the co-detection of TRPM8 (green) and ATP synthase (red). The gallery on the right shows enlarged images of red (top left) and green (top right) fluorescence from the boxed (cyan box, left) region, and their overlay (bottom left), as well as further enlargement of the boxed (yellow and magenta boxes) regions (bottom right). White arrowheads point to juxtapositions of TRPM8 (expressed in the ER) and ATP synthase (expressed in mitochondria). Scale bar: 1 µm. **B,** Immunofluorescence confocal image of two epithelial cells freshly isolated from human prostate (top left) shows a co-detection of the TRPM8 (green) and ATP synthase (red). The gallery (bottom left) shows enlarged images of red and green fluorescence from the boxed (cyan box, top left) region, and their overlay (from left to right, respectively). Representation of the green fluorescence image with "green-fire-blue" lookup table (see color scale bar) highlights non-uniformities in the TRPM8 distribution (top right). The overlay of the enlarged images of red fluorescence and "green-fire-blue"-coded green fluorescence from the boxed region (cyan and red boxes, respectively) intensifies correlation in spatial distribution of the TRPM8-enriched ER microdomains and mitochondria. Scale bar: 5 µm. Experiments has been performed three times independently.

Simultaneous detection of Calnexin and HA-tagged TRPM8(17'-28), coding for TRPM8-38 and TRPM-35 isoforms (**Fig. 3E-G**), often revealed both molecules in

ARTICLE 13

MAMs, although Calnexin and TRPM8 were also detectable in membranes of the ER elements more distant from mitochondria.Another line of evidence confirming localization of TRPM8 isoforms in MAMs was obtained from cell membrane fractioning experiments followed by a separation of organelles on Iodixanol gradient.

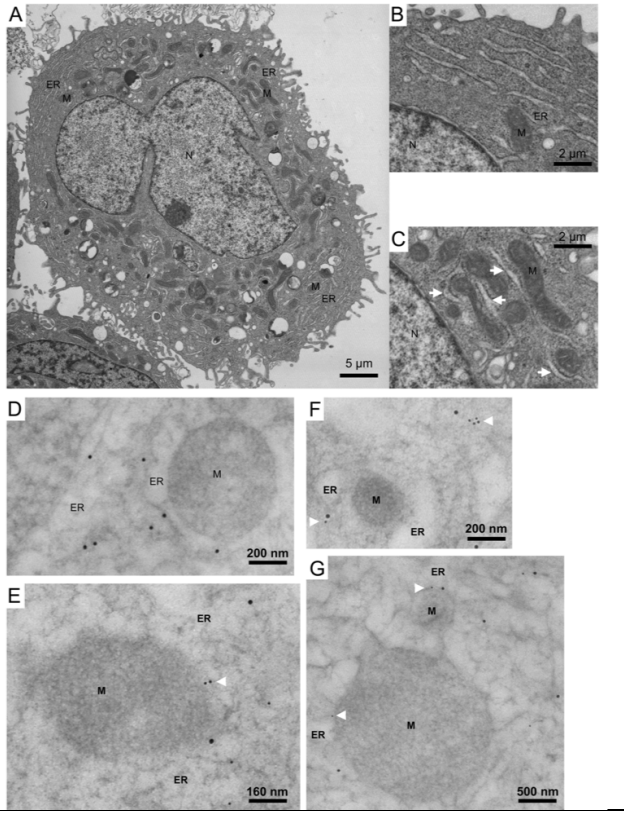

FIGURE 3. *Ultrastructural and immunogold TEM reveals localization of TRPM8-35 in ER membranes in close association with mitochondria in LNCaP C4-2b cells.* **A,** Ultrastructural TEM micrograph shows the nucleus (N), endoplasmic reticulum tubules (ER) and mitochondria (M) in LNCaP C4-2b cell. **B-C,** Higher magnification TEM micrographs from the same call highlights close associations (white arrows) between the endoplasmic reticulum cisternae and mitochondria. **D-G,** Immunogold labeling of calnexin (antibody conjugated to big gold particles) and TRPM8-35-HA (anti-HA antibody conjugated to small gold particles) detect Calnexin but no TRPM8 in the ER membranes of non-transfected cells (**D**). In TRPM8-35-HA overexpressing cells (**E-G**), TRPM8 can be seen in close proximity with calnexin (white arrow heads) suggesting its expression in the ER membranes. Note that both Calnexin and TRPM8-35 were observed in close proximity to mitochondria (white arrow heads; **F** and **G**).

We assessed the presence of TRPM8 proteins, ER marker (Calnexin), Golgi apparatus marker (Golgin 97) and mitochondria marker (VDAC) in these fractions with immunoblotting (**Fig. 4A**). Both TRPM8-35 and TRPM8-40 isoforms were detected at high level in the mitochondria-enriched fractions rich in VDAC and poor in Golgin 97. The full-length classical TRPM8, identified in total membrane protein extract, was not detected in any of the organelles-enriched fractions. Note that TRPM8-38 and calnexin were detected indistinctively in all organelles-enriched fractions, demonstrating the presence of the ER membranes others than the ones purified in the microsomal fraction. Altogether these observations suggest that either (1) TRPM8-40 and TRPM8-35 isoforms are expressed in mitochondria or (2) these TRPM8 isoforms are expressed in the ER membranes tightly associated with mitochondria, i.e. MAMs, which do not segregate with microsomes in our cell membrane fractioning experiments. Although TRPM8-35 was never observed inside mitochondria in TEM images (**Fig. 3D-G**), to discriminate further between these two possibilities we performed immunodetection of TRPM8 and ATP synthase in the organelles-enriched fraction F1 (**Fig. 4A**) set on a polylysin-pretreated glass slide. No significant spatial overlap in the fluorescent signal from the two molecules was detected in the projections of the 3-D reconstructed image, indicating that TRPM8 is not localized in mitochondria (**Fig. 4B**) and is rather expressed in MAMs.

To assess the ER-mitochondrial coupling in living prostate cells, we analysed the motility of these organelles in LNCaP C4-2b cells. The ER and mitochondria were stained with Brefeldin A BODIPY 558/568 and MitoTracker® Green FM (MTG), respectively (**Fig. 4C**), and motility of the two organelles (see Supplementary Animation) was visualized using *x-y* time series confocal imaging. The local maxima of the MTG and Brefeldin A BODPY fluorescence within two regains of interest (**Fig. 4D**) were computed and their time-depended displacements were analysed. This revealed extremely high correlation in the step-by-step displacements of the ER elements and adjacent mitochondria (**Fig. 4E**). Such a coordinated motility of the two organelles implies that mitochondria are "anchored" to the adjacent ER elements. Summing up, the above results unequivocally demonstrate that the membranes of mitochondria and the ER are tightly coupled and that the TRPM8 isoforms are expressed in microdomains of the ER membrane associated with mitochondria, i.e. MAMs (for review see (Giorgi et al, 2009)), as well as in the membranes of the ER distant from mitochondria.

TRPM8 isoforms are functional channels in MAMs of prostate cancer epithelial cells.

As TRPM8 is a Ca^{2+}-permeable ion channel (Thebault et al., 2005), we hypothesized that the expression of TRPM8 isoforms in MAMs may serve to couple the TRPM8-mediated Ca^{2+} release from the SR to mito
chondrial Ca^{2+} uptake. To test this hypothesis we stimulated the cell with TRPM8 agonists, menthol an icilin, and monitor changes in cytosolic and mitochondrial Ca^{2+} concentration ($[Ca^{2+}]$). Several previous studies have demonstrated that menthol or icilin application in LNCaP cells triggers Ca^{2+} release from the ER (Thebault et al, 2005; Zhang & Barritt, 2004). This Ca^{2+} release could be the result of activation of either full-length classical TRPM8 or TRPM8 isoform(s), or both. In order to discriminate between these possibilities, we analyzed the effects of the TRPM8 knocked down or TRPM8-35 overexpression on the TRPM8-mediated Ca^{2+} responses.
.

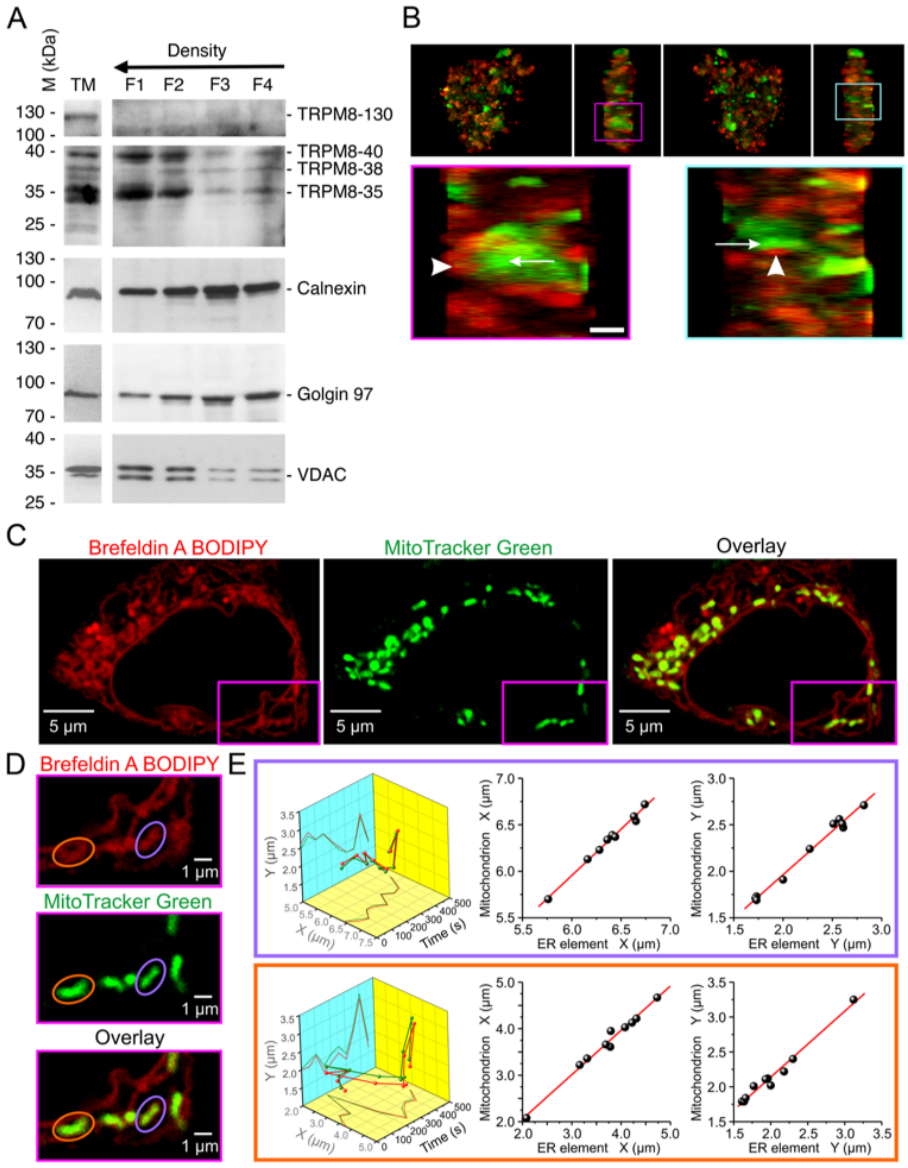

FIGURE 4. *The ER-mitochondria coupling in PCa epithelial cells: mitochondria-associated membranes (MAMs) of the ER are enriched with TRPM8 isoforms.* **A,** Immunoblotting of TRPM8, Calnexin (the ER marker), Golgin-97 (the Golgi apparatus marker) and voltage-dependent anion channel, VDAC (the mitochondrial marker) reveals a distinct pattern of expression either in total membrane protein extract (TM) or in Iodixanol gradient-purified organelles-enriched membranes of LNCaP C4-2b cells. The heaviest fraction (F1) is primarily formed by mitochondrial and associated ER membranes, while the lightest fraction (F4) is mainly composed of Golgi membranes. 80 µg of proteins were loaded for each fraction. **B,** The result of the confocal z-sectioning of the F1 extract, labeled with anti-TRPM8 (green) and anti-ATP synthase (red), is presented as rotation of the 3-D reconstructed image around *y* axis with 90° step. Enlarged images of the boxed regions are shown below, respectively. Juxtaposition of TRPM8 and ATP synthase is highlighted by the arrow and arrowhead, respectively. **C-E**, Coordinated motility confirms tight coupling between the ER elements and mitochondria in LNCaP C4-2b cell. The ER and mitochondria were visualized using Brefeldin A BODIPY 558/568 and MitoTracker® Green FM (MTG), respectively. The gallery shows confocal images of Brefeldin A BODIPY and MTG fluorescence from a single LNCaP cell, and their overlay, as indicated (**C**). Enlarged images of the boxed region are shown from top to bottom, respectively (**D**). Results of motility analysis, conduced for 2 outlined (orange and violet ellipses in **D**) mitochondria and adjacent ER elements are presented in 2 boxed panels, outlined in corresponding colour (**E**). The *x* and *y* positions of the local maxima of the MTG and Brefeldin A BODPY fluorescence were computed and plotted over time. In each panel (**E**), the 3D plot (left) shows the trajectory of the mitochondrion (green) and adjacent ER element (red) motion. The *x* and *y* positions of the organelles in time are seen in the *X-Y* and *X-Z* projections, respectively. The *x* vs. *x* and *y* vs. *y* positions for each mitochondrion and adjacent ER element are plotted (middle and right, respectively). Linear regression analysis revealed high correlation between the parameters in both cases: R = 0.995, P<0.0001 (top middle); R = 0.994, P<0.0001 (top right); R = 0.992, P<0.0001 (bottom middle); R = 0.989, P<0.0001 (bottom right).

ARTICLE 13

Changes in Ca^{2+} concentration in cytosol ($[Ca^{2+}]_c$) and in mitochondria ($[Ca^{2+}]_m$) were monitored using x-y time series imaging of fluo-4 and rhod-2 fluorescence, respectively, in control and TRPM8 knock-down LNCaP C4-2b cell line (**Fig. 5A and 5B, respectively**), and in control and TRPM8 knock-down human prostate cancer primary culture epithelial cells, PrPCa (**Fig. 5D and 5E, respectively**). The cells were bathed in Ca^{2+}-free solution and stimulated with either 10 µM icilin (**Fig. 5A-B**) or 200 µM menthol (**Fig. 5D-E**) In both cell types, application of the TRPM8 agonist triggered the Ca^{2+} release from the ER and concurrent mitochondrial Ca^{2+} uptake. These responses were virtually completely abolished by the TRPM8 knock-down (**Fig. 5C and F**). Mitochondrial origin of rhod-2 signal was confirmed in separate experiments (**Fig. S3**) where icilin-induced rhod-2 responses were obtained in LNCaP cells stained with MitoTracker® Green FM.

Since knockdown of TRPM8 proteins with siRNA targeting the channel pore region (siM8-20) causes suppression of all TRPM8 channel isoforms, including the full-length one, to demonstrate the specific involvement of TRPM8-35 isoform we compared the mitochondrial Ca^{2+} responses to stimulation with 200 µM menthol in control HEK cells, which do not express TRPM8, and HEK cells expressing TRPM8(17')-encoding vector. While no changes in rhod-2 fluorescence in response to TRPM8 stimulation was observed in HEK cells expressing an empty vector (**Fig. S5A**), the expression of TRPM8-35 isoform resulted in menthol-induced Ca^{2+} uptake into mitochondria (**Fig. S5B**), similar to that observed in human prostate cancer primary culture epithelial cells (**Fig. 5D**). This implies that TRPM8-35 isoform, expressed in MAMs (see Figs 3 and 4A-B), may function as Ca^{2+}-permeable channel which couples Ca^{2+} release from the ER to mitochondrial Ca^{2+} uptake.To directly demonstrate that TRPM8-35 isoform functions as an ion channel we performed patch- clamp recordings of the single channel activity on the giant unilamellar vesicles (GUVs) prepared from the ER-containing membrane fraction produced from HEK293 cells expressing TRPM8-35 isoform. In approximately 1 out of 12 patches we have an activity demonstrating characteristic properties of the TRPM8 channel: stimulation of activity by menthol and a specific TRPM8 agonist ws-12 and sensitivity to TRPM8 inhibitor BCTC (**Fig. 6A and C**, n=9, 7 and 3), while no responses to stimulation by menthol or ws-12 could be observed in the GUVs prepared from control HEK293 cells or the cells expressing TRPM8-35 but in the absence of PiP_2. Further biophysical properties typical of of TRPM8 channel, such as a characteristic voltage-dependence and single channel conductance of 65.1 ± 2.5 pS (n = 12) are presented in **Figures 6D-F**.

The results presented above demonstrates that TRPM8-40 and TRPM8-35 isoforms are expressed as functional Ca^{2+}-permeable ion channel in the MAM compartments of the ER and that activation of this channel couples the ER Ca^{2+} release to the mitochondrial Ca^{2+} uptake

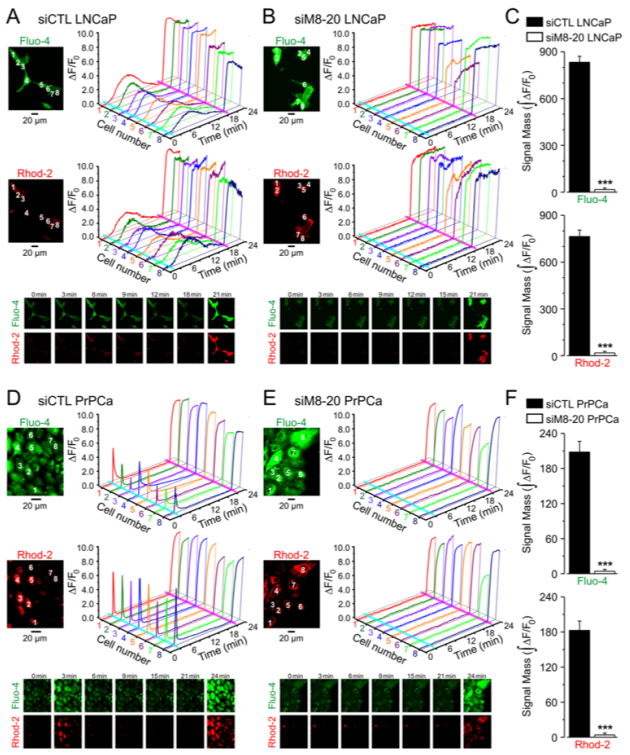

FIGURE 5. *Knockdown of TRPM8 with siM8-20 abolishes the channel-mediated Ca^{2+} fluxes in human prostate cancer cells.* Changes of Ca^{2+} concentration in cytosol ($[Ca^{2+}]_c$) and mitochondria ($[Ca^{2+}]_m$) were monitored in LNCaP cell line, LNCaP C4-2b (**A-B**), and primary culture of human prostate cancer cells, PrPCa (**D-E**), using x-y time series imaging of fluo-4 and rhod-2 fluorescence, respectively. The images were acquired at 0.15 Hz from confocal optical slice below 2 µm. The cells were bathed in Ca^{2+}-free solution and TRPM8 was stimulated with either 10 µM icilin (**A-B**) or 200 µM menthol (**D-E**). The fluorescence intensity (F) was normalized to the averaged fluorescence intensity before TRPM8 agonist application (F_0). Relative changes in the fluorescence intensity ($\Delta F/F_0$), averaged within each of 8 cells, denoted by the numbers on the images (left), are plotted over time, respectively (right). TRPM8 agonist and ionomycin applications are depicted on the 3-D plots by vertical cyan and magenta bars, respectively. The galleries below the plots demonstrate the images of fluo-4 and rhod-2 fluorescence (as indicated) captured at times depicted above the images. Bar diagram plots compare masses, $\int(\Delta F / F_0)$, of the fluo-4 and rhod-2 signals, as indicated, during the period between application of the TRPM8 agonist and application of ionomycin in (**C**) siM8-20 LNCaP cells (n=30) versus siCTL LNCaP cells (n=42), and in (**F**) siM8-20 PrPCa cells (n=41) versus siCTL PrPCa cells (n=59). ***P<0.001.

Does spontaneous basal activity of this channel affects Ca^{2+} homeostasis in the ER and mitochondria? To address this issue we analyzed the effect of TRPM8-40/35 suppression on the steady-state $[Ca^{2+}]$ in the ER and mitochondria of non-stimulated cells. Measurement of the steady-state $[Ca^{2+}]$ in organelles is entangled by the

number of factors, such as a degree of specificity of localization of the probe in particular cellular compartment, variations in the level of the probe accumulation, the probe photostability, etc. (Demaurex & Frieden, 2003).

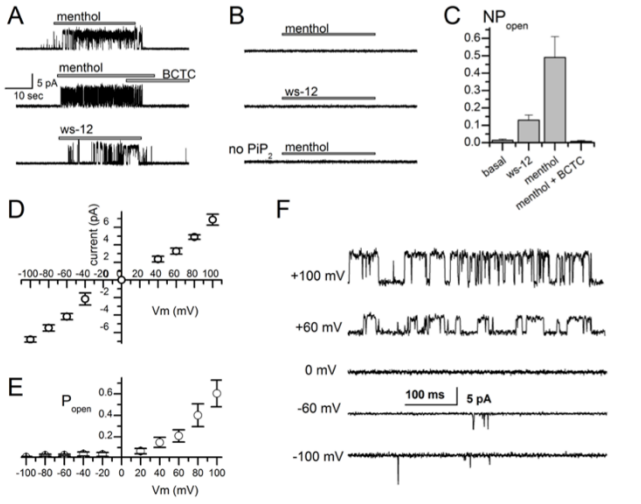

FIGURE 6. *Intracellularly localized TRPM8-35 isoform forms a functional channel in the ER membrane.* **A**. Sample response to 200 μM menthol stimulation followed by wash (upper panel) or 10 μM BCTC application (middle panel) or to stimulation by 10 μM of a specific TRPM8 agonist ws-12 in patches made to artificial liposomes prepared from the ER fraction of HEK293 cells expressing TRPM8-35. **B**. Sample responses to stimulation by 200 μM menthol (upper) or 10 μM ws-12 (middle panel) in patches made to artificial liposomes prepared from the ER fraction of control HEK293 cells show absence of characteristic activity. Similarly, no response was observed in artificial liposomes prepared from TRPM8-35 expressing HEK293 cells upon stimulation by menthol but in the absence of PiP_2 . The mean levels of activity of TRPM8-35 upon stimulation are summarized in panel **C**. **D**. Dependence of the amplitude of the single-channel current on command voltage. Individual points show mean ± S.E.M. current amplitudes at the indicated voltages (n = 12). Straight line presents a linear fit yielding the mean channel conductance of 65.1 ± 2.5 pS. **E.** NP_{open} representing average level of TRPM8-35 activity as a function of the applied voltage (n = 12). Note the characteristic dependence of open probability on the command potential. Sample activity of TRPM8-35 at different potentials, indicated on the left, is presented in panel **F**.

Development of genetically encoded probes provided assurance on their organelle-specific localization and significantly minimized complications caused by variations in the level of accumulation of a Ca^{2+}-sensitive probe in particular organelle. The effect of this "concentration artifact" can be completely eliminated by the use fluorescence lifetime imaging microscopy (FLIM), which derives ionic concentration from the decay in the lifetime of the dye fluorescence rather than the fluorescence intensity (Agronskaia et al, 2004; Lakowicz, 1996; Szmacinski & Lakowicz, 1995). Furthermore, FLIM is widely used as an efficient marker to visualize Fluorescence Resonance Energy Transfer (FRET) and thus can be performed on Cameleon Ca^{2+} biosensors. Improved variants of Cameleon are less sensitive to pH and less prone to interact with wild type calmodulin than those initially available on the market (Miyawaki et al, 1999). In order to measure the steady-state $[Ca^{2+}]$ in the ER ($[Ca^{2+}]_{ER}$) and mitochondria ($[Ca^{2+}]_m$) of LNCaP C4-2b cells, we performed time-domain FLIM using time-correlated single photon counting (TCSPC) approach on Cameleon biosensors expressed either in ER, D1ER (Palmer et al, 2004), or in mitochondria, MitoCam-conjugated 4mTM3cpv (Palmer et al, 2006). Although cyan variant of green fluorescent protein (CFP) displayed a bi-exponential lifetime (Tramier et al, 2002), we estimated the mean lifetime, τ_{mean}, in each pixel of the FLIM images using the phasor plot method (Digman et al, 2008) and a custom-developed software (Leray et al, 2009). To account for variations in the lifetime between the samples, we calculated the averaged τ_{mean} for every single cell and performed statistical analysis. In these experiments, LNCaP C4-2b cells were transfected with siRNA for 3 days and with plasmids encoding Cameleon biosensors (D1ER or MitoCam) for 24h before FLIM was commenced (**Fig. 7A**). We found that suppression of the full-length TRPM8 (siM8-7) did not alter the averaged lifetime of MitoCam: 2.37 ± 0.08 ns (siCTL) vs. 2.38 ± 0.08 ns (siM8-7). The averaged lifetime of D1ER was slightly reduced by suppression of the full-length TRPM8 (siM8-7): from 2.61 ± 0.08 ns (siCTL) to 2.47 ± 0.08 ns (siM8-7) (**Fig. 7B**). Simultaneous knockdown of the full-length TRPM8 and TRPM8-40/35 isoforms (siM8-20) significantly increased the averaged lifetime of Cameleon fluorescence in mitochondria (2.49 ± 0.06 ns) and decreased the averaged lifetime of Cameleon fluorescence in ER (2.42 ± 0.06 ns).

In a two-component system (free and bound donor), the mean fluorescence lifetime depends on the two factors, the FRET efficiency (E) and the fraction of donor (f_D) that undergoes FRET, the relative effect of which is impossible to determine in the case of a multi-lifetime donor like CFP. To overcome this problem we used an alternate method based on calculation of the minimal percentage of donor molecule involved in FRET, mf_D (Leray et al, 2013; Padilla-Parra et al, 2008) from τ_{mean}. For a biosensor with equal quantity of donor and acceptor of FRET, mf_D corresponds to the minimal fraction of ligand-bound biosensor, which is directly proportional to the ligand concentration, namely $[Ca^{2+}]$. Calculated mf_D revealed a significant increase of the steady-state $[Ca^{2+}]_{ER}$ in LNCaP C4-2b cells transfected with siM8-7 (mfD = 35 ± 5 %) or with siM8-20 (mf_D = 40 ± 4 %) vs. the cells transfected with siCTL (mf_D = 26 ± 5 %) (**Fig. 7A** and **7C**). While the steady-state $[Ca^{2+}]_m$ was not altered by the knockdown of the full-length TRPM8, it was significantly decreased by simultaneous knockdown of the full-length TRPM8 and TRPM8-40/35 isoforms: mf_D = 42 ± 5 % (siM8-7) and mf_D = 34 ± 4 % (siM8-20) vs. mf_D = 43 ± 5 % (siCTL), respectively. These results strongly suggest that TRPM8-40/35 channels are endogenously active in the ER membranes and participate in the regulation of the steady-state $[Ca^{2+}]$ in mitochondria and the ER of prostate cells.

ARTICLE 13

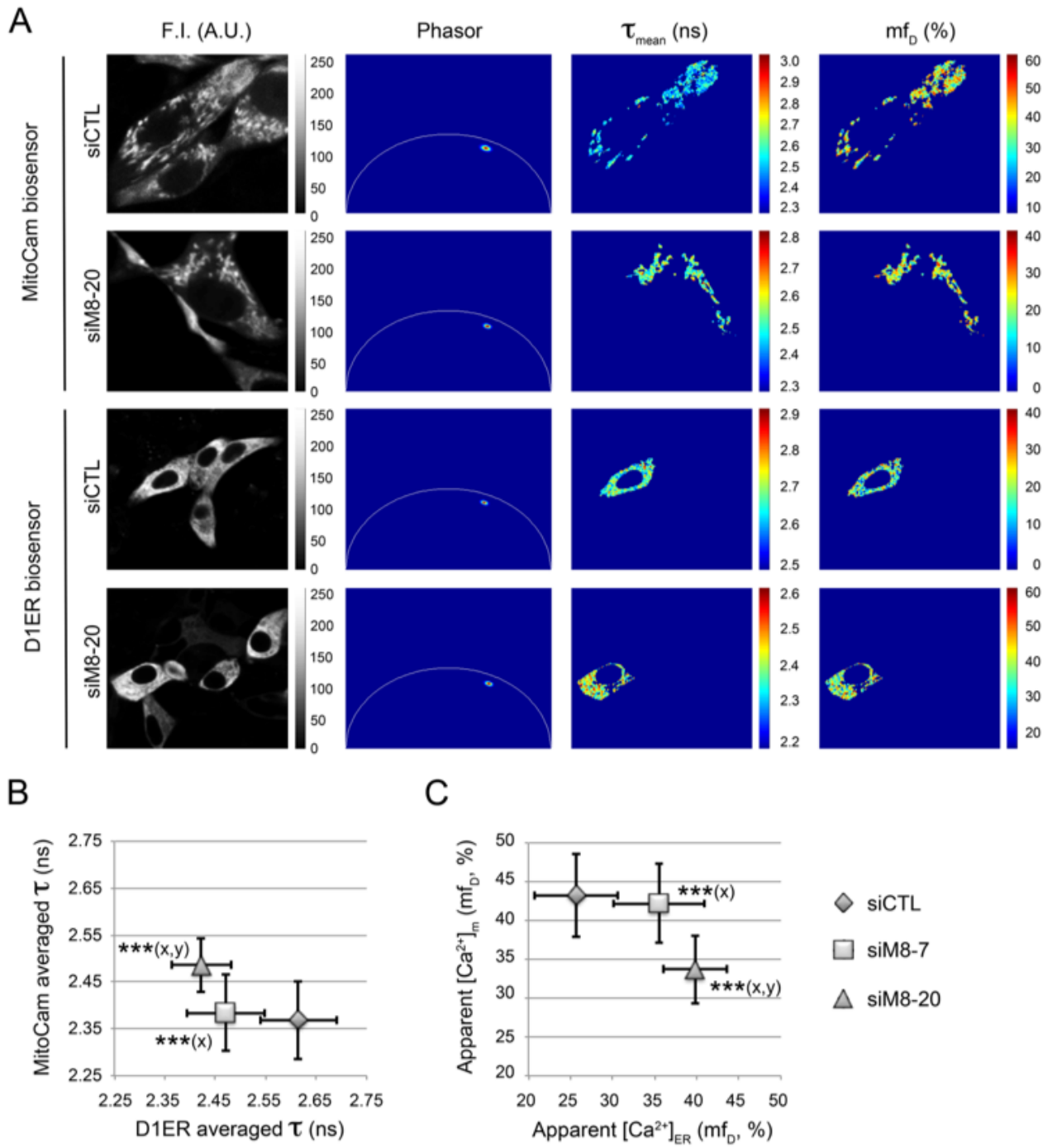

FIGURE 7. *Knockdown of TRPM8 isoforms impairs calcium homeostasis in both mitochondria and ER.* **A,** $[Ca^{2+}]$ in mitochondria and the ER was assessed by measuring FRET with the time-domain fluorescence lifetime imaging microscopy (TM FLIM) in LNCaP C4-2b cells transfected concomitantly with siRNA and plasmids encoding either ER targeted Camelon biosensor (D1ER) or mitochondria-targeted Cameleon biosensor (MitoCam). Time-correlated photon counting (TCSPC) approach was chosen to achieve a good spatial resolution, which would allow discriminating between the organelles. Gray-scale coded fluorescence images (fluorescence intensity in arbitrary units) were analyzed by the phasor plot method (Phasor) to compute FLIM images (τ_{mean}) showing the mean lifetime, recalculated pixel-by-pixel from TCSPC histograms and images of the minimal fraction of Ca^{2+}-bound Cameleon (mf_D). **B,** Histogram shows the averaged distribution of cells as a function of Cameleon lifetime in both the ER and mitochondria. LNCaP C4-2b cells have been transfected with control siRNA (siCTL) or siRNA targeting full length TRPM8 (siM8-7) or siRNA targeting TRPM8 and TRPM8-35 (siM8-20) for 3 days. **C.** Histogram shows the averaged distribution of cells as a function of apparent calcium concentration in mitochondria ($[Ca^{2+}]_m$) and endoplasmic reticulum ($[Ca^{2+}]_{ER}$), as estimated by the minimal fraction of Ca^{2+}-bound Cameleon biosensor (mf_D, %). * $p<0.001$. (x) or (x,y) statistical significance in x axis, or x,y axes.

The increase of the $[Ca^{2+}]_{ER}$ by the knockdown of TRPM8-40/35 isoforms, but not by the knockdown of the full-length TRPM8, was confirmed in independent experiments, where Ca^{2+} releasable from the ER of the fura-2-loaded LNCaP C4-2b cells in response to application of 5 µM ionomycin was used as a measure of the ER Ca^{2+} load. This revealed that the amplitude of the ionomycin-induced $[Ca^{2+}]_i$ transient was significantly increased in the cells transfected with siM8-20, but was not altered in the cells transfected with siM8-7.

In conclusion, we demonstrated that TRPM8-40 and TRPM8-35 isoform forms a 4 transmembrane domain Ca^{2+}-permeable channel, which is expressed in the MAMs of prostate cancer cells and participates in calcium homeostasis of the ER and mitochondria.

DISCUSSION

In the current study we report on 3 major findings. First, as we cloned and characterized N-terminal truncated TRPM8 channels in prostate cells. Surprisingly, the 4 transmembrane domain (TM) structure of TRPM8-35 and TRPM8-38 diverges from the TRP archetype (6TM). Second, these isoforms are residents of ER membranes and are spread in mitochondria associated membranes (MAMs) and in a second type of microdomain away from mitochondria. Third and last, TRPM8-agonists induce ER Ca^{2+} release dependent of TRPM8-35 isoform and this isoform participate to the definition of the steady-state $[Ca^{2+}]$ in mitochondria.

Novel archetype of TRP channel as tool to understand structure-activation of TRP channels. For 15 years TRP channels have been characterized as tetramers of 6 TM proteins. However, the number of TM varies greatly among all channel families: 2 TM for the epithelial Na+ channel, ENaC (Giorgi et al, 2009), 4 TM for 2 pore K^+ channel, TWIK-1 (Lesage et al, 1996), 6 TM for voltage-gated K^+ channels (Santos et al, 2012), 7 TM for large-conductance Ca^{2+}-activated K^+ (BK) channel (Atkinson et al, 1991). Behind this apparent diversity of channel structures, every gene has been thought to encode a single channel archetype and consequently diversity is based on different genes. TRPM8 was reported to follow this rule, although we showed that the *trpm8* gene also codes for truncated non-channel proteins (Bidaux et al, 2011; Fernandez et al, 2011). In this study, we reveal that a diversity of channel structures is also encoded in the alternate transcripts of a single gene.

Studying comparatively different kind of TRPM8 channels gives new insights in the relationship between structure and activation/inhibition mechanisms. The structural difference between full-length TRPM8 and TRPM8-35 isoform is important regarding their apparent sizes (130 and 35 kDa, respectively) and regarding the loss of specific domains, TM1 and TM2, in TRPM8-35. In this study, we demonstrated that TRPM8-35 is a functional channel *per se*. This implies that its 4TM structure may be consider as a minimal channel structure. Along this line, TRPM8-35 activation with menthol demonstrates that neither N-terminal loop, TM1 nor TM2 are required. This looks like paradoxical since Bandell *et al* suggested that menthol could interact with S2 (Bandell et al, 2006). Nevertheless, menthol-mediated activation of TRPM8 is a complex mechanism that could involve different domain of the channel. Indeed, the TM4 voltage-sensor (Voets et al, 2007) and the C-terminus (Bandell et al, 2006; Brauchi et al, 2006) are involved in menthol-mediated TRPM8 activation, even though they did not impaired TRPM8 sensitivity to menthol. Furthermore, we demonstrated that the interaction of short non-channel isoforms with the C-terminus of TRPM8 could partially inhibit menthol-mediated TRPM8 activation (Bidaux et al, 2011; Fernandez et al, 2011) while it did not impair iciline-mediated TRPM8 activation. Consequently, we suggest that, although menthol activation may indeed involve a binding pocket localized between TM1 and TM2 in full length TRPM8, it also requires another mechanism requiring a conformational coupling between the C-terminus and the p-helix. In the light of these data, TRPM8-35 activation by menthol appears fathomable.

TRPM8-35 isoform is a functional resident of MAMs. Except its structure, another striking feature of TRPM8-35 isoform comes from its localization in the so-called mitochondria-associated membranes (MAMs), which are ER microdomains in close association with mitochondria. We recently proposed that one TRPM8 isoform showing this 4 TM archetype, TRPM8-40, is expressed and functional in ER microdomains of keratinocytes (Bidaux et al, unpublished data). On the one hand, MAMs are essential for the functional coupling between ER Ca^{2+} stores and the fine-tuning of the Ca^{2+} concentration in mitochondria, $[Ca^{2+}]_m$ (Ishii et al, 2006; Rizzuto et al, 2004; Shkryl & Shirokova, 2006). $[Ca^{2+}]_m$ is an essential regulator of the activity of the tricarboxylic cycle(Denton et al, 1980; Hansford & Zorov, 1998; McCormack & Denton, 1980) that consecutively modifies the rate of ATP synthesis (Jouaville et al, 1999). Moreover, MAMs could be involved in the lipid metabolism of ceramids (Bionda et al, 2004), phospholipids and fatty acid (Rusinol et al, 1994). Consequently, they could participate to the secretory pathways connecting ER to Golgi by regulating the assembling of apolipoprotin B (Rusinol et al, 1994). Nowadays, only inositol trisphosphate receptors (InsP3R) have been postulated to primarily regulate $[Ca^{2+}]_m$ via tight ER-mitochondria connections (Robb-Gaspers et al, 1998a; Robb-Gaspers et al, 1998c). On the other hand, full length TRPM8, these latter could be endogenous lipids such as phosphatidylinositol 4,5-bisphosphate, PiP_2 (Brauchi et al, 2007; Rohacs et al, 2005), lysophospholipids, LPLs (Vanden Abeele et al, 2006b) which activate TRPM8 and polyunsaturated fatty acids, PUFAs reported as TRPM8 inhibitors (Andersson et al, 2007). By analogy with TRPM8 regulation by lipids, and due to its localization in MAMs TRPM8-35 might participate in cell bioenergetics, lipid metabolism or both.

TRPM-35 isoform in prostate. The *trpm8* gene was historically assumed to code for the cold and menthol receptor in the neurons of the dorsal root ganglia. It is, however, very unlikely that epithelial prostate cells have to sense cold or others external stimuli. We thereby assumed that TRPM8-35 would probably be endogenously regulated. This hypothesis is supported by the modification of Ca^{2+} homeostasis in the mitochondria and ER of TRPM8 knockdown prostate cells. We hypothesized that TRPM8-35 behaves as an ER leak Ca^{2+}

channel, meaning it is autonomously activated by intracellular signals, and that it directly participates to the definition of the Ca^{2+} concentration in mitochondria. It should be further studied whether TRPM8-35 isoforms might promote bioenergetics and/or lipid metabolism in prostate cancer cells and could consequently be used as a target in anti-cancer therapies.

MATERIALS AND METHODS

Cell line culture. LNCaP and PC-3 cell lines have been purchased from the American Type Culture Collection (ATCC). LNCaP C4-2b cell line was a generous gift from Dr. F. Cabon, Paris. Cells have been amplified in RPMI medium 1640 (Gibco®) supplemented with 10% FCS and kanamycin (100 µg/ml).

Primary culture of epithelial cells from human prostate resection specimens. Human prostate tissue specimens have been obtained from resection surgeries performed on clinical indications in the Urology Department at Hôpital St Philibert (Lille, France). All tissue specimens came from patients who had not received any anti-androgen therapy. In addition, all resection specimens have been diagnosed by an anatomopathological examination. After patient surgery, the conjunctive tissues were eliminated and the epithelial nodules were cut into small fragments of about 1-2 mm^3 in a 100 mm diameter dish filled with 3 ml of RPMI medium 1640 (Gibco®). Explants have been plated in KSF medium (Keratinocyte Serum-Free; Gibco-BRL) containing 2% fetal bovine serum and antibiotics (100 mg/ml kanamycin, 100 mg/ml gentamycin), supplemented with 50 mg/ml bovine pituitary extract and 50 ng/ml epidermal growth factor in 100 mm diametercoated dishes (Nunc). Epithelial cells were amplified as primary culture for at least 4 weeks. Alternatively, freshly isolated epithelial cells have been prepared as reported elsewhere (Bidaux et al, 2005). All experiments on human tissues have been performed according to the "CP 01/33" regulations issued by the "Comité Consultatif de Protection des Personnes dans la Recherche Biomedicale de Lille" (CCPPRB).

Transfection. Plasmid transfection was carried out with X-tremeGENE HP DNA Transfection Reagent (Roche) at the concentration of 4 µg per million cells. Transfection of 50 nM siRNA was achieved with HiPerfect transfection reagent (Qiagen). Sense sequences of siRNA were: 5'-CUUACGCUGAGUACUUCGAdTdT-3' for the control siRNA targeted Luciferase (siLuc), 5'-UCUCUGAGCGCACUAUUCA(dTdT)-3' for the siRNA anti-TRPM8 targeted exon 7 (siM8-7) and 5'-UAUUCCGUUCGGUCAUCUAdTdT-3' for the siRNA anti-TRPM8 targeted exon 20 (siM8-20).

5'-RACE-PCR. 5'-extremities of TRPM8 mRNAs were cloned with SMART RACE-PCR as described previously (Bidaux et al, 2011). cDNA has been amplified with a TRPM8-specific primer (5'-GGTGCCCACCGTGTAGCCAA-3') and the universal primer targeting the 5'-adaptor. After cleaning up the PCR products (Nucleospin extract II, Macherey Nagel), a Nested-PCR has been performed with Phusion Hot Start II High-Fidelity DNA Polymerase (Takara) on 1 µl of RACE purified DNAs. Amplicons have been visualized on agarose gels with SYBER® Green (Invitrogen) on a Dark reader transilluminator (Ozyme). DNA has been extracted prior to terminal adenylation and cloned in pGem-T easy vector (Promega). Colonies have been controlled by EcoR I digestion and positive plasmids have been sequenced.

Cloning of TRPM8 mRNAs. 3 µg of Human prostate mRNA have been reverse transcribed with PrimeScript Reverse Transcriptase (Takara). Specific primers (see **Table 1**) targeting the new 5'-extremties of TRPM8 mRNAs have been used to amplify Human prostate cDNA with Phusion Hot Start II High-Fidelity DNA Polymerase (Takara). PCR products have been ligated in pGem-T easy vector (Promega) before transformation in JM109 chemo-competent bacteria. TRPM8 DNAs have been transferred from pGem-T easy vector to pcDNA4.TO.A vector (Invitrogen) with a double Sac II/Not I restriction.

HA-tag fusion proteins. HA-tagged TRPM8 isoforms have been generated by PCR with a forward PCR oligonucleotide including a Not I restriction site and the endogenous Kozak sequence of original mRNA, plus a backward degenerated PCR oligonucleotide incorporating an in frame HA sequence followed with a Xho I restriction site. PCR products have been digested overnight at 37°C with Not I and Xho I restrictases. After an agarose gel purification, TRPM8 DNAs have been extracted with Wizard® SV gel (Promega) and consecutively ligated in pcDNA4.TO.A vector with a T4 ligase (New England Biolabs) overnight at 4°C. After transformation in JM109 chemo-competent bacteria, plasmids were extracted and checked by sequencing.

Quantitative real-time PCR analysis. After total mRNA extraction and purification with TRI REAGENT® (Sigma-Aldrich), mRNA have incubated with 0.25 µl DNAse (Ambion) per µg of RNA for 25 min at 25°C. Afterwards, mRNA have been mixed in a V/V phenol/chloroform/AIA solution (Fluka) with 5% Sodium Acetate 3 M, incubated for 20 min on ice and finally centrifuged at 15,000 xG for 10 min. The upper phase, transferred in a clean 1.5 ml tube, has been completed with 0.1 Volume of Sodium Acetate 3M and 2.5 Volume of 100% Ethanol. After vortexing, tubes have been incubated at -20°C overnight to precipitate mRNA. After a brief wash in 70% Ethanol, pellets were left to dry and then re-suspended in 30 µl water. After checking of mRNA quality on agarose gel, 2 µg of mRNA have been reverse transcribed as reported elsewhere (Gackiere et al, 2006). Real-time quantitative PCR has been performed on a Cfx C1000 system (Biorad). For each reaction, 12.5 ng of cDNA has been placed in a final reaction mixture of 15 µl containing 7.5 µl of 2x SsoFast™ EvaGreen® Supermix (Biorad) and 200 nM primer pairs (see **Table 1**). The housekeeping gene Glyceraldehyde-3-phosphate dehydrogenase (GAPDH) has been used as an endogenous control to normalize gene expression with the comparative ΔΔCt method (Livak & Schmittgen, 2001). The PCR protocol was: an initial 30 sec denaturation step at 95° C, and 40 cycles of [4 sec at 95° C, 30 sec at 60° C] and a final dissociation curve to control the specificity of the amplification.

Purification of mitochondria and associated microdomains of endoplasmic reticulum membranes. Methods has been described elsewhere (Shapovalov et al., manuscript submitted for publication). Briefly, 5 to 10 75cm^2-flasks of LNCaP C4-2 cells have been mechanically detached in PBS solution, pelleted by centrifugation at 250 ***g***, 4°C for 10 min and consecutively suspended in 5 ml of solution B (0.85% (w/v) NaCl, 10 mM Tricine-NaOH, pH 7.4). After mechanical disruption of cells with a glass potter homogenizer in 5 ml of solution B, the lysate was filled to 30 ml with solution B before centrifugation at 500 ***g***, 4°C for 15 min (*step 1*). The resulting pellet has been suspended in 5 ml of solution B and centrifuged at 1,000 ***g***, 4°C for 10 min. Top pellet resulted from the accumulation of free nuclei (post-nuclear fraction), while bootom pellet resulted from non-disrupted cells. The supernatant of *step 1* has been centrifuged once more at 500 ***g***, 4°C for 15 min and the resulting pellet thrown away. The supernatant was centrifuged at 17,000 ***g***, 4°C for 20 min, and the resulting pellet has been suspended in 1 ml of solution B prior to be loaded on 10%:30% Iodixanol gradient prepared with OptiPrep™ Density Gradient Medium (SIGMA). Tubes were centrifuged on a SV40 rotor at 100,000 ***g***, 4°C for 2h. Four visible rings of biological matter were divided in four fractions (from 1 to 2 ml), completed with 6 ml of HEPES buffer and subjected to a second ultracentrifugation on a 50Ti rotor at 100,000 ***g***, 4°C for 1h. All pellets isolated from the whole procedure have been either solubilized in an ice-cold buffer (as described in immunoblotting section, below) and sonicated prior to perform immunoblotting, or dried-out before solubilization in a 1:3 methanol/chloroform solution in order to incorporate proteins in GUV as described elsewhere (Shapovalov et al., manuscript submitted for publication)

Immunoblotting. An ice-cold buffer (pH 7.2) containing 10 mM PO4Na2/K buffer, 150 mM NaCl, 1 g/100 ml sodium deoxycholate, 1% Triton X-100, 1% NP40, a mixture of protease inhibitors (Sigma-Aldrich), and a phosphatase inhibitor (sodium orthovanadate; Sigma-Aldrich) has been applied to previously PBS-washed cells in dishes. After 30 min incubation on ice, the protein extract has been transferred to 1.5 ml tubes and subjected to sonication. After 10 minutes of centrifugation at 15,000 g, the pellet has been transferred into a clean tube prior to a determination of the protein concentration using a BCA Protein Assay (Pierce). 25 µg of total protein have been loaded onto a 10% polyacrylamide gel before an SDS-page has been performed. After electrophoresis, proteins have been transferred to a Polyvinylidene Difluoride (PVDF) membrane using a semi-dry electroblotter (Bio-Rad). The membrane has been blocked in a TNT +5% (W/V) milk (15 mM Tris buffer, pH 8, 140 mM NaCl, 0.05% Tween 20, and 5% non-fat dried milk) for 30 min at room temperature, then soaked in primary antibody diluted in TNT +1% milk for either 2 h at room temperature or overnight at +4°C. After three washes in TNT, the membrane has been soaked in secondary antibody diluted in TNT+1% milk for 1h at room temperature. The membrane has been processed for chemiluminescence detection using Luminata Forte Western HRP Substrate (Millipore) according to the manufacturer's instructions. After a 10 min bath in Re-blot PLus Mild SOlution (Millipore), membrane has been blotted again. The primary antibodies were: rabbit anti-TRPM8 (Ab109308, Abcam), rabbit anti-HA tag (Ab9110, Abcam), mouse anti-Calnexin (MAB3126, Millipore), mouse anti-VDAC (sc-58649, Santa Cruz), and anti-Golgin-97 (A21270, Invitrogen).

Immunofluorescence. Cells have been plated on 35 mm glass bottom dishes (MatTek Inc) and grown in the desired medium. Before immunofluorescence (ICF), cells have been fixed with 4% formalin in PBS for 10 min on ice prior to 3 PBS washes. Afterwards, cells have been subjected to blocking and permeabilization with PBS + 1.2% gelatine + 0.2% Tween + 0.2M glycine for 30 min at 37°C. The cells have then been incubated with primary antibodies 2 h at 37°C. After thorough rinsing in PBS/gelatine, the dishes have been treated with the corresponding secondary antibody: either Dye light 488-labeled anti-rabbit IgG (Jackson ImmunoResearch; dilution, 1/2000) or Alexa fluor 546-labeled anti-mouse IgG (Molecular Probes; dilution, 1/4000) diluted in PBS/gelatine for 1 h at ambient temperature. After rinsing twice in PBS/gelatine and once in PBS with 1/200 Dapi for 10 min at ambient temperature, the slides have been mounted with Mowiol® and examined under a confocal microscope. The primary antibodies used were: rabbit anti-TRPM8 (Anti-TRPM8(extracellular), Cat.ACC-049, lot.AN-03, Alomone, 2009 batch) and mouse anti-ATP synthase (xxxxxxxxCalbiochem).

Morphology analysis by Transmission Electron Microscopy. For morphology analysis, cells were fixed in 2.5% glutaraldehyde dissolved in 0.1 M cacodylate buffer and were post-fixed in 1% osmium tetroxide in the same buffer. After acetonitril dehydration, the pellets were embedded in Epon. Serial thin sections (90 nm) were cut using a Leica UC7 ultramicrotome and collected on 150 mesh hexagonal barred copper grids. After staining with 2% uranyl acetate prepared in 50% ethanol and incubation with a lead citrate solution (Reynolds), sections were observed on a Hitachi H-600 transmission electron microscope at 75kV.

High-pressure Freezing, Freeze Substitution (HPF/FS) and Immuno-Electron Microscopy. Cells were scratched and collected by centrifugation at 200g for 5 min. The cell pellet was gently suspended in a low volume of 20% BSA as a cryoprotective agent. The mixture was transferred into the 3 mm specimens carriers (Leica Microsystems Inc, Vienna, Austria), then high-pressure frozen with a Leica EM HPM100 High Pressure Freezer (Leica Microsystems Inc, Vienna, Austria) at -197°C, 210 KPa and maintained under liquid nitrogen.

Samples were then cryo-substituted in a Leica AFS2 system (Leica Microsystems, Vienna, Austria) prior to be transferred under liquid nitrogen to freeze substitution medium consisting of methanol and PAF 0.5%. Samples were thereafter incubated at -85°C for 1h30, and were subsequently warmed to -45°C over a period of 14 hr. Samples were washed three times with 100% methanol prior to embedding in K4M resin. Polymerization was performed under UV light for 36 hr. Ultrathin sections (90nm) were obtained as described above.

ARTICLE 13

For immuno-electron microscopy, sections were incubated in blocking medium (0.2 M glycin, 5% donkey serum, 0.2% BSA-c™, 0.1% fish gelatin in PBS buffer) for 30 min, then with primary antibodies: 1/50 anti-calnexin (MAB3126, Millipore) and 1/30 anti-HA (715500, Invitrogen) overnight at room temperature. After washing, sections were incubated at room temperature for 2 hr in the corresponding secondary gold conjugates (Jackson ImmunoResearch) diluted in PBS + 1.2% gelatin. Following a final thorough wash in PBS alone then in water, sections were stained with 0.5% uranyl acetate for 12 min. Observations were performed on Hitachi H600 transmission electron microscope at 75 kV accelerating voltage.

Wide-field Ca^{2+} imaging. Calcium imaging experiments have been performed as described previously (Thebault et al, 2005). Briefly, $[Ca^{2+}]_c$ was measured using ratiometric dye fura-2 and quantified according to Grynkiewicz equation (Grynkiewicz et al, 1985). The bath solution contained in mM: NaCl 140, KCl 5, $CaCl_2$ 2, $MgCl_2$ 2, Na_2HPO_4 0.3, KH_2PO_4 0.4, $NaHCO_3$ 4, glucose 5, HEPES 10; pH adjusted to 7.3 with NaOH; osmolality 330 mosmol/l.

Confocal microscopy. Experimental chambers with the cells were placed on the stage of Axiovert 200M inverted microscope attached to a LSM 510 META laser-scanning unit (Zeiss, Oberkochen, Germany). The SCSi interface of the confocal microscopes was hosted by a Pentium PC (32-bit Windows NT 4.0 operating system) running LSM 510 software (Zeiss, Oberkochen, Germany). During time series protocol, the x-y confocal images of the fluo-4, rhod-2, Brefeldin A BODIPY 558/568 or MitoTracker Green fluorescence were acquired at 0.1–0.5 Hz using a Zeiss plan-Apochromat 40× 1.3 N.A. or 63× 1.4 N.A. oil-immersion objectives. Fluo-4 and MitoTracker Green fluorescence was excited by the 488 nm line of a 500 mW argon ion laser (Laser-Fertigung, Hamburg, Germany) and was captured at wavelengths 505-530 nm. Rhod-2 and Brefeldin A BODIPY 558/568 fluorescence was exited by the 543 nm line of 15 mW helium/neon ion laser and detected at wavelengths 560-615 nm. The illumination intensity was attenuated to 0.5-6 % (depending on the laser line) with an acousto-optical tunable filter (Zeiss, Oberkochen, Germany). To optimize signal quality the pinhole was set to provide a confocal optical section 0.5–1.8 µm, depending on experimental protocol. To avoid any bleed-through of the fluorescence signal in multi-staining experiments, fluorochromes with well separated excitation and emission spectra were used and imaging was performed using the frame-by-frame multitrack mode of the confocal scanner: sequential acquisition via well-separated optical channels of the x-y images produced by fluorescence of different fluorochromes. The photomultiplier gain and offset in each optical channel were set individually to achieve similar signal intensity at each channel and remove sub-signal noise from the images.

Experimental solutions. In confocal microscopy experiments the cells were bathed in physiological salt solution (PSS) containing (in mM): NaCl 140, KCl 5, $MgCl_2$ 1, glucose 10, HEPES 10; pH adjusted to 7.4 with NaOH. PSS was supplemented with 0.5 mM EGTA or 2 mM $CaCl_2$, depending on experimental protocol, as described in the text.

Visualization of the endoplasmic reticulum (ER) and mitochondria. The ER was visualised using Brefeldin A BODIPY 558/568 (Povstyan et al, 2011; Vanden Abeele et al, 2006a), which was loaded by 20-min incubation of the cells with 2 µM of the dye followed by 1.5-hour wash. The mitochondria were visualised using MitoTracker® Green FM, which was loaded by 30-min of the cells with 2 µM of the dye followed by 30-min wash.

Visualization of agonist-induced changes of Ca^{2+} concentration in cytosol ($[Ca^{2+}]_c$) and mitochondria ($[Ca^{2+}]_m$). Changes of $[Ca^{2+}]_c$ were imaged using the high-affinity fluorescent Ca^{2+} indicator fluo-4, as described previously (Povstyan et al, 2011; Thebault et al, 2005). Fluo-4 was loaded by 1-hour incubation of the cells with 5 µM fluo-4 acetoxymethyl ester (fluo-4 AM; diluted from a stock containing 2 mM fluo-4 AM and 0.025% (w/v) pluronic F-127 in dimethyl sulphoxide). Changes of $[Ca^{2+}]_m$ were imaged using fluorescent Ca^{2+} indicator rhod-2: 50 µg of rhod-2 AM was dissolved in 20 µL of DMSO (containing 0.025% (w/v) pluronic F-127), which was then mixed with 20 mL of PSS and superfused to the experimental chamber for 20 min. The incubation of the cells with the dyes was followed by a 1-hour wash in PSS containing 1.7 mM $CaCl_2$ to allow time for de-esterification. The dye loading was performed at room temperature. The cells were then kept for 30 min at 37ºC. Before imaging was commenced the cells were superfused with PSS containing 70 µM $CaCl_2$ and supplemented with 10 µM $LnCl_3$ to eliminate capacitative Ca^{2+} entry, unless stated otherwise. The cells were stimulated with either 200 µM menthol or 10 µM icilin. The intensity of fluo-4 or rhod-2 fluorescence (F) was normalised to the average fluorescence intensity in the images acquired before agonist application (F_0). The temporal profiles of the agonist-induced $[Ca^{2+}]_c$ and $[Ca^{2+}]_m$ transients are illustrated by the plots showing time course of the normalised fluo-4 or rhod-2 fluorescence intensity (F/F_0) averaged within confocal optical slice of the cell.

Time domain-fluorescence lifetime imaging microscopy (TM-FLIM). For live-cell imaging, cells were placed on 35mm glass bottom dishes (MatTek Corporation, USA), filled with L-15 medium without phenol red (Life technologies), and kept at 37°C using a stage incubator (Life Imaging Services, Switzerland). FLIM was performed with a Leica TCS SP5 X confocal head (Leica Microsystems, Germany) with the SMD upgrade, mounted on an inverted microscope (DMI6000, Leica Microsystems, Germany). A pulsed diode laser, PDL 800-B (PicoQuant GMBH, Germany), delivered 40 MHz repetitive rate pulses at 405nm. The confocal pinhole was set to 1 Airy, for a 0.921 µm optical slice. Single photon events originated from the illuminated voxel were collected through a 63x/1.2NA water-immersion objective and recorded by a TCSPC detector (HydraHarp 400; PicoQuant GMBH, Germany). Fluorescence was detected through a 483/32 single-bandpass filter (Semrock, USA) on Single Photon Avalanche Photodiodes, SPAD (MPD, Italy), set up at 256 x 256 pixels. Arrival time of single photons was

measured with SymPhoTime software (PicoQuant GMBH, Germany) while image were taken with LAS AF software (Leica Microsystems, Germany. In order to obtain the best resolution of organelles, a 5-fold zoom factor was applied, giving a pixel size of 0.193 µm and an image size of 49.21x49.21 µm. Since the statistical determination of the distribution of single photon arrival time requires a minimum of 100 photons per pixel, 120 frames were acquired at 200Hz and summed in the final image.

Preparation of giant unilamelar vesicules (GUVs). Isolation of the ER-containing membrane fraction from eTRPM8 expressing HEK293 cells and preparation of the GUVs were carried out as described elsewhere (Shapovalov et al., manuscript submitted for publication). GUVs were prepared from the 1:5 mixtures of the ER-containig fraction with 10:1 diphytanoylphosphatidylcholine (DPhPC)/cholesterol lipid combination (5 mM). This mixture was supplemented by 0.2 mM phosphatidylinositol 4,5-bisphosphate (PiP_2) in order to sustain TRPM8 activity (Rohacs et al, 2005).

Electrophysiology. For GUVs Patch-clamp experiments, we used Axopatch 200B amplifier and pClamp 10.0 software (Molecular Devices, Union City, CA) for data acquisition and analysis. Patch pipettes were fabricated from borosilicate glass capillaries (World Precision Instr., Inc., Sarasota, FL) on horizontal puller (Sutter Instruments Co., Novato, CA) and had a resistance in the range of 7-10 MΩ. Prepared vesicles were immersed in a bath solution containing, in mM, 150 NaCl, 5 glucose, 10 Hepes, pH 7.2. In order to prevent activity of IP3R and RyR channels, commonly present in ER, this solution was supplemented by 1 mM $MgCl_2$, 1 mM EGTA and 1 µM dantrolene (Nelson et al, 1996). Patch pipettes were filled with the same solution, supplemented by 2 µM PiP_2 and 1 mM MgATP in order to enhance TRPM8 activity (Rohacs et al, 2005).

Data analysis. Each experiment was repeated at least three times and the results were expressed as mean ± S.D. The data were analyzed and graphs plotted using Origin 5.0 software (Microcal, Northampton, MA). InStat3 (GraphPad Software Inc, SanDiego, USA) was used for statistical analysis and mean values were compared using either unpaired t test with Welch's corrected test (2 groups) or One-way ANOVA with Dunnett multiple comparison post-test (≥3 groups). Statistical significance was denoted by (*) for $P<0.05$, (**) for $P<0.01$ or (***) for $P<0.001$.

FOOTNOTES.

This work was supported by grants from INSERM, Ministère de l'Education Nationale, Ligue Nationale Contre le Cancer, the Region Nord-Pas-de-Calais, SIRIC OncoLILLE, Association de Recherche sur les Tumeurs de la Prostate.

Dr. Dmitri Gordienko is supported by SFFR (F 46.2/001).

Dr. Anne-sophie Borowiec is supported by Fondation pour la recherche médicale.

D1ER cameleon and mt Cameleon are generous gift of Prof Tsien R., La Jolla, CA, USA.

REFERENCES.

Agronskaia AV, Tertoolen L, Gerritsen HC (2004) Fast fluorescence lifetime imaging of calcium in living cells. *J Biomed Opt* **9:** 1230-1237

Andersson DA, Nash M, Bevan S (2007) Modulation of the cold-activated channel TRPM8 by lysophospholipids and polyunsaturated fatty acids. *J Neurosci* **27:** 3347-3355

Atkinson NS, Robertson GA, Ganetzky B (1991) A component of calcium-activated potassium channels encoded by the Drosophila slo locus. *Science* **253:** 551-555

Bandell M, Dubin AE, Petrus MJ, Orth A, Mathur J, Hwang SW, Patapoutian A (2006) High-throughput random mutagenesis screen reveals TRPM8 residues specifically required for activation by menthol. *Nat Neurosci* **9:** 493-500

Bidaux G, Beck B, Zholos A, Gordienko D, Lemonnier L, Flourakis M, Roudbaraki M, Borowiec AS, Fernandez J, Delcourt P, Lepage G, Shuba Y, Skryma R, Prevarskaya N (2011) Regulation of transient receptor potential melastatin 8 (TRPM8) channel activity by its short isoforms. *J Biol Chem*

Bidaux G, Flourakis M, Thebault S, Zholos A, Beck B, Gkika D, Roudbaraki M, Bonnal JL, Mauroy B, Shuba Y, Skryma R, Prevarskaya N (2007) Prostate cell differentiation status determines transient receptor potential melastatin member 8 channel subcellular localization and function. *J Clin Invest* **117:** 1647-1657

Bidaux G, Roudbaraki M, Merle C, Crepin A, Delcourt P, Slomianny C, Thebault S, Bonnal JL, Benahmed M, Cabon F, Mauroy B, Prevarskaya N (2005) Evidence for specific TRPM8 expression in human prostate secretory epithelial cells: functional androgen receptor requirement. *Endocrine-related cancer* **12:** 367-382

Bionda C, Portoukalian J, Schmitt D, Rodriguez-Lafrasse C, Ardail D (2004) Subcellular compartmentalization of ceramide metabolism: MAM (mitochondria-associated membrane) and/or mitochondria? *Biochem J* **382:** 527-533

Brauchi S, Orta G, Mascayano C, Salazar M, Raddatz N, Urbina H, Rosenmann E, Gonzalez-Nilo F, Latorre R (2007) Dissection of the components for PIP2 activation and thermosensation in TRP channels. *Proc Natl Acad Sci U S A* **104:** 10246-10251

Brauchi S, Orta G, Salazar M, Rosenmann E, Latorre R (2006) A hot-sensing cold receptor: C-terminal domain determines thermosensation in transient receptor potential channels. *J Neurosci* **26:** 4835-4840

Demaurex N, Frieden M (2003) Measurements of the free luminal ER Ca(2+) concentration with targeted "cameleon" fluorescent proteins. *Cell Calcium* **34:** 109-119

Denton RM, McCormack JG, Edgell NJ (1980) Role of calcium ions in the regulation of intramitochondrial metabolism. Effects of Na+, Mg2+ and ruthenium red on the Ca2+-stimulated oxidation of oxoglutarate and on pyruvate dehydrogenase activity in intact rat heart mitochondria. *Biochem J* **190:** 107-117

Digman MA, Caiolfa VR, Zamai M, Gratton E (2008) The phasor approach to fluorescence lifetime imaging analysis. *Biophys J* **94:** L14-16

ARTICLE 13

Fernandez JA, Skryma R, Bidaux G, Magleby KL, Scholfield CN, McGeown JG, Prevarskaya N, Zholos AV (2011) Short isoforms of the cold receptor TRPM8 inhibit channel gating by mimicking heat action rather than chemical inhibitors. *J Biol Chem*

Fuessel S, Sickert D, Meye A, Klenk U, Schmidt U, Schmitz M, Rost AK, Weigle B, Kiessling A, Wirth MP (2003) Multiple tumor marker analyses (PSA, hK2, PSCA, trp-p8) in primary prostate cancers using quantitative RT-PCR. *Int J Oncol* **23:** 221-228

Gackiere F, Bidaux G, Lory P, Prevarskaya N, Mariot P (2006) A role for voltage gated T-type calcium channels in mediating "capacitative" calcium entry? *Cell Calcium* **39:** 357-366

Giacomello M, Drago I, Bortolozzi M, Scorzeto M, Gianelle A, Pizzo P, Pozzan T (2010) Ca2+ hot spots on the mitochondrial surface are generated by Ca2+ mobilization from stores, but not by activation of store-operated Ca2+ channels. *Mol Cell* **38:** 280-290

Giorgi C, De Stefani D, Bononi A, Rizzuto R, Pinton P (2009) Structural and functional link between the mitochondrial network and the endoplasmic reticulum. *Int J Biochem Cell Biol* **41:** 1817-1827

Grynkiewicz G, Poenie M, Tsien RY (1985) A new generation of Ca2+ indicators with greatly improved fluorescence properties. *J Biol Chem* **260:** 3440-3450

Hansford RG, Zorov D (1998) Role of mitochondrial calcium transport in the control of substrate oxidation. *Mol Cell Biochem* **184:** 359-369

Harris DA, Das AM (1991) Control of mitochondrial ATP synthesis in the heart. *Biochem J* **280 (Pt 3):** 561-573

Hubbard MJ, McHugh NJ (1996) Mitochondrial ATP synthase F1-beta-subunit is a calcium-binding protein. *FEBS Lett* **391:** 323-329

Ishii K, Hirose K, Iino M (2006) Ca2+ shuttling between endoplasmic reticulum and mitochondria underlying Ca2+ oscillations. *EMBO Rep* **7:** 390-396

Jouaville LS, Pinton P, Bastianutto C, Rutter GA, Rizzuto R (1999) Regulation of mitochondrial ATP synthesis by calcium: evidence for a long-term metabolic priming. *Proc Natl Acad Sci U S A* **96:** 13807-13812

Kiessling A, Fussel S, Schmitz M, Stevanovic S, Meye A, Weigle B, Klenk U, Wirth MP, Rieber EP (2003) Identification of an HLA-A*0201-restricted T-cell epitope derived from the prostate cancer-associated protein trp-p8. *Prostate* **56:** 270-279

Kozak M (1986) Point mutations define a sequence flanking the AUG initiator codon that modulates translation by eukaryotic ribosomes. *Cell* **44:** 283-292

Kozak M (2002) Pushing the limits of the scanning mechanism for initiation of translation. *Gene* **299:** 1-34

Lakowicz JR (1996) Emerging applications of fluorescence spectroscopy to cellular imaging: lifetime imaging, metal-ligand probes, multi-photon excitation and light quenching. *Scanning Microsc Suppl* **10:** 213-224

Leray A, Padilla-Parra S, Roul J, Heliot L, Tramier M (2013) 827Spatio-temporal quantification of FRET in living cells by fast time-domain FLIM: a comparative study of non-fitting methods. *PLoS One* **8:** e69335

Leray A, Spriet C, Trinel D, Heliot L (2009) Three-dimensional polar representation for multispectral fluorescence lifetime imaging microscopy. *Cytometry A* **75:** 1007-1014

Lesage F, Guillemare E, Fink M, Duprat F, Lazdunski M, Romey G, Barhanin J (1996) TWIK-1, a ubiquitous human weakly inward rectifying K+ channel with a novel structure. *EMBO J* **15:** 1004-1011

Levine T, Rabouille C (2005) Endoplasmic reticulum: one continuous network compartmentalized by extrinsic cues. *Curr Opin Cell Biol* **17:** 362-368

Lewin TM, Van Horn CG, Krisans SK, Coleman RA (2002) Rat liver acyl-CoA synthetase 4 is a peripheral-membrane protein located in two distinct subcellular organelles, peroxisomes, and mitochondrial-associated membrane. *Archives of biochemistry and biophysics* **404:** 263-270

Livak KJ, Schmittgen TD (2001) Analysis of relative gene expression data using real-time quantitative PCR and the 2(-Delta Delta C(T)) Method. *Methods* **25:** 402-408

McCormack JG, Denton RM (1980) Role of calcium ions in the regulation of intramitochondrial metabolism. Properties of the Ca2+-sensitive dehydrogenases within intact uncoupled mitochondria from the white and brown adipose tissue of the rat. *Biochem J* **190:** 95-105

Miyawaki A, Griesbeck O, Heim R, Tsien RY (1999) Dynamic and quantitative Ca2+ measurements using improved cameleons. *Proc Natl Acad Sci U S A* **96:** 2135-2140

Nelson TE, Lin M, Zapata-Sudo G, Sudo RT (1996) Dantrolene sodium can increase or attenuate activity of skeletal muscle ryanodine receptor calcium release channel. Clinical implications. *Anesthesiology* **84:** 1368-1379

Padilla-Parra S, Auduge N, Coppey-Moisan M, Tramier M (2008) Quantitative FRET analysis by fast acquisition time domain FLIM at high spatial resolution in living cells. *Biophys J* **95:** 2976-2988

Palmer AE, Giacomello M, Kortemme T, Hires SA, Lev-Ram V, Baker D, Tsien RY (2006) Ca2+ indicators based on computationally redesigned calmodulin-peptide pairs. *Chem Biol* **13:** 521-530

Palmer AE, Jin C, Reed JC, Tsien RY (2004) Bcl-2-mediated alterations in endoplasmic reticulum Ca2+ analyzed with an improved genetically encoded fluorescent sensor. *Proc Natl Acad Sci U S A* **101:** 17404-17409

Phelps CB, Gaudet R (2007) The role of the N terminus and transmembrane domain of TRPM8 in channel localization and tetramerization. *J Biol Chem* **282:** 36474-36480

Poburko D, Fameli N, Kuo KH, van Breemen C (2008) Ca2+ signaling in smooth muscle: TRPC6, NCX and LNats in nanodomains. *Channels (Austin)* **2:** 10-12

Povstyan OV, Harhun MI, Gordienko DV (2011) Ca2+ entry following P2X receptor activation induces IP3 receptor-

mediated Ca2+ release in myocytes from small renal arteries. *Br J Pharmacol* **162:** 1618-1638

Rizzuto R, Duchen MR, Pozzan T (2004) Flirting in little space: the ER/mitochondria Ca2+ liaison. *Sci STKE* **2004:** re1

Robb-Gaspers LD, Burnett P, Rutter GA, Denton RM, Rizzuto R, Thomas AP (1998a) Integrating cytosolic calcium signals into mitochondrial metabolic responses. *EMBO J* **17:** 4987-5000

Robb-Gaspers LD, Rutter GA, Burnett P, Hajnoczky G, Denton RM, Thomas AP (1998c) Coupling between cytosolic and mitochondrial calcium oscillations: role in the regulation of hepatic metabolism. *Biochim Biophys Acta* **1366:** 17-32

Rogozin IB, Kochetov AV, Kondrashov FA, Koonin EV, Milanesi L (2001) Presence of ATG triplets in 5' untranslated regions of eukaryotic cDNAs correlates with a 'weak' context of the start codon. *Bioinformatics* **17:** 890-900

Rohacs T, Lopes CM, Michailidis I, Logothetis DE (2005) PI(4,5)P2 regulates the activation and desensitization of TRPM8 channels through the TRP domain. *Nat Neurosci* **8:** 626-634

Rusinol AE, Cui Z, Chen MH, Vance JE (1994) A unique mitochondria-associated membrane fraction from rat liver has a high capacity for lipid synthesis and contains pre-Golgi secretory proteins including nascent lipoproteins. *J Biol Chem* **269:** 27494-27502

Sabnis AS, Shadid M, Yost GS, Reilly CA (2008) Human lung epithelial cells express a functional cold-sensing TRPM8 variant. *Am J Respir Cell Mol Biol* **39:** 466-474

Santos JS, Asmar-Rovira GA, Han GW, Liu W, Syeda R, Cherezov V, Baker KA, Stevens RC, Montal M (2012) Crystal structure of a voltage-gated K+ channel pore module in a closed state in lipid membranes. *J Biol Chem* **287:** 43063-43070

Shkryl VM, Shirokova N (2006) Transfer and tunneling of Ca2+ from sarcoplasmic reticulum to mitochondria in skeletal muscle. *J Biol Chem* **281:** 1547-1554

Stone SJ, Vance JE (2000) Phosphatidylserine synthase-1 and -2 are localized to mitochondria-associated membranes. *J Biol Chem* **275:** 34534-34540

Szmacinski H, Lakowicz JR (1995) Possibility of simultaneously measuring low and high calcium concentrations using Fura-2 and lifetime-based sensing. *Cell Calcium* **18:** 64-75

Thebault S, Lemonnier L, Bidaux G, Flourakis M, Bavencoffe A, Gordienko D, Roudbaraki M, Delcourt P, Panchin Y, Shuba Y, Skryma R, Prevarskaya N (2005) Novel role of cold/menthol-sensitive transient receptor potential melastatine family member 8 (TRPM8) in the activation of store-operated channels in LNCaP human prostate cancer epithelial cells. *J Biol Chem* **280:** 39423-39435

Tramier M, Gautier I, Piolot T, Ravalet S, Kemnitz K, Coppey J, Durieux C, Mignotte V, Coppey-Moisan M (2002) Picosecond-hetero-FRET microscopy to probe protein-protein interactions in live cells. *Biophys J* **83:** 3570-3577

Tsavaler L, Shapero MH, Morkowski S, Laus R (2001) Trp-p8, a novel prostate-specific gene, is up-regulated in prostate cancer and other malignancies and shares high homology with transient receptor potential calcium channel proteins. *Cancer Res* **61:** 3760-3769

Vanden Abeele F, Bidaux G, Gordienko D, Beck B, Panchin YV, Baranova AV, Ivanov DV, Skryma R, Prevarskaya N (2006a) Functional implications of calcium permeability of the channel formed by pannexin 1. *J Cell Biol* **174:** 535-546

Vanden Abeele F, Zholos A, Bidaux G, Shuba Y, Thebault S, Beck B, Flourakis M, Panchin Y, Skryma R, Prevarskaya N (2006b) Ca2+-independent phospholipase A2-dependent gating of TRPM8 by lysophospholipids. *J Biol Chem* **281:** 40174-40182

Voets T, Owsianik G, Janssens A, Talavera K, Nilius B (2007) TRPM8 voltage sensor mutants reveal a mechanism for integrating thermal and chemical stimuli. *Nature chemical biology* **3:** 174-182

Wang HJ, Guay G, Pogan L, Sauve R, Nabi IR (2000) Calcium regulates the association between mitochondria and a smooth subdomain of the endoplasmic reticulum. *J Cell Biol* **150:** 1489-1498

Zhang L, Barritt GJ (2004) Evidence that TRPM8 is an androgen-dependent Ca2+ channel required for the survival of prostate cancer cells. *Cancer Res* **64:** 8365-8373

ARTICLE 13

	5'-forward-3'	5'-reverse-3'
Cloning / Full length PCR		
TRPM8	GAGAGACCAGCAGGATCCTTGG	TCAAGGTCTCAGCACACTAGG
TRPM8(15a)	GTGCTGATGTCGCTGTAGAGC	TCAAGGTCTCAGCACACTAGG
TRPM8(16a)	GAAGAAAGTTTGCATGGCATCCTG	TCAAGGTCTCAGCACACTAGG
TRPM8(17')	GTGTGCATTTAGCTACTAAGTCAC	TCAAGGTCTCAGCACACTAGG
TRPM8(17'')	AGGGACATGGGGTGGGAGT	TCAAGGTCTCAGCACACTAGG
TRPM8(18a)	GGACATTTAAAAATCTGGAAATGGTTG	TCAAGGTCTCAGCACACTAGG
Real-time PCR		
GAPDH	ACCCACTCCTCCACCTTTG	CTCTTGTGCTCTTGCTGGG
TRPM8 ex(8-9)	CTGTCATGGACATCCCACTG	GGGATCTTGCCACCATAGTT
TRPM8 ex(21-22)	CGGTCATCTACGAGCCCTAC	CACACACAGTGGCTTGGACT

TABLE 1: list of oligonucleotides used in this study.

SUPPLEMENTAL FIGURES

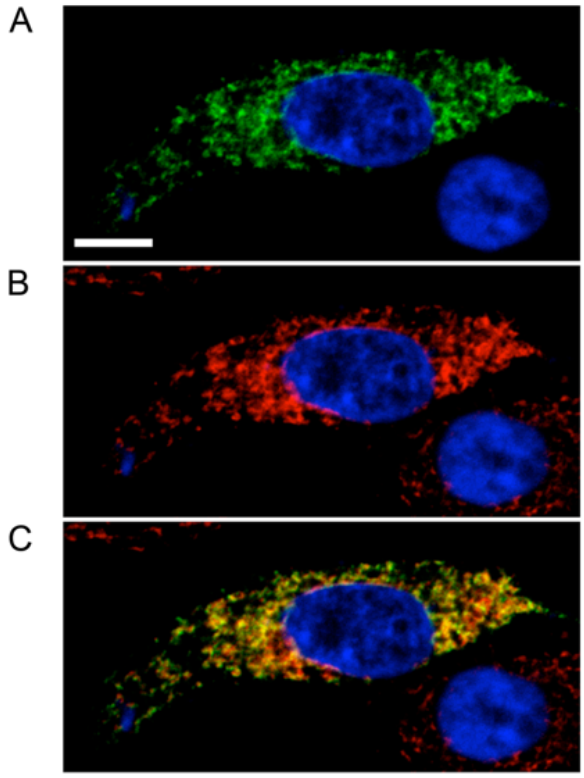

FIGURE S1. *TRPM8 isoforms are expressed in the ER membranes*. Immunodetection of TRPM8 (green, **A**) and the ER protein Calnexin (red, **B**) in LNCaP C4-2 cells revealed their colocalization (overlay, **C**). Scale bar: 5 µm. Experiments has been performed three times independently.

ARTICLE 13

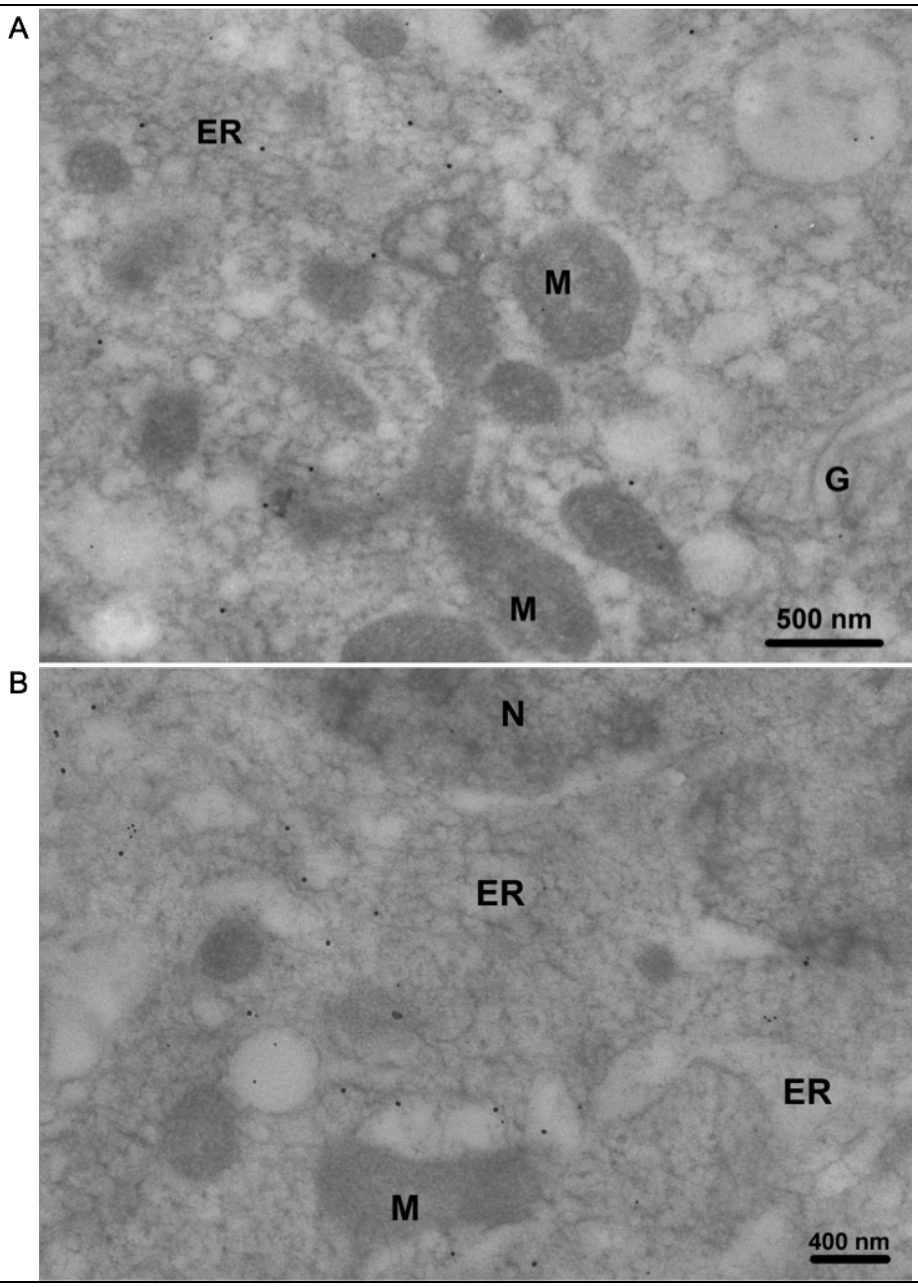

FIGURE S2. *Spatial distribution of TRPM8-35 isoform in LNCaP C4-2b cells.* Immunogold detection of calnexin (big gold particles) and TRPM8-HA (small gold particles) after cryosubstitution. TEM micrograps show the localisation of calnexin and TRPM8-35-HA in non-transfected LNCaP C4-2b cells (**A**) and in TRPM8-35-HA-transfected LNCaP C4-2b cells (**B**). Immunolabelling was performed with anti-HA antibody as described in the Methods.

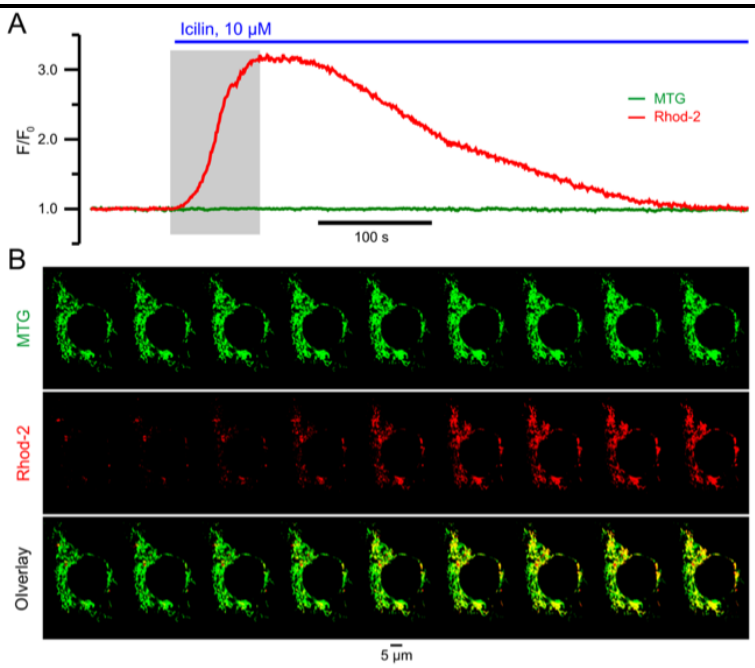

FIGURE S3. *Visualization of mitochondria with MitoTracker® Green FM (MTG) confirms mitochondrial origin of rhod-2 response to stimulation of TRPM8 with icilin in LNCaP cells.* The plot (**A**) shows the time course of self-normalized (F/F_0) MTG and rhod-2 fluorescence, as indicated. The fluorescence intensity (F) was normalized to the averaged fluorescence intensity before icilin application (F_0). The galleries (**B**) demonstrate the images of MTG fluorescence (top), rhod-2 fluorescence (middle) and their overlay (bottom): every 10th image captured from a single LNCaP cell during the period, highlighted on the plot by grey background (**A**), is shown (from left to right). Note that elevation of mitochondrial Ca^{2+} concentration ($[Ca^{2+}]_m$) is reported in the overlay images by change in color of mitochondria from green (dominating MTG fluorescence) to yellow (the overlay of MTG and elevated rhod-2 fluorescence).

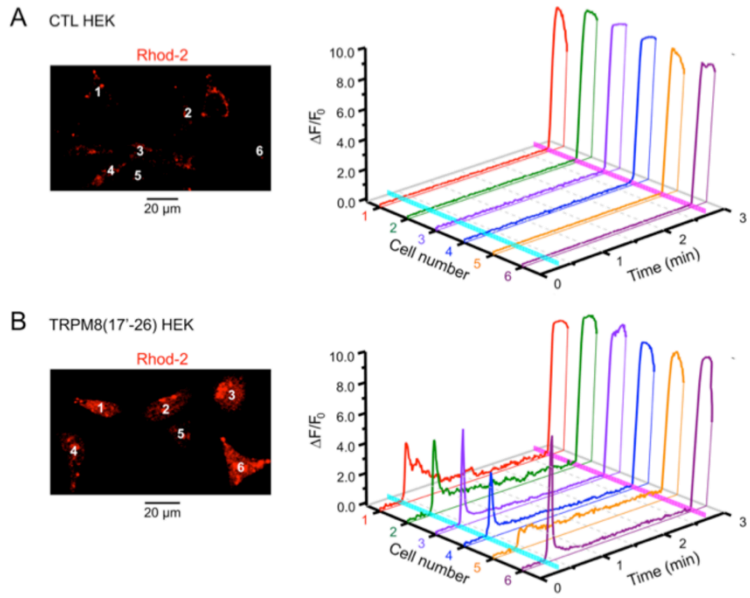

FIGURE S4. *Menthol-induced mitochondrial Ca^{2+}uptake depends on TRPM8 isoform expression.* Changes of Ca^{2+} concentration in mitochondria ($[Ca^{2+}]_m$) were monitored in (**A**) control HEK cells and (**B**) HEK cells transfected with TRPM8(17'-26) plasmid using x-y time series imaging of rhod-2 fluorescence. The images were acquired at 1.5 Hz from confocal optical slice below 2 µm. The celles were bathed in Ca^{2+}-free solution and stimulated with 200 µM menthol. To estimate the rhod-2 load, the cells were exposed to 2.5 µM ionomycin at the end of the experiment. The fluorescence intensity (F) was normalized to the averaged fluorescence intensity before menthol application (F_0). Relative changes in the fluorescence intensity ($\Delta F/F_0$), averaged within each of 6 cells, denoted by the numbers on the images (left), are plotted over time, respectively (right). Menthol and ionomycin applications are depicted on the 3D plots by vertical cyan and magenta bars, respectively.

ARTICLE 13

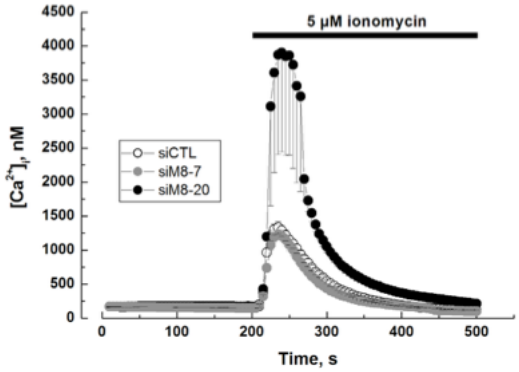

FIGURE S5. *Knockdown of TRPM8-35 isoform but not the full-length TRPM8 increases $[Ca^{2+}]_{ER}$ in LNCaP C4-2b cells.* Ionomycin-induced $[Ca^{2+}]_i$ responses detected with wide-field imaging in fura-2-loaded LNCaP C4-2b cells pre-treated for 48 hours with control siRNA (siCTL, n=223), siRNA targeting M8-7 (siM8-7, n=177) or siRNA targeting M8-20 (siM8-20, n=119). The cells were bathed in Ca^{2+}-free solution. Results are presented as values ± SEM.

IV. ARTICLE 15

ARTICLE 15

Epidermal TRPM8 channel isoform controls the balance between keratinocyte proliferation and differentiation in a cold-dependent manner.

Gabriel Bidaux[1,2,a], Anne-Sophie Borowiec[1], Dmitri Gordienko[1,6,§], Benjamin Beck[1,7], George Shapovalov[1], Lemonnier Loïc[1], Matthieu Flourakis[1,8], Matthieu Vandenberghe[1], Christian Slomianny[1], Etienne Dewailly[1], Philippe Delcourt[1], Emilie Desruelles[1], Abigaël Ritaine[1], Renata Polakowska[3], Jean Lesage[4], Mounia Chami[5], Roman Skryma[1,§] and Natalia Prevarskaya[1,§,b]

[1]Inserm U-1003, Equipe labellisée par la Ligue Nationale contre le cancer et LABEX, Université Lille1, 59655 Villeneuve d'Ascq, France
[2]Laboratoire de Physique des Lasers, Atomes & Molécules, Equipe Biophotonique Cellulaire Fonctionnelle, Parc scientifique de la Haute Borne, Villeneuve d'Ascq, France.
[3]Inserm U837, Jean-Pierre Aubert Research Center, Institut pour la Recherche sur le Cancer de Lille (IRCL), 59045 Lille, France
[4]Université Lille Nord de France, Unité Environnement Périnatal et Croissance, EA 4489, Equipe dénutritions maternelles périnatales, Université Lille 1, 59655 Villeneuve d'Ascq, France
[5]Institut de Pharmacologie Moléculaire et Cellulaire, UMR7275 CNRS/UNSA, équipe labellisée "Fondation pour la Recherche Médicale" 1 and "Excellence laboratory Distalz", 660 Route des Lucioles, 06560 Valbonne, France

Running title: eTRPM8 regulates epidermal homeostasis.

Key words: eTRPM8; mild cold; epidermal homeostasis; endoplasmic reticulum; calcium signaling; mitochondria; ATP; superoxide; proliferation; differentiation.

Abstract

Deviation of the ambient temperature is one of the most ubiquitous stimuli which continuously affect mammals' skin. While role of the warmth receptors in epidermal homeostasis (EH) was elucidated in recent years, the mystery of the keratinocyte mild-cold sensor remains unsolved.

Here we report the cloning and characterization of new functional epidermal isoform of TRPM8 mild-cold receptor, dubbed eTRPM8, which is localized in the keratinocyte endoplasmic reticulum membrane and controls mitochondrial Ca^{2+} concentration ($[Ca^{2+}]_m$). In turn, $[Ca^{2+}]_m$ modulates ATP and superoxide ($O_2^{\bullet-}$) synthesis in a cold-dependent manner. We report that this fine tuning of ATP and $O_2^{\bullet-}$ levels by cooling, controls the balance between keratinocyte proliferation and differentiation. Finally, to ascertain eTRPM8 role in EH *in vivo* we developed new functional KO mouse strain by deleting the pore domain of TRPM8 and demonstrated that eTRPM8 knockout impairs adaptation of the epidermis to low temperatures.

Significance Statement

Epidermis, the outer layer of skin, is a protective barrier and a sensing interface. Although deviation of the ambient temperature is one of the most ubiquitous stimuli affecting the skin, the influence of mild cold on epidermal homesostasis is not well understood.

Using a large range of techniques we identified a novel mild-cold sensor protein in keratinocytes, and demonstrate its location in the membrane of the endoplasmic reticulum, a major calcium store of the cell, and forms Ca^{2+}-permeable ion channel. Activation of this channel links the Ca^{2+} release to mitochondrial Ca^{2+} uptake and, thereby, modulates synthesis of ATP and superoxide involved in control of epidermal homeostasis. Molecular inactivation of this mild-cold sensor protein in mice impairs normal epidermal homeostasis.

Introduction

The skin epidermis provides a protective barrier that guards the body against an uncongenial environment. Under influence of a variety of ambient factors the skin epidermis undergoes continuous regeneration through so-called epidermal homeostasis (EH): the fine-tuning of the balance between proliferation, directional migration, differentiation and death of keratinocytes. EH involves complex molecular and chemical pathways, regulating dynamic and continuous transition of keratinocytes from proliferating state in the basal layer to non-proliferating state in the suprabasal layer prior to beginning of the differentiation in the *stratum spinosum* and *stratum granulosum*. The terminal differentiation step, characterized by keratinocyte death, transforms keratinocytes into corneocytes, which form the waterproof, mechanically resistant sheath of *stratum corneum* (1).

Deviation of the ambient temperature is one of the most important stimuli which constantly affect mammals' skin. At ambient temperatures from +10°C to +30°C, the unprotected human skin temperature settles at mean steady-state values within the range of +24°C to +33°C, respectively (2). Temperature is perceived by thermoreceptors, the ion channels which belong to the transient receptor potential (TRP) super family (for review see (3)). Of these, TRPV1 and TRPV2 are activated by heat (above 42°C and above 52°C, respectively) (4), whereas TRPM8 and likely TRPA1 are activated by mild (5, 6) and noxious (7-9) cold, respectively. Heat-stimulated keratinocytes have been shown to secrete ATP (10) and, taking into account that purinergic receptors are expressed in keratinocytes (11), TRPV3 is invloved in a paracrine heat-induced regulator of EH. Surprisingly, Grifford *et al* (2012) recently reported that local heating of human skin does not result in accumulation of interstitial ATP (12), what refutes

significance of TRPV thermoreceptors in normal temperature-dependent EH. TRPV3 also was suggested to be important for corneocyte formation through Ca^{2+}-dependent activation of cross-linking enzymes such as Transglutaminase (13-15). Apart heat-activated TRP, no successful attempt elucidating the role of cold-sensitive TRP channels in EH has been reported yet. The range of thermo-activation of TRPM8 channel fits well with human unprotected skin temperature, +24°C to +33°C (5, 6). Apart from the observation that topical application of TRPM8 chemical agonists can improve epidermal regeneration (16), no solid evidence for the expression of functional TRPM8 in epidermal keratinocytes was presented yet and no alterations in epidermal homeostasis have been reported in *trpm*$8^{-/-}$ null mutant mice suppressing the full length TRPM8 cold receptor (17, 18). However, suppression of the full length TRPM8 expression does not necessary affect expression of TRPM8 isoforms (19).

Here we report the cloning and characterization of a new 4-trasmembrane-domain epidermal isoform of the TRPM8 cold receptor-channel, dubbed eTRPM8. We demonstrate that eTRPM8 is localized and functions in the keratinocyte endoplasmic reticulum (ER) membrane where its activation within ER-mitochondria contact sites sustains mitochondrial Ca^{2+} uptake, thus, affecting mitochondrial Ca^{2+} concentration ($[Ca^{2+}]_m$). In turn, $[Ca^{2+}]_m$ modulates ATP and superoxide ($O_2^{\bullet-}$) synthesis in a cold-dependent manner. We report that this fine-tuning of ATP and $O_2^{\bullet-}$ levels by cooling temperatures controls the balance between proliferation and differentiation of keratinocytes. Finally, to ascertain eTRPM8's role in EH *in vivo* we developed new functional KO mouse line by deleting the active pore domain in all TRPM8 channel isoforms and demonstrated that eTRPM8 knockout impairs the epidermis adaptation to low temperatures and general skin homeostasis.

Results & Discussion

Novel TRPM8 isoform identified in human keratinocytes is composed of 4 transmembrane domains. Using differential PCR screenings to characterize TRPM8 mRNA in human keratinocytes, we found that in both HaCaT human keratinocyte cell line and human normal epidermal keratinocytes (hNEK) TRPM8 mRNA is 5'-truncated. Indeed, in both cell types, PCR analysis reported the product of amplification of the pore encoding mRNA region, but not exon 2 to 7 or exon 11 to 14 in the 5' region of TRPM8 mRNA (Fig. 1A). Controls on primary prostate epithelial cells (PrPE) were positive for all three regions tested, what validates the primers used for the detection of the classical TRPM8 mRNA. This demonstrates that the classical full length TRPM8 is not expressed in keratinocytes. This conclusion was confirmed further by Western blot analysis that demonstrates the classical TRPM8 (the 130 kDa doublet) in total protein extract from human prostate, but not from hNEK and HaCaT cells (Fig. 1B). The 5'-RACE PCR, performed from pore encoding exon 20, revealed a new alternate starting exon, labeled as 15a. It was located upstream and was adjacent to core exon 15, which was renamed as 15b, respectively (Fig. S1A). Internal quality control for the RACE PCR was performed with the cloning of the 5' extremity of classical TRPM8 mRNA in human prostate. We succeeded in amplifying 2,900 bp (GenBank accession number: KC692993) and improved the definition of the first transcribed nucleotide (+1) of the TRPM8 mRNA, since we detected 10 additional bases upstream to the published +1 (NM_024080.4). This makes the new +1 nucleotide to be located 25 bases downstream of the TATAA box. Although previously published +1 nucleotide was identified to be located 35 bases downstream (20), this does not match consensus distance between TATAA box and +1 (from 15 to 25 bp). As presented in Figure S1A, two sequences were cloned from hNEK mRNA: an alternate TRPM8 mRNA from exon 15a to exon 26, labeled TRPM8(15a) - (GenBank accession number: KC692994), and a splice variant of this alternate mRNA with skipping of exon 16, labeled TRPM8(15a/δ16) - (GenBank accession number: KC692995). TRPM8(15a) was found in human prostate, testis, skin and brain, while TRPM8(15a/δ16) was detected in human skin and colon (Fig. 1C). Quantification of TRPM8(15a) mRNAs in keratinocytes demonstrated similarly low level of the mRNAs in HaCaT cell line and basal hNEK, while induction of hNEKs (see Methods) was associated with significant increase in the level of TRPM8(15a) mRNAs (Fig. S1B). Furthermore, we verified eTRPM8 expression in human epidermis with *In Situ* hybridization and immunohistofluorescence. *In Situ* hybridization showed a positive detection of the pore-encoding region in epidermis, specifically with the anti-sense probe (Fig. S1C). Immunodetection of eTRPM8 with the antibody against the P-loop of the TRPM8 channel confirmed epidermis-specific expression of eTRPM8 showing marked increase of the channel expression in differentiated layers of epidermis (Fig. 1D).

Surprisingly, the putative open reading frames (ORFs) of the two mRNA were quite similar, however TRPM8(15a/δ16) revealed an additional longer ORF (Fig. S1A). After quantification of TRPM8(15a) mRNA and TRPM8(15a/δ16) mRNA intensities with a gel imager, TRPM8(15a) in skin was about 4 times more expressed than its splice form, we focused on TRPM8(15a) and defined its putative protein as epidermal TRPM8 (eTRPM8). Note that 5'-truncation removes the first 14 exons (Fig. S1A), what indicates that the two longest, putative ORFs encode 4-transmembrane domain (4-TD) proteins, including TD3 to 6 and the P-loop forming pore segment, with molecular weight of 40.94 kDa and 35.77 kDa, respectively (Fig. S1D). Immunoblotting of wild type (*wt)* eTRPM8 or HA-tagged eTRPM8 expressed in HEK cells revealed a major 39-40 kDa doublet and a minor 35-36 kDa doublet (Fig. 1E), which were referred to as eTRPM8-40 and eTRPM8-36, respectively. Native eTRPM8 expression was confirmed in two independent hNEK samples (Fig. 1F) and it should be noted that rather low level of the protein expression correlates with low level of eTRPM8 mRNA in keratinocytes.

Cold (<32°C) and cooling agents, such as menthol and icilin, activate the TRPM8 channel (5, 6). Although precise position of the menthol and icilin binding sites in classical TRPM8 is not yet clearly identified, there are growing evidence that both agonists

ARTICLE 15

interact with transmembrane domains 3 and 4 of the channel (reviewed in (21)).

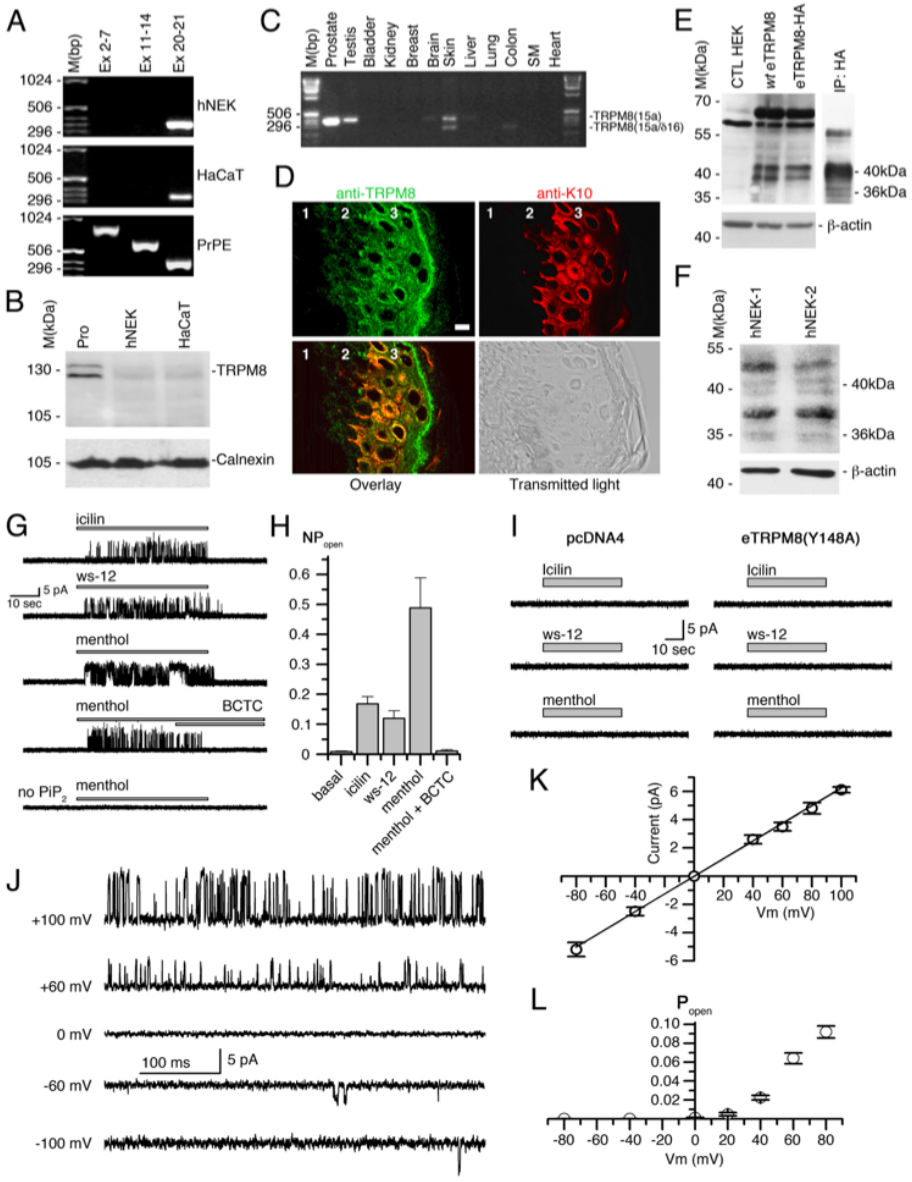

Figure 1. *Trpm8 gene encodes alternate TRPM8 mRNA variants and their associated proteins in human keratinocytes.* **A,** Representative PCR fingerprinting (n=5) revealed expression of pore-encoding region (exon 20-21) in the keratinocyte HaCaT cell line, in human normal epidermal keratinocytes (hNEK) and in primary culture of human prostate epithelial (PrPE) cells. Note that segments from exons 2 to 7 and from exons 11 to 14, encoding the cytosolic N-terminus of the TRPM8 channel, were detected in PrPE cells but not in keratinocytes. **B,** Representative immunoblotting (n=3) of 100 µg total protein extracts from human prostate (Pro), human normal epidermal keratinocytes (hNEK) and HaCaT cell line. Classical full length TRPM8 channel (126-128 kDa) was detected with rabbit anti-TRPM8 antibody (Alomone Labs, batch of 2009). Calnexin protein was used as a reporter of equal loading. **C,** Full length PCR illustrates human tissue profiling of alternate TRPM8(15a) transcripts (n=3). **D,** The gallery shows fluorescent confocal images of human female breast skin sections (n=3) with immunostained eTRPM8 (top left, green) and keratin 10 (top right, red), and their overlay (bottom left) and corresponding transmitted light image (bottom right). Numbers on the images depict: 1 – dermis, 2 - basal layer of epidermis and 3 - spinal and granular layers of epidermis. Scale bar:5 µm. **E,** W*ild type* and HA-tagged eTRPM8 (*wt* eTRPM8 and eTRPM8-HA, respectively), detected with anti-TRPM8 antibody in total protein extract from HEK cells, show strong doublet at 39-40 kDa and much weaker doublet at 35-36 kDa. β-actin was used as control of the protein loading. Immunoprecipitation with anti-HA antibody followed by immunoblotting with anti-TRPM8 antibody (right panel, IP: HA)) confirms specificity of both doublets and invalidates non-specific bands between 55 and 70 kDa. The same results were obtained in 3 independent samples. **F,** Native eTRPM8 protein detected with anti-TRPM8 immunoblotting in two independent samples (hNEK-1 and -2) of the induced hNEKs. β-actin was used as control of the protein loading. **G**, Sample activity of eTRPM8 in responce to application of 10 µM icilin, 500 nM ws-12 and 200 µM menthol, as well as inhibition by 10 µM BCTC, with levels of eTRPM8 activity summarized in panel **H**. **I,** Typical records upon application of icilin, ws-12 and menthol to liposomes

prepared from cells expressing the non-functional pore mutant eTRPM8(Y148A) or transfected with empty vector (pcDNA44). **J**, Sample activity of eTRPM8 at different potentials, indicated on the left. Note the characteristic dependence of open probability on the command potential. Dependence of the amplitude (**K**) and P_{open} (**L**) of the single-channel current on command voltage. Individual points show mean ± S.E.M. current amplitudes at the indicated voltages. Straight line presents a linear fit yielding the mean channel conductance of 63.1 ± 2.4 pS.

This indirectly suggests that both agonists may bind to eTRPM8. Besides, since the cold sensor domain is located in the carboxy-terminus of classical TRPM8 (22), it is likely that eTRPM8 may function as a cold-sensitive protein. Nevertheless, no changes in transmembrane ion currents, recorded under whole-cell voltage clamp in eTRPM8-expressing HEK cells, were detected in response to cold, menthol or icilin. This ruled out eTRPM8 as plasma membrane functional channel. Based on our previous findings (19) we hypothesized that, similarly to TRPM8 in prostate cancer cells, eTRPM8 in keratinocytes may function as the endoplasmic reticulum (ER) Ca^{2+}-release channel. To test this hypothesis, we, first of all, conducted double-immunostaining of eTRPM8 and the ER protein calnexin. This revealed (Fig. S2) that eTRPM8 clusters coincide with the ER elements in CTL and eTRPM8 overexpressing HaCaT cells, and in hNEKs. Since eTRPM8 is expressed in the ER of keratinocytes, to measure eTRPM8-mediated single channel current we conducted patch-clamp recording on the giant unilamellar vesicles (GUVs) containing the proteins extracted from the ER membrane fractions of HEK293 cells expressing eTRPM8 (Fig. 1 G-L).

Biophysical properties of the single channel activity measured in these conditions were characteristic for TRPM8 channel: (1) single channel conductance of 63.1 ± 2.4 pS and dependence of P_{open} on applied voltage (n= 37), (2) sensitivity to all currently known specific activators and inhibitors of TRPM8 and (3) PiP_2-dependance. The single channel current was activated by 10 µM icilin (n=16), 500 nM ws-12 (23) (n=18) or 200 µM menthol (n=31), required the presence of PiP_2 in GUVs and was blocked by 10 µM BCTC (n=13). . Stimulation with these activators of the patches made to the GUVs prepared from cells expressing the empty vector (n=290) or non-functional mutant eTRPM8(Y148A) (n=258) failed to induce the single channel activity.

Thus, we have cloned a new kind of TRP channel, eTRPM8, which, in contrast to all previously known members of TRP family, has the 4-TD structure. Furthermore, we demonstrated that keratinocytes express eTRPM8 instead of classical TRPM8, what raised the question about its role in epidermal homeostasis.

Functional TRPM8 knockout impairs skin differentiation in mouse. Several *trpm8*$^{-/-}$ mouse strains have been generated by deletion of either the first translated exon, or exons in the first half of TRPM8 sequence (17, 18). These mutations, however, did not target the pore region and, therefore, failed to suppress eTRPM8 expression and activity. In contrast, based on our previous detection of amino-terminal truncated TRPM8 isoforms (19), we have designed a functional KO mouse line by deleting exons 18, 19 and 20, which encode the active pore domain (Fig. 2A and Fig. S1A). Here we assessed the expression of mouse orthologous eTRPM8. PCR amplification of TRPM8(15a) was successfully achieved from exon 16 to exon 23 in total mRNA extracts (Fig. 2B), not only from skin sections of wild-type mice but also from primary culture of wild-type mouse keratinocytes (*wt* mPK) grown with 2% FCS + 1.8 mM Ca^{2+}, (24).

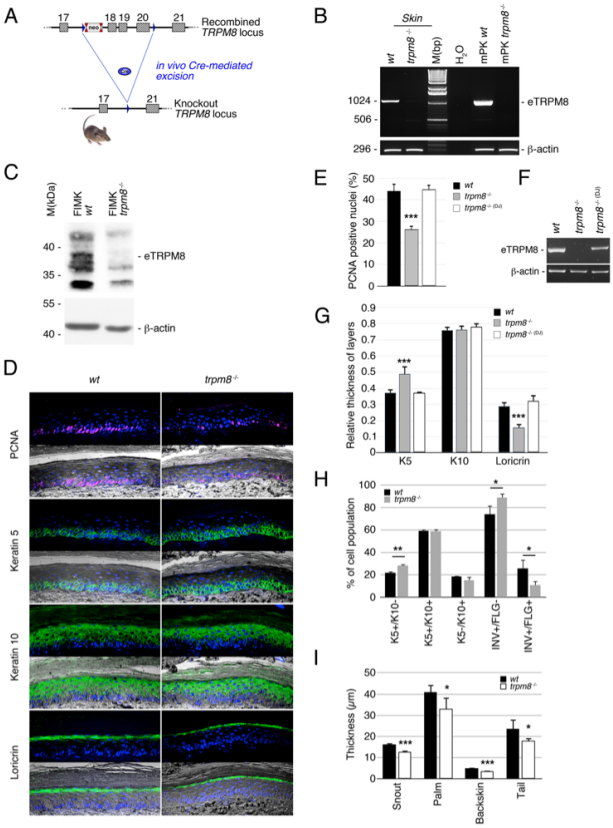

Figure 2. *Epidermal TRPM8 isoform (eTRPM8) ablation in mouse epidermis partially impairs epidermal homeostasis.* **A.** Schematic representation of the strategy used to establish the *trpm8* $^{-/-}$ mouse line. **B.** PCR amplification from exon 16 to exon 22 demonstrates expression of mouse eTRPM8 mRNA in *wild type* (*wt*) skin as well as in mPKs derived from *wt* mouse skin and grown with 2% FCS and 1.8 mM Ca^{2+} (mPK *wt*). Note that no eTRPM8 expression was detected in keratinocytes derived from *trpm8* $^{-/-}$ mouse skin (mPK *trpm8* $^{-/-}$) (n=3). **C.** Immunoblotting shows ~38 kDa protein in the skin of *wt* but not *trpm8* $^{-/-}$ mice (1 out of 4 readings for each mouse strain). β-actin was used as control of the protein loading. **D.** Representative immunohistofluorescence images of *wt* and *trpm8* $^{-/-}$ mouse palm skin reveals a decreased number of cycling cells in *trpm8* $^{-/-}$ epidermis (reported by PCNA) and a thicker granular layer (reported by loricrin, LN). **E.** Bar diagram plot compares fractions of the cells with PCNA-positive nuclei in the keratin 5

ARTICLE 15

(K5)-positive cell compartment counted in the images of skin sections of 5 *wt*, 7 *trpm8* $^{-/-}$ mice and 5 *trpm8* $^{-/-\,(DJ)}$ mice (lacking full length TRPM8 channel only). Note, that *trpm8* $^{-/-}$ mouse skin section (**D**) has thicker basal layer (K5-positive cells) but thinner granular layer (LN-positive cells), while total thickness of *SS* + *SG* remains unaltered. **F.** PCR amplification from exon 16 to exon 22 demonstrates expression of mouse eTRPM8 mRNA in skin sections of *wt*, *trpm8* $^{-/-}$ mice and *trpm8* $^{-/-\,(DJ)}$ mice. **G.** Bar diagram plot compares relative thickness (see Methods) of K5-, K10- and LR-positive compartments in 5 *wt*, 7 *trpm8* $^{-/-}$ mice and 5 *trpm8* $^{-/-\,(DJ)}$ mice. **H.** Distribution of keratinocyte phenotypes in the suspension of cells, freshly isolated from the back skin samples of 5 *wt* and 5 *trpm8* $^{-/-}$ mice, was measured with flow cytometry and compared. The phenotypes detected include: basal cells (K5+/K10-), suprabasal and early spinal cells (K5+/K10+), late spinal cells (K10+/INV+/FLG-) and granular cells (INV+/FLG+). **I.** Thickness of *corneosum stratum* (*CS*) was measured in trichrome-stained slides of paraffined skin samples obtained from the different skin regions (as indicated) and compared for 5 *wt* and 5 *trpm8* $^{-/-}$ mice.

This implies that eTRPM8, detected in the skin sections, is hosted by keratinocytes. Moreover, the lack of amplification products for exon 14 to 23 is indicative of truncation of the first half of 5' exon characteristic for eTRPM8 sequence. Specificity of TRPM8 detection was validated in the samples from TRPM8 KO-mice which do not express TRPM8. Finally, we checked eTRPM8 protein expression in freshly isolated mouse keratinocytes (FIMK) and detected a doublet of protein near 39 kDa from *wt* cells, which was not present in FIMK from *trpm8*$^{-/-}$ mice (Fig 2C).

To address involvement of eTRPM8 in epidermal homeostasis (EH) we tested whether eTRPM8 knockout (KO) would impair EH. Immuhistofluorescence analysis revealed a significant decrease of the number of proliferating cell nuclear antigen (PCNA) positive cells in *trpm8*$^{-/-}$ basal/suprabasal compartments (B/SbS) labeled with keratin 5 (K5) (Fig 2D and 2E). This suggests that the proliferation level of the *stratum basale* (*SB*) is impaired in eTRPM8 KO epidermis.

Since suppression of the channel pore region abolishes the activity of both eTRPM8 and classical TRPM8, to eliminate any possible involvement of the TRPM8 KO to the measurements (even though we obtained no evidence for the TRPM8 expression in keratinocytes) we conducted additional control experiments on *trpm8*$^{-/-\,(DJ)}$ mouse strain, where only classical TRPM8, but not eTRPM8 is suppressed (Fig. 2F). No changes in the proportion of PCNA positive cells in comparison with *wt* mice were detected in these experiments (Fig. 2G). Furthermore, measurements of the thickness of the different epidermal layers (Fig 2D and G) revealed a significant increase of B/SbS, no change in *stratum spinosum* (SS) + *stratum granulosum* (SG), and a significant decrease of the SG. These data indicate that the SS thickness is increased in proportion to the decrease of SG one, so that total thickness of the two layers remains unchanged. The observed alterations were further confirmed by assessing the percentage of FIMK positive for a specific epidermal layer marker (Fig. 2H). We have found that FIMK from *trpm8*$^{-/-}$ mice were enriched in the number of basal K5-positive, keratin 10(K10)-negative ($K5^+/K10^-$) proliferating cells, as well as in Involucrin (INV)-positive, filaggrin (FLG)-negative (INV^+/FLG^-) late spinosum cells, but they were slightly depleted of filaggrin-positive (INV^+/FLG^+) granulosum cells, as compared to the *wt* FIMK. Finally, consistent with the decrease of proliferation and increase in late differentiation, we have detected the decrease in the thickness of the *stratum corneum* (SC) in the skin samples of different body regions from *trpm8*$^{-/-}$ mice: snout, palm, backskin and tail (Fig. 2I).

Altogether, our data in the *trpm8*$^{-/-}$ mouse model demonstrated an impairment of EH, which was characterized by the decrease of proliferation rate and accumulation of keratinocytes in basal/suprabasal layers and early SS paralleled with a partial depletion of the cells in SG and SC. We, therefore, have concluded that eTRPM8 is an important modulator of EH. This prompted us to study molecular mechanisms of eTRPM8-dependent EH regulation.

eTRPM8 is the endoplasmic reticulum (ER) Ca^{2+}-release channel, activity of which affects mitochondrial Ca^{2+} concentration ($[Ca^{2+}]_m$). To assess immediate consequences of eTRPM8 activation in keratinocytes, we monitored menthol-induced changes of the ionized Ca^{2+} concentration in cytosol ($[Ca^{2+}]_c$) and mitochondria ($[Ca^{2+}]_m$) using fluorescence confocal imaging. In these experiments, to eliminate possible contribution of capacitative Ca^{2+} entry and, thereby, to enable the detection of Ca^{2+} flow among intracellular compartments only, external solution, containing 70 µM Ca^{2+}, was supplemented with 10 µM La^{3+} (25). Changes of $[Ca^{2+}]_c$ and $[Ca^{2+}]_m$ in response to external application of 200 µM menthol were simultaneously monitored at 37°C using fluo-4 and rhod-2, respectively. The $[Ca^{2+}]_c$ and $[Ca^{2+}]_m$ transients detected in mPKs from wild-type mice (Fig. 3A) were virtually abolished (Fig. 3C) in mPKs from *trpm8*$^{-/-}$ mice (Fig. 3B), while the transients observed in control HaCaT cells (Fig. 3D) were significantly augmented (Fig. 3F) following eTRPM8 overexpression (Fig. 3E). Induction (see Methods) of hNEKs also increased the amplitude of both $[Ca^{2+}]_c$ and $[Ca^{2+}]_m$ transients (Fig. S3A and S3B) what correlates with elevation of eTRPM8 protein expression (Fig. 1D). The sensitivity of eTRPM8 to menthol, icilin, cold and WS-12 (synthetic TRPM8 agonist) was further confirmed by wide-field microscopy of the fura-2 responses (Fig. S3C and S3D). Moreover, to verify the origin of Ca^{2+}, giving rise to $[Ca^{2+}]_c$ and $[Ca^{2+}]_m$ transients, we monitored icilin-induced changes of the ER Ca^{2+} concentration ($[Ca^{2+}]_{ER}$) in permeabilized HaCaT cells. This revealed (Fig. S3E) that decrease of $[Ca^{2+}]_{ER}$ in response to 10 µM icilin, observed in control HaCaT cells, was abolished following eTRPM8 knockdown (KD), achieved by transfection of HaCaT cells with shRNA targeting the eTRPM8-pore-encoding sequence (shM8). Mitochondrial origin of rhod-2 signal was confirmed by visualization of the mitochondria with MitoTracker® Green FM (Fig.

S2F). Another line of evidence, confirming that eTRPM8 functions as Ca^{2+}-permeable channel, was derived from the experiments on mutation of the channel pore region. We generated a pore-killer mutant of classical TRPM8 channel by substituting Tyrosine 905 with Alanine that completely abolished the current through homotetrameric channel and had a partial dominant negative effect (Fig. S4A).

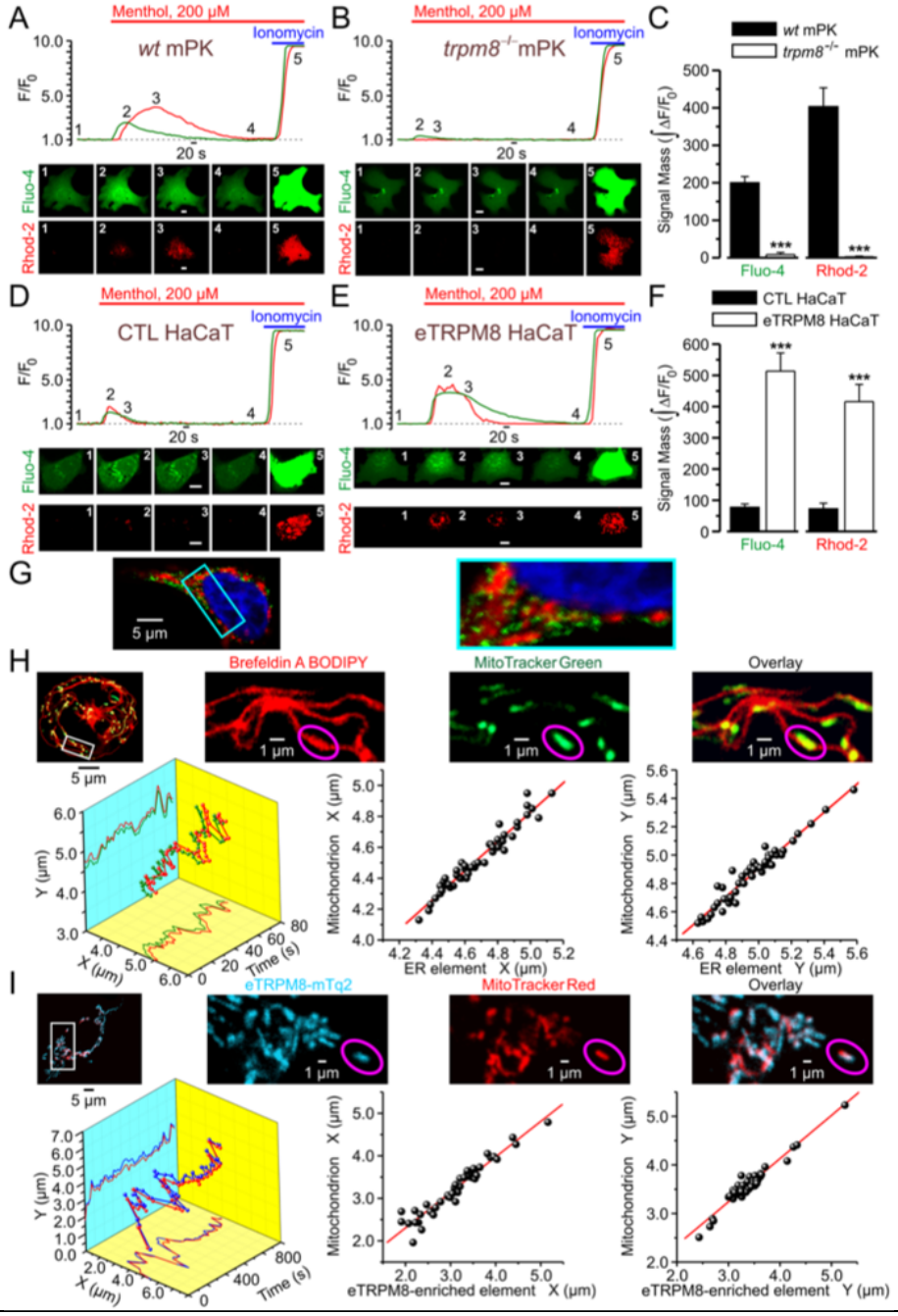

Figure 3. *eTRPM8 couples Ca^{2+} release from the ER to mitochondrial Ca^{2+} uptake.* Changes of Ca^{2+} concentration in cytosol ($[Ca^{2+}]_c$) and mitochondria ($[Ca^{2+}]_m$) in response to external application of 200 µM menthol were monitored using *x-y* time series imaging of fluo-4 and rhod-2 fluorescence, respectively, in primary culture of (**A**) *wild type* mouse keratinocytes (*wt* mPK) and (**B**) *trpm8* $^{-/-}$ mouse keratinocytes (*trpm8* $^{-/-}$ mPK), and in (**D**) control HaCaT cells (CTL HaCaT) and (**E**) HaCaT cells overexpressing eTRPM8 (eTRPM8 HaCaT). The plots show the time course of normalized fluorescence (F/F_0) of fluo-4 (green traces) and rhod-2 (red traces). The galleries below the plots demonstrate the images of fluo-4 and rhod-2 fluorescence (as indicated), captured at the moments depicted by the numbers on the plots, respectively. Scale bar: 10 µm. To eliminate capacitative Ca^{2+} entry, external solution, containing 70 µM Ca^{2+}, was supplemented with 10 µM La^{3+}. To estimate the load of the Ca^{2+}-sensitive indicators, the cells were exposed to 2.5 µM of ionomycin at the end of each experiment. Bar diagram plots compare masses, $\int \Delta F / F_0$, of the fluo-4 and rhod-2 signals (as indicated) during the period between application of menthol and application of ionomycin in (**C**) *trpm8* $^{-/-}$ mPKs (n=35) versus *wt* mPKs (n=27), and in (**F**) eTRPM8 HaCaT cells (n=15) versus CTL HaCaT cells (n=16). Immunodetection (**G**) of overexpressed eTRPM8 (green) in HaCaT cells expressing a DsRed targeted to

mitochondria (red) illustrates that eTRPM8-expressing ER microdomains are in close proximity to mitochondria. Right: enlarged image of the boxed region. Coordinated motility confirms tight coupling between eTRPM8-enriched ER elements and mitochondria in HaCaT cells (**H-I**). The ER elements were either stained with Brefeldin A BODIPY 558/568 (**H**) or identified by mTurquoise2 (mTq2) fluorescence, following eTRPM8-mTq2 expression (**I**). The mitochondria (**H** and **I**) were stained with either MitoTracker® Green FM (MTG) or MitoTracker® Red FM (MTR), respectively. Spatial distribution of the ER elements and mitochondria was analyzed using *x*-*y* time series confocal imaging. The galleries (top right) show enlarged images of Brefeldin A BODIPY and MTG fluorescence (**H**) or mTq2 and MTR fluorescence (**I**) captured from the boxed region (top left), and their overlays, as indicated. Motility analysis was conduced for the outlined (magenta ellipses) mitochondrion and the adjacent ER element. The *x* and *y* positions of the local maxima of the MTG and Brefeldin A BODPY fluorescence (**H**) or mTq2 and MTR fluorescence (**I**) were computed and plotted over time. The 3D plots (bottom left) shows the trajectory of the motion of mitochondrion (**H**: green; **I**: red) and adjacent (**H**: red) ER element or (**I**: blue) eTRPM8-enriched ER element. The *x* and *y* positions of the organelles in time are seen in the X-Y and X-Z projections on the 3D plot, respectively. The *x* vs. *x* and *y* vs. *y* positions for the mitochondrion and the ER element are plotted (bottom middle and bottom right, respectively). Linear regression analysis revealed high correlation between the parameters in all four cases: R = 0.973 (**H**: bottom middle), R = 0.970 (**H**: bottom right), R = 0.963 (**I**: bottom middle) and R = 0.967 (**I**: bottom right).

By analogy, we created an identical pore-killer mutant for eTRPM8, eTRPM8(Y148A), and overexpressed it in HaCaT cells. In this experimental model no Ca^{2+} release from the ER and concurrent mitochondrial Ca^{2+} uptake was ever observed (Fig. S4B), while the protein expression was confirmed in Western-blot experiments. This implies that the pore-killer mutation abolishes the channel activity of eTRPM8, as it does in classical TRPM8 (Fig. S4A), and further confirms that the ER Ca^{2+} release leading to mitochondrial Ca^{2+} uptake is mediated via eTRPM8 (Fig. S4B).

This suggests tight coupling between the ER and mitochondria, which facilitates mitochondrial Ca^{2+} uptake either by robust increase of Ca^{2+} concentration in the ER-mitochondria "nanodomains" (26) or via direct "Ca^{2+} tunneling" from the ER to mitochondria (27). Immunofluorescence detection of native eTRPM8 in HaCaT cells, overexpressing DsRed targeted to mitochondria, revealed that eTRPM8 foci surround mitochondria (Fig. 3G). Another evidence that eTRPM8-enriched ER elements are tightly coupled to mitochondria was obtained from the analysis of motility of the ER elements and mitochondria in living HaCaT cells (see Supporting Videos). This revealed extremely high correlation in the step-by-step displacements of the ER element, visualized either with Brefeldin A BODIPY staining (Fig. 3H; n = 8) or following eTRPM8-mTurquoise2 expression (Fig. 3I; n = 10), and adjacent mitochondrion. The coordinated motility of the organelles indicates that mitochondria are "anchored" to the adjacent eTRPM8-enriched ER elements.

Taken together the above results imply that eTRPM8 is an ER functional channel, which, forming calcium nanodomains, couples the ER Ca^{2+} release to mitochondrial Ca^{2+} uptake in keratinocytes. We, therefore, analyzed the downstream molecular events engaged by eTRPM8 activation.

eTRPM8 facilitates mitochondrial ATP synthesis at 37°C and adjusts ATP production to mild cold adaptation requirements.

In pancreatic and hepatic cells, a correlated Ca^{2+} oscillation in both cytosol and mitochondria have been shown to support a cell specific pacing of metabolism, which coordinates with cell function (28-30). Mitochondrial Ca^{2+} transients have been reported to increase mitochondrial dehydrogenase (DHase) activity that in turn enhances ATP synthesis. Besides, three key DHases of the tricarboxylic acid cycle (TCA) have been reported to be Ca^{2+} dependent, suggesting that mitochondrial Ca^{2+} regulates NADH/NAD^{+} ratio, which, in turn, controls ATP synthesis (31-33). We, therefore, tested whether eTRPM8 expression and activity may influence ATP synthesis in keratinocytes. The eTRPM8 KD HaCaT cells showed almost 40% decrease of steady-state $[Ca^{2+}]_m$ (Fig. 4A), what correlates with 40% fall in steady-state $[ATP]_m$ detected with mitochondrial luciferase (Fig. 4B). Mitochondrial ATP is thought to represent between 40 to 60% of total cell ATP depending on cell model and physiology. We, therefore, expected that the eTRPM8-dependent mitochondrial ATP synthesis would have a global impact on cell energy stores. Consistent with this, measurements of total intracellular ATP content ($[ATP]_i$) in the eTRPM8 KD HaCaT cells and mPKs from *trpm8*$^{-/-}$ mice revealed a significant decrease compared to the respective controls (left panels, Fig. 4C and 4D).

Apart from being involved in all energy-dependent cellular processes, ATP is excreted as paracrine/autocrine messenger, which may contribute to EH. Indeed, purinergic receptors are expressed in the plasma membrane of keratinocytes and their activation modulates proliferation (34). Bearing this in mind, we measured extracellular ATP concentration ($[ATP]_e$) and, as in the case of $[ATP]_i$, detected $[ATP]_e$ decrease with both the KD HaCaT cells and mPKs from *trpm8*$^{-/-}$ mice (right panels, Fig. 4C and 4D). This revealed that $[ATP]_e$ represents a good correlate of $[ATP]_i$. Altogether these data demonstrate that eTRPM8 is involved in modulation of mitochondrial ATP synthesis that defines both intra- and extracellular ATP concentration at 37°C.

As eTRPM8 is a cold sensor, we tested whether mild cold could stimulate ATP production. The notion that ATP production could be enhanced by cold seems to be counterintuitive, since it is well appreciated that optimal temperature for enzyme activity is 37°C. To verify whether keratinocyte metabolism is sensitive to acute and chronic cold as expected, we assessed the

temperature dependence of the total DHase activity in hNEKs, and found that total DHase activity is gradually reduced during acute cooling for 1h (Fig. 4E). Conversely, keratinocyte acclimatization to cold within 24h prior measuring total DHase activity at 37°C, revealed no difference with DHase activity in keratinocytes grown at 37°C. This suggests that intrinsic temperature dependence of the enzyme activity dominates and masks much weaker, if any, effect of the keratinocyte adaptation on DHase activity (i.e. increased expression, protein modifications increasing activity). We, therefore, assessed ATP content in the culture medium of control HaCaT cells grown at temperatures of 37, 31 and 25°C for 24h. This revealed no statistically significant alterations of $[ATP]_e$ (Fig. 4F), what is hardly consistent with the notion of decreased global metabolism at lowered temperatures. Overexpression of eTRPM8 increased $[ATP]_e$. relative to control HaCaT cells at all tested temperatures, while eTRPM8 knock down (shM8) had an opposite effect. It is noteworthy, that overexpression of the eTRPM8 pore-killer mutant (eTRPM8(Y148A)) reversed the effect observed with overexpression of functional eTRPM8, suggesting that eTRPM8 channel activity is required for full-scale ATP production, especially under mild cold conditions. Nevertheless, the $[ATP]_e$ levels, observed in control HaCaT cells and following eTRPM8(Y148A) expression, were not statistically different, suggesting that the mutant is not negative dominant (Fig. 4F). Unexpectedly, $[ATP]_e$ in control mPKs gradually decreased with cooling, and was reduced in mPKs from *trpm8* $^{-/-}$ mice with a maximal drop (about 50%) at 31°C (Fig. S5A). In contrast, $[ATP]_e$ in hNEKs increased with cooling at 31°C, and was reduced by siTRPM8 expression (Fig. S5B). Thus, all cell models tested support the notion that eTRPM8 is involved in control of ATP synthesis. Despite the difference in temperature-dependence of $[ATP]_e$ in different cell models, reflecting some contribution of eTRPM8 independent mechanisms, the impact of eTRPM8 on ATP synthesis was always maximal around 31°C (Fig. 4G) and correlated with eTRPM8-dependent fraction of $[Ca^{2+}]_m$ (Fig. 4G, inset). While an increase in the eTRPM8-dependent fraction of $[ATP]_e$ at 31°C can be attributed to elevation of the mitochondrial ATP synthesis boosted by the uptake of Ca^{2+} released from the ER via activated eTRPM8, subsequent decrease of this fraction at 25ºC cannot be explained by temperature-dependence of TRPM8 and likely reflects an intrusion of different mechanism, which decreases ATP synthesis despite elevated mitochondrial Ca^{2+} uptake. One of the possible candidates for such a mechanism is mitochondrial superoxide ($O_2^{\bullet-}$) production, which was reported to correlate well with metabolic rate (35, 36). It should be emphasized that keratinocytes are more prone to $O_2^{\bullet-}$ accumulation than other cell types due to reduced super oxide dismutase (SOD) activity (37).

eTRPM8 activation facilitates superoxide production in mitochondria and triggers its accumulation under mild cold conditions.

To test the above hypothesis we compared mitochondrial $O_2^{\bullet-}$ accumulation in response to eTRPM8 stimulation with 10 µM icilin in control (Fig. 5A) and eTRPM8-overexpressing (Fig. 5B), HaCaT cells, and in *wt* mPKs and mPKs from *trpm8*$^{-/-}$ mice (Fig. S6A), using x-y time series confocal imaging of MitoSOX^{TM} Red fluorescence in the living cells (see Methods). This revealed that $O_2^{\bullet-}$ accumulation was augmented in eTRPM8-overexpressing HaCaT cells and was suppressed in mPKs from *trpm8*$^{-/-}$ mice. Indeed, mean rate of $O_2^{\bullet-}$ accumulation, estimated as mass of MitoSOX fluorescent signal per second following icilin application, was found to be 9 times higher in eTRPM8-overexpressing HaCaT than control HaCaT cells (Fig. 5C), and 7.5 times lower in mPKs from *trpm8*$^{-/-}$ mice than in *wt* mPKs (Fig. 5D).

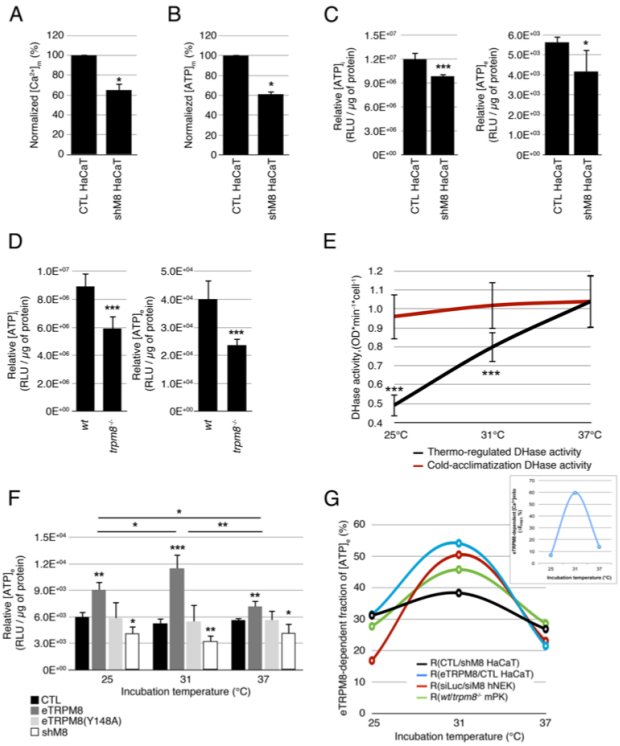

Figure 4. *eTRPM8 conveys cold-dependent enhancement of ATP synthesis.* **A.** A steady-state $[Ca^{2+}]_m$ was assessed using mtAEQmut probe in control and eTRPM8 KD HaCaT cells (CTL HaCaT and shM8 HaCaT, respectively). Bar diagram plot compares mean ± SEM values in CTL HaCaT cells (n=13) and ShM8 HaCaT cells (n=11) in three independent experiments, after rescaling the mean control value to 100%. **B.** Basal ATP concentration within mitochondria ($[ATP]_m$) was measured with mitochondria targeted ATP-dependent luciferase in CTL HaCaT (n=12) and shM8 HaCaT (n=12) cells at 37°C. Decrease of $[ATP]_m$ in shM8 HaCaT cells (presented as % of control) is summarized in the bar diagram plot. **C.** Intracellular and extracellular ATP concentrations ($[ATP]_i$ and $[ATP]_e$) were quantified using luciferase assay (see Methods) in CTL HaCaT and shM8 HaCaT cells at 37°C and compared (n=5). **D.** The same as (**C**) but for mPKs from *wt* and *trpm8* $^{-/-}$ mice (n=5). **E.** Dehydrogenase (DHase) activity assay performed at either 37°C, 31°C or 25°C demonstrates strong temperature dependence of DHase activity in hNEKs cultured at 37°C (black curve; thermo-regulated DHase activity). No significant deviations in DHase activity

ARTICLE 15

associated with cold-acclimatization of hNEKs cultured at either 37°C, 31°C or 25°C was detected by DHase assay performed at 37°C (red curve; clod-acclimatization DHase activity). n=3. **F.** Quantification of $[ATP]_e$ HaCaT cells cultured at either 37°C, 31°C or 25°C for 24 h following transfection with either empty vector (CTL), eTRPM8, pore-killer mutant eTRPM8(Y148A) or shRNA targeting eTRPM8 (shM8). n=5. **G.** Contribution of eTRPM8 to regulation of ATP synthesis was estimated from TRPM8-dependent fraction of $[ATP]_e$: (1) the differences between *wt*/CTL/siLuc and KO/shM8/siTRPM8 $[ATP]_e$ values were divided by corresponding *wt*/CTL/siLuc $[ATP]_e$ values, for mPKs, HaCaT cells and hNEKs, respectively and (2) the difference between eTRPM8 HaCaT and CTL HaCaT $[ATP]_e$ values was divided by eTRPM8 HaCaT $[ATP]_e$ value. Inset: using the same strategy the eTRPM8-dependent component of a steady-state $[Ca^{2+}]_m$ was assessed by the measurements of 4mTM3cpv Cameleon FRET efficacy (E_{FRET}) in HaCaT and eTRPM8 HaCaT cells. Smooth curves show parabolic interpolation of the mean values (n= 5). Note, that in all cases, an impact of eTRPM8 activity on $[ATP]_e$ is maximal around 31°C. Also note correlation between eTRPM8-dependent $[Ca^{2+}]_m$ and $[ATP]_e$.

As natural stimulus activating TRPM8 is cold, and since long-term incubation of keratinocytes in mild-cold condition affects the ATP content (see above), we also tested the effect of long-term cooling on $O_2^{\bullet-}$ accumulation in different keratinocyte models using CellRox® Deep Red Reagent, a non specific ROS probe, previously reported to be confined to the cytosol. In contrast to reported previously, we found that this probe accumulates in mitochondria, since it was colocalized with mitochondria-targeted GFP (Fig. S6B). Furthermore, we detected that CellRox® Deep Red Reagent fluorescence decreased with increasing concentration of hydrogen peroxide, H_2O_2 (Fig. S6C). This indicates that an increase in the intensity of CellRox fluorescence is not a reporter of $-H_2O_2$ accumulation. On the other hand, a 30 min pre-treatment of keratinocytes with MnTBAP, a superoxide ($O_2^{\bullet-}$) and peroxynitrite ($ONOO^-$) scavenger, results in strong decrease of CellRox fluorescence. Since peroxynitrites are down-products of $O_2^{\bullet-}$ (38, 39), CellRox® Deep Red Reagent seems to be a good reporter of the $O_2^{\bullet-}$ catalytic chain activity in mitochondria. Bearing this in mind, we assessed steady-state superoxide concentration $[O_2^{\bullet-}]$ in living hNEKs (Fig. 5E) or HaCaT cells (Fig. 5F) after 72- or 24-h culturing at either 37°C, 31°C or 25°C. The hNEKs were transfected either with control siRNA (siLuc) or with siRNA targeting the pore-encoding sequence of TRPM8 (siTRPM8), while HaCaT cells were transfected with empty vector (CTL), eTRPM8 plasmid or eTRPM8 + SOD1 plasmids. Imaging of CellRox® Deep Red fluorescence was preformed using confocal microscope equipped with CO_2 incubator. The $O_2^{\bullet-}$-specific signals (see Methods), obtained under different siRNA conditions were normalized to that in corresponding controls (37ºC; hNEKs, transfected with siLuc, or HaCaT cells, transfected with empty vector) and compared. This revealed that transfection of hNEKs with siRNA targeting the pore-encoding sequence of TRPM8 partially but significantly suppress $O_2^{\bullet-}$ accumulation at all 3 temperatures tested (Fig. 5E and Fig. S6E).

Bearing in mind that $O_2^{\bullet-}$ content depends on both its synthesis and dismutation by superoxide dismutases, we tested in HaCaT cells whether the effect of eTRPM8 overexpression can be reversed by overexpression of the Cu/Zn superoxide dismutase (SOD1). This revealed that significant increase of $O_2^{\bullet-}$ accumulation caused by eTRPM8 overexpression at all temperatures tested was partially reversed by concomitant overexpression of SOD1 (Fig. 5F). Furthermore, SOD1 overexpression suppress cold-dependence of $O_2^{\bullet-}$ accumulation, thus, suggesting that the balance between $O_2^{\bullet-}$ dismutation and synthesis remains the same regardless of the temperature. However, simultaneous overexpression of eTRPM8 and SOD1 resulted in small but significant increase of $O_2^{\bullet-}$ accumulation relative to cell transfected with empty vector (CTL) at all tested temperatures. This suggests that, with gradual cooling, elevation of eTRPM8 activity progressively overrides a native SOD activity, while when SOD1 is overexpressed a cold-dependent increase of TRPM8 activity is masked.

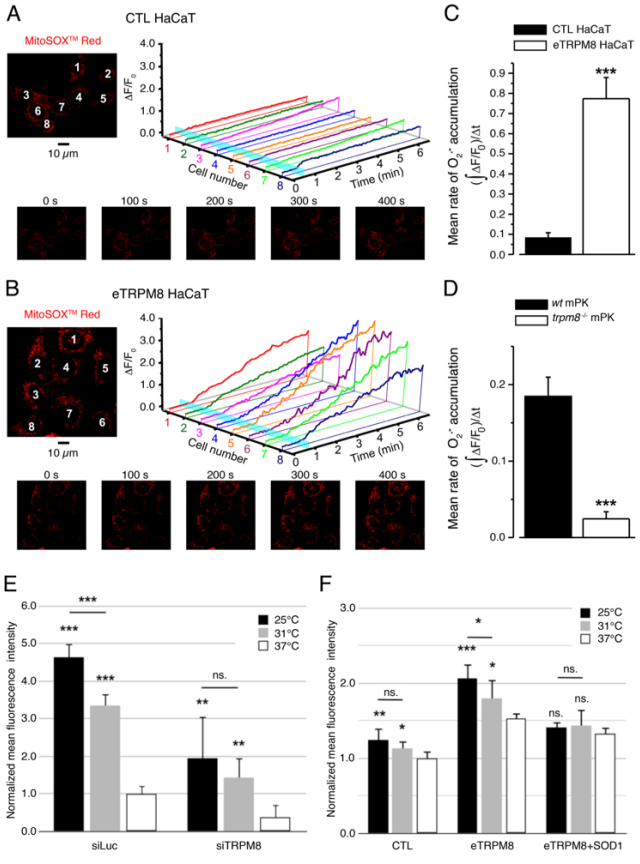

Figure 5. *Icilin- and cold-induced $O_2^{\bullet-}$ accumulation depends on the level of eTRPM8 expression.* Confocal images of MitoSOX™ Red fluorescence revealed distinct mitochondrial staining in control HaCaT cells, CTL HaCaT (**A**), and HaCaT cells overexpressing epithelial TRPM8, eTRPM8 HaCaT (**B**). Changes in the MitoSOX fluorescence in response to stimulation with 10 μM icilin were monitored using x-y time series imaging protocol. The MitoSOX fluorescence intensity (F) was normalized

to the averaged fluorescence intensity before agonist application (F_0). In (**A**) and (**B**), relative changes in the fluorescence intensity ($\Delta F/F_0$), averaged within each of 8 cells denoted by the numbers on the images (top left), are plotted over time, respectively (top right). Icilin application is depicted by vertical cyan bar. The galleries (bottom) show the images of MitoSOX fluorescence captured at times indicated above the images. Mean rates of $O_2^{\bullet-}$ accumulation were estimated as masses of MitoSOX fluorescent signal per second following icilin application, $\left(\int \Delta F / F_0\right) / \Delta t$, in CTL HaCaT (n = 28), eTRPM8 HaCaT (n = 20), in primary cultures of either *wt* mouse keratinocytes (*wt* mPK), (n = 8), or *trpm8* $^{-/-}$ mouse keratinocytes (*trpm8* $^{-/-}$ mPK), (n = 10), and compared in (**C**) and (**D**), respectively. **E**, Steady-state superoxide concentration [$O_2^{\bullet-}$] was assessed in living hNEKs after 72-h culturing at either 37°C, 31°C or 25°C, using CellRox® Deep Red Reagent. Cells were transfected either with control siRNA (siLuc) or with siRNA targeting the pore-encoding sequence of TRPM8 (siTRPM8). For each temperature and siRNA condition the measurements were performed in 3 Petri dishes, sequentially mounted on the microscope stage at the ambient temperature corresponding to the pre-incubation temperature. In each Petri dish confocal imaging of CellRox® Deep Red fluorescence was performed from 4 fields of view, 230x230 µm (1024x1024 pixels) each. The $O_2^{\bullet-}$- specific increases in the CellRox® Deep Red signal mass (see Methods) for each condition were averaged, normalized to the mean value detected at 37ºC in siLuc-transfected hNEKs, and compared. **F**, The same as **E**, but for HaCaT cells transfected with empty vector (CTL), eTRPM8 plasmid or eTRPM8 + SOD1 plasmids, and cultured for 24 h at 37°C, 31°C or 25°C. The data were normalized to the mean value detected at 37ºC in HaCaT cells transfected with empty vector, and compared. Note, that the difference between corresponding values for different expression conditions (in **E** and **F**) are statistically significant at all 3 temperatures tested with $p<0.05$. Experiments (in **E** and **F**) were performed 3 times and include more than 200 cells per experiment.

Altogether, our data demonstrate that activation of eTRPM8 in the ER leads to the increase of $[Ca^{2+}]_m$ that consequently enhances ATP and $O_2^{\bullet-}$ production in mitochondria. In a line with this, 24-72 h incubation of keratinocytes under mild-cold conditions elevates both $[ATP]_i$ and $[O_2^{\bullet-}]_i$. These findings are of great physiological importance, since ATP has been reported to be a key inducer of keratinocyte proliferation, whereas $O_2^{\bullet-}$ is involved in keratinocyte differentiation. Indeed, SOD1 was shown to be expressed in basal layer, but to disappear in differentiated layers of epidermis (40). Based on this observation the authors speculated that in proliferating keratinocytes (which have elevated energy metabolism) SOD1 serves to maintain $O_2^{\bullet-}$ at low level and, thereby, to protect the cells from oxidation, while in differentiated cells (which have lowly energy metabolism) enhanced accumulation of $O_2^{\bullet-}$ and, perhaps, peroxinitrites, resulting from downregulation of SOD1, may be involved in regulation of keratinocyte differentiation. The latter was further supported by observation of correlation between ROS concentration and degree of keratinocyte differentiation (41, 42). We, therefore, hypothesized that eTRPM8-dependent production of both ATP and $O_2^{\bullet-}$ may control the proliferation/differentiation balance of keratinocytes.

eTRPM8 regulates proliferation in temperature-dependent manner.

To test whether background, non-stimulated eTRPM8 activity at 37°C is relevant to EH, hNEKs transfected with either control siRNA or anti-TRPM8 siRNA were subjected to a growth assay at 37°C. The eTRPM8 KD hNEKs showed reduced growth rate in virtual absence of apoptosis (less than 1%), suggesting that lack of eTRPM8 suppresses proliferation (Fig. 6A). Assessment of thermo-sensitivity of keratinocyte proliferation revealed that control HEKs showed gradual decrease of growth rate with cooling, as expected, whereas eTRPM8 knockdown reduces the proliferation rate only at 37°C (Fig. 6B), consistent with the notion that eTRPM8 activity at 37°C encourages proliferation. eTRPM8 overexpression did not modify the growth at 37°C, but significantly suppressed it at 25°C. The latter was reversed by concomitant overexpression of SOD1, thus, suggesting that the effect was mediated by $O_2^{\bullet-}$ (Fig. 6B and 6C, middle and right panels). Conversely, eTRPM8+SOD1 co-transfection reduced proliferation at both 37°C and 31°C, as compared to control and eTRPM8-overexpressing cells. Paradoxically, even though eTRPM8+SOD1-overexpressing cells had higher ATP content than both control cells and eTRPM8-overexpressing cells at 37°C (Fig. 6C, left panel), their growth rate was significantly reduced (Fig. 6C, right panel).

To assess the extent of eTRPM8 recruitment to keratinocyte proliferation *in vivo*, we examined whether cold/menthol stimulation of mouse epidermis would affect cell proliferation in *SB*. As the most of the mouse skin is protected from variations of ambient temperature by fur, which acts as a thermal insulator, we shaved the two sides of mice but kept the fur on the back, as control. We applied 1 mM of menthol twice a day for 3 weeks on the right side, while the left side remained untreated. Furred back skin was shaved after sacrifice, and 3 skin samples were compared: control (from the back), shaved (from the left side) and menthol-treated shaved (from the right). Immuhistofluorescence detection of K14-positive cells, which are forming basal transit amplifying compartment of epidermis cells (43), and PCNA-positive cells, which reflect the cell population undergoing cell cycle, was performed with confocal microscope. The proliferation rate was then estimated by dividing the number of $PCNA^+/K14^+$ cells by the number of $PCNA^-/K14^+$ cells. In control conditions (unshaved mice), this ratio was significantly reduced in *trpm8*$^{-/-}$ epidermis, what reveals a TRPM8-dependent, cold-independent regulatory component of keratinocyte proliferation. We also detected significant decrease of this ratio in shaved *trpm8*$^{+/+}$ epidermis and its further reduction in shaved *trpm8*$^{+/+}$ epidermis subjected to menthol treatment (Fig. 6D), what

ARTICLE 15

demonstrates that cooling reduces proliferation *in vivo*. It should be emphasized, that in all skin samples from *trpm8*$^{-/-}$ mice this ratio was reduced to the same extent, independently of shaving and menthol treatment. This result suggests that the decrease of the keratinocyte proliferation rate *in vivo* in response to cooling cannot be explained solely by customary temperature-dependence of metabolic rate. Altogether, these results confirm that *in vivo* mild cold reduces number of proliferating keratinocytes in an eTRPM8-dependent manner. Nevertheless, variations in the number of PCNA^{+} cells can be explained by either slowing down of the cell cycle or by an increase of proliferation rate. The effect of eTRPM8 knock down in HaCaT cells at 37°C on the cell growth (Fig. 6B) undoubtedly favors the second hypothesis and confirms that eTRPM8 expression is required for full-scale proliferation of basal keratinocytes at 37°C, and that mild cold reduces the proliferation rate of keratinocytes in a TRPM8-dependent manner. Regardless of the mechanism linking eTRPM8 expression to full-scale keratinocyte proliferation, reduction of keratinocyte proliferation rate may involve two different mechanisms: cell cycle arrest associated with quiescence phase or induction of differentiation.

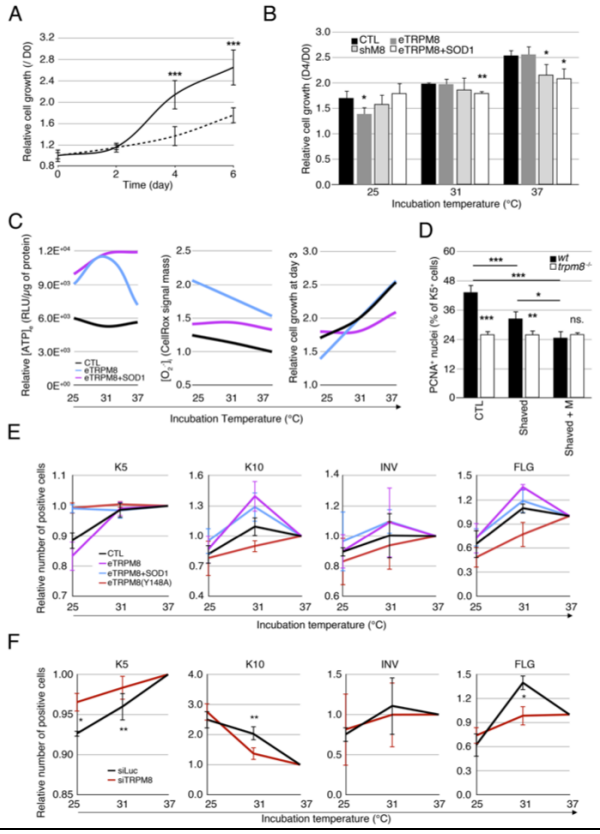

Figure 6. *Mild cold suppresses proliferation and facilitates differentiation of keratinocytes in eTRPM8-dependent manner.* **A.** The graph illustrates growth of induced (see Methods) hNEKs transfected with either control siRNA (black line) or anti-TRPM8 siRNA (dashed line) during 6 days. Data are presented as fold increase of the cell number from day 0. n=3. **B.** Bar diagram plot compares growth of HaCaT cells transfected with empty vector (CTL), eTRPM8 vector (eTRPM8), shRNA anti-TRPM8 vector (shM8) or cotransfected wit eTRPM8 and SOD1 vectors (eTRPM8+SOD1) at 25ºC, 31°C and 37ºC. n=3. **C.** Charts illustrate dependence of $[ATP]_e$ (left panel), $[O_2^{\bullet-}]_i$ (middle panel) and cell growth (right panel) on ambient temperature for HaCaT cells transfected with either empty vector (CTL), eTRPM8 vector (eTRPM8), or cotransfected with eTRPM8 and SOD1 vectors (eTRPM8+SOD1). Smooth curves are the result of parabolic interpolation of the mean values (n=3). **D.** Count of PCNA-positive nuclei in basal epidermis compartment was performed on slices from three different areas of skin (see Methods): furred (CTL), shaved (Shaved) and shaved with application of 1mM Menthol twice a week (Shaved+M). 6 *Wt* and 7 *trpm8* $^{-/-}$ mice were treated for 3 weeks before analysis was commenced. Bar diagram plot shows the ratio of the number of PCNA-positive cells divided by the number DAPI-positive nuclei in basal compartment identified with anti-keratin 14 antibodies. **E.** Distribution of keratinocyte phenotypes of HaCaT cells induced at 37°C, 31°C or 25°C for 24 hours was measured with flow cytometry and compared for HaCaT cells transfected with either empty vector (CTL), eTRPM8 vector (eTRPM8), eTRPM8 mutant vector (eTRPM8(Y148A)) or cotransfected with eTRPM8 and SOD1 vectors (eTRPM8+SOD1). The distribution of keratinocyte phenotypes was estimated on the basis of the percentage of cells expressing basal differentiation marker, K5, early spinal differentiation marker, K10, late spinal differentiation marker, INV, and granular differentiation marker, FLG. Cold-dependency of keratinocytes differentiation was figured out with normalization of values from cells grown at 25°C and 31°C by values from cells grown at 37°C. Data are presented as mean ± SD (n=3). Statistical significance was calculated for eTRPM8 (1), eTRPM8+SOD1 (2) and eTRPM8(Y148A) (3) compared to control cells. **F.** Same as (E) but for hNEKs transfected with either control siRNA (siLuc) or anti-TRPM8 siRNA (siTRPM8) for 4 days. Experiments (in **E** and **F**) were performed 3 times and include more than 100000 cells per experiment. Data are presented as mean ± SD.

Stimulation of eTRPM8 with mild cold induces keratinocyte differentiation.

Upon quantification of the differentiation rate in 2D cultures of keratinocytes several issues have to be taken into account. Firstly, it relies on the assumption that initial proportion of different keratinocyte phenotypes (basal, spinous, granular, corneocytes) is well defined and constant in all Petri dishes. Secondly, induced changes in the proportion of the keratinocyte phenotypes, interpreted as differentiation, are generally assessed with Western-blot. This procedure, however, only gives information on the total expression of the so-called differentiation markers in the cell population, but does not provide any information on either the number of cells in each phenotype or the mean expression level of differentiation markers in single cells. Thirdly, on many occasions, quantification of the differentiation rate is based on detection of early differentiation markers only. Therefore, to quantify eTRPM8-linked cold-dependency of the keratinocyte differentiation, we recently shown the

efficiency of flow cytometry (24), as in the case of keratinocytes freshly isolated from mouse skin (see Fig. 2G). While the experiments were conducted with simultaneous detection of two out of four markers (Fig. S7), to simplify visualization, the data are presented in charts showing the relative proportion of cells expressing one marker. Surprisingly, about 90% of cultured keratinocytes revealed the expression of basal markers K5 and K14, while less than 10% of the cells expressed differentiation markers K10 and INV. This could explain why we failed to detect any specific alterations of basal marker expression in HaCaT cells (Fig. 6E) and hNEKs (Fig. 6F) incubated at 31°C, even though when cells were incubated at 25°C significant decrease in the expression of these markers was observed. Intriguingly, in the case of eTRPM8 overexpression there were more K10-positive HaCaT cells at 37ºC than at 31°C, while in the case of concomitant overexpression of SOD1 the situation was the opposite. This suggests a permissive role of $O_2^{\bullet-}$ in early differentiation. This hypothesis is supported by the observation that progressive cooling causes gradual increase of K10 expression in hNEKs, which are known to express endogenous SOD1 at early stage of differentiation. Expression of late *SS* and *SG* INV marker was found to be weakly dependent on eTRPM8 expression and stimulation with mild cold. In contrast, the size of fraction of cells with granular marker, FLG, depended strongly on eTRPM8 expression/activity and showed a bell-shaped cold sensitivity with an optimum at the human physiological skin temperature of about 31°C. Note, that this bell-shaped cold sensitivity in eTRPM8-overexpressing HaCaT cell population is identical to that of hNEKs. Furthermore, this cold sensitivity correlates with the cold sensitivity of ATP synthesis, suggesting that terminal differentiation of keratinocytes is a highly ATP-dependent process. These data, altogether, demonstrate that eTRPM8 is involved in the differentiation of keratinocytes not only in mouse (Fig. 2G) but also in human (Fig. 6E-F) epidermis and conveys cold sensitivity of this process.

In conclusion, we have characterized new archetype of TRP channel encoded by a single gene. This channel is TRPM8 isoform expressed in the endoplasmic reticulum of keratinocytes and serves as a central element of signaling pathways engaged in cold-sensitivity of epidermal homeostasis (EH). Our results revealed a key role of eTRPM8 in keratinocyte bioenergetics: arbitration of the keratinocyte proliferation/differentiation balance (within the range of mild cold temperatures) via orchestrating the Ca^{2+}/ATP/$O_2^{\bullet-}$ triad (Fig. S8). This eTRPM8–mediated temperature-dependent energy metabolism and signaling in keratinocytes might provides skin with the capacity to adapt to large variations of environmental temperature.

Materials and Methods

Cell culture. See supplemental information.

Establishment of *trpm8*$^{-/-}$ mice. To suppress ion channel activity of every channel-like TRPM8 isoforms, we inserted LoxP sites with homologous recombination in introns 17 and 20. This ultimately led to a 2500 bp deletion including exons 18, 19 and 20, which encode transmembrane domains 3, 4 and 5 in addition to the first part of the P-loop of TRPM8 channel. Please refer to Supplemental Information for extended description of the methods.

Molecular Biology & Biochemistry. See supplemental information.

Electrophysiology. See supplemental information.

Visualization of the endoplasmic reticulum (ER) and mitochondria. See supplemental information.

Visualization of agonist-induced changes of Ca^{2+} concentration in cytosol ($[Ca^{2+}]_c$) and mitochondria ($[Ca^{2+}]_m$). Changes of $[Ca^{2+}]_{c\ and}$ $[Ca^{2+}]_m$ were imaged using the high-affinity fluorescent Ca^{2+} indicator fluo-4, and Ca^{2+} indicator rhod-2. Mitochondrial Ca^{2+} signal was also evaluated 48 h after transfection of M8-CTL and M8-KD cells with adenoviral mutated mitochondria-targeted aequorin probe (mtAEQmut). For extended procedures, refer to supplemental information.

Superoxide assessment. Steady-state superoxide concentration [$O_2^{\bullet-}$] was assessed in living hNEKs or HaCaT cells after 72- or 24-h culturing at either 37°C, 31°C or 25°C, using CellRox® Deep Red Reagent (Molecular Probes), loaded by 30-min incubation of the cells with 2.5 μM of the dye at 37°C. Please refer to Supplemental Information for extended description of the methods.

Time domain-fluorescence lifetime imaging microscopy (TM-FLIM) was achieved to estimate difference in steady-state $[Ca^{2+}]_m$ with Cameleon bioindicator. For details, See supplemental information.

Data analysis and statistical procedures. Each experiment was repeated at least three times independently. Data are expressed as mean ± S.D when not indicated in legends. The data were analyzed and graphs plotted using Origin 5.0 software (Microcal, Northampton, MA, USA). InStat3 (GraphPad Software Inc, SanDiego, USA) was used for statistical analysis and the mean values were compared using either unpaired *t*-test with Welch's corrected test (2 groups) or One-way ANOVA with Dunnett multiple comparison post-test (≥3 groups). Statistical significances were: * $p<0.05$; ** $p<0.01$; *** $p<0.001$. Smooth curves on the graphs were obtained by interpolation of data points using parametric Lagrange 2nd degree polynomial: parabola for interpolation of 3 data points.

Footnotes.

[a]Correspondence to: gabriel.bidaux@gmail.com
Present address: Dr Gabriel BIDAUX, Laboratoire de Physique des Lasers, Atomes & Molécules, Equipe Biophotonique Cellulaire Fonctionnelle, Parc scientifique de la Haute Borne, Villeneuve d'Ascq, France; Tel.: 33-3-62-53-17-33
[b]Correspondence to: Natacha.Prevarskaya@univ-lille1.fr.
Prof Natacha Prevarskaya, Laboratoire de Physiologie Cellulaire, INSERM U1003, Bâtiment SN3, USTL, 59655 Villeneuve d'Ascq, France; Tel.: 33-3-20-43-4077; Fax: 33-3-20-43-4066

[§]Share senior authorship.

ARTICLE 15

[6]Present address: Laboratory of Molecular Pharmacology and Biophysics of Cell Signalling, State Key Laboratory of Molecular and Cell Biology, Bogomoletz Institute of Physiology, Kiev, Ukraine

[7]Present address: Institut de Recherche Interdisciplinaire en Biologie Humaine et Moléculaire (IRIBHM), 808 route de Lennik, 1070 Brussels, Belgium.

[8]Present address: Department of Neurobiology and Physiology, Northwestern University, Evanston, IL 60208, USA.

Acknowledgements:

trpm8$^{-/-}$ mouse line has been designed by Dr. Gabriel Bidaux and Genoway Inc. Trpm8$^{-/-}$ mouse line has been established by Genoway Inc. and housed in Charles River Laboratories. Authors would like to thanks Marie Norbert and all Genoway team for their support and their competences.

trpm8$^{-/-\,(DJ)}$ mouse line is a generous gift from Prof. David Julius. We thank Dr Jérôme Busserolles for providing us these animals.

D1ER cameleon and mt Cameleon are generous gift of Prof Tsien R., La Jolla, CA, USA.

This work has been supported by grants from: INSERM, Ministère de l'Education Nationale, Ligue Nationale Contre le Cancer, Region Nord-Pas-de-Calais and ANR Grant: number.

The Cosmetics department of Johnson & Johnson laboratories supported Dr. Gabriel Bidaux.

Dr. Anne-sophie Borowiec is supported by Fondation pour la recherche médicale.

Dr. Dmitri Gordienko is supported by State Found for Fundamental Research (F 46.2/001).

Dr. Benjamin Beck was supported by the French association "Fondation pour la Recherche Médicale".

Authors thank Prof. Julien J-P. at the centre de recherché CHU Laval, QUEBEC, for his generous gift of pcDNA3-FlagN-SOD1 plasmid.

We would like to thanks Delphine Taillieu and Mélanie Besegher for their technical assistance for animals housing at "Animalerie High-Tech de l'Institut de Médecine Prédictive et de Recherche Thérapeutique de Lille" and for their help for menthol experiment on shaved mice.

Bibliography

1. Fuchs E (1990) Epidermal differentiation: the bare essentials. *J Cell Biol* 111(6 Pt 2):2807-2814.
2. Smith AD, Crabtree DR, Bilzon JL, & Walsh NP (2010) The validity of wireless iButtons and thermistors for human skin temperature measurement. *Physiol Meas* 31(1):95-114.
3. Lumpkin EA & Caterina MJ (2007) Mechanisms of sensory transduction in the skin. *Nature* 445(7130):858-865.
4. Caterina MJ & Julius D (2001) The vanilloid receptor: a molecular gateway to the pain pathway. *Annu Rev Neurosci* 24:487-517.
5. McKemy DD, Neuhausser WM, & Julius D (2002) Identification of a cold receptor reveals a general role for TRP channels in thermosensation. *Nature* 416(6876):52-58.
6. Peier AM, *et al.* (2002) A TRP channel that senses cold stimuli and menthol. *Cell* 108(5):705-715.
7. Story GM, *et al.* (2003) ANKTM1, a TRP-like channel expressed in nociceptive neurons, is activated by cold temperatures. *Cell* 112(6):819-829.
8. Kwan KY, *et al.* (2006) TRPA1 contributes to cold, mechanical, and chemical nociception but is not essential for hair-cell transduction. *Neuron* 50(2):277-289.
9. Obata K, *et al.* (2005) TRPA1 induced in sensory neurons contributes to cold hyperalgesia after inflammation and nerve injury. *J Clin Invest* 115(9):2393-2401.
10. Mandadi S, *et al.* (2009) TRPV3 in keratinocytes transmits temperature information to sensory neurons via ATP. *Pflugers Arch* 458(6):1093-1102.
11. Koizumi S, Fujishita K, Inoue K, Shigemoto-Mogami Y, & Tsuda M (2004) Ca2+ waves in keratinocytes are transmitted to sensory neurons: the involvement of extracellular ATP and P2Y2 receptor activation. *Biochem J* 380(Pt 2):329-338.
12. Gifford JR, Heal C, Bridges J, Goldthorpe S, & Mack GW (2012) Changes in dermal interstitial ATP levels during local heating of human skin. *J Physiol* 590(Pt 24):6403-6411.
13. Moqrich A, *et al.* (2005) Impaired thermosensation in mice lacking TRPV3, a heat and camphor sensor in the skin. *Science* 307(5714):1468-1472.
14. Peier AM, *et al.* (2002) A heat-sensitive TRP channel expressed in keratinocytes. *Science* 296(5575):2046-2049.
15. Cheng X, *et al.* (2010) TRP channel regulates EGFR signaling in hair morphogenesis and skin barrier formation. *Cell* 141(2):331-343.
16. Denda M, Tsutsumi M, & Denda S (2010) Topical application of TRPM8 agonists accelerates skin permeability barrier recovery and reduces epidermal proliferation induced by barrier insult: role of cold-sensitive TRP receptors in epidermal permeability barrier homoeostasis. *Exp Dermatol* 19(9):791-795.
17. Bautista DM, *et al.* (2007) The menthol receptor TRPM8 is the principal detector of environmental cold. *Nature* 448(7150):204-208.
18. Dhaka A, *et al.* (2007) TRPM8 is required for cold sensation in mice. *Neuron* 54(3):371-378.
19. Bidaux G, *et al.* (2007) Prostate cell differentiation status determines transient receptor potential melastatin member 8 channel subcellular localization and function. *J Clin Invest* 117(6):1647-1657.
20. Bidaux G, *et al.* (2005) Evidence for specific TRPM8 expression in human prostate secretory epithelial cells: functional androgen receptor requirement. *Endocrine-related cancer* 12(2):367-382.
21. Latorre R, Brauchi S, Orta G, Zaelzer C, & Vargas G (2007) ThermoTRP channels as modular proteins with allosteric gating. *Cell Calcium* 42(4-5):427-438.
22. Brauchi S, Orta G, Salazar M, Rosenmann E, & Latorre R (2006) A hot-sensing cold receptor: C-terminal domain determines thermosensation in transient receptor potential channels. *J Neurosci* 26(18):4835-4840.
23. Beck B, *et al.* (2007) Prospects for prostate cancer imaging and therapy using high-affinity TRPM8 activators. *Cell Calcium* 41(3):285-294.
24. Borowiec AS, Delcourt P, Dewailly E, & Bidaux G (2013) Optimal differentiation of in vitro keratinocytes requires multifactorial external control. *PLoS One* 8(10):e77507.

25. Vanden Abeele F, Roudbaraki M, Shuba Y, Skryma R, & Prevarskaya N (2003) Store-operated Ca2+ Current in Prostate Cancer Epithelial Cells. ROLE OF ENDOGENOUS Ca2+ TRANSPORTER TYPE 1. *J Biol Chem* 278(17):15381-15389.
26. Poburko D, Fameli N, Kuo KH, & van Breemen C (2008) Ca2+ signaling in smooth muscle: TRPC6, NCX and LNats in nanodomains. *Channels (Austin)* 2(1):10-12.
27. Shkryl VM & Shirokova N (2006) Transfer and tunneling of Ca2+ from sarcoplasmic reticulum to mitochondria in skeletal muscle. *J Biol Chem* 281(3):1547-1554.
28. Pralong WF, Spat A, & Wollheim CB (1994) Dynamic pacing of cell metabolism by intracellular Ca2+ transients. *J Biol Chem* 269(44):27310-27314.
29. Hajnoczky G, Robb-Gaspers LD, Seitz MB, & Thomas AP (1995) Decoding of cytosolic calcium oscillations in the mitochondria. *Cell* 82(3):415-424.
30. Jouaville LS, Pinton P, Bastianutto C, Rutter GA, & Rizzuto R (1999) Regulation of mitochondrial ATP synthesis by calcium: evidence for a long-term metabolic priming. *Proc Natl Acad Sci U S A* 96(24):13807-13812.
31. McCormack JG & Denton RM (1980) Role of calcium ions in the regulation of intramitochondrial metabolism. Properties of the Ca2+-sensitive dehydrogenases within intact uncoupled mitochondria from the white and brown adipose tissue of the rat. *Biochem J* 190(1):95-105.
32. Denton RM, McCormack JG, & Edgell NJ (1980) Role of calcium ions in the regulation of intramitochondrial metabolism. Effects of Na+, Mg2+ and ruthenium red on the Ca2+-stimulated oxidation of oxoglutarate and on pyruvate dehydrogenase activity in intact rat heart mitochondria. *Biochem J* 190(1):107-117.
33. Hansford RG & Zorov D (1998) Role of mitochondrial calcium transport in the control of substrate oxidation. *Mol Cell Biochem* 184(1-2):359-369.
34. Pillai S & Bikle DD (1992) Adenosine triphosphate stimulates phosphoinositide metabolism, mobilizes intracellular calcium, and inhibits terminal differentiation of human epidermal keratinocytes. *J Clin Invest* 90(1):42-51.
35. Perez-Campo R, Lopez-Torres M, Cadenas S, Rojas C, & Barja G (1998) The rate of free radical production as a determinant of the rate of aging: evidence from the comparative approach. *J Comp Physiol B* 168(3):149-158.
36. Sohal RS & Allen RG (1985) Relationship between metabolic rate, free radicals, differentiation and aging: a unified theory. *Basic Life Sci* 35:75-104.
37. Hornig-Do HT, *et al.* (2007) Human epidermal keratinocytes accumulate superoxide due to low activity of Mn-SOD, leading to mitochondrial functional impairment. *J Invest Dermatol* 127(5):1084-1093.
38. Bringold U, Ghafourifar P, & Richter C (2000) Peroxynitrite formed by mitochondrial NO synthase promotes mitochondrial Ca2+ release. *Free Radic Biol Med* 29(3-4):343-348.
39. Radi R, Cassina A, Hodara R, Quijano C, & Castro L (2002) Peroxynitrite reactions and formation in mitochondria. *Free Radic Biol Med* 33(11):1451-1464.
40. Carraro C & Pathak MA (1988) Characterization of superoxide dismutase from mammalian skin epidermis. *J Invest Dermatol* 90(1):31-36.
41. Tamiji S, *et al.* (2005) Induction of apoptosis-like mitochondrial impairment triggers antioxidant and Bcl-2-dependent keratinocyte differentiation. *J Invest Dermatol* 125(4):647-658.
42. Muramatsu S, *et al.* (2005) Differentiation-specific localization of catalase and hydrogen peroxide, and their alterations in rat skin exposed to ultraviolet B rays. *J Dermatol Sci* 37(3):151-158.
43. Rangarajan A, *et al.* (2001) Notch signaling is a direct determinant of keratinocyte growth arrest and entry into differentiation. *EMBO J* 20(13):3427-3436.
44. Thebault S, *et al.* (2005) Novel role of cold/menthol-sensitive transient receptor potential melastatine family member 8 (TRPM8) in the activation of store-operated channels in LNCaP human prostate cancer epithelial cells. *J Biol Chem* 280(47):39423-39435.
45. Sakuntabhai A, *et al.* (1999) Mutations in ATP2A2, encoding a Ca2+ pump, cause Darier disease. *Nat Genet* 21(3):271-277.
46. Prasad V, *et al.* (2005) Haploinsufficiency of Atp2a2, encoding the sarco(endo)plasmic reticulum Ca2+-ATPase isoform 2 Ca2+ pump, predisposes mice to squamous cell tumors via a novel mode of cancer susceptibility. *Cancer Res* 65(19):8655-8661.
47. Robb-Gaspers LD, *et al.* (1998) Integrating cytosolic calcium signals into mitochondrial metabolic responses. *EMBO J* 17(17):4987-5000.
48. Robb-Gaspers LD, *et al.* (1998) Coupling between cytosolic and mitochondrial calcium oscillations: role in the regulation of hepatic metabolism. *Biochim Biophys Acta* 1366(1-2):17-32.
49. Harris DA & Das AM (1991) Control of mitochondrial ATP synthesis in the heart. *Biochem J* 280 (Pt 3):561-573.
50. Hubbard MJ & McHugh NJ (1996) Mitochondrial ATP synthase F1-beta-subunit is a calcium-binding protein. *FEBS Lett* 391(3):323-329.
51. Dixon CJ, *et al.* (1999) Regulation of epidermal homeostasis through P2Y2 receptors. *Br J Pharmacol* 127(7):1680-1686.
52. Burrell HE, *et al.* (2005) Human keratinocytes release ATP and utilize three mechanisms for nucleotide interconversion at the cell surface. *J Biol Chem* 280(33):29667-29676.
53. Lee WK, *et al.* (2001) Purinoceptor-mediated calcium mobilization and proliferation in HaCaT keratinocytes. *J Dermatol Sci* 25(2):97-105.
54. Inoue K, Denda M, Tozaki H, Fujishita K, & Koizumi S (2005) Characterization of multiple P2X receptors in cultured normal human epidermal keratinocytes. *J Invest Dermatol* 124(4):756-763.
55. Greig AV, Linge C, Cambrey A, & Burnstock G (2003) Purinergic receptors are part of a signaling system for keratinocyte proliferation, differentiation, and apoptosis in human fetal epidermis. *J Invest Dermatol* 121(5):1145-1149.
56. Thiele JJ, Hsieh SN, Briviba K, & Sies H (1999) Protein oxidation in human stratum corneum: susceptibility of keratins to oxidation in vitro and presence of a keratin oxidation gradient in vivo. *J Invest Dermatol* 113(3):335-339.

ARTICLE 15

Supporting Information Inventory

- Supporting discussion.
- Supporting figures & legends.
- Supporting Table
- Supporting Materials and Methods.
- Supporting references.

Supporting Discussion

In this study, we have characterized new archetype of TRP channel encoded by a single gene. This channel is TRPM8 isoform expressed in the endoplasmic reticulum of keratinocytes and serves as a central element of signaling pathways engaged in cold-sensitivity of epidermal homeostasis (EH). Our results revealed a key role of eTRPM8 in keratinocyte bioenergetics: arbitration of the keratinocyte proliferation/differentiation balance (within the range of mild cold temperatures) via orchestrating the Ca^{2+}/ATP/$O_2^{\bullet-}$ triad.

eTRPM8: new architecture of functional TRP channel

Our results show that a single gene from TRP-channel family may in fact encode two fully functional channel isoforms with different transmembrane architecture, a classical TRPM8 with 6-transmembrane domains (TD) and an unconventional eTRPM8 channel that consists of only 4-TD.

Recently it has been reported that topical application of TRPM8 agonists accelerated epidermal barrier recovery after tape stripping (16). Since the authors failed to demonstrate the expression and localization of the classical cold-menthol receptor in keratinocytes, they speculated that "TRPM8-like" protein is involved. In the present study we addressed this intriguing issue and report cloning of two TRPM8 variants referred to as TRPM8(15a) and TRPM8(15a/δ16). Our study was then focused on the TRPM8(15a) mRNA and its related protein, eTRPM8, which forms functional Ca^{2+}-release channel in the endoplasmic reticulum (ER). Patch clamp recordings on the GUVs formed from the ER membrane fractions of the HEK293 cells expressing this isoform have shown a characteristic activity, including its responsivity to conventional TRPM8 activators such as cold, menthol, icilin and the specific agonist ws-12, as well as an inhibition by BCTC. In a view of these results, it seems likely that the N-terminal cytosolic segment and the first two TD of the classical full-size TRPM8 channel do not play any principal role in its activation. The detailed study of the biophysical properties of this isoform, including the kinetic analysis of single-channel activity is a subject of further independent study.

eTRPM8: a novel path for Ca^{2+} channeling from the ER to mitochondria

The existence of TRPM8 isoform that does not translocate to the plasma membrane, but is restricted to the ER membranes, where its activation triggers Ca^{2+} release, was demonstrated in our previous studies on human prostate cells (19, 44). Given the importance of Ca^{2+} homeostasis in keratinocyte differentiation, the role of the ER as major intracellular Ca^{2+} store and the lead of Ca^{2+} signaling impairment in pathology, the fact that Ca^{2+}-permeable eTRPM8 channel is specifically expressed in the ER grades this molecule as a potentially important therapeutic target. Indeed, it was recently demonstrated that in patients with Darier disease mutation of the *atp2a2* gene encoding the ER Ca^{2+} pump, SERCA2b, impairs growth of keratinocytes and leads to the alteration of epidermis structure, while the same mutation in mice induces squamous-cell carcinoma (45, 46). Here we demonstrated that *trpm8*$^{-/-}$ mice are characterized by the reduced number of basal proliferating cells, a significant accumulation of spinal cells and thinner granular and corneal compartments, what is indicative of the EH impairment.

Till now only inositol trisphosphate receptor ($InsP_3R$) have been postulated to primarily regulate $[Ca^{2+}]_m$ via tight ER-mitochondria connections (47, 48). We found that elevated steady-state $[Ca^{2+}]_m$ correlates with the level of eTRPM8 expression and that eTRPM8 activation releases Ca^{2+} within ER-mitochondria functional nanodomains, what facilitates mitochondrial Ca^{2+} uptake leading to an abrupt elevation of $[Ca^{2+}]_m$. In turn, $[Ca^{2+}]_m$ plays an important role in cell bioenergetics and ATP synthesis in particular. Ca^{2+}-dependent regulation of ATP synthesis involves several mechanisms, including tricarboxylic acid cycle's Ca^{2+}-dependent dehydrogenase regulation (for review see (49)) and Ca^{2+} binding by ATP synthase beta subunit (complex F1) itself (50).

eTRPM8 signaling in keratinocytes proliferation

ATP synthesized in keratinocytes is not only used in energy-dependent processes, but it is also secreted into interstitial compartment (51, 52) to support paracrine purinergic signaling. This signaling primarily targets metabotropic P2Y receptors, activation of which in basal keratinocytes stimulates their proliferation (53). Of P2Y-receptor subtypes, ADP/ATP-sensitive P2Y1 (EC_{50} ~10-50 nM for ADP and ~180-320 nM for ATP) and ATP/UTP-sensitive P2Y2 (EC_{50} ~100-500 nM for ATP and UDP) were found in basal and suprabasal compartments [ref]. Induction of proliferation in *stratum basale* (*SB*) by extracellular ATP was demonstrated to be independent on extracellular Ca^{2+} and to involve Ca^{2+} release from the ER (54), what favors recruitment of P2Y vs. P2X receptors. In our ATP quantification assay, we estimated that $[ATP]_e$ in the media with basal non-stimulated keratinocytes grown at 37°C ranges from 10 to 100 nM, what is close to the effective concentrations for P2Y receptors activation. This suggests that cold-induced eTRPM8 activation may promote purinergic signaling via enhanced synthesis and secretion of ATP. Indeed, our data demonstrate that both increased eTRPM8 expression and activity elevate ATP concentration in keratinocytes as well as in

surrounding medium. Together with previous studies showing that optimal in vivo ATP secretion by keratinocytes is achieved at about 31°C [ref], our data indicate that ATP synthesis and/or secretion can be regarded as cold-dependent processes in which eTRPM8-mediated Ca^{2+} signaling plays an important role.

We have also demonstrated that eTRPM8 expression and activity correlates with accumulation of superoxide ($O_2^{\bullet-}$) and likely a concomitant accumulation of peroxinitrite in mitochondria. Both matrix mitochondrial Mn superoxide dismutase (SOD2) and Cu/Zn cytosolic and interspace mitochondrial superoxide dismutase (SOD1) are expressed in basal/suprabasal keratinocytes and provide antioxidant defense of these cells by catalysis of $O_2^{\bullet-}$ dismutation (40). Our data suggest a minor role, if any, of $O_2^{\bullet-}$ in eTRPM8-dependent proliferation of basal keratinocytes. The proposed signaling pathways by which eTRPM8 stimulates proliferation of basal keratinocytes are summarized in **Figure 7 (top left panel)**.

eTRPM8 signaling in keratinocytes differentiation

We have found that eTRPM8 expression is increased in differentiated layer of epidermis and that exposure to mild cold stimulates its activity. Furthermore, we have demonstrated that mild cold enhances the differentiation rate of keratinocytes in an eTRPM8-dependent manner. Although involvement of ATP in keratinocyte differentiation currently lacks direct evidence, the fact that proportion of FLG-positive cells shows the same cold-dependence as ATP synthesis strongly supports this idea. In addition to P2Y receptors, keratinocytes also express Ca^{2+}-permeable ionotropic P2X purinoceptors. Homomeric P2X5 receptor (EC_{50} ~5-10 μM for ATP) was identified in the basal, suprabasal and spinal compartment (55), whereas homomeric P2X7 receptor (EC_{50} ~100 μM for ATP) was detected in the late spinal and granular layers, where it seems to be involved in late differentiation by mediating Ca^{2+}-dependent activation of TGM1 and, thus, leading to keratinocyte death: transformation of keratinocytes into corneocytes.

We also demonstrated that mild cold stimulates eTRPM8-dependent accumulation of $O_2^{\bullet-}$. Our data indicate that, at least partially, this $O_2^{\bullet-}$ originates from mitochondria, though it remains unclear whether long-term activation of eTRPM8 induces NADPH oxidase-dependent $O_2^{\bullet-}$ synthesis in cytosol. ROS and more specifically $O_2^{\bullet-}$ have been shown to be involved in keratinocyte differentiation (41). Furthermore, ROS gradient from basal to upper layers is characteristic for epidermis (56). However, strong accumulation of $O_2^{\bullet-}$ induces an increase of the number of suprabasal/spinal cells paralleled with the decrease of the quantity of granular cells. Thus, our results suggest that differentiation of keratinocyte is a fine-tuned process involving $O_2^{\bullet-}$ accumulation and elevation of ATP concentration in eTRPM8-dependent manner. The optimal progression of this process is achieved at physiological skin temperature of about 31°C. Based on this findings we summarized in **Figure 7 (top and bottom right panels)** the signaling pathways involved in the cold-stimulated eTRPM8-dependent differentiation of keratinocytes.

eTRPM8 vs. TRPV3 in epidermal homeostasis

Identified in keratinocytes warmth-activated TRPV3 has been proposed to participate in activation of Transglutaminase (13, 14) and, as consequence, to be involved in terminal differentiation of keratinocytes. However, for healthy human mean physiological skin temperature is about 32°C (2), what is slightly below the threshold for TRPV3 activation. Interestingly, TRPV3 and eTRPM8 complement each other in thermosensitivity (i.e. activation by warmth vs. cooling) and Ca^{2+} signaling mechanisms they engage (i.e. mediation of Ca^{2+} entry vs. Ca^{2+} release). Thus, relative expression and activity of eTRPM8 and TRPV3 may provide skin with an adaptive capacity to variations in environmental temperatures.

In conclusion, we report the identification of new TRPM8 isoform, eTRPM8, which enables cold-dependent regulation of epidermal homeostasis. eTRPM8 is a key controller of temperature-dependent energy metabolism and signaling in keratinocytes that provides skin with the capacity to adapt to large variations of environmental temperature.

ARTICLE 15

Supporting Figures

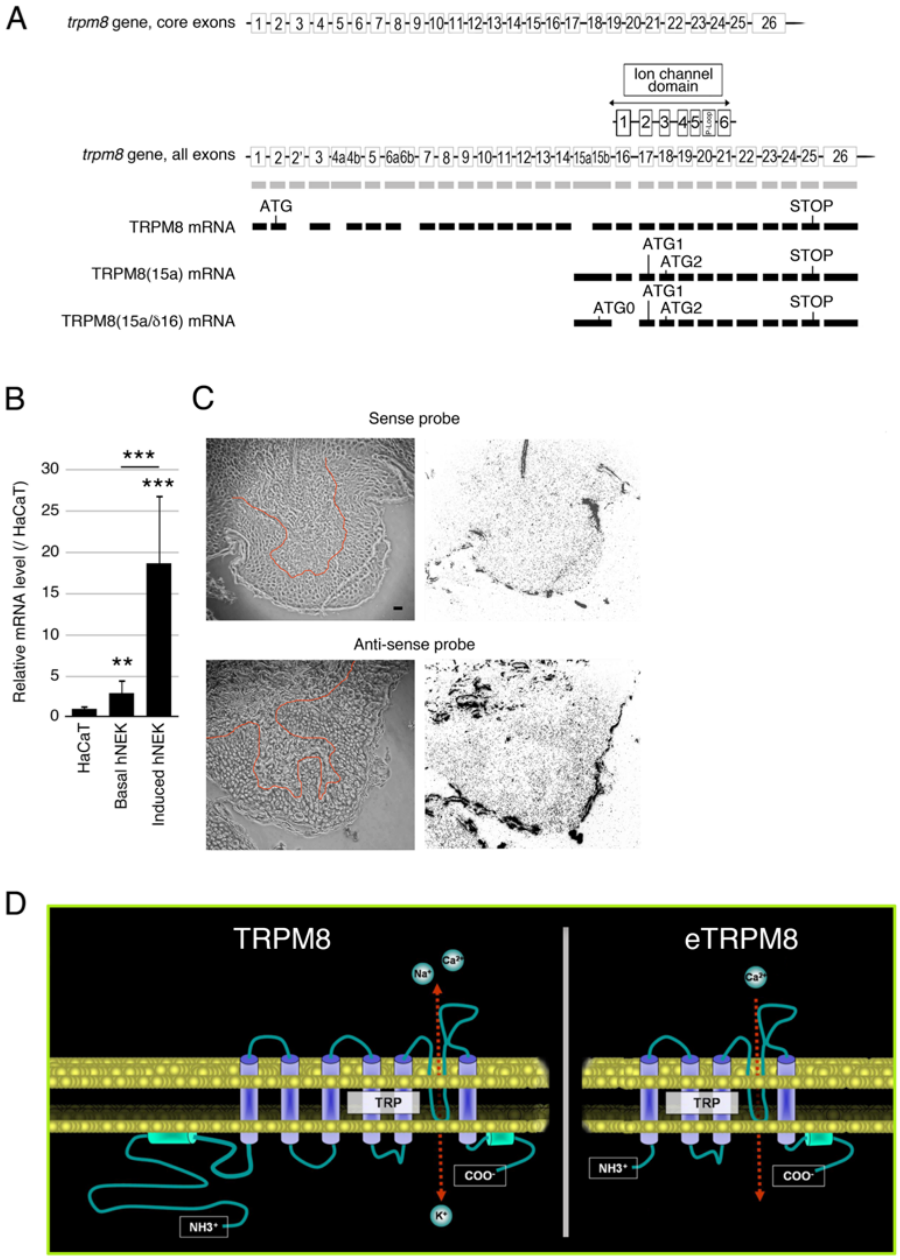

Figure S1. *TRPM8 mRNA variants encode a 4 transmembrane domain monomer.* **A.** Non-at-scale genomic structure of the *trpm8* gene aligned with exonic structure of classical TRPM8, TRPM8(15a) and TRPM8(15a/δ16) mRNAs. Transmembrane domains and P-loop segment are positioned in accordance with their DNA encoding sequences. Putative first ATG codon and STOP codon are presented. **B.** Real-time PCR compares quantity of TRPM8(15a) mRNA in HaCaT cells and in basal or induced (see Methods) hNEKs (n=3). **C.** Expression of eTRPM8 mRNA in human female breast skin sections (n=3) detected with *in situ* hybridization using a either a anti-sens probe targeting the pore region of TRPM8 (top right panel) or its sense counterpart (down right panel). The boundary between epidermis and dermis is outlined (red) in the transmitted light images of the skin sections (left panels, respectively). Scale bar: 10 µm. **D.** Schematic representation of the predicted tertiary structure of TRPM8 and eTRPM8 monomers and their cellular location. **E.** Western blot showing the presence of eTRPM8 and non-functional mutant, eTRPM8(Y148A) in ER membranes-enriched extracts of transfected HEK cells. Control experiment was achieved by the transfection of an empty vector in HEK cells. eTRPM8 was detected as the expected size of 40kDa. Internal control for protein amount was perform through the detection of Calnexin.

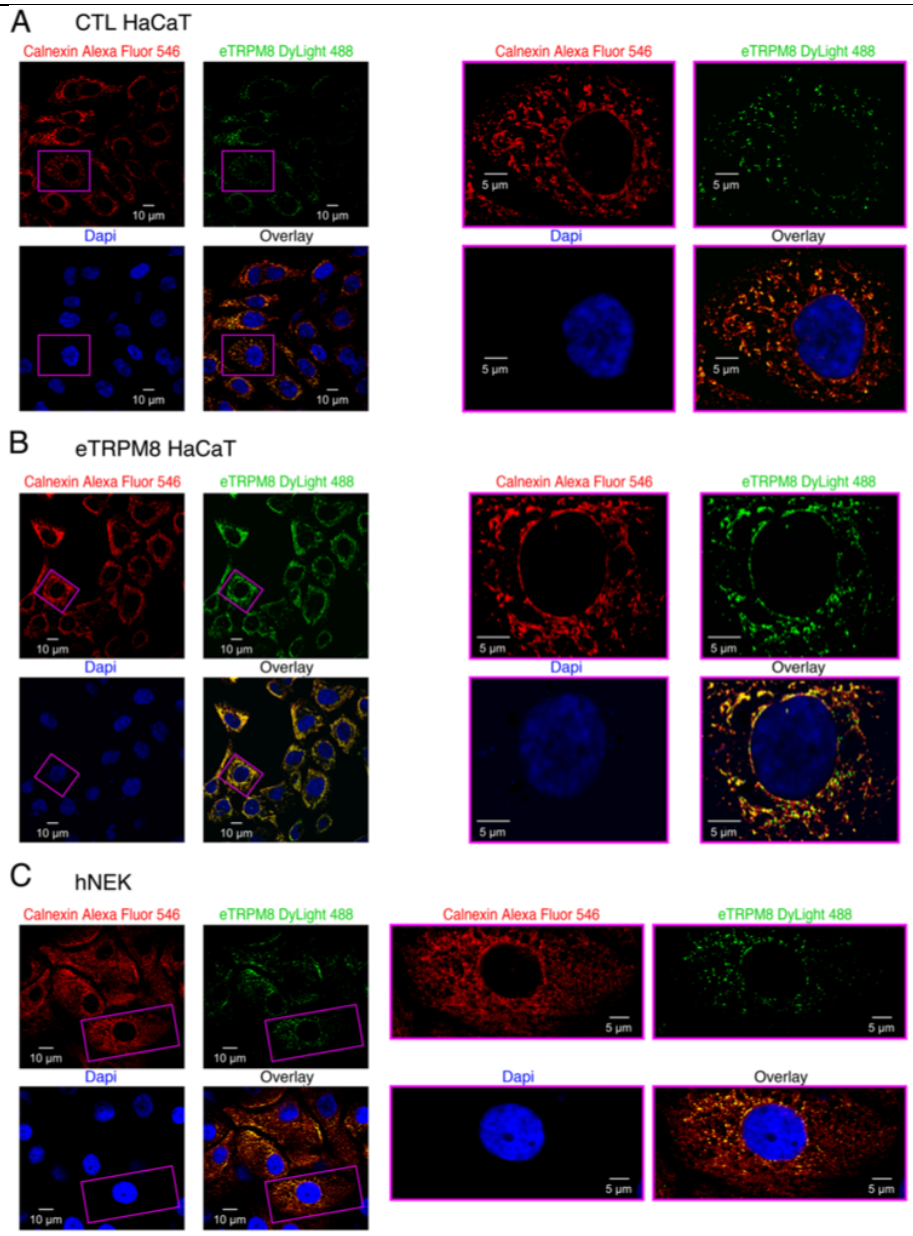

Figure S2. eTRPM8 is expressed in the keratinocyte endoplasmic reticulum (ER) but not in the cell plasma membrane. *Detection of eTRPM8 and the ER marker, calnexin, was performed in (**A**) control HaCaT cells (CTL HaCaT), (**B**) HaCaT cells overexpressing epidermal TRPM8 (eTRPM8 HaCaT) and (**C**) human normal epidermal keratinocytes (hNEK) using indirect immunostaining. Primary antibody-specific binding to eTRPM8 and calnexin was visualized with DyLight 488- and Alexa Fluor 546-conjugated IgGs, respectively. Galleries (left) show confocal images of Alexa Fluor 546 (the ER elements; red), DyLight 488 (eTRPM8; green), DAPI (nuclei; blue) fluorescence and their overlay, as indicated. Enlarged images of the boxed regions are shown on the right, respectively.*

ARTICLE 15

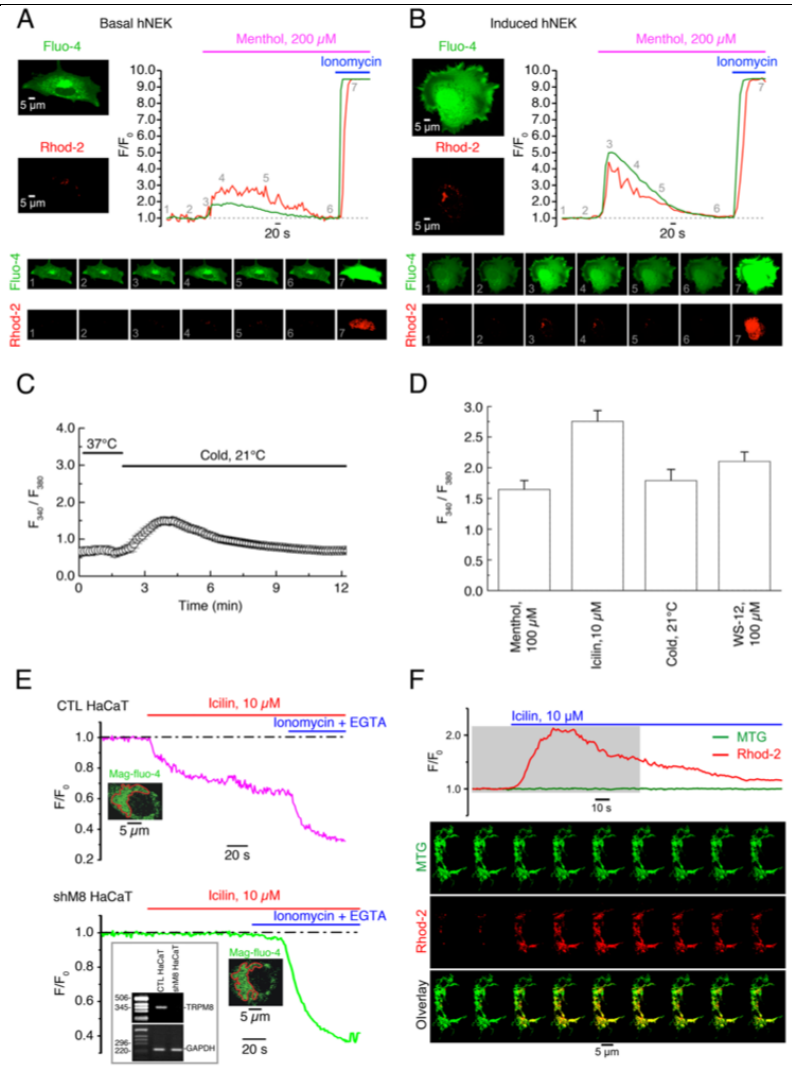

Figure S3. *eTRPM8-mediated Ca^{2+} release results in mitochondrial Ca^{2+} uptake in human keratinocytes.* Changes of Ca^{2+} concentration in cytosol ($[Ca^{2+}]_c$) and mitochondria ($[Ca^{2+}]_m$) elicited by external application of 200 μM menthol were monitored using x-y time series imaging of fluo-4 and rhod-2 fluorescence, respectively, in (**A**) primary culture of basal and (**B**) induced (see Methods) human primary culture keratinocytes (hPK). To eliminate capacitative Ca^{2+} entry, external solution, containing 70 μM Ca^{2+}, was supplemented with 10 μM La^{3+}. To estimate the load of the Ca^{2+}-sensitive indicators, the cells were exposed to 2.5 μM of ionomycin at the end of each experiment. The fluorescence intensity (F) was normalized to the averaged fluorescence intensity before menthol application (F_0). The plots show the time course of normalized fluorescence (F/F_0) of fluo-4 (green traces) and rhod-2 (red traces). The galleries below the plots demonstrate the images of fluo-4 and rhod-2 fluorescence (as indicated) captured at the moments, depicted by the numbers on the plots, respectively. **C**. Application of cold solution (21°C) induces $[Ca^{2+}]_c$ transients in keratinocytes bathed in Ca^{2+}-free medium. Bar diagram plot show mean amplitudes of the fura-2 responses (fluorescence intensity ratio at 340 nm and 380 nm) to 100 μM menthol (n= 30), 10 μM icilin (n= 32), 0.1 μM WS-12 (n= 25) and mild cold (21ºC) (n= 20) in the cells bathed in Ca^{2+}-free solution (**D**). Changes in the ER luminal Ca^{2+} concentration $[Ca^{2+}]_{ER}$ were monitored at 37°C in digitonin-permeabilized keratinocytes using the low affinity Ca^{2+} indicator mag-fluo-4 (**E**). Application of 10 μM icilin induces gradual decrease of the normalized mag-fluo-4 fluorescence (F/F_0) in control HaCaT cells (CTL HaCaT; top) but not in eTRPM8 KD HaCaT cells (shM8 HaCaT; bottom). To verify whether mag-fluo-4 response reflects the decrease of $[Ca^{2+}]_{ER}$, the ER was depleted at the end of the experiment by exposure of the cells to the solution containing 1 μM ionomycin and 10 μM EGTA. The traces on the graphs show the time course of the normalized mag-fluo-4 fluorescence (F/F_0) averaged within outlined (red) regions. Visualization of mitochondria with MitoTracker® Green FM (MTG) confirms mitochondrial origin of rhod-2 response to stimulation of eTRPM8 with icilin in HaCaT cells (**F**). The plot shows the time course of self-normalized (F/F_0) MTG and rhod-2 fluorescence, as indicated. The fluorescence intensity (F) was normalized to the averaged fluorescence intensity before icilin application (F_0). The galleries below the plot demonstrate the images of MTG fluorescence (top), rhod-2 fluorescence (middle) and their overlay (bottom): every 12th image captured from a single HaCaT cell during the period, highlighted on the plot by grey background, is shown (from left to right). Note that elevation of mitochondrial Ca^{2+} concentration ($[Ca^{2+}]_m$) is reported in the overlay images by change in color of mitochondria from green (dominating MTG fluorescence) to

yellow (the overlay of MTG and elevated rhod-2 fluorescence).

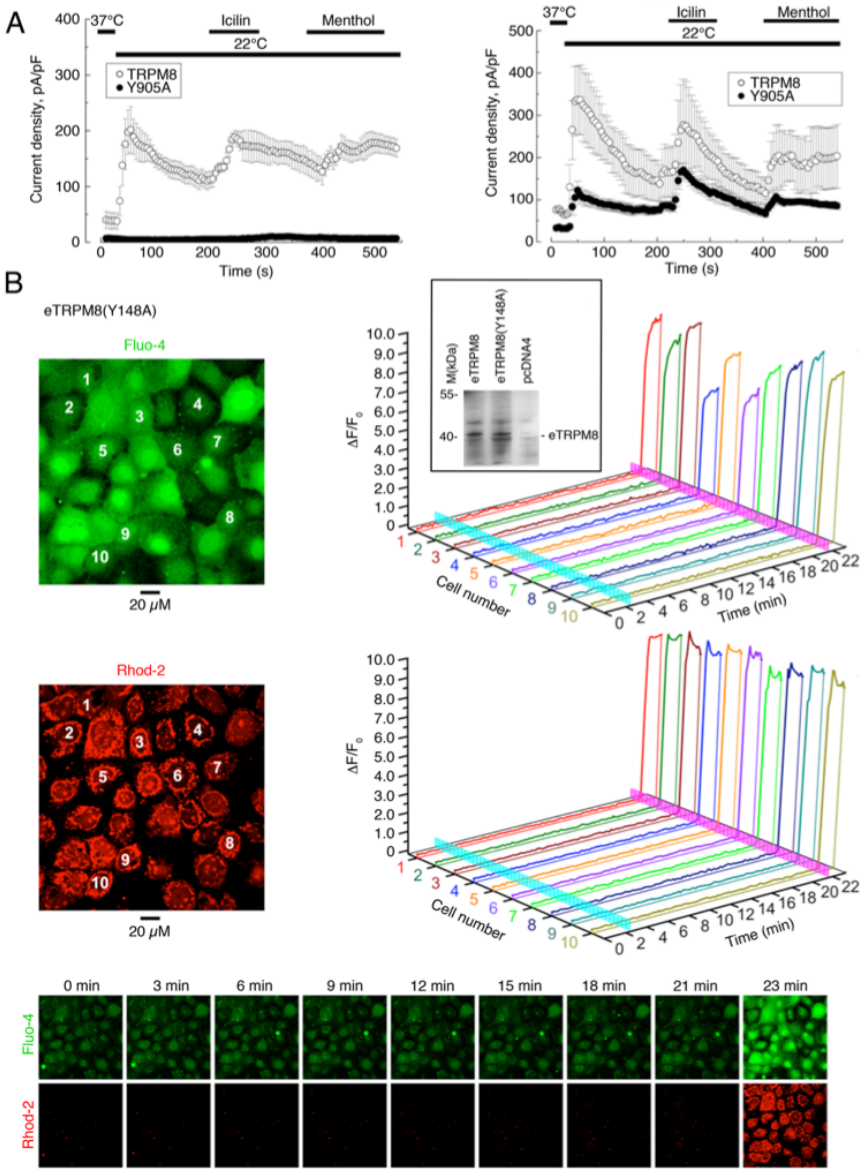

Figure S4. *Mutation in TRPM8 or eTRPM8 pore region abolishes the channel-mediated Ca^{2+} fluxes.* **A.** Whole-cell patch clamp recordings were conducted in *wt*TRPM8-, TRPM8(Y905A)- and *wt*TRPM8+ TRPM8(Y905A)-transfected HEK cells. The cell membrane potential was repetitively altered by voltage ramps from -100 to +100 mV (applied at 0.2 Hz). The changes in the mean current density at +100 mV, elicited by the exposure to cold (22°C), 500 µM menthol and 10 µM icilin were compared in *wt*TRPM8- versus TRPM8(Y905A)-transfected cells (left panel; n=20 and n=7, respectively), and in *wt*TRPM8- versus *wt*TRPM8+ TRPM8(Y905A) co-transfected cells (right panel; n=15 and n=8, respectively). Cotransfection of *wt*TRPM8 and TRPM8(Y905A) was performed at a 1:3 ratio. **B**. No detectable changes of Ca^{2+} concentration in cytosol ($[Ca^{2+}]_c$) and mitochondria ($[Ca^{2+}]_m$) were observed in response to 200 µM menthol in HaCaT cells expressing eTRPM8(Y148A). Changes of $[Ca^{2+}]_c$ and $[Ca^{2+}]_m$ were monitored using x-y time series imaging of fluo-4 and rhod-2 fluorescence, respectively. To eliminate capacitative Ca^{2+} entry, external solution, containing 70 µM Ca^{2+}, was supplemented with 10 µM La^{3+}. The fluorescence intensity (F) was normalized to the averaged fluorescence intensity before menthol application (F_0). Relative changes in the fluorescence intensity ($\Delta F/F_0$), averaged within each of 10 cells, denoted by the numbers on the images (left), are plotted over time, respectively (right). To estimate the load of the Ca^{2+}-sensitive indicators, the cells were exposed to 2.5 µM of ionomycin at the end of the experiment. Menthol and ionomycin applications are depicted on the 3D plots by vertical cyan and magenta bars, respectively. The galleries below the plots demonstrate the images of fluo-4 and rhod-2 fluorescence (as indicated), captured at times indicated above the images. Inset shows the immunodetection of *wt* eTRPM8 and eTRPM8(Y148A) expressed in HEK cells. Negative control is achieved with protein extract from HEK transfected with the empty vector pcDNA4.

ARTICLE 15

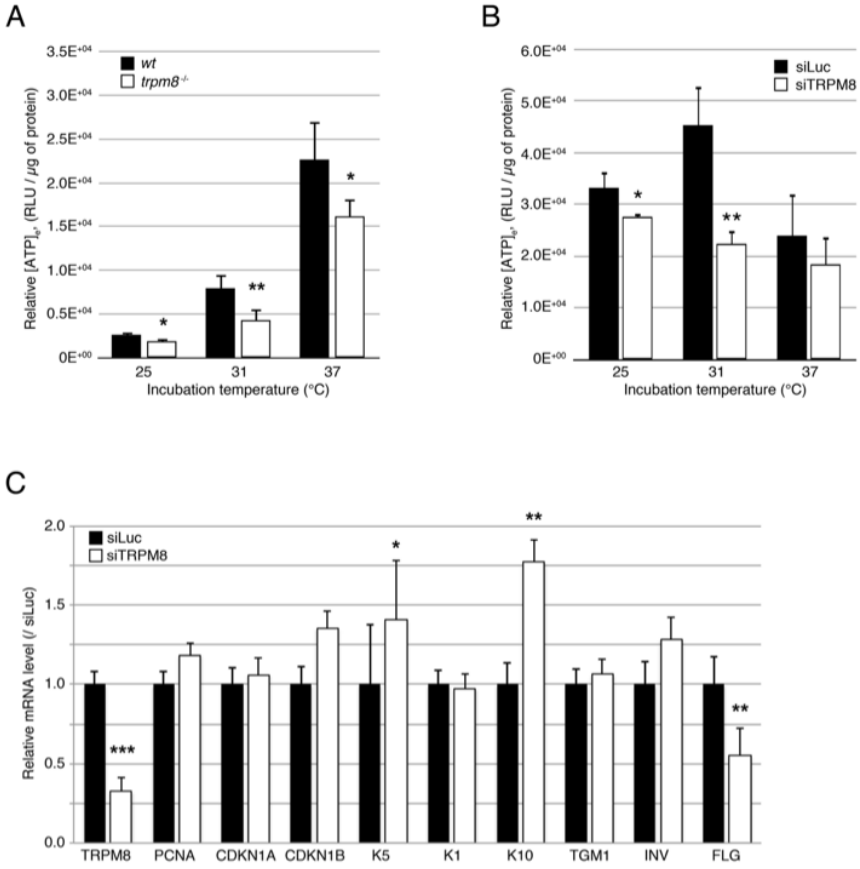

Figure S5. A. Extracellular ATP concentration ($[ATP]_e$) assessed in the media with cultured keratinocytes, isolated from wild type mouse (*wt* mPK) and *trpm8* knock-out mouse (*trpm8* $^{-/-}$ mPK) and grown at 25°C, 31°C or 37°C for 3 days. Data are shown as mean ± SD for 6 *wt* mice and 6 *trpm8* $^{-/-}$ mice. **B.** Same as (**A**) but for induced hNEKs transfected with either control siRNA (siLuc) or siRNA targeting TRPM8 (siTRPM8) and cultured at 25°C, 31°C or 37°C for 3 days. **C**. Real-time PCR experiment demonstrates the effect of eTRPM8 silencing (60% decrease) in hNEK cells (siTRPM8 vs. siLuc) on the expression of genes encoding PCNA, CDKN1A, CDKN1B, keratin 5 (K5), keratin 1 (K1), keratin 10 (K10), transglutaminase 1 (TGM1), involucrin (INV) and filaggrin (FLG). Experiment was performed 3 times, and values are presented as mean ± SD. The mean values on the plot are re-scaled so that mean value in siLuc-treated cells for each gene tested is 1 ± SD. * $p < 0.05$, ** $p < 0.01$, *** $p < 0.001$.

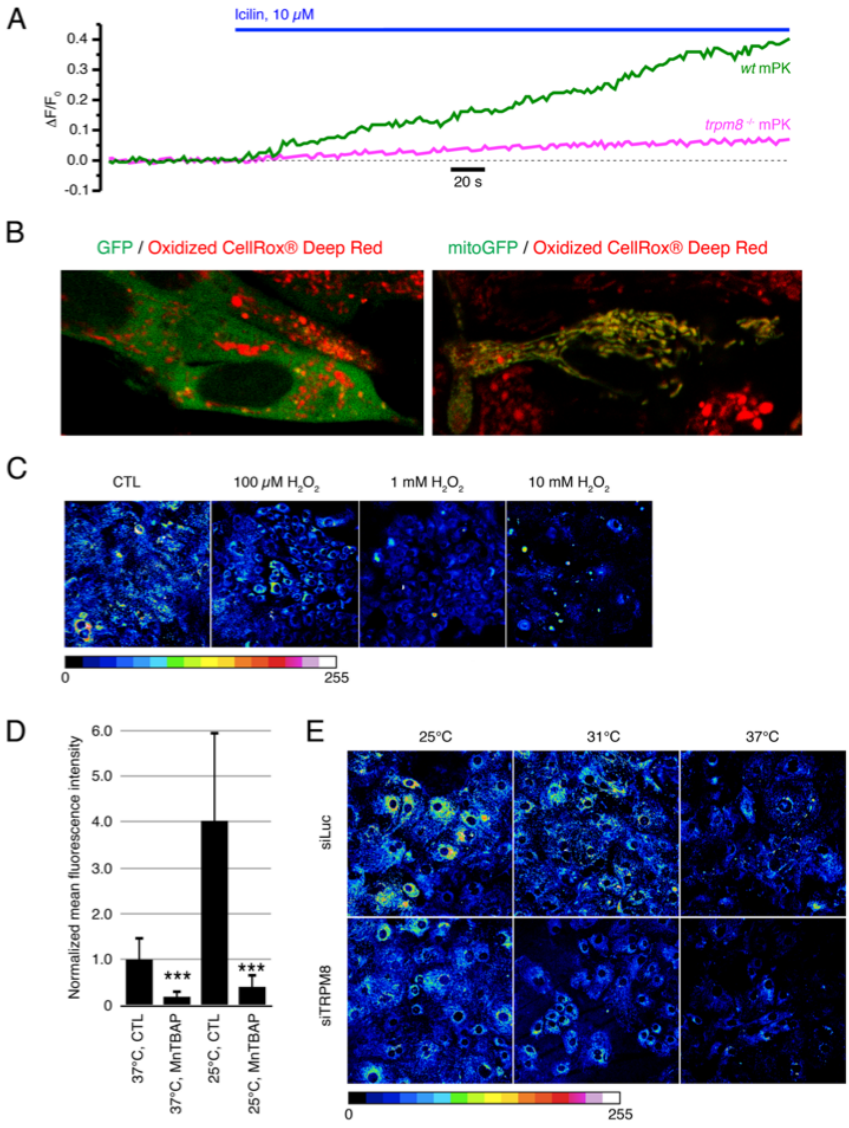

Figure S6. *Icilin-induced $O_2^{\bullet-}$ production is significantly reduced in primary culture of keratinocytes from trpm8$^{-/-}$ TRPM8 mice.* **A.** Relative changes in the MitoSOX^{TM} Red fluorescence intensity ($\Delta F/F_0$), detected using confocal x-y time series imaging in primary culture of keratinocytes from wild type mice, *wt* mPK (green trace), and keratinocytes from *trpm8* $^{-/-}$ TRPM8 mice, *trpm8* $^{-/-}$ mPK (magenta trace), reflect the time course of $O_2^{\bullet-}$ accumulation in response to application of 10 µM icilin. **B.** Confocal images of oxidized CellRox® deep red reagent in cells transfected with either GFP (left panel) or mitoGFP (right panel) revealed mitochondrial localization of CellRox® deep red reagent. **C.** Confocal images of CellRox® deep red-loaded hNEKs incubated in solutions containing vehicle only (water; CTL) or increasing concentrations of hydrogen peroxide (H_2O_2), as indicated. The CellRox® deep red fluorescence intensity was color-coded as indicated by the bar. The same illumination intensity, photomultiplier gain and offset were used in all the experiments (n=3). **D.** Bar diagram plot compares mean intensity of the normalized CellRox® deep red fluorescence in control hNEK (CTL) with that in hNEK pre-treated with 100 µM MnTBAP for 30 min (MnTBAP) after 3-day cell culturing at either 37°C or 25°C, as indicated (n=3). **E.** Confocal images of CellRox® deep red-loaded hNEKs transfected with either control siRNA (siLuc) or siRNA targeting TRPM8 (siTRPM8). Induced (see Methods) cells were cultured at 25°C, 31°C or 37°C for 3 days. The CellRox® deep red fluorescence intensity was color-coded as indicated by the bar. The same illumination intensity, photomultiplier gain and offset were used in all the experiments (n=3).

ARTICLE 15

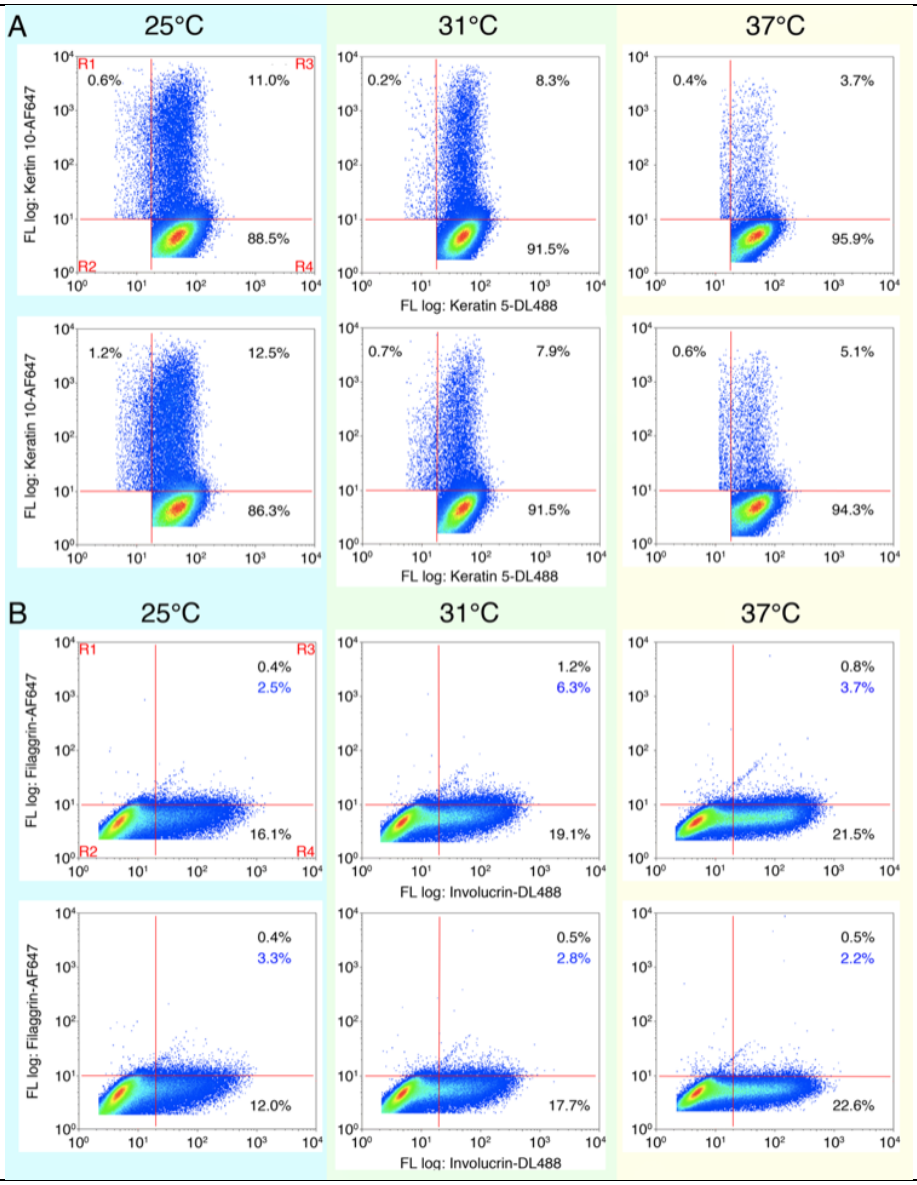

Figure S7. *Mild cold effect on distribution of the induced hNEKs according to the expression of differentiation markers.* **A.** Flow cytometry co-detection of keratin 5 and keratin 10 in hNEKs transfected with either control siRNA (siLuc) or siRNA targeting TRPM8 (siTRPM8) and grown at 25°C, 31°C or 37°C for 4 days. After compensation, regions of interest were chosen to highlight 4 cell populations (panels A and B, top left): (R1) cells expressing single marker indicated on Y axis, (R2) cells expressing non-specific markers, (R3) cells co-expressing two markers indicated on X and Y axes, and (R4) cell expressing single marker indicated on X axis. For each population (except R2) its factional contribution is expressed as percentage in corresponding quadrant on the plots. Differentiation markers denoted on X-axis were immunodetected with Dyelight-488-conjugated IgG, while differentiation denoted on Y-axis were immunodetected with AlexaFluor-647-conjugated IgG. **B.** Same as (A) for co-detection of involucrin and filaggrin labeled with Dyelight-488- and AlexaFluor-647-conjugated IgG, respectively.

ARTICLE 15

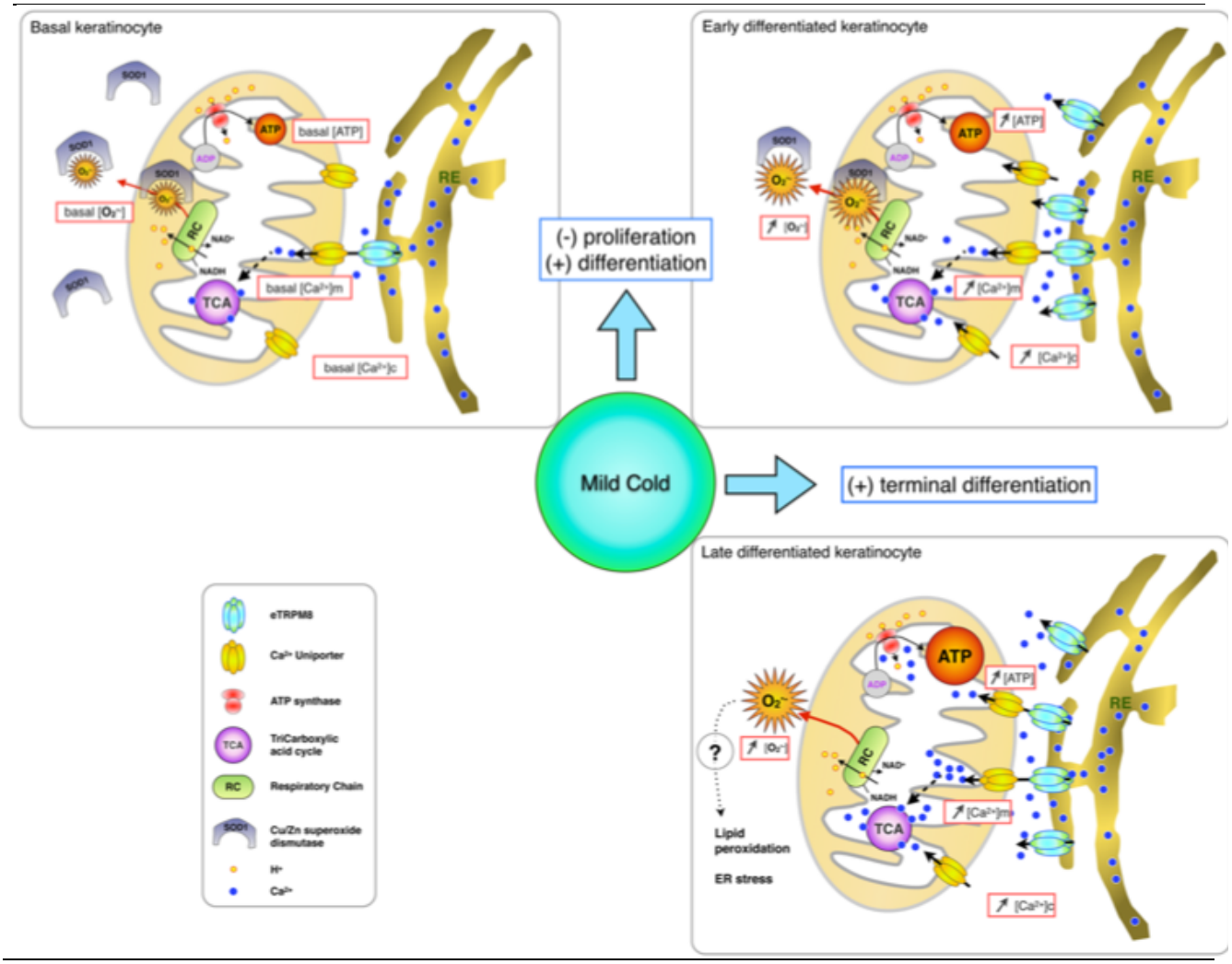

Figure S8. *Schematic representation of the proposed mechanism by which eTRPM8 increases proliferation of basal keratinocytes and mediates cold-dependent potentiation of keratinocyte differentiation.* In basal keratinocytes (top left) the level of expression of eTRPM8 is lower while the level of expression of superoxide dismutase 1 (SOD1) is higher than in early differentiated keratinocytes (top right). Activation of eTRPM8 in basal keratinocytes will, therefore, cause a moderate increase of mitochondrial Ca^{2+} concentration ($[Ca^{2+}]_m$), which, in turn, could potentiate tricarboxylic acid cycle (TCA), and, as a result, increase the activity of the respiratory chain (RC), and ATP synthesis and secretion. However, concomitant $O_2^{\bullet-}$ accumulation will be limited by SOD1 activity. Moderate increase in ATP concentration will initiate cell cycle progression through paracrine activation of P2Y receptors.. Induction of differentiation is associated with an increase of eTRPM8 expression and a decrease of SOD1 expression in differentiating keratinocytes (top right and bottom right). Therefore activation of eTRPM8 in differentiated keratinocytes will boost ATP and $O_2^{\bullet-}$ synthesis. Augmented ATP secretion and accumulation in interstitial space will induce robust elevation of cytosolic Ca^{2+} concentration, $[Ca^{2+}]_c$ (e.g. via activation of P2X-mediated Ca^{2+} entry). Enhanced $O_2^{\bullet-}$ synthesis will overcome the activity of downregulated SOD1, thus, resulting in accumulation of $O_2^{\bullet-}$, what, in turn, will induce lipid peroxydation and ER stress. This, accompanied by a sustained $[Ca^{2+}]_c$ elevation, will induce terminal differentiation of keratinocytes.

Video. *eTRPM8 and Mitochondria coordinated motility.* Concomitant motion of the mTurquoise2-tagged eTRPM8 and mitochondria was visualized in control HaCaT cells (CTL HaCaT) using confocal imaging of mTuquoise2 and MitoTracker® Green FM (MTG) fluorescence, respectively. Images were acquired at 0.05 Hz.

Video. *Mitochondria and ER coordinated motility.* Concomitant motion of the endoplasmic reticulum (ER) elements and mitochondria was visualized in control HaCaT cells (CTL HaCaT) using confocal imaging of Brefeldin A BODIPY 558/568 and MitoTracker® Green FM (MTG) fluorescence, respectively. Images were acquired at 0.625 Hz.

ARTICLE 15

Supporting Table S1

	5’ forward 3’	5’ reverse 3’
Cloning		
TRPM8(15a)	TAAGAATGGACTCACGCACAGG	TCTCAAGGTCTCAGCACACTA
PCR		
hTRPM8(ex 2-7)	GAAGGAATGACACTCTGGAC	GCCATTGTCCACGAGCAGC
hTRPM8 (11-14)	GATTTTCACCAATGACCGCCG	CCCCAGCAGCATTGATGTCG
hTRPM8 (20-21)	TGCTGCAGAGGATGCTGATCG	GGTGCCCACCGTGTAGCCAA
hTRPM8 (15a-17)	GTGCTGATGTCGCTGTAGAGC	GAGGAAGGCGATGTAGAAGACC
mTRPM8(ex16-18)	CGAGACACGAAGAACTGGAAG	CTGCCTCACTTCATCACAGAAG
mGAPDH	CTGCGACTTCAACAGCAACTC	TCCACCACCCTGTTGCTGTA
Real-time PCR		
GAPDH	ACCCACTCCTCCACCTTTG	CTCTTGTGCTCTTGCTGGG
TRPM8	CGGTCATCTACGAGCCCTAC	CACACACAGTGGCTTGGACT
PCNA	CGACACCTACCGCTGCGACC	TAGCGCCAAGGTATCCGCGT
CDKN1A	TCAGGGTCGAAAACGGCGGC	TTTGAGGCCCTCGCGCTTCC
CDKN1B	AGCGGAGCAATGCGCAGGAA	GGCGTCTGCTCCACAGAACCG
Keratin 1	ATTTCTGAGCTGAATCGTGTGATC	CTTGGCATCCTTGAGGGCATT
Keratin 5	CTGCTGGAGGGCGAGGAATGC	CCACCGAGGCCACCGCCATA
Keratin 10	TGATGTGAATGTGGAAATGAATGC	GTAGTCAGTTCCTTGCTCTTTTCA
Involucrin	CTGCCTCAGCCTTACTGTGA	GGAGGAGGAACAGTCTTGAGG
Filaggrin	CTGGACACTCAGGTTCCCAT	TTTCGTGTTTGTCTGCTTGC
Transglutaminase 1	TCACTGTTTCATTGTCTCCA	CCCTCACCAATGTCGTCTTC

Supporting Discussion

In this study, we have characterized new archetype of TRP channel encoded by a single gene. This channel is TRPM8 isoform expressed in the endoplasmic reticulum of keratinocytes and serves as a central element of signaling pathways engaged in cold-sensitivity of epidermal homeostasis (EH). Our results revealed a key role of eTRPM8 in keratinocyte bioenergetics: arbitration of the keratinocyte proliferation/differentiation balance (within the range of mild cold temperatures) via orchestrating the Ca^{2+}/ATP/$O_2^{\bullet-}$ triad.

eTRPM8: new architecture of functional TRP channel

Our results show that a single gene from TRP-channel family may in fact encode two fully functional channel isoforms with different transmembrane architecture, a classical TRPM8 with 6-transmembrane domains (TD) and an unconventional eTRPM8 channel that consists of only 4-TD.

Recently it has been reported that topical application of TRPM8 agonists accelerated epidermal barrier recovery after tape stripping [1]. Since the authors failed to demonstrate the expression and localization of the classical cold-menthol receptor in keratinocytes, they speculated that "TRPM8-like" protein is involved. In the present study we addressed this intriguing issue and report cloning of two TRPM8 variants referred to as TRPM8(15a) and TRPM8(15a/δ16). Our study was then focused on the TRPM8(15a) mRNA and its related protein, eTRPM8, which forms functional Ca^{2+}-release channel in the endoplasmic reticulum (ER). Patch clamp recordings on the GUVs formed from the ER membrane fractions of the HEK293 cells expressing this isoform have shown a characteristic activity, including its responsivity to conventional TRPM8 activators such as cold, menthol, icilin and the specific agonist ws-12, as well as an inhibition by BCTC. In a view of these results, it seems likely that the N-terminal cytosolic segment and the first two TD of the classical full-size TRPM8 channel do not play any principal role in its activation. The detailed study of the biophysical properties of this isoform, including the kinetic analysis of single-channel activity is a subject of further independent study.

eTRPM8: a novel path for Ca^{2+} channeling from the ER to mitochondria

The existence of TRPM8 isoform that does not translocate to the plasma membrane, but is restricted to the ER membranes, where its activation triggers Ca^{2+} release, was demonstrated in our previous studies on human prostate cells [2,3]. Given the importance of Ca^{2+} homeostasis in keratinocyte differentiation, the role of the ER as major intracellular Ca^{2+} store and the lead of Ca^{2+} signaling impairment in pathology, the fact that Ca^{2+}-permeable eTRPM8 channel is specifically expressed in the ER grades this molecule as a potentially important therapeutic target. Indeed, it was recently demonstrated that in patients with Darier disease mutation of the *atp2a2* gene encoding the ER Ca^{2+} pump, SERCA2b, impairs growth of keratinocytes and leads to the alteration of epidermis structure, while the same mutation in mice induces squamous-cell carcinoma [4,5]. Here we demonstrated that *trpm8*$^{-/-}$ mice are characterized by the reduced number of basal proliferating cells, a significant accumulation of spinal cells and thinner granular and corneal compartments, what is indicative of the EH impairment.

Till now only inositol trisphosphate receptor ($InsP_3R$) have been postulated to primarily regulate $[Ca^{2+}]_m$ via tight ER-mitochondria connections [6,7]. We found that elevated steady-state $[Ca^{2+}]_m$ correlates with the level of eTRPM8 expression and that eTRPM8 activation releases Ca^{2+} within ER-mitochondria functional nanodomains, what facilitates mitochondrial Ca^{2+} uptake leading to an abrupt elevation of $[Ca^{2+}]_m$. In turn, $[Ca^{2+}]_m$ plays an important role in cell bioenergetics and ATP synthesis in particular. Ca^{2+}-dependent regulation of ATP synthesis involves several mechanisms, including tricarboxylic acid cycle's Ca^{2+}-dependent dehydrogenase regulation (for review see [8]) and Ca^{2+} binding by ATP synthase beta subunit (complex F1) itself [9].

eTRPM8 signaling in keratinocytes proliferation

ATP synthesized in keratinocytes is not only used in energy-dependent processes, but it is also secreted into interstitial compartment [10,11] to support paracrine purinergic signaling. This signaling primarily targets metabotropic P2Y receptors, activation of which in basal keratinocytes stimulates their proliferation [12]. Of P2Y-receptor subtypes, ADP/ATP-sensitive P2Y1 (EC_{50} ~10-50 nM for ADP and ~180-320 nM for ATP) and ATP/UTP-sensitive P2Y2 (EC_{50} ~100-500 nM for ATP and UDP) were found in basal and suprabasal compartments [ref]. Induction of proliferation in *stratum basale* (*SB*) by extracellular ATP was demonstrated to be independent on extracellular Ca^{2+} and to involve Ca^{2+} release from the ER [13], what favors recruitment of P2Y vs. P2X receptors. In our ATP quantification assay, we estimated that $[ATP]_e$ in the media with basal non-stimulated keratinocytes grown at 37°C ranges from 10 to 100 nM, what is close to the effective concentrations for P2Y receptors activation. This suggests that cold-induced eTRPM8 activation may promote purinergic signaling via enhanced synthesis and secretion of ATP. Indeed, our data demonstrate that both increased eTRPM8 expression and activity elevate ATP concentration in keratinocytes as well as in surrounding medium. Together with previous studies showing that optimal in vivo ATP secretion by keratinocytes is achieved at about 31°C [ref], our data indicate that ATP synthesis and/or secretion can be regarded as cold-dependent processes in which eTRPM8-mediated Ca^{2+} signaling plays an important role.

We have also demonstrated that eTRPM8 expression and activity correlates with accumulation of superoxide ($O_2^{\bullet-}$) and likely a concomitant accumulation of peroxinitrite in mitochondria. Both matrix mitochondrial Mn superoxide dismutase (SOD2) and Cu/Zn cytosolic and interspace mitochondrial superoxide dismutase (SOD1) are

expressed in basal/suprabasal keratinocytes and provide antioxidant defense of these cells by catalysis of $O_2^{\bullet-}$ dismutation [14]. Our data suggest a minor role, if any, of $O_2^{\bullet-}$ in eTRPM8-dependent proliferation of basal keratinocytes. The proposed signaling pathways by which eTRPM8 stimulates proliferation of basal keratinocytes are summarized in **Figure 7 (top left panel)**.

eTRPM8 signaling in keratinocytes differentiation

We have found that eTRPM8 expression is increased in differentiated layer of epidermis and that exposure to mild cold stimulates its activity. Furthermore, we have demonstrated that mild cold enhances the differentiation rate of keratinocytes in an eTRPM8-dependent manner. Although involvement of ATP in keratinocyte differentiation currently lacks direct evidence, the fact that proportion of FLG-positive cells shows the same cold-dependence as ATP synthesis strongly supports this idea. In addition to P2Y receptors, keratinocytes also express Ca^{2+}-permeable ionotropic P2X purinoceptors. Homomeric P2X5 receptor (EC_{50} ~5-10 μM for ATP) was identified in the basal, suprabasal and spinal compartment [15], whereas homomeric P2X7 receptor (EC_{50} ~100 μM for ATP) was detected in the late spinal and granular layers, where it seems to be involved in late differentiation by mediating Ca^{2+}-dependent activation of TGM1 and, thus, leading to keratinocyte death: transformation of keratinocytes into corneocytes.

We also demonstrated that mild cold stimulates eTRPM8-dependent accumulation of $O_2^{\bullet-}$. Our data indicate that, at least partially, this $O_2^{\bullet-}$ originates from mitochondria, though it remains unclear whether long-term activation of eTRPM8 induces NADPH oxidase-dependent $O_2^{\bullet-}$ synthesis in cytosol. ROS and more specifically $O_2^{\bullet-}$ have been shown to be involved in keratinocyte differentiation [16]. Furthermore, ROS gradient from basal to upper layers is characteristic for epidermis [17]. However, strong accumulation of $O_2^{\bullet-}$ induces an increase of the number of suprabasal/spinal cells paralleled with the decrease of the quantity of granular cells. Thus, our results suggest that differentiation of keratinocyte is a fine-tuned process involving $O_2^{\bullet-}$ accumulation and elevation of ATP concentration in eTRPM8-dependent manner. The optimal progression of this process is achieved at physiological skin temperature of about 31°C. Based on this findings we summarized in **Figure 7 (top and bottom right panels)** the signaling pathways involved in the cold-stimulated eTRPM8-dependent differentiation of keratinocytes.

eTRPM8 vs. TRPV3 in epidermal homeostasis

Identified in keratinocytes warmth-activated TRPV3 has been proposed to participate in activation of Transglutaminase [18,19] and, as consequence, to be involved in terminal differentiation of keratinocytes. However, for healthy human mean physiological skin temperature is about 32°C [20], what is slightly below the threshold for TRPV3 activation. Interestingly, TRPV3 and eTRPM8 complement each other in thermosensitivity (i.e. activation by warmth vs. cooling) and Ca^{2+} signaling mechanisms they engage (i.e. mediation of Ca^{2+} entry vs. Ca^{2+} release). Thus, relative expression and activity of eTRPM8 and TRPV3 may provide skin with an adaptive capacity to variations in environmental temperatures.

In conclusion, we report the identification of new TRPM8 isoform, eTRPM8, which enables cold-dependent regulation of epidermal homeostasis. eTRPM8 is a key controller of temperature-dependent energy metabolism and signaling in keratinocytes that provides skin with the capacity to adapt to large variations of environmental temperature.

Supporting Materials and Methods

Cell culture. HaCaT cell line was grown in Dulbecco's minimal essential media (DMEM) (Gibco) supplemented with 2% fetal calf serum (FCS) and Kanamycin (100 µg/ml), and [Ca^{2+}] was adjusted to 1.8 mM to induce differentiation. hNEK cells were obtained from Lifescience Inc. and plated in 10 cm round Petri dishes in basal KSF-SFM media at density of 500k cells/dish. Basal KSF-SFM media was supplemented with bovine pituitary extract, EGF, glutamine and kanamycin (Invitrogen). Induction of differentiation, "Induced cells", was achieved by adding 2% FCS and 1.8 mM Ca^{2+} to basal KSF-SFM, as described previously [21].

Establishment of *trpm8*$^{-/-}$ mice. To suppress ion channel activity of every channel-like TRPM8 isoforms, we inserted LoxP sites with homologous recombination in introns 17 and 20. This ultimately led to a 2500 bp deletion including exons 18, 19 and 20, which encode transmembrane domains 3, 4 and 5 in addition to the first part of the P-loop of TRPM8 channel. After homologous recombination in 129SV/PAS ES cells and G418 selection, insertion of vectors was controlled with Southern-blot and PCR. Selected ES cells were used for blastocyte injection and led to the generation of male chimeras. These were bred with CMV-Cre C57BL/6J females to generate an heterozygous TRPM8 knockout. Agouti-colored pups were selected for transmission of mutant chromosome in the germ line prior PCR validation of the deletion for the TRPM8 knockout line. F1 animals were interbreeding to obtain F2 homozygote *trpm8*$^{-/-}$ mice as well as control homozygote *trpm8*$^{+/+}$ mice, as confirmed by PCR after blood collection. Scale-up of *trpm8*$^{-/-}$ colonies was achieved by backcrossing *trpm8*$^{-/-}$line with control *trpm8*$^{+/+}$ line. According to the Jackson laboratory recommendations for breeding strategies, interbreeding was performed for eight generations in order to prevent sub-strain apparition and genetic divergence. This study was carried out in strict accordance with the recommendations in the Guide for the Care and Use of Laboratory Animals of the French National Institute for Medical Research (INSERM). The protocol has been approved by the Committee on the Ethics of Animal Experiments of the University of Lille 2. All efforts were made to minimize animal suffering.

Primary culture of mouse keratinocytes (mPK). After sacrifice, back skin of C57BL/6J mice was shaved prior to skin removal. Pieces of skin were either fixed in formol prior inclusion in paraffin or used for keratinocyte isolation. To isolate the cells, subcutaneous tissues were removed and pieces of the skin, dermis side down, were put into the solution supplemented with 0.25% trypsin. Freely floating pieces of the skin (with unsubmerged epidermis) were incubated overnight at 4°C. Then dermis was removed and remaining epidermal tissue was cut into 250 mm^2 pieces, which were transferred to Defined-SFM media (Gibco) supplemented with 10% FCS to inhibit trypsin. The pieces of epidermis were then triturated with a wide bore pipette and residual hair, connective tissue and debris were removed from the suspension by sieving with a 70 µm nylon mesh. The cell suspension was then centrifuged for 10 min at 250 g and, keratinocytes were re-suspended in serum-free Defined-SFM media (to suppress fibroblast growth) and were grown in Petri dishes. After 5 days in culture the cells were transferred to the serum-free Ca^{2+}-free Keratinocyte-SFM media to stimulate the cell growth without differentiation. When required, induction of differentiation was achieved by adding 2% FCS and 1.8 mM Ca^{2+} to Keratinocyte-SFM media.

Transient expression studies. Plasmid transfection was carried out with X-tremeGENE HP DNA Transfection Reagent (Roche) at the concentration of 4 µg per million cells. SiRNA transfection was performed with 50 nM of HiPerfect transfection reagent (Qiagen). hNEKs transfection was conducted twice with a 2-day interval to improve the transfection rate.

RACE-PCR and cloning of eTRPM8. RACE-PCR was performed as reported previously [22]. Briefly, 5' extremities were cloned from total mRNA after the first RACE amplification followed by a Nested-RACE PCR using materials derived from SMART RACE-PCR kit (Clonetech). Full-length variants were cloned from the same set of total mRNA using Prime Script Reverse Transcriptase. Long-distance PCR was conducted using Phusion polymerase (Finnzymes), GC rich buffer and specific primers design on extremities of RACE-amplified DNA (for primers: see table 1). DNA amplification procedure included 30 s denaturation at 98°C, followed by 15 cycles of 5 s at 98°C, 15 s at 68°C, 30 s/kbp at 72°C, and 20 cycles of 5 s at 98°C, 15 s at 64°C, 30 s/kbp at 72°C, and, finally, 5 min at 72°C. After agarose gel purification and DNA recovery, amplicons were subjected to terminal adenylation with TaqGold polymerase (Applera) and cloned overnight in pGem-T easy vector with T4 ligase at 14°C. Finally, wild type inserts were transferred in pcDNA4-TO-A vector with appropriate restrictases. Alternatively, inserts were modified with a consensus KOZAK sequence and fused in frame with HA tag at their C-terminus.

siRNA and shRNA plasmids were built in pENTER vector (Invitrogen) following manufacturer's recommendations. Control shRNA targeted TRPM8 exon 7 and shRNA anti-eTRPM8 targeted exon 20. shRNA sense sequences are: CACCAtctctgagcgcactattcaGAGAGtgaatagtgcgctcagaga and CACCAtattccgttcggtcatctaGAGAGtagatgaccgaacggaata (Capital letters refer to the structure of the short hairpin RNA and small letters refer to the siRNA sequence). Control of silencing efficiency was achieved by immunoblotting of total proteins extracted from Hek cells, co-transfected with either shCTL + eTRPM8pcDNA4 or shM8 + eTRPM8pcDNA4.
Control siRNA targeted Luciferase (siLuc) and siRNA anti-eTRPM8 (siTRPM8) targeted exon 20. The sense sequences

are CUUACGCUGAGUACUUCGA(dTdT) and GUAUUCUGGACGAGUCAUU(dTdT), respectively.

Analysis of TRPM8 mRNA expression. Total RNA was isolated from different cell lines using Tri Reagent mix (Sigma-Aldrich). After a DNase I (Invitrogen) treatment and phenol/chloroform purification, 2 µg of total RNA was reverse transcribed into cDNA at 42°C using random hexamer primers (Applera) and MuLV reverse transcriptase (Applera).
Qualitative PCR was performed with TaqGold polymerase (Applera) and controlled on agarose gel.
Real-time quantitative PCR was performed on a Cfx C1000 system (Biorad). For each reaction, 12.5 ng of cDNA was placed in 15 µl of final reaction medium containing 7.5 µl of 2x SsoFast™ EvaGreen® Supermix (Biorad) and 200 nM primer pairs (see **Table 1**). The housekeeping gene Glyceraldehyde-3-phosphate dehydrogenase (GAPDH) was used as an endogenous control to normalize variations in RNA extracts, the degree of RNA degradation and variability in RT efficiency. To quantify the results, we used the comparative Ct method. PCR protocol consisted of: 30 s denaturation at 95°C followed by 40 cycles of [4 s at 95°C and 30 s at 60°C], and final dissociation curve to control specificity of the amplification.

***In Situ* Hybridization (ISH).** Human skin sections were obtained from resections specimens after breast reduction surgery according to the Declaration of Helsinki Principles and the guidelines of ethical committee of the Medical Center, CHRU Lille prepared in agreement with the French law. The skin sections (10 µm thick) were mounted onto gelatin-coated slides, and air-dried. After PCR amplification, the sense and antisense probe sequences were cloned into pcR2.1 TA cloning (Invitrogen) and checked for sequencing. The vector was linearized, and the probes were transcribed with the SP6/T7 transcription kit (Roche diagnostics) and [^{35}S]-dUTP (1,300 Ci/mmol, Amersham Biosciences). *In situ* hybridization was performed as previously described [23], and finally radioactivity was revealed using X-ray film (Biomax-MR, Kodak) prior to digitalization. Sense sequence of the probe (318 bp) was cloned with forward primer: CGTTCGGTCATCTACGAGC and backward primer: GCAGTACTCCTGCACCAGG and correspond to the sequence of the pore domain. Antisense probe was generated using the complementary primer sequences.

Immunoblotting. Tissues were collected and stored in liquid nitrogen until protein extraction. Pieces of skin were transferred in beads containing tubes and 500µl of an ice-cold buffer (pH 7.2) containing 10 mM PO4Na2/K buffer, 150 mM NaCl, 1 g/100 ml sodium deoxycholate, 1% Triton X-100, 1% NP40, a mixture of protease inhibitors (Sigma-Aldrich), and a phosphatase inhibitor (sodium orthovanadate; Sigma-Aldrich) was added. Protein extraction was achieved with 2 cycles of 30 sec at 6,500 xG in a high-throughput PRECELLYS®24 tissue homogenizer cooled down with CRYOLIS® at 4°C.
Cultured cells were collected in a phosphate buffered saline solution, then pellet prior extraction in the ice cold buffer described above. After 30 min incubation on ice, the protein extract was further subjected to sonication and debris were pelleted at 15,000 xG at 4°C for 10 min. Protein concentration was measured by the mean of a BCA Protein Assay (Pierce). 25 µg of total protein were loaded onto a 10% polyacrylamide gel before an SDS-page was performed. After electrophoresis, proteins were transferred to a nitrocellulose membrane using a semi-dry electroblotter (Bio-Rad). The membrane was blocked in a TNT +5% (W/V) milk (15 mM Tris buffer, pH 8, 140 mM NaCl, 0.05% Tween 20, and 5% non-fat dried milk) for 30 min at room temperature, then soaked in primary antibody diluted in TNT +1% milk for either 2 h at room temperature or overnight at +4°C. After three washes in TNT, the membrane was soaked in secondary antibody diluted in TNT+1% milk for 1h at room temperature. The membrane was processed for chemiluminescence detection using Luminata Forte Western HRP Substrate (Millipore) according to the manufacturer's instructions. After a 10 min bath in Re-blot PLus Mild SOlution (Millipore), membrane was blotted again. The primary antibodies were: rabbit **anti-TRPM8 channel (Anti-TRPM8(extracellular), Cat.ACC-049, lot.AN-03, Alomone, 2009 batch) or anti-TRPM8 channel (Anti-TRPM8 ab109308, lot.GR47573-2, Abcam, 2011-2012 batches) at 1 µg/ml,** rabbit anti-HA tag (Sc-805, Santa Cruz; 1/200), mouse anti-actin (Lab Vision CO; 1/1000) and **mouse anti-Calnexin (MAB3126, Millipore ; 1/1000)**.

Immunohistofluorescence (IHF). Experiments were performed on 6 µm - thick sagittal slices of the palm skin from *wt*, 5 *trpm8*$^{-/-}$ mice or 5 *trpm8*$^{-/-}$ *(DJ)* mice, obtained with Microm HM355S (Thermo Scientific Inc). After paraffin removal, antigen retrieval was achieved in a citrate buffer boiled 4 times for 5 minutes in a microwave oven. After three washes in PBS, the tissue sections were blocked with PBS supplemented with 1.2% gelatin (PBS/gelatin) for 30 min at 37 °C, and then co-incubated with primary antibodies diluted in PBS/gelatin for 2 h at 37°C. After thorough rinsing in PBS/gelatine, the slides/dishes were treated with the corresponding secondary antibody: either Dye light 488-labeled anti-rabbit IgG (Jackson ImmunoResearch; dilution, 1/2000) or Alexa fluor 546-labeled anti-mouse IgG (Molecular Probes; dilution, 1/4000) diluted in PBS/gelatine for 1 h at RT. After rinsing, twice in PBS/gelatine and once in PBS with 1/200 DAPI for 10 min at RT, the slides were mounted with Mowiol® and examined under a confocal microscope. Primary antibodies used were: anti-Keratin 5, K5, (Covance) at 1/2000 dilution, anti-Keratin 10, K10, (Covance) at 1/10 dilution, anti-Involucrin, INV, (Sigma) at 1/1000 dilution, anti-Loricrin, LR, (Abcam) at 1/1000 dilution, anti-PCNA (SantaCruz) at 1/100 dilution, anti-TRPM8 channel (Anti-TRPM8(extracellular), Cat.ACC-049, lot.AN-03, Alomone, 2009 batch) or anti-TRPM8 channel (Anti-TRPM8 ab109308, lot.GR47573-2, Abcam, 2011-2012 batches) at 1 µg/ml. The two anti-TRPM8 antibodies recognize close regions TRPM8 pore encoded by exon 21-22 and 21

respectively, and can thus detected classical full length TRPM8 and TRPM8 isoforms as well. Analysis of the epidermis structure was performed using LSM 780 confocal workstation (Zeiss, Oberkochen, Germany). In each skin slice, imaging was performed on 4 randomly selected 500 µm - wide regions of interest (ROI). In each ROI, the thickness of K5-, K10- and LN- positive compartments was measured at 3 *x* positions. The measurements were performed on the slices from 5 *wt* and 5 *trpm8*$^{-/-}$ mice, giving in total 60 measurements per condition. To compensate for the effect of deviations in the cut angle on the apparent thickness of the epidermis cross-cuts, the thickness of either K5- or K10-, or LR-positive compartments was normalized to the total thickness of *stratum basale* (SB) + *stratum spinosum* (SS) + *stratum granulosum* (SG), measured from the overlay of transmitted light image and confocal image of DAPI fluorescence. Mean ± SED values were compared for *wt* and *trpm8*$^{-/-}$ mice.

Measurement of the *stratum corneum* thickness. Deparaffinized slides of mouse skin from snout, palm, back skin and tail were subjected to Hemalum-erythrosin-safran trichrome staining. The slides were analyzed on an upright Axio Imager.A1 microscope (Zeiss, Germany). Images were acquired with an AxioCam MRc5 digital camera (Zeiss, Germany) and the Axionvision software was used for analysis. Measurements were performed on intact samples of stratum corneum of 8 *wt* mice and 8 *trpm8-/-* mice.

Flow cytometry was conducted with CyAn™ ADP Analyser. Cells were harvested, split in 1 million samples in 15 ml tubes and fixed overnight with 1ml of 70% ethanol at -20°C. Cells were then washed twice with PBS, supplemented with 4% BSA and 0.1% Triton X100, and incubated at RT for 30 min. After that, the cells were transferred for 1 h to PBS-BT supplemented with the primary antibodies at the same dilutions as described above. After two cycles of washout in PBS the cells were incubated for 30 min at RT with secondary antibodies: anti-rabbit IgG coupled to DL-488 and anti-mouse IgG coupled to AF-647, diluted at 1/2000 and 1/4000 respectively. Following 3 washout cycles at RT flow cytometry was commenced. Flow cytometer was calibrated with rainbow beads before each experiment. The laser lines of 488 nm and 642 nm were used. Data were analyzed with FlowJo software (v 8.7).

DeHydrogenase (DHase) quantization assay. The cells were trypsinized, counted and transferred to 96 well plates: 20,000 cells per well in 100 µl of medium. After 2-4 hours of recovery at the desired incubation temperature (37, 31 or 25°C), the cells were subjected to CellTiter 96® AQ_{ueous} Non-Radioactive Cell Proliferation Assay (Promega). Although this assay kit is commonly used for quantization of growth, it is based on the assessment of DHase activity by means of measuring of optical density (OD) reflecting absorption of light by formazan at 490 nm. We modified this procedure to measure DHase activity by fixing the cell number at constant level. Briefly, 100 µl of MTS solution (see manufacturer data sheet) was added in each well and OD was measured at 30, 60, 90 and 120 minutes later. Apparent enzymatic activity (OD/min) was estimated from the fit of linear function $f_{(OD)}=a \bullet T_{(min)}+b$ to the data, after correction for the background OD, measured in cell-free well containing 100 µl of medium and 100 µl of MTS solution.

Electrophysiology. Membrane currents in TRPM8-expressing HEK cells were recorded in the whole-cell configuration using the patch-clamp technique and a computer-controlled EPC-9 amplifier (HEKA Electronic, Germany. Patch pipettes were made using a P-97 puller (Sutter, USA) from borosilicate glass capillaries (WPI, USA). Patch-pipettes (resistance 3 to 5 MΩ) were filled with the following solution (in mM): 120 Cs-Met, 10 CsCl, 6 $MgCl_2$, 10 BAPTA, 2.5 $CaCl_2$ (calculated free Ca^{2+} concentration: 150 nM), 10 HEPES, pH adjusted to 7.3 with CsOH (osmolality: 305 mosmol/l). Extracellular solution used to record TRPM8 current contained (in mM): NaCl 140, KCl 5, $CaCl_2$ 10, $MgCl_2$ 2, Na_2HPO_4 0.3, KH_2PO_4 0.4, $NaHCO_3$ 4, glucose 5, HEPES 10; pH adjusted to 7.3 with NaOH; osmolality: 330mosmol/l.
For giant unilamelar vesicles (GUV) patch-clamp experiments, we used Axopatch 200B amplifier and pClamp 10.0 software (Molecular Devices, Union City, CA) for data acquisition and analysis. Patch pipettes were fabricated from borosilicate glass capillaries (World Precision Instr., Inc., Sarasota, FL) on horizontal puller (Sutter Instruments Co., Novato, CA) and had a resistance in the range of 7-10 MΩ. Prepared vesicles were immersed in a bath solution containing, in mM, 150 NaCl, 5 glucose, 10 Hepes, pH 7.2. In order to prevent activity of IP_3R and RyR channels, commonly present in the ER, this solution was supplemented with 1 mM $MgCl_2$, 1 mM EGTA and 1µM dantrolene [24]. Patch pipettes were filled with the same solution, supplemented by 2 µM PiP_2 and 1 mM MgATP in order to enhance TRPM8 activity [25].

Experimental solutions. In confocal microscopy experiments the cells were bathed in physiological salt solution (PSS) containing (in mM): NaCl 140, KCl 5, $MgCl_2$ 1, glucose 10, HEPES 10; pH adjusted to 7.4 with NaOH. PSS was supplemented with 70 µM or 1.7 mM $CaCl_2$, depending on experimental protocol, as described in the text.

Preparation of giant unilamelar vesicles (GUVs).
GUVs were prepared from the 1:5 mixtures of the ER-containing fraction with 10:1 diphytanoylphosphatidylcholine (DPhPC)/cholesterol lipid combination (5 mM). This mixture was supplemented by 0.2 mM phosphatidylinositol 4,5-bisphosphate (PiP_2) in order to sustain TRPM8 activity [25].

Wide-field Ca^{2+} imaging. Calcium imaging experiments have been performed as described previously [3]. Briefly,

ARTICLE 15

$[Ca^{2+}]_c$ was measured using ratiometric dye fura-2 and quantified according to Grynkiewicz equation [26]. The bath solution contained in mM: NaCl 140, KCl 5, $CaCl_2$ 2, $MgCl_2$ 2, Na_2HPO_4 0.3, KH_2PO_4 0.4, $NaHCO_3$ 4, glucose 5, HEPES 10; pH adjusted to 7.3 with NaOH; osmolality 330 mosmol/l.

Visualization of the endoplasmic reticulum (ER) and mitochondria. The ER was visualized using Brefeldin A BODIPY 558/568 [27,28], which was loaded by 20-min incubation of the cells with 2 µM of the dye followed by 1.5-hour wash. The mitochondria were visualized using MitoTracker® Green FM, which was loaded by 30-min incubation of the cells with 2 µM of the dye followed by 30-min wash.

Visualization of agonist-induced changes of Ca^{2+} concentration in cytosol ($[Ca^{2+}]_c$) and mitochondria ($[Ca^{2+}]_m$). Changes of $[Ca^{2+}]_c$ were imaged using the high-affinity fluorescent Ca^{2+} indicator fluo-4, as described previously [3,28]. Fluo-4 was loaded by 1-hour incubation of the cells with 5 µM fluo-4 acetoxymethyl ester (fluo-4 AM; diluted from a stock containing 2 mM fluo-4 AM and 0.025% (w/v) pluronic F-127 in dimethyl sulphoxide). Changes of $[Ca^{2+}]_m$ were imaged using fluorescent Ca^{2+} indicator rhod-2: 50 µg of rhod-2 AM was dissolved in 10 µl of DMSO (containing 0.025% (w/v) pluronic F-127), which was then mixed with 4 ml of PSS and superfused to the experimental chamber for 20 min. The incubation of the cells with the dyes was followed by a 1-hour wash in PSS containing 1.7 mM $CaCl_2$ to allow time for de-esterification. The dye loading was performed at RT. The cells were then kept for 30 min at 37ºC. Before imaging was commenced the cells were superfused with PSS containing 70 µM $CaCl_2$ and supplemented with 10 µM $LaCl_3$ to eliminate capacitative Ca^{2+} entry, unless stated otherwise. The cells were stimulated with either 200 µM menthol or 10 µM icilin. The intensity of fluo-4 or rhod-2 fluorescence (F) was normalized to the average fluorescence intensity in the images acquired before agonist application (F_0). The temporal profiles of the agonist-induced $[Ca^{2+}]_c$ and $[Ca^{2+}]_m$ transients are illustrated by the plots showing time course of the normalized fluo-4 or rhod-2 fluorescence intensity (F/F_0) averaged within confocal optical slice of the cell.

Superoxide assessment. The hNEKs were transfected either with control siRNA (siLuc) or with siRNA targeting the pore-encoding sequence of TRPM8 (siTRPM8), while HaCaT cells were transfected with empty vector (CTL), eTRPM8 plasmid or eTRPM8 + SOD1 plasmids. Cells were incubated in the medium supplemented with 2.5 µM CellRox® Deep Red reagent for 30 min at 37°C. After two washes, cells were incubated for 30 min at 37°C prior to confocal imaging. For each temperature and siRNA condition, the measurements were performed in 3 Petri dishes, sequentially mounted on the microscope stage at the ambient temperature corresponding to the pre-incubation temperature. In each Petri dish, confocal imaging of CellRox® Deep Red fluorescence was performed from 4 regions of interest, 230x230 µm (1024x1023 pixels) each. The same illumination intensity, photomultiplier gain and offset were used in all the experiments. Data were processed with ImageJ64 freeware. After setting offset (pixel fluorescence intensity below 20 a.u.) and the mean cell background (pixel fluorescence intensity 100 a.u.) in the control condition (cells grown at 37°C), specific to $O_2^{\bullet-}$ increase in the CellRox® Deep Red fluorescence was computed according to the formula $\sum Pix_{I(100-255)} / \sum Pix_{I(20-255)}$, where $Pix_{I(20-255)}$ and $Pix_{I(100-255)}$ are the pixels with intensities lying within the range of 20-255 and 100-255 a.u., respectively. The $O_2^{\bullet-}$- specific increases in the CellRox® Deep Red signal mass for each condition were averaged, normalized to the mean value, detected at 37ºC either in hNEKs, transfected with siLuc, or HaCaT cells, transfected with empty vector, and compared. Data are presented as mean ± S.D.
Specificity of CellRox® Deep Red oxidation by superoxide or peroxinitrite was assessed with Mn(III)tetrakis(4-benzoic acid)porphyrin Chloride, MnTBAP. Cells were incubated for 30 min at 37°C in the medium supplemented with 100 µM MnTBAP. After 3 washes in MnTBAP-free medium, the cells were then incubated with CellRox® Deep Red as described above.
Icilin-induced $O_2^{\bullet-}$ accumulation in mitochondria was performed using MitoSOX™ Red. Briefly, 50 µg of MitoSOX™ Red was dissolved in 20 µL of DMSO (containing 0.025% (w/v) pluronic F-127) and aliquoted at 2 µL. One aliquot was then dissolved in 2 mL of external solution and superfused to the experimental chamber. The cells were stained for 10 min followed by 30-min wash, all at 37ºC. Mean rates of $O_2^{\bullet-}$ accumulation were estimated as mass of MitoSOX™ fluorescent signal per second following icilin application, $\left(\int \Delta F / F_0\right) / \Delta t$. Experiments were conducted at 37ºC.

ATP quantization assay. Intra- and extracellular ATP concentrations were quantified with the ATP bioluminescence Assay Kit HS II (Roche). For extracellular ATP, 500 µl of 24 h-conditioned media was picked up and filtered with 0.2 µm filters to remove floating cells. 100 µl of media was mixed with luciferase-containing solution prior to luminescence quantization in a LUMAT LB 9507 system (Berthold LUMAT LB 9507). Intracellular ATP was measured as following. After trypsinization 1 million cells were gently spun down at 180 xG for 8 min. The pellet was then re-suspend in lysis buffer for 10 min on ice, and the cells were spun down again at 12,000 xG for 10 min. Supernatant (100 µl) was then diluted 10 and 100 times with dilution buffer and finally 100 µl of diluted solution was mixed with 100 µl of luciferase-containing solution prior luminescence quantization. For both intra- and extracellular ATP quantization, the cells were counted and total cellular protein was extracted. The protein extracts were quantified with BCA Protein Assay and luminescence intensity (RLU) was normalized to the weight of the extracted protein (RLU/µg).

Confocal microscopy. Experimental chambers with the cells were placed on the stage of Axiovert 200M inverted microscope attached to a LSM 510 META laser-scanning unit (Zeiss, Oberkochen, Germany). The SCSi interface of the confocal microscopes was hosted by a Pentium PC (32-bit Windows NT 4.0 operating system) running LSM 510 software (Zeiss, Oberkochen, Germany). During time series protocol, the x-y confocal images of the fluo-4, rhod-2, MitoSOX Red, Brefeldin A BODIPY 558/568 or MitoTracker Green fluorescence were acquired at 0.1–0.5 Hz using a Zeiss plan-Apochromat 40× 1.3 N.A. or 63× 1.4 N.A. oil-immersion objectives. Fluo-4 and MitoTracker Green fluorescence was excited by the 488 nm line of a 500 mW argon ion laser (Laser-Fertigung, Hamburg, Germany) and was captured at wavelengths 505-530 nm. Rhod-2, Brefeldin A BODIPY 558/568 and MitoTracker Red fluorescence was exited by the 543 nm line of 15 mW helium/neon ion laser and was detected at wavelengths 560-615 nm or above 560 nm. The mTurquoise2 fluorescence was excited by 405 nm line of blue diode laser and was captured at wavelengths 475-525 nm. The MitoSOX^{TM} fluorescence was excited by 514 nm line of a 500 mW argon ion laser and was captured at wavelengths above 560 nm. The illumination intensity was attenuated to 0.5-6 % (depending on the laser line) with an acousto-optical tunable filter (Zeiss, Oberkochen, Germany). To optimize signal quality the pinhole was set to provide a confocal optical section 0.5–1.8 µm, depending on experimental protocol. To avoid any bleed-through of the fluorescence signal in multi-staining experiments, fluorochromes with well separated excitation and emission spectra were used and imaging was performed using the frame-by-frame multitrack mode of the confocal scanner: sequential acquisition via well-separated optical channels of the x-y images produced by fluorescence of different fluorochromes. The photomultiplier gain and offset in each optical channel were set individually to achieve similar signal intensity at each channel and remove sub-signal noise from the images. The adequacy of the imaging protocol applied to the multi-labeled cells was confirmed by control experiments on the mono-labeled cells.

Time domain-fluorescence lifetime imaging microscopy (TM-FLIM). For live-cell imaging, cells were placed on 35mm glass bottom dishes (MatTek Corporation, USA), filled with L-15 medium without phenol red (Life technologies), and kept at 37°C using a stage incubator (Life Imaging Services, Switzerland).FLIM was performed with a Leica TCS SP5 X confocal head (Leica Microsystems, Germany) with the SMD upgrade, mounted on an inverted microscope (DMI6000, Leica Microsystems, Germany). A pulsed diode laser, PDL 800-B (PicoQuant GMBH, Germany), delivered 40 MHz repetitive rate pulses at 405nm. The confocal pinhole was set to 1 Airy, for a 0.921 µm optical slice. Single photon events originated from the illuminated voxel were collected through a 63x/1.2NA water-immersion objective and recorded by a TCSPC detector (HydraHarp 400; PicoQuant GMBH, Germany). Fluorescence was detected through a 483/32 single-bandpass filter (Semrock, USA) on Single Photon Avalanche Photodiodes, SPAD (MPD, Italy), set up at 256 x 256 pixels. Arrival time of single photons was measured with SymPhoTime software (PicoQuant GMBH, Germany) while image were taken with LAS AF software (Leica Microsystems, Germany. In order to obtain the best resolution of organelles, a 5-fold zoom factor was applied, giving a pixel size of 0.193 µm and an image size of 49.21x49.21 µm. Since the statistical determination of the distribution of single photon arrival time requires a minimum of 100 photons per pixel, 120 frames were acquired at 200Hz and summed in the final image.

Aequorin measurements. Mitochondrial Ca^{2+} signal was evaluated 48 h after transfection of M8-CTL and M8-KD cells with adenoviral mutated mitochondria-targeted aequorin probe (mtAEQmut). mtAEQ was reconstituted with 5 µM coelenterazine for 2 h at 37°C in Krebs-Ringer modified buffer composed of (in mM): NaCl 125, KCl 5, $MgSO_4$ 1, Na_3PO_4 1, glucose 5.5, HEPES 20, pH adjusted to 7.4 with NaOH. Aequorin measurements were carried out in a purpose built luminometer. The experiments were terminated by the cell lysis with 100 µM digitonin in a hypotonic Ca^{2+}-rich solution (10 mM $CaCl_2$ in H_2O), what discharges the remaining aequorin pool. The light signal was collected and calibrated into [Ca^{2+}] values, as previously described [29].

Data analysis and statistical procedures. Each experiment was repeated at least three times independently. Data are expressed as mean ± S.D when not indicated in legends. The data were analyzed and graphs plotted using Origin 5.0 software (Microcal, Northampton, MA, USA). InStat3 (GraphPad Software Inc, SanDiego, USA) was used for statistical analysis and the mean values were compared using either unpaired *t*-test with Welch's corrected test (2 groups) or One-way ANOVA with Dunnett multiple comparison post-test (≥3 groups). Statistical significances were: * $p<0.05$; ** $p<0.01$; *** $p<0.001$. Smooth curves on the graphs were obtained by interpolation of data points using parametric Lagrange 2nd degree polynomial: parabola for interpolation of 3 data points.

ARTICLE 15

Supporting Reference.

1. Denda M, Tsutsumi M, Denda S (2010) Topical application of TRPM8 agonists accelerates skin permeability barrier recovery and reduces epidermal proliferation induced by barrier insult: role of cold-sensitive TRP receptors in epidermal permeability barrier homoeostasis. Exp Dermatol 19: 791-795.
2. Bidaux G, Flourakis M, Thebault S, Zholos A, Beck B, et al. (2007) Prostate cell differentiation status determines transient receptor potential melastatin member 8 channel subcellular localization and function. J Clin Invest 117: 1647-1657.
3. Thebault S, Lemonnier L, Bidaux G, Flourakis M, Bavencoffe A, et al. (2005) Novel role of cold/menthol-sensitive transient receptor potential melastatine family member 8 (TRPM8) in the activation of store-operated channels in LNCaP human prostate cancer epithelial cells. J Biol Chem 280: 39423-39435.
4. Sakuntabhai A, Ruiz-Perez V, Carter S, Jacobsen N, Burge S, et al. (1999) Mutations in ATP2A2, encoding a Ca2+ pump, cause Darier disease. Nat Genet 21: 271-277.
5. Prasad V, Boivin GP, Miller ML, Liu LH, Erwin CR, et al. (2005) Haploinsufficiency of Atp2a2, encoding the sarco(endo)plasmic reticulum Ca2+-ATPase isoform 2 Ca2+ pump, predisposes mice to squamous cell tumors via a novel mode of cancer susceptibility. Cancer Res 65: 8655-8661.
6. Robb-Gaspers LD, Burnett P, Rutter GA, Denton RM, Rizzuto R, et al. (1998) Integrating cytosolic calcium signals into mitochondrial metabolic responses. EMBO J 17: 4987-5000.
7. Robb-Gaspers LD, Rutter GA, Burnett P, Hajnoczky G, Denton RM, et al. (1998) Coupling between cytosolic and mitochondrial calcium oscillations: role in the regulation of hepatic metabolism. Biochim Biophys Acta 1366: 17-32.
8. Harris DA, Das AM (1991) Control of mitochondrial ATP synthesis in the heart. Biochem J 280 (Pt 3): 561-573.
9. Hubbard MJ, McHugh NJ (1996) Mitochondrial ATP synthase F1-beta-subunit is a calcium-binding protein. FEBS Lett 391: 323-329.
10. Dixon CJ, Bowler WB, Littlewood-Evans A, Dillon JP, Bilbe G, et al. (1999) Regulation of epidermal homeostasis through P2Y2 receptors. Br J Pharmacol 127: 1680-1686.
11. Burrell HE, Wlodarski B, Foster BJ, Buckley KA, Sharpe GR, et al. (2005) Human keratinocytes release ATP and utilize three mechanisms for nucleotide interconversion at the cell surface. J Biol Chem 280: 29667-29676.
12. Lee WK, Choi SW, Lee HR, Lee EJ, Lee KH, et al. (2001) Purinoceptor-mediated calcium mobilization and proliferation in HaCaT keratinocytes. J Dermatol Sci 25: 97-105.
13. Inoue K, Denda M, Tozaki H, Fujishita K, Koizumi S (2005) Characterization of multiple P2X receptors in cultured normal human epidermal keratinocytes. J Invest Dermatol 124: 756-763.
14. Carraro C, Pathak MA (1988) Characterization of superoxide dismutase from mammalian skin epidermis. J Invest Dermatol 90: 31-36.
15. Greig AV, Linge C, Cambrey A, Burnstock G (2003) Purinergic receptors are part of a signaling system for keratinocyte proliferation, differentiation, and apoptosis in human fetal epidermis. J Invest Dermatol 121: 1145-1149.
16. Tamiji S, Beauvillain JC, Mortier L, Jouy N, Tual M, et al. (2005) Induction of apoptosis-like mitochondrial impairment triggers antioxidant and Bcl-2-dependent keratinocyte differentiation. J Invest Dermatol 125: 647-658.
17. Thiele JJ, Hsieh SN, Briviba K, Sies H (1999) Protein oxidation in human stratum corneum: susceptibility of keratins to oxidation in vitro and presence of a keratin oxidation gradient in vivo. J Invest Dermatol 113: 335-339.
18. Moqrich A, Hwang SW, Earley TJ, Petrus MJ, Murray AN, et al. (2005) Impaired thermosensation in mice lacking TRPV3, a heat and camphor sensor in the skin. Science 307: 1468-1472.
19. Peier AM, Reeve AJ, Andersson DA, Moqrich A, Earley TJ, et al. (2002) A heat-sensitive TRP channel expressed in keratinocytes. Science 296: 2046-2049.
20. Smith AD, Crabtree DR, Bilzon JL, Walsh NP (2010) The validity of wireless iButtons and thermistors for human skin temperature measurement. Physiol Meas 31: 95-114.
21. Borowiec AS, Delcourt P, Dewailly E, Bidaux G (2013) Optimal differentiation of in vitro keratinocytes requires multifactorial external control. PLoS One 8: e77507.
22. Bidaux G, Beck B, Zholos A, Gordienko D, Lemonnier L, et al. (2011) Regulation of transient receptor potential melastatin 8 (TRPM8) channel activity by its short isoforms. J Biol Chem.
23. Lesage J, Blondeau B, Grino M, Breant B, Dupouy JP (2001) Maternal undernutrition during late gestation induces fetal overexposure to glucocorticoids and intrauterine growth retardation, and disturbs the hypothalamo-pituitary adrenal axis in the newborn rat. Endocrinology 142: 1692-1702.
24. Nelson TE, Lin M, Zapata-Sudo G, Sudo RT (1996) Dantrolene sodium can increase or attenuate activity of skeletal muscle ryanodine receptor calcium release channel. Clinical implications. Anesthesiology 84: 1368-1379.
25. Rohacs T, Lopes CM, Michailidis I, Logothetis DE (2005) PI(4,5)P2 regulates the activation and desensitization of TRPM8 channels through the TRP domain. Nat Neurosci 8: 626-634.
26. Grynkiewicz G, Poenie M, Tsien RY (1985) A new generation of Ca2+ indicators with greatly improved fluorescence properties. J Biol Chem 260: 3440-3450.
27. Vanden Abeele F, Bidaux G, Gordienko D, Beck B, Panchin YV, et al. (2006) Functional implications of calcium permeability of the channel formed by pannexin 1. J Cell Biol 174: 535-546.
28. Povstyan OV, Harhun MI, Gordienko DV (2011) Ca2+ entry following P2X receptor activation induces IP3 receptor-mediated Ca2+ release in myocytes from small renal arteries. Br J Pharmacol 162: 1618-1638.
29. Chami M, Ferrari D, Nicotera P, Paterlini-Brechot P, Rizzuto R (2003) Caspase-dependent alterations of Ca2+ signaling in the induction of apoptosis by hepatitis B virus X protein. J Biol Chem 278: 31745-31755.

V. ARTICLE 16

ARTICLE 16

Cold/menthol channels initiate the cold shock response and protect germ cells from cold shock mediated oxydation

Anne-sophie Borowiec[1], Benoit Sion[2], Frédéric Chalmel[3], Antoine Rolland[3], Loïc Lemonnier[1], Tatiana De Clerck[1], Alexandre Bokhobza[1], Sandra Derouiche[1], Etienne Dewailly[1], Christian Slomianny[1], Claire Mauduit[4], Mohamed Benhamed[4], Morad Roudbaraki[1], Bernard Jégou[3], Natalia Prevarskaya[1], and Gabriel Bidaux[1]

[1] Inserm, U-1003, Equipe labellisée par la Ligue Nationale contre le cancer, Villeneuve d'Ascq, F-59655 France; Université Lille 1, Villeneuve d'Ascq, F-59655 France.
I[2]Pharmacologie Fondamentale et Clinique de la Douleur, France Inserm, U 1107, Neuro-Dol, Clermont Université, Université d'Auvergne, F-63001 Clermont-Ferrand, France

[3]INSERM U1085-Irset, Campus de Beaulieu, Bâtiment 13, 35042 Rennes

[4]Inserm, Nice

Running title: TRPM8 channels and cold shock in testis.
To whom correspondences should be addressed: Gabriel Bidaux gabriel.bidaux@gmail.com
Laboratoire de Physique des Lasers, Atomes et Molécules, Equipe Biophotonique Cellulaire Fonctionnelle, UMR 8523, Parc scientifique de la Haute Borne, Villeneuve d'Ascq, France.

Keywords: TRPM8 channels, hypothermia, cold shock response, ROS, oxidation, spermatogenesis, apoptosis.

SUMMARY

Testes of most male mammals present the particularity of being externalized from the body. Consequently, mean testis temperature is slightly cooler than core body temperature (4-8°C below). While most human-related enzymatic reactions are optimal at 37°C, mild-heat, as found in cryptorchidism, has been reported to damage DNA and trigger apoptosis of germ cells leading to infertility. Conversely, testis hypothermia is known to increase germ cells apoptosis, even though little is known about the underlying molecular mechanisms including cold sensors, transduction pathways and apoptosis triggers.

In DRG neurons, the cold and menthol-activated TRPM8 channel is associated to cold sensation. However, little is known about its function in other tissues. In this study, using a functional knockout of TRPM8 in mouse, we demonstrated that under resting conditions, TRPM8 knockout in germ cells is correlated with an increased level of cell death. Apoptosis increased proportionally to cooling level in control mice but was independent of temperature in KO's. We also observed that the rate of germ cell death was correlated to both ROS level and expression of the detoxifying enzymes.

We therefore conclude that TRPM8 channel participates to ROS homeostasis in testis by indirectly controlling detoxifying enzymes expression that helps to increase viability of germ cells exposed to hypothermia.

INTRODUCTION

In male mammals the mean testis temperature is about 4-8°C below the core body temperature. Internalization of testes in cryptorchidism and mild heat of testes as well, have been reported to damage DNA and trigger apoptosis of germ cells leading to infertility (1). Surprisingly, testis cooling triggers similar effects. Indeed testis hypothermia was reported to increase germ cells apoptosis in both adult rats (2-4) and Red-Bellied Newts (5). Concomitant to cell death, authors described an increase of abnormal spermatozoa, a slight decrease of fertility and a strong decrease of viable embryos. Among all germ cells, pachytene spermatocytes at stages XII–I were the most sensitive to cooling. These studies emphasize the thermo-sensitivity of gametogenesis and suggest that specific molecular protective pathways could intervene to control cell viability under mild temperature variations. Because hyperthermia is related to a human disease, it has been extensively studied, while testes hypothermia has been only described on a macroscopic scale. Studying cold transduction mechanisms and molecular pathways leading to germ cells death may therefore give new insight on infertility.

In afferent fibers innervating skin, the cold and menthol-activated TRPM8 channel is devoted to cold sensing (6-8). This cationic channel has been reported to be a thermodynamic sensor detecting cool temperatures in the range of 15°C-33°C (9-11). Outside of its expression in dorsal root ganglia neurons and inner tissues such as prostate (12), TRPM8 channel is expressed in keratinocytes (13) where it regulates cold-dependent epidermal homeostasis (Bidaux et al, PNAS, revision). Recent advances in the molecular mechanisms induced by TRPM8 activation have revealed that its cold transducer activity is tightly coupled to the level of reactive oxygen species, ROS (14, 15) (Bidaux et al, PNAS, revision). In spermatozoa, low ROS levels facilitate capacitation, when at higher concentrations they trigger tissue injury through cell death (16, 17). Based on the knowledge that TRPM8 is expressed in spermatozoa (18-20), and that ROS are well-known inducers of cell death, our goal was here to understand whether hypothermia-mediated apoptosis of

male germ cells could be triggered by the cold transducer, TRPM8.

In this study, we demonstrate that the *trpm8* gene is mostly expressed in pachytene spermatocytes and that cold stimulation of rodent germ cells triggers calcium mobilization from internal stores. We have previously demonstrated that TRPM8-mediated Ca^{2+} mobilization from internal stores can be elicited by either the full length TRPM8 or by its N-terminally truncated isoforms (12, 21). In the present study, we show that the latters are expressed in rodent germ cells, and could therefore account for the observed cold-induced store depletion.

By mean of a functional KO of TRPM8 channels in mice, we show that, at ambient temperature, loss of TRPM8 correlates to an increased level of germ cells death and to variation in the type of spermatozoa abnormality. We also report that TRPM8 expression increased viability of control (29°C) and cooled spermatozoa (17°C), but did not protect them from cold-induced apoptosis at 4°C. This protective effect of TRPM8 is related to a concomitant overexpression of anti-oxidant enzymes, namely the superoxide dismutase (SOD1) and glutathione peroxidases (GPx2, 4 and 5), and the decoupling protein, UCP3. This TRPM8-dependent induction of protective agents is correlated to a tight control of ROS concentration absent in TRPM8 KO germ cells.

In summary, we show that TRPM8 channels are required for the protection of germ cells against testis hypothermia, *via* a tight control of cell ROS concentration.

EXPERIMENTAL PROCEDURES

Cell culture. The HEK cell line was purchased from the American Type Culture Collection (ATCC). Cells were amplified in DMEM (Gibco®) supplemented with 10% FCS and kanamycin (100 µg/ml).

Establishment of *trpm8*$^{-/-}$ mice. To suppress ion channel activity of every channel-like TRPM8 isoforms, we inserted LoxP sites with homologous recombination in introns 17 and 20. This ultimately led to a 2500 bp deletion including exons 18, 19 and 20, which encode transmembrane domains 3, 4 and 5 in addition to the first part of the P-loop of TRPM8 channel. After homologous recombination in 129SV/PAS ES cells and G418 selection, insertion of vectors was controlled with Southern-blot and PCR. Selected ES cells were used for blastocyte injection and led to the generation of male chimeras. These were bred with CMV-Cre C57BL/6J females to generate an heterozygous TRPM8 knockout. Agouti-colored pups were selected for transmission of mutant chromosome in the germ line prior to PCR validation of the deletion for the TRPM8 knockout line. F1 animals were interbred in order to obtain F2 homozygote *trpm8*$^{-/-}$ mice as well as control homozygote *trpm8*$^{+/+}$ mice, as confirmed by PCR after blood collection. Scale-up of *trpm8*$^{-/-}$ colonies was achieved by backcrossing *trpm8*$^{-/-}$ line with control *trpm8*$^{+/+}$ line. According to the Jackson laboratory recommendations for breeding strategies, interbreeding was performed for eight generations in order to prevent sub-strain apparition and genetic divergence. This study was carried out in strict accordance with the recommendations in the Guide for the Care and Use of Laboratory Animals of the French National Institute for Medical Research (INSERM). The protocol has been approved by the Committee on the Ethics of Animal Experiments of the University of Lille 2. All efforts were made to minimize animal suffering.

Cold shock of mouse testes.

Heat treatment mice were anaesthetized with an i.p. injection xylazine 10 mg/Kg ketamine 100mg/kg. Following anesthesia, the scrotum of each male was passed through a hole which was then placed in a circulating water bath at 0° or 15 °C for 45 min. Control animals received anesthesia only. After waking all animals were returned to their cages. Mice from each group were killed by cervical dislocation and their testis and epididymis were removed. Testes were weighted. Spermatozoa have been prepared from minced epididymis which were incubated in 3 ml of BWW under stirring during 15 minutes. An aliquot was diluted with a sodium acid carbonate-formaldehyde solution and placed into the chamber of a haemocytometer (Thomas Sci. Inc.). Spermatozoa were counted according to the techniques described by the World Health Organization (22). Mice from each group were killed by cervical dislocation and their. Sperm preparation smears were made and allowed to dry in air. 200 spermatozoa were examined at 400-fold magnifications.

Isolation and culture of germ cells.

After sacrifice, testes of C57BL/6J mice were collected. The tunica albuginea of testes was removed. Tubules were then digested in F12/DMEM (1:1) containing 0.5 mg/ml collagenase at 32°C for 15 min under gently agitation. Seminiferous tubules were harvested by low-speed centrifugation and washed twice with F12/DMEM without enzyme. The pellet was resuspended in F12/DMEM supplemented with antibiotics and containing 0.5 mg/ml collagenase and 10 µg/ml DNase. Seminiferous tubules were then cut in fragments with two lancets and digested as above. The dispersed seminiferous cords and cells were collected by centrifugation (1000 rpm, 8 min), washed and gently resuspended in culture medium F12/DMEM supplemented with 5% fetal calf serum, MEM vitamin (1x), ITS liquid media supplemented (1x), Sodium pyruvate (1mM), antibiotic/antimycotic.

Transfection. HEK cells were transfected with plasmids according to manufacturer instructions using Nucleofector technology (Lonza). Briefly, 1 million cells were transfected with 2 µg of total vectors and plated on dishes precoated with polylysine.

mRNA-seq.

Total testis extract and *Spermatogonia, pachytene spermatocytes, round spermatids* and *Sertoli cells* were prepared as previously described (23).

Microarray.

PCR. A classical reverse transcription polymerase chain reaction (RT-PCR) protocol was used, as described elsewhere (24). Oligonucleotide are presented in Table 1.

Quantitative real-time PCR analysis. After total mRNA extraction and purification with TRI REAGENT® (Sigma-Aldrich), mRNAs were subjected to DNAse treatment (Ambion) at 0.25µl DNAse per µg of RNA for 25 min at 25°C. Afterwards, 10 µg mRNA were purified

in a V/V phenol/chloroform/AIA solution (Fluka) with 5% Sodium Acetate 3M. The upper phase was supplemented with 10% Sodium Acetate 3M and 2.5V 100% Ethanol, and kept at -20°C overnight for precipitation. After a brief wash in 70% Ethanol, pellets were left to dry and then re-suspended in 30 µl water. After an agarose gel check of mRNA quality, 2µg of mRNA were subjected to reverse transcription as reported elsewhere (25). Real-time quantitative PCR was performed on a Cfx C1000 system (Biorad). For each reaction, 12.5 ng of cDNA were placed in a final reaction mixture of 15ul containing 7.5ul of 2x SsoFast™ EvaGreen® Supermix (Biorad) and 200nM primer pairs (see **Table 1**). The PCR protocol was: an initial 30 sec denaturation step at 95° C, and 40 cycles of [4 sec at 95° C, 30 sec at 60° C] and a final dissociation curve to control the specificity of the amplification. Quantification of gene expression was performed by the $\underline{\underline{\Delta C}}_T$ method, where $-\underline{\underline{\Delta C}}T = 2^{-(C_T,x-C_T,ref)}$ with efficiency of primer pairs close to 100%. However, in case of tissue analysis and multiple biological variables, proper selection of reference genes cannot be achieved randomly. After microarray analysis, we therefore selected the three most stable genes (GA3PDH, GID2 and CTDNEP1) expressed in the different subtypes of germ cells and in the different cell types constituting testis tissue as well (**Fig Supp S5 A**). We checked the stability of expression of the reference genes in CTL and KOM8 testis subjected or not to mild and strong hypothermia (**Fig Supp S5 B,C**). Since we detected minor asymmetric variations, we concluded that the three reference genes should be used for normalization instead of arbitrarily selecting one or two of them. C_T,ref was substituted by a normalization factor, C_q, calculated by geometric averaging of the C_T of the three reference genes (26). Scattered plots of GA3PDH, GID2 and CTDNEP1 C_T values in function of C_q revealed a better correction of gene expression (**Fig Supp S5 D**).

Immunoblotting. Tissues were collected and stored in liquid nitrogen until protein extraction. Pieces of testes were transferred in beads-containing tubes and 500µl of an ice-cold buffer (pH 7.2) containing 10 mM PO4Na2/K buffer, 150 mM NaCl, 1 g/100 ml sodium deoxycholate, 1% Triton X-100, 1% NP40, a mixture of protease inhibitors (Sigma-Aldrich), and a phosphatase inhibitor (sodium orthovanadate; Sigma-Aldrich) were added. Protein extraction was achieved with 2 cycles of 30 sec at 6,500 xG in a high-throughput PRECELLYS®24 tissue homogenizer cooled down with CRYOLIS® at 4°C.

Cultured cells were collected in a phosphate buffered saline solution, then pelleted prior to extraction in the ice cold buffer described above. After a 30 min incubation on ice, the protein extract was further subjected to sonication and debris were pelleted at 15,000 xG at 4°C for 10 min. Protein concentration was measured by the mean of a BCA Protein Assay (Pierce). 25 µg of total proteins were loaded onto a 10% polyacrylamide gel before an SDS-page was performed. After electrophoresis, proteins were transferred to a nitrocellulose membrane using a semi-dry electroblotter (Bio-Rad). The membrane was blocked in a TNT +5% (W/V) milk (15 mM Tris buffer, pH 8, 140 mM NaCl, 0.05% Tween 20, and 5% non-fat dried milk) for 30 min at room temperature, then soaked in primary antibody diluted in TNT +1% milk for either 2 h at room temperature or overnight at +4°C. After three washes in TNT, the membrane was soaked in secondary antibody diluted in TNT+1% milk for 1h at room temperature. The membrane was processed for chemiluminescence detection using Luminata Forte Western HRP Substrate (Millipore) according to the manufacturer's instructions. After a 10 min bath in Re-blot PLus Mild SOlution (Millipore), membrane was blotted again. The primary antibodies were: HSPA1 1/500 (sc-1060 Santa-Cruz); HSPA2 1/2000 (ab83204, abcam); HSF1-C5 1/500 (sc-17756, Santa-Cruz); HSF2 1/500 (sc-13056, Santa-Cruz); CIRP 1/200 (sc-161012, Santa-Cruz); Ki67 1/500 (Ab15580, Abcam); SOD1 1/500 (sc-11407, Santa-Cruz); SOD2 1/500 (sc-133254, Santa-Cruz); GPx4 1/200 (sc-50497, Santa-Cruz); GPx5 1/200 (sc-54826, Santa-Cruz), b-actin 1/4000 (A-2228, Sigma); Protamin 2 1/200 (sc-23102, Santa-Cruz); p-FRAP (ser2448) 1/200 (sc-101738, Santa-Cruz); FRAP 1/200 (sc-8319, Santa-Cruz)

Histology. Deparaffinized slides of testis from 8 *wt* and 8 *trpm8-/-* mice were subjected to Hemalum-erythrosin-safran trichrome staining. The slides were analyzed on an upright Axio Imager.A1 microscope (Zeiss, Germany). Images were acquired with an AxioCam MRc5 digital camera (Zeiss, Germany) and the Axionvision software was used for analysis.

Immunohistofluorescence. After paraffin removal, antigen retrieval was achieved in a citrate buffer boiled 4 times for 5 minutes in a microwave oven. After three washes in PBS, the tissue sections were blocked with PBS supplemented with 1.2% gelatin (PBS/gelatin) for 30 min at 37 °C, and then co-incubated with primary antibodies diluted in PBS/gelatin for 2 h at 37°C. After thorough rinsing in PBS/gelatine, the slides/dishes were treated with the corresponding secondary antibody: either Dye light 488-labeled anti-rabbit IgG (Jackson ImmunoResearch; dilution, 1/2000) or Texas Red-labeled anti-goat IgG (Jackson ImmunoResearch; dilution, 1/800) diluted in PBS/gelatine for 1 h at RT. After rinsing, twice in PBS/gelatine and once in PBS with 1/200 DAPI for 10 min at RT, the slides were mounted with Mowiol® and examined under a confocal microscope.

TUNEL (terminal deoxynucleotide transferasemediated dUTP—biotin nickend labelling) was achieved on deparaffinized slides of mouse testis, by the mean of TUNEL-TMR red (Roche), incubated at room temperature for 30 min. After rinsing twice in PBS/gelatine and once in PBS with 1/200 Dapi for 10 min at ambient temperature, the slides were mounted with Mowiol®. Images were acquired with an AxioCam MRc5 digital camera (Zeiss, Germany) and the Axionvision software was used for analysis.

Flow cytometry. ROS contents in freshly isolated mouse germ cells were measured by the mean of fluorescent reporters analyzed by a CyAn™ ADP flow cytometer. Briefly, after the dissociation of mouse testis, germ cells were incubated concomitantly with 2.5 µM CellRox® Deep Red reagent and 2.5 µM CellRox® Green reagent for 45 min. After two 5-minute washes,

cells were incubated for 1h at 32, 20 or 8°C prior to flow cytometer analysis. Fluorescent reagents were excited specifically by mean of 488nm and 633nm lines and emission was filtered with series of specific filters in order to avoid any bleed-through. The flow cytometer was calibrated with rainbow beads before each experiment. 405, 488 and 642 wavelength lasers were used according to fluorescent reporters. Data were analyzed with FlowJo software (v 8.7).

Wide-field Ca^{2+} imaging. Calcium imaging experiments have been performed as described previously (21). Briefly, $[Ca^{2+}]_c$ was measured using ratiometric dye fura-2 and quantified according to Grynkiewicz equation (27). The bath solution contained in mM: NaCl 140, KCl 5, $CaCl_2$ 2, $MgCl_2$ 2, Na_2HPO_4 0.3, KH_2PO_4 0.4, $NaHCO_3$ 4, glucose 5, HEPES 10; pH adjusted to 7.3 with NaOH; osmolality 330 mosmol/l.

Electrophysiology. Membrane currents were recorded in the whole-cell configuration using the patch-clamp technique and a computer-controlled EPC-9 amplifier (HEKA Electronic, Germany). Patch pipettes were made using a P-97 puller (Sutter, USA) from borosilicate glass capillaries (WPI, USA). Patch-pipettes (resistance 3 to 5 MΩ) were filled with the following solution (in mM): 140 CsCl, 10 HEPES, 8 EGTA, 1 $MgCl_2$, and 4 $CaCl_2$ (100 nM free Ca^{2+}), pH 7.2 (adjusted with CsOH); osmolality: 290 mosmol/l. The extracellular solution contained (in mM): 150 NaCl, 5 KCl, 10 HEPES, 10 Glucose, 1 $MgCl_2$, 2 $CaCl_2$, pH 7.3 (adjusted with NaOH); osmolality: 310 mosmol/l.

Data analysis. Each experiment was repeated at least three times and the results were expressed as mean ± S.D. The data were analyzed and graphs plotted using Origin 5.0 software (Microcal, Northampton, MA). GraphPad Prism (GraphPad Software Inc, SanDiego, USA) was used for statistical analysis. and mean values were compared using either unpaired t test with Welch's corrected test (2 groups) or One-way ANOVA with Turkey's multiple comparison post-test (≥3 groups). Statistical significance was denoted by (*) for $P<0.05$, (**) for $P<0.01$ or (***) for $P<0.001$.

RESULTS

TRPM8 isoforms are expressed in meiotic germ cells and Leydig cells in rodent testis. Full length TRPM8 channel has been previously detected in mouse spermatozoa where it could participate to acrosome reaction or to chemotaxis (18-20). However the expression of TRPM8 through male gametogenesis has not been reported yet. Besides, while TRPM8 isoforms have been described in prostate (12), lung (28) and epidermis (Bidaux et al, PNAS, revision), their expression in testis has never been studied. By the mean of mRNA sequencing and computer-assisted prediction of mRNA sequences, we sorted out four alternative TRPM8 transcripts in addition of the full length cold and menthol receptor mRNA as well. While full length TRPM8 mRNA sequence includes exon 1 to exon 26, the first isoform of TRPM8 mRNA excludes the first exon (**Fig. 1A**). Comparatively, alternate mRNAs 2, 3 and 4 are likely transcribed from internal promoters ahead exon 15', 17a and 19' that would result in the partial loss of TRPM8 N-terminal cytosolic loop and transmembrane segments (**Fig. S1A**). PCR amplifications confirmed the expression of TRPM8 core exons in both mouse testis and 3-day primary cultures of mouse germ cells (**Fig. 1B**). The profiling of TRPM8 isoforms expression in different germ cell subtypes and in somatic cells was achieved by all-exom microarray as described by Chalmel et al (23). Dataset demonstrated higher expression of TRPM8 isoforms than full length TRPM8 in pachytene spermatocytes, although significant levels were also detected in spermatids and Leydig cells (**Fig. 1C**). It has to be noted that peritubular and Sertoli cells did not express TRPM8 isoforms, and neither did spermatogonium.

Several *trpm8*$^{-/-}$ mouse strains have been generated over the years by deleting either the first translated exon, or exons in the first half of TRPM8 sequence (8, 29). These mutations that did not target the pore region therefore failed to suppress an amino-terminal truncated TRPM8 isoform expression and activity in skin (Bidaux et al, PNAS, revision). In this study, we designed a functional KO mouse line (KOM8) by deleting exons 18, 19 and 20, which encode the active pore domain (**Fig. S1A** and **S1B**). Videofluorimetry using fura-2AM probe showed that menthol induced a calcium mobilization in primary cultures of germ cells isolated from wild type mouse (**Fig. 1D**). Conversely, KOM8 germ cells were characterized by an absence of $[Ca^{2+}]_i$ variation. Since $[Ca^{2+}]_i$ increase could have been generated by either a transient activation of the full length TRPM8 in plasmalemma or by TRPM8 channels-mediated Ca^{2+} release from internal stores (12). Electrophysiological recordings failed to detect any TRPM8 currents in mouse germ cells plasma membrane (**Fig. S2**), while the positive controls done in HEK cells transfected with a TRPM8 were characterized by the typical cold-activated outwardly rectifying current (6, 7, 12). These data suggest that functional TRPM8 channels located within ER membrane participate to ER Ca^{2+} signaling in germ cells, possibly impacting gametogenesis. Because TRPM8 proteins incorporate a cold sensor in their C-terminus (30), we wondered whether TRPM8 channels, either full length or isoforms, could participate to testis response to hypothermia.

TRPM8 suppression sensitizes mouse germ cells to apoptosis. Hypothermia of mouse scrotum was obtained by immersion of scrotum, posterior legs and tail in cold water. This protocol offers the advantage of a rapid cooling of testis while limiting core hypothermia, thus increasing overall survival. In order to calibrate cooling speed and efficiency, we measured core and scrotum temperature of mice partially immerged in cool (14°) and cold water (0°C) for 45 min. As presented in supplementary **figure S3**, scrotum temperature dropped and stabilized at 4-5°C within 5 minutes (rate of decrease was 6.2°C per minute). By comparison, the rate of body temperature cooling was about 0.38°C per minute. After 45 minutes of immersion, mice were in severe hypothermia, preventing us to prolong the experiment (with these experimental conditions, mice viability was 100% three days after immersion).

ARTICLE 16

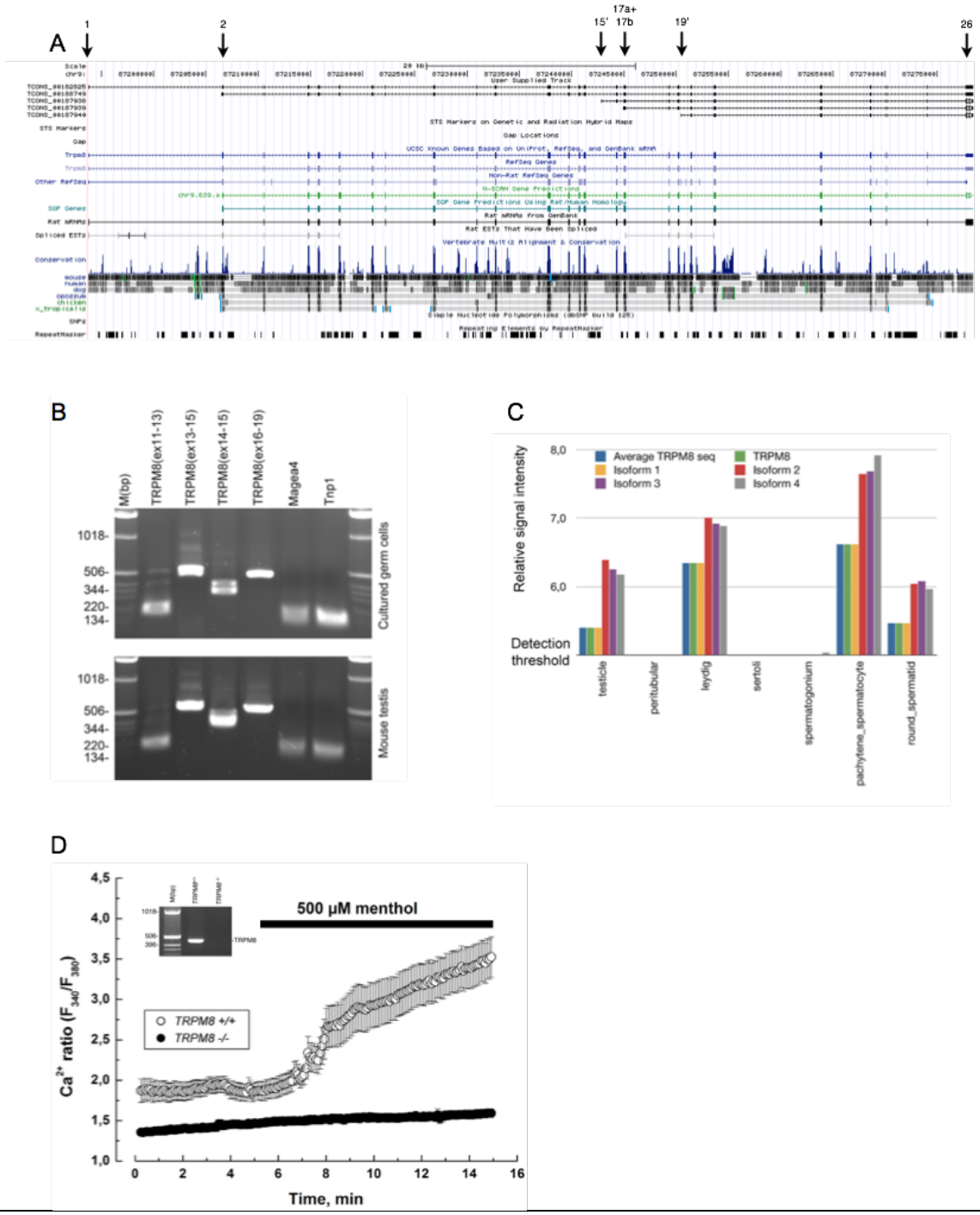

FIGURE 1. *N-terminal truncated TRPM8 isoforms and full length TRPM8 are expressed but functionally restricted to intracellular membrane of mouse germ cells.* **A.** mRNA seq-based prediction of TRPM8 mRNA in rodent testis. 4 TRPM8 alternate mRNA were detected (Constructs 00188749/00187936/00187939/00187940) in addition of the full length cold an menthol receptor (Constructs 00182825). Genomic map of each constructs were aligned with the TRPM8 gene from different species and with alternate mRNA detected. **B.** PCR detection of different regions of the *TRPM8* gene in cultured germ cells (top panel) and in whole extracts of mouse testis (bottom panel). PCR fragments were amplified from exon X to exon Y and reported as TRPM8(exX-Y). Melanoma antigen family A, 4 (Magea 4) and transition protein (Tnp1) were used as reporters of spermatogonia and spermatids respectively. **C.** All-exon transcriptomic datasets sorts TRPM8 mRNAs according to their expression pattern in the different testicular cell types (Leydig cell, Sertoli cell, spermatogonium, spermatocyte, spermatid). Detection level was assumed to be significant above 6. **D.** Calcium imaging experiments realized with Fura2-AM fluorescent probe show an increased cytosolic Ca^{2+} concentration in 2-days isolated CTL mouse germ cells (n=20) after addition of 500 µM menthol. No Ca^{2+} variation was detected in germ cells of TRPM8 knock-out mice (KOM8, n=83).

As expected when inactivating the cold sensor, whose range of activation spanned from 15°C to 32°C, KOM8 mice showed a defect of adaptive thermogenesis resulting in a fast hypothermia in mild cold condition. Indeed, cooling down testis at 17°C for 45 minutes reduced KOM8 mice core body temperature to 22.1±0.8 °C, a value significantly lower than the 25.6±1.5 °C recorded in wild type animals (**Fig. 2A**). This differential amplitude of mice hypothermia was attenuated when animals were stalled at 4°C. This suggests that TRPM8-stimulated thermogenesis cannot attenuate strong cold-induced hypothermia. After a 3-day recovery period, mice were sacrificed and testes collected. We did not measure any difference in testis weight (**Fig. 2B**), spermatozoa count (**Fig. 2C**) and percentage of abnormal spermatozoa (**Fig. 2D**) between KOM8 and CTL mice, even though the proportions of each spermatozoa abnormal phenotype were different (**Fig. S4**). Histological analysis revealed significantly higher number of empty seminiferous tubules in KOM8 testis (**Fig. 2E**). Altogether, our data mostly differed from anterior publications showing that hypothermia triggered massive cell death and increased the number of seminiferous tubules as well as the proportion of abnormal spermatozoa (2, 3, 5). However, in line with these previous studies, we found a significant increase in apoptotic germ cells (**Fig. 2F**). KOM8 germ cells exhibited a cold-independent apoptotic population, while apoptosis of CTL germ cells was doubled by cold (**Fig. 2G**).

Furthermore, basal apoptosis observed in KOM8 germ cells was higher than the one of CTL cells at 29°C, but similar to the one recorded in CTL cells at 4°C. These results suggest that TRPM8 channels protect germ cells, exposed to mild cold (17 to 29°C), against apoptosis. This latter range of temperature is similar to the window of TRPM8 activation by cold. To decipher how TRPM8 may protect germ cells against cold-induced cell death, we looked for potential deregulation of gene families in germ cells of CTL mice subjected to hypothermia.

Hypothermia exerts a TRPM8-dependent regulation of gene expression in testis. By mean of qPCR, we specifically screened the expression of genes involved in cell cycle, mitochondrial uncoupling, oxidation, and of genes activated by cold. To avoid false-positive variations in gene expression, we firstly carefully defined a normalizing factor as described in experimental procedures section. This factor was selected among the most invariant genes detected in CTL and KOM8 testes subjected or not to hypothermia (**Fig. S5**). Because cold could have modified the rate of gametogenesis and unbalanced the proportion between germ cells subtypes, we also controlled that their markers were expressed at a similar level under our experimental conditions. No significant variation of genes expression was detected, which suggests that the proportions of spermatogonium, spermatocytes and spermatids are similar in KOM8 and CTL testes, and are therefore hypothermia-insensitive (**Fig. S6**). Based on these observations, we then assumed that any variation in gene expression detected in the following experiments would solely results from a true shift in the transcription rate, and not from major changes in cell population heterogeneity.

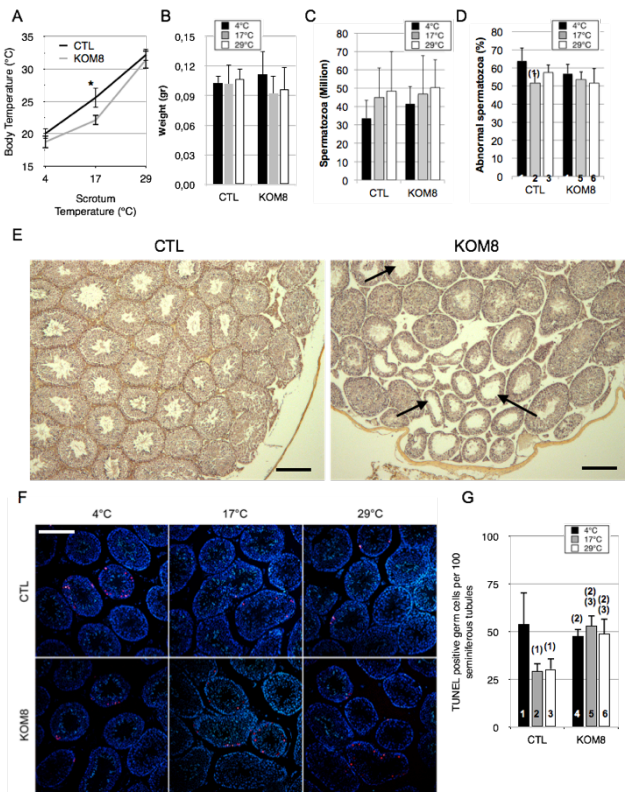

FIGURE 2. *TRPM8 channels expression protects germ cells from apoptosis at rest and during mild cold but not noxious cold exposure.* **A.** Control (CTL) and TRPM8-knockout (KOM8) mice were subjected to a 45 minutes cold shock (as described in experimental procedures section) and both body and scrotum temperatures were measured concomitantly. Mild cold (17°C) revealed an impaired thermogenesis of KOM8 testis while no alteration appeared under noxious cold conditions (4°C). Testicular weight, spermatozoa concentration and percentage of abnormal spermatozoa in CTL and KOM8 mouse testes subjected to cold shocks of different magnitudes did not show any significant difference 3 days after treatment (**B**, **C** and **D**, respectively). Statistical significance was assumed when $p<0.05$ and is shown above the tested column as the number of the column it was paired to. **E.** Anatomopathological analysis confirmed the presence of near-empty seminiferous tubules (arrows) in trichromatic-stained paraffin-embedded sections of KOM8 mouse testis. Scale bar: 200 µm. **F.** Terminal deoxynucleotidyl transferase dUTP nick end labeling (*TUNEL*) with nucleotides coupled to tetramethyl rhodamine (red) revealed apoptotic germ cells. Nuclei were counterstained with Dapi (blue). Apoptotic cells were counted and normalized by 100 seminiferous tubules. Scale bar: 200 µm. (**G**). Histogram shows statistical analysis of the counting of apoptotic germ cells. Values are presented as mean ± SD for CTL (n=6) and KOM8 (n=6) mice.

We secondly controlled that the level of TRPM8 transcripts was stable in both KOM8 and CTL testis, independently of the incubation temperature, by quantifying the expression of exons 21 to 22 downstream of the deleted region in KOM8 (**Fig. 3A**). In addition of

ARTICLE 16

dedicated proteins, heat shock proteins are also regulated by cold shock (31, 32)..

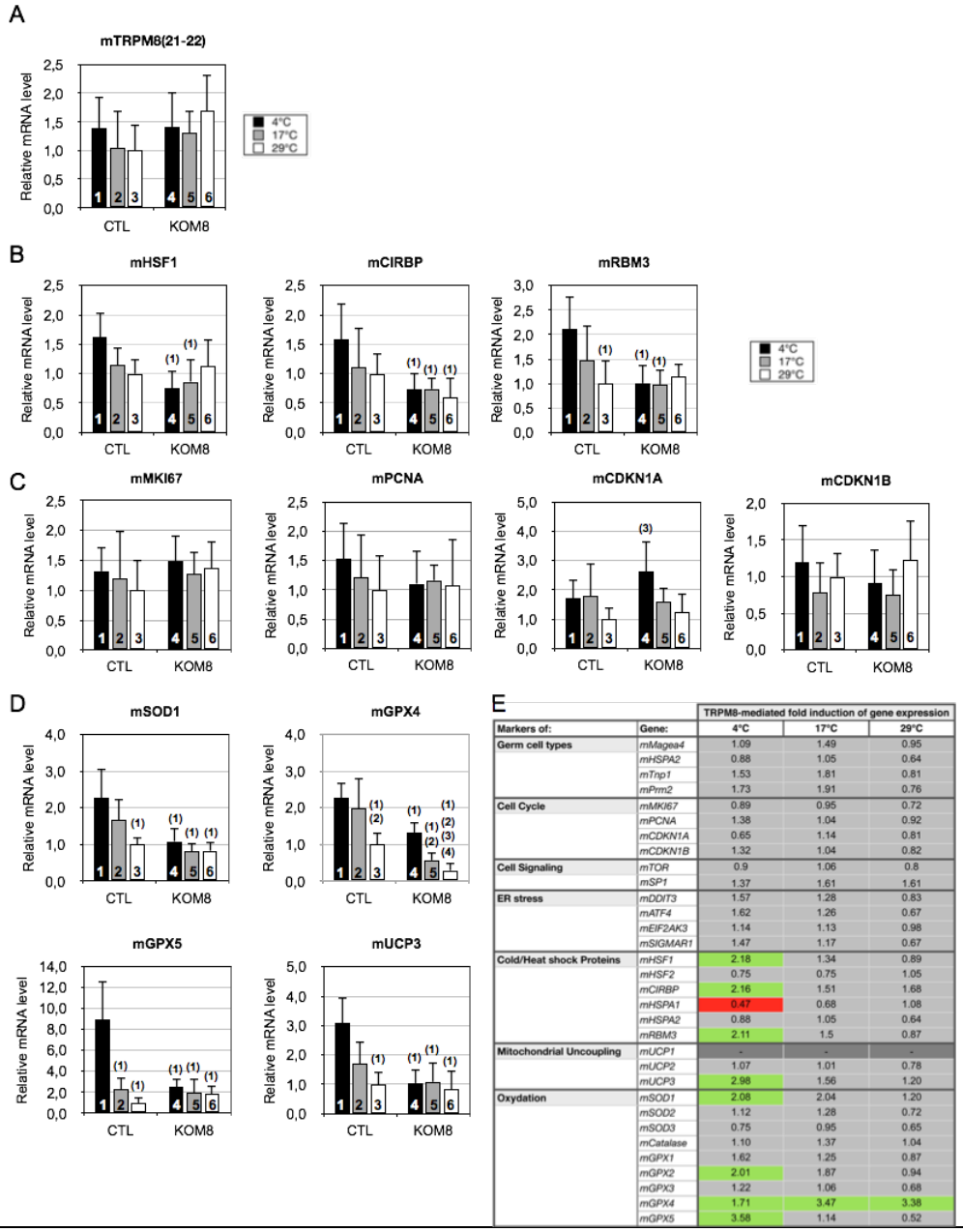

Markers of:	Gene:	TRPM8-mediated fold induction of gene expression 4°C	17°C	29°C
Germ cell types	mMagea4	1.09	1.49	0.95
	mHSPA2	0.88	1.05	0.64
	mTnp1	1.53	1.81	0.81
	mPrm2	1.73	1.91	0.76
Cell Cycle	mMKI67	0.89	0.95	0.72
	mPCNA	1.38	1.04	0.92
	mCDKN1A	0.65	1.14	0.81
	mCDKN1B	1.32	1.04	0.82
Cell Signaling	mTOR	0.9	1.06	0.8
	mSP1	1.37	1.61	1.61
ER stress	mDDIT3	1.57	1.28	0.83
	mATF4	1.62	1.26	0.67
	mEIF2AK3	1.14	1.13	0.98
	mSIGMAR1	1.47	1.17	0.67
Cold/Heat shock Proteins	mHSF1	2.18	1.34	0.89
	mHSF2	0.75	0.75	1.05
	mCIRBP	2.16	1.51	1.68
	mHSPA1	0.47	0.68	1.08
	mHSPA2	0.88	1.05	0.64
	mRBM3	2.11	1.5	0.87
Mitochondrial Uncoupling	mUCP1	-	-	-
	mUCP2	1.07	1.01	0.78
	mUCP3	2.98	1.56	1.20
Oxydation	mSOD1	2.08	2.04	1.20
	mSOD2	1.12	1.28	0.72
	mSOD3	0.75	0.95	0.65
	mCatalase	1.10	1.37	1.04
	mGPX1	1.62	1.25	0.87
	mGPX2	2.01	1.87	0.94
	mGPX3	1.22	1.06	0.68
	mGPX4	1.71	3.47	3.38
	mGPX5	3.58	1.14	0.52

FIGURE 3. *Screening of specific genes networks reveals the TRPM8-dependence of genes encoding cold shock proteins and anti-oxidant enzymes.* **A.** Real-time PCR shows no significant variation of *TRPM8* gene expression (exons 21-22) in CTL and KOM8 mouse subjected to cold shocks of different amplitudes (scrotum temperatures were 29°C, 17°C and 4°C). mRNA quantification was also performed for the following heat and cold shock factors (**B**): heat shock factor 1 (HSF1), cold inducible RNA binding protein (CIRBP) and RNA binding motif (RNP1, RRM) protein 3 (RBM3); for proliferation markers (**C**): antigen identified by monoclonal antibody Ki 67 (MKi67) and proliferating cell nuclear antigen (PCNA); inhibitors of cell cycle: cyclin-dependent kinase inhibitor 1A and 1B (CDKN1A and CDKN1B respectively) also known as $p21^{cip1/waf1}$ and $p27^{kip}$; and for antioxidant enzymes (**D**): superoxide dismutase 1, Cu^{2+}/Zn^{2+} (SOD1), glutathione peroxidases 4 and 5 (GPx4 and GPx5 respectively) and uncoupling protein 3 (UCP3). Values are presented as mean ± SD for CTL (n=5) and KOM8 (n=5) mice. Statistical significance was assumed when $p<0.05$ and is shown above the tested column as the number of the column it was paired to. **E**. Summary table showing the TRPM8-dependence of gene expression in mouse germ cells subjected to cold shock and subsequently to a 3-day recovery period. When variation of expression between CTL and KOM8 is found significant, TRPM8-dependent gene repression is colored in orange, and TRPM8-dependent gene induction is colored in green. Values represent the ratio of averaged gene expression obtained by dividing CTL value by KOM8 value. Grey shading was applied when no significant variations between CTL and KOM8 samples were detected.

We found a weak induction of heat shock factor 1 (*HSF1)*, cold-induced RNA-binding protein (*CIRBP*) and RNA-binding motif protein 3 (*RBM3*) in CTL testis subjected to strong hypothermia (4°C), which was suppressed in KOM8 testis (**Fig. 3B**). This suggests a TRPM8-dependant and cold-dependent up regulation of these genes. Conversely, the expression of Heat shock protein 70 *(HSPA1)* was decreased under cold induction in CTL mouse testis but stay unchanged in KOM8 mouse testis (**Fig. S7**) Cell cycle regulators: Ki67 *(MKI67)*, PCNA, and $p27^{kip1}$ *(CDKN1B)* were not affected by cold, while $p21^{cip1}$ *(CDKN1B)* was preferentially induced by cold in KOM8 testis (**Fig. 3C**). Cold could, thus, slow down cell cycle rate. Since TRPM8 has been implicated in modifications of ROS homeostasis (15), and because elevated [ROS] could induce an increased apoptosis of germ cells paired with modifications in spermatozoa phenotype and survival (33), we measured the expression level of genes coding for the detoxifying enzymes superoxide dismutase 1 and 2 (SOD1 and SOD2), glutathione peroxydases 1-5 (GPX1-5), and catalase. Because the uncoupling protein 3 (UCP3) has been reported to participate to ROS homeostasis (34), we also measured the expression of UCP3. As shown in figures **3D and S7**, *SOD1*, *GPX2*, *GPX5* and *UCP3* were induced by cold in CTL testis, but not in KOM8's. Surprisingly, mild cold (17°C)-induction of the testis-specific peroxidase, GPX4, was restricted to CTL mice, although strong cold (4°c) induces *GPX4* gene in both CTL and KOM8 mouse testes (**Fig. 3D**). We finally tested genes involved in ER-stress response and cell signaling, but no significant variations were detected (**Fig. S7**). These results, altogether, indicated that cold (4°C) induction of *HSF1*, *CIRBP*, *RBM3*, *SOD1*, *GPX2*, *GPX5* and *UCP3* genes and cold repression of the *HSPA1* gene required TRPM8 channels (**Fig. 3E**). It should be noted that the highest *GPX4* induction is reached with mild cold (17°C) stimulation.

Immunoblotting partially confirmed the above results for HSPA1, SOD1, GPX4 and GPX5 proteins in extracts of mouse testis 3 days after hypothermia. Note that, thought its expression was unchanged at mRNA level, we observed a down-regulation of HSPA2 protein in CTL testis subjected to hypothermia and in KOM8 mice at 32°C (**Fig. 4A and 4B**). This suggests a cold-dependent post-transcriptional regulation of HSPA2 protein. Immunolabelling of CTL mouse testis sections confirmed this decrease in HSPA2 expression after hypothermia while CIRBP appeared stable (**Fig. 4C**). In the same line of evidence, KOM8 mice showed decreased level of CIRBP expression (**Fig. 4D**), confirming that variation in immunoblotting are mostly related to decrease of expression per cell instead of a decreased proportion of cell population in testis.

Although testis responses to hypothermia were measured 3 days after cold shock, the observed gene deregulation represented long-term responses following apoptosis kinetic. Induction of detoxifying enzymes suggests that cold shock could be concomitant with a boost of [ROS], which would explain the induction of apoptosis reported here. However, since we analyzed whole testis tissue, we could not clearly state that the observed gene regulations occurred in germ cells instead of occurring in spermatozoa, interstitial and endothelial cells. This is of primordial interest since cold-induced apoptosis was restricted to germ cells. We next studied the response of isolated germ cells to an acute cold shock (22°C or 8°C versus 32°C) in order to characterize the immediate cold-stimulated TRPM8-dependent responsive genes.

Cold-transduction *via* TRPM8 induced immediate up-regulation of GPX4 and 5 concomitantly to an increase in [ROS] in mouse germ cells. By the mean of qPCR, in order to demonstrate germ cells enrichment of the extracts, we normalized the expression of several germ cells markers in isolated germ cells extract by their expression level in whole testis extracts. A 100-fold increase in the expression of Magea4 (marker of spermatogonium), Trnp1 and Prm2 (markers of spermatids) respectively, demonstrated the successful enrichment in germ cells in both CTL and KOM8 samples (**Fig. 5A**). Interestingly, *TRPM8*, *HSPA1*, *HSF2* and *SOD1* were significantly enriched in the germ cells preparation, while *RBM3* was decreased almost 100 times. Since *RBM3* is mainly expressed in Sertoli cells (31), this observation confirms the enrichment in germ cells of our preparations. After exposing isolated germ cells to a cold shock, we performed qPCR fingerprinting of gene expression. A cold-mediated down-regulation of *HSPA2* and *HSF1* was detected only in KOM8 germ cells, suggesting that TRPM8 expression prevents this cold-dependency (**Fig. 5B and 5C**). Nevertheless, one could also associate this decrease in *HSPA2* expression to a decrease of spermatocytes proportion at 20°C and 29°C, or to a down-regulation of gene expression. Because CTL and KOM8 germ cells were prepared in similar conditions, and because incubations were performed for 1 hour, we assumed that the former explanation was unlikely. Besides, the absence of variation of spermatogonium (*Magea4*) and spermatids proportions (*Trnp1* and *Prm2*) confirmed the identical distribution of germ cell subtypes in the different samples. Contrary to these results, and in line with our whole testis analysis (**Fig. 3E**), we found that both *GPX4* and *GPX5* were differentially upregulated by TRPM8 channels in germ cells subjected to a large range of cold temperatures (**Fig. 5B and 5C**). Another type of response was observed with SOD1 and GPX2, which showed a TRPM8-dependent regulation in whole testis analysis 3 days after testis hypothermia, but no variation in their expression in germ cells subjected to acute cold. While GPX4 and GPX5 genes could be directly regulated by acute cold, SOD1 and GPX2 upregulation could result either from their increased expression in other testis cell types, or from a later process taking place after the time point of the present measurement. Our results, altogether, suggest that ER TRPM8 channels are playing the role of cold-transducers inducing an increased expression of anti-oxidant enzymes in germ cells.

ARTICLE 16

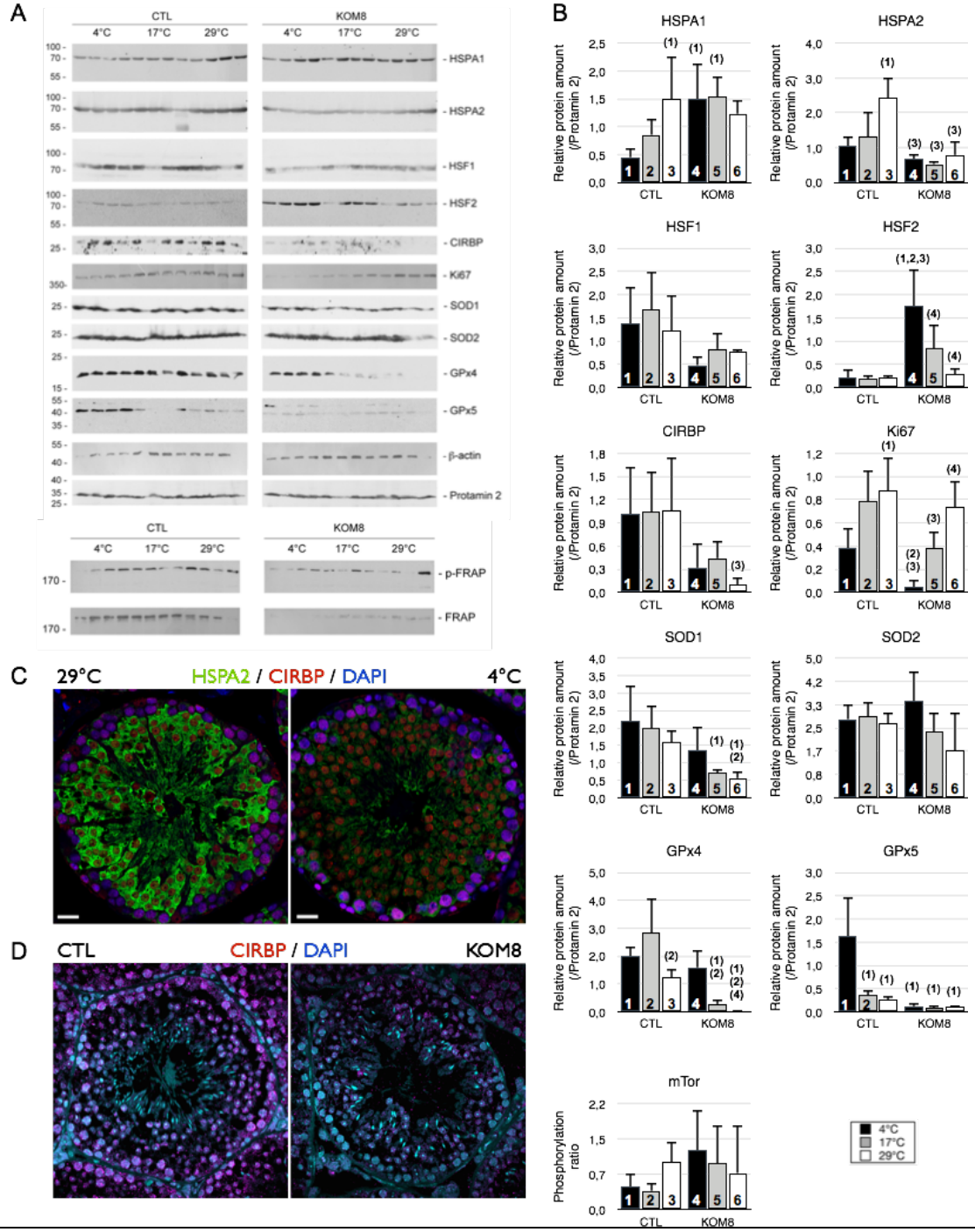

FIGURE 4. *TRPM8 channels participate to the regulation of specific proteins expression in a cold-dependent and cold-independent way.* **A.** Immunoblottings showing the variation of key proteins expression in testis of 4 control and 4 TRPM8-knockout mice 3 days after cold shock (scrotum temperatures were either 29°C, 17°C or 4°C). B-actin and protamine 2 were used as invariant reporters. FKBP-rapamycin associated protein was detected both in its non-phosphorylated form and in its phosphorylated one (Ser^{2448}). Quantification of the protein levels and statistical significance are reported in panel **B**. Protein amount was normalized with protamin2 which appeared much more stable than actin or GAPDH (not shown). Values are presented as mean ± SD for CTL (n=4) and KOM8 (n=4) mice. Statistical significance was assumed when $p<0.05$ and is shown above the tested column as the number of the column it was paired to. **C**. Immunohistofluorescence confirmed the decreased expression of HSPA2 (green) in CTL germ cells subjected to hypothermia (right panel) compared to control (left panel). CIRBP (red) expression appears stable in both conditions. However, CIRBP (red) was found downregulated in KOM8 testis (**D**, right panel) when compared to CTL (**D**, left panel). Nuclei were counterstained with Dapi. Scale bar 20 µm.

We finally measured ROS levels to understand why GPX4 and GPX5 were so quickly and efficiently induced after an acute cold shock in mouse germ cells. Isolated germ cells were loaded with the cytosolic CellRox® Deep

Red reagent and the nuclear CellRox® Green reagent, and then exposed to a 1 hour cold shock at 8°C, 20°C or 32°C.

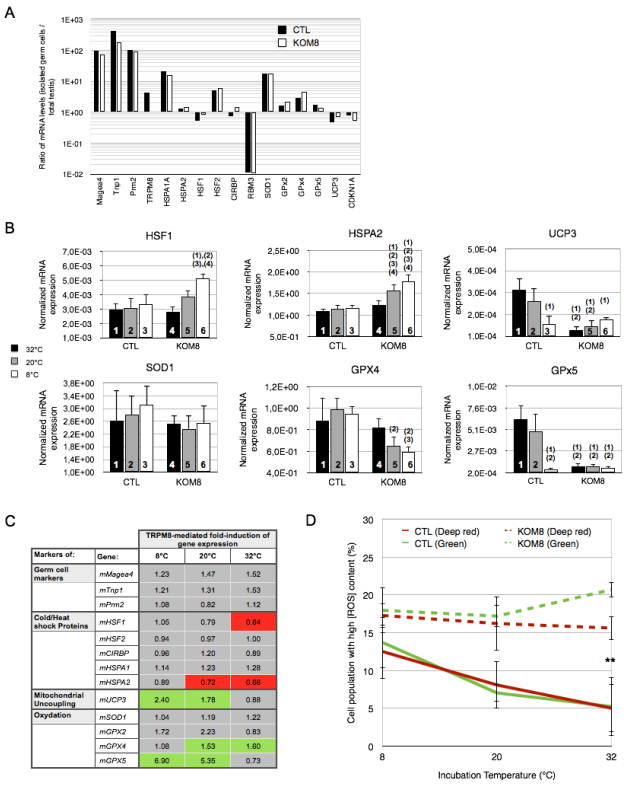

FIGURE 5. *Cold-induced TRPM8 channels activity triggers cold shock response and ROS production.* **A**. Expression level of genes of interest in freshly isolated germ cells from either control (CTL; black bars) or TRPM8 knock-out mice (KOM8; white bars). Values are expressed as ratio of gene expression on total mouse testis expression. RBM3 is the sole gene whose expression drastically drops in isolated germ cells. Conversely, HSPA1, HSF2, SOD1 and GPX2 exhibited a preferential expression in germ cells. **B**. Real-time based quantification of mRNA levels of HSF1, HSPA2, UCP3, SOD1, GPx4 and GPx5 in freshly isolated CTL or KOM8 mouse germ cells subjected to a 1h-incubation at 8°C (black bars), 20°C (grey bars) or 32°C (white bars). Statistical significance was assumed when $p<0.05$ and is shown above the tested column as the number of the column it was paired to. **C**. Summary table showing the TRPM8-dependence of gene expression in mouse germ cells subjected to mild or strong cold shocks. TRPM8-dependent repression is colored in red, and TRPM8-dependent induction is colored in green. Values represent the fold variations of gene expression between CTL and KOM8 samples. Grey shading was applied when no significant variations between CTL and KOM8 samples were figured out. **D.** Freshly isolated mouse germ cells were loaded with the nuclear CellROX Green Reagent (green lines) and the cytosolic/mitochondrial CellROX deep Red Reagent (red lines) before being subjected to a 1-hour cold shock (8°C, 20°C) or kept at control temperature (32°C). Cytometer analysis reveals a significant cold-dependent accumulation of ROS in CTL germ cells (solid lines) while stable ROS concentration was observed in KOM8 germ cells (dashed lines). Values: mean ± SD for CTL (n=4) and KOM8 (n=4) mice.

Fluorescence of ROS reporters was measured by flow cytometry and revealed that the proportion of CTL germ cells showing high [ROS] was increasing gradually with cooling (**Fig. 5D**). Although the population of KOM8 germ cells with high ROS content did not vary with cold shock, its abundance was about 3 times greater than in CTL cells at 32°C. [ROS] was characterized by the same cold- and TRPM8-dependency that the apoptosis induction observed in germ cells as shown in the figure 2G. This clearly emphasizes the relationship between high ROS content and apoptosis, as previously reported in spermatozoa (16, 17). Furthermore, our results validate the hypothesis that functional TRPM8 channels are required in germ cells to modulate [ROS] and to prevent its increase during mild hypothermia.

DISCUSSION

In this study, we show that mouse germ cells express variants of the cold and menthol receptor, TRPM8, in addition to the full-length channel. We demonstrate that TRPM8 activation by menthol triggers Ca^{2+} mobilization from ER stores of germ cells. We also confirm that hypothermia of germ cells triggers an increase in [ROS] which correlates to the increased rate of apoptosis of meiotic cells. Finally, we show that TRPM8 channels are required for cold-mediated induction of GPX4 and GPX5 that in turn protect germ cells from deleterious effects of ROS.

Thermo-sensitivity of spermatogenesis

In mammals, testis presents the original characteristic to stay at a lower temperature, 32°C, than inner organs. Besides, numerous studies previously reported testis vulnerability to both hypothermia (2-5) and hyperthermia (1, 31, 35, 36). While the latter has been extensively studied, the former is still poorly understood. Cold shock, below 32°C, has been reported to stimulate expression of cold-induced proteins like cold-induced RNA-binding protein (CIRBP) and RNA-binding motif protein 3 (RBM3) in numerous tissues (31, 32). These observations probably explain why both CIRBP and RBM3 are constitutively expressed in testis. Conversely to cold shock proteins, heat shock proteins are down-regulated during hypothermia. The heat shock factor family, *HSF1*, *HSF2* and *HSF4* in mammals, are sensitive to heat and oxidation, and transduce stress signals to *HSP* genes. However, how changes in temperature may induce this HSF-dependent pathway is still unknown. Our results clearly demonstrate the requirement of cold detectors, namely TRPM8 isoforms, in controlling the steady-state expression of *HSF1/HSF2/HSPA2/CIRBP* genes. This suggests that TRPM8 channels activation initiates the cold shock response in testis, which may protect germ cells from cold-mediated death.

The reactive oxygen species (ROS) and their derived reactive nitrogen species have been characterized as the main contributors to cell death in hyperthermia (36). In this study, we have correlated the cold response to an increase of both [ROS] and apoptosis of spermatocytes. Our results emphasize the preponderant role of oxidation in deleterious events occurring in

hypothermic germ cells. Strikingly, cooling and heating induce similar pathways including synthesis of chaperones (heat *vs* cold shock proteins), stress, and oxidation. This means that optimal spermatogenesis requires a tightly controlled temperature and shield mechanisms to protect germ cells against strong and/or transient variations of temperature. While the control of scrotum temperature can be partially achieved by body's responses such as adaptation of blood circulation and nutriment availability, thermo-shielding mechanisms must be incorporated in germ cells to guarantee the quickest and the most efficient response to oxidation. Dedicated enzymes such as superoxide dismutase, catalase and glutathione peroxidase perform ROS scavenging in all cells. Studies have reported in endotherms (37, 38), and ectotherms (39) as well, that cold conditioning was correlated to an increased activity of glutathion peroxidases and catalase. Authors suggested that this increased GPX activity would enhance detoxification of ROS and consequently increase cell survival (16, 17, 35).

Amplitude of cold exposure differentially induces ROS-scavenging enzymes in germ cells.

Our study is the first to report a cold-mediated induction of ROS-scavenging enzymes in mammal testis. While GPX4 and GPX5 are mainly expressed in the male genital tract, SOD1 and GPX2 are found in all tissues. GPX4 is a selenium-dependent scavenger that metabolizes reactive H_2O_2 and complexes organic peroxidized molecules in H_2O (for review, see (40)). Suppression of the mitochondrial GPX4 increases ROS content and triggers infertility (41) – demonstrating its critical role in ROS detoxification. GPX5 is a selenium-dependent scavenger which is mainly expressed in epididymis spermatozoa. GPX5 deletion increases ROS content in spermatozoa and decreases viability of resulting embryos (42). Our results clearly demonstrate that TRPM8 is required for GPX4 sustained expression between 17°C and 32°C, while *GPX5* gene is upregulated in germ cells *via* TRPM8 at a colder range of temperatures (below 20°C). Taking into account that TRPM8 range of activity is between 15°C-32°C, it is noteworthy that GPX4 and GPX5 are differentially regulated by the same cold-activated TRPM8 response. This suggests that GPX4 and GPX5 are likely regulated by different pathways or require different levels of TRPM8 activation.

Another regulator of ROS content, which is not *per se* a ROS-scavenger, has recently emerged in the literature. Except in thermogenic tissues, uncoupling has been postulated to participate to ROS homeostasis. Superoxides activate UCP3 which triggers proton leak, and consequently mild uncoupling (43). This, in turn, decreases the rate of production of new superoxide anions and then modulates [ROS] in cells (34, 44). Hyperthermia stimulates UCP2 expression that in turn increases uncoupling and prevents the production of high levels of ROS (45). In our hands, UCP3 regulation by cold is similar to GPX5's and requires functional TRPM8 channels. Conversely to GPX4, UCP3 and GPX5 expression levels fit well with the proportion of CTL germ cells characterized by a high ROS content. This suggests that at basal temperature, GPX4 may be the main ROS scavenger active in germ cells, while during mild hypothermia both GPX5 and UCP3 are activated in order to enhance ROS scavenging.

Altogether, these mechanisms confer to rodent germ cells graduated responses to cold-mediated ROS induction that efficiently protect them from cell death during an hypothermia ranging from 17°C to 30°C. However, acute cold, below 15°C, probably triggers many more effects which cannot be completely prevented by the triad TRPM8/GPX4/GPX5.

TRPM8 protects rodent spermatocytes from cold-mediated ROS-induced apoptosis

An increasing number of evidences propose ROS as crucial second messengers (46). This function implies that ROS homeostasis must be finely tuned in order to maintain enough ROS for cell signaling while preventing surges of ROS that would invariably lead to cell death (47). The latter may arise from an increased synthesis of ROS coupled to a basal or decreased activity of ROS-scavenging enzymes (48). At scrotum physiological temperature, TRPM8 exerts a protective effect by indirectly up-regulating GPX4 level, which probably explains why ROS content is lower in CTL germ cells than in KOM8 cells. Although the thermo-regulated TRPM8 activity is very low at 32°C, the channel can still be regulated by lipids (49, 50). TRPM8 activation by cold clearly induces GPX5/UCP3 expression concomitantly to an increase in ROS content. This appears paradoxical since increased expression of ROS-scavenging enzymes is expected to stabilize or down-regulate ROS content. However, though a 1-hour cold stimulation is probably too short to induce functional ROS scavenging enzymes, it is sufficient to increase ROS production. We recently showed that a similar isoform of TRPM8 induces Ca^{2+} channeling from ER microdomains to mitochondria in keratinocytes. This phenomenon boosts TCA activity and the associated superoxide production (ref Bidaux et al). It is therefore likely that cold stimulation of germ cells stimulates ROS production through a Ca^{2+}-dependent mechanism.

REFERENCES.

1. Chowdhury AK & Steinberger E (1970) Early changes in the germinal epithelium of rat testes following exposure to heat. *Journal of reproduction and fertility* 22(2):205-212.
2. Macdonald J & Harrison RG (1954) Effect of low temperatures on rat spermatogenesis. *Fertility and sterility* 5(3):205-216.
3. Blanco-Rodriguez J & Martinez-Garcia C (1997) Mild hypothermia induces apoptosis in rat testis at specific stages of the seminiferous epithelium. *Journal of andrology* 18(5):535-539.
4. Zhang Z*, et al.* (2004) Functional analysis of the cooled rat testis. *Journal of andrology* 25(1):57-68.
5. Yazawa T*, et al.* (2003) Abnormal spermatogenesis at low temperatures in the Japanese red-bellied newt, Cynops pyrrhogaster: possible biological significance of the cessation of spermatocytogenesis. *Molecular reproduction and development* 66(1):60-66.

6. McKemy DD, Neuhausser WM, & Julius D (2002) Identification of a cold receptor reveals a general role for TRP channels in thermosensation. *Nature* 416(6876):52-58.
7. Peier AM*, et al.* (2002) A TRP channel that senses cold stimuli and menthol. *Cell* 108(5):705-715.
8. Bautista DM*, et al.* (2007) The menthol receptor TRPM8 is the principal detector of environmental cold. *Nature* 448(7150):204-208.
9. Brauchi S, Orio P, & Latorre R (2004) Clues to understanding cold sensation: thermodynamics and electrophysiological analysis of the cold receptor TRPM8. *Proc Natl Acad Sci U S A* 101(43):15494-15499.
10. Latorre R, Brauchi S, Madrid R, & Orio P (2011) A cool channel in cold transduction. *Physiology (Bethesda)* 26(4):273-285.
11. Voets T*, et al.* (2004) The principle of temperature-dependent gating in cold- and heat-sensitive TRP channels. *Nature* 430(7001):748-754.
12. Bidaux G*, et al.* (2007) Prostate cell differentiation status determines transient receptor potential melastatin member 8 channel subcellular localization and function. *J Clin Invest* 117(6):1647-1657.
13. Denda M, Tsutsumi M, & Denda S (2010) Topical application of TRPM8 agonists accelerates skin permeability barrier recovery and reduces epidermal proliferation induced by barrier insult: role of cold-sensitive TRP receptors in epidermal permeability barrier homoeostasis. *Exp Dermatol* 19(9):791-795.
14. Nocchi L, Daly DM, Chapple C, & Grundy D (2014) Induction of oxidative stress causes functional alterations in mouse urothelium via a TRPM8-mediated mechanism: implications for aging. *Aging cell* 13(3):540-550.
15. Zhu S*, et al.* (2014) Involvement of transient receptor potential melastatin-8 (TRPM8) in menthol-induced calcium entry, reactive oxygen species production and cell death in rheumatoid arthritis rat synovial fibroblasts. *European journal of pharmacology* 725:1-9.
16. Aitken RJ & Baker MA (2013) Causes and consequences of apoptosis in spermatozoa; contributions to infertility and impacts on development. *The International journal of developmental biology* 57(2-4):265-272.
17. Aitken RJ*, et al.* (2012) Electrophilic aldehydes generated by sperm metabolism activate mitochondrial reactive oxygen species generation and apoptosis by targeting succinate dehydrogenase. *J Biol Chem* 287(39):33048-33060.
18. De Blas GA*, et al.* (2009) TRPM8, a versatile channel in human sperm. *PLoS One* 4(6):e6095.
19. Gibbs GM*, et al.* (2011) Cysteine-rich secretory protein 4 is an inhibitor of transient receptor potential M8 with a role in establishing sperm function. *Proc Natl Acad Sci U S A* 108(17):7034-7039.
20. Martinez-Lopez P*, et al.* (2011) TRPM8 in mouse sperm detects temperature changes and may influence the acrosome reaction. *J Cell Physiol* 226(6):1620-1631.
21. Thebault S*, et al.* (2005) Novel role of cold/menthol-sensitive transient receptor potential melastatine family member 8 (TRPM8) in the activation of store-operated channels in LNCaP human prostate cancer epithelial cells. *J Biol Chem* 280(47):39423-39435.
22. World Health O (2001) [Laboratory manual of the WHO for the examination of human semen and sperm-cervical mucus interaction]. *Ann Ist Super Sanita* 37(1):I-XII, 1-123.
23. Chalmel F*, et al.* (2007) The conserved transcriptome in human and rodent male gametogenesis. *Proc Natl Acad Sci U S A* 104(20):8346-8351.
24. Bidaux G*, et al.* (2005) Evidence for specific TRPM8 expression in human prostate secretory epithelial cells: functional androgen receptor requirement. *Endocrine-related cancer* 12(2):367-382.
25. Gackiere F, Bidaux G, Lory P, Prevarskaya N, & Mariot P (2006) A role for voltage gated T-type calcium channels in mediating "capacitative" calcium entry? *Cell Calcium* 39(4):357-366.
26. Vandesompele J*, et al.* (2002) Accurate normalization of real-time quantitative RT-PCR data by geometric averaging of multiple internal control genes. *Genome biology* 3(7):RESEARCH0034.
27. Grynkiewicz G, Poenie M, & Tsien RY (1985) A new generation of Ca2+ indicators with greatly improved fluorescence properties. *J Biol Chem* 260(6):3440-3450.
28. Sabnis AS, Shadid M, Yost GS, & Reilly CA (2008) Human lung epithelial cells express a functional cold-sensing TRPM8 variant. *Am J Respir Cell Mol Biol* 39(4):466-474.
29. Dhaka A*, et al.* (2007) TRPM8 is required for cold sensation in mice. *Neuron* 54(3):371-378.
30. Brauchi S, Orta G, Salazar M, Rosenmann E, & Latorre R (2006) A hot-sensing cold receptor: C-terminal domain determines thermosensation in transient receptor potential channels. *J Neurosci* 26(18):4835-4840.
31. Danno S, Itoh K, Matsuda T, & Fujita J (2000) Decreased expression of mouse Rbm3, a cold-shock protein, in Sertoli cells of cryptorchid testis. *The American journal of pathology* 156(5):1685-1692.
32. Nishiyama H*, et al.* (1997) A glycine-rich RNA-binding protein mediating cold-inducible suppression of mammalian cell growth. *J Cell Biol* 137(4):899-908.
33. Wang X*, et al.* (2003) Oxidative stress is associated with increased apoptosis leading to spermatozoa DNA damage in patients with male factor infertility. *Fertility and sterility* 80(3):531-535.
34. Liu D*, et al.* (2012) Human stanniocalcin-1 suppresses angiotensin II-induced superoxide generation in cardiomyocytes through UCP3-mediated anti-oxidant pathway. *PLoS One* 7(5):e36994.
35. Ishii T*, et al.* (2005) Accelerated impairment of spermatogenic cells in SOD1-knockout mice under heat stress. *Free radical research* 39(7):697-705.
36. Pino JA*, et al.* (2013) Differential effects of temperature on reactive oxygen/nitrogen species production in rat pachytene spermatocytes and round spermatids. *Reproduction* 145(2):203-212.
37. Kaushik S & Kaur J (2003) Chronic cold exposure affects the antioxidant defense system in various rat tissues. *Clinica chimica acta; international journal of clinical chemistry* 333(1):69-77.
38. Selman C, McLaren JS, Himanka MJ, & Speakman JR (2000) Effect of long-term cold exposure on antioxidant enzyme activities in a small mammal. *Free Radic Biol Med* 28(8):1279-1285.
39. Voituron Y, Servais S, Romestaing C, Douki T, & Barre H (2006) Oxidative DNA damage and antioxidant defenses in the European common lizard (Lacerta vivipara) in supercooled and frozen states. *Cryobiology* 52(1):74-82.

40. Chabory E, *et al.* (2010) Mammalian glutathione peroxidases control acquisition and maintenance of spermatozoa integrity. *Journal of animal science* 88(4):1321-1331.
41. Schneider M, *et al.* (2009) Mitochondrial glutathione peroxidase 4 disruption causes male infertility. *FASEB J* 23(9):3233-3242.
42. Chabory E, *et al.* (2009) Epididymis seleno-independent glutathione peroxidase 5 maintains sperm DNA integrity in mice. *J Clin Invest* 119(7):2074-2085.
43. Papa S & Skulachev VP (1997) Reactive oxygen species, mitochondria, apoptosis and aging. *Mol Cell Biochem* 174(1-2):305-319.
44. Echtay KS, *et al.* (2002) Superoxide activates mitochondrial uncoupling proteins. *Nature* 415(6867):96-99.
45. Zhang K, *et al.* (2007) Uncoupling protein 2 protects testicular germ cells from hyperthermia-induced apoptosis. *Biochem Biophys Res Commun* 360(2):327-332.
46. Imai H & Nakagawa Y (2003) Biological significance of phospholipid hydroperoxide glutathione peroxidase (PHGPx, GPx4) in mammalian cells. *Free Radic Biol Med* 34(2):145-169.
47. Ray PD, Huang BW, & Tsuji Y (2012) Reactive oxygen species (ROS) homeostasis and redox regulation in cellular signaling. *Cell Signal* 24(5):981-990.
48. Circu ML & Aw TY (2010) Reactive oxygen species, cellular redox systems, and apoptosis. *Free Radic Biol Med* 48(6):749-762.
49. Vanden Abeele F, *et al.* (2006) Ca2+-independent phospholipase A2-dependent gating of TRPM8 by lysophospholipids. *J Biol Chem* 281(52):40174-40182.
50. Andersson DA, Nash M, & Bevan S (2007) Modulation of the cold-activated channel TRPM8 by lysophospholipids and polyunsaturated fatty acids. *J Neurosci* 27(12):3347-3355.

FOOTNOTES.

trpm8$^{-/-}$ mouse line has been designed by Dr. Gabriel Bidaux and Genoway Inc. Trpm8$^{-/-}$ mouse line has been established by Genoway Inc. and housed in Charles River Laboratories. Authors would like to thank Marie Norbert and the whole Genoway team for their support and their competences.

This work has been supported by grants from: INSERM, Ministère de l'Education Nationale, Ligue Nationale Contre le Cancer, Region Nord-Pas-de-Calais and ANR Grant: TRPM8/REPROD.

Dr. Anne-sophie Borowiec was supported by Fondation pour la recherche médicale.

We also wish to thank Delphine Taillieu and Mélanie Besegher for their technical assistance for animals housing at "Animalerie High-Tech de l'Institut de Médecine Prédictive et de Recherche Thérapeutique de Lille".

TABLE 1

	5' forward 3'	5' reverse 3'
PCR		
mTRPM8(ex13-14)	TGAAGCTTCTGCTGGAGTGG	GAGTTCCACATCCAAGTCCTC
mTRPM8(ex15-17)	CTGCAAGCTCTCTTCATCTGG	CTGCCTCACTTCATCACAGAAG
mTRPM8(ex16-17)	ATATGAGACCCGAGCAGTGG	CTGCCTCACTTCATCACAGAAG
mTRPM8(ex18-21)	CGAGACACGAAGAACTGGAAG	ATCCGTTGCAGAATTATAATCTGGG
mTRPM8(ex16-21)	ATATGAGACCCGAGCAGTGG	ATCCGTTGCAGAATTATAATCTGGG
b-actin	CAGAGCAAGAGAGGTATCCT	GTTGAAGGTCTCAAACATGATC
Real-time PCR		
mGAPDH	CTGCGACTTCAACAGCAACTC	TCCACCACCCTGTTGCTGTA
mGID2	GGAATACGACGTGATCGTGC	CAGCGGTGTTATAGACGCACT
mCTDNEP1	ACAAACACCCAGTCCGGTTT	TGCCACAGCAGAGCCATAAA
mTRPM8	CACATATGACTTCTCCCACTGT	AGAGCATGTAGATGCACACCA
mMAGEA4	GGGAGTTAGACAATGTTCAGGCT	GGAGAGGAGGCTCTTTGAGG
mHSPA2	CGCTTTCGTCCTAACGTTGC	CGATGATCTCCACCTTGCCA
mTNP1	CTCACAAGGGCGTCAAGAGA	CATTGCCGCATCACAAGTGG
mPRM2	CATAGGATCCACAAGAGGCG	TGCCTCCTACATTTCCTGCAC
mMKI67	TCTTGGCACTCACAGCCCAGC	TGTCCTCGGTGGCGTTATCCC
mPCNA	TCTGCAAGTGGAGAGCTTGGCA	AGAGCAAACGTTAGGTGAACAGGCT
mCDKN1A	CGGTGTCAGAGTCTAGGGGA	AGGATTGGACATGGTGCCTG
mCDKN1B	GCTGGGTTAGCGGAGCAGTGT	AGCGTTCGGGGAACCGTCTG
mTOR	GCATTCCGACCGTCCGCCTT	CTGGAACGCCGCAGTCCGTT
mSP1	GTGCCGCCTTTTCTCAGACT	CAATTCTGCTGCAGGTTGCT
mDDIT3	TGCAGGAGGTCCTGTCCTCAGAT	AGCCAAGCTAGGGACGCAGG
mATF4	CATGGGTTCTCCAGCGACAA	TCCAACATCCAATCTGTCCCG
mEIF2AK3	CAAGCCAGAGGTGTTTGGGA	AGATTCGAGCAGGGACTCCA
mSIGMAR1	AGGGCACCACGAAAAGTGAGGT	GGTCCCCACTCCAGAGCCGT

ARTICLE 16

mHSF1	GCCTCCCCAGGCAGGAGCATA	AGGGCTCGCCTCCAGTACCC
mHSF2	CATCACCTGGAGTCAGAATGGA	GCACTACTTTTCGGAAGCCA
mCIRBP	GGAGCTCGGGAGGGTCCTACA	GACGATCTGGACGCGGAGGG
mHSPA1	TGGCCTTGAGGACTGTCATT	AGCCCACGTGCAATACACAA
mRBM3	CGTGGTCGCAGTTACTCTAG	TGAGTAGCGGTCATAGCCAC
mUCP1	AGGAGTCCGAAGTCGCGGGT	TGGAGGGCAGAGAGGCGTGA
mUCP2	TCTGCACCACCGTCATCGCC	GACCTGCGCTGTGGTACTGGC
mUCP3	CCGAAGTGCCTCCCACAACGG	ACGGACCTTGGCGGTGTCCA
mSOD1	GCGGTGAACCAGTTGTGTTG	GCACTGGTACAGCCTTGTGT
mSOD2	ACAACTCAGGTCGCTCTTCAG	TCCAGCAACTCTCCTTTGGG
mSOD3	CTGACAGGTGCAGAGAACCTC	GGTCAAGCCTGTCTGCTAGG
mCATALASE	GCCAATGGCAATTACCCGTC	GAGGCCAAACCTTGGTCAGA
mGPX1	TCTCTCTGAGGCACCACGAT	CATTCTCCTGGTGTCCGAACT
mGPX2	CTGCAATGTCGCTTTCCCAG	CCCCAGGTCGGACATACTTG
mGPX3	GCATCCTGCCTTCTGTCCC	CGATGGTGAGGGCTCCATAC
mGPX4	GTACTGCAACAGCTCCGAGT	ATGCACACGAAACCCCTGTA
mGPX5	TGTGAAAGGCACCATCTACG	GACCGCAATAGGTAGCCACA

TABLE 1: list of oligonucleotides used in this study.

SUPPLEMENTAL FIGURES

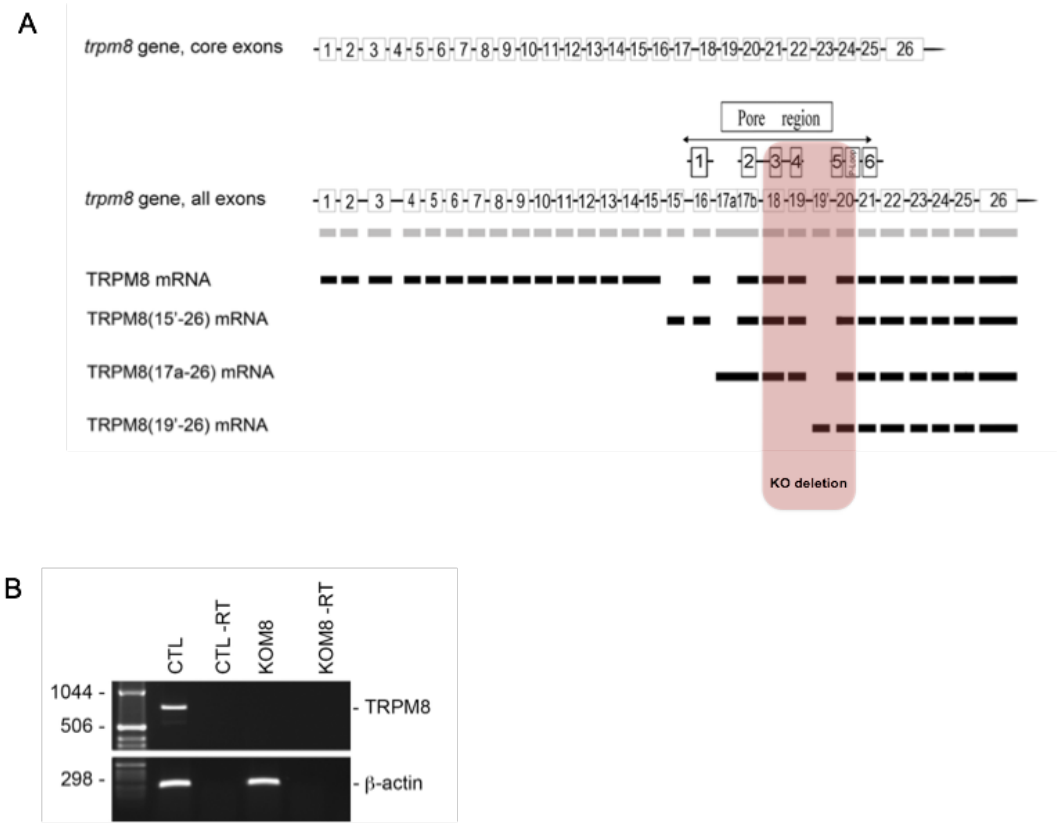

FIGURE 1. *Alternate TRPM8 mRNAs, generated by means of internal promotors, encode different putative TRPM8 channel structures in mouse germ cells.* **A.** Schematic representation of the *trpm8* gene with its core exons (top). In schematic representation (*trpm8* gene, all exons) of both core and new alternate exons (middle) the labeling reflects: "comas" – a cassette exon, a small letter - 5' or 3' supplemental part of a core exon. Transmembrane domains (TM) and p-loop of the channel pore (pore region) are aligned with their encoding exons. Exon structure (bottom) of alternate TRPM8 mRNAs: TRPM8(15'), TRPM8(17a), TRPM8(19'). Putative ATG and STOP codons are indicated. Note that in KOM8, exons 18,19 and 20 are suppressed. **B**. PCR shows detection of TRPM8 cDNA between exon14 and 19 in CTL but not in KOM8 mouse testis. The presence of contaminant DNA was assessed by removing polymerase from the reversion transcription step (-RT). β-actin reports equal cDNA loading and reverse transcription quality.

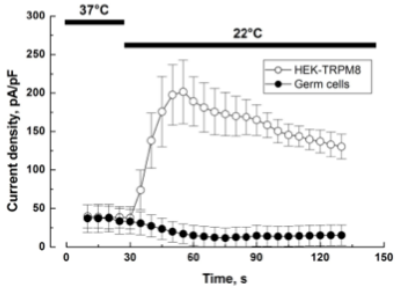

FIGURE 2. *TRPM8 is expressed in isolated germ cells but no TRPM8 current is detected.* Whole-cell patch clamp recordings were conducted in TRPM8-transfected HEK cells (n=7, white circles) and CTL mouse germ cells (n=9, black circles). The cells were repetitively stimulated by voltage ramps (from -100 to +100 mV) and changes in the mean current density at +100 mV elicited by exposure to cold (22°C) are presented as time courses for both cell types.

ARTICLE 16

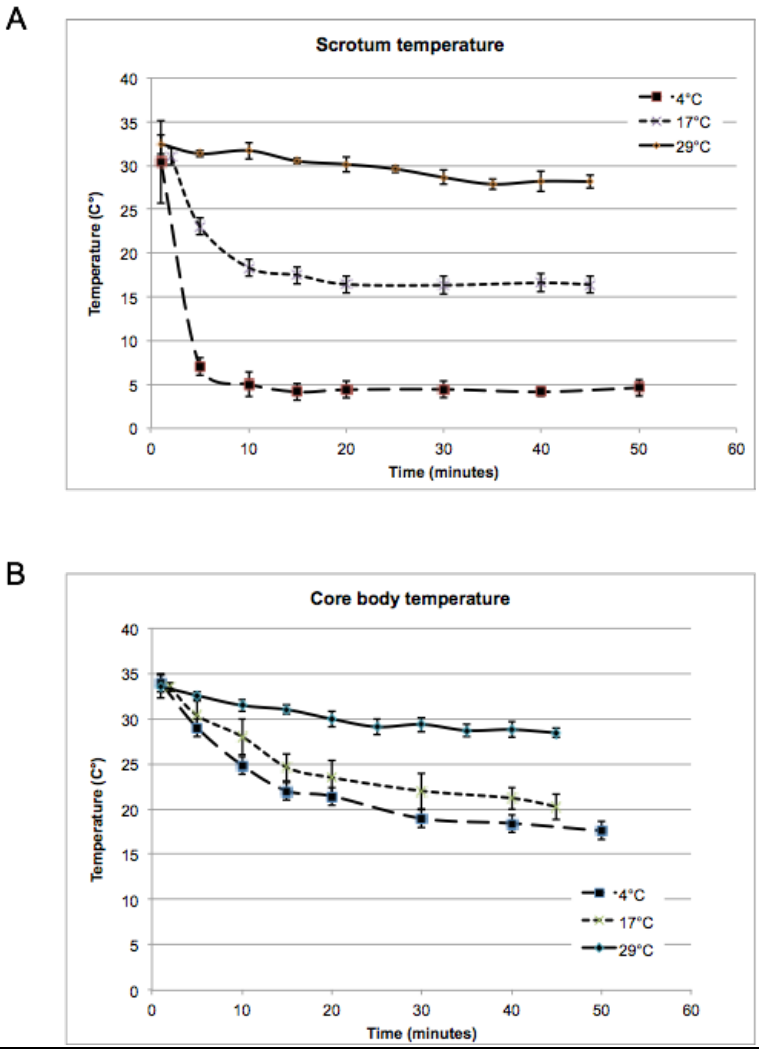

FIGURE 3. *Experimental calibration of the cold shock inducing setup.* The temperature was measured in the scrotum and in peritoneum. The scrotum of anesthetized mice was immersed in a water bath at 0 °, 14 ° C for 45 minutes. For control the mice stayed at room temperature. Mean and standard deviation were shown.(n=3).

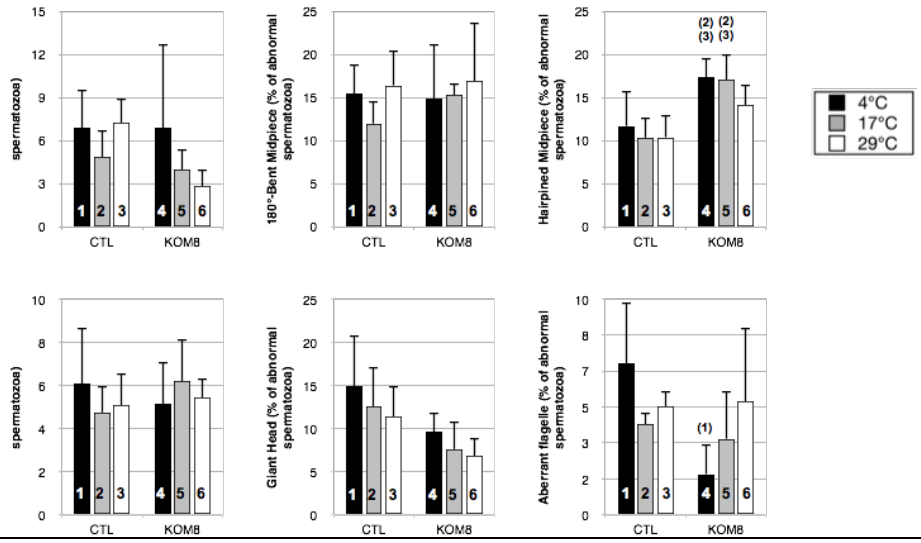

FIGURE 4. *Distribution of abnormal spermatozoa phenotypes*. Midpiece, Head and flagella aberrant morphology were counted and normalized on the total number of abnormal spermatozoa. Statistical

significance was assumed when $p<0.05$ and is shown above the tested column as the number of the column it was paired to.

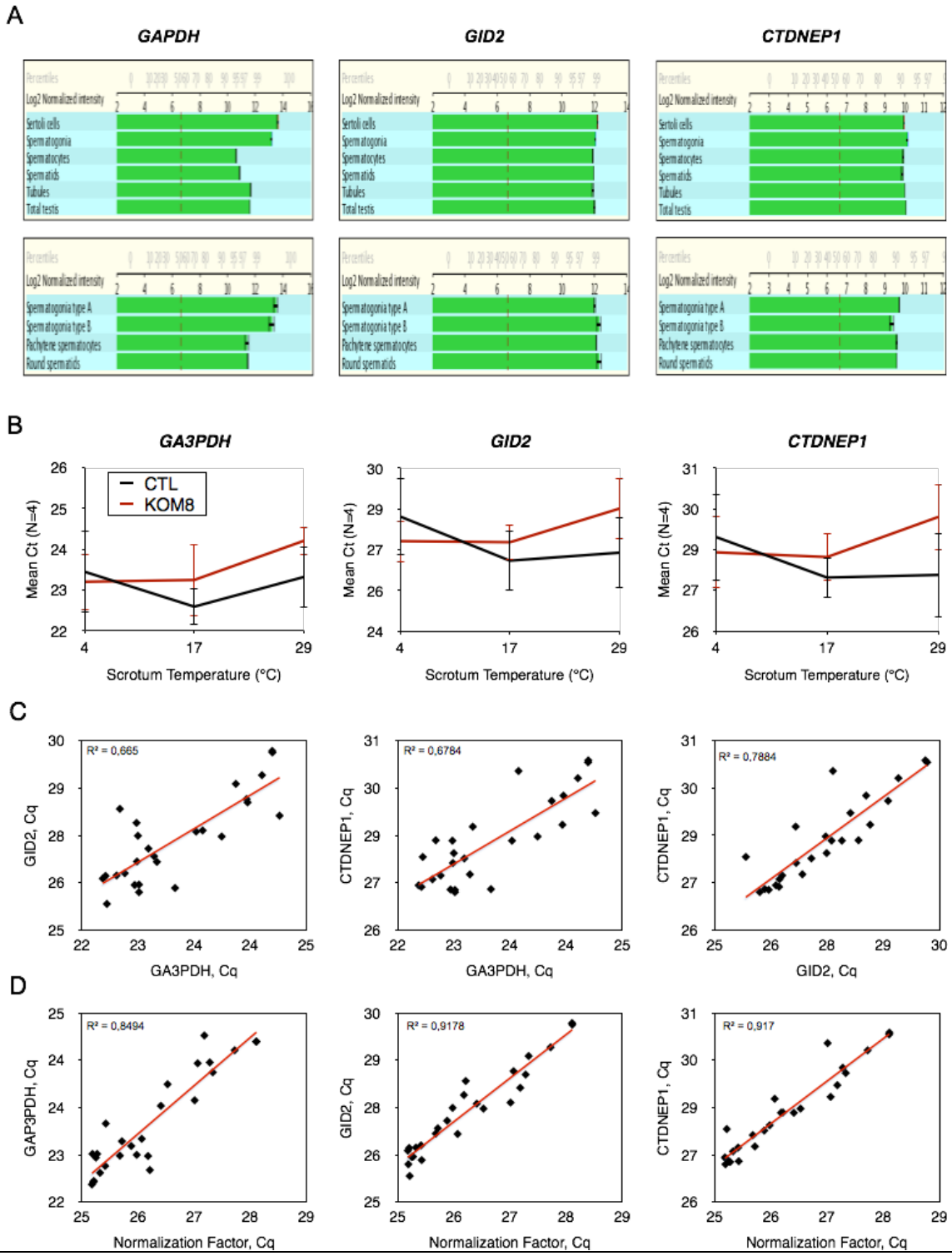

FIGURE 5. *Characterization of the most invariant genes in testis and calculation of real-time PCR correction factor.* **A.** DNA microarrays sorting of *GAPDH*, *GID2* and *CTDNEP1* gene expression levels in the different cell subtype in rodent testis. **B.** Averaged Cq of *GAPDH*, *GID2* and *CTDNEP1* genes in mouse testis 3 days after cold shock. Values are presented as mean ± SD. **C.** Pairwise distribution of the Cq values of the reference genes. The red line shows the linear correlation and R^2 is the correlation factor. **D.** Distribution of the Cq value of a reference gene with the Cq value of the normalization factor.

ARTICLE 16

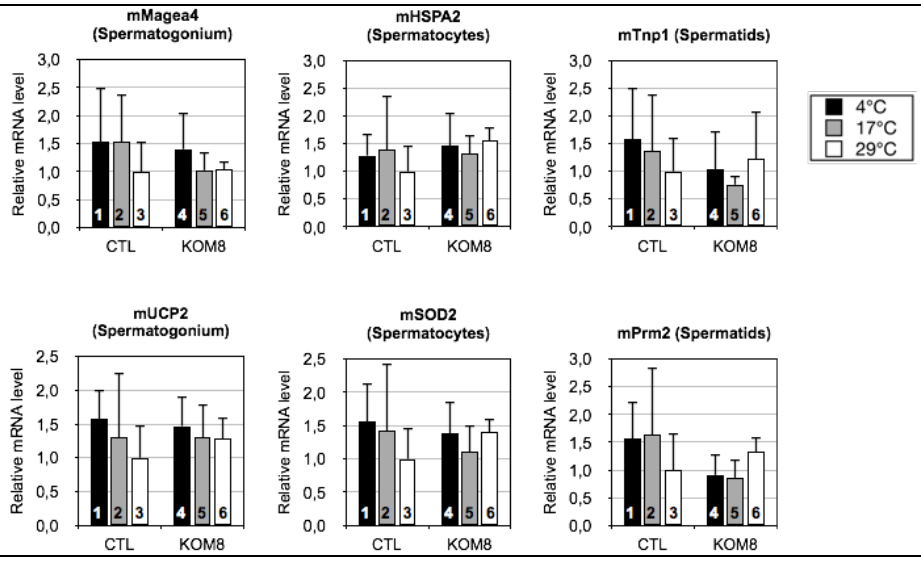

FIGURE 6. *Cold-induced TRPM8 channels activity triggers cold shock response and ROS production.* Real-time PCR demonstrates that there are no significant variations of mRNA levels of germ cell type markers in testis of CTL and KOM8 mice subjected to hypothermia prior to a 3-day recovery period. Melanoma antigen family A, 4 (Magea 4) and Uncoupling protein 2 (UCP2) in Spermatogonia; heat shock protein 2A (HSPA2) and superoxide dismutase 2 (SOD2) in spermatocytes; transition protein (Tnp1) and protamine 2 (Prm2) in spermatids. Statistical significance was assumed when $p<0.05$ and is shown above the tested column as the number of the column it was paired to.

ARTICLE 16

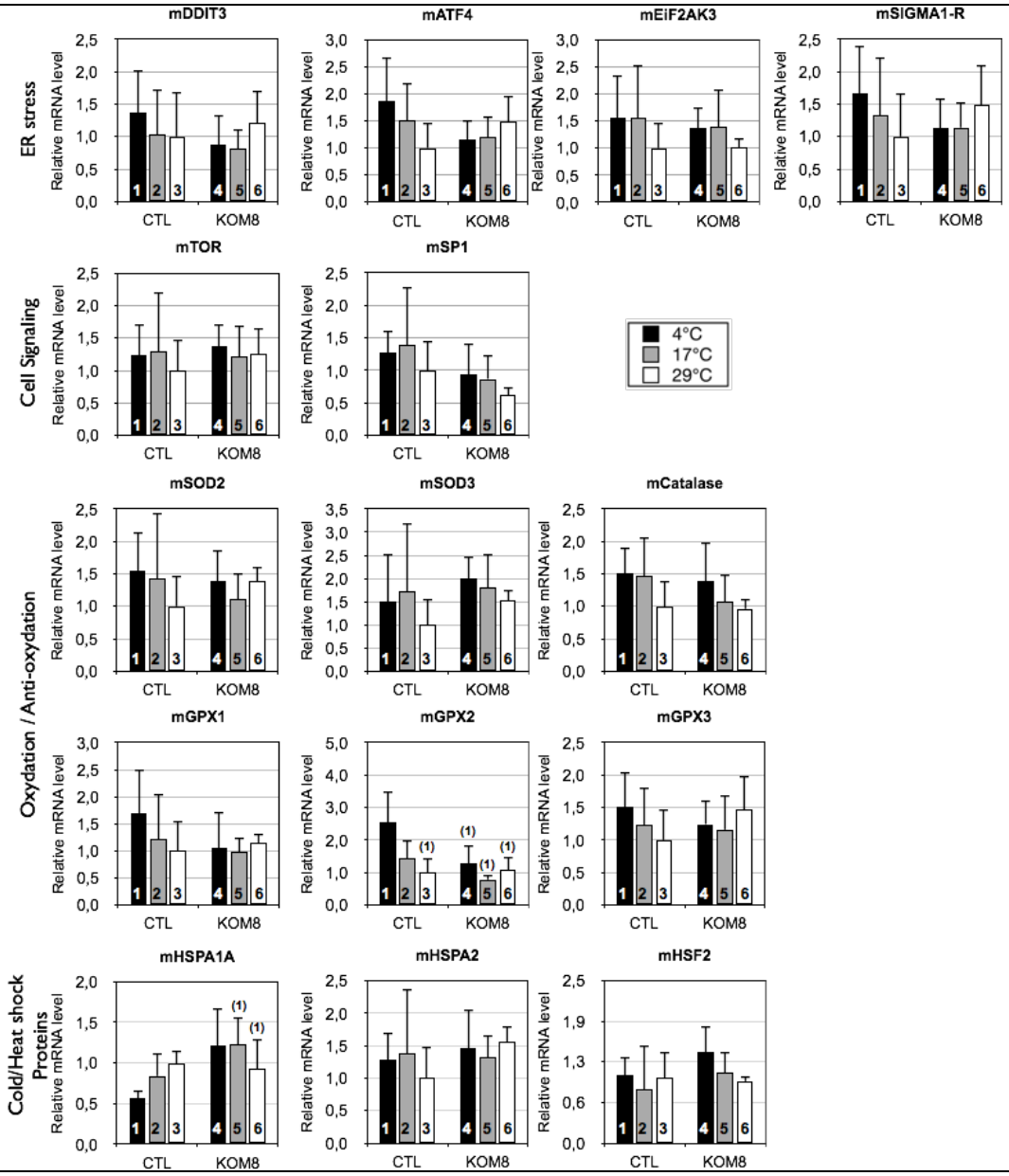

FIGURE 7. *Real-time PCR screening of several genes families in mouse testis 3 days after cold shocks.* Real-time PCR quantification of mRNA levels of genes involved in ER stress, cell signaling, oxidation/anti-oxidation, cold/heat shock proteins and uncoupling was performed on testis of CTL and KOM8 mice subjected to hypothermia prior to a 3-day recovery period. ER stress markers are: DNA-damage-inducible transcript 3 (DDIT3), activating transcription factor 4 (ATF4), eukaryotic translation initiation factor 2-alpha kinase 3 (EIF2AK3), sigma non-opioid intracellular receptor 1 (SIGMAR1). Cell signaling markers: mechanistic target of rapamycin (serine/threonine kinase) (MTOR) and Sp1 transcription factor (SP1). Oxidation/anti-oxidation enzymes: superoxide dismutase 2 and 3 (SOD2 and SOD3 respectively); Catalase; Glutathione peroxidase 1, 2 and 3 (GPx1, GPx2 and GPx3 respectively). Cold/heat shock induced genes: heat shock protein 1A and 2A (HSPA1 and HSPA2 respectively) and heat shock factor 2 (HSF2). Statistical significance was assumed when $p<0.05$ and is shown above the tested column as the number of the column it was paired to.

RÉSUMÉ

Le récepteur au froid et au menthol, TRPM8, est une protéine-canal fonctionnant comme un senseur thermodynamique et est responsable de la détection du froid de part son expression dans les neurones innervant l'épiderme. Après avoir cloné 35 ARN alternatifs et ARN épissés issus du gène *trpm8*, nous avons réalisé un travail de caractérisation moléculaire, biophysique et cellulaire de ces variantes du récepteur au froid. Nous avons, en parallèle, essayé de comprendre leurs rôles dans les grandes fonctions physiologiques comme l'homéostasies de l'épiderme, la réponse au froid dans des cellules germinales ou encore le métabolisme. Le problème intrinsèque des tentatives d'association des niveaux moléculaires et cellulaires avec la physiologie est qu'il est facile de trouver des corrélations mais techniquement beaucoup plus complexe de démontrer des liens de causalité. Or, la compréhension des mécanismes moléculaires, hormis la beauté de la compréhension de l'infiniment petit, n'a de sens en biologie que lorsqu'on arrive à expliquer les effets macroscopiques. C'est dans le respect de cette démarche, que ces 2 dernières années, j'ai acquis des compétences en biophysique et en microscopie photonique avancée. En effet, le développement des outils de fluorescence permet maintenant d'envisager l'observation quantitative de mécanismes moléculaire en cellule vivante unitaire, mais aussi dans l'organisme. L'association du génie génétique, de la photonique et des modèles animaux permet donc d'envisager le développement de la physiologie moléculaire dans les prochaines années.